J. Waugh, S. Aaleti, S. Sritharan, J. Zhao

Nonlinear Analysis of Rectangular and T-Shaped Concrete Walls

ISU-ERI-Ames Report ERI-09327

Submitted to the National Science Foundation for Research Grant No. CMS-0324559

DECEMBER 2008

Final

REPORT

IOWA STATE UNIVERSITY
OF SCIENCE AND TECHNOLOGY

Department of Civil, Construction and Environmental Engineering

Nonlinear Analysis of Rectangular and T-Shaped Concrete Walls

by

Jonathan Waugh
Graduate Research Assistant, Iowa State University

Sriram Aaleti
Graduate Research Assistant, Iowa State University

Sri Sritharan
Associate Professor, Iowa State University and Principal Investigator

Jian Zhao
Assistant Professor, University of Wisconsin-Milwaukee
(formerly a Post-doctoral Researcher at Iowa State University)

ISU-ERI-Ames Report ERI-09327

A Final Report to the National Science Foundation for the PreNEESR Research Project Funded under Grant No. CMS-0324559

Department of Civil, Construction and Environmental Engineering
Iowa State University
Ames, IA 50011

December 2008

ABSTRACT

Structural walls are frequently used in buildings to resist earthquake lateral loads because they have proved to be very effective at limiting building drifts and minimizing damage to both structural and non-structural elements. In a collaborative project involving researchers from the University of Minnesota (UMN), Iowa State University (ISU) and the University of Puerto Rico at Mayagüez as well as a consulting engineer from the Nakaki Bashaw Group, Inc. in California, five large-scale concrete structural walls were designed and tested at the Multi-Axial Subassemblage Testing (MAST) facility at UMN. MAST is one 15 experimental facilities established by the National Science Foundation (NSF) as part of the George E. Brown, Jr. Network for Earthquake Engineering Simulation (NEES). The experimental program included in-plane testing of three rectangular walls and multi-directional load testing of two T-walls. This report focuses on the pre-test and/or post-test analyses of all five walls that were accomplished using fiber-based models developed using OpenSees–an open source finite element package. These models were aimed at accurately capturing both the global and local responses of walls as compensation of errors can lead to good prediction of the global responses, thus failing to identify any shortcomings of the analysis models.

Three notable enhancements to OpenSees were undertaken in this study in order to improve the accuracy of the analytical simulation of wall responses. First, a new concept and a bond slip model with hysteresis rules suitable for capturing strain penetration effects in flexural response of concrete members subjected to monotonic and cyclic loadings were introduced. Second, a new cyclic concrete model was added to OpenSees by modifying an advanced, complex model that was found in the literature. Finally, an approach to deal with shear-lag effects in T-walls was addressed. The benefits of these new OpenSees capabilities are significant and they are demonstrated throughout this report.

When global force-displacement responses of the structural walls obtained from the OpenSees analyses are compared with the experimentally measured responses, good agreements were seen with the measured forces being within 5 to 10% of the experimental values at a given displacement. Furthermore, the contribution of various displacement components were examined at the peak displacements and they also compared well with experimental data. In addition to accounting for the strain penetration effects and using an advanced concrete model, an accurate

simulation of the T-wall response was found to be severely dependent on capturing the shear lag effects in the flange-in-tension direction loading parallel to the web. When shear lag was appropriately modeled, the response of the T-walls was successfully simulated by the OpenSees model.

Besides the global force-displacement responses, the local responses including the lateral displacement at the first floor level as well as location of the neutral axis, curvature, and strain profiles in the critical regions were examined. Satisfactory comparisons between the theoretical and measured local responses were generally found. However, it is concluded that further improvements to the OpenSees analysis could be achieved through introduction of a rational model to capture the shear deformation, which was handled in all wall analysis using an existing material model that was aimed at characterizing pinching behavior and was adapted for the shear deformation behavior of the structural walls. The pinching model was not capable of capturing all the critical points in the shear deformation response recorded during testing. However, it did adequately simulate the response envelope and improve the accuracy of the simulation.

Given the state of knowledge and current analysis capabilities, the fiber based modeling approach used in this investigation of the structural walls was very successful and achieving similar accuracy using models more sophisticated than fiber-based approach may not be possible because of the challenges associated with incorporating the concrete confinement and strain penetration effects. Furthermore, this report summarizes: 1) the outcomes of supplemental research performed with funding from the NSF's International Research and Education in Engineering (IREE) program, in which testing of a precast concrete wall system was performed successfully at the National Center for Research on Earthquake Engineering (NCREE) in Taiwan; and 2) evaluates the benefits of the NEES IT tools that have been developed for research collaboration and makes recommendations for future advancements.

ACKNOWLEDGEMENTS

The study presented in this report is based upon the work supported by the National Science Foundation (NSF) under Grant No. CMS-0324559. The authors gratefully acknowledge the support of Drs. Steven McCabe, Douglas Foutch and M. P. Singh, who have served as NSF Program Directors for this grant. The collaborators of this project are Professor Cathy French, Ms. Suzanne Nakaki and Professor Ricardo López and the authors are indebted to their valuable guidance, feedback and support during the course of the project. The authors also thank Dr. Win Aung of NSF who served as Program Director for the the International Research and Education in Engineering (IREE) supplemental award received for the grant, National Science Council of Taiwan for supporting the experimental program of the IREE award, and Dr. K. C. Tsai, the Director of National Center for Research on Earthquake Engineering (NCREE), Taiwan for his hospitality, coordination, and contribution to the successful completion of the IREE award.

In addition, the following individuals assisted the authors at various stages of the research project: 1) Beth Brueggen and Ben Johnson of UMN by providing the processed experimental data; 2) Drs. Silvia Mazzoni and Frank McKenna of University of California, Berkeley, by providing technical support for OpenSees; 3) Dr. Lelli Van Den Einde, Wei Den, Jason Hanley and Paul Hubbard of University of California at San Diego by providing technical assistance with the NEESit collaborative tools; 4) Mohammad Fraiwan and Tam Chantem of ISU by coding the MAST-RSVtool with input from Professor Manimaran Govindarasu; 5) Drew Daugherty and Chen Wan of MAST laboratory by making the test data available in real time; 6) Sujith Padiyara and Quincy Ma of University of Auckland (UoA), New Zealand, by making the real-time remote participation in tests feasible for the PI during his sabbatical through their telepresence laboratory; 7) Dr. Kevin Liu and other research associates of NCREE for providing assistance with testing of the precast wall; 8) Professor John Wallace by sharing past experimental data on concrete walls; and 9) Rick Henry for proof reading the report. The authors thank all individuals for their contributions, without which this research would not have been successfully completed.

Any opinions, findings, and conclusions or recommendations expressed in this report are those of the authors and do not necessarily reflect the views of NSF.

TABLE OF CONTENTS

LIST OF FIGURES

LIST OF TABLES

Chapter 1
Introduction

1.1 Structural Walls

Many concrete buildings in seismic regions use structural walls to limit lateral deformations of structures and minimize damage to nonstructural elements. Structural walls, which have been generally referred to as shear walls, are designed to resist lateral loads and control the lateral deformations due to their high in-plane stiffness along the length of the wall. These walls are often incorporated into features such as elevator shafts and stairwells so that these required building elements can also perform the primary structural functions. Structural walls can be used to resist gravity loads either alone or in combination with columns, depending on the needs of the owner.

In seismic design of buildings the life safety of the occupants is of paramount importance. For loads representative of wind or small, frequent earthquakes, structural walls are typically designed to respond in an elastic manner. However, during larger, less frequent earthquakes, the walls are designed to undergo inelastic deformations, but without experiencing significant strength degradation. This allows the walls to be smaller in cross-section and more economical than would be possible if the walls had to maintain elastic behavior without compromising the safety of the occupants. The American Concrete Institute (ACI 318, 2002) has adopted this concept in the building code, stating that "*the use of design forces representing earthquake effects requires that the lateral-force resisting system retain a substantial portion of its strength into the inelastic range under displacement reversals.*" The ACI Building Code requires different levels of energy dissipation in the structure depending on the seismic region where the structure is located. This code classifies these regions as having low, moderate, or high seismic risk, based on the maximum expected intensity of the ground motion.

Walls have been proven an effective means for maintaining structural strength under various strengths of ground motions [Fintel, 1995]. This researcher gives examples of the wide use of structural walls in numerous buildings in highly active seismic zones all over the world, including cities located in Chile, Macedonia, Venezuela, California, and Mexico. Based on the

observed damage from past earthquakes in these locations, Fintel noted that buildings with structural walls experienced minimal damage, while ductile moment-resisting frame buildings experienced severe structural damage. For example, a 14-story Party Headquarters Building located in Macedonia had a structural wall-frame system and was subjected to a large earthquake in 1953. The earthquake measured 6.2 on the Richter scale, despite the building swaying considerably and throwing desks across the building, no structural or nonstructural damage occurred to this building, not even to the glass windows. Fintel (1995) concluded that because of over 30 years of the observed superior performance, no building in a seismic zone should be built without structural shear walls to resist lateral seismic loads.

Figure 1.1 shows the Plaza 1 Apartment Building that experienced the 1967 Caracas, Venezuela, earthquake. The building utilized structural walls and had no apparent damage to the structure. In contrast, Figure 1.2 shows the internal second story columns of the Macuto Sheraton Hotel, which had extensive damage to the columns and stairwells during the same Caracas earthquake. The structural walls on the upper stories, which were terminated at the top of the second story columns, were not damaged in the earthquake. Figure 1.3 shows the failure of a beam-column joint in the Cypress Gardens Building during the Caracas earthquake. As witnessed in the 1967 Caracas earthquake and documented by Fintel [1995], structural walls provide buildings with very good seismic performance.

In moderate to large earthquakes, inelastic flexural actions are designed to occur over the lower portion of the walls. In this region, especially at the ends, structural walls are expected to experience very high compressive and tensile flexural strains, thus require special transverse reinforcement. These areas requiring special reinforcement consideration are known as the boundary elements. Dependable lateral load behavior of walls is thus dictated by the boundary elements being adequately reinforced to ensure the satisfactory design and acceptable performance. The transverse reinforcement required in boundary elements allows the concrete to achieve high compressive strains due to confinement effects and helps prevent buckling of the longitudinal reinforcement. If more transverse reinforcement is used than required, the wall will perform well under earthquake loads; however, the cost of the wall will increase and the constructability will decrease. Insufficient reinforcement can cause premature failure of the structural wall due to crushing of the concrete or buckling of the longitudinal reinforcement,

causing rapid strength degradation. In this context, if the wall's behavior under lateral loads can be accurately predicted in the design process, the designer can develop efficient, cost-effective structural wall systems for buildings that will be adequate to resist large ductile deformations.

Figure 1.1 Plaza 1 Apartment Building that was undamaged during the Caracas Earthquake [1]

Figure 1.2 Damage to the 2nd Story Columns of the Macuto Sheraton due to the Caracas Earthquake [2].

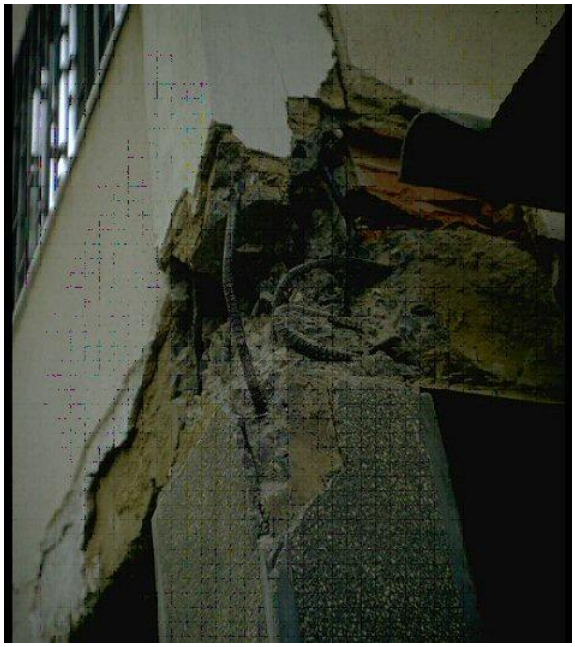

Figure 1.3 Joint Failure in the Cypress Gardens Building due to the Caracas Earthquake [3]

Structural walls can be symmetrical, such as rectangular or barbell walls, or asymmetrical, also known as non-rectangular, such as T-, L- or C-shaped walls, as shown in Figure 1-4. Symmetric walls have been extensively studied. Abrams [1991] lists numerous studies on symmetrical structural walls. However, non-rectangular wall sections have not been as thoroughly studied. Asymmetrical shapes for walls may occur because of irregular building geometry and/or due to specific space requirements from the owner or architect. When two or more walls in different directions are joined together, one acts as the flange and has a significant impact on the ductility, strength, and stiffness of the other wall(s) [Thomsen and Wallace, 1995]. The impact of the flange varies depending on the direction, in which the load is applied. This direction dependence must be accounted for in the analysis and design of the structural wall.

Figure 1.4 Common Wall Sections

Since the flange plays an important role in the behavior of a non-rectangular wall, it is essential that the design community understands how the flange affects the lateral load response of this wall type. Accurate prediction of the wall behavior is important in determining the reinforcement required for these structural elements in new buildings, as well as to evaluate retrofit techniques for existing structures containing this type of concrete walls. Given the complexity of wall behavior, models for predicting both symmetric and asymmetric wall behavior must be calibrated adequately against experimental data. Furthermore, since the direction of earthquake ground motions is random, the model representing non-rectangular walls should be able to capture the wall response regardless of the direction of the earthquake attack.

1.2 Methods of Analysis

Various methods have been used to analyze structural walls and to predict their behavior under reversed cyclic loads. These methods have ranged from simple calculations based on moment-curvature relationships to general finite element analysis of the walls. For the current study, a fiber-based finite element analysis approach was chosen to model and analyze the structural walls. The fiber concept represents a reinforced concrete section of a structural element with a group of uniaxial fibers and assigns the uniaxial concrete or steel behavior to these fibers. Three dimensional effects on material behavior are typically incorporated into the uniaxial behavior of the material in order to improve the accuracy of the analysis. Taucer *et al.* [1991] used this concept to develop a beam-column element for seismic response analysis of structural systems and demonstrated that, it significantly improves the computation efficiency over the traditional finite element approaches. The main benefit of using this fiber-based element is that it allows the use of uniaxial stress-strain relationships that are well established, providing accurate force-displacement responses for structural members under lateral loads. An inherent assumption used in the fiber-based element is that plane sections remain plane after bending. When a section of a structural member does not satisfy this assumption such as a flanged wall, this assumption can lead to inaccurate strains and curvature at the critical sections. Consequently, the analysis would lead to inaccurate estimate of damage and force-displacement responses as they are significantly dependent on local responses in the critical regions. Another drawback of the fiber-based analysis is that it typically ignores the effects of bond slip of longitudinal reinforcement resulting from strain penetration.

The open source finite element program OpenSees [Mazzoni *et al.,* 2006] was used for the study in this report because it was capable of using a fiber section in conjunction with beam-column elements. Access to the source code of the program allowed new section definitions and material models to be added to the program to overcome the challenges identified above and improve the simulation of the structural walls under applied multi-directional lateral loads.

1.3 Project Description

In parallel with establishment of the George E. Brown, Jr. Network for Earthquake Engineering Simulation (NEES) (http://www.nees.org/) in October 2004, the National Science Foundation (NSF) funded an unsolicited collaborative research proposal to a team of researchers from the University of Minnesota (UMN), Iowa State University (ISU) and the University of Puerto Rico at Mayagüez. The focus of this research proposal was to experimentally and analytically study the behavior of nonrectangular structural walls subjected to the effects of multi-directional loading. In addition to addressing this fundamental problem, this project was aimed at examining the IT capability available for collaboration NEES research and verifying the capabilities of the Multi-Axial Subassemblage Testing (MAST) facility at UMN, which is one of 15 experimental facilities in the NSF's shared NEES network. This is one of three such projects to be awarded by NSF prior to establishing the NEES Research (NEESR) awards through a special solicitation for proposals that would utilize the unique capabilities of the NEES network. Consequently, these three projects funded through the unsolicited proposal scheme were referred to as the PreNEESR projects.

As part of this PreNEESR research project described in this report, three rectangular and two T-shaped large-scale concrete walls were tested at the MAST facility at UMN. All researchers of the project participated locally or remotely in testing; researchers at ISU also remotely controlled some of the testing and examined the IT capabilities available through NEESit (http://it.nees.org/software/index.php) at the time of testing of each wall.

The major focus of the ISU research team was on the analysis of concrete walls using an open source computer package (i.e., OpenSees). A motivation for using OpenSees for the analytical simulation of both rectangular and T-shaped concrete walls under prescribed sets of loading was that it was selected as the simulation component for NEES. In addition, the ISU team contributed to the design and instrumentation of the test walls and played a lead role in the evaluation of the NEES collaborative tools. The ISU team also received supplementary funding from the NSF International Research and Education in Engineering (IREE) program. This funding enabled integration of international collaboration into the project through partnership with National Center for Research on Earthquake Engineering (NCREE) in Taiwan and introduction of a new precast wall system.

Presented in this report are various components of the PreNEESR research completed by the ISU team with major emphasis on the analytical investigation while the experimental portion of the research is summarized in a separate report to be published by the University of Minnesota. At the beginning of this PreNEESR research project, it was realized that a significant drawback of OpenSees was that it lacked the ability to account for the strain penetration effects in the analytical simulation of flexural members. Hence, this issue was first addressed by introducing Bond-SP01 element in OpenSees, which is now being used by OpenSees users worldwide. The technical information on the development and implementation of Bond-SP01 and the associated benefits has been published in a journal paper [Zhao and Sritharan 2007]. Therefore, this information is not included in the main body of this report, but reproduced in Appendix A. Similarly, outcomes of three other project activities are summarized in Appendices B, C and D. Appendix B presents a draft of a paper on the verification of a new concrete model presented in Chapter 3 and the dynamic analysis capabilities of OpenSees. Appendix C summarizes the IREE research component, which has information about the observed experimental performance of a new precast wall system tested at NCREE, Taiwan. Finally, Appendix D reproduces an invited summary paper that has focused on the IT activities undertaken as part of the PreNEESR project along with conclusions and recommendations. In consideration of the NEES IT capabilities available at the beginning of the project, a Real-time System Visualization tool (RSVtool) was developed by the ISU team to improve the collaboration between researchers during testing of the walls, which is also discussed in this appendix. With this arrangement, the main body of this report is dedicated to the implementation of a concrete model in OpenSees and nonlinear analysis of rectangular and T-shaped concrete walls to monotonic, cyclic and/or dynamic earthquake loading. More details on the report layout are presented in Section 1.6.

1.4 Research Objectives

In the context of the above described project, current state of the knowledge and the shortcomings of OpenSees, the objectives of the study presented in this report are as follows:

- Implement a robust concrete model into OpenSees and verify its capabilities
- develop an analytical model for rectangular and T- shaped concrete walls that is

computationally efficient, easy to build and understand; Model should be simple enough to be used by the design community when appropriate;

- accurately model the response of rectangular walls with different anchorage details such as mechanical couplers and lap splices;
- accurately model the response of T-walls to multidirectional loading; including the force-displacement response, strain profile, and location of the neutral axis;
- model the contributions of the displacement components due to flexure, shear and strain penetrations to the total top displacement;
- calibrate the model technique against existing data, and predict the response of T-walls before testing using available material properties;

The investigation focuses on the experimental data from the testing of three rectangular walls with different anchorage details and two T-walls completed at the Multi-Axial Subassemblage Testing (MAST) facility at the University of Minnesota. The T-walls were subjected to multidirectional displacements parallel to the web, parallel to the flange, in skewed directions, and under two multidirectional displacement paths, whereas the rectangular walls were subjected to in plane cyclic loading.

1.5 Definition of Terms

Provided below is a list of the various terms used throughout the report that may not be familiar to all readers. The definition of the term is provided here to allow readers to refer back if a term is unclear. This is not an exhaustive list, but rather the key terms and concepts used in the report.

Aspect ratio: ratio of the wall height to the wall length that is used to determine if the wall behavior is shear or flexure dominated

Bond slip due to strain penetration: slip along a portion of adequately anchored longitudinal reinforcement of a flexural member into a footing (or an adjoining connecting member) due to localized crushing of concrete surrounding a portion of the anchored bar in the connecting element, which in turn introduces rotation to the flexural member at the connection interface

Boundary elements: the ends of the wall that require special consideration including additional transverse reinforcement to ensure adequate seismic performance of concrete walls when high

strains are expected in the concrete and reinforcement bars in these regions

Fiber section analysis: a method for determining strains and stresses on a section of a structural member, thereby characterizing the member behavior by discretizing and analyzing the section as a group of uniaxial fibers

Integration points: points along the length of a beam-column element where strains and the corresponding stresses are calculated by satisfying the strain compatibility and equilibrium conditions.

Neutral axis: location of zero strain on a section due to flexural bending

Shear lag: refers to the phenomenon when the bending strain is unevenly distributed across a flange of a structural member subjected to moment in the direction perpendicular to the flange, limiting the effective flange participation in resisting moment.

Plastic hinge length: the length over which all the plastic action maybe assumed to occur in lumped plasticity models, which is much shorter than the length of the actual plastic region

Plastic region – region in a flexural member where inelastic strains are expected to develop in concrete and steel fibers.

1.6 Report Layout

This report consists of seven chapters and four appendices. The following chapter reviews the available literature on experimental tests of non-rectangular walls, the various analysis techniques that have been used to analyze structural walls, and investigations of the effects of shear lag in non-rectangular sections. Chapter 3 discusses a new concrete model that was implemented in OpenSees in order to improve the simulation of structural walls. Chapter 4 presents the post-test analysis of three rectangular walls tested at the MAST facility with comparisons to the recorded global and local responses. Chapter 5 presents the analysis of the first T-wall, NTW1, tested at the MAST facility. Both pre-test and post-test analyses of this wall subjected to multidirectional loading are presented. The various responses recorded during the test are compared to the OpenSees simulation results. Chapter 6 presents the pre-test analysis of the second T-wall, NTW2. The global force-displacement responses are presented and compared to the force-displacement results from the OpenSees analysis; similarly, selected local responses are also compared. Chapter 7 presents conclusions from the investigation and recommendations

for future research on the analysis of T-walls. Appendix A presents the strain penetration material model developed by Zhao and Sritharan that was used in the analysis of the structural walls. Appendix B presents a model used in the blind prediction contest conducted by the University of California at San Diego (UCSD) on the response of a 7-story building slice. This model is similar to the models used for the analysis of NTW1 and NTW2 and showed the modeling approach can be used for a dynamic analysis. Appendix C presents the summary of results for the lateral load behavior of the new precast wall system, which was tested at NCREE, Taiwan as part of an international collaboration made possible by the IREE supplemental award. Appendix D reproduces an invited summary paper that has focused on the IT activities undertaken as part of the PreNEESR project along with conclusions and recommendations.

Chapter 2
Literature Review

2.0 Introduction

The lateral load behavior of symmetric walls especially with rectangular cross section was extensively investigated in the literature. Numerous experimental investigations have been conducted to understand the effect of various design parameters on lateral load behavior of these walls. However, structural walls with T, C-and L shape cross section have not been thoroughly tested and analyzed by the research community. This chapter outlines the existing experimental research that has been conducted on rectangular and nonrectangular structural walls, the nonlinear analysis of structural walls, and investigations of shear lag in nonrectangular walls.

2.1 Symmetric Wall Sections

Symmetric wall sections are walls that have typically either a rectangular or a barbell shaped cross section. These walls have been studied and the effects of various types and configurations have been investigated. Some of the types are briefly outlined below, with references to studies on this subject for those interested in exploring the topic further. Abrams (1991) gives a complete listing classified similar to the terms used here, however none of these configurations were the focus of this study so they are not discussed in detail.

2.1.1 Squat Shear Walls

The aspect ratio of the wall will determine if the wall behavior is dominated by flexure or shear. Squat walls are walls with an aspect ratio of 1 or less and their behavior is dominated by shear. Shear failures are typically a brittle failure, with decreased energy dissipating capacity and fail prematurely compared to flexural dominated systems. Most research has been conducted to determine how to prevent shear failures because they are an abrupt brittle failure. Paulay et al. (1982) found that the effects of shear were early strength and stiffness degradation and increased "pinching" in the hysteresis loops. However, if properly detailed, inelastic flexural response can

develop (Paulay et al., 1982). Abrams (1991) and Ali and Wight (1990) give references for research on previous squat walls.

2.1.2 Slender Walls

Slender walls are walls that have an aspect ratio greater than 2, and their behavior is dominated by flexure. Walls with an aspect ratio of less than 2 and greater than 1 are in the transition between flexure and shear dominated behavior, and both may have significant influence on the wall performance. Both rectangular and T-walls which were analyzed in this study, are isolated slender walls. There are numerous references on the analysis, design and behavior of isolated slender walls and few of the experimental studies conducted on slender walls are summarized below.

2.1.2.1 Portland Cement Association (PCA)

The most extensive study was conducted at the Construction Technology Laboratories in Skokie, Illinois. The study consisted of three phases, in the first two phases (Oesterle et al., 1976; Oesterle et al., 1979) sixteen 1/3-scale structural walls were constructed. The walls tested had rectangular, barbell, and flanged cross sections, and were designed in accordance to the 1971 ACI Building code (Oesterle et al., 1979). The walls tested were 15 ft. tall, 75 in. long and 4 in. thick. The flanged walls had 36 in. by 4 in. flanges on each end, while the barbell walls had 12 in. square boundary elements, see Figure 2.1. The concrete strength varied with each wall specimen from 3165 to 7775 psi, and the yield strength of the reinforcement varied from 59.5 to 74.2 ksi. The axial load applied to the walls ranged from zero to approximately 9% of f_c'. The walls were loaded in the plane of the web under increasing reversed cyclical displacements.

Oesterle et al. (1979) found that the different cross section shapes were associated with different patterns of behavior. The rectangular wall had limited out-of-plane stiffness due to the small width of the wall, making it more susceptible to instability in the compression zone under large load reversals resulting in out-of-plane buckling of the boundary element (Oesterle et al., 1979). This was observed in the failure of one rectangular test specimen tested with in-plane lateral displacements. Oesterle et al. noted that rectangular walls exhibited lower flexural capacity compared to the barbell or flanged sections, of equal length and web thickness. The barbell shape prevents horizontal sliding shear failure by providing large dowel action in the

boundary elements. The large boundary elements also provide high out-of-plane stiffness that limits its instability. The large area of steel in the boundary element allows high flexural capacities to develop. Crushing of the web concrete was the primary failure mechanism observed in the tests because of the high strains that develop in the plastic region. The researchers recommended that barbell walls be designed for high shear stresses on the section. The flanged sections had a performance similar to the barbell shaped sections, with high flexural capacities developing and the requirement that high shear stresses must be designed for in the wall.

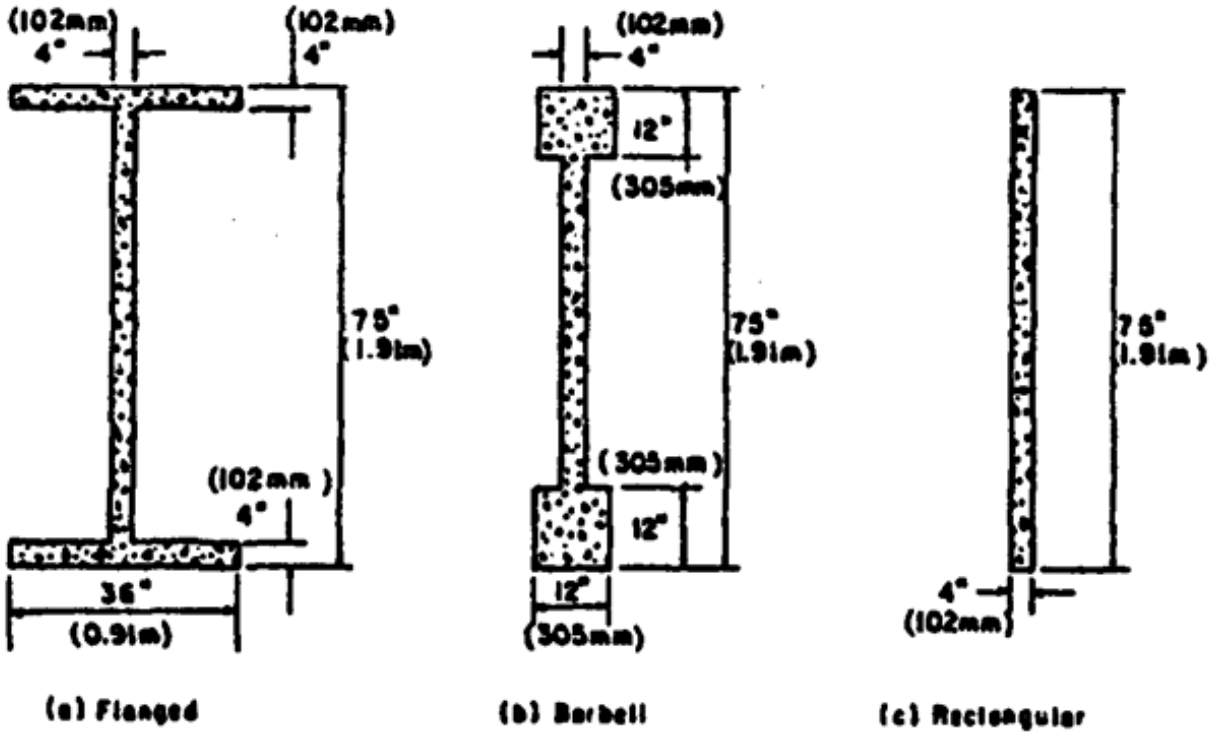

Figure 2.1 Wall sections tested by Oesterle et al. (1979).

Two failure mechanisms were observed in the walls tested corresponding to the level of shear stress on the wall. Walls with low maximum shear stress (i.e., $V < 3\sqrt{f_c'}$) the wall's displacement capacity was limited by buckling of the longitudinal reinforcement in the boundary elements and failure of the confined concrete. For walls with high maximum shear stress (i.e. $V > 7\sqrt{f_c'}$) the displacement capacity was limited by crushing of the web concrete. The ductility of

a wall, determined from measured rotations, decreased with increased shear stress ranging from approximately 8 to 3. The researchers also noted that for walls subjected to high shear stress where crushing of the web concrete limited the performance, uniform axial load of 0.1 $f_c^{'}$ increased the ductility of the section (Oesterle et al., 1979).

The third phase (Shiu et al., 1981) consisted of testing of two 1/3-scale rectangular structural walls. The walls were 18 ft tall, 6.25 ft long, and had a uniform thickness of 4 in., simulating a six story shear wall, see Figure 2.2. With the exception of openings the two walls were identical; one specimen had 12.5 in. by 18 in. openings cut into each story level simulating typical window openings. In the test, the wall without openings carried 14% more load; however there were material property differences between the walls. In particular the yield strength of the primary reinforcement was different between the two walls. When the data for the two walls is normalized with respect to the reinforcing yield strength, the response is very similar leading the researchers to conclude that the presence of openings has little impact on the load versus deformation response of the walls. The primary effect of openings was that a diagonal compression strut could not form across the wall between the floor levels because of the interruption, reducing the initial shear stiffness of the wall with openings. These compression struts were observed in the wall without openings and helped resist the load. The failure to form the compression struts did not affect its lateral load or deformation capacity. Both walls experienced shear failures; the wall without openings due to horizontal sliding and the wall with openings due to shear compression failure of the boundary elements.

The researchers concluded that walls with openings should be designed as isolated walls without openings. Lintels should be designed to fully couple the wall piers and should not yield prior to developing yielding at the base of the wall. The design practice of placing interrupted steel evenly distributed along the opening performed well in the tests, and does not need to be changed.

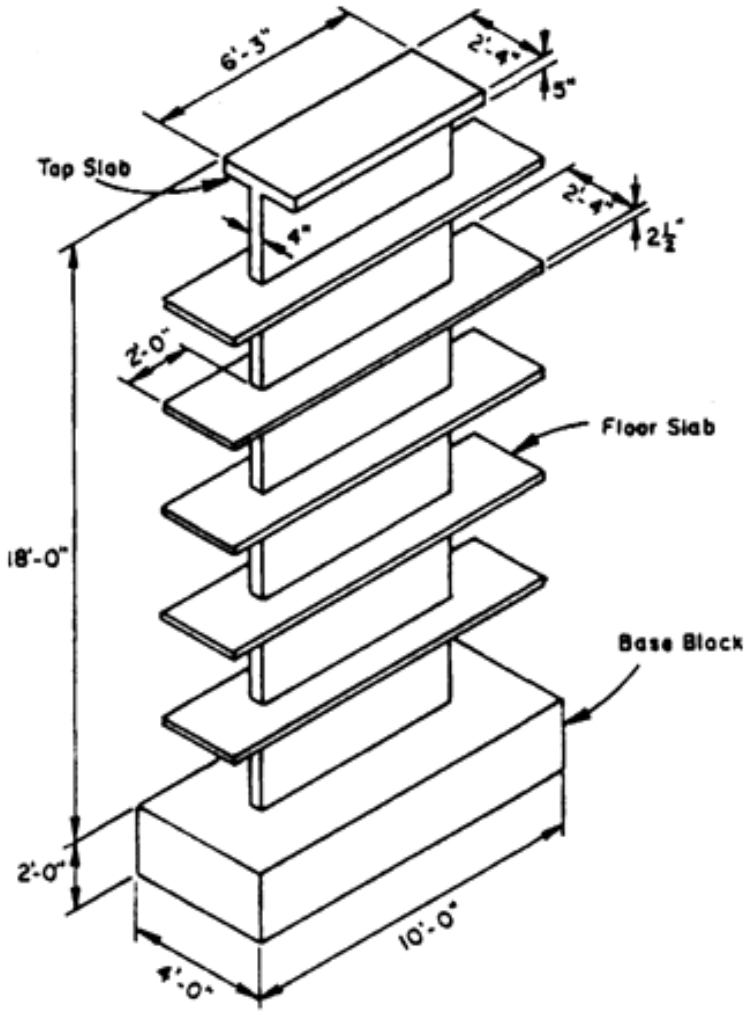

Figure 2.2 Wall specimen from Shin et al. (1981).

2.1.2.2 Loannis D. Lefas and Michael D. Kotsovos (1990)

The main focus of the study was to investigate the effect of loading history and structural repair methods on the lateral load behavior of reinforced concrete walls. Four identical rectangular wall specimens (SW30, SW31, SW32 and SW33) were tested as part of this study. The walls were ½.4 scaled specimens with an aspect ratio of 2. The walls were 650 mm wide, 1300 mm high and 65 mm thick. In all the specimens the walls were monolithically constructed with the bottom and top beam. The longitudinal reinforcement was continuous across the wall-foundation interface and was properly anchored. All the four specimens were designed according

to the ACI building code (ACI 318-86). The wall specimens were subjected variable cyclic loading histories and were repaired after the walls experienced failure and retested under cyclic loading. From the experimental observations it was concluded that the strength and deformational response of the walls were independent of the cyclic loading regime. The walls also dissipated considerable amounts of energy before failure. It was also found that repairing only the damaged regions of the compressive zone was sufficient to fully restore wall strength, thus implying that the compressive zone is the main contributor to shear resistance.

2.1.2.3 Kypros Pilakoutas and Amr Elnashai (1995)

Pilakoutas and Elnashai (1995) tested six 1/2.5-scale rectangular concrete walls with an aspect ratio of 2 to quantify the ductility and the energy dissipation potential of reinforced concrete walls. The test specimens namely SW4 to SW9 were 1.2 m high, 0.6 m wide and 60 mm thick. The walls were designed in three pairs; each pair had equal flexural reinforcement but different shear reinforcement. The flexural reinforcement was concentrated in the boundary elements to maximize the flexural capacity. All the test specimens were subjected to cyclic displacement with two full cycles at each peak displacement. It was observed that the cracks propagated from the wall boundaries toward centers and from the bottom upward. The cracks in the boundaries were horizontal, while further away they were inclined and the inclination increased along the height of the wall. As the applied displacement increased the crack density in the boundaries increased, while the main web cracks were limited to three to four on each side. Based on the study the researchers concluded that the strength and deformational characteristics of specimens were not affected significantly by shear reinforcement in excess of the amount needed to resist maximum applied load. It was also noted that the bulk of the energy dissipation was due to flexural action. Shear deformations, though significantly contributed to the total displacement of the wall, cannot be considered toward overall energy dissipation. It was also found that the longitudinal strains on the reinforcement near the top of the walls were found to be significantly higher than analytically expected, indicating the mobilization of possible arch and tie mechanism for shear resistance.

2.1.2.4 Tasnimi (2000)

Tasnimi (2000) conducted an experimental investigation of rectangular concrete walls.

The objective of the study was to experimentally investigate the lateral load behavior of structural walls used in mid-rise buildings, designed according to the Iranian seismic design code. As part of this study, four 1/8-scale rectangular wall specimens SHW1, SHW2, SHW3 and SHW4 with an aspect ratio of 3 were tested under cyclic loading. The walls were 1.5 m tall, 0.5 m long and 50 mm thick. All the four walls were constructed with identical in dimensions and reinforcement details. The walls were monolithic; the longitudinal reinforcement was continuous across the wall-foundation interface and was well anchored into the foundation block. The specimens were subjected to cyclic displacements with increasing amplitude. All four specimens developed flexural cracks and inclined cracks in the critical region as expected for a flexural dominant wall. At failure, horizontal crack was formed near the wall-foundation interface, causing the lateral load carrying capacity of the specimens to drop abruptly.

2.1.2.5 Yunfeng zhang and Zhihao Wang (2000)

Four rectangular walls (SW7, SW8, SW9 and SWCW12) were tested to understand the influence of high axial load ratio on the lateral load behavior of flexural dominant walls. Each specimen was tested under combined action of constant axial load and horizontal load reversals. Two parameters were considered and varied in the specimen design, that is, axial-load ratio and shear compression ratio. It was found from past experiments that the shear compression ratio is an important parameter that affects the post yielding behavior of shear walls. The specimens were designed to experience flexural failure mode. All the walls were 1.75m tall, 0.7m long and 100 mm thick. The longitudinal reinforcement was continuous across the wall-foundation interface and was well anchored into the foundation. All the four walls experienced similar crack pattern along the wall height, except that the load at which first crack was noticed varied depending on the axial load ratio. Axial-load ratio had an important effect on the failure mode, stiffness, and ductility of the walls. In this study, the wall specimen subjected to a high axial-load ratio of 0.35 exhibited an undesirable out-of-plane buckling failure mode in the post yielding stage, whereas the wall specimen with an axial-load ratio of 0.25 and shear compression ratio of 0.11 exhibited a more favorable boundary element crushing failure mode with relatively high ductility. It was also found that the shear compression ratio affected the post yielding behavior of shear walls. Higher shear compression ratio resulted in development of extensive criss-crossing cracks in the web of the wall.

2.1.2.6 Riva, Meda and Giuriani (2003)

In this study, Riva et al. (2003) experimentally investigated the lateral load behavior of a full scale rectangular concrete wall. The scope of the research was to partially fill the gap concerning full scale tests on slender walls, and also analyzing the behavior with a particular attention to the ductility, energy dissipation capability and the resisting mechanisms. The test specimen was representative of four storey shear building and was designed according to the Eurocode8 (EC8). The wall was 12.5 m high, 2.8 m wide and 300 mm thick. The longitudinal reinforcement was continuous across the wall-foundation interface. Due to the size of specimen and readily available test setup, the wall specimen was tested horizontally. The wall subjected to cyclic loads with increasing amplitude. The loads were applied at two points by means of hydraulic jacks. The position of the jacks was defined to obtain the same bending moment and shear force around the critical section as the one resulting from the analysis of the four storey building.

Prior to the yielding of the longitudinal reinforcement, the main cracks in the critical zone have limited inclination, proving that the behaviour is governed by bending. The crack distance was close to the stirrup spacing in the external chords, where longitudinal reinforcement was concentrated, while in the middle part of the critical section the cracks were tend to merge into a lower number of cracks, characterized by larger opening and greater inclination, thus showing the influence of shear stress. In the post-yielding stage, a progressive damage with increased imposed displacement was observed. The damage was mainly localized at the critical section, with a wide crack (50mm at mid depth of the wall) observed near the base of the wall. Concrete spalling, crushing of concrete, rebar yielding was observed in confined regions. At the end the wall specimen was failed in shear along the wide crack. It was due to shear as a consequence of a lack of longitudinal reinforcement in the wall web (between the chords or boundary elements). In fact, the amount of web reinforcement provided in accordance to EC8 was not enough to limit the observed crack opening, and friction contribution to shear strength resulted in being much smaller than expected.

To summarize the experimental investigations, the later load behavior and failure modes of slender walls depends on the axial load ratio, shear reinforcement distribution, confinement steel in boundary elements, shear compression ratio etc. It is important to notice that in all the

experimental investigations, the longitudinal steel was continuous at the wall-foundation interface. However, in practice for ease of construction, it is common to splice the longitudinal reinforcement at the wall-foundation interface using either mechanical couplers or lap splices. It was noticed from the literature review that there are no studies done to understand the influence of splicing of reinforcement on the lateral load behavior of structural walls.

2.2 Nonrectangular Wall Tests

2.2.1 Goodsir [1985]

Goodsir tested a 1/3-scale, T-shaped reinforced concrete wall as part of an experimental study. The wall had a 51 in. long web with a 27.5 in. wide flange and had a uniform thickness of 4 in. The wall specimen was constructed to give an aspect ratio of approximately 2.2 in the web direction, with a wall height of 112 inches. When tested under cyclic loads, this wall achieved a displacement ductility of 6 and failed due to crushing of the unconfined concrete immediately adjacent to the confined concrete of the boundary element. Goodsir stated that the wall failure was due to the high ductility demand and eccentric loading arising from out-of-plane displacement. Goodsir concluded that the transverse reinforcement in the boundary element should be extended further into the section of the T-walls if large compressive zones were expected due to large displacements. The extent to which the boundary element should be extended was recommended for further study.

2.2.2 Sittipunt and Wood [1993]

Sittipunt and Wood conducted an analytical and experimental study of C-shaped structural walls. The objective of their research was to investigate a) the inelastic cyclic response and energy dissipation, b) the effective stiffness at various displacement levels, and c) the influence of web reinforcement on the response of C-walls. The wall section had a 60 in. long flange, with two parallel 36 in. long webs. The two walls, CLS and CMS, were 9 ft tall and 3 in. thick; a schematic of the wall is shown in Figure 2.3a. The researchers reported that the "60 in. flange width was chosen to be longer than the effective width defined for a T-beam with a 3 in. flange in Section 8.10.2 and 8.10.4 of the 1989 ACI Building Code" [Sittipunt and Wood, 1993].

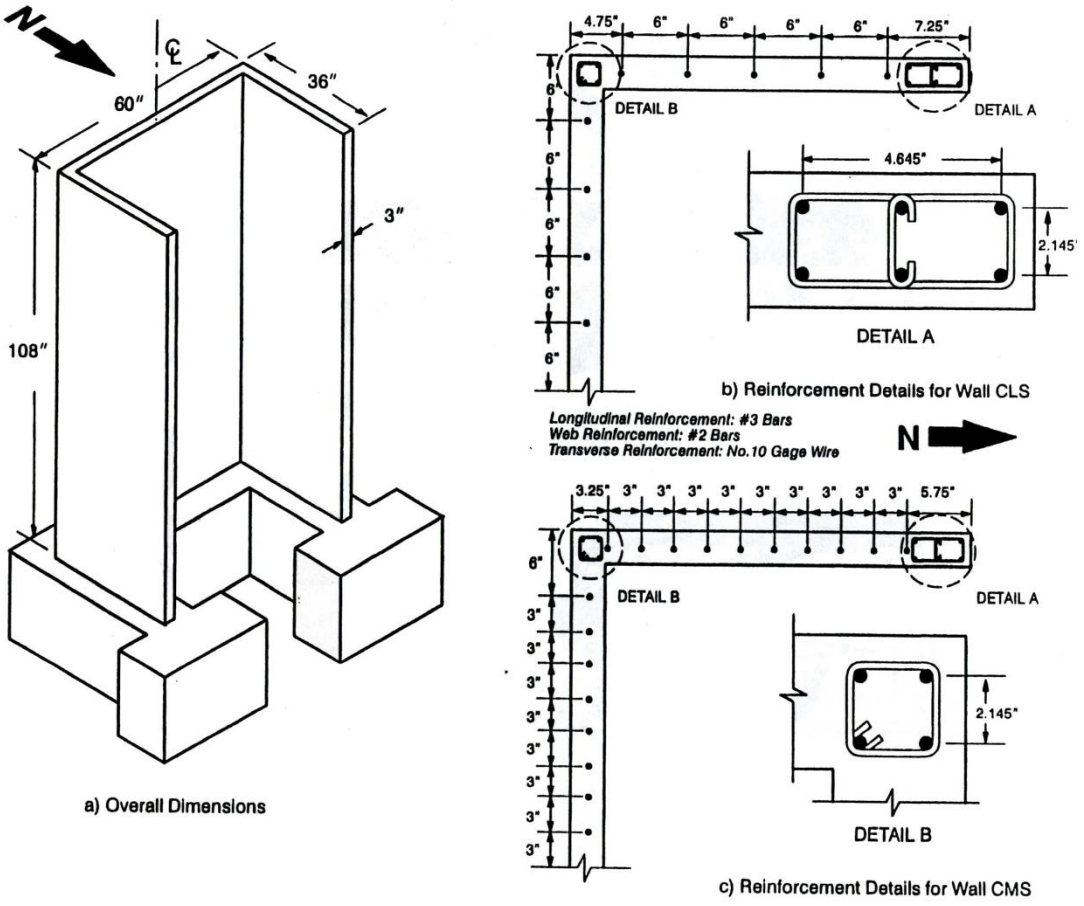

Figure 2.3 Overall Dimensions and reinforcement details of the C-Walls tested by Sittipunt and Wood [1993]

The reinforcement details for each C-wall, called CMS and CLS, is shown in Figure 2.3b and 2.3c. The same amount of flexural reinforcement was provided in the boundary of both walls, with 10 #3 bars in each web. Four of these bars were placed in the boundary element at the intersection between the flange and web, and the remaining six bars were placed in the web stem. The difference between the two C-shaped walls was the amount of distributed reinforcement in the web and flanges. One wall (CLS) had the minimum distributed reinforcement allowed in the 1989 ACI Building Code with a web reinforcement ratio of 0.0025, while the other wall (CMS) had twice as much reinforcement. The reinforcement ratios in the horizontal and vertical directions of each wall were equal. A single layer of #2 bars were used to provide the distributed reinforcement in both walls. Wall CLS used a nominal spacing of 6 in.

whereas CMS used a 3 in. nominal spacing, doubling the reinforcement ratio of the wall, see Figure 2.3(b) and (c).

Transverse reinforcement consisted of square spirals made of No. 10 gauge wire around the four bar boundary element, while the same gauge wire rectangular spirals with cross ties were used for the six bar boundary element, see "Detail A" and "Detail B" in Figure 2.3. The spacing of the transverse reinforcement in both boundary elements was two inches. Both walls were designed such that their nominal flexural strength was less than the nominal shear strength; the shear capacity was calculated to be 22%-42% higher than the shear demand expected at full development of the full flexural capacity for CLS depending on if an elasto-plastic or strain hardening stress-strain relationship was used the reinforcement. The shear strength of CMS was 54%-87% higher than the flexural capacity, which allowed the walls to experience a ductile flexure dominated response rather than a brittle shear response.

Both walls were loaded at the top with quasi-static lateral load reversals in the web direction. An axial load of 100 kips was applied to both test specimens through the centroid of the section, which induced a uniform stress of 265 psi to the walls. The walls were subjected to cycles of ±10 kips, ±1.0 in. of displacement, ±1.5 in. of displacement, and then cycles of greater than ±2.0 in. of displacement The force displacement responses measured for both CLS and CMS are shown in Figure 2.4.

Sittipunt and Wood used the test data to calibrate a general finite element model so that they could investigate the effects of various reinforcement details and the effective flange width on the response of C-walls. They developed a general two-dimensional model of concrete using the smeared crack model with fixed orthogonal directions for crack propagation. The reason for using this concrete model was largely based on the observations made during testing of the C-walls and the response of walls tested by Oesterle et al. [1979]. In the finite element model, they used a discrete steel model because it allowed them to more accurately model the specimens. Sittipunt and Wood used linear isoparametric 4-node elements with a 2x2 integration rule to represent the concrete and a 2-node bar element to represent the reinforcing. While the discrete steel model allows the use of linkage elements to include the effects of bond slip due to strain penetration, they did not use linkage elements in their finite element model. However, the possibility of using link elements to model the bond slip was suggested by Sittipunt and Wood.

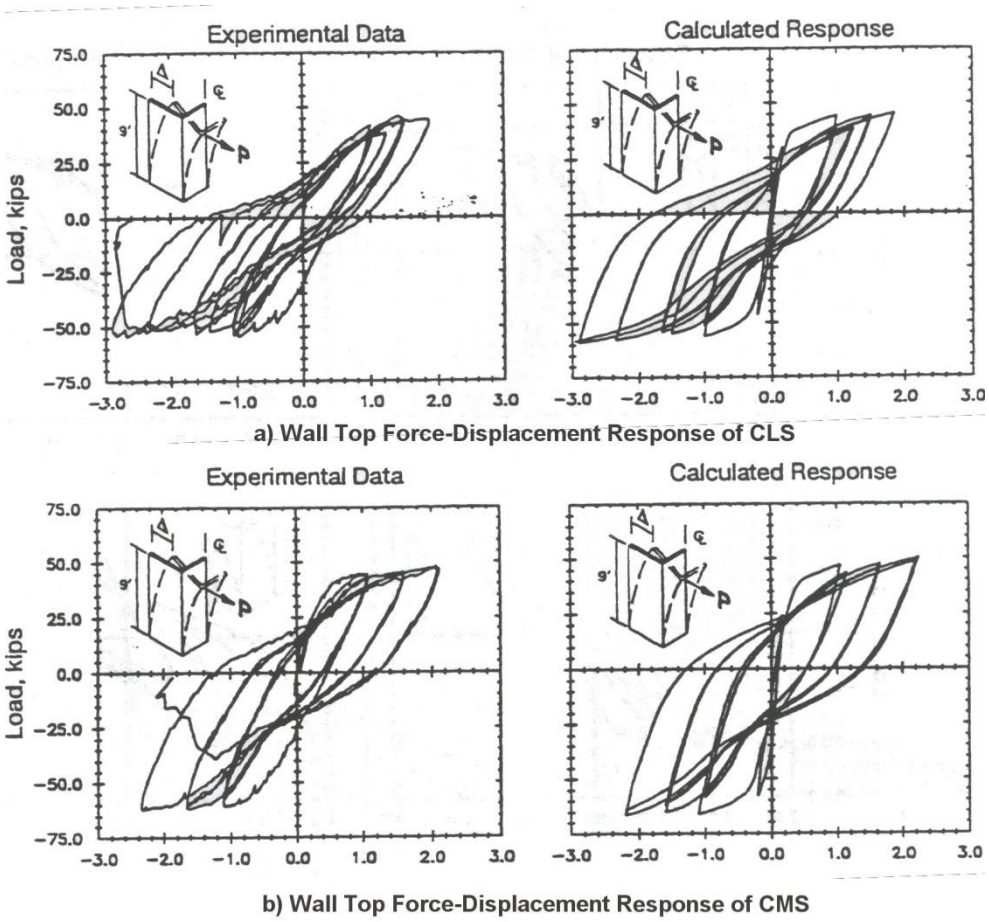

Figure 2.4 Experimental and Analytical Force-Displacement Response of CLS and CMS [Sittipunt and Wood, 1993]

Their model captured the global behavior of the wall adequately, with the calculated load versus deflection correlating acceptably with the recorded experimental response, as shown in Figure 2.4. Both the experimental data and analysis of the wall showed good energy dissipation and no strength degradation prior to crushing of concrete in the web tip boundary elements. However, no comparisons of the strain and curvature simulations were presented. The local response parameters such as, strains, curvature, location of the neutral axis, etc. are important predictors of damage and their accurate prediction is required in performance-based seismic design.

Sittipunt and Wood concluded from their testing and analytical models that the effective flange width can be larger than that recommended by 1989 ACI Building Code for the effective flange width of T-beams. Furthermore, they suggested that using the 1989 ACI code

recommendations for effective flange width is conservative when the flange is in compression; however, when the flange is placed in tension, using a too small effective flange width greatly underestimates the strength of the section, which can potentially lead to premature crushing of the concrete in the boundary elements in the web. This result from more tension reinforcing steel being mobilized and allowing the section to carry a larger moment than was implied by the 1989 ACI code recommendations. The extra moment places additional strain demand on the concrete in the web tips and can lead to crushing of the confined concrete at lower displacement levels than anticipated. However, they made no specific recommendation on how large and effective flange width should be used for C-walls; rather they recommended further research to determine the proper effective flange width.

2.2.3 Thomsen and Wallace [1995]

Thomsen and Wallace conducted an investigation on the behavior of structural walls with rectangular and T-shaped cross-sections. The walls were selected based on a prototype building multi-story office building located in a high seismic region; see Figure 2.5 for the floor plan of the prototype building. The building was six stories tall, and incorporated both rectangular and T-shaped walls as well as moment resisting concrete frames to resist lateral and gravity loads.

Thomsen and Wallace used a displacement-based design procedure to determine estimates of the lateral roof displacement and story drifts of the prototype structure. In this procedure, individual walls are designed based on the required global deformations The section analysis program BIAX [Thomsen & Wallace, 1995] was used in the design procedure to determine the flexural strength of walls, transverse steel in the boundary elements, and the required shear strength of the wall. They wanted to show that their displacement-based design method effectively designed both rectangular and nonrectangular walls. The rectangular wall was designed considering the forces corresponding to the in-plane response, while the T-shaped wall was designed considering the forces in the plane of the flange and in the plane of the web.

The prototype rectangular wall was 192 in. long by 16 in. thick. The prototype T-wall was 192 in. wide at the flange and was 192 in. deep; both the flange and the web were 16 in. thick. The rectangular and T-walls were 864 in. tall in the prototype structure. Once the designs for the rectangular and T-shaped walls in the prototype structure were completed, four 1/4-scale test specimens were designed and constructed. They were identified as RW1, RW2, TW1, and

TW2. Figures 2.6 and 2.7 shows the dimensions and reinforcement details of Thomsen and Wallace's rectangular specimens RW1 and RW2. RW2 differed from RW1 by using a closer spacing for the transverse reinforcing steel in the boundary elements to suppress buckling of the longitudinal reinforcement and allow the confined concrete to control the lateral load behavior of the wall. However, the diameter of the transverse reinforcement was not changed, increasing the volumetric ratio by 50% and thereby greatly increasing the confinement effects to the concrete.

Figure 2.8 shows the reinforcement details for the first T-wall, TW1. TW1 was designed by taking two rectangular walls and joining them together without considering the T-wall behavior. On the other hand, TW2 was designed considering the T-wall behavior and its reinforcement details were significantly different from those of TW1. Figure 2.9 shows the reinforcement details of TW2. The modified details of TW2 with respect to TW1 include: 1) the boundary element in the web tip was significantly longer to accommodate the high strains and location of the neutral axis expected when the flange is in tension, 2) the spacing of the transverse reinforcement in the web tip boundary element was reduced, and 3) the number of longitudinal bars in the web tip boundary element was increased by adding two #2 bars.

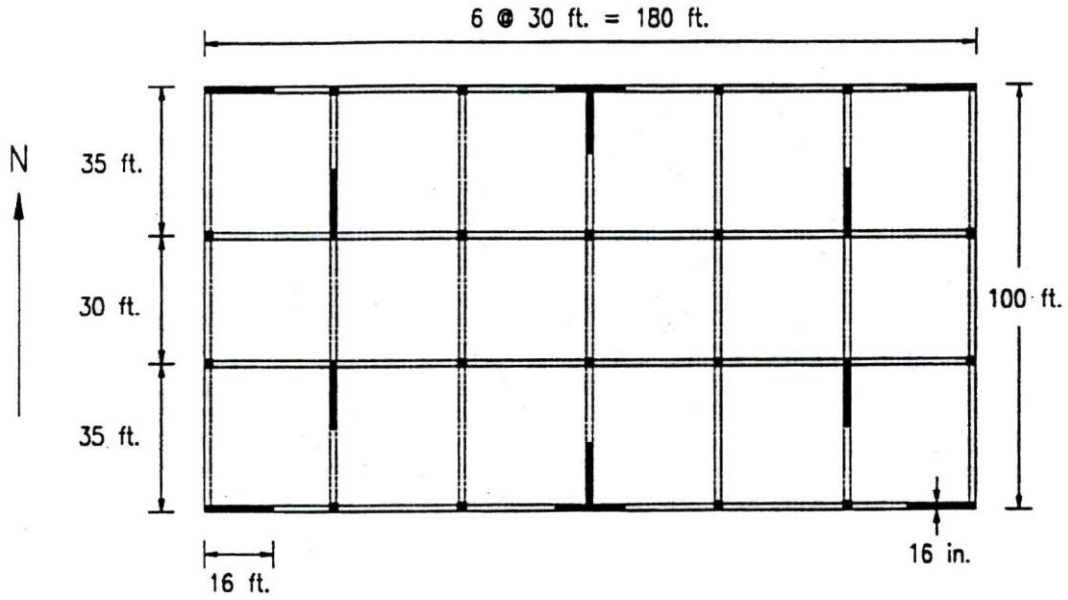

Figure 2.5 The Floor Plan of the Prototype Building chosen by Thomsen & Wallace [1995]

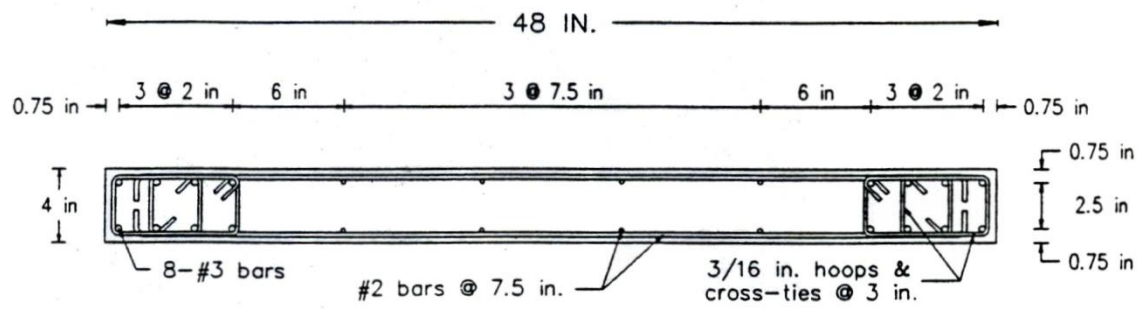

Figure 2.6 Section of Rectangular Wall RW1 Tested by Thomsen and Wallace [1995]

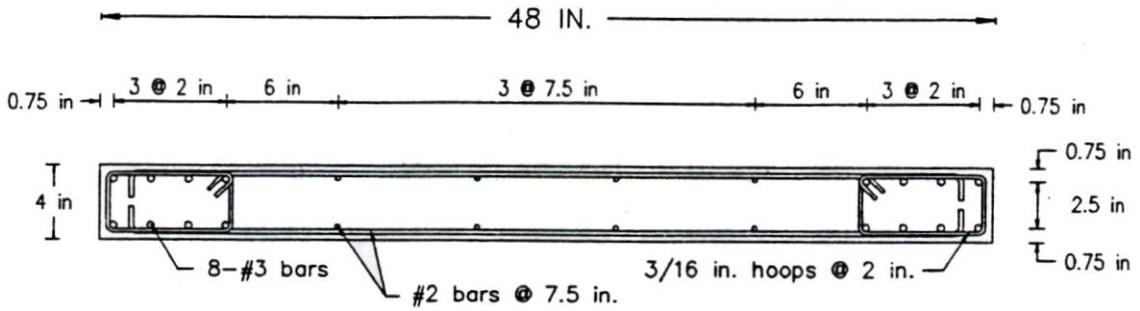

Figure 2.7 Section of Rectangular Wall RW2 Tested by Thomsen and Wallace [1995]

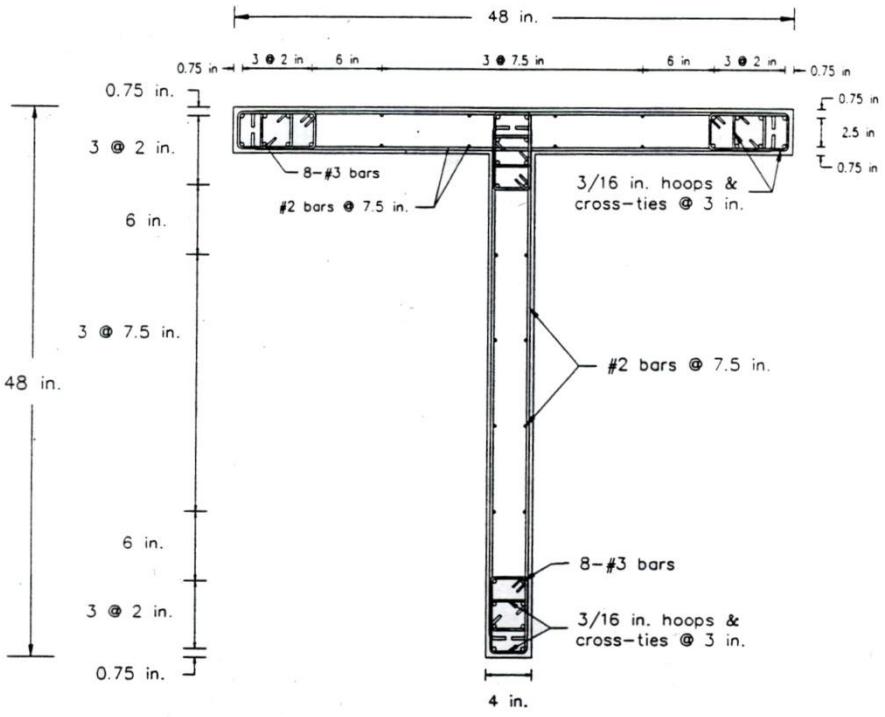

Figure 2.8 Wall Section TW1 Tested by Thomsen and Wallace [1995]

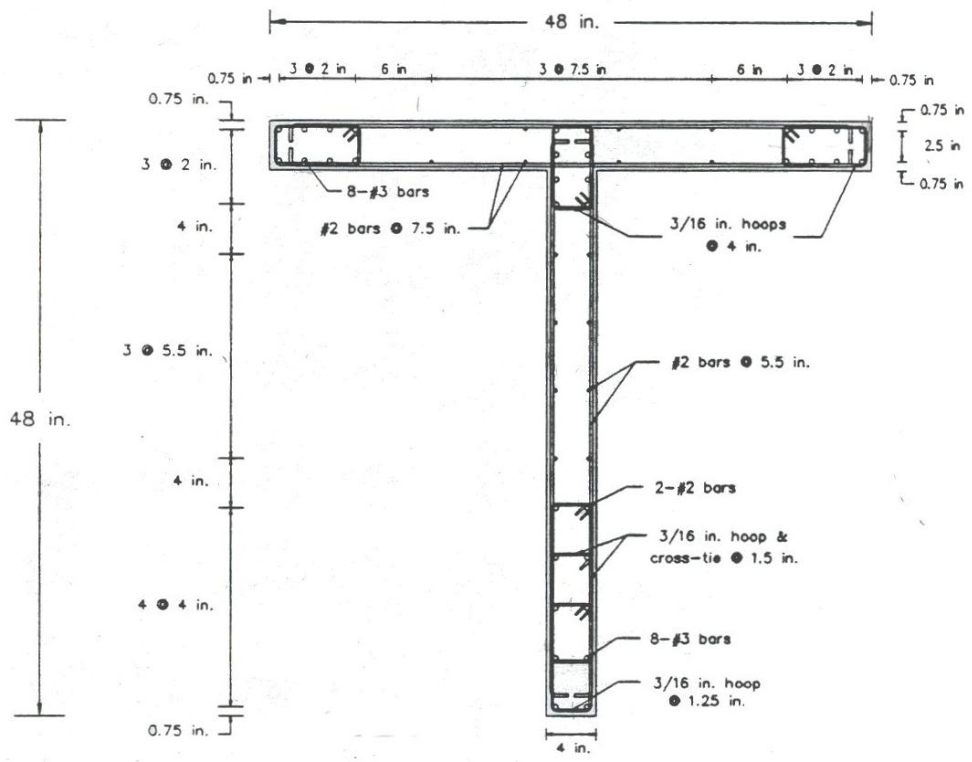

Figure 2.9 Wall Section TW2 Tested by Thomsen and Wallace [1995]

Prior to testing them lateral load, all walls were subjected to axial loads in the range of 0.07Agf'c to 0.1Agf'c, where Ag is the gross cross-sectional area and f'c is the measured concrete strength. The actual axial load ratio applied to each wall is noted in the force-displacement plots in Figures 2.10 to 2.13, where f'c values were 4.58 ksi, 6.33 ksi, 4.92 ksi, 6.048 ksi for RW1, RW2, TW1, and TW2, respectively. The rectangular walls were loaded in the plane of the wall and cycled at least twice at each level of target story drift. The drift targets were 0.25%, 0.50%, 0.75%, 1.0%, 1.5%, 2.0%, and 2.5% drift. The T-walls were loaded in the plane of the web, causing compression or tension in the flange depending on the direction of the load. With good detailing, specimen RW1, RW2, and TW2 were expected to provide adequate ductility with no strength degradation, TW1 was expected to perform poorly and was intended to show the effects of treating a T-wall as separate rectangular walls in each direction, thus ignoring the effects of the flange on the response. Figure 2.10 and 2.11 show the response of rectangular walls, which experienced a symmetric response in terms of strength and ductility when loaded alternatively in the positive and negative directions. RW1 failed by buckling of all eight longitudinal bars in the boundary element between the transverse reinforcement at 1.5% drift. RW2 also failed due to

buckling of the longitudinal reinforcement between the transverse reinforcement; however, the reduced spacing of the transverse reinforcement delayed buckling until 2.5% lateral drift. However, the response of the T-walls, seen in Figure 2.12 and 2.13, was different depending on if the flange was in compression or tension. When the flange was in compression, the wall had a lower lateral force resistance; however, the ductility of the section was higher. The higher ductility results from the small neutral axis depth and low compressive strains in the flange. The tension steel is located far from the neutral axis and experiences very large strains allowing the steel to utilize its entire post-yield strain capacity. The lower lateral strength was due to the reduced amount of reinforcement area in the web tip when compared to the steel area in the flange. When the load was reversed and the flange was placed in tension, the lateral load resistance increased and the ductility of the wall was decreased. The increased load came from the large longitudinal steel area in the flange, allowing a higher flexural strength to be developed at the critical wall section. The neutral axis was located high in the web such that the compression and tension strains were approximately equal, leading to reduced strain demand in the steel and a lower ductility for the wall.

The flexural strength of the wall when the flange was in tension was almost twice as large as when the flange was in compression. This placed a larger shear demand on the wall. However, as seen in Figure 2.14, the shear deformation near the wall base was the largest when the flange was in compression, even though the corresponding shear demand was lower. Thomsen & Wallace [1995] offer the following explanation:

> "When the flange is in compression, the depth of the compression zone is extremely small (~3 in.), and large inelastic tensile strains are developed in the web, resulting in substantial flexural and shear cracking (diagonal shear cracks extend the entire length of the web). The inelastic shear distortions measured under this loading condition are relatively high, even though the measured shear force is comparatively low (half as large as the shear expected under reversed loading condition). When the flange is in tension, the wall stiffness increases and the depth of the compression zone is approximately half the wall length. Under this loading condition, less damage (diagonal cracking) was witnessed; therefore relatively small shear distortions were measured, even though the

shear force was approximately twice as large."

TW1 failed due to global buckling of the entire web tip boundary element. The brittle buckling failure was expected due to the poor detailing, but was intended to show the brittle behavior that result from poor conceptual design and detailing. TW2 failed due to crushing of the confined concrete core at 2.5% lateral drift, the confined concrete was observed pushing out through the hoops and ties. The crushing of the confined core resulted in out-of-plane instability on subsequent cycles.

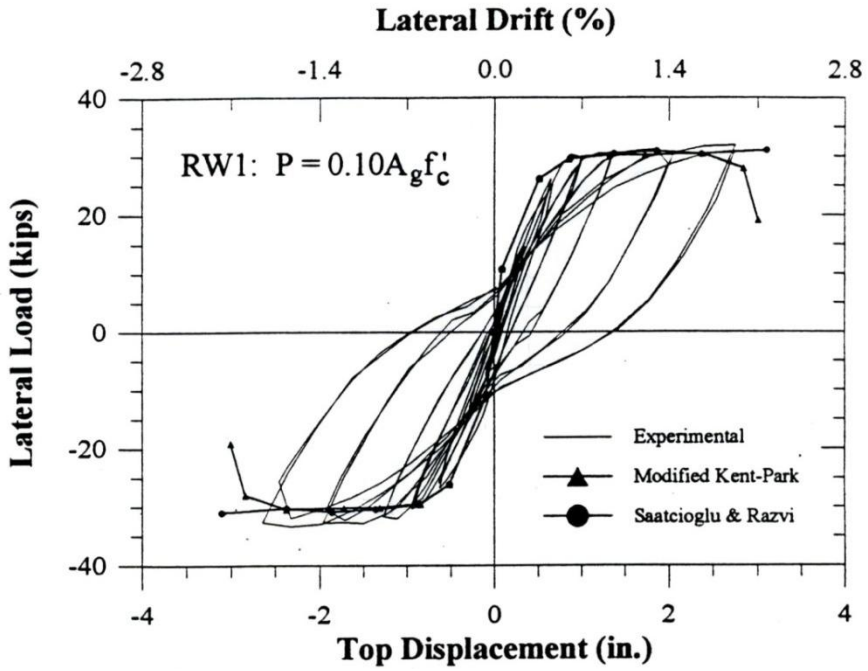

Figure 2.10 Measured & Analytical Response of RW1 [Thomsen & Wallace, 1995]

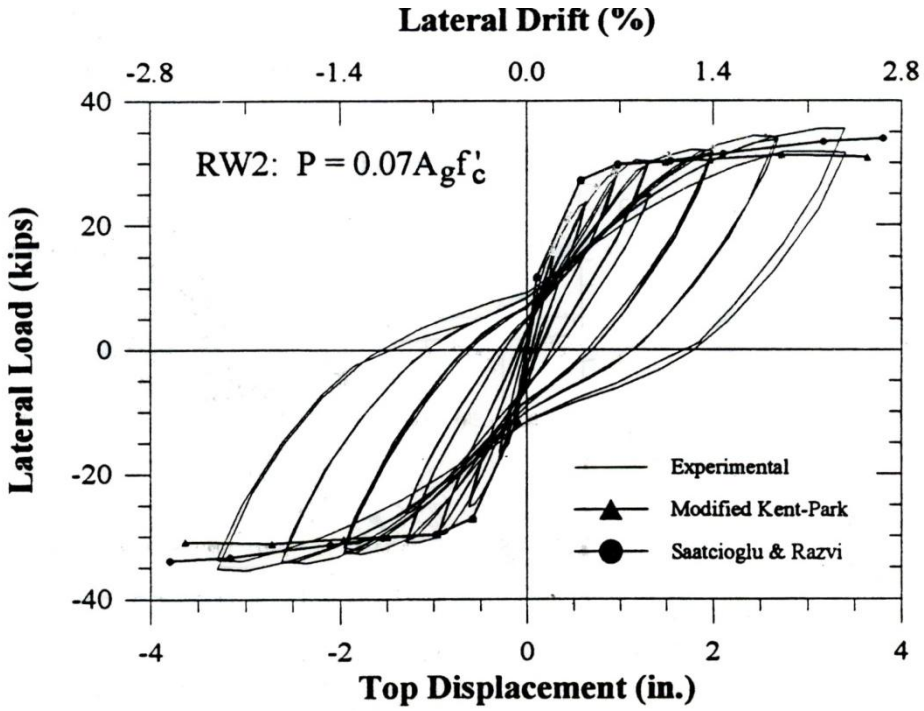

Figure 2.11 Measured & Analytical Response of RW2 [Thomsen & Wallace, 1995]

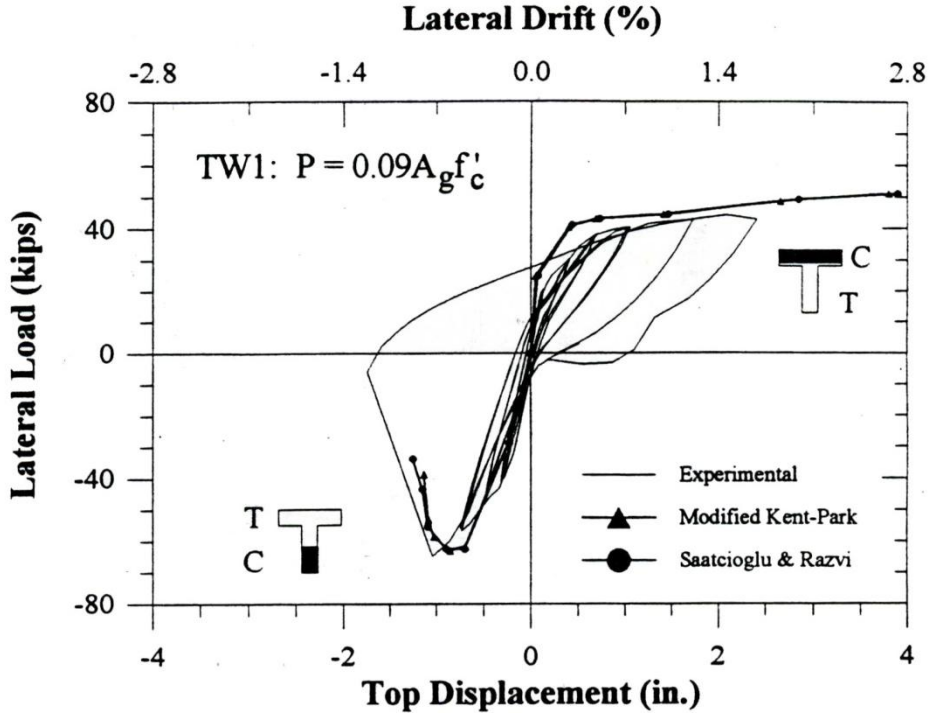

Figure 2.12 Measured & Analytical Response of TW1 [Thomsen & Wallace, 1995]

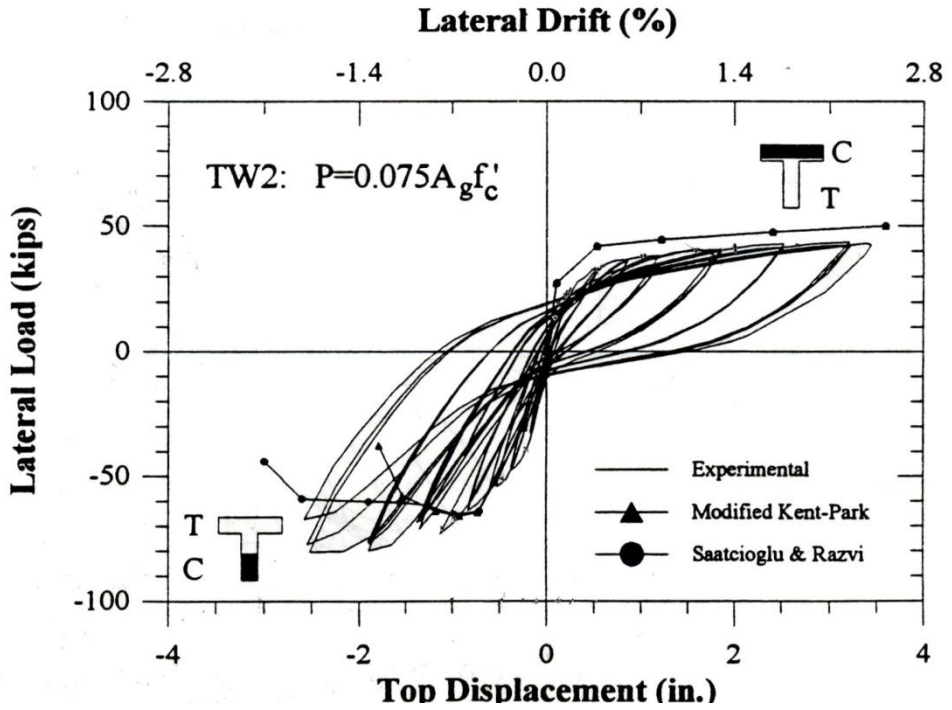

Figure 2.13 Measured & Analytical Response of TW2 [Thomsen & Wallace, 1995]

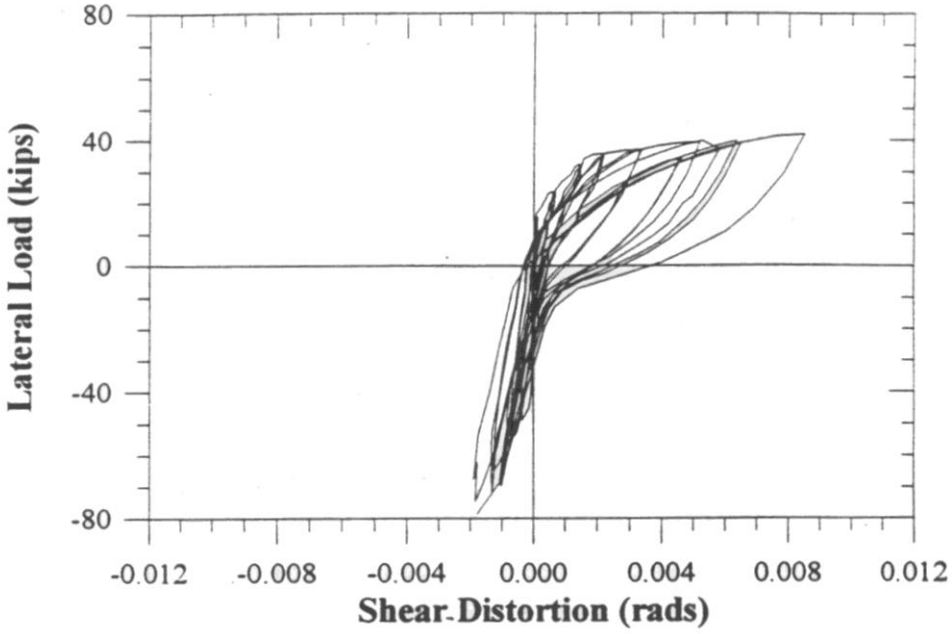

Figure 2.14 TW2 First Floor Shear Distortion [Thomsen & Wallace, 1995]

Thomsen and Wallace compared the predicted force-displacement response of the wall based on the moment-curvature results of the section analysis program BIAX [Wallace and Moehle, 1989] with the response recorded during the experiment. BIAX has different material

models that can be used to simulate the behavior of the concrete. Thomsen and Wallace ran two separate analyses of each wall one using a Modified Kent-Park [Park, Priestley and Gill, 1982] concrete model and the other using the Sastcioglu & Razvu [1992] concrete model. Figure 2.10 shows that the BIAX results showed a slightly stiffer response predicted than that was observed in the elastic region; however, the lateral capacity of the wall was well predicted for RW1. Figure 2.11 compares similar results for RW2, and it appears that BIAX predicted the stiffness adequately, but somewhat under predicted the lateral strength of the wall. As shown in Figure 2.12, BIAX over predicted the strength and stiffness of TW1 when the flange was in compression, and greatly underestimated the stiffness for the flange-in-tension direction. The comparison of results for TW2 is shown in Figure 2.13. Similar to TW1, the strength and stiffness of the wall were over predicted for the flange-in-compression direction loading, while the stiffness in the flange-in-tension direction was under predicted. Additionally, the lateral capacity of the wall was significantly under predicted by the analysis, particularly at large displacement levels.

Based on a follow up analytical study, Orakcal and Wallace [2006] presented an improved analysis model for predicting lateral load behavior of reinforced concrete structural walls. Using the data recorded in the experiment, they concluded that shear-flexure interaction had a significant impact on the response of the wall. Consequently, they created a special type of element called the "Multi-Component-in-Parallel Model" (MCPM) to capture the flexure-shear interaction. The MCPM model is similar to the multiple-vertical-line-element models that will be discussed in the next section. The force-displacement response comparison between their analytical model and the experimental response shows an excellent match for RW2 seen in Figure 2.15. However, the data from RW2 was used to calibrate the parameters used in the MCPM model; a prediction of the response for a wall using the MCPM has not been presented.

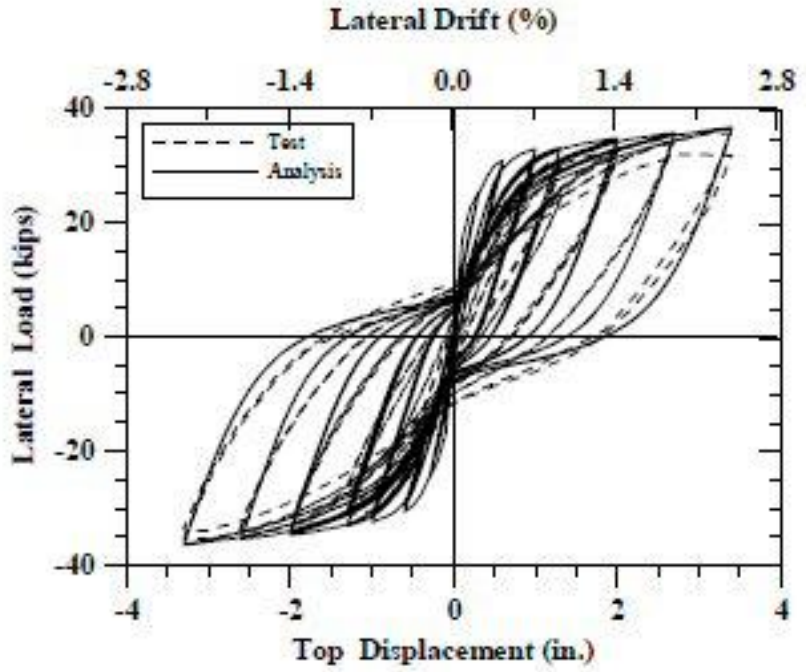

Figure 2.15 Comparison of results from the MCPM model of RW2 with the Measured Response [Orakcal and Wallace, 2004].

2.3 Analytical Studies

This section presents the various analytical approaches presented in literature for modeling the response of structural walls. Any of these techniques can be used for nonrectangular walls. Structural walls have been modeled and analyzed using a number of different approaches by researchers. Rather than making an extensive listing of all the analytical studies done on structural walls, a summary of various modeling approaches used for walls studies are presented, followed by a representative sample of analyses and commentary on the advantages and disadvantages of the different approaches.

2.3.1 Solid (Brick) Elements

The behavior of structural walls has been simulated using solid or brick elements. Solid elements have been used by a number of researchers [Deshmukh et al., 2006; Moaveni et al., 2006] to simulate the structural wall behavior under lateral loads. This modeling approach has the advantage of allowing the strain and corresponding stress to vary across the section without the user having to specify a particular distribution such as that based on the plane section remains

plane assumption. Additionally the shear stiffness of the wall is determined for the individual elements. In this approach, the longitudinal and transverse reinforcement can be smeared across the solid element or modeled discretely using truss elements. The 3D nature of the model allows bi-directional lateral loads to be applied to the wall. However, solid elements have some significant disadvantages. These include incorporating an accurate 3D concrete material model that can accurately model the initiation, propagation, and orientation of cracks as they form in concrete elements as well as the loading and unloading paths. A large number of solid elements may be required to model the concrete and reinforcement of a wall accurately, which may require significant computational time to run the analysis. Including the effects of strain penetration is challenging and typically ignored in the analysis [e.g., Moaveni et al, 2006; Deshmukh, 2006].

Deshmukh et al. [2006] modeled the 7-Story building slice tested at UCSD, which included gravity columns, floor slabs, a rectangular wall bending about its strong axis, and a rectangular wall bending about its weak axis. A complete description of the 7-story building slice is described in Appendix B. Deshmukh et al. modeled the 7-Story building slice in SAP 2000 using brick elements and the concrete material model available in SAP 2000. The steel reinforcement was modeled separately, and linked to the displacement of the nodes of the concrete solid elements through constraint equations. The SAP 2000 model used over 7000 solid elements to simulate the UCSD Building Slice.

2.3.2 Plane stress, Plane Strain, or Shell Elements

Plane stress, plane strain, and shell elements have also been used to simulate the response of structural walls in 2D. Studies conducted by Sittipunt and Wood [1993], Palermo and Vecchio [2004], and Kelly [2006, 2007] are good examples of this modeling approach. This approach has some of the same advantages and disadvantages as the solid element. A reliable 2D concrete model is required for the analysis that should include the effects of cracking and appropriate unloading/reloading rules. In addition to the concrete model, complexity and number of elements, these models are be limited to unidirectional loading only. Similar to solid elements, including the effects of strain penetration is difficult and commonly ignored [e.g. Sittipunt and Wood, 1993].

Kelly [2006] also modeled the 7-Story Building slice discussed in Appendix A. Kelly

used nonlinear plane stress elements to model the web wall, flange wall, and post-tensioned column. The effects of strain penetration were modeled using pairs of nonlinear gap-truss elements to model the reinforcement at the base of each wall. The gap truss elements allowed for a large crack to form at the base of the wall, simulating the base rotation due to strain penetration. The model had 686 degrees-of-freedom which is relatively low. The comparison of the calculated and measured displacement profiles is shown in Figure 2.16, which that the model predicted the displacement response envelope for events EQ1 and EQ4. The relatively low number of degrees of freedom (DOF) makes this modeling approach well suited for the analysis of a complete building in a design office.

Hachem [2006] also used plane stress elements to model the response of 7-Story building slice. The web wall was modeled using 4-node, 8-degree-of-freedom plane stress elements with a nonlinear concrete material model that simulated both cracking and crushing of concrete. The reinforcement was modeled using truss elements connected to the nodes of plane stress elements. The effects of strain penetration were ignored in building the analytical model. The model consisted of a total of 3143 elements, of which 804 plane stress elements represented the web wall and 2322 truss elements represented the longitudinal reinforcement of the web wall. Figure 2.17 shows the displacement profile analytical and experimental profile for the 7-Story building slice.

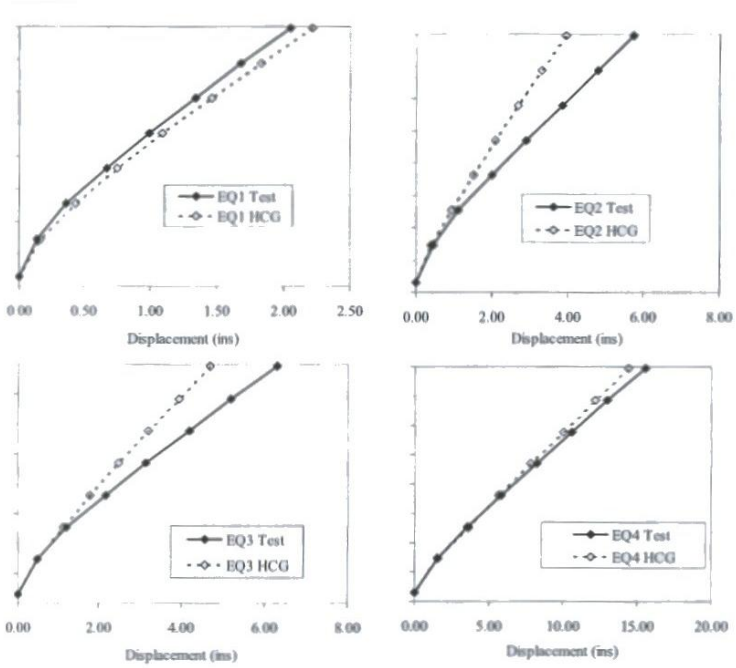

Figure 2.16 Displacement Profile Comparison [Kelly, 2006]

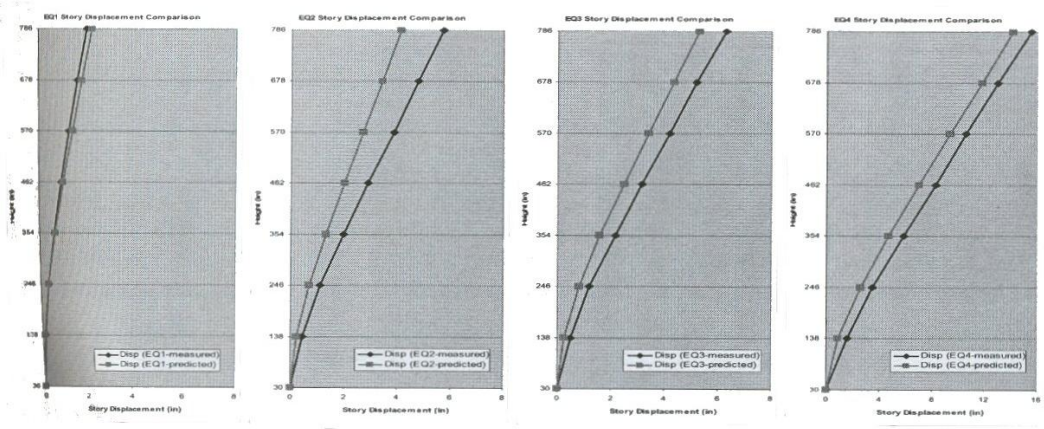

Figure 2.17 Displacement Profile Comparison [Hachem, 2006]

2.3.3 Macro Model Elements

Macro model elements are a type of element that instead of specifying microscopic behaviors, such as stress-strain relationships, global response parameters are specified directly. Typically, macro models lump various behaviors into one element to simplify the analysis and increase the computational efficiency of the analysis. Macro model elements are used to capture

regions of nonlinear behavior, while linear elements are used for regions that will remain elastic during the analysis.

One example of a macro model element is the multiple-vertical-line-element-models (MVLEM) that have been shown to capture the response of structural walls [Fischinger and Isakovic, 2006; Orakcal et al., 2004]. This modeling approach simulates the behavior of rectangular walls using a series of vertical and shear springs connected by rigid beams at the top and bottom of the element. Figure 2.18 shows the MVLEM schematically. The force-displacement characteristics of the springs can be defined to incorporate the various response components of the structural walls.

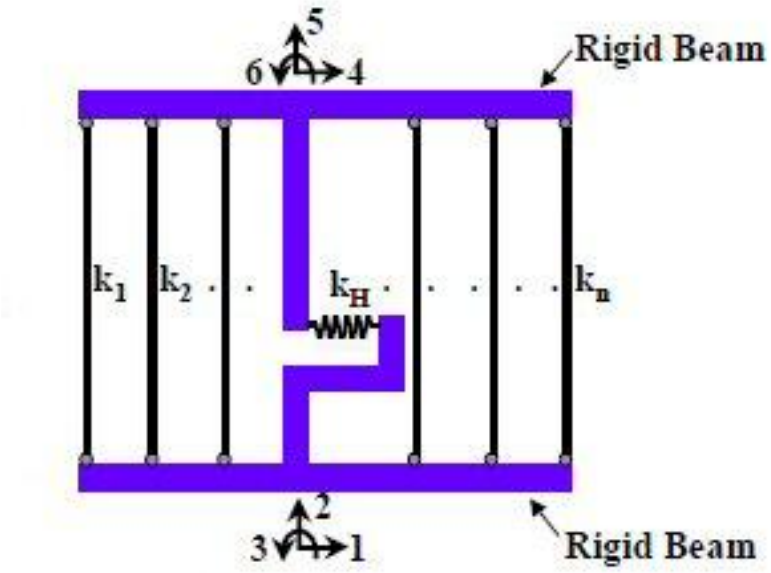

Figure 2.188 Multiple Vertical Line Element Model

A "beam with hinges" is another example of a macro model used to simulate structural walls [Bolander and Wright, 1991]. This model lumps all the nonlinear behavior at the ends through the use of axial and rotational springs. The spring behavior is then defined to give almost any type of response that is desired by the user.

The primary advantage of macro model elements is that they are very computationally efficient and provide good simulation of the global wall behavior. However, macro model elements require experience and knowledge to determine the force-displacement relationships for the springs, rather than stress-strain relationships of the material that are more familiar to most

engineers. Additionally, strain penetration and other behaviors are lumped together in the spring behavior, potentially leading to inaccurate simulation at the local level.

Fischinger and Isakovic [2006] successfully modeled the UCSD 7-Story Building slice using the MVLEM approach. The web wall was modeled using a stack of MVL elements, of which four of them were used in the first story and one element in all the other stories. Five vertical springs were used to simulate the entire cross section of the wall and the compressive strength of the vertical spring was based on the compressive strength of the confined concrete, neglecting the steel reinforcement in compression. Empirically verified values were used to define the hysteretic relations in the vertical springs. The shear behavior was assumed to remain elastic. Figure 2-19 shows the predicted and measured maximum displacement profiles.

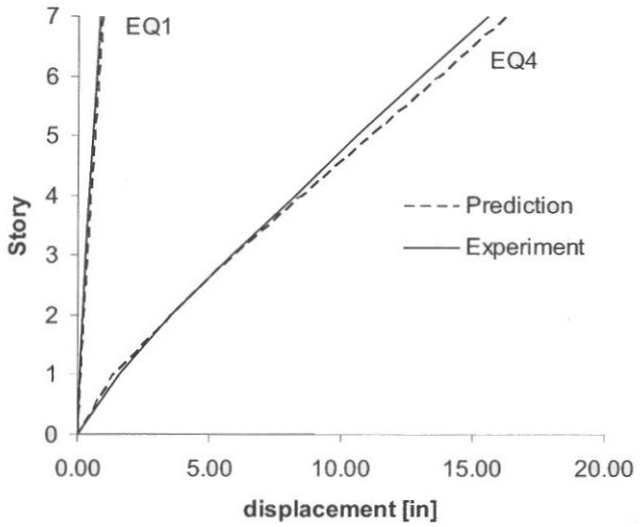

Figure 2.19 Predicted and Experimental Displacement Profiles

2.3.4 Beam-Column Elements

Beam-column elements with fiber sections have been used to simulate response of structural walls [e.g. Martinelli and Filippou, 2006; Grange et al., 2006; Dazio, 2006]. These models allow the user to specify uniaxial stress-strain behavior of longitudinal reinforcement as well as that of confined and unconfined concrete including the effects in the transverse direction. A large variety of models are available that can be used to characterize the behavior of different materials in order to capture the section and member responses accurately. Since the model is

based on the uniaxial stress-strain behavior of groups of fibers, the models are easier to build and understand. The disadvantage of fiber beam-column elements is that the strain distribution at the section level is typically predefined. Additionally, some fiber based elements require the shear deformation to be handled separately. In this case, the beam-column element only considers the axial and bending deformations on the element, and no shear stiffness is included in the element stiffness. In order to include the effects of shear deformation, a separate material model must be used to define the global shear force-deformation relationship for the beam column element. The shear material model can be placed in parallel to the beam-column, thus including the shear stiffness in the global structural stiffness matrix.

2.4 Shear Lag Behavior

The Bernoulli-Euler assumption that plane sections before bending remain plane after bending is often used for the analysis of beams. This assumption states that the longitudinal strain is constant at all points in a flange section of a member located at the same distance from the neutral axis. However, this approximation fails to include the appropriate effects of shear flow on the section. The shear flow causes shear distortion in the flange causing the longitudinal strains at regions away from the flange-web junction to lag behind the strains at the flange-web junction [Kwan, 1996]. An example of shear lag effects is shown in Figure 2.20 which depicts the longitudinal bending stress distribution on a closed rectangular tube with and without shear lag. As shown, higher strains are observed at the flange-web junction than in the center of the flange. In a T-wall the strains would decrease along the flange towards the tips.

The effects of shear lag are due to distortion of the flange due to the shear flow in the cross-section. Thus increasing the shear stiffness of the flange will decrease the effects of shear lag; conversely, decreasing the shear stiffness of the flange will increase the shear lag effects. The shear stiffness of the flange is dependent on the length and thickness of the flange, a short, thick flange will have much higher shear stiffness than a wide, thin flange. The distribution of both the longitudinal and transverse steel will affect the shear stiffness, well distributed longitudinal steel is better in shear than steel concentrated in the ends. The transverse reinforcement is generally designed as shear reinforcement, and a closer spacing of the transverse reinforcement increases the shear stiffness of the flange. Height of the wall will

influence the shear stiffness; with shorter walls have higher shear stiffness.

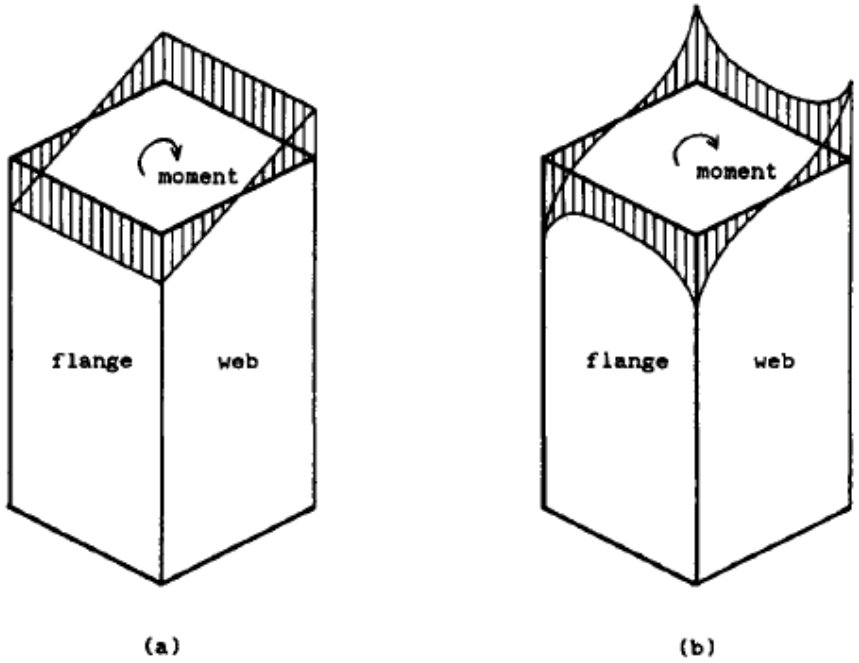

Figure 2.200 Longitudinal Stress Distribution a) without shear lag and b) with shear lag [Kwan 1996]

The shear lag reduces the effective width of the flange by changing the strain along the length of the flange and therefore stress distribution across the flange. The problems of shear lag has been studied by a number of researchers [Song and Scordelis, 1984a,b; Kwan, 1996; Haji-Kazemi and Company, 2002; Foutch and Chang, 1982]. However, most of the investigations have focused on "closed" section such as box girders [Foutch and Chang, 1982; Evans and Taherian, 1977, Chang, 2004] or tubular structures [Kwan, 1996; Haji-Kazemi and Company, 2002]. The studies have historically focused on the shear lag effect in bridge girders connected with concrete decks, rather than in structural walls.

Kwan [1996] examined shear lag in structural core walls and reviewed a number of techniques that are available to analyze the shear lag behavior. Kwan grouped the analytical methods into the following categories: 1) folded plate methods; 2) harmonic analysis methods; 3) finite stringer methods; 4) finite element methods; and 5) semiemperical methods.

The folded plate methods [Defries-Skene and Scordelis, 1964] treat the structure as a series of plates joined along their longitudinal edges. A Fourier series harmonic functions are

used to express the forces and displacements along the joints. Each plate is analyzed considering bending and membrane forces. The joint displacements can then be placed in a stiffness matrix and the external loads are then represented as a Fourier series. The final results can then be expressed by summing the partial results from each term in the Fourier expansion.

Harmonic analysis methods [Song and Scordelis, 1984a,b] represents the externally applied load using a Fourier harmonic expansion. However, the analysis is simplified by disregarding any out-of-plane bending of the flange plates. In the model, the web plates are simplified by assuming bending only, thus allowing the analysis of the flange alone. The analysis of the flange is then carried out in a manner similar to the folded plate analysis. This analysis determines a stress function; however, strain is not a function of stress, i.e. More than one strain can correspond to a given stress. This makes this method of analysis in appropriate for concrete if post peak behavior is considered.

The finite stringer method also assumes that only bending occurs in the web plates; however, the flange is simplified as a series of stringers connected by plates. The plates carry only shear forces, while the stringers carry the axial forces. Separating the axial and shearing forces in the flange simplifies the governing equations and makes them simpler to solve. This methodology is only appropriate for linear behavior for converting the strains to stresses to determine the stress distribution.

Finite element has been used to investigate the effects of shear lag. Moffatt and Dowling [1975] carried out an extensive parametric study of shear lag in bridge decks. The web was modeled considering bending only, and the bridge deck was modeled using one layer of solid elements. However, fine meshes were required for the deck panels. The finite element results were used to create a set of design values to estimate the effect of shear lag in bridge decks. Finite element analysis could be used to investigate the shear lag phenomenon for concrete structural walls in the nonlinear range. It would be dependent on the accuracy of the concrete material model. The analysis would need to be conducted using either solid, shell, or plane stress/strain elements. A fine mesh would need to be used in order to capture the variation across the flange. Moffatt and Dowling [1975] noted that a fine mesh was needed over the length and width of the flange, particularly near supports or point loads.

Additionally, various researchers [Coull and Bose, 1975; Coull and Abu El Magd, 1980] have used semiemperical methods based on energy formulation to determine the effects of shear lag. These methods use simplifying assumptions about the longitudinal stress distribution in the web and the flange. Solutions are then reached by minimizing the strain energy or the total potential energy. While these methods are easier to use, they are not as accurate as the other more rigorous methods. Energy methods are more difficult for nonlinear systems, and the inaccuracy of the approach is undesirable.

As previously stated, most of these studies have focused on box or tubular sections; only two of these studies conducted by Song and Scordelis [1984a, b] and Coull and Abu El Magd [1980] examined T-shaped sections. While these two studies present equations for the stress distribution in T-walls, the equations are not useful in the current investigation. In both studies, the equations were developed in terms of the longitudinal stress assuming elastic behavior of the T-beam; a T-wall is essentially a cantilevered T-beam. However, this investigation focuses on T-wall behavior in both the elastic and inelastic ranges. The equations developed by Song and Scordelis, and Coull and Abu El Magd, are complex and cannot be easily implemented in a framework like OpenSees. The equations are dependent on the location of the section of interest and the particular loading applied to the beam or wall. In OpenSees, shear lag would have to be handled at the section level because it is the section level that knows the particular details of the cross section and the location and type of each fiber; however, a section does not know its location in the global system, nor the particular external loading applied to it. In addition to the difficulty with implementation due to the constraints of a section in the OpenSees framework, the proposed shear lag equations would cause a significant increase in the computational time required for an analysis.

Chapter 3
Concrete Model

3.0 Introduction

Analysis of walls tested by Thomsen and Wallace [1993] showed that the concrete model was limiting the accuracy of the simulation of the wall behavior, particularly the unloading and reloading behavior, as well as the residual displacements. The cross-section of the second of two rectangular walls tested by Thomsen and Wallace, referred to as RW2, is shown in Figure 3.1. RW2 was 144 in. tall, 48 in. long and 4 in. thick. This wall was first modeled in OpenSees using beam-column elements with fiber sections. The confined and unconfined concreter fibers were modeled using the Kent and Park concrete model available in OpenSees [Mazzoni et al., 2006]. Figure 3.2 shows the simple unloading and reloading rules for the hysteretic behavior of the concrete model. The confined concrete behavior was based on the model proposed by Mander et al. [1988] and the unconfined concrete properties were as recorded by Thomsen and Wallace. Figure 3.3 shows the force-displacement response of RW2 observed by Thomsen and Wallace and the response given by the OpenSees analysis.

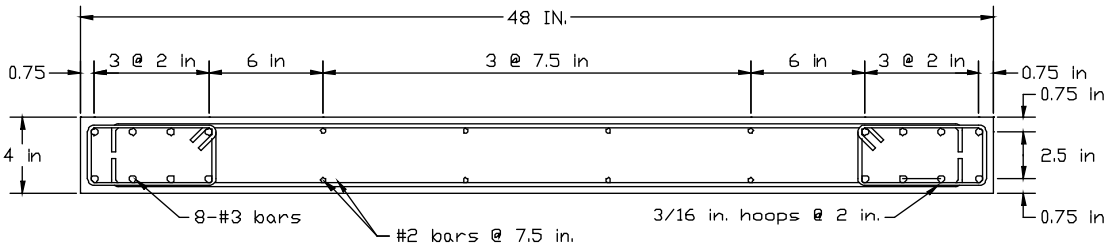

Figure 3.1 Cross-section details of Thomsen and Wallace's specimen RW2

The reloading stiffness is not well captured by the analysis; particularly near zero displacement. Also, the OpenSees results show a significant change in stiffness and a kink in the response near zero displacement. This kink is due to how the concrete model handles crack closure. The Kent-Park concrete model does not allow compression stress to develop until after the tension strain is completely removed as shown in Figure 3.2. This is unrealistic due to the presence of crushed concrete in open cracks. Additionally, the residual displacement is

significantly underestimated by the analysis. Improving the concrete model will help address these issues.

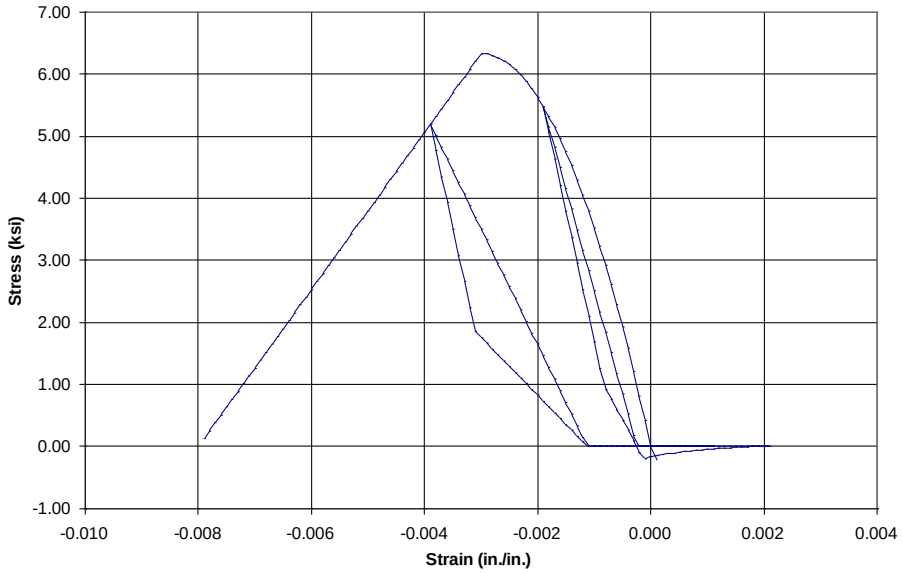

Figure 3.2 Response of OpenSees Concrete03 model based on Kent and Park Model

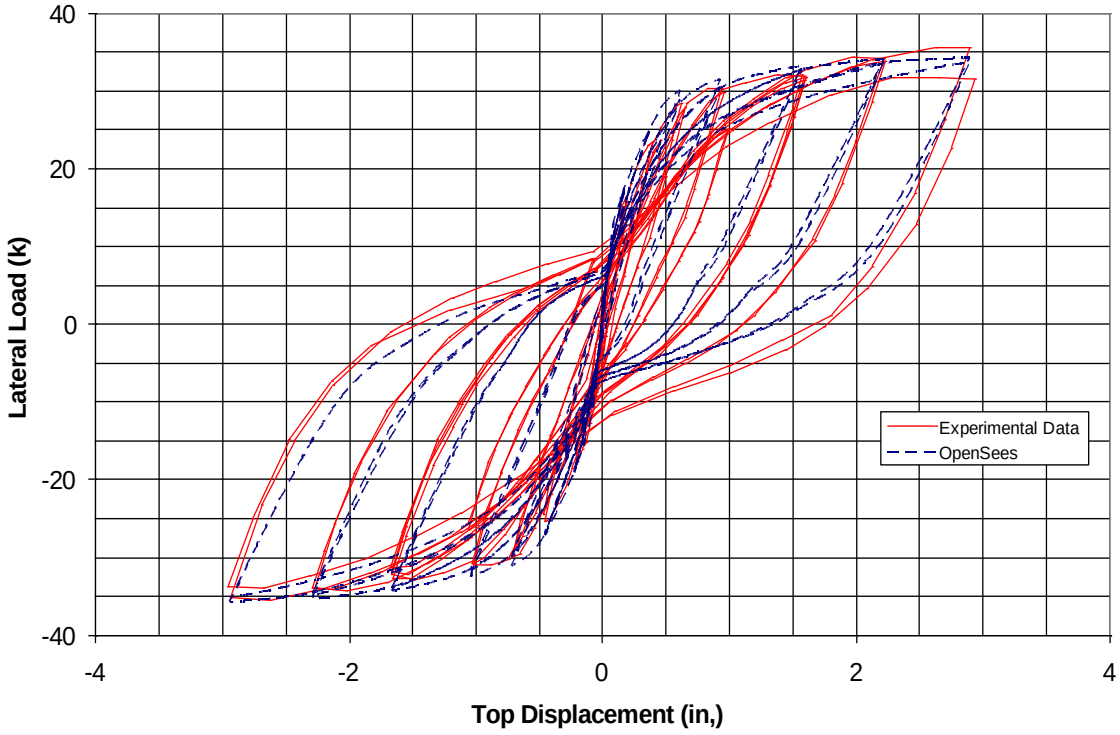

Figure 3.3 Force vs. Displacement response of RW2

To overcome the aforementioned challenges, the concrete model proposed by Chang and Mander [1994] was selected for implementation in OpenSees for a number of reasons. First, this model assumes that wedging action occurs in the cracks causing compression stress to develop prior to crack closure. Second, the model has different behavior depending on when the strain reversal occurs, providing a more robust hysteretic behavior. Third, the confined concrete model proposed by Mander et al. [1988] has become widely used to determine the confined concrete properties, and the Chang and Mander model extends the 1988 model to include the behavior of unconfined and high strength concrete. Fourth, Chang and Mander used a large number of cyclic concrete tests to validate the model behavior.

The implementation of the Chang and Mander [1994] concrete model is presented in the chapter. First the original model as described by Chang and Mander is presented; next, the challenges associated with the original model and steps taken to overcome these challenges are presented. Then, a simplified version of the Chang and Mander model is introduced. Finally, the improvement of the simulation of RW2 due to the use of new concrete model is then shown.

3.1 Model Description:

Chang and Mander [1994] proposed a hysteretic material model for the simulation of cyclic behavior of both confined and unconfined concrete. The proposed model was an advanced rule-based model in comparison to other concrete models and the ability to simulate the hysteretic behavior of both ordinary (<6 ksi) and high strength (6-12 ksi) concrete in both cyclic compression and tension. The model incorporates the degradation that occurs due to incomplete unloading cycles in addition to that due to completed unloading cycles. A complete cycle is unloading from the monotonic envelope in one direction to the envelope in the other direction. The effects of both partial and complete reloading to the monotonic envelope is also incorporated. The model pays particular attention to effects of opening and closing of cracks. Chang and Mander noted that most models assumed sudden crack closure with a rapid change in the section modulus, but this assumption is not supported by experimental results obtained on lightly loaded columns.

The general shape of the concrete stress-strain curve of their model is shown in Figure 3.4 and has certain characteristics: (1) the initial slope of the curve at the origin is the elastic modulus (E_c), (2) it reaches a maximum value at the peak stress and corresponding strain (ε_c, f'_c), and (3) it has both an ascending and descending branch. Controlling the slope of the ascending and descending branches of the model is important because they are different for confined and unconfined concrete. For unconfined concrete, the slope of the ascending and descending curves becomes steeper. In confined concrete, the slope of the descending branch is dependent on both the level of confinement and strength of the concrete. Chang and Mander investigated a number of different curves to use for describing the envelope response, and selected Tsai's (1988) equation. The equation has the following form:

$$x = \frac{\varepsilon_c}{\varepsilon'_c} \tag{3.1}$$

$$y = \frac{f_c}{f'_c} \tag{3.2}$$

$$y = \frac{nx}{1 + (n - \frac{r}{r-1})x + \frac{x^r}{r-1}} \tag{3.3}$$

where x, y, n, and r are parameters to control the shape of the curve.

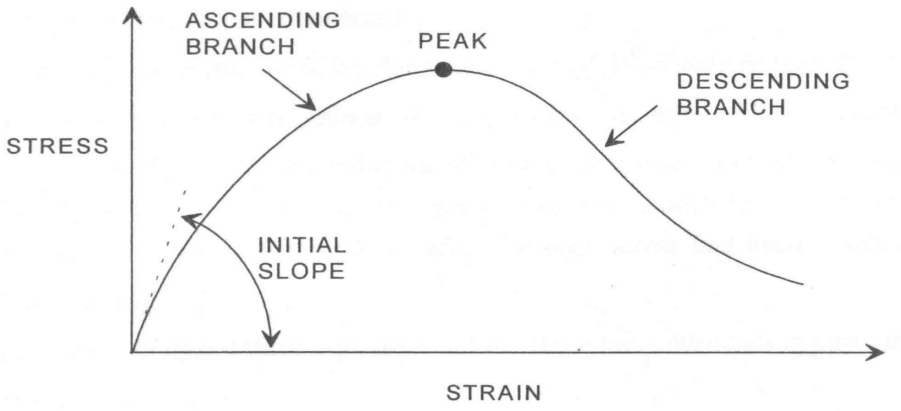

Figure 3.4: General Characteristics of a Concrete Material Model

3.2 Recommended Stress-Strain Parameters

3.2.1 Unconfined Concrete Behavior

Chang and Mander proposed suitable values to be used in Tsai's equation to represent the stress-strain response of concrete. They proposed the following equations for determining the modulus of elasticity for both normal and high strength concrete:

$$E_c = 185{,}000\,(f'_c)^{3/8}\ psi \quad \text{or} \tag{3.4a}$$

$$E_c = 8{,}200\,(f'_c)^{3/8}\ MPa \tag{3.4b}$$

The strain at which the peak compression stress occurs for both ordinary and high strength concrete can be obtained using the following equations:

$$\varepsilon'_c = \frac{(f'_c)^{1/4}}{4{,}000}\ psi \quad \text{or} \tag{3.5a}$$

$$\varepsilon'_c = \frac{(f'_c)^{1/4}}{28}\ MPa \tag{3.5b}$$

To control the descending branch, Tsai's equation uses parameter *r*; the value of this parameter is determined by the following formulas:

$$r = \frac{f'_c}{750} - 1.9\ psi \quad \text{or} \tag{3.6a}$$

$$r = \frac{f'_c}{5.2} - 1.9\ MPa \tag{3.6b}$$

The other parameter, *n,* that controls the ascending branch of the curve is defined as:

$$n = \frac{E_c \varepsilon'_c}{f'_c} \tag{3.7}$$

which, if Eqs. 3.1 and 3.2 for E_c and ε'_c are substituted in and simplified, reduces to:

$$n = \frac{46}{(fi_c)^{3/8}}\ psi \quad \text{or} \tag{3.8a}$$

$$n = \frac{7.2}{(f'_c)^{3/8}}\ MPa \tag{3.8b}$$

3.2.2 Confined Concrete Behavior

When axial load is applied to concrete, the section will attempt to dilate in the transverse direction due to the Poisson's effect. Restraining this dilation leads to an increase in strength, peak strain, and ductility of the concrete section. Chang and Mander proposed the following equation to calculate the increase in peak strength of the concrete.

$$f'_{cc} = f'_{c0} * (1 + k_1 * x') \tag{3.9}$$

where,

f'_{cc} = peak concrete strength of confined concrete

f'_{c0} = unconfined peak concrete strength

$$k_1 = A * \left(0.1 + \frac{0.9}{1 + B * x'}\right) \tag{3.10}$$

$$x' = \frac{f_{l1} + f_{l2}}{2f'_{c0}} \tag{3.11}$$

$$A = 6.886 - (0.6069 + 17.275\mathrm{r})\, e^{-4.989\gamma} \tag{3.12}$$

$$B = \frac{4.5}{\frac{5}{A}(0.9849 - 0.6306\, e^{-3.8939\gamma}) - 0.01} \tag{3.13}$$

where A and B are factors that determine the increased strength from lateral confinement.

$$\gamma = \frac{f_{l1}}{f_{l2}} \qquad f_{l2} \geq f_{l1} \tag{3.14}$$

$$\varepsilon_{cc} = \varepsilon_{c0}(1 + k_2 * x') \tag{3.15}$$

$k_2 = 5\mathrm{k}_1$ Normal strength transverse reinforcement ($F_y \leq 60$ ksi)

$k_2 = 3\mathrm{k}_1$ High strength transverse reinforcement ($F_y > 60$ ksi)

$$E_c = 185{,}000 * (f'_c)^{\frac{3}{8}} \tag{3.16}$$

The model description by Chang and Mander does not give directions on determining the descending branch parameter for confined concrete. However, the confined concrete model proposed by Mander *et al.* (1988) uses Popovics' (1973) equation for the shape of the concrete

stress-strain diagram. Popovics' equation can be shown to be a constrained version of Tsai's equation [Chang and Mander, 1994]. Using the relationship between Popovics' and Tsai's equations and the concrete model of Mander *et al.* [1988], the descending branch parameter, *r*, of the confined concrete model was determined according to the following:

$$n = \frac{E_c * \varepsilon_{cc}}{f'_{cc}} \tag{3.17}$$

$$r = \frac{n}{n-1} \tag{3.18}$$

3.3 Cyclic Behavior of Confined and Unconfined Concrete

3.3.1 Compression Envelope Curves

The compression envelope shown in Figure 3.5 is defined by the initial slope (E_c), the coordinate of the peak stress (ε'_{cc}, f'_{cc}), Tsai's equation parameters (r and n), and a nondimensional critical strain (x^-_{cr}) to define the spalling strain of the concrete.

Chang and Mander used Tsai's equation in for both the tension and compression envelope curves and can be written in nondimensional form by using the following equations:

$$y(x) = \frac{n\,x}{D(x)} \tag{3.19}$$

$$z(x) = \frac{(1-x^r)}{[D(x)]^2} \tag{3.20}$$

where,

$$D(x) = 1 + (n - \frac{r}{r-1})\,x + \frac{x^r}{r-1} \quad \text{when } r \neq 1 \tag{3.21}$$

$$D(x) = 1 + (n - 1 + \ln x)\,x \quad \text{when } r = 1 \tag{3.22}$$

Let n and x be defined as:

$$n^- = \frac{E_c \varepsilon'_{cc}}{f'_{cc}} \tag{3.23}$$

The spalling nondimensional strain can be calculated using:

$$x_{sp}^{-} = x_{cr}^{-} - \frac{y(x_{cr}^{-})}{n^{-} z(x_{cr}^{-})} \tag{3.24}$$

Where n^{-} is the n value for the compressions curve, f'_{cc} is the peak compressive strength of the concrete, E_c is the initial Young's Modulus for concrete, ε'_{cc} is the strain at peak stress, x^{-}_{cr} is the nondimensional critical strain in compression used to determine the tangent line up to spalling strain, x^{-}_{sp} is the nondimensional spalling strain, ε_c is the concrete strain, $y(x)$ is the nondimensional stress function, and $z(x)$ is the nondimensional tangent modulus function. The stress and tangent Young's Modulus at any strain on the envelope is then given by:

a) For $x^{-} < x^{-}_{cr}$ (Tsai's equation) **(Rule 1)**

$$f_c^{-} = f'_{cc}\, y(x^{-}) \tag{3.25}$$

$$E_t^{-} = E_c\, z(x_{cr}^{-}) \tag{3.26}$$

b) For $x^{-}_{cr} < x^{-} < x^{-}_{cr}$ (Straight Line) **(Rule 1)**

$$f_c^{-} = f'_{cc}[\, y(x_{cr}^{-}) + n^{-} z(x_{cr}^{-})(x^{-} - x_{cr}^{-})] \tag{3.27}$$

$$E_t^{-} = E_c\, z(x_{cr}^{-}) \tag{3.28}$$

c) For $x^{-} > x^{-}_{sp}$ (Spalled) **(Rule 5)**

$$f_c^{-} = E_t^{-} = 0 \tag{3.29}$$

Where E^{-}_{t} is the tangent modulus and f'_{cc} is the concrete stress. After the concrete has spalled, it has zero stress and stiffness from that moment onwards. For confined concrete, a large value of x^{-}_{cr} should be chosen since confined concrete does not spall. The minus signs in Eqs. 3.20-3.26 refer to the compression side of the stress-strain behavior.

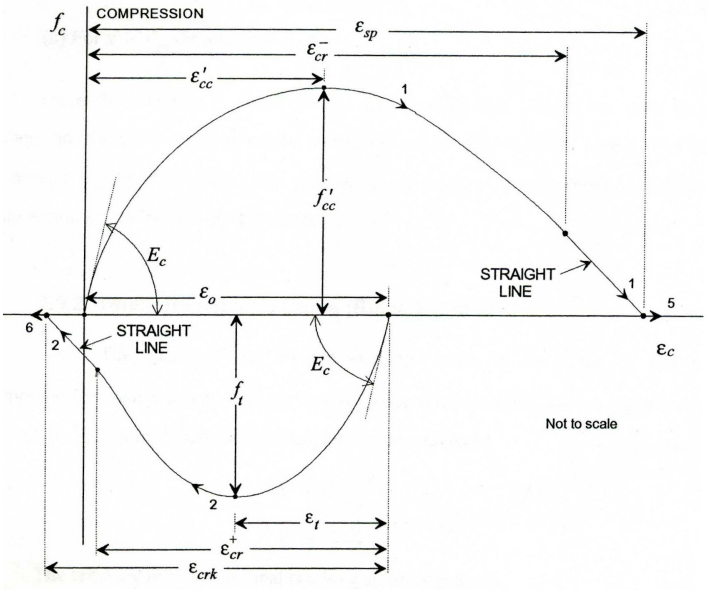

Figure 3.5: Compression and Tension Envelope Curves from Chang and Mander [1994]. (Numerals shown on the figure identify the rule number)

3.3.2 Tension Envelope Curves

Chang and Mander uses the same shape for the tension side of the envelope as for the compression side. Chang and Mander shifts the origin of the tension side by a parameter ε_0; however, this was left out of the implementation in OpenSees because the reason for the shift was not explained. Consequently, the nondimensional parameters are as follows:

$$x^+ = \left| \frac{\varepsilon_c - \varepsilon_0}{\varepsilon_t} \right| \tag{3.30}$$

$$n^+ = \frac{E_c \varepsilon_t}{f_t} \tag{3.31}$$

The cracking nondimensional strain is calculated from the positive critical nondimensional strain by:

$$x_{sp} = x_{cr}^+ - \frac{y(x_{cr}^+)}{n^+ z(x_{cr}^+)} \tag{3.32}$$

The stress and tangent modulus for any strain on the tension envelope are given by:

a) For $x^+ < x^+_{cr}$ (Tsai's equation) **(Rule 2)**

$$f_c^+ = f_t\, y(x^+) \tag{3.33}$$

$$E_t^- = E_c\, z(x^+) \tag{3.34}$$

b) For $x^+_{cr} < x^+ < x^+_{cr}$ (Straight Line) **(Rule 2)**

$$f_c^+ = f_t[\, y(x^+_{cr}) + n^+\, z(x^+_{cr})(x^+ - x^+_{cr})] \tag{3.35}$$

$$E_t^+ = E_c\, z(x^+_{cr}) \tag{3.36}$$

c) For $x^- > x^-_{sp}$ (Spalled) **(Rule 6)**

$$f_c^+ = E_t^+ = 0 \tag{3.37}$$

Where y and z are the same as defined previously for the compression envelope. Once the concrete has cracked it is assumed to have zero tension carrying capacity due to the crack opening. However, gradual crack closure is considered to occur by allowing compression stress to develop immediately upon strain reversal. The gradual crack closure behavior will be discussed later in Section 3.3.4.

3.3.3 Pre-Cracking Unloading and Reloading Curves

The basic elements of the unloading and reloading curves are addressed in this section. Every rule has a smooth curve that starts at a starting point with an initial slope and ends at a second point with a final slope. The curve for the transition in terms of the stresses and strains is as follows:

$$f_c = f_I + (\varepsilon_c - \varepsilon_I)[\, E_I + A\left|(\varepsilon_c - \varepsilon_I)^R\right|] \tag{3.38}$$

$$E_t = E_I + A(R+1)\left|\varepsilon_c - \varepsilon_I\right|^R \tag{3.39}$$

$$R = \frac{E_F - E_{SEC}}{E_{SEC} - E_I} \tag{3.40}$$

$$A = \frac{E_{SEC} - E_I}{\left|\varepsilon_F - \varepsilon_I\right|^R} \tag{3.41}$$

$$E_{SEC} = \frac{f_F - f_I}{\varepsilon_F - \varepsilon_I} \tag{3.42}$$

Where I is the initial value, F is the final value, E_{SEC} is the secant modulus of elasticity, and R and A are equation parameters.

In order to define the cyclic properties of concrete, a number of statistical regressions were carried out on the tests conducted by Sinha, Gerstle and Tulin [1964], Karsan and Jirsa [1969], Spooner and Dougill [1975], Okamoto [1976], and Tanigawa [1979]. The model parameters obtained by Chang and Mander are shown in Figure 3.6, and the results of the regression analysis are as follows:

$$\bar{E}_{SEC} = E_c \left(\frac{\left| \frac{\bar{f}_{un}}{E_c \varepsilon'_{cc}} \right| + 0.57}{\left| \frac{\bar{\varepsilon}_{un}}{\varepsilon'_{cc}} \right| + 0.57} \right) \tag{3.43}$$

$$\bar{E}_{pl} = 0.1 E_c e^{-2\left|\frac{\bar{\varepsilon}_{un}}{\varepsilon'_{cc}}\right|} \tag{3.44}$$

$$\Delta \bar{f} = 0.09 \bar{f}_{un} \sqrt{\left| \frac{\bar{\varepsilon}_{un}}{\varepsilon'_{cc}} \right|} \tag{3.45}$$

$$\Delta \bar{\varepsilon} = \frac{\bar{\varepsilon}_{un}}{1.15 + 2.75 \left| \frac{\bar{\varepsilon}_{un}}{\varepsilon'_{cc}} \right|} \tag{3.46}$$

The derived variables are:

$$\bar{\varepsilon}_{pl} = \bar{\varepsilon}_{un} - \frac{\bar{f}_{un}}{\bar{E}_{SEC}} \tag{3.47}$$

$$\bar{f}_{new} = \bar{f}_{un} - \Delta \bar{f} \tag{3.48}$$

$$\bar{E}_{new} = \frac{\bar{f}_{new}}{\bar{\varepsilon}_{un} - \bar{\varepsilon}_{pl}} \tag{3.49}$$

$$\bar{\varepsilon}_{re} = \bar{\varepsilon}_{un} + \Delta \bar{\varepsilon} \tag{3.50}$$

$$\bar{f}_{re} = \bar{f} \left(\left| \frac{\bar{\varepsilon}_{re}}{\varepsilon'_{cc}} \right| \right) \tag{3.51}$$

$$\bar{E}_{re} = \bar{E} \left(\left| \frac{\bar{\varepsilon}_{re}}{\varepsilon'_{cc}} \right| \right) \tag{3.52}$$

For cyclic behavior in tension, the statistical regression showed that slightly different values should be used for the parameters. Hence, the parameters for the hysteretic response of concrete in tension are given by:

$$E^{+}_{SEC} = E_c \left(\frac{\left| \frac{f^{+}_{un}}{E_c \varepsilon_t} \right| + 0.67}{\left| \frac{\varepsilon^{+}_{un} - \varepsilon_0}{\varepsilon_t} \right| + 0.67} \right) \tag{3.53}$$

$$E^{-}_{pl} = \frac{E_c}{\left| \frac{\varepsilon^{-}_{un} - \varepsilon_0}{\varepsilon_t} \right|^{1.1} + 1} \tag{3.54}$$

$$\Delta f^{-} = 0.15 f^{+}_{un} \tag{3.55}$$

$$\Delta \varepsilon^{-} = 0.22 \varepsilon^{+}_{un} \tag{3.56}$$

Similarly:

$$\varepsilon^{+}_{pl} = \varepsilon^{+}_{un} - \frac{f^{+}_{un}}{E^{+}_{SEC}} \tag{3.57}$$

$$f^{+}_{new} = f^{+}_{un} - \Delta f^{+} \tag{3.58}$$

$$E^{+}_{new} = \frac{f^{+}_{new}}{\varepsilon^{+}_{un} - \varepsilon^{+}_{pl}} \tag{3.59}$$

$$\varepsilon^{+}_{re} = \varepsilon^{+}_{un} + \Delta \varepsilon^{+} \tag{3.60}$$

$$f^{+}_{re} = f^{+} \left(\left| \frac{\varepsilon^{+}_{re}}{\varepsilon_t} \right| \right) \tag{3.61}$$

$$E^{+}_{re} = E^{+} \left(\left| \frac{\varepsilon^{+}_{re}}{\varepsilon_t} \right| \right) \tag{3.62}$$

Where ε_{un} is the unloading strain from the envelope curve, f_{un} is the unloading stress, ε_{pl} is the plastic strain, E_{pl} is the tangent modulus at the plastic strain, f_{new} is the new stress at the unloading strain, E_{new} is the tangent modulus at the unloading strain, and ε_{re}, f_{re}, and E_{re} are respectively the strain, stress, and tangent modulus at the point where the envelope response is rejoined.

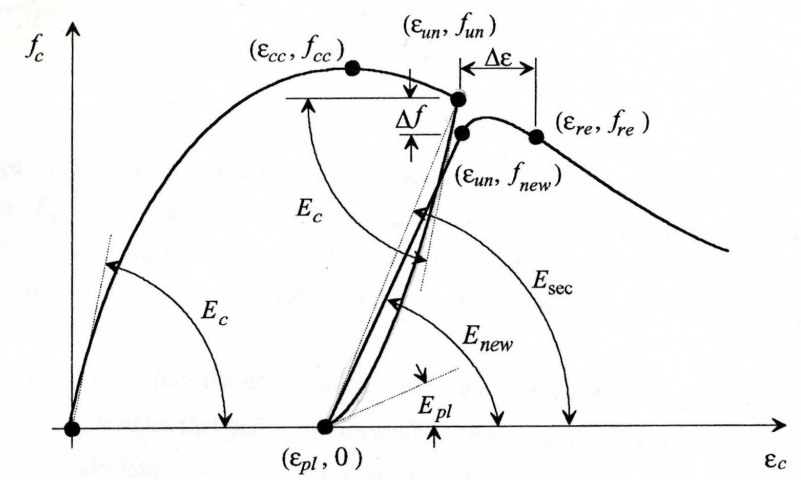

Figure 3.6: Cyclic Properties for Concrete in Compression as per Chang and Mander [1994].

The rules and parameters for the connecting curves for the reversal from compression envelope curve shown in Figure 3.7 are defined as:

$$\begin{aligned} \varepsilon_I &= \varepsilon^-_{un} \\ f_I &= f^-_{un} \\ E_I &= E_c \\ \varepsilon_F &= \varepsilon^-_{pl} \\ f_F &= 0 \\ E_F &= E^-_{pl} \end{aligned} \qquad \textbf{Rule 3} \qquad (3.63)$$

$$\begin{aligned} \varepsilon_I &= \varepsilon^-_{pl} \\ f_I &= 0 \\ E_I &= E^-_{pl} \\ \varepsilon_F &= \varepsilon^+_{un} \\ f_F &= f^+_{new} \\ E_F &= E^+_{new} \end{aligned} \qquad \textbf{Rule 9} \qquad (3.64)$$

$$\varepsilon_I = \varepsilon^+_{un}$$
$$f_I = f^+_{new}$$
$$E_I = E^+_{new} \qquad \textbf{Rule 8} \qquad (3.65)$$
$$\varepsilon_F = \varepsilon^+_{\text{re}}$$
$$f_F = f^+_{\text{re}}$$
$$E_F = E^+_{\text{re}}$$

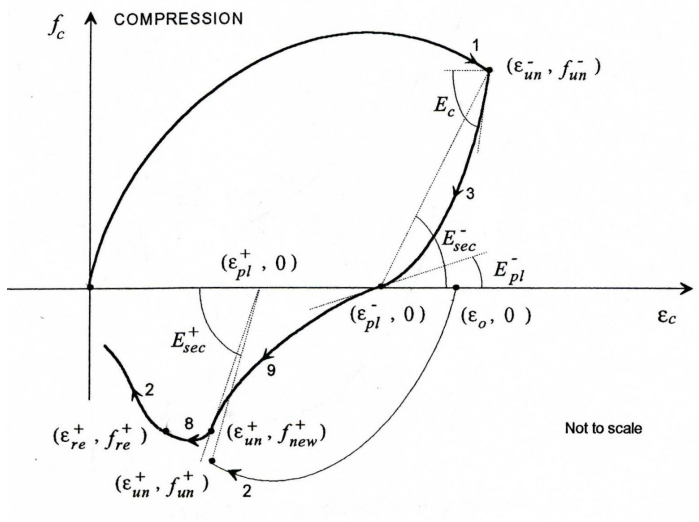

Figure 3.7: Complete Unloading Branch from the Compression Envelope per Chang and Mander [1994]. (Numerals shown on the figure identify the rule number)

Similarly, a reversal from the tension envelope curve, shown in Figure 3.8, is defined by:

$$\varepsilon_I = \varepsilon^+_{un}$$
$$f_I = f^+_{un}$$
$$E_I = E_c \qquad \textbf{Rule 4} \qquad (3.66)$$
$$\varepsilon_F = \varepsilon^=_{pl}$$
$$f_F = 0$$
$$E_F = E^+_{pl}$$

$$\varepsilon_I = \varepsilon^+_{pl}$$
$$f_I = 0$$
$$E_I = E^+_{pl}$$
$$\varepsilon_F = \varepsilon^-_{un}$$
$$f_F = f^-_{new}$$
$$E_F = E^-_{new}$$

Rule 10 (3.67)

$$\varepsilon_I = \varepsilon^-_{un}$$
$$f_I = f^-_{new}$$
$$E_I = E^-_{new}$$
$$\varepsilon_F = \varepsilon^-_{\mathrm{re}}$$
$$f_F = f^-_{\mathrm{re}}$$
$$E_F = E^-_{\mathrm{re}}$$

Rule 7 (3.68)

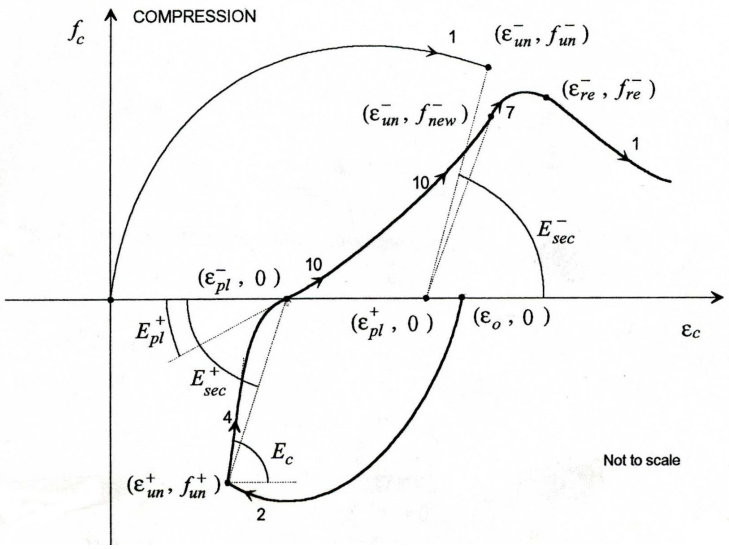

Figure 3.8: Complete Loading Branch Reversed from Tension Envelope per Change and Mander [1994]. (Numerals shown on the figure identify the rule number)

3.3.4 Post-Cracking Unloading and Reloading Curves

After cracking of the concrete is considered to have occurred, the tension capacity is assumed to be zero. Therefore, the tension side of the hysteresis behavior will not exist. Figure 3.9 shows after unloading to the plastic strain (Rule 3), the crack opens (Rule 6), and when the strain reverses and gradual crack closure occurs (Rule 13).

$$\begin{aligned} &\varepsilon_I = \varepsilon_r \\ &f_I = 0 \\ &E_I = 0 \\ &\varepsilon_F = \bar{\varepsilon}_{un} \\ &f_F = \bar{f}_{new} \\ &E_F = \bar{E}_{new} \end{aligned} \qquad \textbf{Rule 13} \qquad (3.69)$$

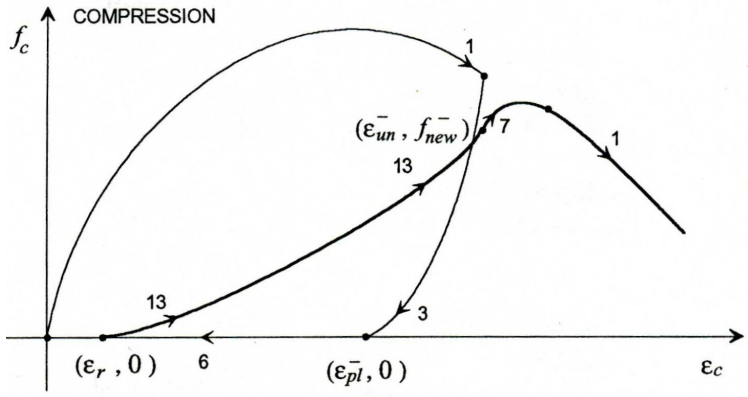

Figure 3.9: Unloading and Reloading Curve in the Post Cracking region per Chang and Mander [1994]. (Numerals shown on the figure identify the rule number)

3.3.5 Pre-Cracking Transition Curves

When a partial loading or unloading from one of the connecting curves occurs, a transition curve is used to move back to another connecting curve. Rules 3, 4, 9, and 10 are all connecting curves, and thus partial loading and unloading on each curve must be considered

separately. Figure 3.10 shows how reversals from Rules 3 and 4 are addressed. When a partial unloading from the compression envelope occurs, a reversal from Rule 3, then f_{new} needs to be changed, and a new stress f_{new^*} is calculated, and the point where the envelope is rejoined ($\varepsilon^-_{re}, f_{re}$) is changed to ($\varepsilon^-_{re^*}, f_{re^*}$). The equations for these modified expressions given by Chang and Mander are:

$$f^-_{\text{new}^*} = f^-_{un} - \Delta f^- \frac{\varepsilon^-_{un} - \varepsilon^-_{ro}}{\varepsilon^-_{un} - \varepsilon^-_{pl}} \tag{3.70}$$

$$E^-_{\text{new}^*} = \frac{f^-_{\text{new}^*} - f^-_{ro}}{\varepsilon^-_{un} - \varepsilon^-_{ro}} \tag{3.71}$$

$$\varepsilon^-_{\text{re}^*} = \varepsilon^-_{un} - \Delta\varepsilon^- \frac{\varepsilon^-_{un} - \varepsilon^-_{ro}}{\varepsilon^-_{un} - \varepsilon^-_{pl}} \tag{3.72}$$

$$f^-_{\text{re}^*} = f^-\left(\left|\frac{\varepsilon^-_{\text{re}^*}}{\varepsilon'_{cc}}\right|\right) \tag{3.73}$$

$$E^-_{\text{re}^*} = E^-\left(\left|\frac{\varepsilon^-_{\text{re}^*}}{\varepsilon'_{cc}}\right|\right) \tag{3.74}$$

The curve for the modified Rule 7 is then given by:

$$\begin{aligned} &\varepsilon_I = \varepsilon^-_{ro} \\ &f_I = f^-_{ro} \\ &E_I = E_c \\ &\varepsilon_F = \varepsilon^-_{un} \\ &f_F = f^-_{\text{new}^*} \\ &E_F = E^-_{\text{new}^*} \end{aligned} \qquad \textbf{Rule 7.1} \quad \left|\varepsilon^-_{ro}\right| \le \left|\varepsilon_c\right| \le \left|\varepsilon^-_{un}\right| \tag{3.75}$$

$$\begin{aligned} &\varepsilon_I = \varepsilon^-_{un} \\ &f_I = f^-_{\text{new}^*} \\ &E_I = E^-_{\text{new}^*} \\ &\varepsilon_F = \varepsilon^-_{\text{re}^*} \\ &f_F = f^-_{\text{re}^*} \\ &E_F = E^-_{\text{re}^*} \end{aligned} \qquad \textbf{Rule 7.2} \quad \left|\varepsilon^-_{un}\right| < \left|\varepsilon_c\right| < \left|\varepsilon^-_{\text{re}^*}\right| \tag{3.76}$$

Similarly, when a reversal from a partial unloading from the tension envelope occurs, reversal from Rule 4, then the $f^+_{\text{new}^*}$ must be determined, and the point at which the tension

envelope is regained $(\varepsilon^{+}_{re*}, f^{+}_{re*})$ must be calculated. The equations to determine these new values are as follows:

$$f^{-}_{new*} = f^{+}_{un} - \Delta f^{+} \frac{\varepsilon^{+}_{un} - \varepsilon^{+}_{ro}}{\varepsilon^{+}_{un} - \varepsilon^{+}_{pl}} \tag{3.77}$$

$$E^{+}_{new*} = \frac{f^{+}_{new*} - f^{+}_{ro}}{\varepsilon^{+}_{un} - \varepsilon^{+}_{ro}} \tag{3.78}$$

$$\varepsilon^{+}_{re*} = \varepsilon^{+}_{un} - \Delta\varepsilon^{+} \frac{\varepsilon^{+}_{un} - \varepsilon^{+}_{ro}}{\varepsilon^{+}_{un} - \varepsilon^{+}_{pl}} \tag{3.79}$$

$$f^{+}_{re*} = f^{+}\left(\left|\frac{\varepsilon^{+}_{re*} - \varepsilon_0}{\varepsilon'_{cc}}\right|\right) \tag{3.80}$$

$$E^{+}_{re*} = E^{+}\left(\left|\frac{\varepsilon^{+}_{re*} - \varepsilon_0}{\varepsilon_t}\right|\right) \tag{3.81}$$

Rule 8 is modified as follows:

$\varepsilon_I = \varepsilon^{+}_{ro}$
$f_I = f^{+}_{ro}$
$E_I = E_c$
$\varepsilon_F = \varepsilon^{+}_{un}$
$f_F = f^{+}_{new*}$
$E_F = E^{+}_{new*}$

Rule 8.1 $\left|\varepsilon^{+}_{ro} - \varepsilon_0\right| \le \left|\varepsilon_c - \varepsilon_0\right| \le \left|\varepsilon^{+}_{un} - \varepsilon_0\right|$ (3.82)

$\varepsilon_I = \varepsilon^{+}_{un}$
$f_I = f^{+}_{new*}$
$E_I = E^{+}_{new*}$
$\varepsilon_F = \varepsilon^{+}_{re*}$
$f_F = f^{+}_{re*}$
$E_F = E^{+}_{re*}$

Rule 8.2 $\left|\varepsilon^{+}_{un} - \varepsilon_0\right| < \left|\varepsilon_c - \varepsilon_0\right| < \left|\varepsilon^{+}_{re*} - \varepsilon_0\right|$ (3.83)

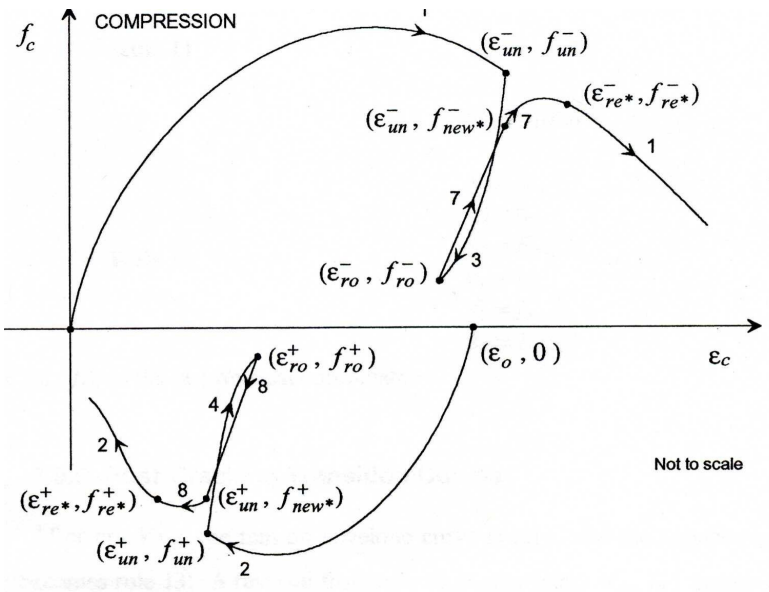

Figure 3.10: Partial Unloading and Reloading from the Tension and Compression Envelope as per Chang & Mander [1994]. (Numerals shown on the figure identify the rule number)

Figure 3.11 shows that reversal from Rule 9 at point A (ε_a, f_a) will target point B (ε_b, f_b) on Rule 10 through Rule 11; incomplete loading on Rule 11 will target point A again through Rule 12. Similarly, reversal from Rule 10 at Point B (ε_b, f_b) will target point A (ε_a, f_a) on rule 9 through Rule 12. The relationship between the target points A and B is expressed by the following:

$$\frac{\varepsilon_a - \varepsilon^-_{pl}}{\varepsilon^+_{un} - \varepsilon^-_{pl}} = \frac{\varepsilon^-_{un} - \varepsilon_b}{\varepsilon^-_{un} - \varepsilon^+_{pl}} \tag{3.84}$$

Rule 11

$$\begin{aligned} \varepsilon_I &= \varepsilon_r \\ f_I &= f_r \\ E_I &= E_c \\ \varepsilon_F &= \varepsilon_b \\ f_F &= f_b \\ E_F &= E_t(\varepsilon_b) \end{aligned} \tag{3.85}$$

$$\varepsilon_I = \varepsilon_r$$
$$f_I = f_r$$
$$E_I = E_c$$
$$\varepsilon_F = \varepsilon_a$$
$$f_F = f_a$$
$$E_F = E_t(\varepsilon_a) \qquad \textbf{Rule 12} \qquad (3.86)$$

where (ε_r, f_r) is the coordinate of the last reversal.

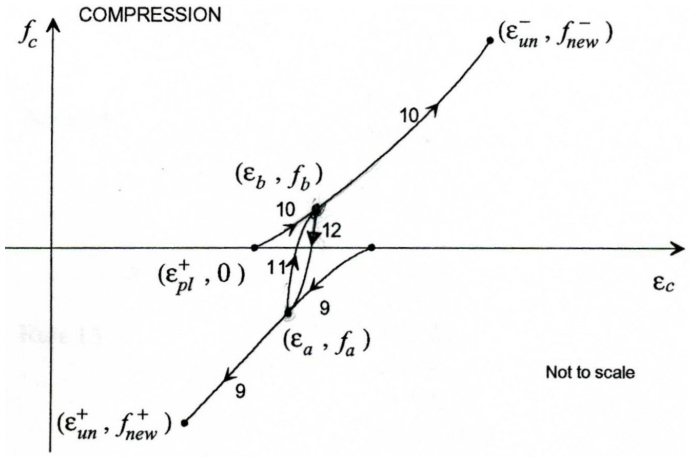

Figure 3.11: Pre-Cracking Transition Curves as per Chang & Mander [1994]. (Numerals shown on the figure identify the rule number)

3.3.6 Post-Cracking Transition Curves

After cracking, the tension envelope follows the x-axis, and the connecting compression curve was Rule 13. Figure 3.12 shows that reversal from Rule 13 at (ε_a, f_a) will target ε_b on the ordinate axis. The target strain, ε_b, is calculated by the following:

$$\varepsilon_b = \varepsilon_a - \frac{f_a}{E_{SEC}^{-}} \qquad (3.87)$$

$$\begin{aligned} \varepsilon_I &= \varepsilon_r \\ f_I &= f_r \\ E_I &= E_c \\ \varepsilon_F &= \varepsilon_b \\ f_F &= 0 \\ E_F &= 0 \\ \varepsilon_I &= \varepsilon_r \end{aligned} \qquad \textbf{Rule 14} \qquad (3.88)$$

$$\begin{aligned} f_I &= f_r \\ E_I &= E_c \\ \varepsilon_F &= \varepsilon_a \\ f_F &= f_a \\ E_F &= E_t(\varepsilon_a) \end{aligned} \qquad \textbf{Rule 15} \qquad (3.89)$$

Where (ε_r, f_r) is the coordinate of the last reversal.

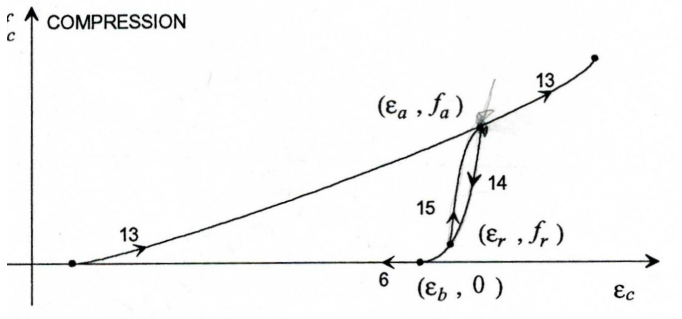

Figure 3.12: Post-Cracking Transition Curves as per Chang & Mander [1994]. (Numerals shown on the figure identify the rule number)

Figure 3.13 summarizes how the rules presented in this section are related. The tension side of the curve has been enlarged for clarity. Figure 3.13 shows all the rules that are defined by Chang and Mander. However, all of these rules are not available at any one time. Rules 2, 4, 6, 8, 8.1, 8.2, 9, 10, 11, 12 are only occur prior to cracking, and Rules 13, 14, 15 only occur after cracking of the model has occurred.

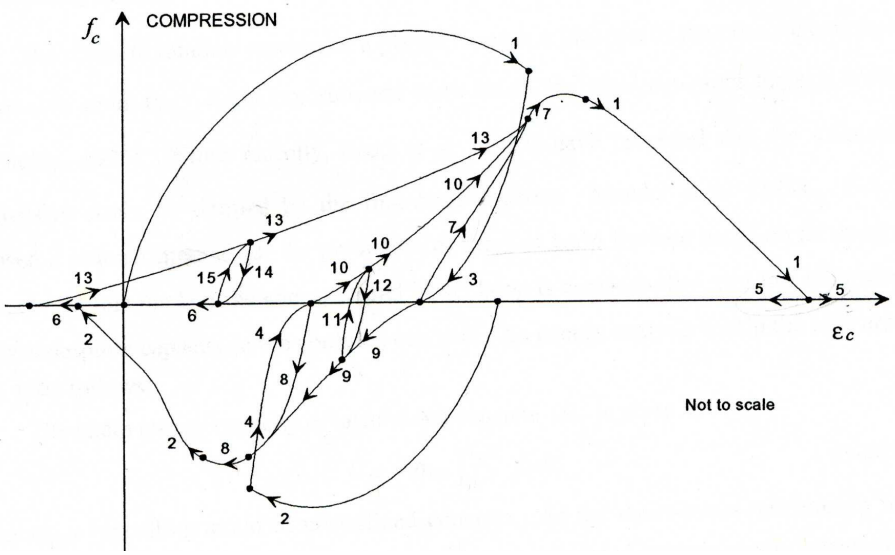

Figure 3.13: Behavior of concrete Model Proposed by Chang & Mander [1994]. (Numerals shown on the figure identify the rule number)

3.4 Challenges with Implementing Chang and Mander's Concrete Model.

Implementing Chang and Mander's concrete model in OpenSees as presented in the previous section exhibited some challenges in the model. This section summarizes the challenges encountered, how they were addressed, and the modifications that were made to the rules presented in the previous sections.

3.4.1 Numerical Stability of the Unloading and Reloading Function

The curve that was used in the original model for the shape of the connecting and transition curves was chosen so that it starts from an initial point (x_0,y_0) with an initial slope (E_0) and ends at a point (x_f,y_f) with a final slope (E_f). The algebraic equation that was selected for the connecting and transition curves had the following general form:

$$y = y_0 + E_0(x - x_0) + A(x - x_0)^B \qquad (3.90)$$

Applying the conditions that at $x = x_0$, $y = y_f$ and $E = E_f$, Eq. 3.90 can be rewritten into the following form:

$$y = y_0 + (x - x_0)[E_0 + A|x - x_0|^R] \quad (3.91)$$

$$y' = E_0 + A(R-1)|x - x_0|^R \quad (3.92)$$

where,

$$R = \frac{E_f - E_{SEC}}{E_{SEC} - E_0} \quad (3.93)$$

$$A = \frac{E_{SEC} - E_0}{|x_f - x_0|^R} \quad (3.94)$$

$$E_{SEC} = \frac{y_f - y_0}{x_f - x_0} \quad (3.95)$$

If E_{SEC} is very close to the value of E_0, then the denominator of the Eq. 3.93 becomes a very small number and the value of R becomes very large. Parameter *A* becomes impossible to calculate because the difference between the x values is less than one and when raised to a large power, it becomes nearly zero. This problem only occurs when E_{SEC} is approximately equal to E_0; if this is the case, then the curve should be represented as a straight line. A straight line occurs when *R* takes a value of zero.

In order to address this problem, a number of "if" statements were added prior to parameter *A* being calculated. The "if" statement set R = 0 when any of the following conditions are true.

i) $0.985 \leq E_{SEC}/E_0 \leq 1.015$

ii) $0.9999 \leq x_f/x_0 \leq 1.0001$

iii) $R > 50$

The second statement noted above covers the case of a small strain increment that causes E_{SEC} to become a large number due to a small denominator. The last condition on R greater than 50 was selected based on the values of parameter *A* during testing of the code. With this change, the stability of the unloading and reloading curves were improved, which was confirmed by performing the analysis of RW2 to ensure the performance of the concrete model.

3.4.2 Strain Reversals Not Considered in Original Description

In a general program, the strain can reverse direction at any time; however, a reversal from Rules 7, 7.1, 7.2, 8, 8.1, and 8.2 was not discussed by Chang and Mander. To ensure convergence and that the program will not stall, rules for these reversals must be defined.

Reversals from Rules 7, 7.2, 8, and 8.2 are handled as if the reversal occurred from the envelope. Rule 3 is followed for reversals from Rules 7 and 7.2 and Rule 4 for reversals from Rules 8 and 8.2. Since Rules 7, 7.2, 8, and 8.2 handle rejoining the envelope response, the rules for unloading from the envelope were felt to be the most appropriate behavior.

A reversal occurring after a partial unloading and reloading cycle was also not considered by the original model. If the model follows Rule 7.1 or 8.1 and a strain reversal occurs, no guidance is given for the unloading path. These reversals are handled by returning on a straight line to the point on Rule 3 where Rule 7.1 started if the reversal occurs from Rule 7.1. Similarly, Rule 4 was used if the reversal occurs from Rule 8.1. Once the unloading reaches Rule 3 or 4, Rule 3 or 4 is followed as defined in Section 3.3.3.

3.5 Model Verification

To provide further verification to the models, four types of confined concrete blocks were constructed and tested in cyclical compression. Although, this attempt was generally unsuccessful, a brief documentation of this effort is included to provide useful information for others interested in similar tests.

The test blocks measured 6 in. wide by 10 in. long, and three of the four types of blocks were 10 in. tall, while one was 5 in. tall. The volumetric ratio of the transverse reinforcement was varied among the blocks. Three of four types had #2 deformed bars spaced at 2.5 in. o.c., while the other type of block had a lower level of transverse reinforcement with #2 hoops at 3.25 in. o.c. The details of the four block types are shown in Figure 3.14. Types 1, 2, and 4 had the same transverse reinforcement ratio; while type 3 had a lower amount of transverse reinforcement. Type 1 blocks had #2 vertical bars in the four corners of the hoops. These vertical bars were greased to prevent them from bonding to the concrete and adding to the axial

strength of the block allowing them to only participate in providing confinement to the concrete. Strain gages were placed on the vertical bars to determine if they were participating in the axial resistance. Type 2 blocks were the same size as Type 1; however, the longitudinal reinforcement was removed. Type 4 blocks were half the height of the Type 1 and 2 blocks to investigate the influence of the size of the specimen on the results. The Type 1 and 2 blocks were intended to determine the influence of the longitudinal reinforcement on the confinement of the section. Type 4 was expected to provide the influence of size of the specimen to be investigated, while Type 3 intended to examine the confined effects for two levels of transverse reinforcement. The blocks were tested in strain control to verify the loading and unloading characteristics of the model. Figures 3-15 and 3-16 show the load frame setup used for testing the concrete blocks. The actuator and load cell were offset from the test specimen because neither the load cell nor the actuator had the expected capacity of the confined concrete blocks. Each block was instrumented by mounting a DCDT on each face of the specimen. The movement of two rods embedded in the concrete block was measured to determine the approximate strain on each side. The gauge length for the strain measurements was approximately 2.5 in.

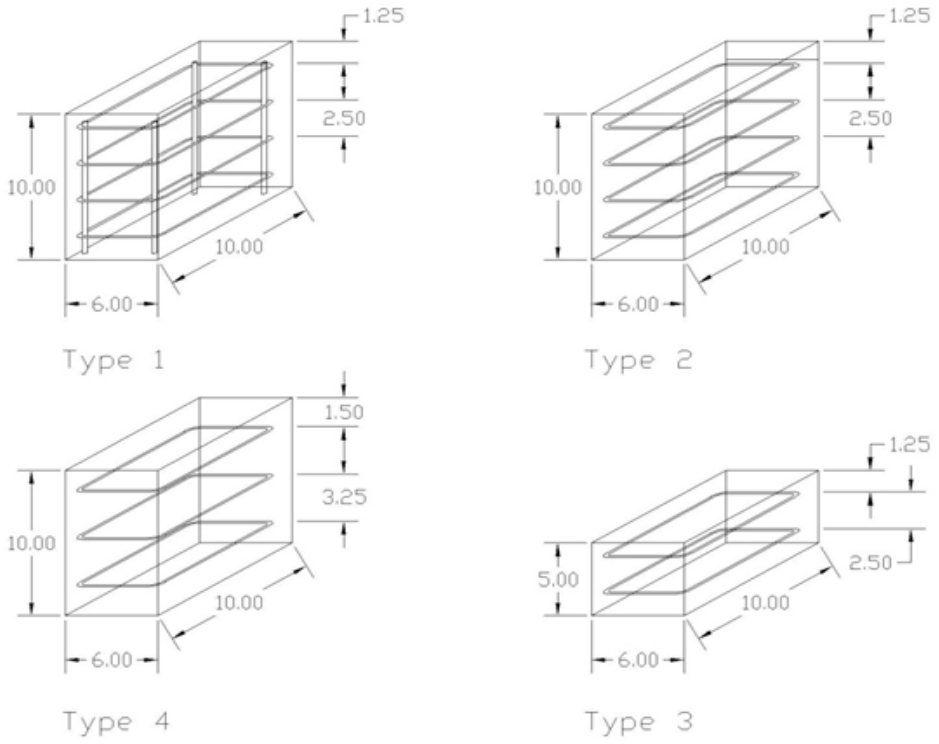

Figure 3.14: Reinforcement Details of Concrete Blocks

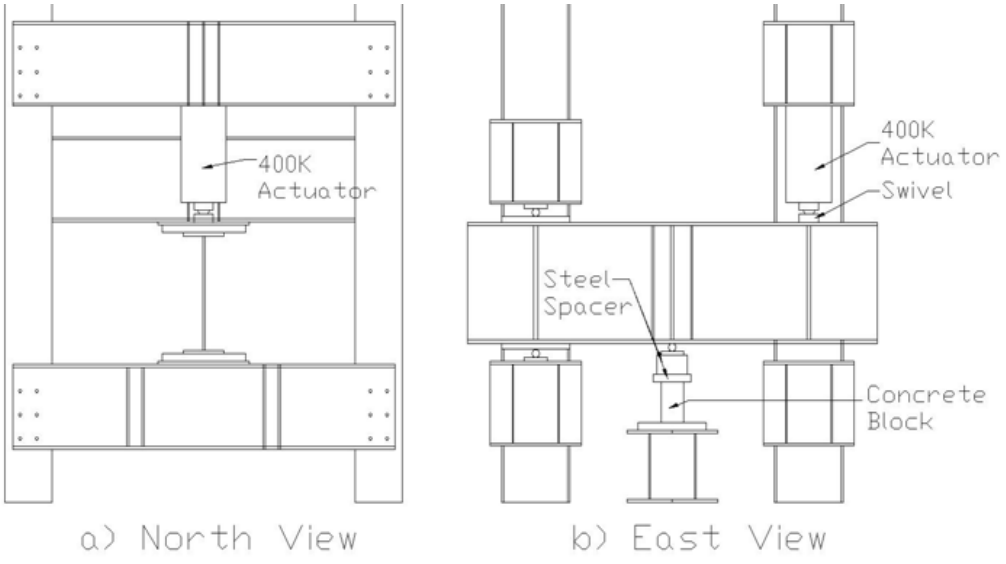

Figure 3.15: Testing Frame Setup

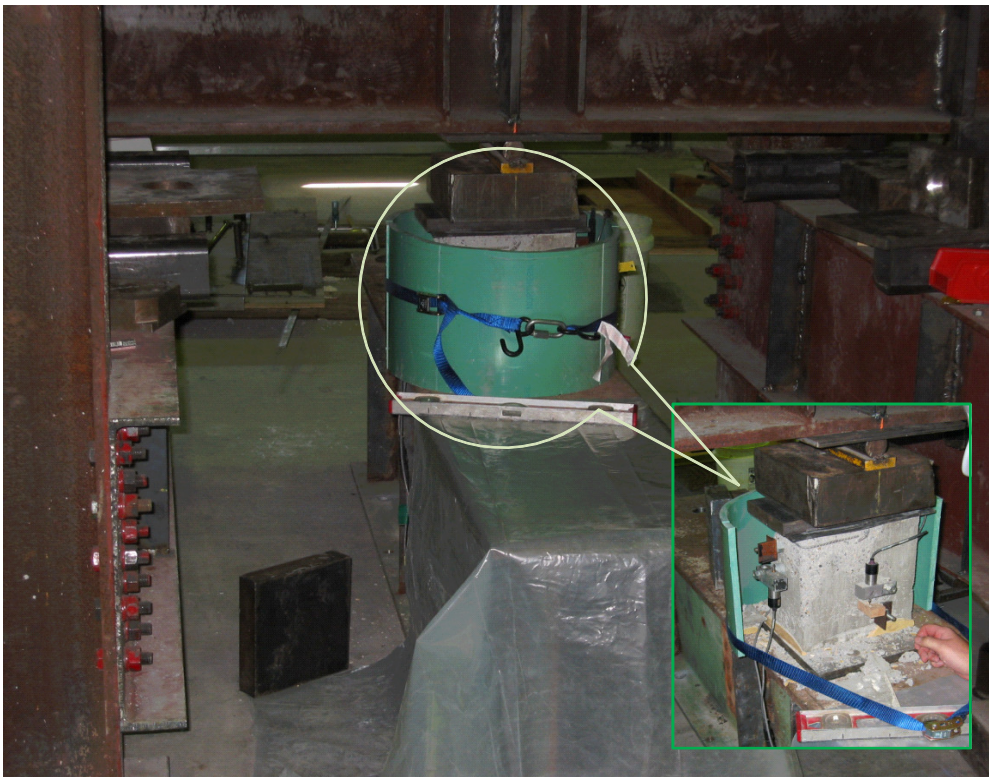

Figure 3.16: Testing Frame Used for Concrete Blocks

In the test setup shown in Figures 3-15 and 3-16, the load on the specimen was twice the load registered by the load cell. However, the test setup caused problems due to curvature of the load beam as well as the inability to ensure uniform stress on the block once cracking occurred as a result of concrete dilation. At the start of the test, the strains measured on each face were approximately equal; however, once cracking occurred in the specimen, the strains were not equal on each face. The four strains measured on one specimen after cracking were -0.0025, 0.0007, -0.006, and -0.005. The unequal strains were due to eccentric loading on the specimen, causing it to experience axial and flexural actions about both axises. However, because of the bending moment the specimens during testing, the data could not provide confirmation of the cyclic behavior of the confined concrete model beyond the validation conducted by Chang and Mander in their original 1994. Additionally, the peak strength was significantly below the expected value from the confined model. The average stress-strain data did show that the

envelope, unloading, and reloading curves follow the shape given by Chang and Mander, see Figure 3.17. Further validation of the concrete model cannot be provided beyond that shown by Chang and Mander.

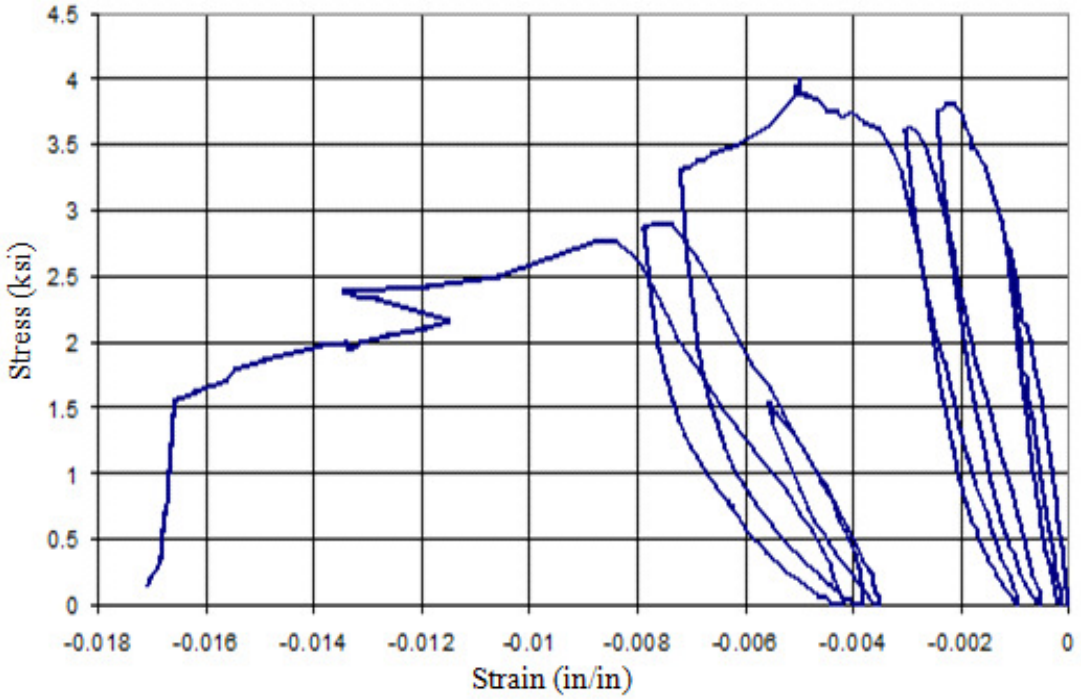

Figure 3.17: Cyclic Behavior of Confined Concrete Blocks

3.6 Simplified Concrete Model

The concrete model described previously was shown to be an adequate by Chang and Mander [1994]. However, the nonlinear nature of the loading and unloading curves can require a number of iterations to converge to solution at the section level. In a large, complex model, the extra iterations can add significantly to the computation time required for the analysis. After implementing the original concrete model of Chang and Mander in OpenSees and experiencing significant time required for convergence of the solution due to the use of this model, a simplified model was created from the original model that would reduce the number of iterations required to achieve the converged state.

The simplified model uses a trilinear approximation to represent the smooth curve used for the loading and unloading portions. The model is assumed to return to the compression or tension envelope at the point where it left. Figure 3.18 shows the trilinear approximation used for the connecting curves. The critical strain for the trilinear relationship is defined in Eq. 3.96, using the following terms: stress, strain, and slope terms used in the original Chang and Mander model

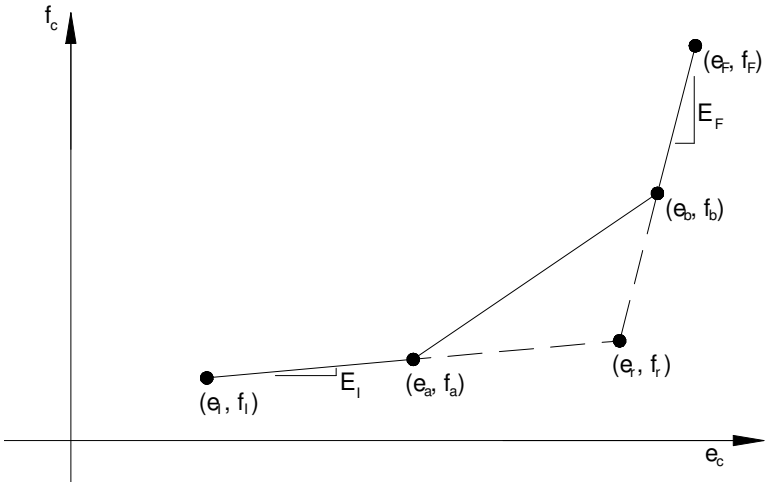

Figure 3.18: Trilinear Approximation used for Loading and Unloading in the Simplified Model

$$\varepsilon_r = \frac{(E_I * \varepsilon_I - E_F * \varepsilon_F - f_I + f_F)}{E_I - E_F} \tag{3.96}$$

If the strain is less than the average of ε_r and ε_I, see Figure 3.18, then the stress is calculated from the initial stress, strain, and slope. If the strain is greater than the average of ε_r and ε_F, then the stress is calculated from the final stress, strain, and slope. The third line section connects the endpoints of the the initial and final line sections.

The initial and final strain, stress, and slopes for the rules in the simplified model are the same as those defined in Section 3.3 However, Rules 7, 7.2, 8, and 8.2 were removed in the simplified model, allowing the model to rejoin the envelope at the same strain where it had previously unloaded from. Removing Rules 7, 7.2, 8, and 8.2 requires modifications to Rules 9,

10, and 13 in order to change their endpoint to a point on the tension or compression envelope. Accordingly,

$$\begin{aligned} \varepsilon_I &= \varepsilon_{pl}^- \\ f_I &= 0 \\ E_I &= E_{pl}^- \\ \varepsilon_F &= \varepsilon_{un}^+ \\ f_F &= f_{un}^+ \\ E_F &= E_{new}^{+*} \end{aligned} \qquad \textbf{Rule 9} \qquad (3.97)$$

$$\begin{aligned} \varepsilon_I &= \varepsilon_{pl}^+ \\ f_I &= 0 \\ E_I &= E_{pl}^+ \\ \varepsilon_F &= \varepsilon_{un}^- \\ f_F &= f_{un}^- \\ E_F &= E_{new}^{-*} \end{aligned} \qquad \textbf{Rule 10} \qquad (3.98)$$

where,

$$E_{new}^{-*} = \frac{f_{un}^-}{\varepsilon_{un}^- - \varepsilon_{pl}^-} \qquad (3.99)$$

$$E_{new}^{+*} = \frac{f_{un}^+}{\varepsilon_{un}^+ - \varepsilon_{pl}^+} \qquad (3.100)$$

Rule 13 uses the power curve proposed by Chang and Mander with the following rules to prevent the numerical instability discussed previously in Section 3.4.1.

i) $0.985 \leq E_{SEC}/E_0 \leq 1.015$

ii) $0.9999 \leq x_\beta/x_0 \leq 1.0001$

iii) $R > 80$

If any of the above conditions is found to be true, then the trilinear connecting curve is used in place of the power function suggested by Chang and Mander. With the trilinear approximation, Rule 13 was:

$$\begin{aligned} \varepsilon_I &= \varepsilon_r \\ f_I &= 0 \\ E_I &= 0.25 * E_{SEC} \end{aligned}$$

$$\varepsilon_F = \varepsilon_{un}^{-} \qquad \textbf{Rule 13} \qquad (3.101)$$
$$f_F = f_{un}^{-}$$
$$E_F = E_{new}^{-*}$$

where E_{SEC} is as defined in Eq. 3.31. The $0.25E_{SEC}$ for E_I was based on the observed response when the numerical instability occurred. Otherwise if numerical the above conditions are false, Rule 13 is defined with the following parameters:

$$\varepsilon_I = \varepsilon_r$$
$$f_I = 0$$
$$E_I = 0.0$$
$$\varepsilon_F = \varepsilon_{un}^{-} \qquad \textbf{Rule 13} \qquad (3.102)$$
$$f_F = f_{un}^{-}$$
$$E_F = E_{new}^{-*}$$

Rules 7.1, 8.1, 11, 12, 14, and 15 are all replaced with straight lines. are defined below:

$$E = \frac{f_{un}^{-} - f_{ro}^{-}}{\varepsilon_{un}^{-} - \varepsilon_{ro}^{-}} \qquad \textbf{Rule 7.1} \qquad (3.103)$$
$$f = E * (\varepsilon - \varepsilon_{ro}^{-}) + f_{ro}^{-}$$

$$E = \frac{f_{un}^{+} - f_{ro}^{+}}{\varepsilon_{un}^{+} - \varepsilon_{ro}^{+}} \qquad \textbf{Rule 8.1} \qquad (3.104)$$
$$f = E * (\varepsilon - \varepsilon_{ro}^{+}) + f_{ro}^{+}$$

$$E = \frac{f_b - f_r}{\varepsilon_b - \varepsilon_r} \qquad \textbf{Rule 11} \qquad (3.105)$$
$$f = E * (\varepsilon - \varepsilon_r) + f_r$$

$$E = \frac{f_a - f_r}{\varepsilon_a - \varepsilon_r} \qquad \textbf{Rule 12} \qquad (3.106)$$
$$f = E * (\varepsilon - \varepsilon_r) + f_r$$

where ε_b and ε_a are calculated using Eq. 3.84.

$$E = \frac{0.0 - f_r}{\varepsilon_b - \varepsilon_r}$$
$$f = E * (\varepsilon - \varepsilon_r) + f_r \qquad \textbf{Rule 14} \qquad (3.107)$$

$$E = \frac{f_a - f_r}{\varepsilon_a - \varepsilon_r}$$
$$f = E * (\varepsilon - \varepsilon_r) + f_r \qquad \textbf{Rule 15} \qquad (3.108)$$

where

$$\varepsilon_b = \varepsilon_r - \frac{f_r}{E_{SEC}^-} \qquad (3.109)$$

where ε_a and E_{SEC}^- are as defined in Eq. 3.84 and 3.43. Figure 3.19 shows the loading and unloading rules for the simplified concrete model. This Figure is equivalent to Figure 3.13.

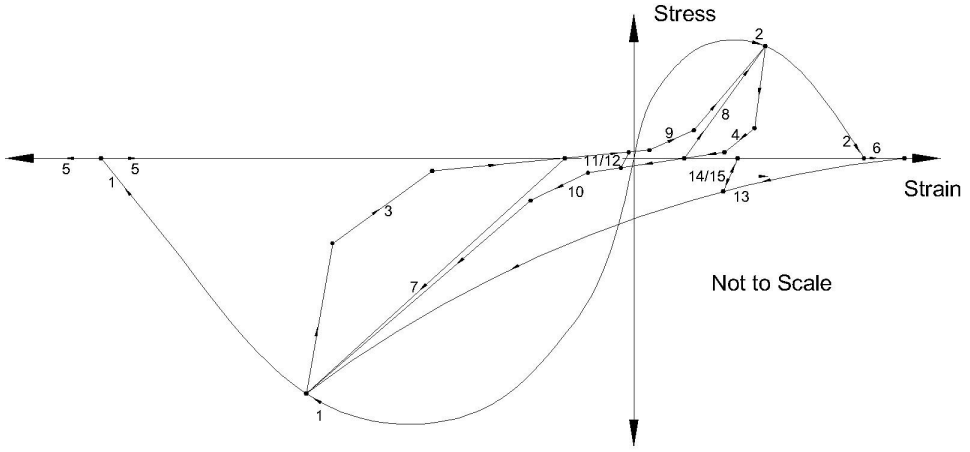

Figure 3.19: Cyclic Behavior of Simplified Chang and Mander Concrete Model. (Numerals shown on the figure identify the rule number)

3.7 Verification of the Simplified Model

The effect of the simplified Chang and Mander model on the overall structural response needs to be examined. The structure chosen for this comparison was the second of the two

rectangular walls, RW2 tested by Thomsen and Wallace (1993) shown earlier in Figure 3.1. The cyclic response of RW2 from OpenSees using the simplified concrete model is shown in Figure 3.20. The deficiencies seen in Figure 3.3 are not present in Figure 3.20. The residual displacement and reloading stiffness are well simulated. The kinking seen near zero displacement that was observed in Figure 3.3 is not present due to the gradual crack included in the simplified Chang and Mander concrete model.

The difference in the stiffness of the response at low displacement levels is due to shear deformation not being included in the analytical model. Fiber-based elements in OpenSees do not account for shear deformation, and in order to better observe the effect of the concrete model, the shear deformation was left out. If shear deformation effects are included in the model, the monotonic envelope is well simulated. This is shown in Figure 3.21 that confirms inclusion of shear deformation accurately simulates the force-displacement response of RW2 at all displacement levels. Cyclic simulation of RW2 including shear deformation was not conducted because there was not a good material model available to simulate the cyclic shear-distortion of the wall.

Both the simplified model and the original Chang and Mander model were used to model RW2 to determine the effect the simplifications had on the overall response of a structure. Figure 3.22 showed that the simplified model simulates the response as well as the original Chang and Mander models for the loading and unloading stiffnesses, and lateral force resistance. The two models show slightly difference responses near zero lateral force due to how the numerical instability of Rule 13 are handled in the two models. Overall, the simplifications had little effect of the simulation, but significantly increased the computational efficiency.

Due to the improved simulation of wall behavior seen in the simulation of RW2, the simplified concrete material model was submitted to the OpenSees community and was included in version 1.7.4 as Concrete07. The model has already been used by researchers at several universities, who are engaged in analytical simulation of the nonlinear behavior of concrete structures using OpenSees.

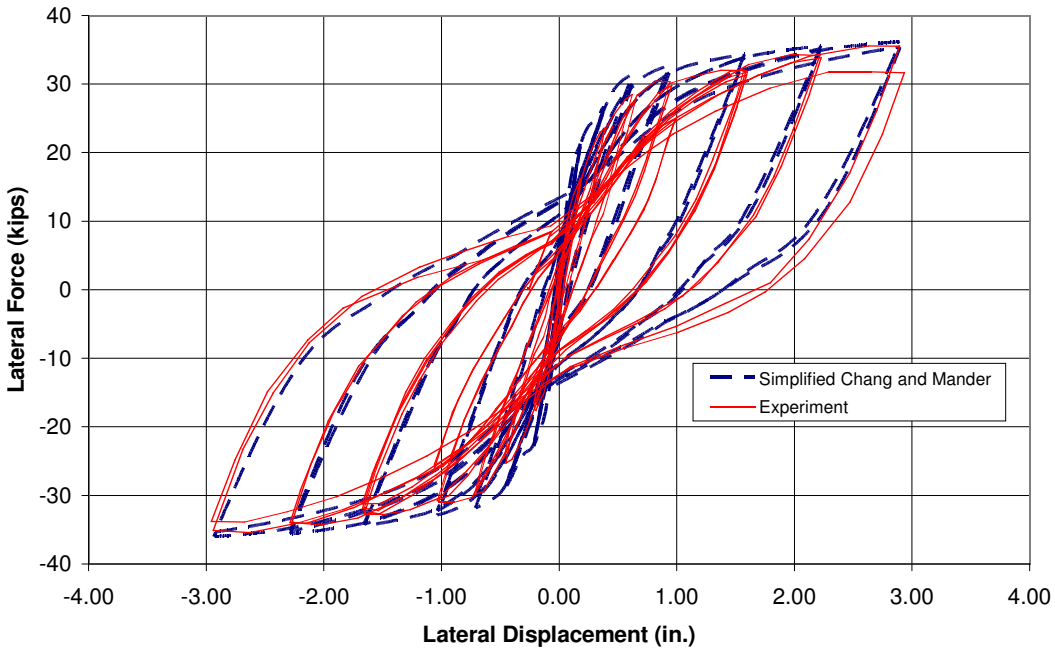

Figure 3.20: RW2 Cyclic Response Comparison using Simplified Chang and Mander Concrete Material Model.

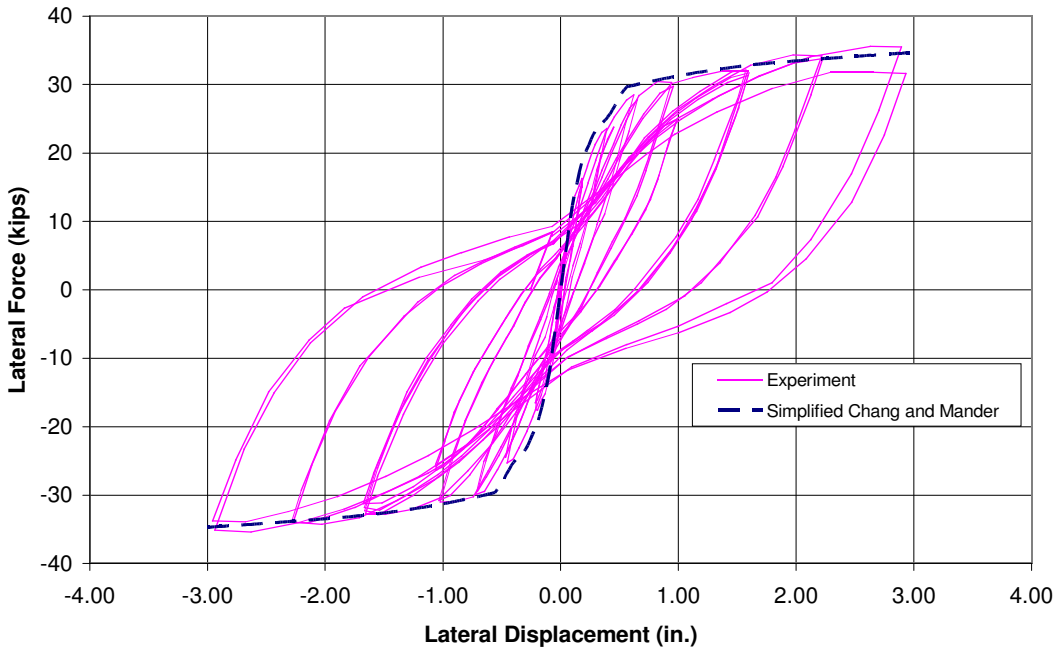

Figure 3.21: Monotonic Envelope Including Shear Deformations

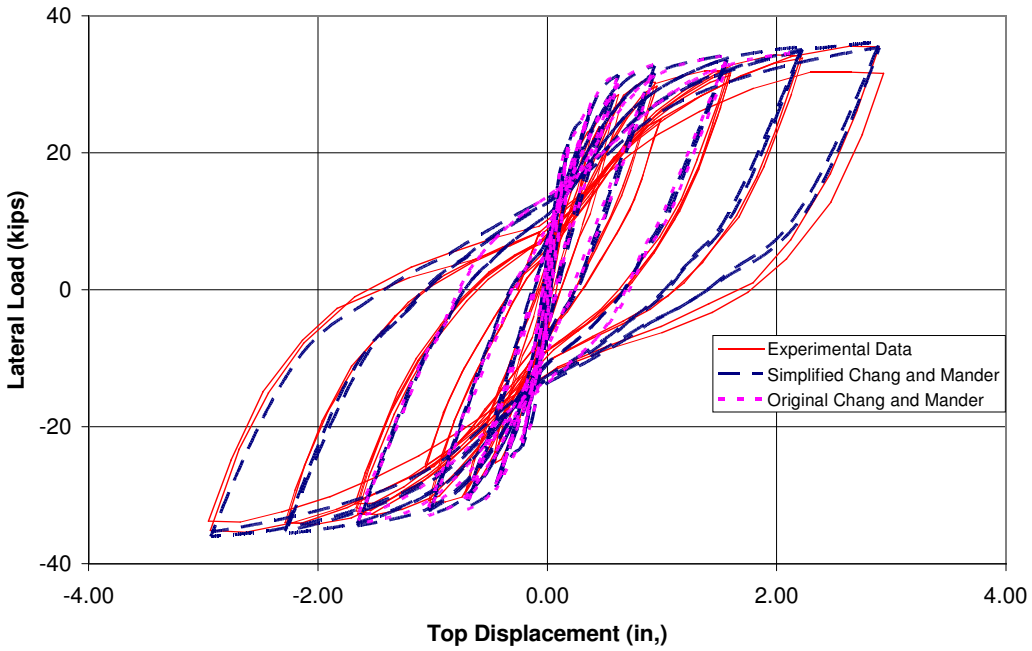

Figure 3.22: Cyclic Response Comparison using Original and Simplified Chang and Mander Concrete Models.

Chapter 4
Analysis of Rectangular Concrete Walls

4.0 Introduction

As previously noted, the experimental part of this collaborative PreNEESR project included characterization of lateral load behavior of reinforced concrete structural walls at the MAST Laboratory of the University of Minnesota. As part of this collaborative effort, three structural walls with rectangular cross section and two walls with T-shaped cross section were tested. The rectangular walls were subjected to in-plane cyclic loads, whereas the T-walls were subjected to multi-directional loading. Presented in this chapter are the theoretical characterizations of the rectangular walls using fiber-based beam-column elements, while the Chapters 5 and 6 present the same for the two T-walls (i.e. NTW1 and NTW2). The three rectangular walls were identical, except for the fact that they used different anchorage details for the longitudinal reinforcement at the wall-to-foundation interface. These tests were conducted as part of the investigation of the behavior of T-shaped concrete walls and were motivated to understand the impact of different anchorage details on the response of the T-walls. In practice, concrete walls are designed with conventional lap splices at the base of the walls (ACI 318, 2002), whereas experimental research on walls has typically eliminated any splices as this detail often influences the response of concrete walls. Consequently, the rectangular walls were designed to examine the influence of following three different details at the base of the walls: 1) continuous longitudinal reinforcement without any splices 2) couplers and 3) code-based conventional lap splices. When detailing the walls, two different boundary elements were used such that the wall response in the two different in-plane directions would correspond to the flange in tension and flange in compression response of a T-wall loaded in the web direction (Johnson, 2007). All three rectangular walls were subjected to cyclic loading with full reversals. Analytical Investigation of all walls was conducted using the OpenSees software (OpenSees 2007). In addition to presenting a summary of the tests, this chapter presents the analytical responses of the rectangular walls with comparison to experimental results wherever possible. To ensure that the analytical model satisfactorily captures measured response, both global and local

parameters, as well as different displacement components are compared. Failure to do this may inadequately validate analytical model since compensation of error may lead to satisfactory structural response at global level as demonstrated by Sritharan et al. (2000)

4.1 Description of Test Walls

The rectangular concrete walls used in this study were designed to replicate the web direction response of a 50% scale prototype T-wall designed for a six story building located in Los Angeles, CA. The details of the prototype T-wall and the six-story prototype building are presented in Chapter 5. Details of the design computations of the prototype T-wall can be found in Narina (2007) and Johnson (2007).

The first wall specimen used continuous longitudinal reinforcement from the footing to the top of the wall, which was identified as RWN (where "RW" represents rectangular wall while "N" stands for no splicing). The second wall specimen used mechanical couplers to splice the longitudinal reinforcement near the wall-to-foundation interface; which was referred to as RWC (where "C" stands for coupler). The third wall specimen used conventional lap splices near the wall-to-foundation interface, which was identified as RWS (where "S" stands for splices). The dimensions and the reinforcement details of the rectangular walls were chosen to closely match the strength of the 50% scaled prototype T-wall in the web direction. The reinforcement in the rectangular walls was designed to ensure that the flexural strain gradient along the wall height and the inelastic curvature at the base will be comparable to that of the T-wall in the flange in tension and flange in compression under web direction loading. This design requirement caused the rectangular walls to have unsymmetrical amounts and distribution of longitudinal steel in the boundary elements. Complete details about the design considerations adopted for the rectangular walls can be found in Johnson (2007).

As shown in Figures 4.1 and 4.2, all three rectangular concrete walls were 254 in. tall, 90 in. long and 6 in. thick. Since these walls were designed to match the moment resistance of a T-wall, they consisted of two different boundary elements: one with #6 (d_b = 0.75 in., where d_b is the bar diameter) and #5 (d_b = 0.625 in.) longitudinal bars, the other with #9 (d_b = 1.125 in.) longitudinal bars. Consequently, the two boundary elements were referred to as No. 6 boundary element and No. 9 boundary element respectively. Between the boundary elements, #4 (d_b = 0.5

in.) longitudinal bars were distributed at 18 in. of spacing. The distributions of the longitudinal reinforcement for the three walls are seen in Figure 4.1 and Figure 4.2.

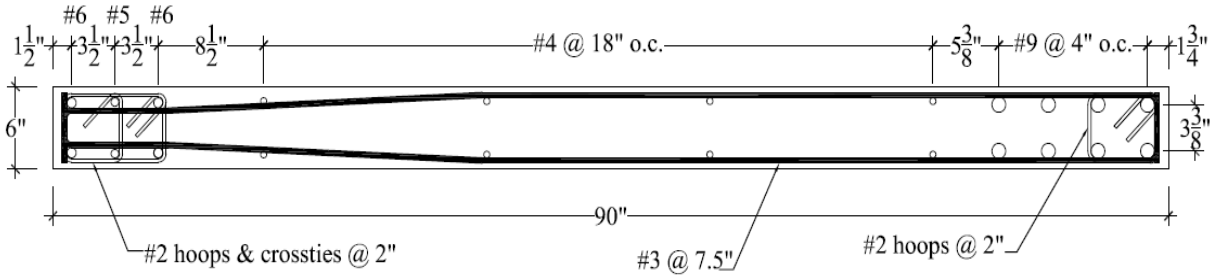

a) RWN with no splices in the longitudinal reinforcement

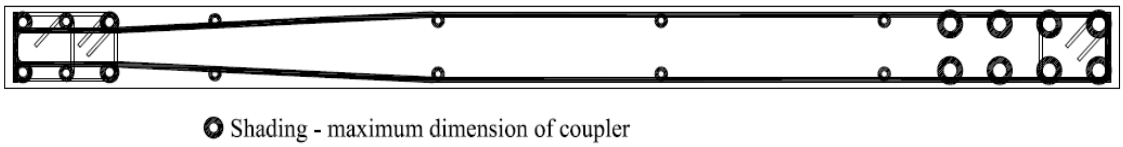

b) RWC with mechanical couplers at the foundation interface

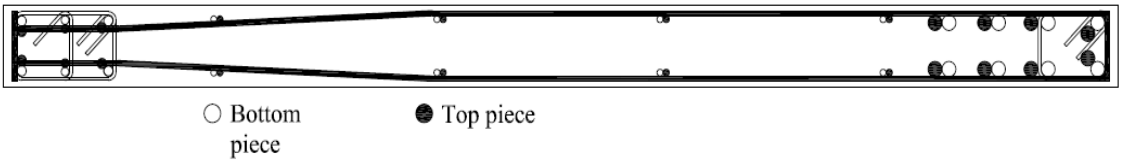

c) RWS with traditional lap splices near the wall base

Figure 4.1 Reinforcement details of the three rectangular walls.

Both boundary elements were also designed with #2 (d_b= 0.25 in.) hoops spaced at 2 in. over the bottom 90 in. of the wall as confinement reinforcement. Since, #2 bars were not readily available, the confinement hoops were made from ASTM A496 D-5 deformed wire. The boundary elements lengths were determined based on the ACI 318-02 requirements (2002). The potential for shear failure to occur in the rectangular walls prior to the development of full flexural moment resistance was avoided in design by adequately designing the shear reinforcement according to the requirements of ACI 38-02 design code, which led to #3 (d_b = 0.75 in.) horizontal bars in the walls spaced at 7.5 in. for the entire height. For splicing of longitudinal bars in RWC, type-2 mechanical couplers (as defined in section 21.1.6 of ACI 318-

02 code) manufactured by Headed Reinforcement Corporation (HRC) (http://www.hrc-usa.com) were used at the wall-to-foundation interface. All mechanical couplers in RWC were located just above the interface (see Figure 4.3). RWS used "Class B" lap splices (lap length is equal to 1.3 times the tensile development length calculated according to 12.2.2 or 12.2.3 of ACI 318-02 code), which were designed according to the ACI-318 (2002) at the interface. The foundation block of each wall was 21 in. tall and provided required anchorage depth for the longitudinal reinforcement. A strut and tie design method according to ACI 318-02 was used for the foundation design to reduce reinforcement congestion (Johnson 2007).

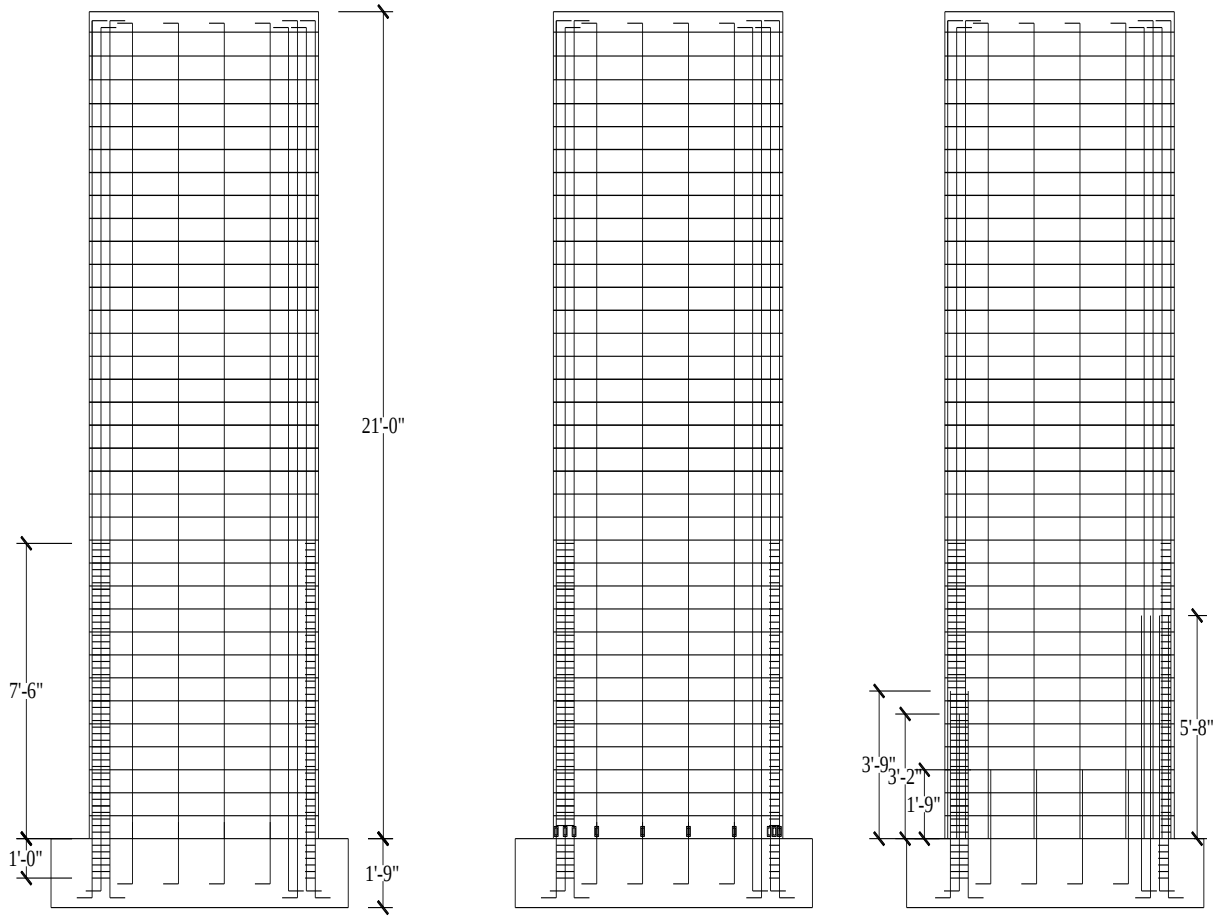

Figure 4.2 Reinforcement details along the wall height in the rectangular walls.

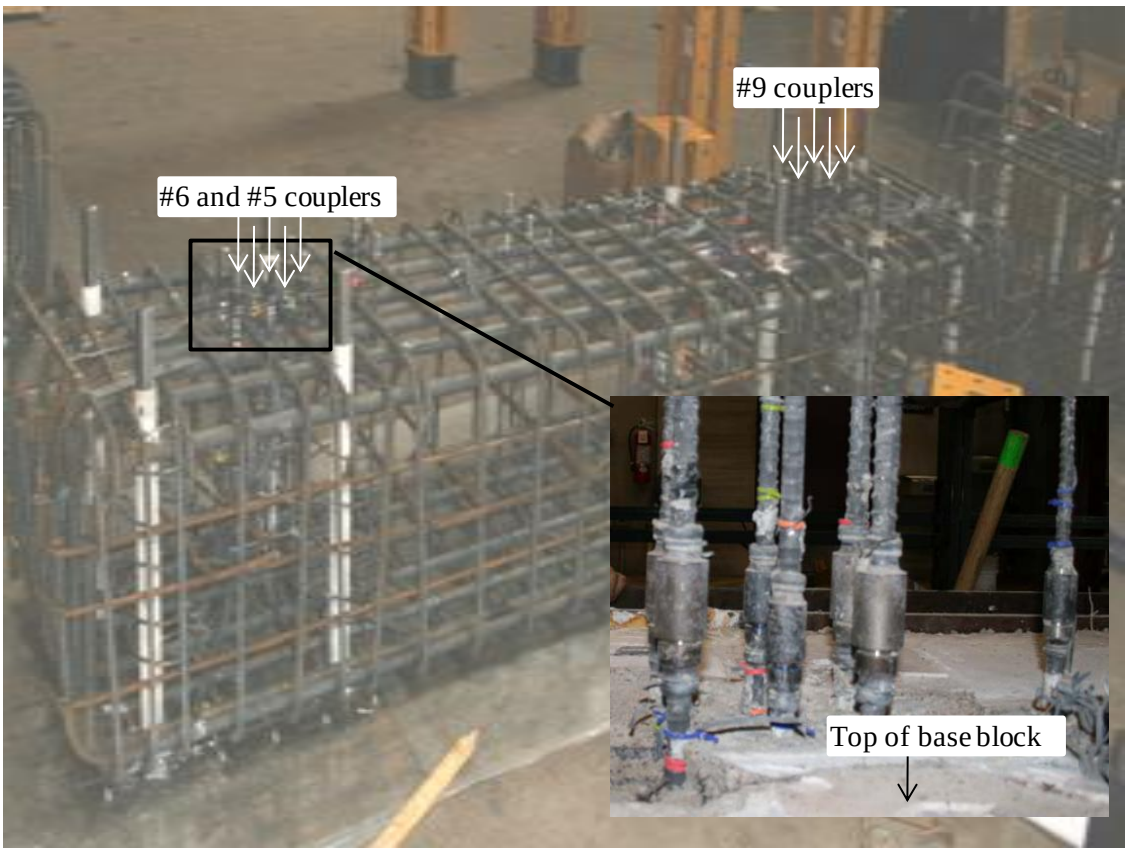

Figure 4.3 Location of the mechanical couplers in RWC.

4.2 Experimental Test Setup, Loading Protocol and Test Observations

4.2.1 Test Setup and Loading Protocol

This section briefly discusses the test setup and the loading protocol used for the experimental investigation of rectangular walls. A schematic of the rectangular wall test setup is shown in Figure 4.4. The base block of each test wall was firmly post-tensioned to the strong floor using 10 three-inch diameter threaded bars. The rectangular walls were subjected to reverse cyclic loading using a ± 220 kip capacity hydraulic actuator mounted horizontally to the MAST reaction wall. In each case, predetermined reversed cyclic displacements were applied to the wall at 20 ft from the foundation-to-wall interface under displacement control. To distribute the applied forces over the entire horizontal length of the wall, the actuator was connected to a pair of steel channels that were clamped to the wall using five one-inch diameter pretensioned rods. The rods were distributed over the horizontal length of wall in a zigzag pattern (see Figure 4.4).

A roller restraint was provided at the top of the wall to prevent any out-of-plane movement of wall during testing. The walls were not subjected to any external vertical load.

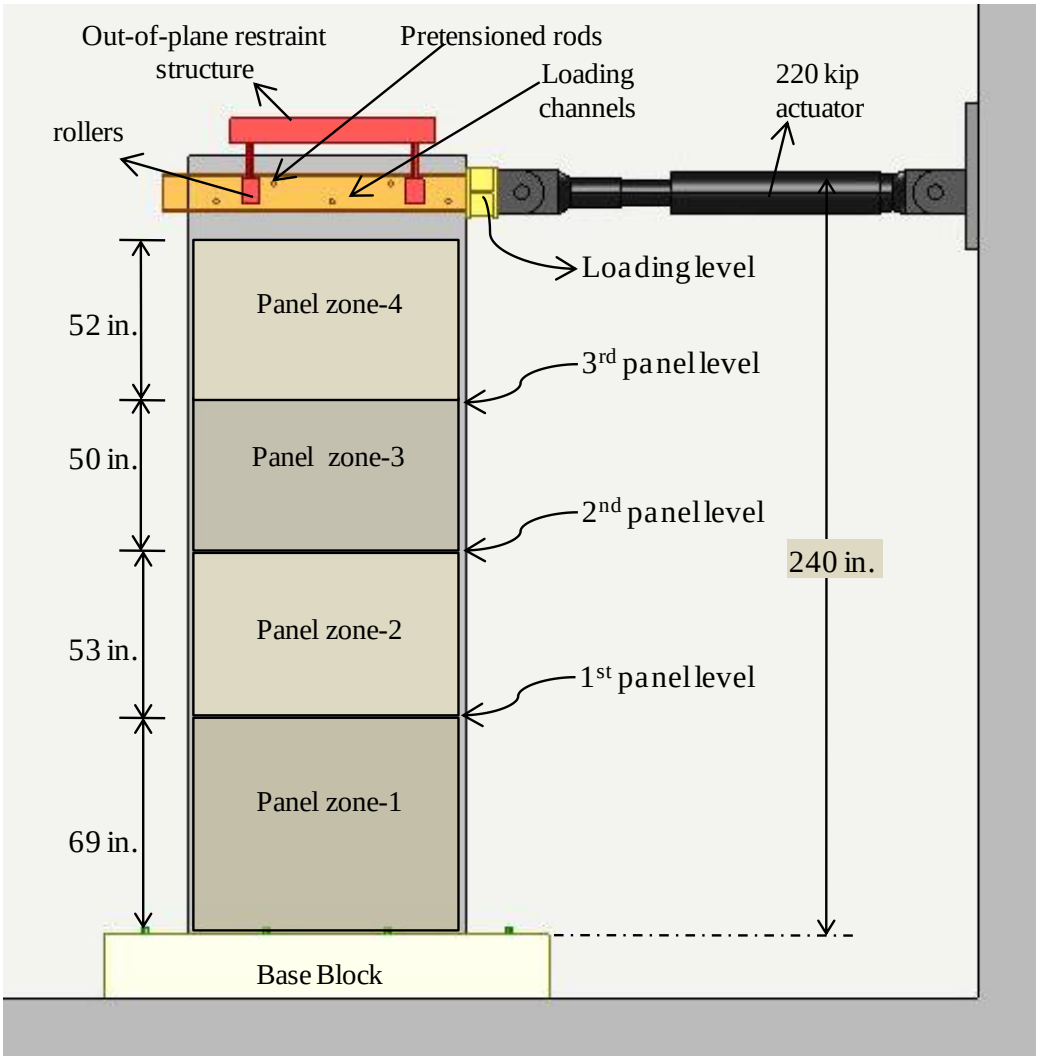

Figure 4.4 Schematic of the test setup used for the rectangular wall tests.

Ignoring the influence of anchorage details, the initial displacement targets for the testing were chosen based on a predicted force-displacement response of the walls that was obtained from a moment-curvature analysis of the wall section. All three walls were subjected to the same displacement history until initiation of failure. Three load cycles were used at each target displacement, to ensure the stability of the force-displacement response at that displacement. The applied displacement history for the three rectangular walls is shown in Figure 4.5. During

testing, the applied lateral displacements to the walls were controlled using an external string potentiometer located at the loading height (i.e. 20 ft from base of the wall). The walls were divided into four panels along the height (see Figure 4.4) to monitor the deformation components and damage within each panel. In addition to recording the wall displacement at the loading height, the lateral displacement at each panel was monitored during testing. Complete details of the test setup can be found in Johnson (2007). All three walls experienced a global buckling failure in the No. 6 confined region during testing at 2% drift cycles as the No.9 confined region was subjected to tension. Consequently, the load histories beyond this point were varied for each wall due to the damage state of each wall at the time of buckling. However, the loading history used after the buckling of the wall was not considered in the analytical investigation presented in this chapter, as this failure mode was not included in the model.

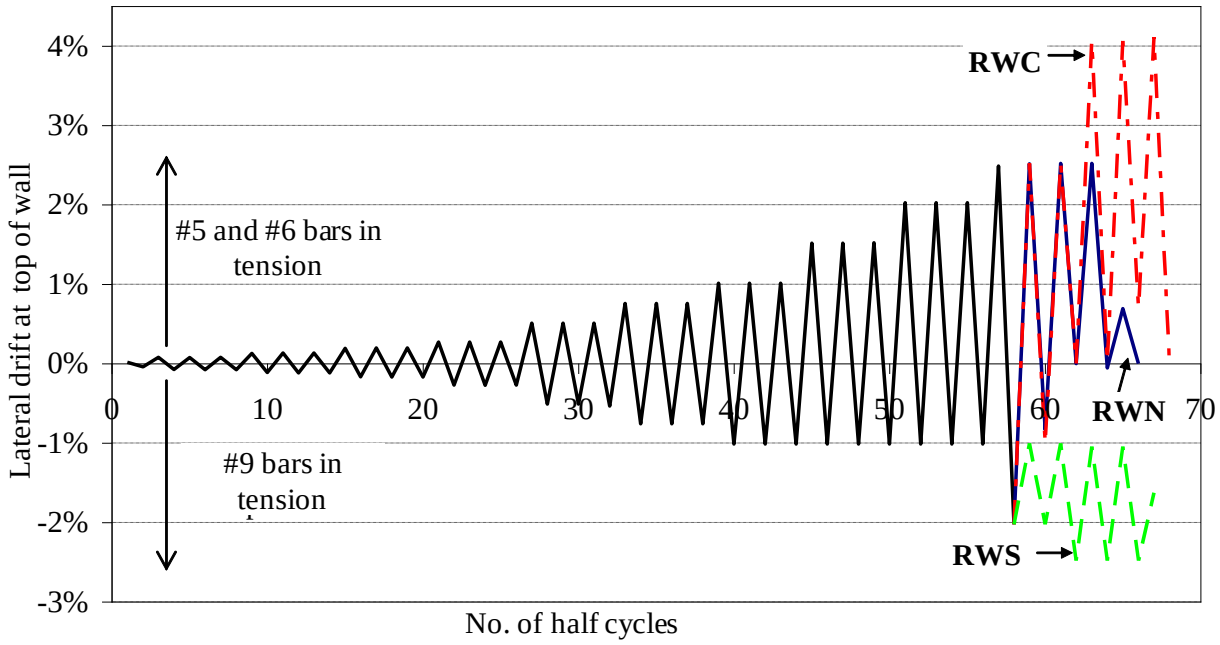

Figure 4.5 The displacement protocol used for testing of the three rectangular walls.

4.2.2 Experimental Observations

The measured cyclic responses of the walls are shown later in section 4.4. All three rectangular walls performed satisfactorily up to 2% lateral drift, when the #5, #6 bars were in tension and up to 1% drift when the #9 bars were in tension. The longitudinal steel in all walls

experienced yielding at a drift of about 0.4 %. The three walls also showed similar responses and crack patterns for drift levels below 1%. However, at larger drifts, the response of RWS was relatively stiff in comparison to other walls, which was expected due to the additional steel in the lap spliced region. Large number of closely spaced flexural cracks formed over the bottom 72 inches of the walls, some of which transitioned into inclined shear cracks outside the confined region (between the confined regions). The shear cracks were much wider when compared to the flexural cracks in the confined region. The crack at the wall-foundation interface was similar in size as the other cracks in the wall until 1% drift. However, in case of RWS the interface gap grew much wider (13 mm wide at 2 % drift), which was caused by the bond degradation in the splice region leading to the slippage of the bars. This large gap opening at the interface caused stress concentration in the bars, leading to local buckling and fracture of longitudinal reinforcement in the No.6 boundary element. In RWS, The flexural cracks at the end of the splice region were much wider than the flexural cracks at other locations. An interesting phenomenon observed during the testing of the walls was shear sliding of the wall along horizontal cracks in the plastic hinge region. This was observed in all the three walls. However, the height of the cracks along which sliding took place were different. When compared to other walls, the sliding in RWS took place at a higher level and outside the spliced region, which is believed to be due to higher amounts of longitudinal steel reinforcement in the splice region.

In summary, the wall with the mechanical couplers performed comparable to that with the continuous reinforcement. The wall with lap splices was stiffer compared to the other two walls and the performance was not as good as the other two walls. The interface crack opening was observed in all the walls but at higher drifts, the interface crack in RWS was nearly 3 to 4 times wider than that was observed in RWN and RWC. In RWN and RWC, the damage was extended up to 65-70 inches from the base, whereas in RWS the damage was concentrated more at the base over a shorter distance, causing the local buckling of the longitudinal reinforcement and thus reducing the energy dissipation capability of RWS. Based on observed performance of RWS, while detailing the NTW2 reinforcement, the lap splice was moved to the first story level to prevent the local buckling of longitudinal reinforcement and the slip along the splice length. More details about the observed experimental behaviour can be found in Johnson (2007).

4.3 OpenSees Models

The lateral load behavior of the three rectangular walls was analytically investigated using fiber based beam-column elements available in OpenSees (OpenSees 2007). The walls were modeled using nonlinear forced-based beam-column elements. Described below are the details of the analytical models developed for the three rectangular walls, which include information on how various anchorage details of the test specimens were modeled.

The base block of each wall was rigidly connected to the strong floor. Lateral movement and rotation of the base block with respect to the strong floor were monitored during testing. Since these measurements were found to be negligible, the base block was modeled with a node (i.e. node 1 in Figure 4.6) in the analytical model and its degrees of freedom were restrained in all the directions. Furthermore, since adequate anchorage was provided for the longitudinal reinforcement in the foundation, the longitudinal bars were assumed to experience no slip in the foundation due to anchorage condition. However, slipping of the bars along a portion of a fully anchored bar should be expected due to strain penetration (Zhao and Sritharan, 2007), which was accounted for in the analytical model as detailed below.

4.3.1 Model for RWN

In order to capture the overall and local responses of the wall accurately, the analysis model should satisfactorily capture the individual deformation components due to flexure, shear and strain penetration. In this section, the analytical model developed for RWN is described. Figure 4.6 shows a schematic of the fiber-based OpenSees model developed for RWN, which consists of five force-based beam-column elements along the height of the wall. Force-based beam-column elements were preferred over the displacement-based beam-column elements for the model because the force-based beam-column element captures the plastic hinge region and the spread of plasticity along the length of a member more accurately than a displacement based beam-column element. Consequently, the force-based element was expected to capture the flexural response more accurately than a displacement-based element.

Previous research has shown that sufficiently anchored longitudinal reinforcement of the flexural members experiences slip along a portion of the bar embedment due to strain penetration along the longitudinal reinforcing bars anchored into a connecting concrete member. It was also demonstrated by Sritharan et al. (2000) and Zhao & Sritharan (2007) that ignoring the strain

penetration effects in analytical models will significantly affect the prediction of the local response parameters. Consequently, as recommended by Zhao & Sritharan (2007) (see Appendix A) a zero-length fiber-based element was used at the interface between the wall and foundation to account for the strain penetration effects. This zero length interface element had the same cross section as the rectangular wall (i.e. cross section-1 for RWN, shown in Figure 4.6). The steel fibers of this zero length section were modeled using the strain penetration material model, which relates the stress in a fully anchored reinforcement with the total slip of the bar at the interface (see Appendix A).

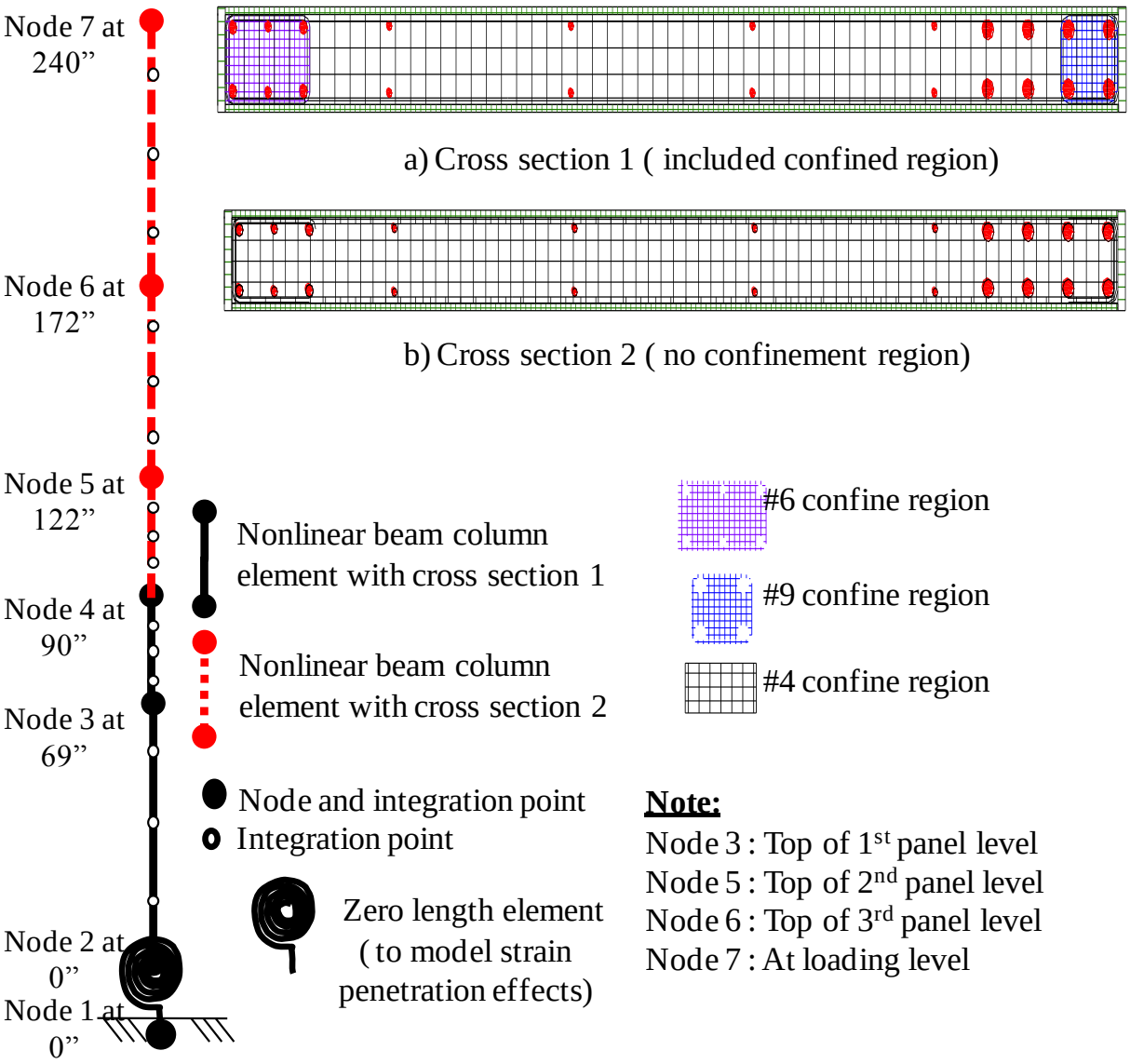

Figure 4.6 Schematic of the nonlinear fiber-based OpenSees model for RWN

Based on the experimental observations and data from RWN, some modifications to the suggested values by Zhao and Sritharan (2007) for the model parameters such as slip at yield were incorporated. A preliminary analysis was carried out with the suggested slip values at the yield stress, which were 0.01373 in. for #5 bar, 0.01541 for #5 bar, 0.01680 for #6 bar and 0.02196 in. for #9 bar respectively. However, after examining the response of the wall and comparing the experimental and analytical slip values and their contributions, the slip at yield stress for #6, #5 and #4 rebars was increased by a factor of 1.5, while the yield slip for #9 bars was increased by a factor of 6. The increase in the yield slip value for #9 bars was high and is suspected to be due to the use of 1.875 in. clear spacing between bars and the associated congestion of the reinforcing bars in the boundary element to match the capacity of T-wall in flange in tension direction.

Except for the second panel, a single force-based beam-column element (i.e. nonlinearBeamColumn in OpenSees) with five integration points along its length modeled each panel of RWN. The location of integration points followed the Gauss-Lobotto scheme. For example, in an element with five integration points, the integration points are located at both ends of the element (-1.0 and 1.0 in an isoparametric formulation), at the center of the element (0.0 in an isoparametric formulation) and at points located at a distance of 0.17267 times the length of the element from both ends (-0.65465367, 0, 0.65465367) of the element. The second panel was modeled with two force-based elements since the boundary elements were extended 21 in. into the second panel, changing the cross section details at 90 in. from the base of the wall. A fiber section was used to represent the cross section of the wall. The details of the fiber sections used for the nonlinear beam-column elements are shown in Figure 4.6. The wall cross sections in the confined and unconfined regions were discretized using fibers approximately 0.2 in. x 0.2 in. The confined and unconfined concrete fibers were modeled to follow the modified Chang and Mander confinement model described in Chapter 3 (i.e., *Concrete07* in OpenSees).

The unconfined concrete strength for the wall specimen was obtained from testing of ten 4 in. x 8 in. cylinders at the end of testing of RWN. The average concrete strength for RWN was 7870 psi for bottom two panels and 6880 psi for the remainder of the wall. The concrete strength was different between the top two and bottom two panels because the wall was cast in two different stages. The concrete tensile strength was taken as $6\sqrt{f_c'}$ (psi) in both cases. However, the tensile strength in the No. 6 boundary region of the first panel was reduced to $3\sqrt{f_c'}$ (psi), to

account for the effects of pre-existed shrinkage cracks in the region near the wall base. The concrete young's modulus was approximated to $57000\sqrt{f_c'}(psi)$ (psi). The confined concrete properties in the boundary regions were obtained using the confined concrete model proposed by Mander et al. (1988) based on the details of the transverse reinforcement.

All longitudinal reinforcement (i.e. #4, #5, #6 and #9 bars) was modeled using the *ReinforcingSteel* material model available in OpenSees. This model has the ability to closely follow the strain response of Grade 60 mild steel reinforcement, especially under cyclic loading.

Table 4.1 Measured properties of reinforcement used in the RWN model

Bar size (dia (in.))	Yield Strength (ksi)	Elastic Modulus (ksi)	Tangent at initial strain hardening (ksi)	Strain hardening strain (in/in)	Ultimate strength (ksi)	Strain at ultimate strength (in/in)
#9 (1.125 in.)	66.74	26546	775	0.0086	90.0	0.10
#6 (0.75 in.)	71.00	28249	800	0.0096	96.5	0.10
#5 (0.625 in.)	71.03	28560	875	0.0095	97.5	0.10
#4 (0.5 in.)	58.00	22282	-	-	90.0	0.10
#3 (0.375 in.)	66.00*	29000*	-	-	-	0.12
#2 (0.25 in.)	79.34	29000*	-		96.3	0.12

* assumed

The #4 reinforcing bar was modeled using the modified Menegotto-Pinto model (i.e., *Steel02* in OpenSees) because the uniaxial testing of #4 rebar did not exhibit any yield plateau. Furthermore, the strain demand in #4 bars was never reported to exceed 0.035 in/in. Figure 4.7 compares the modeled stress-strain response of #4, #5, #6, and #9 bars with the experimental stress-strain behavior obtained from monotonic pull tests. The reinforcement properties used for the OpenSees model of RWN are shown in Table 4.1.

Significant contribution of shear deformations towards the lateral deformation of walls and the existence of shear-flexural coupling in the plastic hinge regions was demonstrated by previous research on flexural dominant rectangular concrete walls with aspect ratios greater than 2.5 (Thomsen & Wallace 1995). These phenomena were also observed in the experimental response of the RWN (Johnson, 2007). Therefore, it follows that to accurately capture the lateral load behavior, it is necessary to account for the shear deformations along the height of the wall.

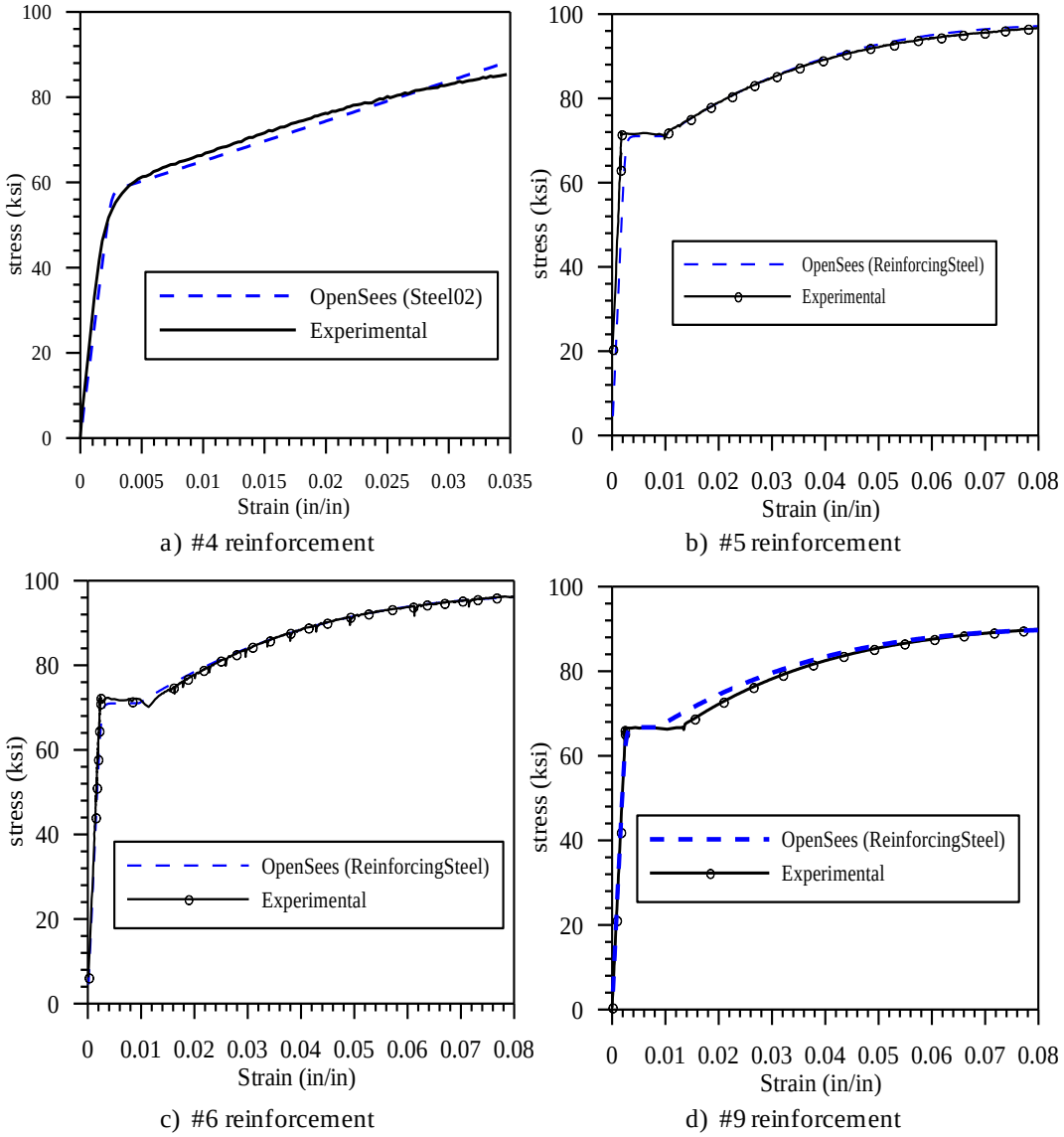

Figure 4.7 Comparison of experimental and theoretical stress-strain responses of RWN longitudinal reinforcement under monotonic loading.

The force-based beam-column element in OpenSees accounts only the flexural response while ignoring the effects of shear mechanism and possible interaction between flexure and shear mechanisms. Although, there are several formulations recommended in literature to account for the shear deformations in the force-based beam-column elements (Petrangeli, 1999 and Martinelli, 2008) no such technique was available in OpenSees to account for the effects of shear deformation. Therefore the shear deformations in RWN were accounted by aggregating a uniaxial material behavior (i.e. *Pinching4* in OpenSees) over the flexural response of the nonlinear beam-column element. Although, the section aggregation method helps in accounting

for the shear deformation, it doesn't account for the effects of flexure-shear interaction. The experimentally observed shear force-distortion relationship of RWN was used to arrive at the model parameters for the *Pinching4* model. Also, with the *Pinching4* material model, the observed degradation of shear stiffness could not be captured and thus the shear degradation is ignored in the model.

4.3.2 Model for RWC

In this section, the analytical model developed for the rectangular wall with couplers near the foundation interface is described. The overall modeling of RWC followed that of the RWN, but it incorporated a sixth force-based beam-column element. This new beam-column element was used to model the region containing the mechanical couplers. Figure 4.8 presents the schematic of the OpenSees model developed for RWC. It was anticipated that the presence of couplers would modify the strain distribution in the bottom region of the wall. A challenge associated with this modeling was that, the length and the area of the couplers varied based on the size of the rebar. Since the response that subjected the #5 and #6 longitudinal bars in tension experienced severe nonlinearity, the length of this beam-column element representing the coupler region was taken as the average length of the #5 and #6 bar couplers. The lengths and cross sectional areas of the couplers used in RWC are presented in Table 4.2. Concrete and longitudinal reinforcement fibers in RWC were modeled as in RWN, while the couplers were modeled with their increased cross sectional area, but with the stress-strain model same as the corresponding longitudinal reinforcing bar. During construction of the test specimen, no confinement hoops were placed within the coupler region as this would not have permitted any cover to the hoop reinforcement. The concrete fibers in the coupler region were therefore, modeled as unconfined concrete. Because the couplers were kept above the wall-to-foundation interface in the specimen, reinforcement fibers in the zero-length section at the wall-to-foundation interface were modeled using the reinforcing bar area instead of couplers area. The strain penetration effect and the shear deformations were included in the same manner as it was done in RWN model.

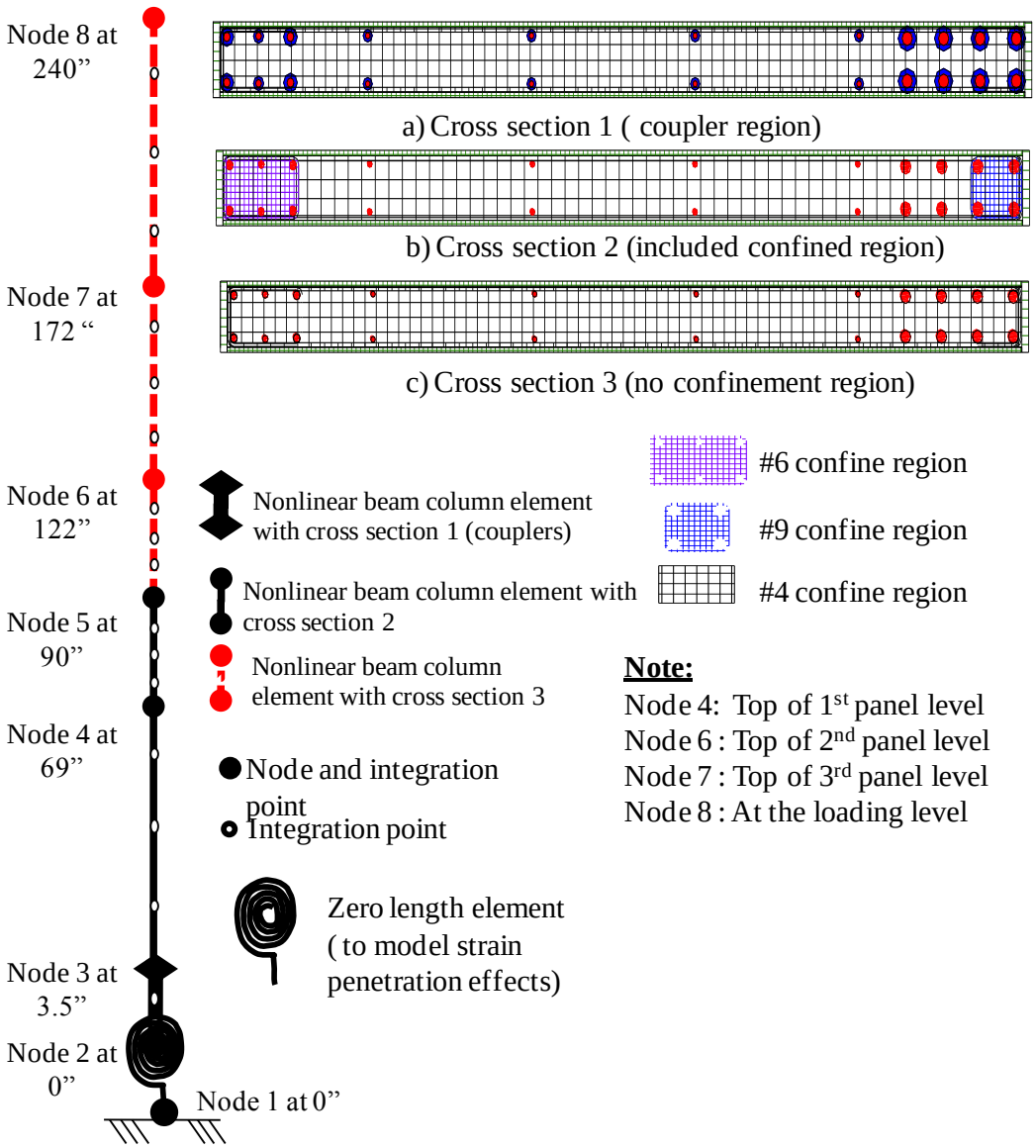

Figure 4.8 Schematic of the nonlinear fiber-based OpenSees model for RWC.

As with RWN, the unconfined concrete strength of the wall specimen was obtained from testing of ten 4 in. x 8 in. cylinders at the end of testing of RWC. The average concrete strength of RWC was 7500 psi for bottom two panels and 9100 psi for the top two panels. The concrete strength was different between the top and bottom halves of the wall due to same reason as RWN. The concrete tensile strength was taken as $6\sqrt{f_c'}$ (psi) in the both cases. However, as with RWN, the tensile strength in the No. 6 boundary region of the first story was reduced to $3\sqrt{f_c'}$ (psi), to account for the effects of pre-existed shrinkage cracks in the bottom panel. The concrete

young's modulus was approximated to $57000\sqrt{f_c^{'}(psi)}$ (psi). The confined concrete properties in the boundary regions were obtained using the confined concrete model proposed by Mander et al. (1988) based on the details of the transverse reinforcement. The longitudinal reinforcement was modeled with same material properties as in RWN.

Table 4.2 Length and cross section area details of the couplers in RWC

Bar Size (dia)	Coupler length (in.)	Coupler dia (in.)	Coupler Area (in^2)
#4 (0.5 in.)	2.75	0.99	1.125
#5 (0.625 in.)	3.00	0.99	1.125
#6 (0.75 in.)	4.00	1.50	1.77
#9 (1.125 in.)	5.00	2.0	3.14

4.3.3 Model for RWS

In this section, the analytical model developed for the rectangular wall with traditional lap splices near the wall base (i.e., in the plastic hinge region), RWS is described. The overall modeling of RWS was done as for RWN, except for introducing five more force-based beam-column elements. These new beam-column elements were used to model the region containing the traditional lap splices. Figure 4.9 presents the schematic of the OpenSees model developed for RWS. It was anticipated that the presence of lap splices in the plastic hinge region would influence the strain distribution in the spliced region. It was also anticipated that along the length of the splice, the effective bar area will be larger than that of one bar in the middle region of the splice because of the conservatism built into the estimation of code based lap splice length as used in RWS. A review of relevant literature indicated that structures with lap splices have been typically modeled with a single rebar effectively representing the lap splice. This is because it is generally accepted that the strength of a spliced bar is almost the same as that of a single embedded bar (Cho and Pincheira, 2006).

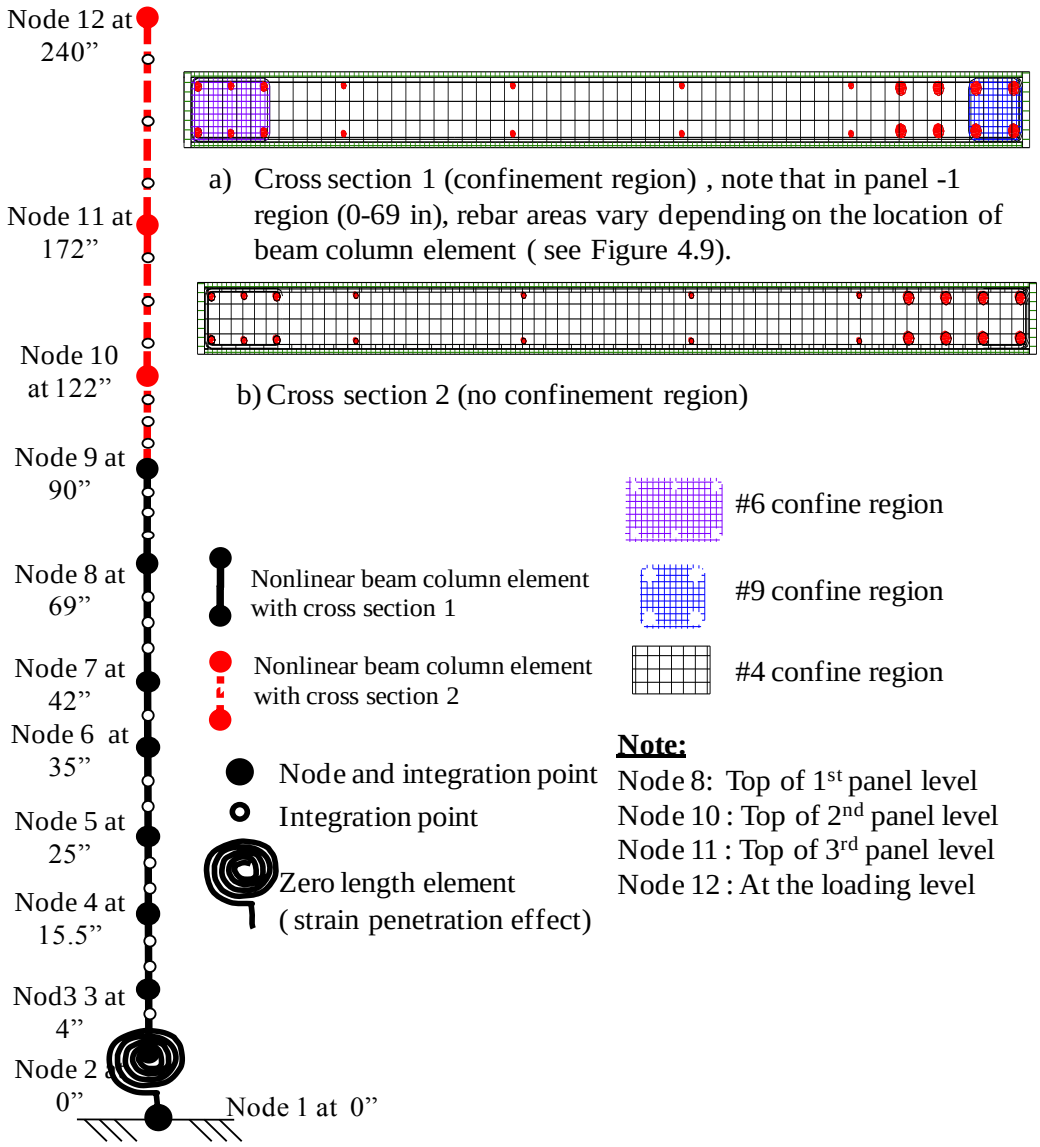

Figure 4.9 Schematic of the nonlinear fiber-based OpenSees model of RWS.

Using this approach, a preliminary analysis of RWS with the lap-splice represented by a single rebar located at the center of the lap splice was conducted. A comparison of the response from the analysis with experimental response did not support this approach (see results in Figure 4.24, presented in Section 4.4.3.1). Consequently, in the RWS model, the lap splice region was modeled using six nonlinear beam-column elements, with effective reinforcing bar areas varying from one bar area to two bar area depending upon the location of the beam-column element. Figure 4.10 shows the assumed effective bar area over the splice length in the RWS model for

different bar sizes, which were obtained based on assumed bond strength of $10\sqrt{f_c'}(psi)$ along the splice region. The strain penetration effect and the shear deformation in this model were handled in the same manner as in the RWN model. During the experiment, slip between the longitudinal bars (predominantly in #6 and #5 bars) in lap splice region was observed. Since there are neither specific experimental studies nor analytical models found in the literature to model the slip within the spliced region, the potential slip of bars in the spliced region was not modeled.

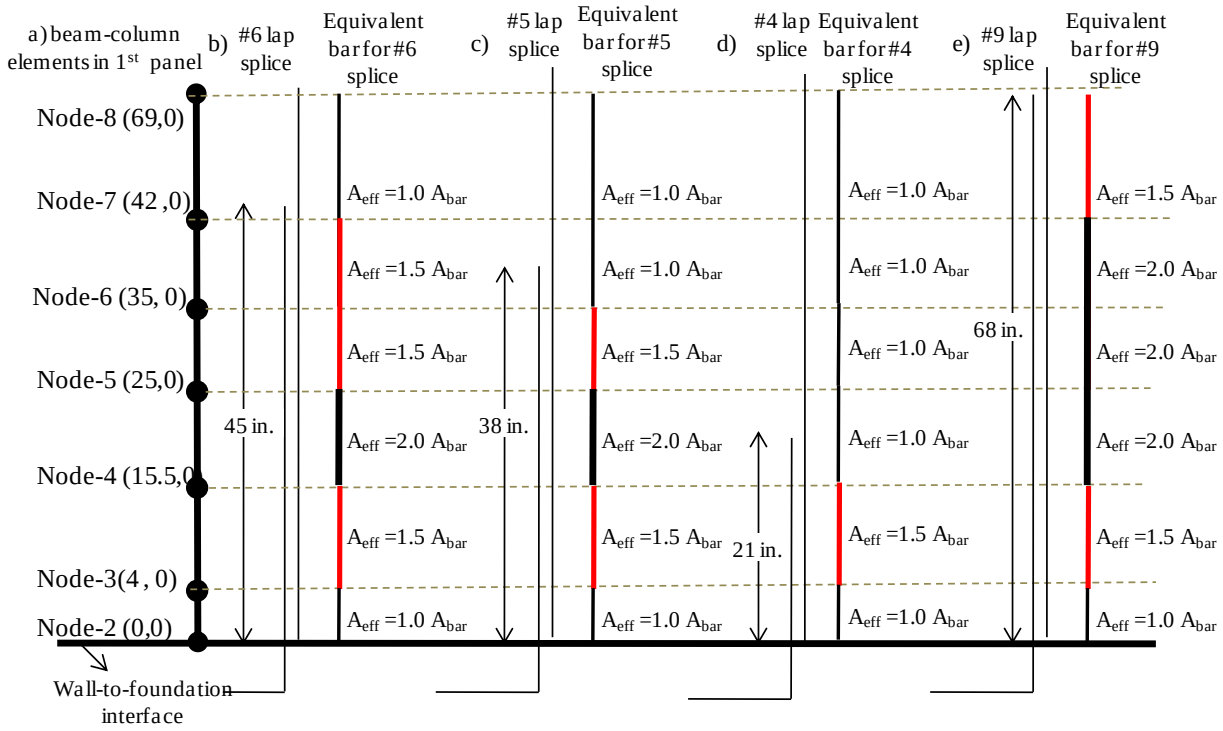

Figure 4.10 Schematic of the effective bar area used over the lap splice length of #4, #5, #6 and #9 in the RWS model

Again, the unconfined concrete strength for the wall specimen was obtained from testing of ten 4 in. x 8 in. cylinders at the end of testing of RWS. The average concrete strength for RWS was 8110 psi for bottom two panels and 6580 psi for the top two panels. The concrete strength was different between the top two and bottom two panels for the same reason as RWN and RWC. The concrete tensile strength was taken as $6\sqrt{f_c'}$ (psi) for the entire wall. The concrete young's modulus was approximated to $57000\sqrt{f_c'}(psi)$ (psi). The confined concrete properties in

the boundary regions were obtained using the confined concrete model proposed by Mander et al. (1988) based on the appropriate details of the transverse reinforcement. The longitudinal reinforcement was modeled as with the RWN model using the same material properties.

4.4 Comparison of Results

4.4.1 RWN

In this section, the OpenSees analytical model and experimentally observed responses of RWN are compared and appropriate comments are made. In addition to the global response, accuracy of the local responses is examined, including the force-displacement response of RWN at different panel levels. Also a comparison of experimental and calculated contribution of various deformation components to the lateral displacement at first panel level and top of wall is presented

4.4.1.1 Cyclic Response

The measured and calculated cyclic responses of RWN when subjected to the loading protocol in Figure 4.4 are shown in Figure 4.11. As seen in this figure, the OpenSees simulation accurately captured the force-displacement response of RWN for the loading direction that subjected the #6 and #5 longitudinal bars in tension. The unloading stiffness, reloading stiffness, and residual displacements were all well simulated by the analysis model in this direction. In the opposite direction, that subjected the #9 bars in tension, the analytical response closely matched the experimental response up to about 2.4 in. of lateral displacement, which was the peak lateral displacement for the majority of testing. However, the agreement is not as good as that observed for the other direction. The calculated peak values were within 3% of the experimental values for up to 2.4 in. (i.e., 1% drift) of lateral displacement in the #9 bars in tension direction. At 4.8 in. lateral displacement, for #9 bars in tension, the analytical model overestimated the lateral force resistance by 7.9%. The over estimation of the load and the underestimation of the residual displacements are due to disregarding of the shear degradation in the OpenSees model, which is further discussed in the next section. The initial stiffness in the both directions was captured with good accuracy.

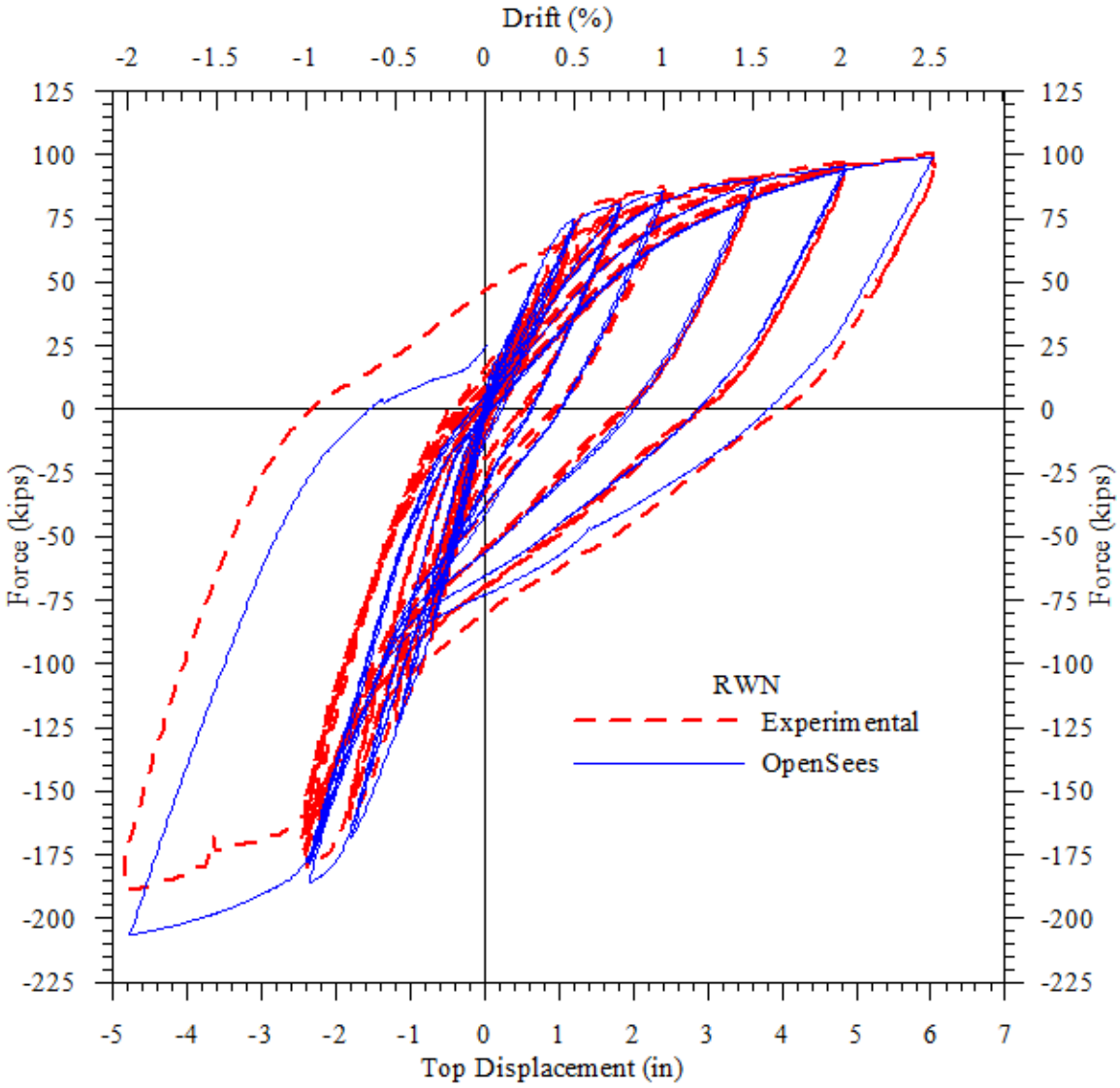

Figure 4.11 Comparison of measured and calculated force-displacement responses of RWN.

4.4.1.2 Response at top of First Panel

To ensure that the OpenSees model adequately captured the different deformation components accurately, the responses at different panel levels were also examined. It was expected that the first panel response would be heavily influenced by the contribution of shear deformation, due to the reduction of shear stiffness caused by the flexural damage and yielding of the longitudinal reinforcement within the first panel. Thus, the comparison of lateral load response at the first panel level provides an opportunity to examine the modeling accuracy of the

shear deformation. The calculated and measured force-displacement responses at the first panel level are shown in Figure 4.12a. The OpenSees model did not capture the first panel response in both loading directions as accurately as it did at the top of the wall. It is seen that the analytical model over predicted the total lateral displacement for the direction that subjected the #6 bars in tension and under predicted the lateral displacement for the #9 bars in tension. However, the analytical model estimated the initial stiffness and the post yield stiffness of the first story level with good accuracy.

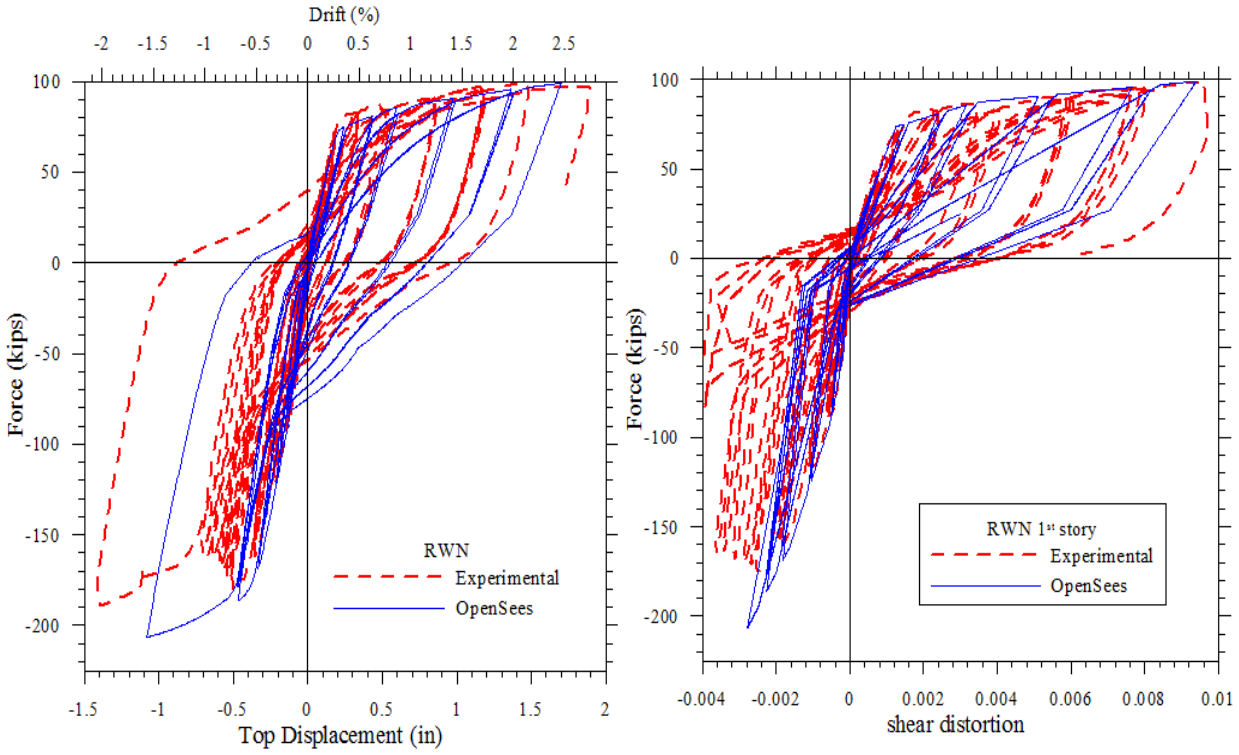

a) force-displacement response at top of 1st panel b) 1st panel force-shear distortion response

Figure 4.12 Overall and the shear distortion responses of RWN at the first panel level.

The under prediction of the lateral displacement response in the #9 bars in tension direction was expected as the *pinching4* model used for capturing the shear response did not account for possible strength degradation and softening of the structure expected due to repeated loading to the same lateral displacement of 2.4 in. (i.e. -1% drift) in #9 bars in tension direction. This can be clearly seen in Figure 4.12 b, which compares the theoretical and experimental shear distortions of the first panel in RWN. The increase in the shear distortion (from -0.002 rad. to -0.0038 rad.) due to the repeated loading to -1% drift was expected due to significant damage

observed in the first panel of RWN during testing. Large inclined shear cracks were developed during the +1.5%, +2.0% loading cycles in the #6 bars in tension direction due to yielding of longitudinal reinforcement. The wall was heavily cracked at +2% drift with minor spalling of cover concrete. Figure 4.13 shows the damage state of the first panel of RWN as the drift in the #6 direction changes from 1% to 2.5 % while a constant drift of -1% was maintained in #9 in tension direction. The level of shear cracking shown in Figure 4.13 at different drift levels supports the measured increase in shear distortion in the first panel in #9 bars in tension direction.

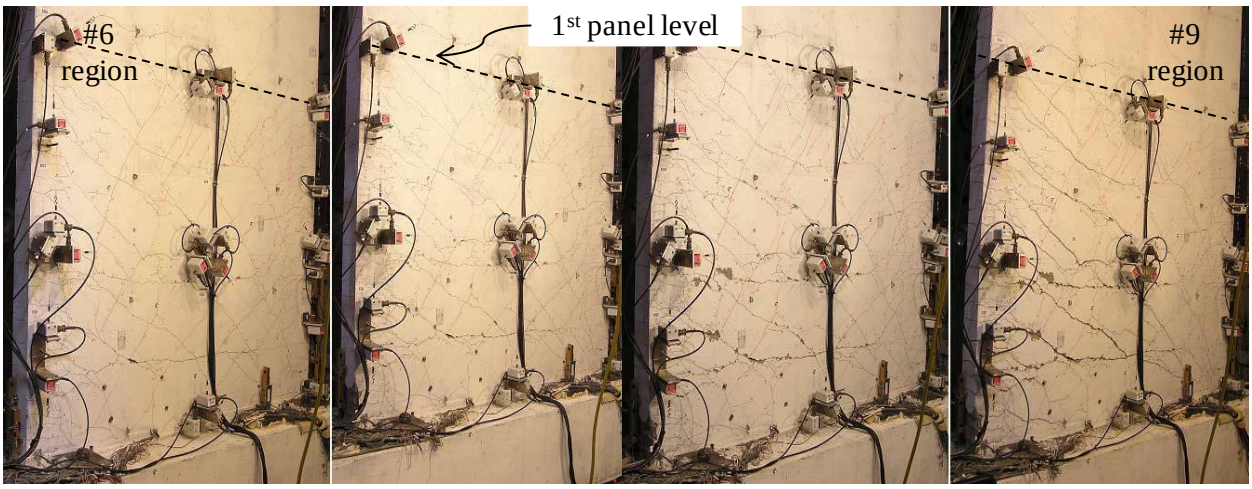

a) at 1% drift b) at 1.5% drift c) at 2% drift d) at 2.5% drift

Figure 4.13 Extent of shear cracking observed at different drift levels within the first panel of RWN.

4.4.1.3 Response at top of Second Panel

The lateral load response of RWN at the top of second panel was also compared to the measured experimental response and is shown in Figure 4.14. The OpenSees model captured the force-displacement behavior at the second panel level with good accuracy in the #6 bars in tension direction. The stiffness of the loading, unloading, reloading paths and residual displacements all are well captured by the model in the #6 bars in tension direction. The initial stiffnesses in both directions were also captured accurately by the OpenSees model. However, the residual displacements in the #9 in tension directions were under predicted as observed for the response at the top of the wall. This observation again reinforces that the discrepancy seen in

the total response of RWN in Figure 4.10 is largely due to the shear distortion error encountered in the first panel of the wall.

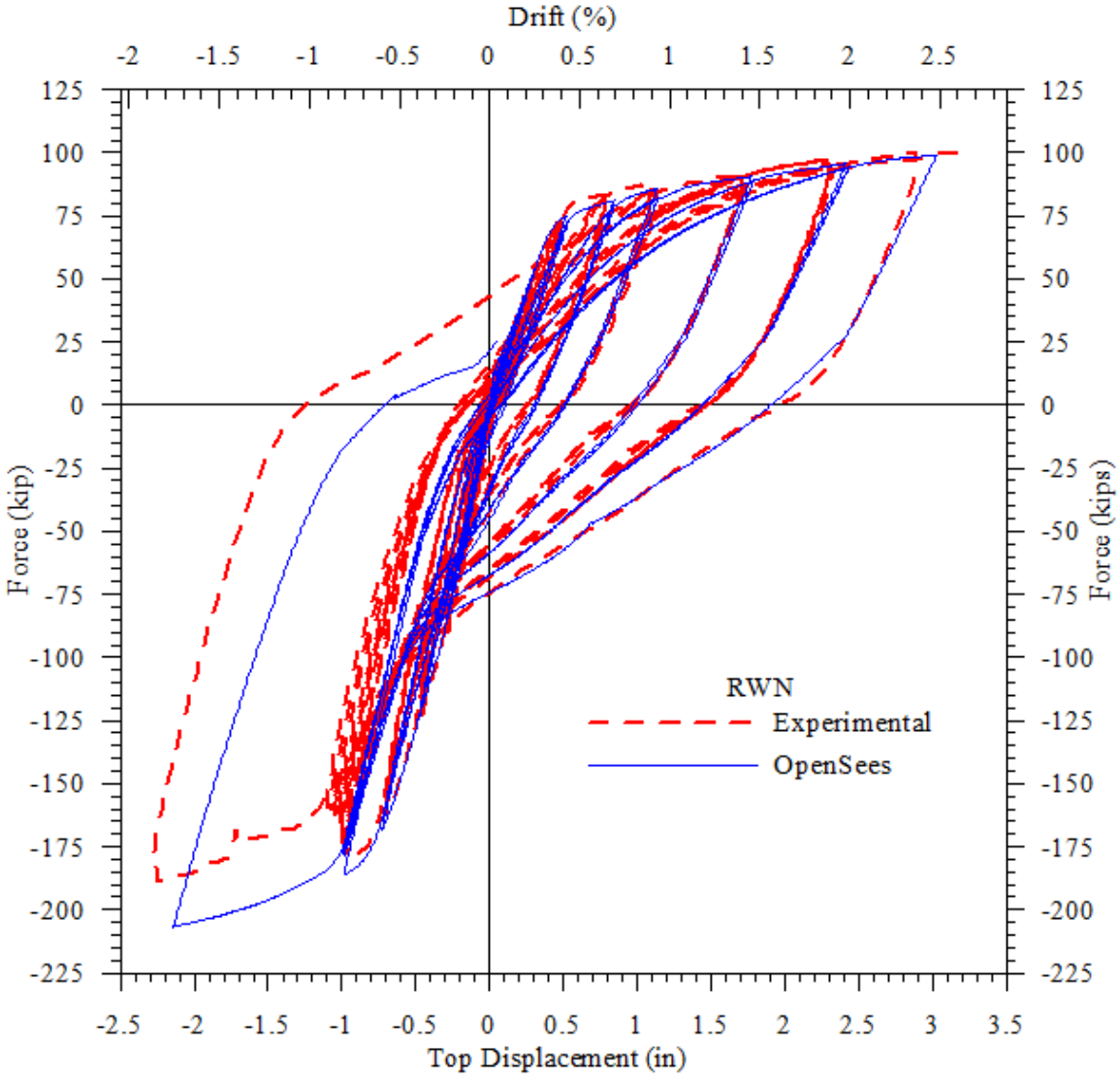

Figure 4.14 Comparison of the measured and calculated force-displacement responses of RWN at the top of the second panel.

4.4.1.4 Comparison of Deformation Components

Calculated and experimental values of various deformation component responses of RWN at the first panel level and the top of the wall during the peak displacements are compared and appropriate comments are presented. Since the #6 and #5 bars in tension direction response was of significant interest, the comparisons are presented for that loading direction only.

The experimentally measured displacements in all the three wall testes were decomposed into various displacement components including those due to flexure, shear and strain penetration. All the four panels of all the three walls were extensively instrumented with string potentiometers arranged in an X-shaped configuration to isolate the shear and flexure contributions towards the total lateral displacement. Few longitudinal bars along the wall length were welded with small studs to measure the slip in the longitudinal reinforcement due to strain penetration effect. Complete details about the instrumentation plan, types of instruments used and the location of instruments can be found in Johnson (2007). A joint method presented by Sritharan (1998) for quantifying the deformation components in the joint regions of column/cap beam tee connections was used for decomposing the lateral displacement at each panel level into various displacement components.

The comparison between the calculated and measured values of various deformation components of RWN at the first panel level and the top of the wall are shown in Figure 4.15 and Figure 4.16 respectively. It can be seen from Figure 4.15 and Figure 4.16 that the analytical model over predicted the localized flexural deformation in the first panel, while accurately predicting the overall flexural deformation of RWN. The shear deformation and the deformation due to strain penetration in the first panel and at the top of RWN were well captured by the model.

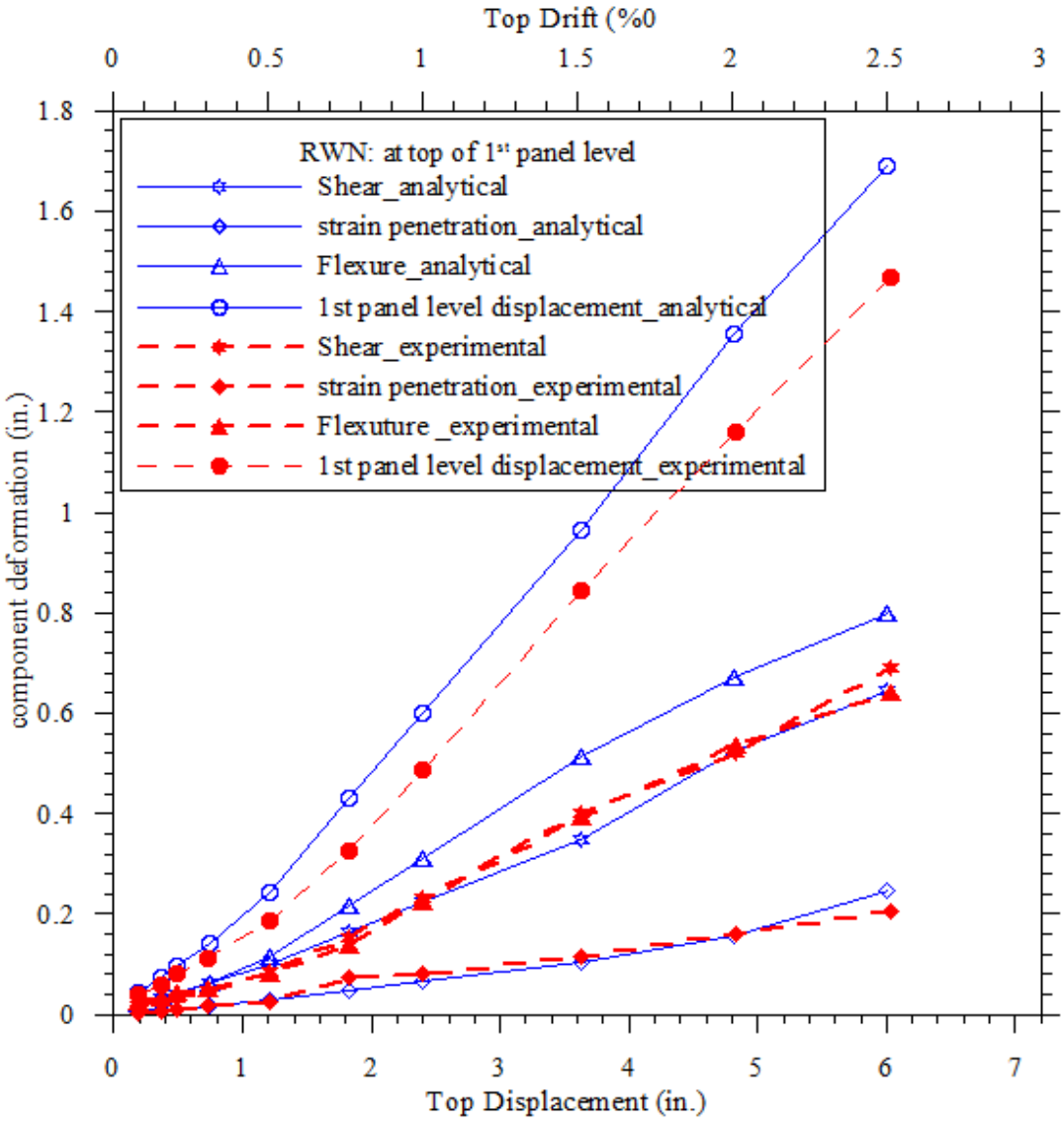

Figure 4.15 Comparison between calculated and experimental deformation component responses at the first panel level of RWN

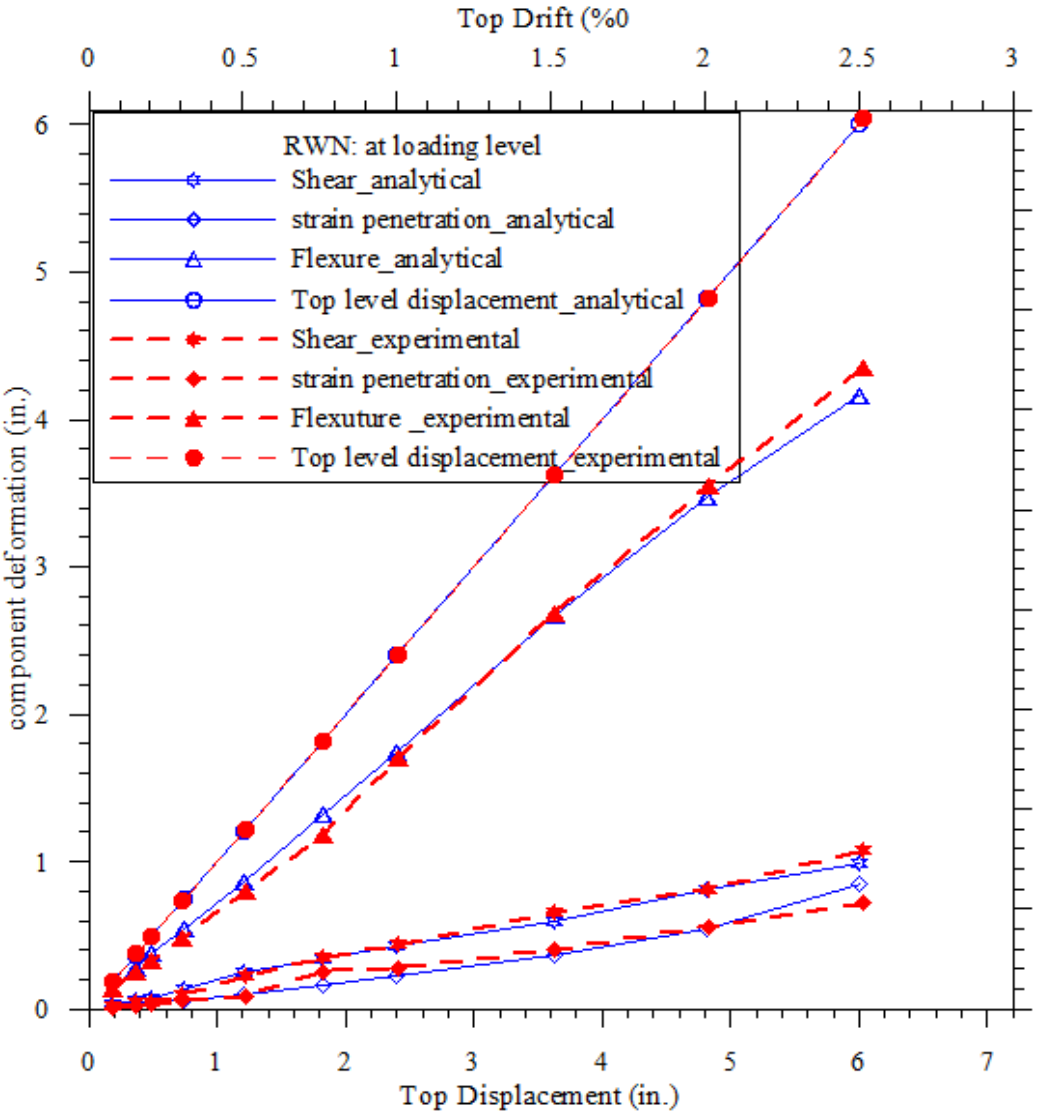

Figure 4.16 Comparison between calculated and experimental deformation component responses at the top of RWN.

4.4.2 RWC

In this section, the OpenSees analytical model and experimentally observed responses of RWC are compared and appropriate comments are made. In addition to the global response, accuracy of the local responses is examined, including the force-displacement response of RWC at different panel levels.

4.4.2.1 Cyclic Response

The measured and calculated cyclic responses of RWC when subjected to the loading protocol in Figure 4.5 are shown in Figure 4.17. As seen in this figure, the OpenSees simulation accurately captured the force-displacement response of RWC for the loading direction that subjected the #6 and #5 longitudinal bars in tension. The unloading stiffness, reloading stiffness,

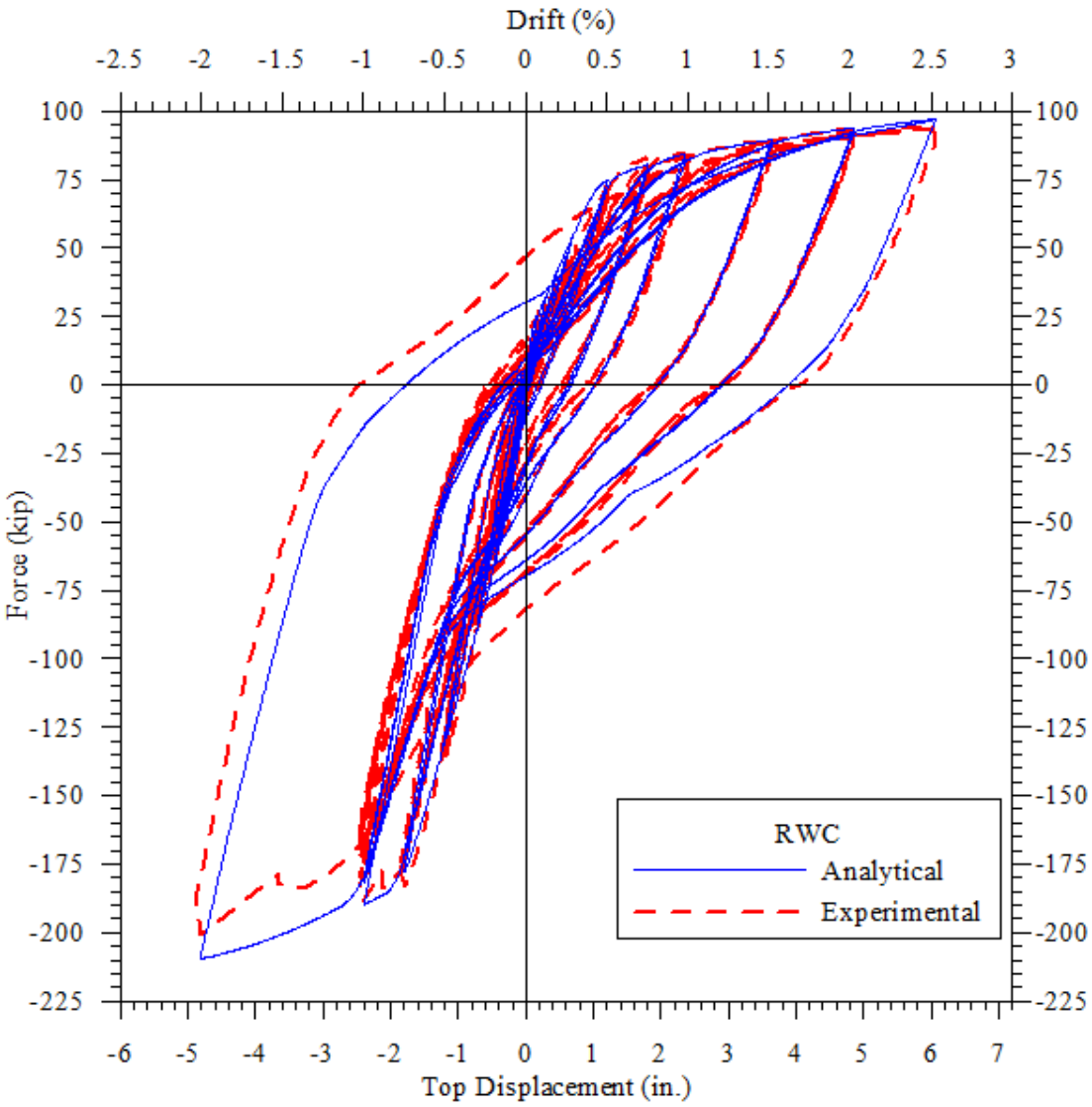

Figure 4.17 Comparison of measured and calculated force-displacement responses of RWC.

and residual displacements were all well simulated by the analysis model up to a lateral displacement of 6.0 in. (i.e., +2.5% drift) in this direction. In the opposite direction, that

subjected the #9 bars in tension, the analytical response accurately captured the experimental response up to a lateral displacement of 2.4 in. (i.e. -1% drift) and the calculated peak values were within 3% of the experimental values. At -2% drift, the analytical model overestimated the load by 5.0%. The over estimation of the load and the underestimation of the residual displacements are due to disregarding of the shear degradation in the OpenSees model, which is further discussed in the next section. The initial stiffness in the both directions was captured with good accuracy.

4.4.2.2 Response at top of First Panel

To ensure that the OpenSees model adequately captured the different deformation components accurately, the responses at different panel levels were examined. As explained in section 4.4.1.2, the comparison of lateral load response at first panel level provides an opportunity to further examine the modeling accuracy, including that of shear. The calculated and measured force-displacement responses at the first panel level are shown in Figure 4.18a.

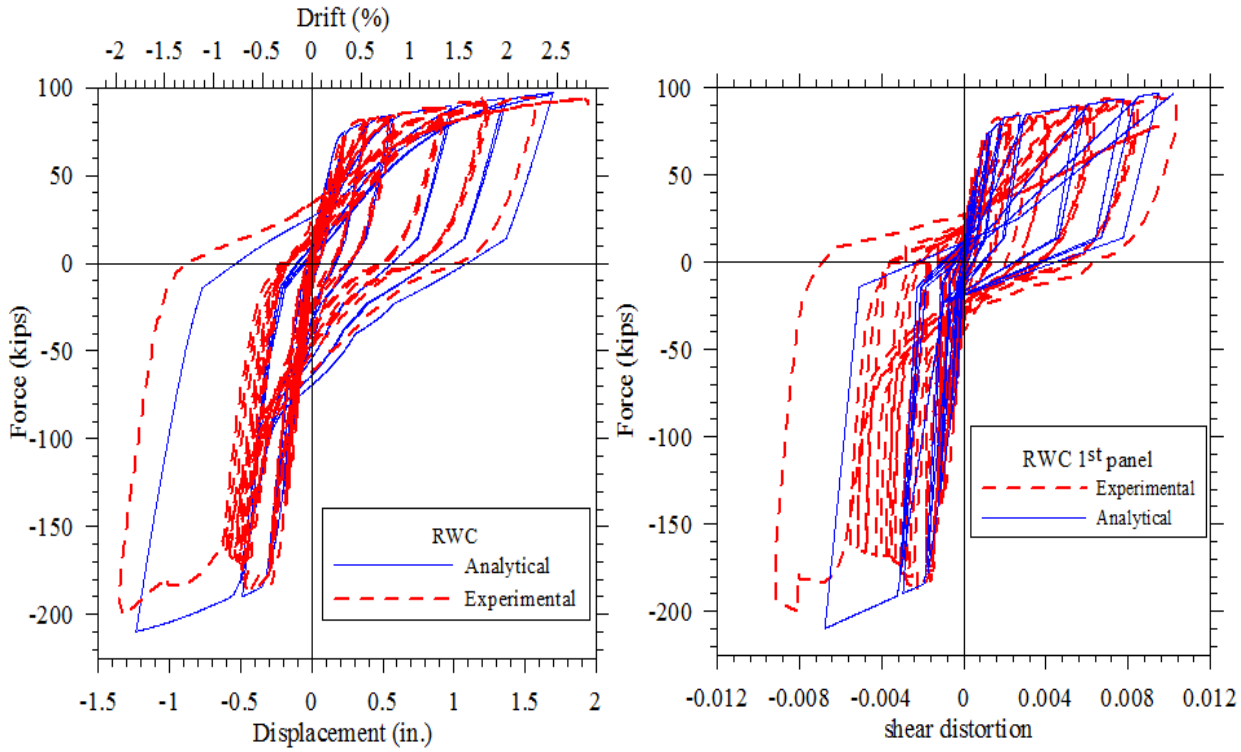

a) force-displacement response at top of 1st panel b) 1st panel force-shear distortion response

Figure 4.18 Overall and the shear distortion responses of RWC at the first panel level.

As observed previously with RWN, the OpenSees model did not capture the first panel response in both loading directions as accurately as it did at the top of the wall. It can be seen that the analytical model over predicted the total lateral displacement in the #6 bars in tension, which was observed previously in RWN. The strength degradation and the increase in the first panel level displacement at -1% drift were not well captured by the analytical model. The unloading stiffness and reloading stiffness were well captured up to a drift of 0.75% in the #6 bars in tension direction. However, the analytical model estimated the initial stiffness and the post yield stiffness of the first panel level with good accuracy. The over prediction of the strength and not capturing the strength degradation at 2.4 in. lateral displacement (i.e., -1% drift) in the #9 bars in tension direction was expected as the *pinching4* model used for capturing the shear response did not account for the strength degradation and softening of the structure expected due to repeated loading to the same lateral displacement of 2.4 in. (i.e. -1% drift) in #9 bars in tension direction. It can be seen in Figure 4.18b, which compares the theoretical and experimental shear distortions of the first panel in RWC. The increase in the shear distortion with the repeated loading to -1% drift was expected based on significant damage observed in the first panel of RWC. Similar to RWN, large inclined shear cracks were developed during the +1.5%, +2.0% loading cycles in the #6 bars in tension direction due to yielding of longitudinal reinforcement. Figure 4.19 shows the damage state of the first panel of RWC at different drift levels.

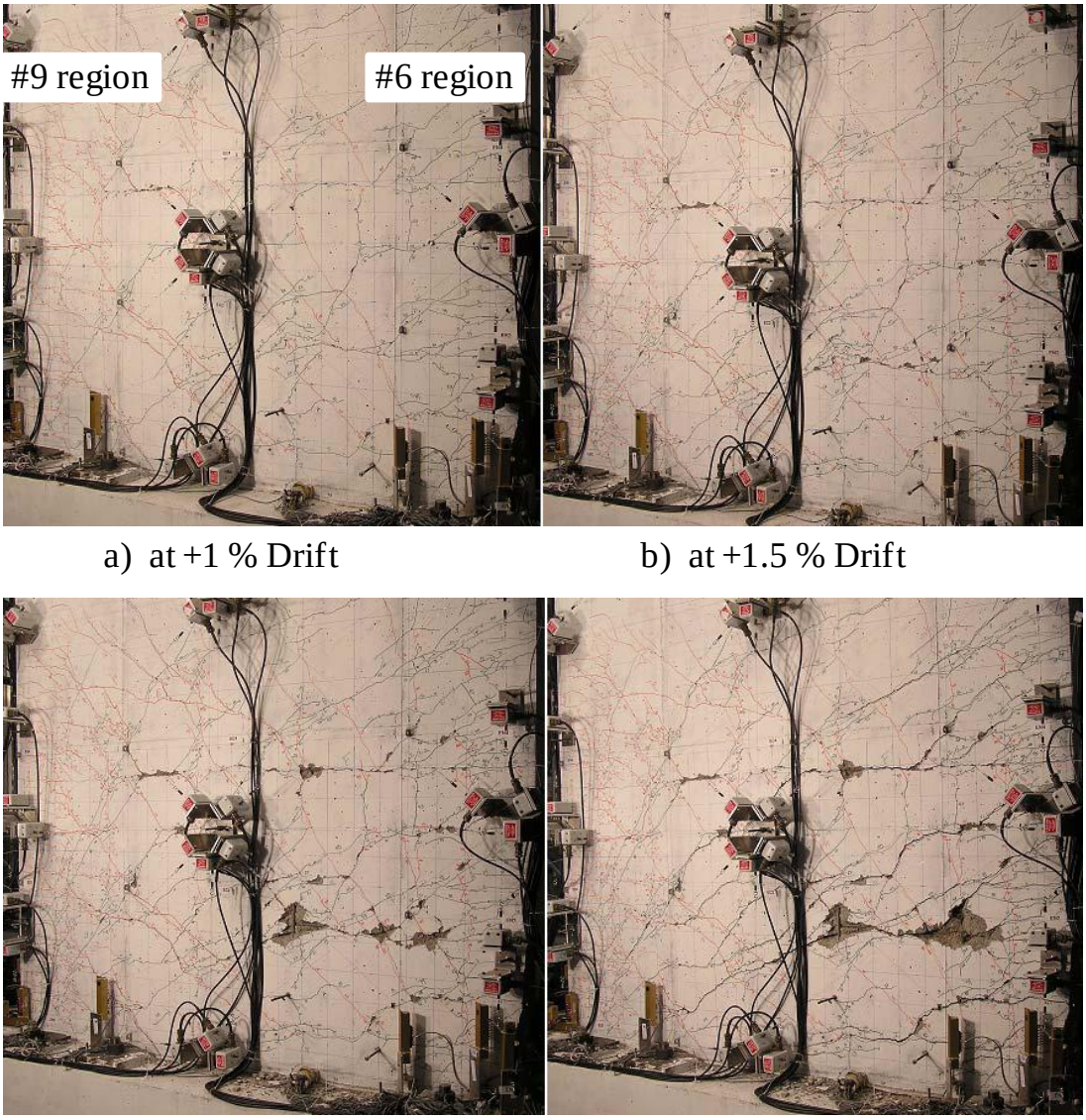

a) at +1 % Drift b) at +1.5 % Drift

c) at +2.0 % Drift d) at +2.5 % Drift

Figure 4.19 Extent of shear cracking observed at different drift levels within the first panel of RWC.

4.4.2.3 Response at top of Second Panel

The lateral load response of RWC at the top of second panel was also compared to the measured experimental response and is shown in Figure 4.20. The OpenSees model captured the force-displacement behavior at second panel level with good accuracy up to 1.5% drift in the #6 bars in tension direction. The stiffness of the loading, unloading, reloading paths and residual displacements were all well captured by the model in the #6 bars in tension direction. The initial stiffnesses in both directions were also captured accurately by the OpenSees model. However,

the residual displacements in the #9 in tension direction were under predicted as observed for the response at the top of the wall, which was also observed in RWN. This further reinforces the discrepancy in capturing the shear distortion by the *pinching 4* model.

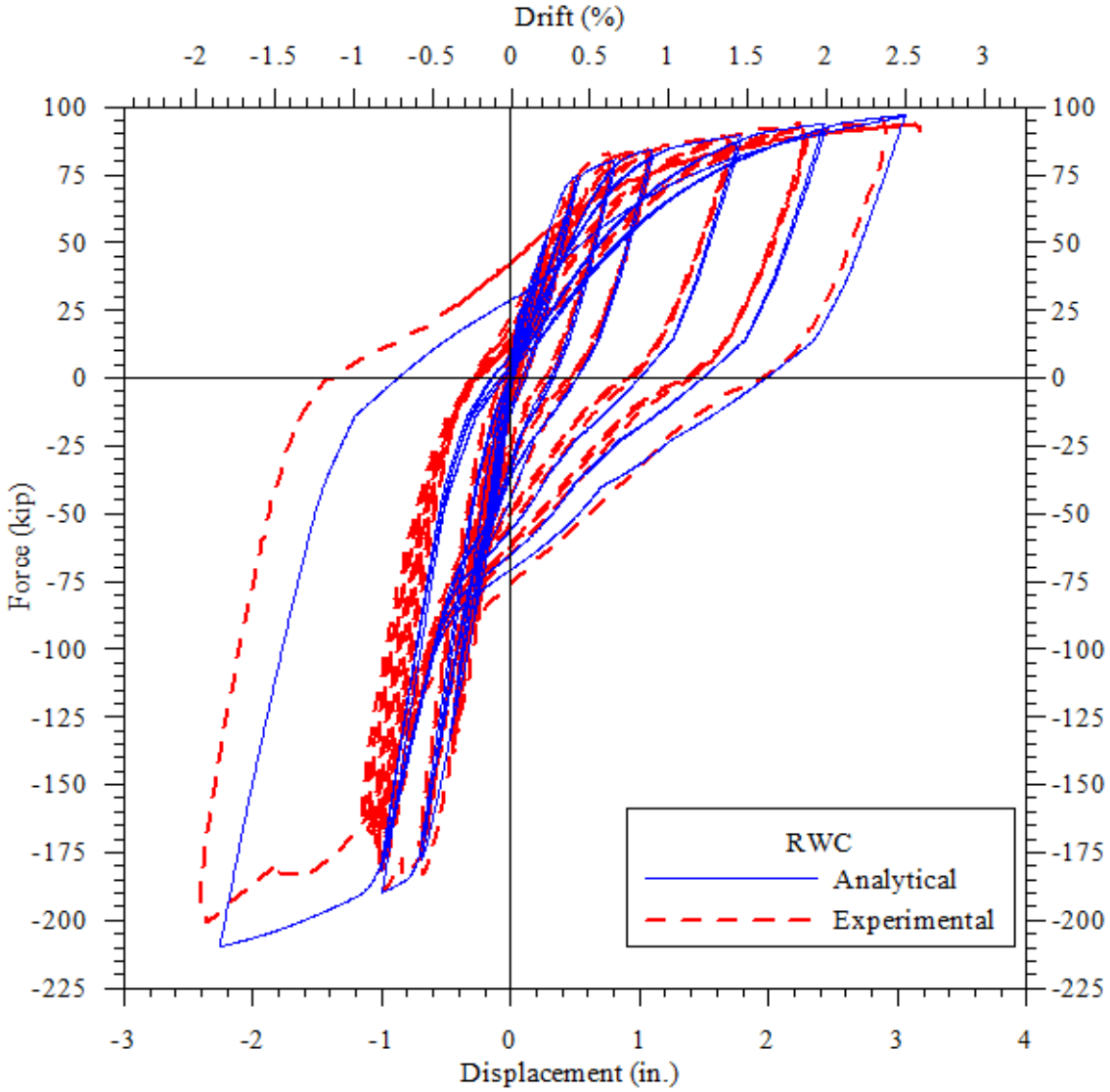

Figure 4.20 Comparison of the measured and calculated force-displacement responses of RWC at the top of the second panel.

4.4.2.4 Comparison of Deformation Components

Calculated and experimental values of various deformation component responses of RWC at the first panel level and the top of the wall during the peak displacements are compared

and appropriate comments are presented. Similar to RWN, the comparisons are presented only in the #6 bars in tension direction.

The comparison between the calculated and measured values of deformation components of RWC at the first panel level and the top of the wall are shown in Figure 4.21 and Figure 4.22 respectively. As observed in RWN, the flexural deformations in the first panel of RWC were

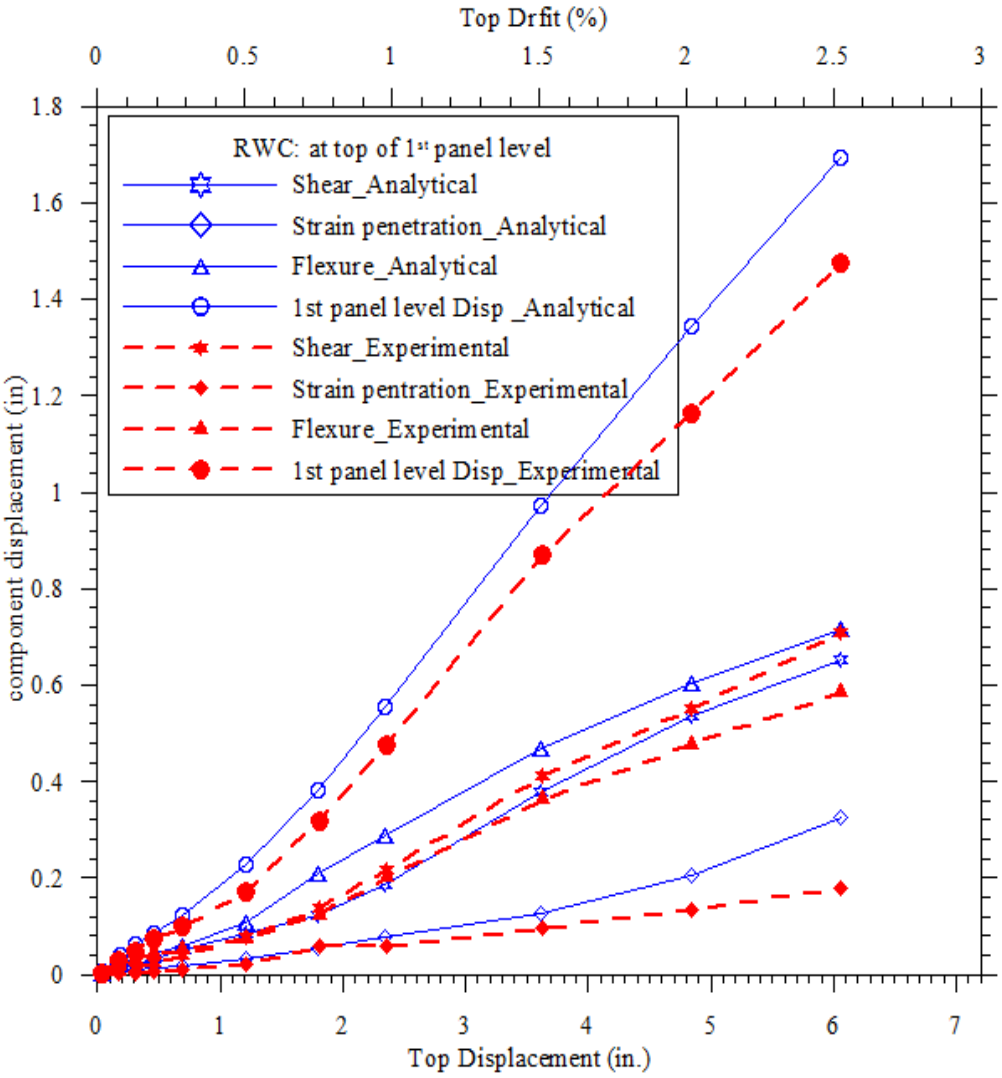

Figure 4.21 Comparison between calculated and experimental deformation component responses at the first panel level of RWC.

over predicted by the model. The deformation due strain penetration was well captured by the model up to a top displacement of 2.4 in. (i.e. 1% drift). The total flexure deformation at the top of wall was well captured by the OpenSees model and can be seen in Figure 4.22. The shear deformation and deformation due to strain penetration were well captured by the model up to a

top displacement of 2.4 in. (i.e. 1% drift). However, beyond 1% drift, the shear deformations and strain penetration deformations were under predicted and over predicted respectively. Consequently the prediction of overall response of RWC was not affected by the inaccurate shear and strain penetration deformations.

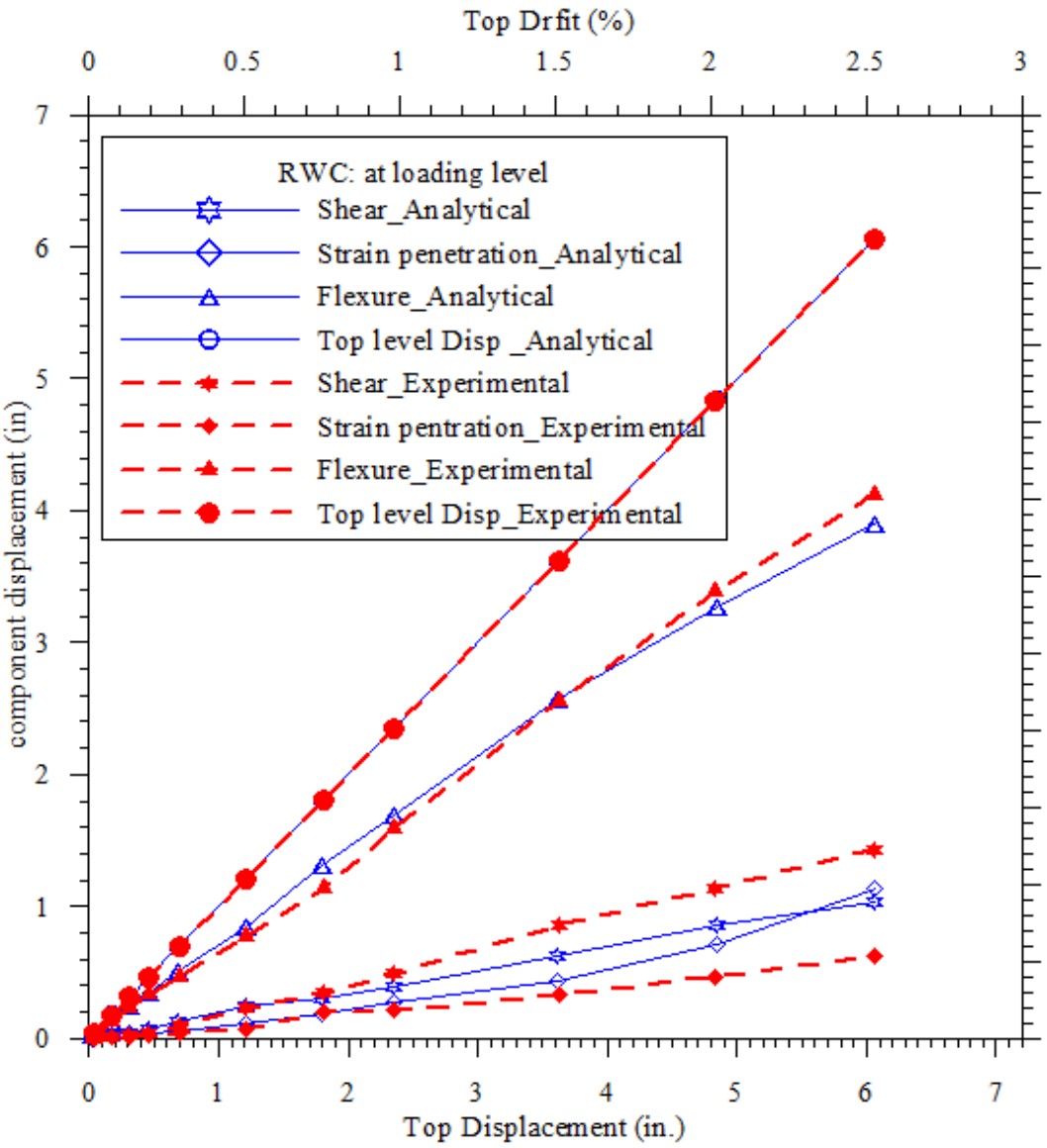

Figure 4.22 Comparison between calculated and experimental deformation component responses at the top of RWC.

4.4.3 RWS

In this section, the OpenSees analytical model and experimentally observed responses of RWS are compared and appropriate comments are made. In addition to the global response, accuracy of the local responses is examined, including the force-displacement response of RWS at different panel levels.

4.4.3.1 Cyclic Response

The measured and calculated cyclic responses of RWS subjected to the loading protocol in Figure 4.4 are shown in Figure 4.23. Figure 4.24 shows the comparison of measured response of RWS with the calculated response obtained by representing the traditional lap splice with a single bar.

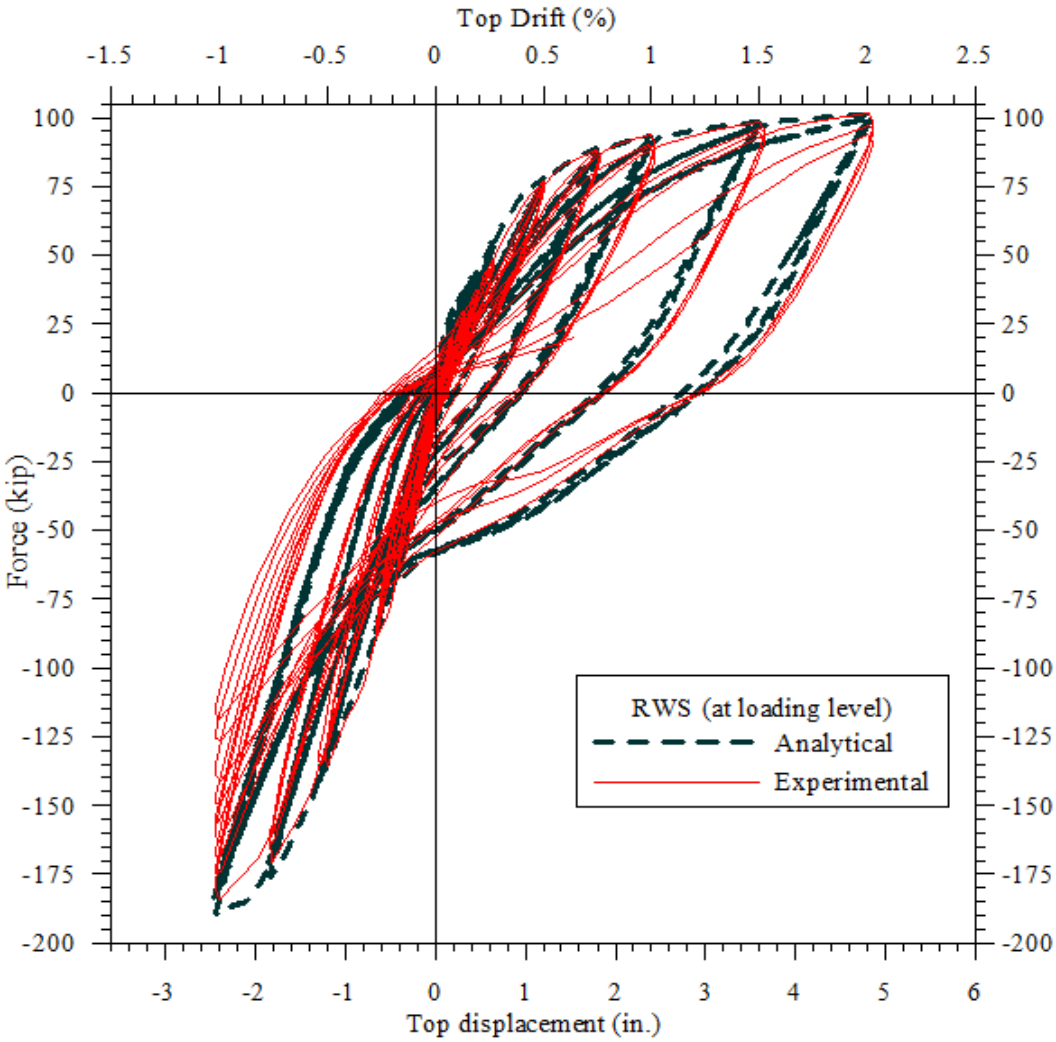

Figure 4.23 Comparison of the measured and calculated force-displacement responses of RWS.

This figure shows that replacing the bars in a lap splice with a single bar area didn't captured the strength of RWS and thus supports that a varying effective bar area along the lap splice length should be used to represent a lap splice region.

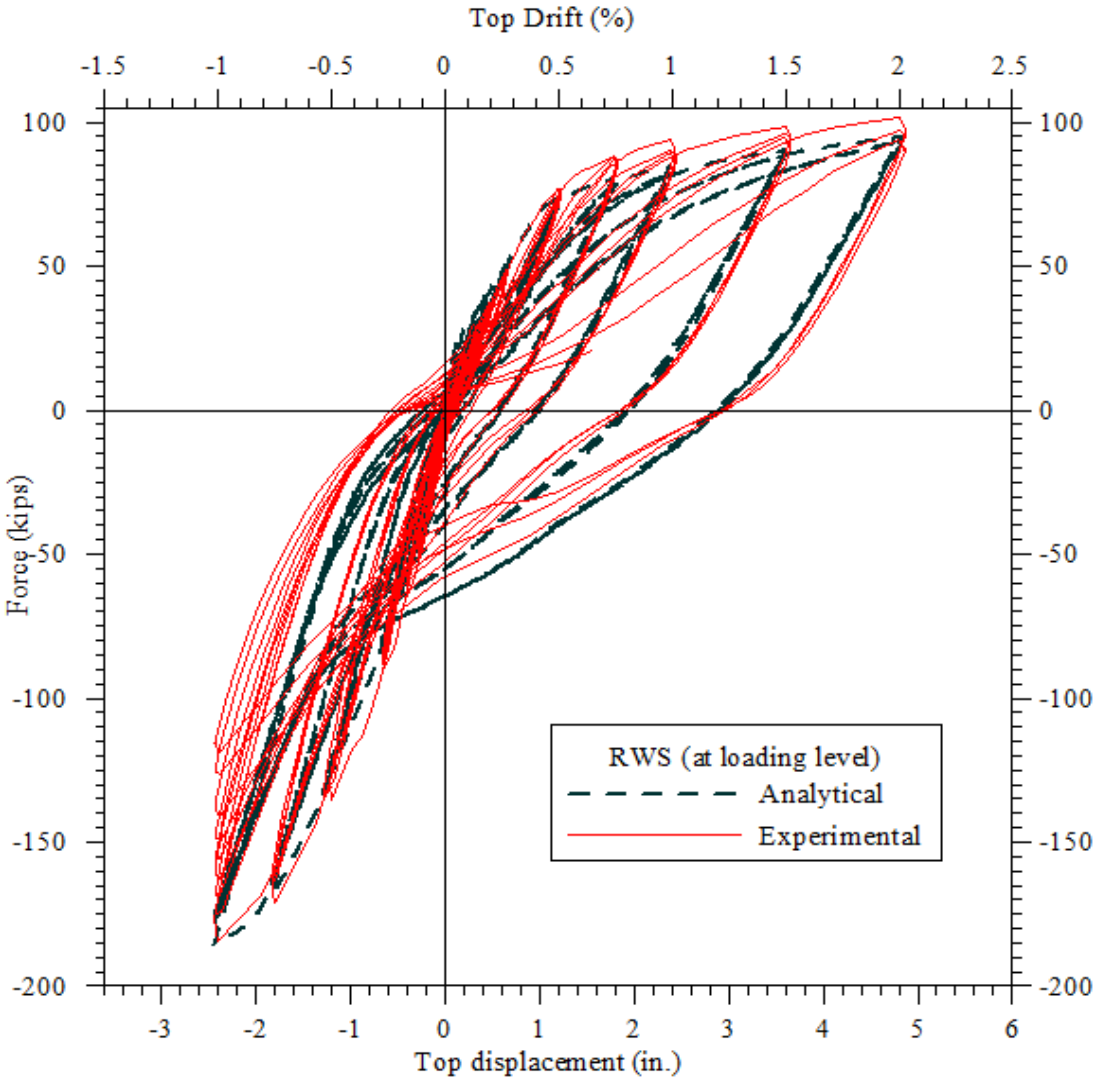

Figure 4.24 Comparison between the measured response of RWS and calculated force-displacement response using single bar assumption for lap splice.

As shown in Figure 4.23, the OpenSees simulation using equivalent effective bar area for lap splices accurately captured the force-displacement response of RWC for the loading direction that subjected the #6 and #5 longitudinal bars in tension. The unloading stiffness, reloading stiffness, and residual displacements were well simulated by the analysis model in this direction. In the direction that subjected #9 bars in tension, the analytical response is closely matched with the experimental response. The calculated peak values were within 3% of the experimental

values for up to a lateral displacement of 2.4 in. (i.e. -1% drift) in #9 bars in tension. The strength degradation observed at -1% drift was not captured by the OpenSees model. The strength degradation in the experimental response was observed due to the slip of longitudinal bars in lap splices (see Figure 4.26) and the shear stiffness degradation due to repeated cyclic loading at the lateral displacement of 2.4 in. (i.e. -1% drift) in the #9 bars under tension direction. As noted before (in section 4.3.3), the model did not account for the local bar slip in the lap splice region. Also, as observed before with RWN and RWC, *Pinching 4* model did not capture the shear stiffness degradation. However, the initial stiffness in the both directions was captured with good accuracy.

4.4.3.2 Response at the top of First Panel

To ensure that the OpenSees model adequately captured the different deformation components accurately, the responses at different panel levels were also examined. As explained in section 4.4.1.2, the comparison of lateral displacement at first panel level provides an opportunity to examine the modeling accuracy of the shear deformation. The calculated and measured force-displacement responses at the first panel level are shown in Figure 4.25a. Similar

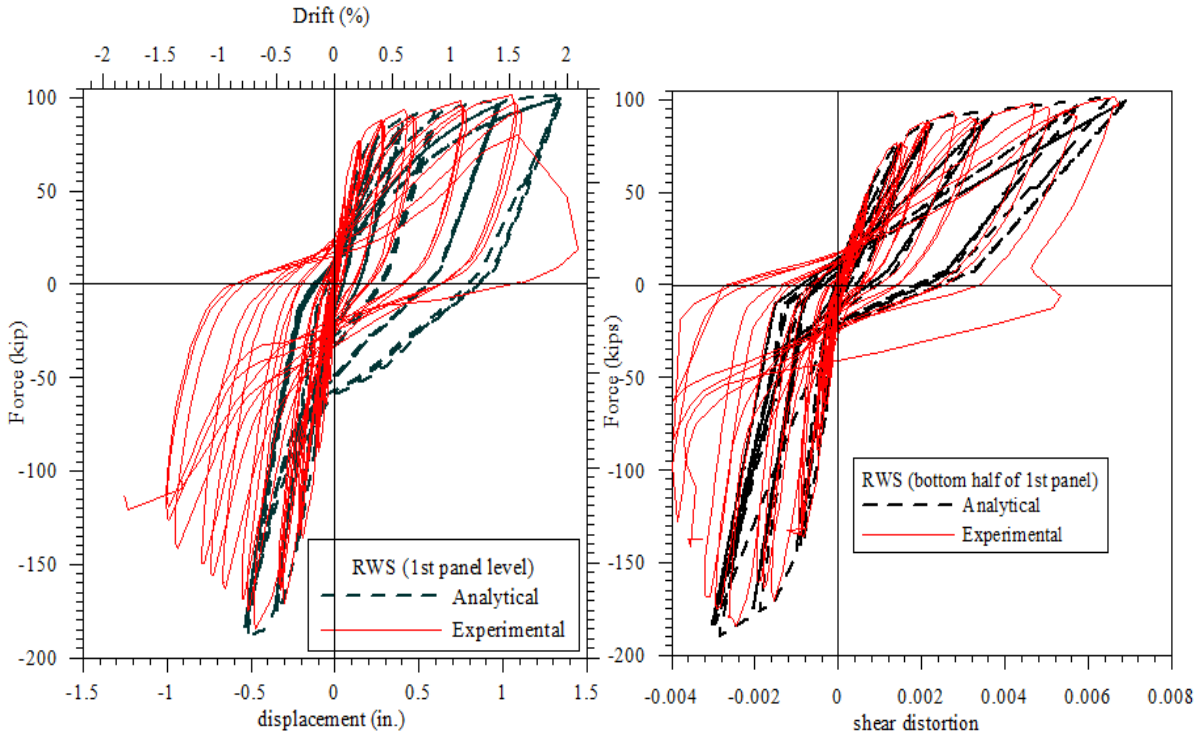

a) force-displacement response at top of 1st panel

b) force-shear distortion response of bottom half of 1st panel

Figure 4.25 Overall and the shear distortion responses of RWS at the first panel level.

to observations made in RWN, the OpenSees model did not capture the first panel response as accurately as it did at the top of the wall in both directions. The analytical model over predicted the displacement response in the #6 bars in tension direction. As observed in the previous walls (RWN and RWC) analyses, the analytical model didn't captured the strength degradation at 2.4 in. displacement in the #9 bars in tension direction (i.e., -1% drift). The analytical model captured the unloading and reloading stiffnesses for the #6 bars in tension direction, the initial and the post yield stiffnesses of the first panel with good accuracy.

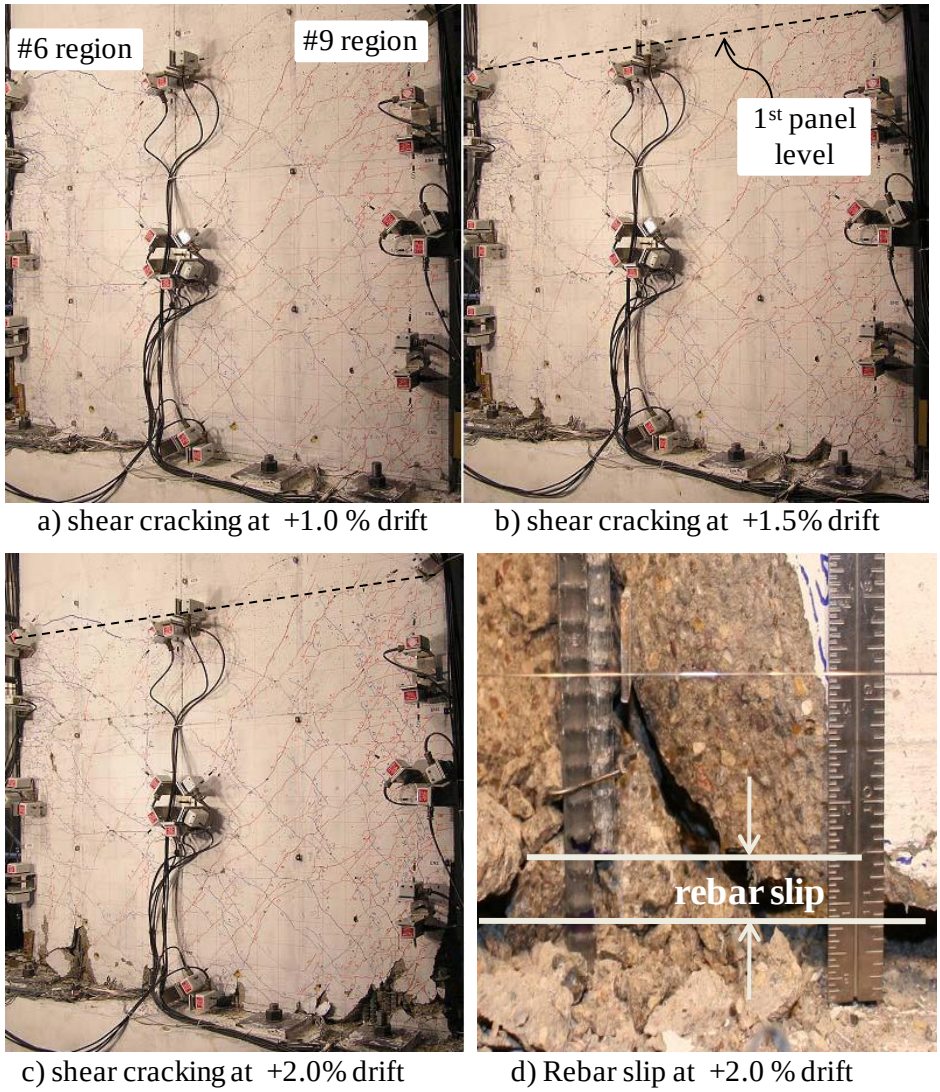

a) shear cracking at +1.0 % drift

b) shear cracking at +1.5% drift

c) shear cracking at +2.0% drift

d) Rebar slip at +2.0 % drift

Figure 4.26 Extent of shear cracking observed at different drift levels in the first panel of RWS and the observed rebar slip at 2%

The over prediction of the strength and not capturing the strength degradation at 1% drift in the #9 bars in tension direction was expected, as the local bar slip in the splice region was not modeled. This can be seen in the Figure 4.25b, which compares the predicted and experimental shear distortions in the bottom half of the first panel of RWS. Figure 4.26 shows the damage to the first panel of the wall at different drift levels and the observed bar slip in the lap splice region at 2% drift.

4.4.3.3 Response at the top of Second Panel

The lateral load response of RWS at the top of second panel level was also compared to the measured experimental response and is shown in Figure 4.27. The OpenSees model captured the force-displacement behavior at the second panel level with good accuracy in the #6 bars in tension direction. The stiffness of the loading, unloading paths and residual displacements were all well captured by the model in the #6 bars in tension direction. The initial stiffnesses in both directions were also captured accurately by the OpenSees model. The pinching of the force-displacement loops at 1.5% and 2.0% drifts were not well captured by the analytical model. However, this was expected because the RWS model did not account for the bar slip occurred in the lap splice region.

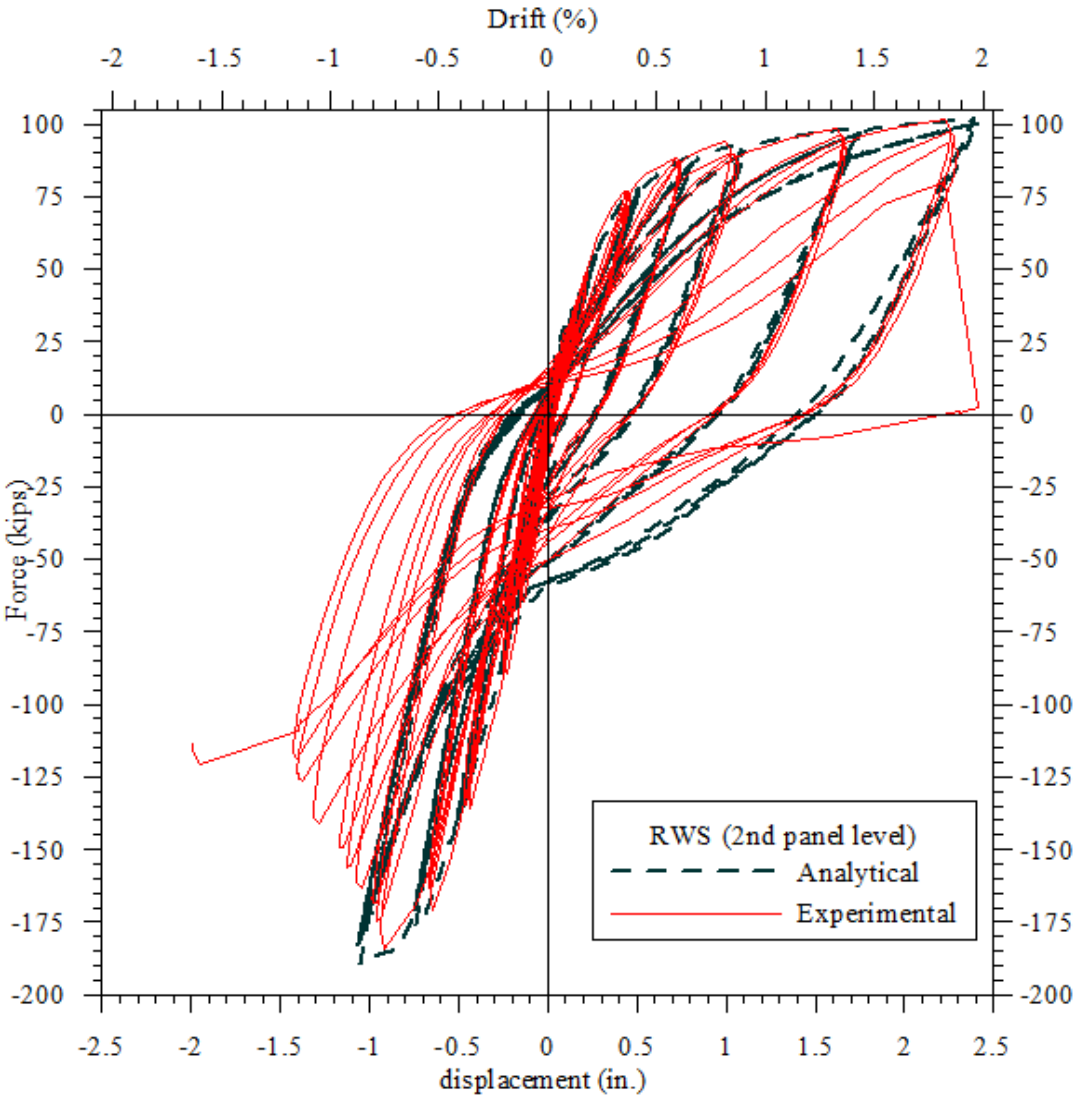

Figure 4.27 Comparison of the measured and calculated force-displacement responses of RWS at the top of the second panel.

4.4.3.4 Comparison of Components of Deformation

The comparison between the calculated and measured values of deformation components of RWS at the first panel level and the top of the wall are shown in Figure 4.28 and Figure 4.29 respectively. OpenSees Simulation overestimated the deformations due to flexure and strain penetration at the first panel level in RWS. However, the flexure deformation at the top the wall was well captured by the analytical model. The deformation due to strain penetration was overestimated by nearly 300%. At the top of the wall, the summation of the experimentally obtained deformation components (flexure, shear and strain penetration deformations) did not

match the measured displacement at the top of the wall. This was expected as local bar slip in the splice region was observed during the experimental testing of RWS (see Figure 4.26d). This local slip contributed to the additional rotation at the wall base and in turn to the lateral displacement of the wall. The instrumentation used for capturing the different deformation components, did not capture the deformation due to bar slip in splice regions. However, the analytical model overestimated the strain penetration deformation, which compensated the deformation due to the rebar slip in the splice regions. Consequently, the RWS model accurately captured the observed force-displacement response (see Figure 4.23).

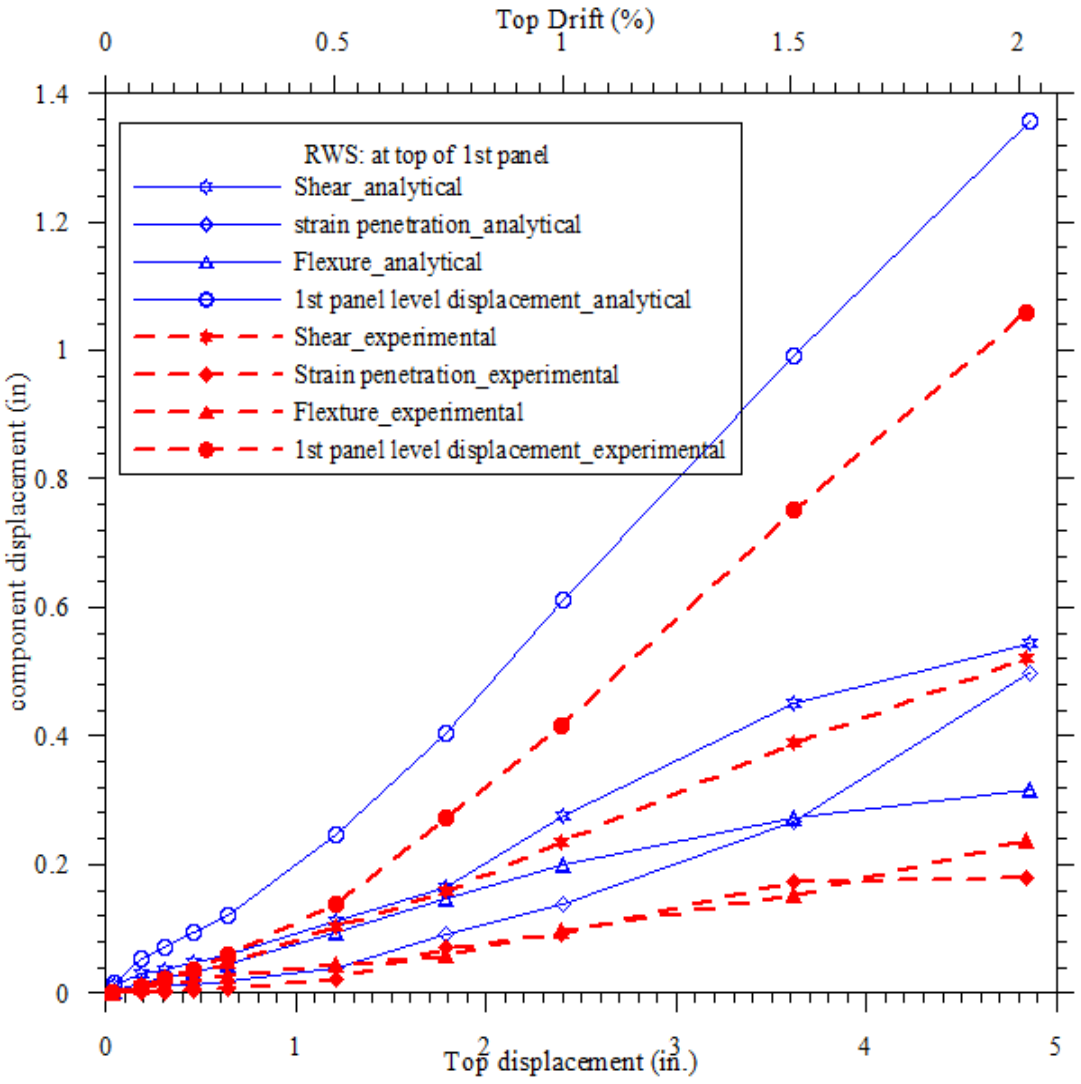

Figure 4.28 Comparison between calculated and experimental deformation component responses at the first panel level of RWS.

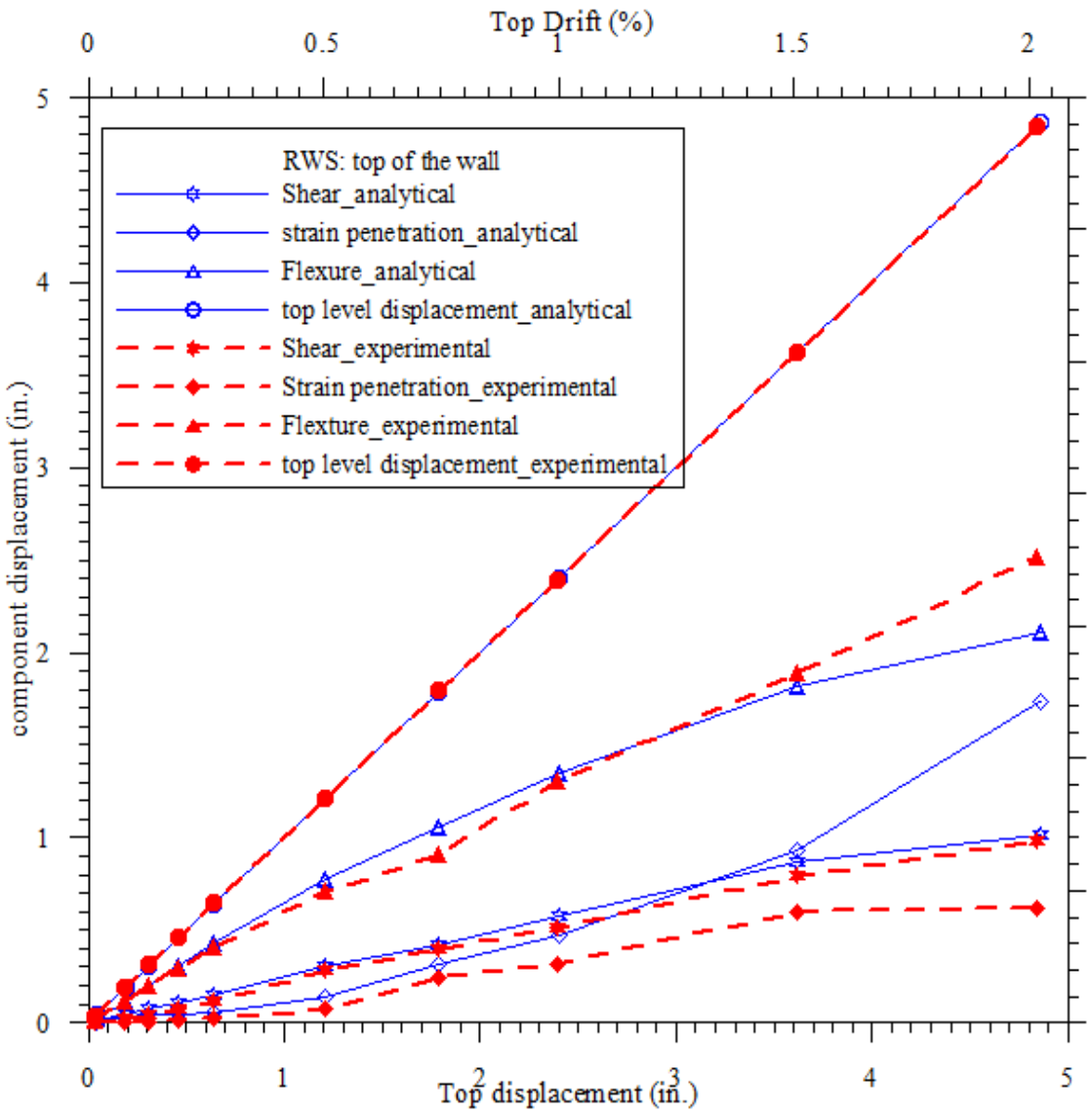

Figure 4.29 Comparison between calculated and experimental deformation component responses at the top of RWS.

Chapter 5
Analysis of NTW1

5.0 Introduction

As previously stated, in this PreNEESR project, two T-walls were constructed at 50 percent scale and tested to multi-directional loading at the NEES-MAST Facility in Minnesota. This chapter discusses the analysis of the first T-wall, NTW1, and the compares to the analysis results recorded during the test.

5.1 Prototype Wall

The prototype T-wall used in this study was a T-wall designed for a six-story prototype building located in Los Angeles, California. The floor plan of the prototype building is shown in Figure 5.1, and it had a 22,500 square foot (SF) floor plan with story heights of 12 feet at all levels. The gravity and lateral loads of the building were resisted by two separate systems. The gravity load system consisted of a 7 in. cast-in-place (CIP) concrete floor slab spanning between CIP or precast beams. The beams were supported on gravity columns located in a 20 ft by 45 ft grid. The lateral load was resisted by CIP concrete structural walls. A total of 10 T-walls resisted all the lateral force in the transverse direction, while additional rectangular walls were required in the building core to resist lateral load in the longitudinal direction.

The T-walls in the prototype building were designed using the IBC [2003] to resist a total building base shear of 351 kips and a base overturning moment of 183,887 kip-ft. These forces resulted in each T-wall having a 15 ft web, 12 ft flange, and a uniform thickness of 12 in. as shown in Figure 5.2, which shows details of a full-size T-wall with a design concrete strength of 5000 psi; the web and flange of the wall were detailed with boundary elements. The longitudinal reinforcement in the boundary element was 12 #11 bars in the flange and web tips. In addition, distributed vertical steel consisted of #5 bars at 18 in. on center (o.c.) was provided on each face of the wall in the regions outside of the boundary elements. The confinement ties were required for the bottom 13 ft 6 in. of the flange reinforcement and 15 ft of the web reinforcement. The

confined region extended 30 in. into the flanges and web. In order to prevent shear failure occurring prior to developing full flexural capacity, the required horizontal shear reinforcement was #5 at 12 in. o.c. on each face of the web and #5 at 18 in. o.c. on each face of the flange. More description of the prototype T-wall design may be found in Brueggen et al. (2009).

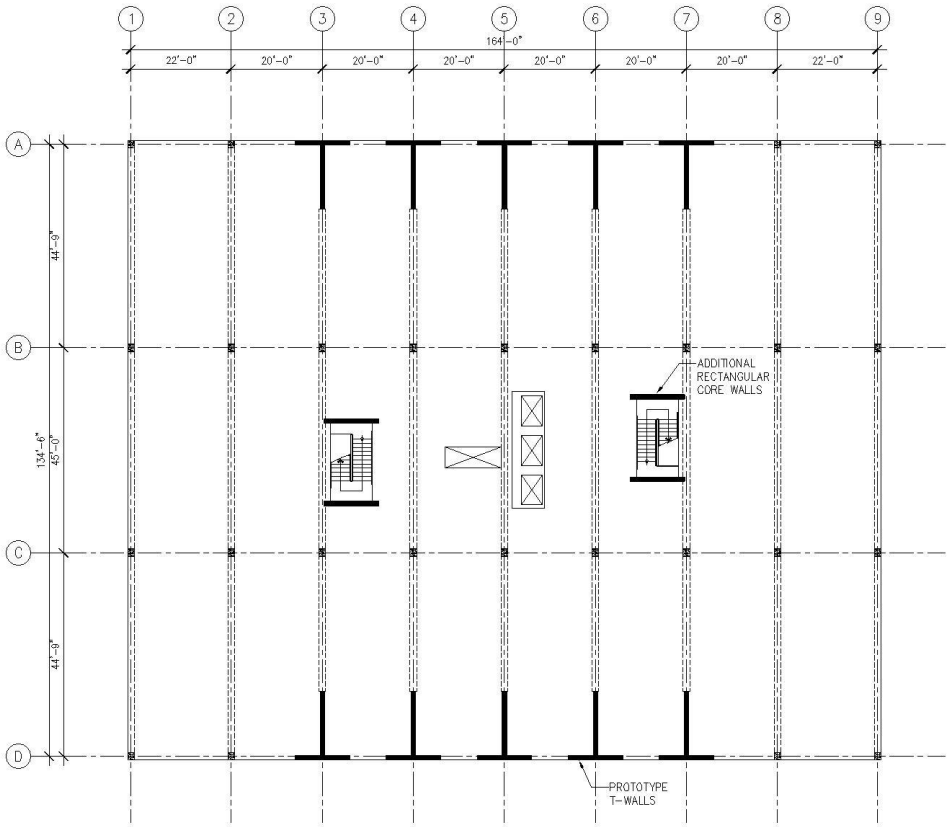

Figure 5.1 Floor Plan of the Six-Story Prototype Building

5.2 Description of NTW1

The first T-wall specimen tested at UMN, referred to as NTW1, and was a 50% scale of the prototype T-wall, shown in Figure 5.3. While the T-walls in the prototype building were six stories high, NTW1 only had four stories but the effect of the missing two stories was included by applying a moment at the top of the wall in addition to the lateral force to simulate the moment gradient along the wall height as accurately as that expected for the prototype wall. NTW1 had a 6 ft long flange and 7 ft 6 in. long web, with a uniform thickness of 6 in. With

concrete design strength of 4,000 psi, NTW1 was designed with eight #6 bars and two #5 bars in the boundary elements in the flange tips. The web tip boundary element was extended by adding two #3 bars to the eight #6 and two #5 bars. This extension was required to meet the length of boundary element required by ACI 318-02 [2002]. The distributed steel in the web of the T-wall outside the boundary element was #3 at 12.5 in. o.c. on each face; while six #3 bars were used in the flange at a spacing of 6.5 in. The shear reinforcement was #3 bars at 7 in. o.c. on each face of the flange and web. The wall was 288 in. tall with 21 in. thick base and top blocks, totaling a specimen height of 330 in.

5.3 Description of Analysis Model

Modeling of NTW1 in OpenSees posed a number of new challenges in comparison to the modeling of the response of rectangular walls presented in Chapter 4. The T-wall model needed to be capable of a) being loaded in a number of load paths in multiple directions, b) accounting for shear lag, and c) accurately simulate the moment and lateral force. The analytical model developed is described in this section, along with how these challenges were overcome.

The base block of NTW1 was connected to the strong floor with ten three-in. diameter threaded Dywidag bars. The height of the base block was expected to provide adequate anchorage for the wall longitudinal reinforcement. Consequently, as with rectangular wall models, the base block was represented with a node in the analysis model and the degrees-of-freedom of this node was fixed in all directions. The base block did not move during the test, satisfying the assumed boundary condition in the model.

The interface between the T-wall and the base block was modeled using a zero-length interface element to account for the strain penetration effects. The interface element had a fiber section with the same cross section as NTW1 except that the steel reinforcement was replaced with the strain penetration material model developed by Zhao and Sritharan [2007].

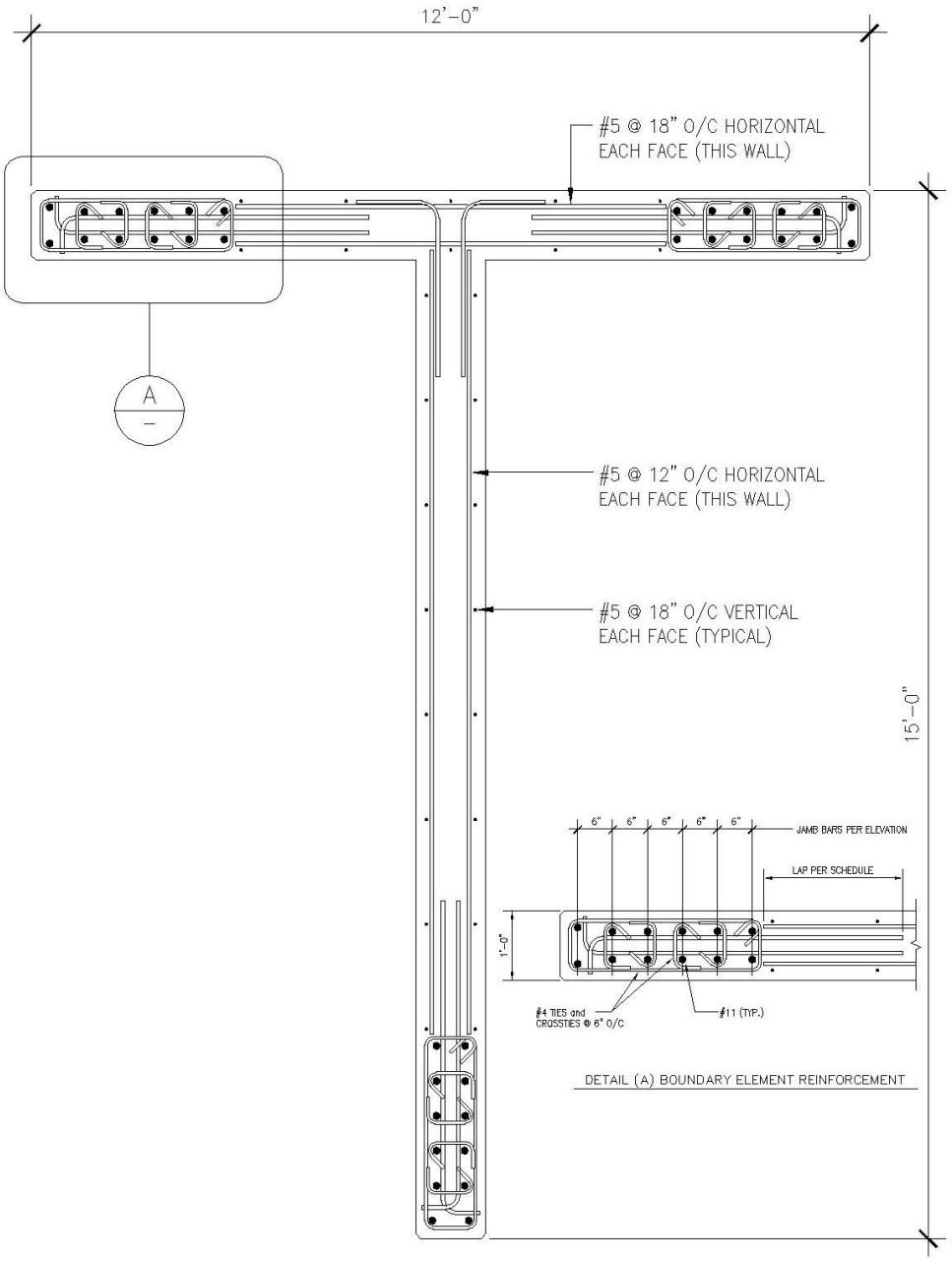

Figure 5.2 Details of T-wall in the Prototype Building

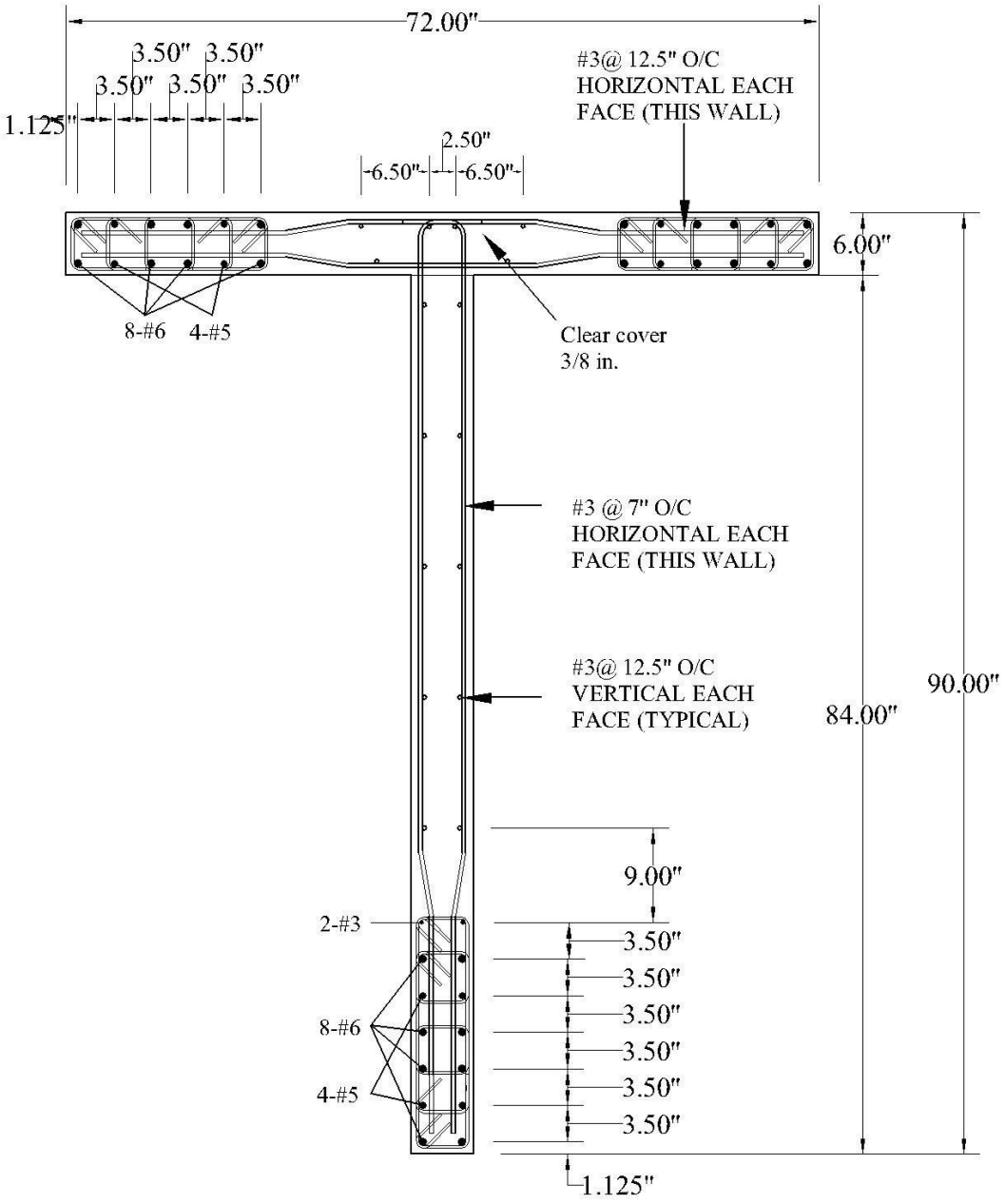

Figure 5.3 Cross-section Details of Test Specimen NTW1

The wall was modeled using a force-based beam-column element developed by Taucer et al. [1991]. A single force-based beam-column with five integration points was used to model the entire height of the wall, resulting five integration points to be located at 0 in., 99.46 in, 144 in., 238.27 in, and 288 in above the base of the wall (see Figure 5.4b). A fiber section was used to

model the cross section of the wall. And it was discretized using fibers approximately 0.25 in. by 0.25 in. for the confined and unconfined concrete regions. The confined and unconfined concrete were modeled using a Kent & Park model with nonlinear tension softening which was available in OpenSees as "*Concrete03*". Implementation of *Concrete07* was not completed prior to testing of NTW1. The peak tension stress of the concrete was assumed to be $7.5\sqrt{f_c'}(psi)$ with the post peak behavior similar to the University of Houston model recommended by Belarbi and Hsu [1991] and Pang and Hsu [1992]. The unconfined concrete was based on 130% of the design concrete strength of 4000 psi with the assumption of peak compressive strain occurring at 0.002. The confined concrete properties were calculated using the confined concrete model proposed by Mander et al. [1998] based on the details of the transverse reinforcement and assumed unconfined concrete. The longitudinal reinforcement was modeled by matching the modified Menegotto-Pinto model available in OpenSees (i.e., *Steel02*) using the average results obtained from testing three tension for the #3, #5, and #6 bars. The reinforcement properties used for the OpenSees model are shown in Table 5.1.

Table 5.1: Analytical Reinforcement Properties Used in the NTW1 Model

Bar Size	Yield Stress (ksi)	Elastic Modulus (ksi)	Strain Hardening Ratio
#3	76.0	29000*	0.02
#5	63.0	29000*	0.02
#6	60.0	29000*	0.02

* assumed value

The top block of NTW1 (see Figure 5.4a) was modeled using a rigid beam-column element, as shown in Figure 5.4b. This element allowed the deformations of NTW1 model at the height of the bottom of the crosshead to be monitored during analysis. This information was critical as the force and displacements were applied to the test specimen at the MAST facility at this location. Additionally, another rigid element was included in the NTW1 model (See Figure 5.4b) to allow load to be applied at 24 in. above the top of the wall because this application point best simulated the moment gradient through the first floor when an inverse triangular load as typically used in design for the original 6 story wall was imposed. Consequently, this point

became the control point in the analysis model; Figure 5.5 shows the moment diagram for the inverse triangular load pattern and the moment diagram for the applied loading. The difference in displacement between the bottom of the crosshead and the control point was less than 0.00001 in.

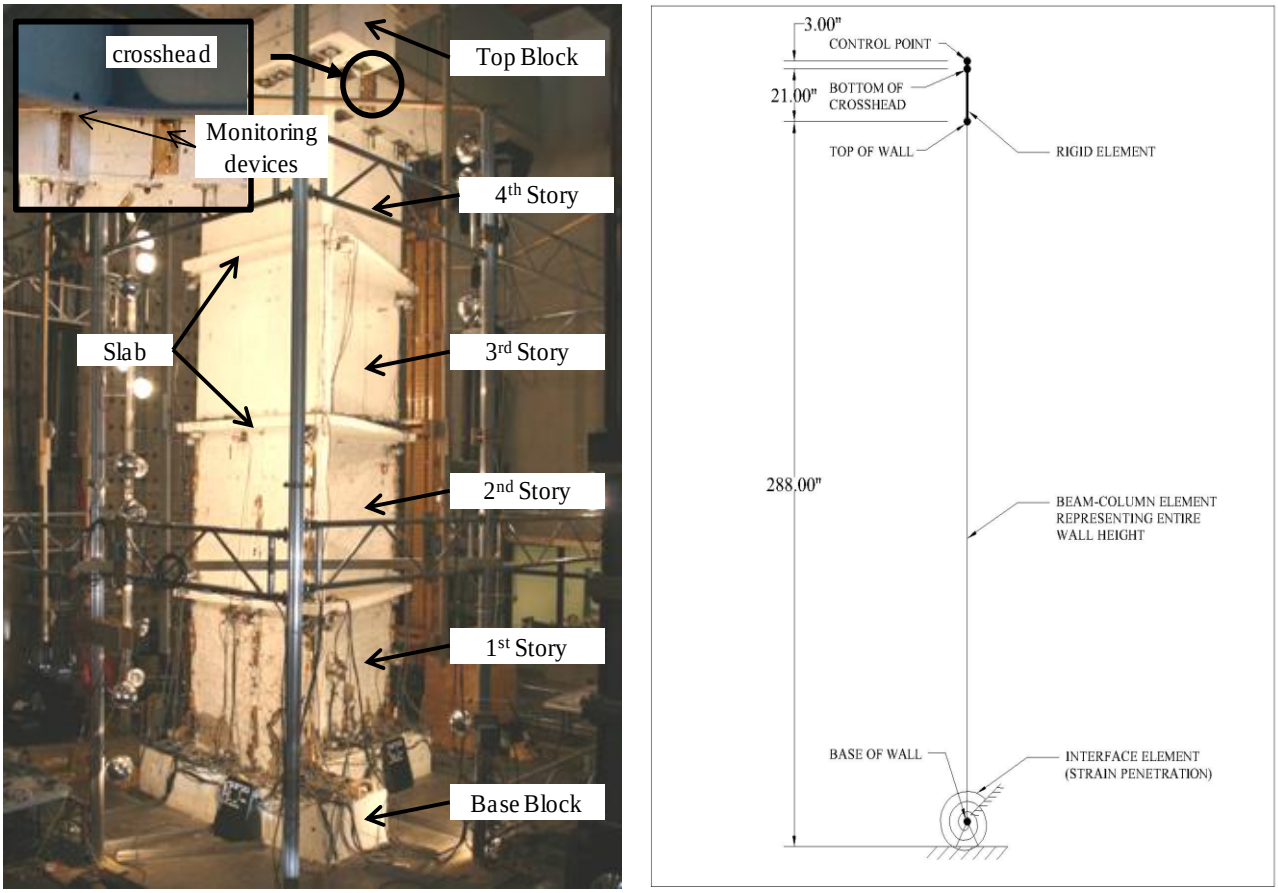

a) Full view of NTW1 specimen

b) Schematic of the analytical model of NTW1

Figure 5.4 Full view of NTW1 test setup and Schematic of the analytical model of NTW1

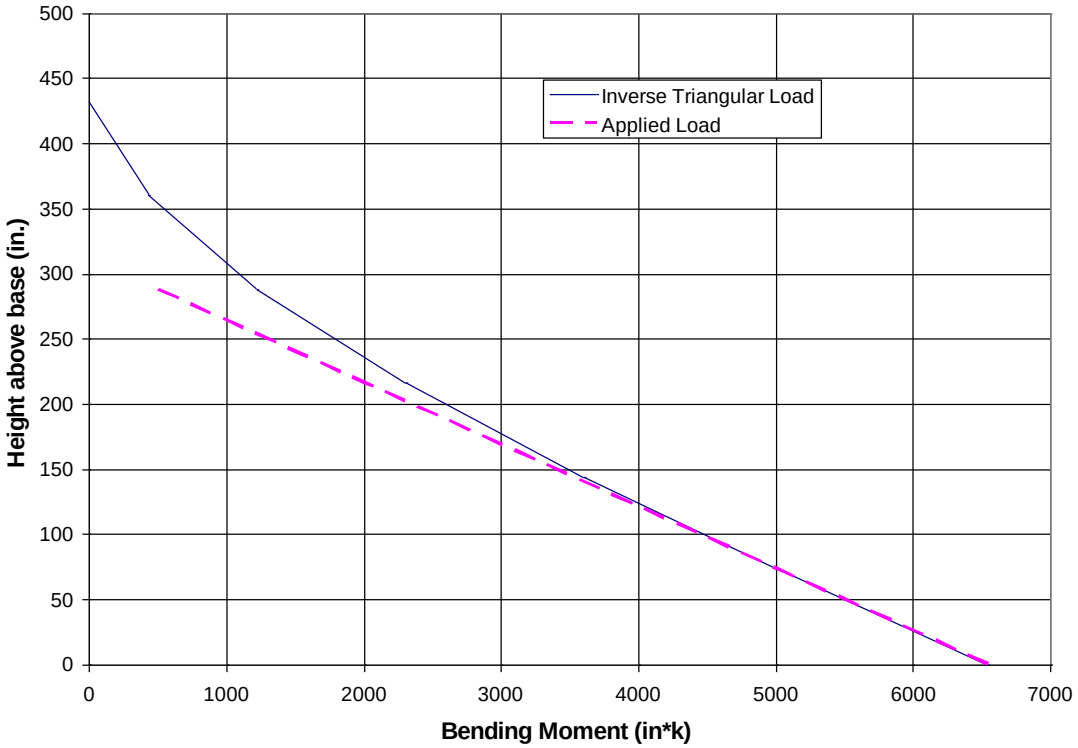

Figure 5.5 Bending Moment Profiles

An axial load of 186.5 kips was applied to NTW1 at the top of the wall. This value was determined based on the prototype building to reflect the axial load effect that would be typical of a T-wall in the prototype structure. In order to apply the displacement in the directions parallel to the web and the flange, boundary constraints were applied to the control point, located 24 in. above the top of the test wall. During analysis, the values of the two lateral displacement degrees-of-freedom (DOF) at the control point were specified at every time step, allowing the wall to be displaced in any desired direction or path.

5.4 Multidirectional Load Path

In order to develop a load path suitable for testing of NTW1, the envelope responses were needed to be defined. In a unidirectional test, the monotonic force-displacement response will define this envelope. In the two dimensional lateral loading used for the T-wall test, the envelope had to be defined by a surface. The two critical points on a monotonic envelope in a one dimensional space are the “first yield” and “ultimate” points. For the first T-wall test, the

"first yield" point in any direction of loading was defined as the displacement when the first bar in the cross section reaches the yield strain of the reinforcement. The "ultimate" point was defined by the strain in the confined concrete at the critical region achieving the compressive strain capacity or the tension strain in the critical longitudinal bar reaching 0.06 to account for bar fracture due to low cycle fatigue. The compressive strain capacity for the confined concrete was calculated based on the model proposed by Mander et al. (1988). However, since the ultimate strain is significantly underpredicted by this model, the strain capacity was increased by 30% over the theoretical value.

It was intended that NTW1 would be displaced in directions parallel to the web, parallel to the flange, and with components parallel to the web and flange. Therefore, the wall model was analyzed in several different directions, and the first yield displacement and the ultimate displacement capacity were defined for each loading direction. These displacements could then be plotted with respect to the direction to develop the yield and failure surface for NTW1. Figures 5.6 and 5.7 show the surfaces in terms of displacement and force, respectively. In the figures throughout this chapter, positive displacements parallel to the web place the flange in compression, while negative displacements in the web direction loading place the flange in tension. The idealized yield displacement is shown in Figure 5.6 as the "ductility 1" surface. The "ductility 1" displacement was calculated by multiplying the first yield displacement in any given direction by the force corresponding to either a strain in the concrete of 0.004 or a tension strain in the reinforcement of 0.015, whichever occurred first and dividing by the first yield lateral force in that direction. These strain limits chosen for the ideal strength of walls followed the recommendation of Priestley et al. (1996). Failure points defined by both concrete and steel strain limits are included in Figures 5.6 and 5.7 to show what controlled the failure surface as a function of loading direction. These figures do not include the effect of shear lag across the flange for the flange-in-tension loading direction. From the results of these analyses, the load path for the test specimen was determined.

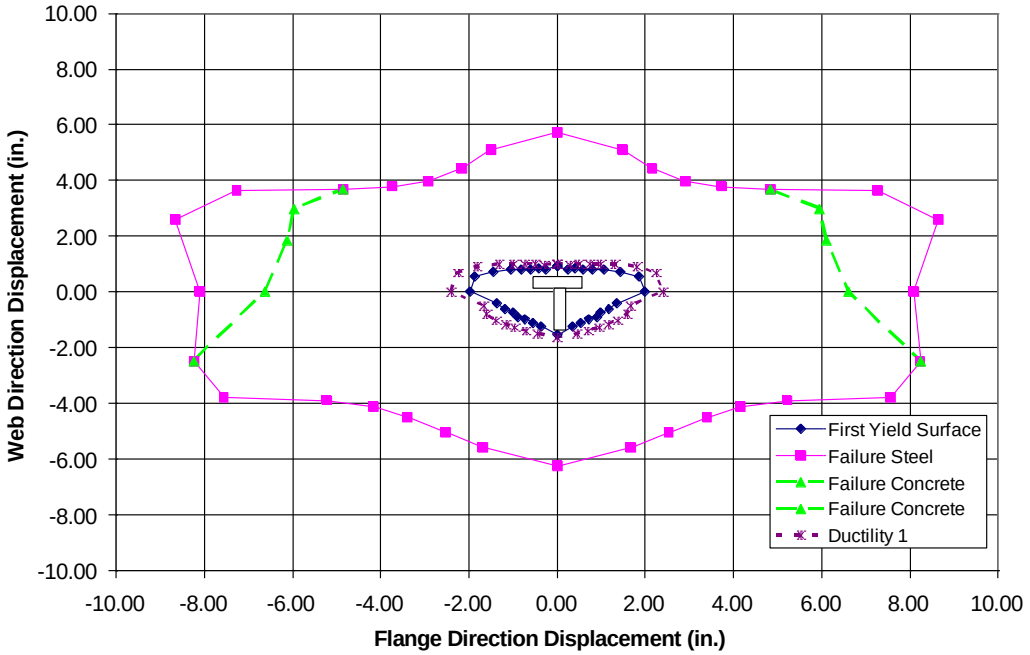

Figure 5.6 Theoretical First Yield and Ultimate Displacement Surfaces Established for NTW1 and Ultimate Displacement Surfaces

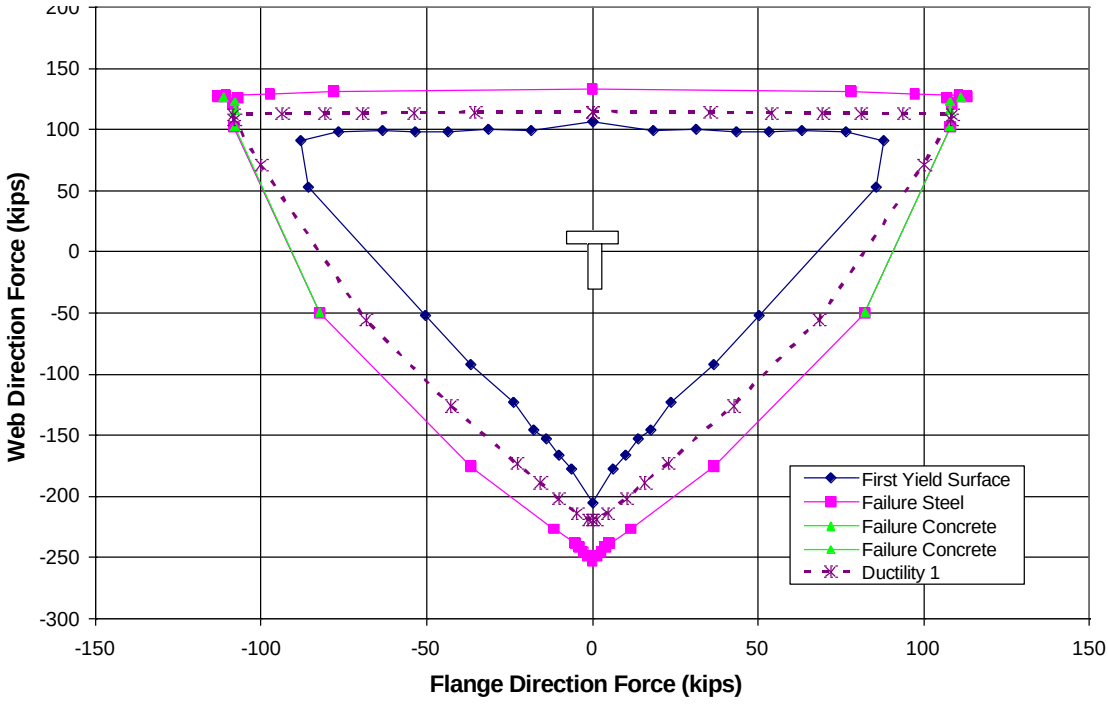

Figure 5.7 Theoretical First Yield and Ultimate Force Surfaces Established for NTW1

For all test cycles, the displacements of the translational degrees-of-freedom (DOF) at the control point, located 24 in. above the top of the top block of NTW1, were specified. The rotational DOF were unconstrained, and thus could take any value required by the analysis. The values of the translational DOF were specified at each time step to allow the wall to be displaced along predicted displacement paths. Although, this approach was initially used for establishing the load paths for the test, the lateral displacements applied by the crosshead were eventually used for the analysis to ensure the analytical model was subjected to the same displacement path as NTW1 for comparing the results. The displacement targets at the bottom of the crosshead were recorded during the tests; these targets were applied at the control point. The 3 in. difference in location resulted in a difference of less than 0.00001 in.

All analyzes were executed using the Krylov-Newton algorithm to minimize the computation time. This algorithm does not update the stiffness matrix at each iteration, saving computational time but may require additional iterations to reach a converged solution. The Krylov-Newton algorithm uses subspace acceleration in order to reduce the number of iterations required to find the converged solution. The convergence was determined based on the displacement increment, and the analysis was allowed up to 200 iterations to find a converged solution. Two hundred iterations allowed the analysis to find a solution; few steps required more than 10 iterations to find a converged solution. If the iteration limit was reached, it was because of an error in the analysis model, or the step was too large and was reduced.

The load path suitable for testing NTW1 was developed in terms of the first yield displacement for any given direction. This resulted in different displacement values in each direction; however, this approach was intended to allow the maximum strains and, therefore, damage in each direction to a similar level prior to moving to the next level of displacement. The selected load paths for testing NTW1 are prescribed in Figures 5.8 through 5.19. These load paths were motivated to gain as much experimental information as possible on the following behavior of walls:

- Shear lag for flange-in-tension direction loading;
- Bond slip due to strain penetration;
- Largest strain demand on the concrete/reinforcement;
- Simulation capability of OpenSees; and

- Effect of 2D lateral load path on T-wall response.

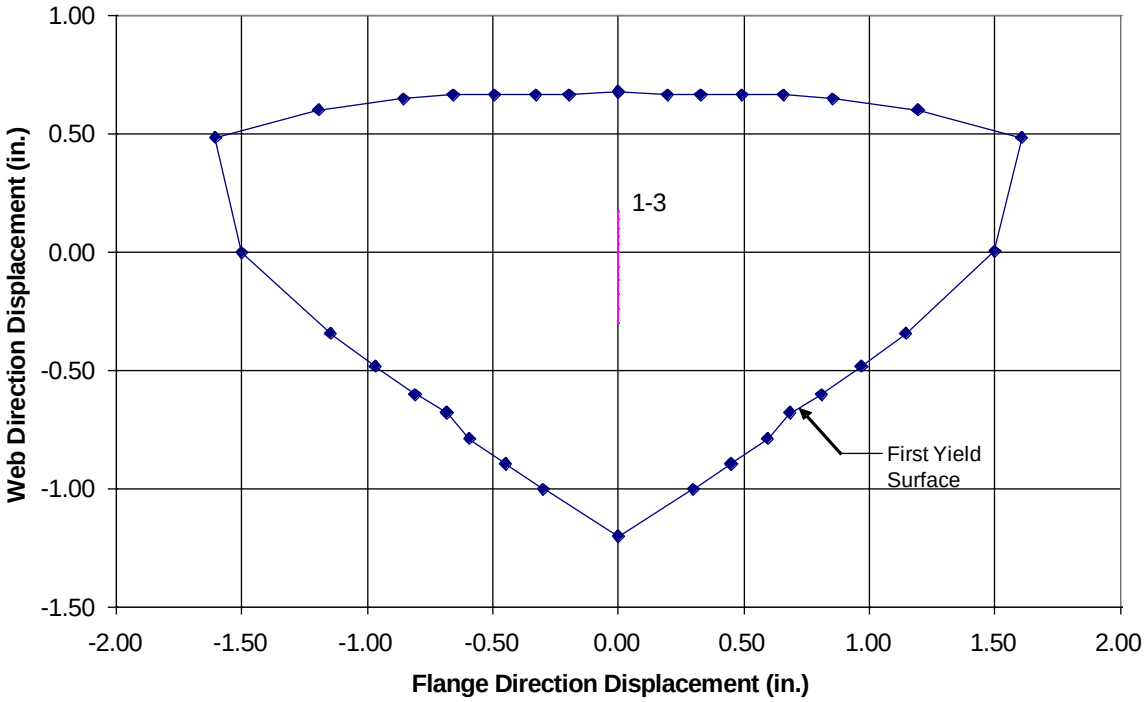

Figure 5.8 Load Steps 1 to 3 to Test in the Web Direction at 25% of the First Yield Displacement.

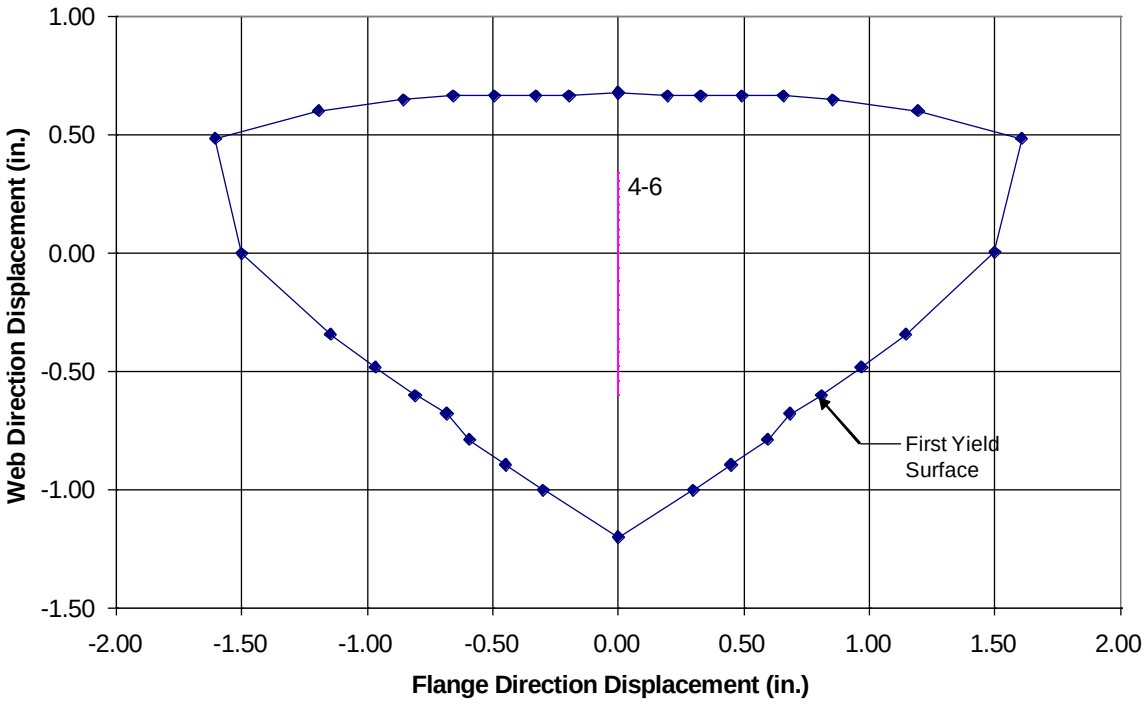

Figure 5.9 Load Steps 4-6 to Test in the Web Direction at 50% of the First Yield Displacement

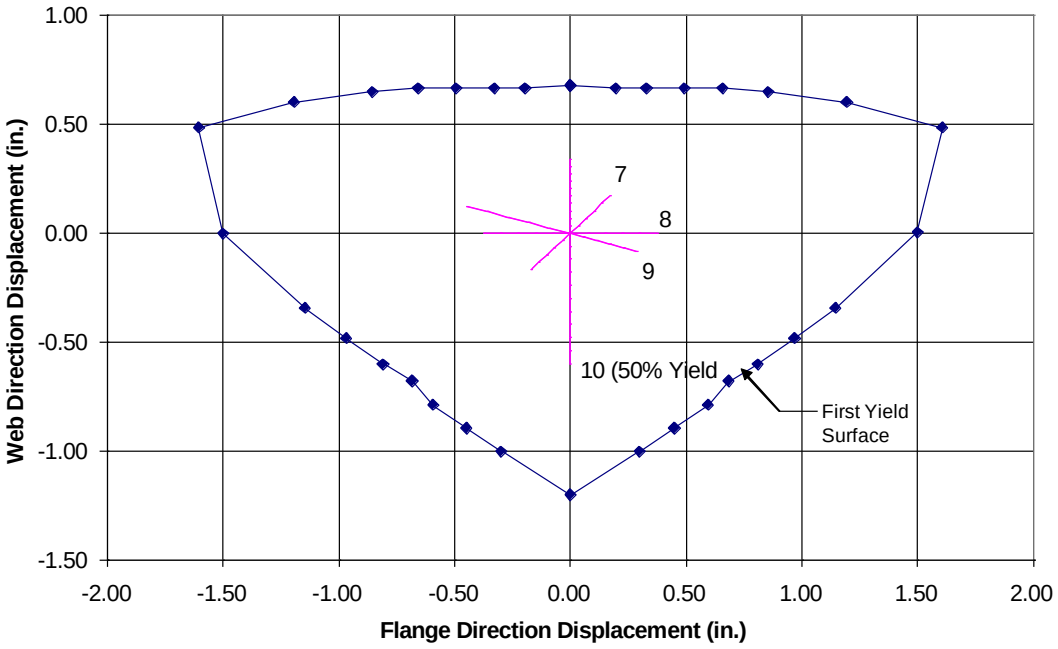

Figure 5.10 Load Steps 7 to 10 to NTW1 at Test 45º, Parallel to the Web, and 100+30 Directions at 25% of First Yield Displacement, and Repeat 50% of the First Yield in the Web Direction

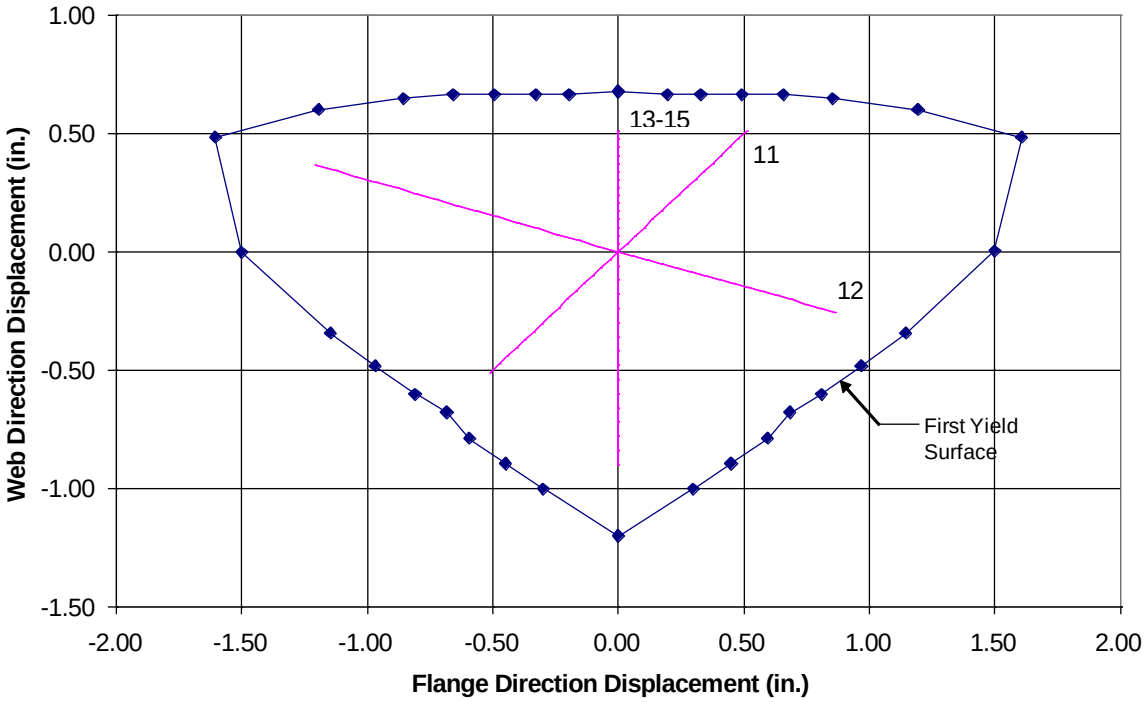

Figure 5.11 Load Steps 11 to 15 to Test NTW1 45º, 100+30, and the Web Direction at 75% of First Yield Displacement

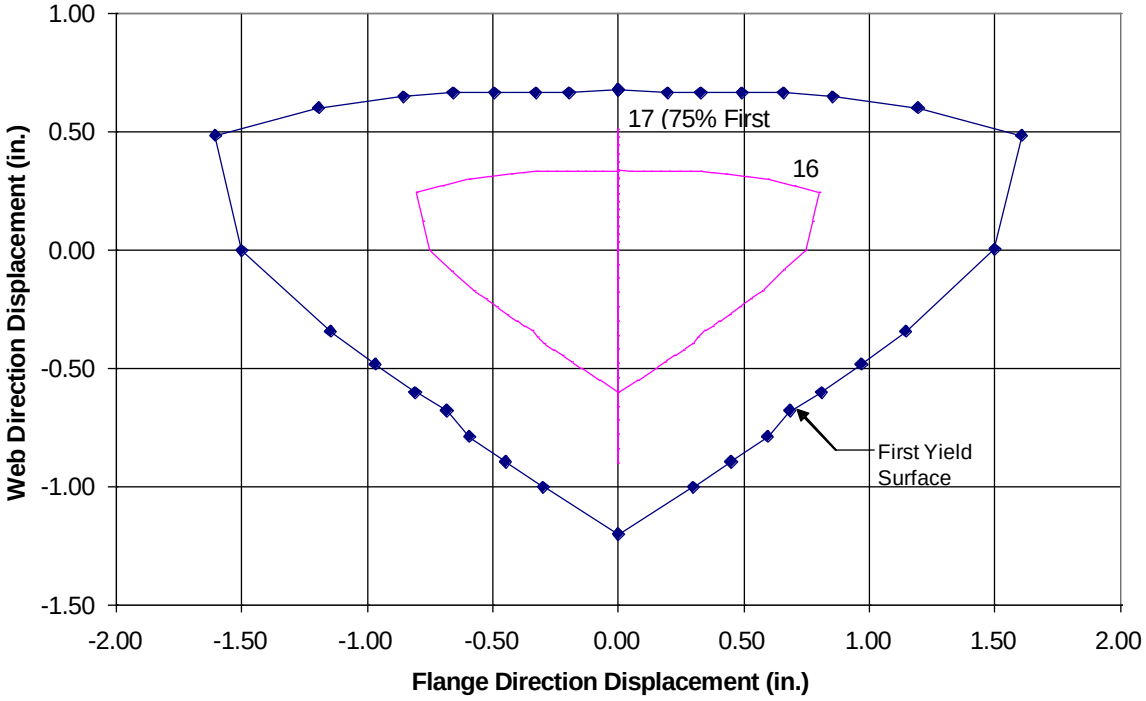

Figure 5.12 Load Steps 16 and 17, to Test NTW1 at 50% First Yield Surface Path and the Web Direction to 75% of the First Yield Displacement

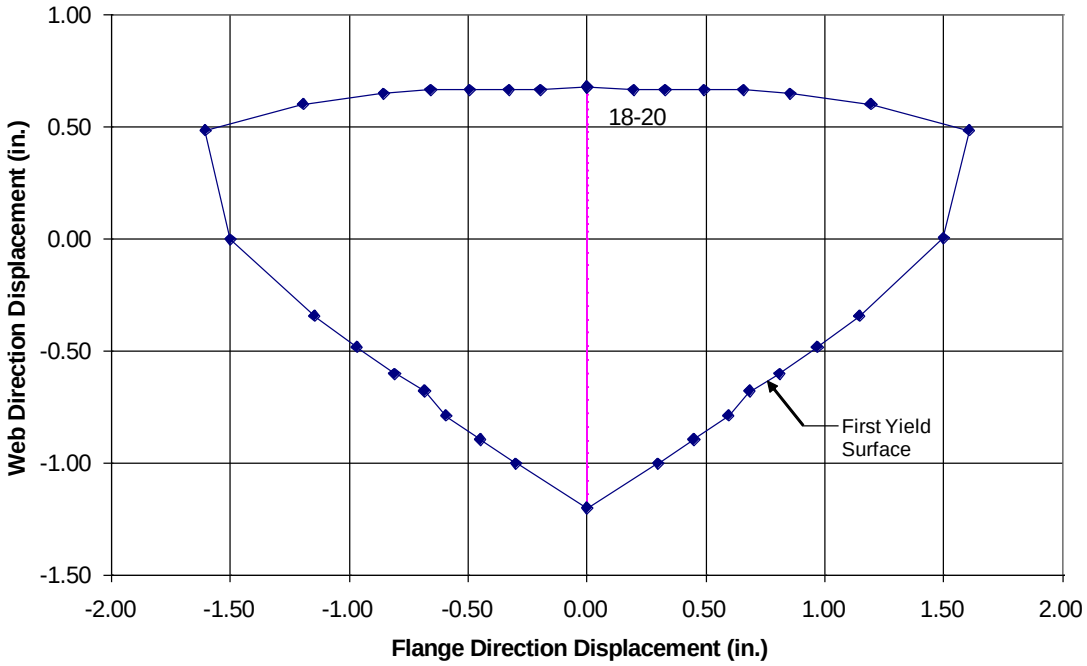

Figure 5.13 Load Steps 18 to 20 to Test NTW1 in the Web Direction of 100% First Yield Displacement

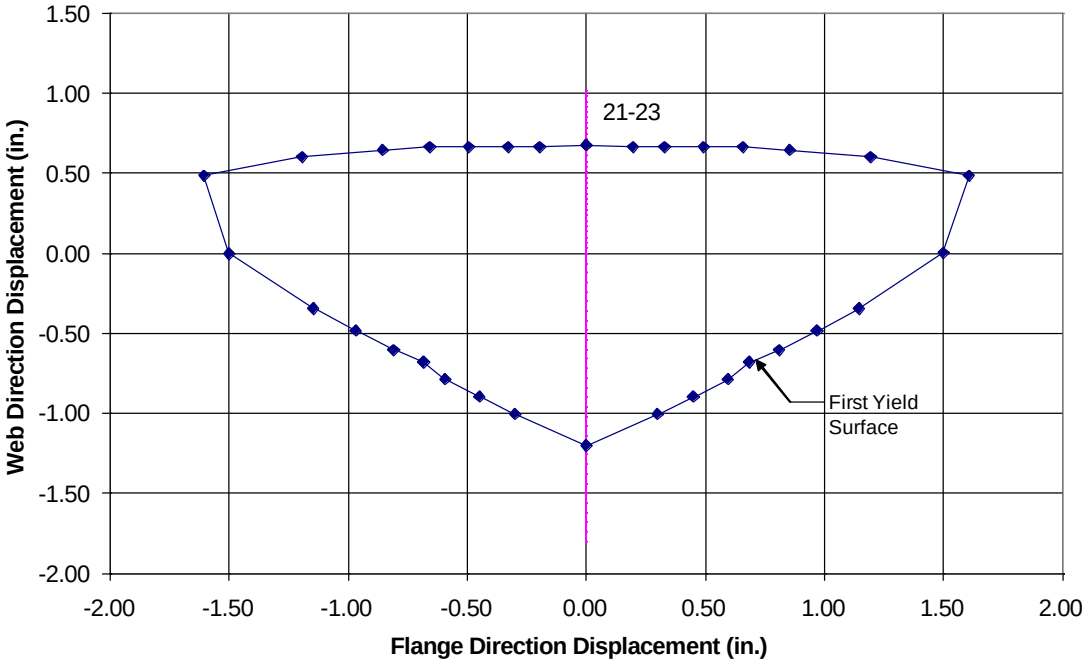

Figure 5.14 Load Steps 21 to 23, to Test NTW1 in the Web Direction of 150% First Yield Displacement

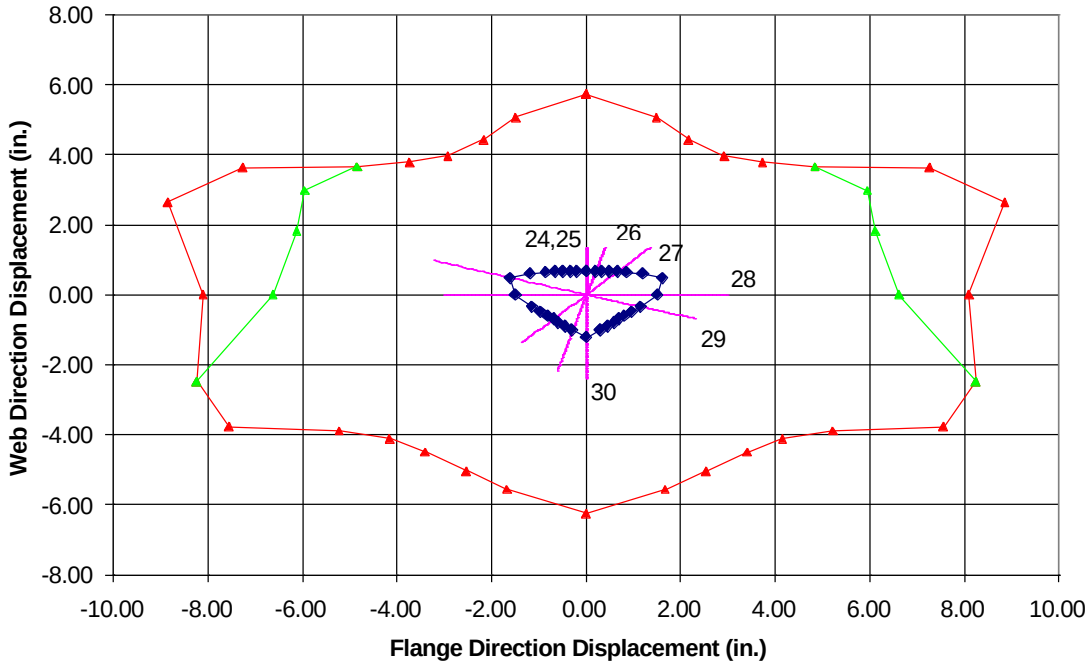

Figure 5.15 Load Steps 24 to 30 to Test NTW1 in Multidirectional Direction at 200% First of the First Yield Displacement

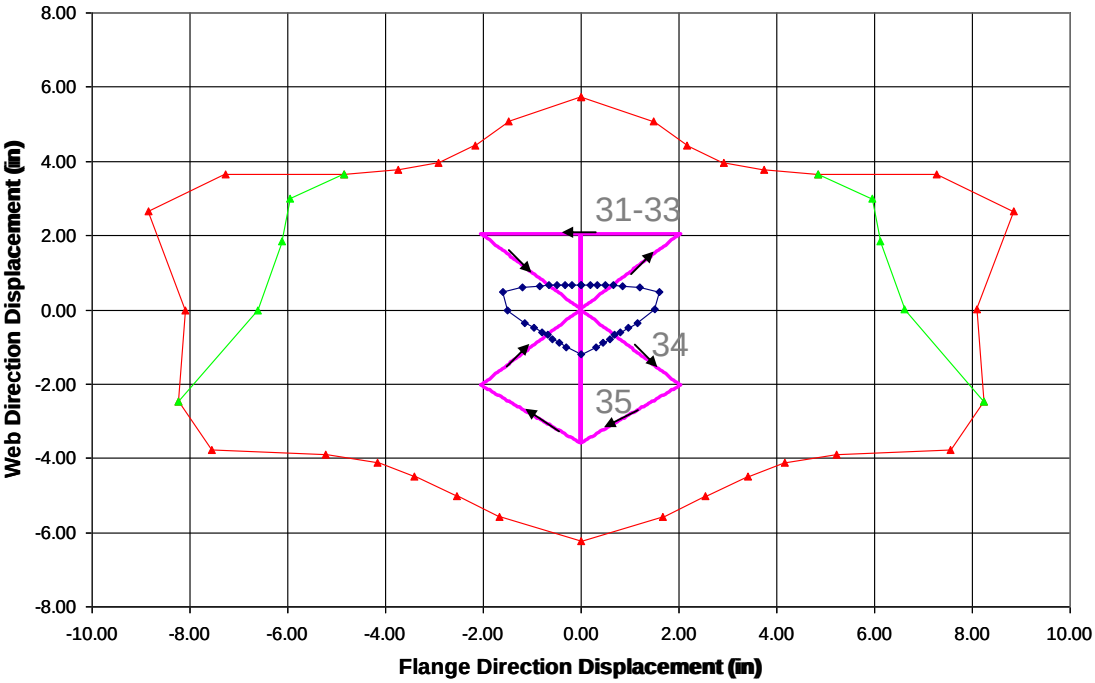

Figure 5.16 Load Steps 31 to 33, and 35 to Test NTW1 in the Web Direction and Load Step 34 to Test NTW1 to Hourglass Path at 300% of the First Yield Displacement

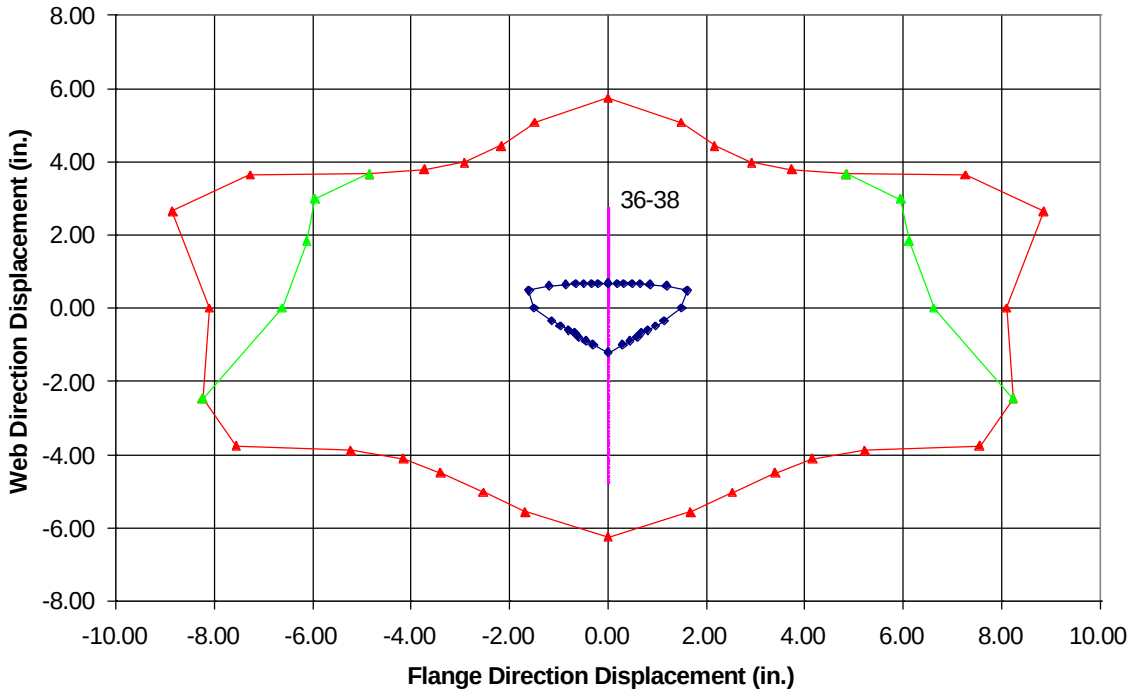

Figure 5.17 Load Steps 36 to 38 to Test NTW1 in the Web Direction at 400% of the First Yield Displacement

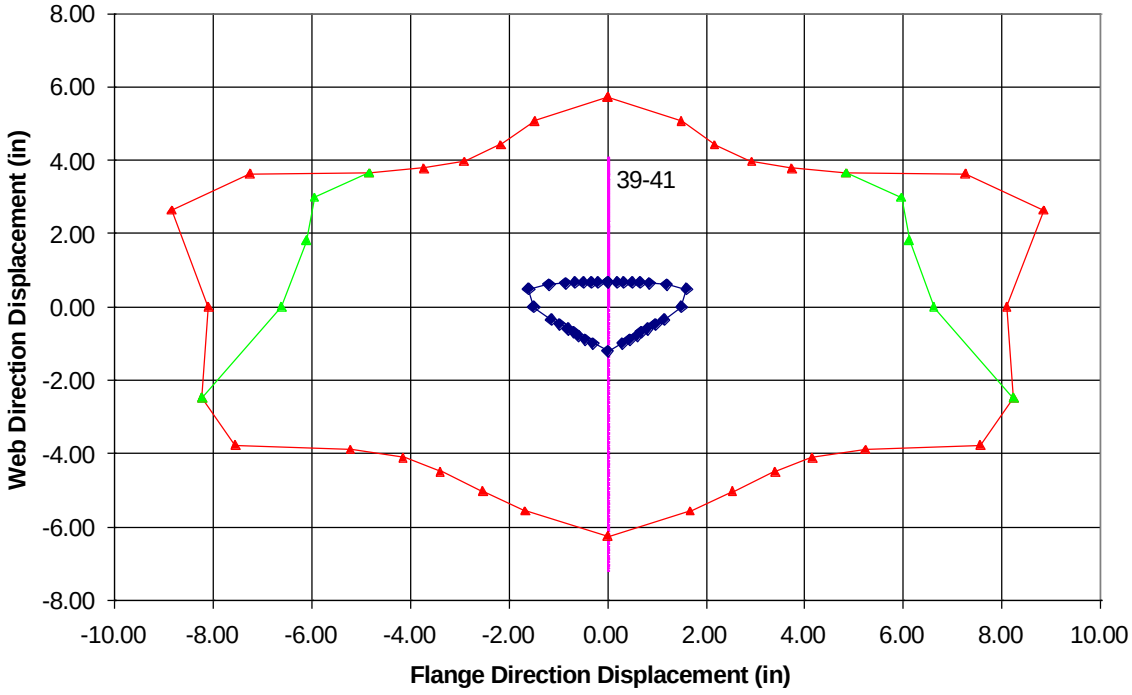

Figure 5.18 Load Steps 39 to 41 to Test NTW1 in the Web Direction at 600% of the First Yield Displacement

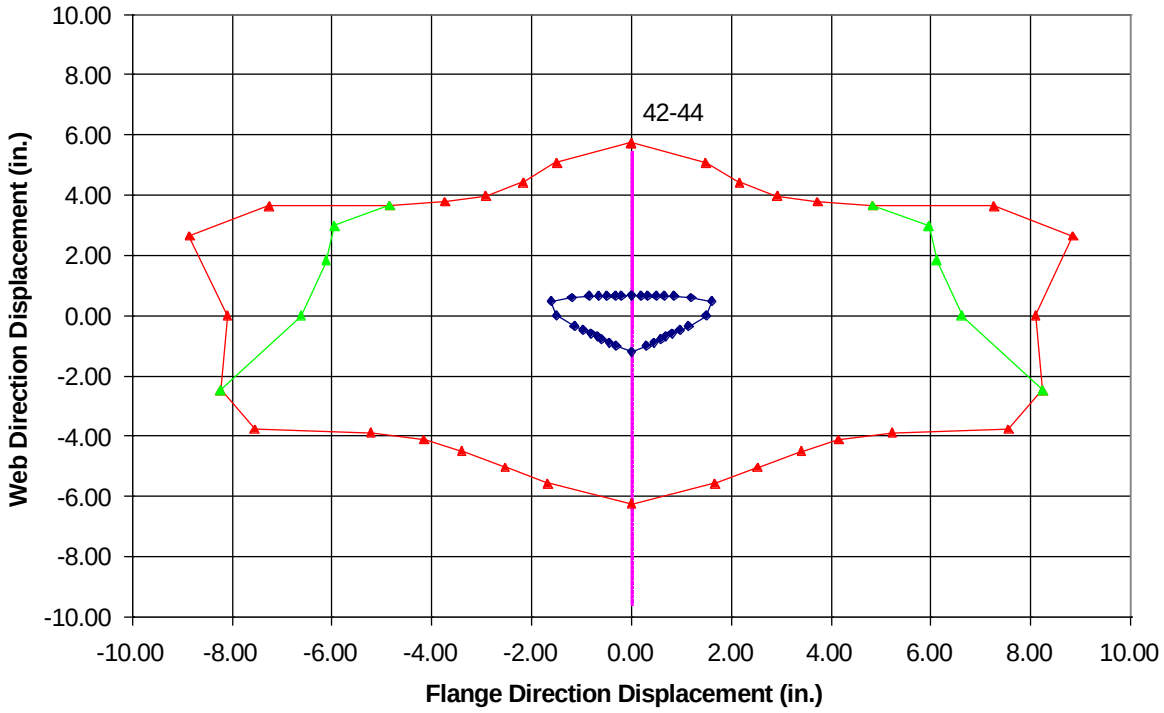

Figure 5.19 Load Steps 42-44 to Test NTW1 in the Web Direction at 800% of the First Yield Displacement

The web direction load cycles were targeted to obtain information on the shear lag and strain penetration behavior. For this reason, the web direction cycles were typically completed first at each new displacement level. The selected inclined load paths subjected the web and flange direction displacements at a constant ratio (e.g., Load Steps 11 and 12 in Figure 5.11) because they placed high demands on the flange and web tip confined regions.

The load paths described above was the one that was developed prior to the testing of the specimen. However, during testing a number of events that led to modifications to the planned loading protocol occurred. These events included:

- Larger shear deformation than those obtained from the OpenSees analysis
- Premature buckling of the longitudinal reinforcement in the web tip.

The planned directions of the load path were generally followed up to approximately 2% drift during testing of NTW2. However, the target displacements correspond to the different load cycles were increased because of the increased contribution of the shear deformations in an

attempt to reach the desired strain levels. After imposing the 150% of first yield displacement during the test, the target displacements were replaced with target drifts instead of relating targets to the first yield displacements. During the hourglass shaped load path at 2% drift level, buckling of the longitudinal reinforcement in the web tip was observed. In order to maximize the data gained from the test, the loading protocol at this point was changed and the specimen was loaded parallel to the flange to reach target lateral drifts of ±1%, ±1.5%, ±2%, ±3%, and ±4%. Table 5.2 summarizes the actual load protocol used during the test. Figures 5.20 and 5.21 shows the displacement components parallel to the web and flange, respectively, versus the load step, defined as a movement from one target point to the next target point. For example, a cycle 0 in the web direction includes two load steps, one moving to 0.08 in. and a second moving to -0.12 in.

Table 5.2: Applied Displacement Targets for NTW1

Cycle No	Displacement level	Flange direction (in.)	Web direction (in.)
0	10% of Yield Displacement Web Direction	0.0	0.08
		0.0	-0.12
1-3	25% of Yield Displacement Web Direction	0.0	0.3
		0.0	-0.4
4-6	50% of Yield Displacement Web Direction	0.0	0.6
		0.0	-1.1
7	25% of Yield Displacement Flange Direction	0.86	0.0
		-0.86	0.0
8	25% of Yield Displacement 45º Direction	0.29	0.29
		-0.30	-0.30
9	25% Yield Displacement 100% Flange + 30% Web	0.66	-0.2
		-0.88	0.27
10	50% of Yield Displacement Web Direction	0.0	0.6
		0.0	-1.1

11	75% of Yield Displacement 45º Direction	0.9	0.9
		-0.71	-0.71
12	75% Yield Displacement 100% Flange + 30% Web	2.0	-0.6
		-2.7	0.8
13-15	75% of Yield Displacement Web Direction	0.0	1.2
		0.0	-1.7
16	Mimic the 50% Yield Surface	0.0	0.8
		0.8	0.8
		1.5	0.55
		1.4	0
		0	1.1
		-1.4	0
		-1.5	0.55
		-0.8	0.8
		0.0	0.9
17	75% of Yield Displacement Web Direction	0.0	1.2
		0.0	-1.6
18-20	100% Yield Displacement Web Direction	0.0	1.56
		0.0	-2.1
21-23	150% Yield Displacement Web Direction	0.0	2.35
		0.0	-3.25
24	1% & 1.5% Drift Web Direction	0.0	3.1
		0.0	-4.7
25	1% & 1.5% Drift 100% Web + 30% Flange	1.0	3.0
		-1.5	-4.5
26	1% Drift Flange Direction	3.2	0.0

		-3.2	0.0
27	1.5% Drift 45º Direction	3.4	3.4
		-3.4	-3.4
28	1.5% Drift Flange Direction	4.8	0.0
		-4.8	0.0
29	1.5% Drift 100% Flange + 30% Web Direction	-4.6	1.4
		4.6	-1.4
30-31	1% & 1.5% Drift Web Direction	0.0	3.1
		0.0	-4.7
32-34	1.5% & 2% Drift Web Direction	0.0	4.8
		0.0	-6.4
35	2.0% Drift Hourglass Displacement Path	4.5	4.5
		-4.5	4.5
		4.5	-4.5
		0	-6.4
		-4.5	-4.6
		0	0
36	1.5% Drift Flange Direction	4.8	0.0
		-4.8	0.0
37-39	2% Drift Flange Direction	6.4	0.0
		-6.4	0.0
40-42	2.5% Drift Flange Direction	8.0	0.0
		-8.0	0.0
43-45	3% Drift Flange Direction	9.6	0.0
		-9.6	0.0

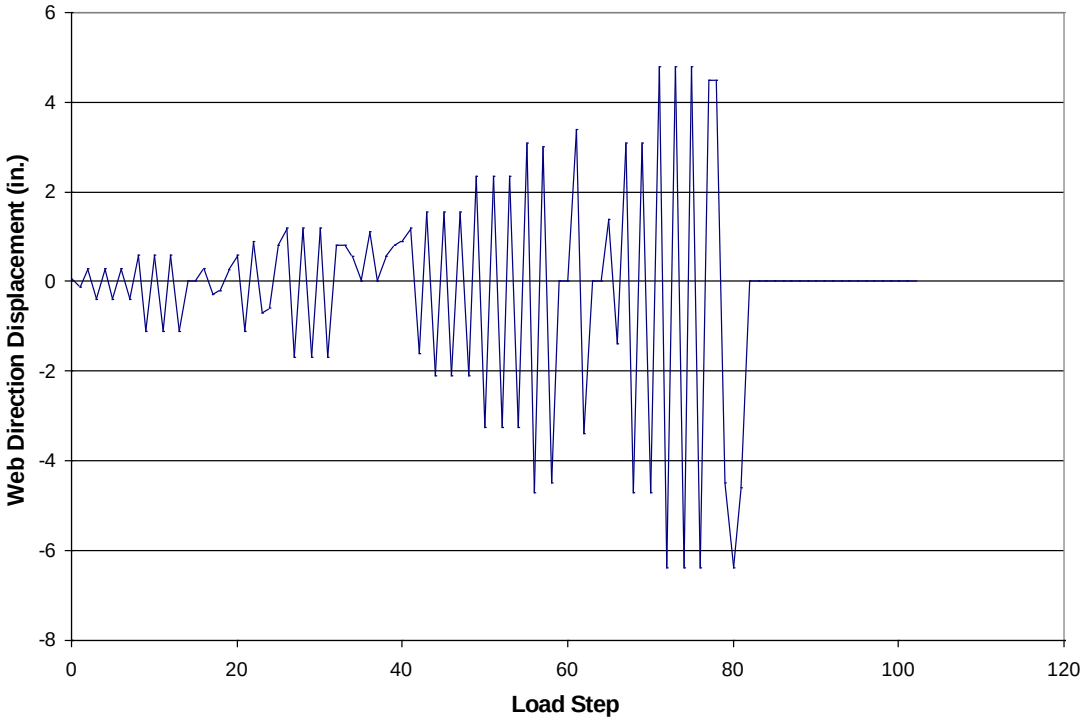

Figure 5.20 Displacement Component of the Load Protocol used for NTW1 Parallel to the Web Direction

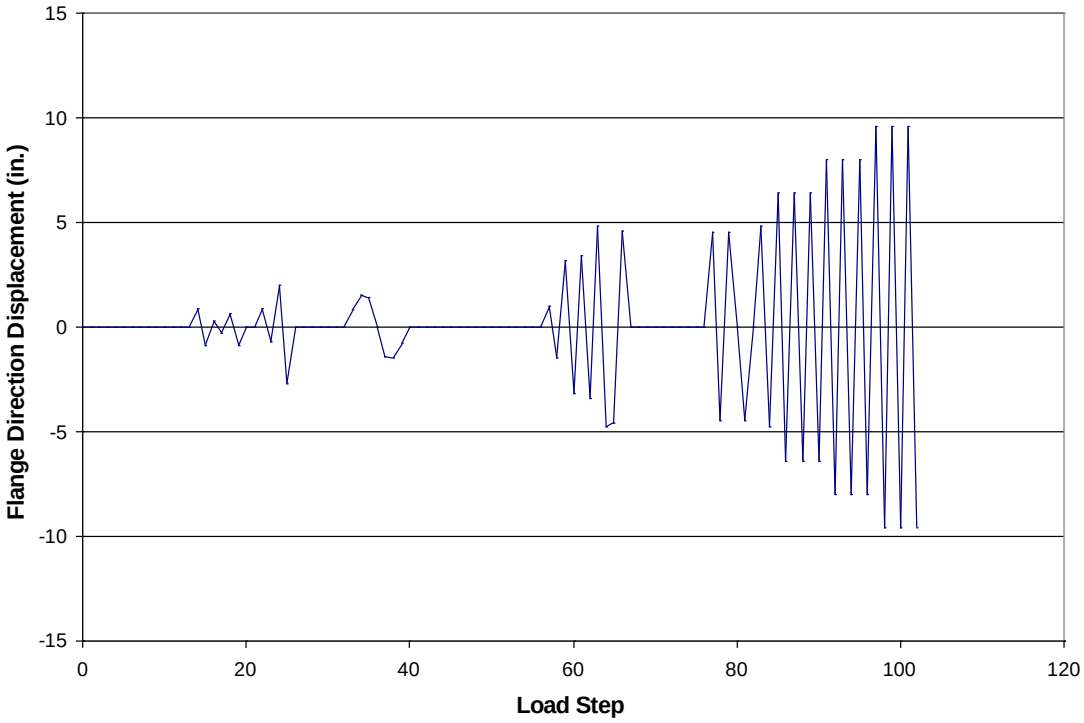

Figure 5.21 Displacement Component of the Load Protocol used for NTW1 Parallel to the Flange Direction

5.5 Summary of NTW1 Experimental Response

NTW1 was subjected to the load protocol summarized in Table 5.2 beginning on June 15, 2006 and was completed on June 28, 2006. The test took 7 days to complete. The observed cracking of the wall followed a specific pattern; cracks were small and well distributed in the boundary elements and then became significantly wider and spaced further apart outside of the boundary elements. The reduced spacing of the longitudinal reinforcement in the boundary elements led to better crack distribution; whereas the large spacing of the longitudinal reinforcement outside of the boundary elements led to large concentrated cracks. This crack pattern is seen in Figure 5.22 for the web, a similar pattern was observed in the flange. The response was very stable in all the loading directions, repeated cycles showed a small drop in the second cycle at a displacement level; however, no drop was observed between the second and third cycle.

Failure was first observed in the web tip during the hourglass shaped load path. As NTW1 approached the -6.4 in. of web direction displacement target buckling of the longitudinal reinforcement in the boundary element was observed. This failure ceased loading in the web direction. The specimen was then cycled to return the specimen as close to zero displacement, zero force in both the web and flange directions.

NTW1 was then cycled parallel the flange in order to maximize the information from the test. The specimen showed a stable response in this direction even after failure in the orthogonal direction. The specimen showed a stable response until failure due to bucking of the longitudinal reinforcement in the boundary element at 3% lateral drift. Upon reversal the bars that had buckled fractured. Figure 5.23 shows NTW1 following failure of the flange boundary element.
NTW1 performed very well overall, with the exception of the large cracks that formed outside the boundary elements in both the flange and the web. More information about the observed experimental behavior of NTW1 can be found in Brueggen (2009).

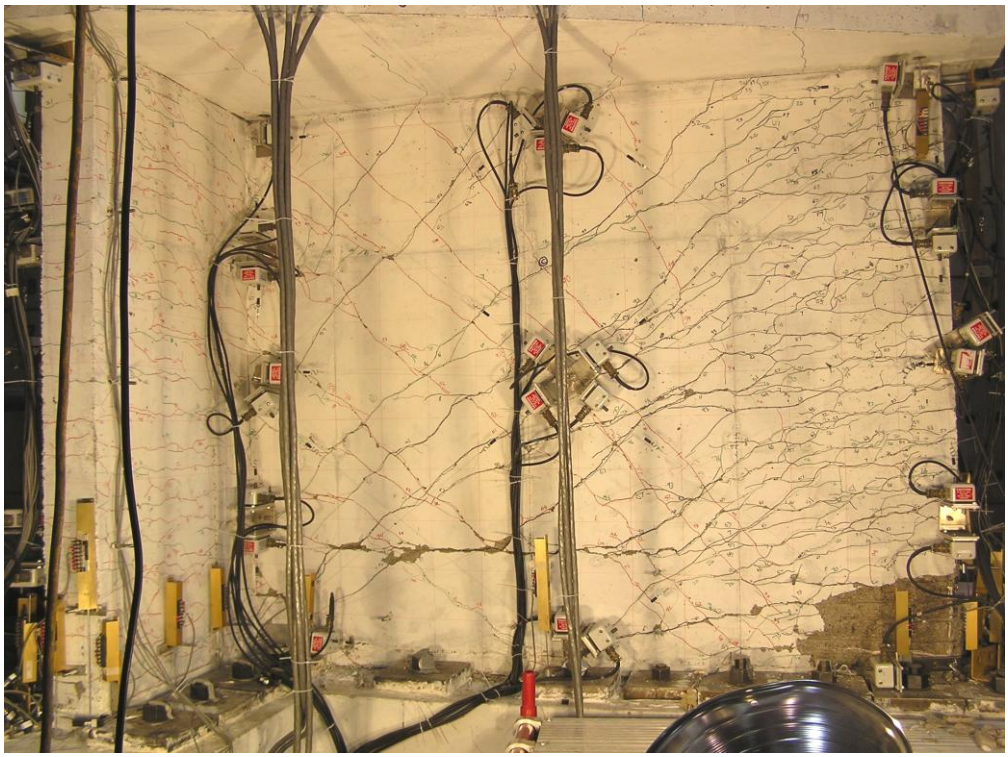

Figure 5.22 Observed cracking of NTW1 in the web

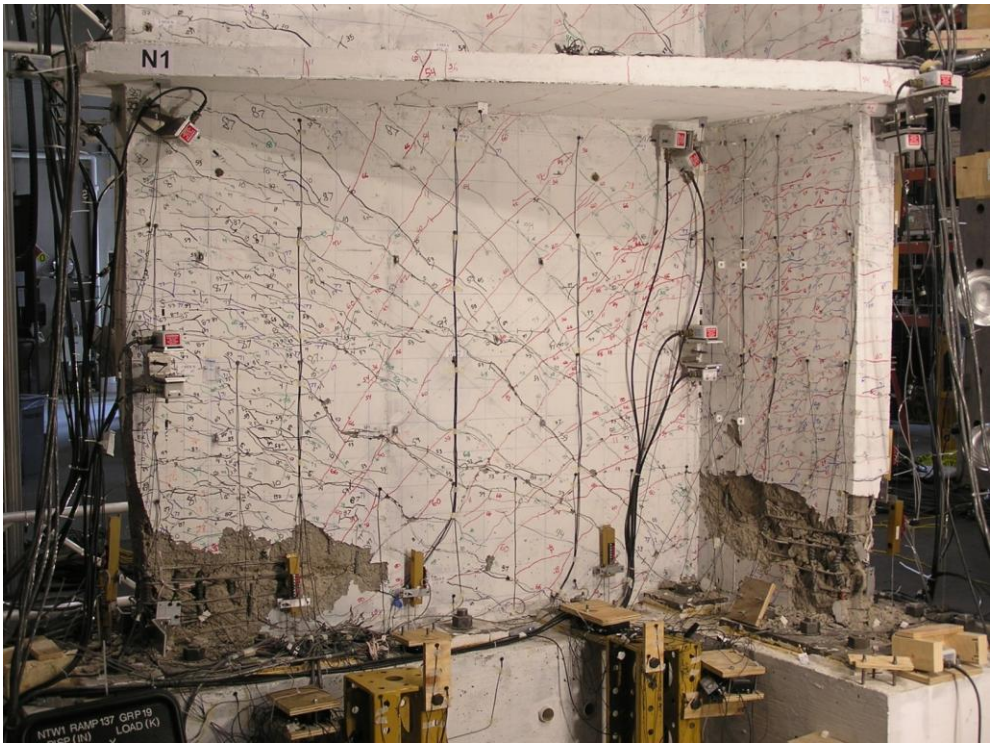

Figure 5.23 NTW1 following completion of the load protocol

5.6 Pretest Analysis Results

The concrete material properties were updated from the estimated properties based on three uniaxial compressive tests of six-inch diameter concrete cylinders tested on the day before testing NTW1 began. The average measured unconfined concrete compressive strength was 7260 psi, the average tensile strength was taken as 880 psi based on split cylinder tests. The confined concrete properties were updated using the average measured concrete strengths and the Mander et. al. (1988) confined concrete model. However, he model used for the prediction of the behavior of NTW1 was generally unsatisfactory and can be seen in the comparison between the analytical monotonic response envelope and experimental response shown in Figure 5.24 for the direction parallel to the web and in Figure 5.25 for the direction parallel to the flange. As can be seen, the OpenSees model failed to capture the elastic stiffness of the wall in both loading directions and over predicted the envelope for the flange direction loading.

The prediction of the cyclic response was generally not satisfactory. The stiffness of the wall was over predicted similar to the monotonic prediction. Additionally, the residual displacement was underpredicted by the analysis, due to the use of Kent-Park concrete model (i.e. *Concrete03* in OpenSees. The cyclic prediction is not presented because of the poor comparison, as expected based on the monotonic prediction.

5.7 Details of Improved Model

Following completion of testing of NTW1, the causes of the discrepancies in Figure 5.24 and 5.25 were investigated. The cause for the discrepancies was largely attributed to neglecting the effects of shear deformation and inaccurate simulation of the shear lag in the flange. The large discrepancies seen in the flange direction response is due to the load protocol emphasizing loading NTW1 in virgin territory in the direction parallel to the web. This caused some damage to the specimen in the flange tips prior to loading the wall in the flange direction, leading to the significant decrease in the lateral force resistance seen in Figure 5.25, demonstrated in the next section through the cyclic analysis of NTW1. In addition to using test day material properties, in the post-test analysis of NTW1, the concrete model for the fibers was also changed from the Kent-Park model to the modified Chang and Mander model described in Chapter 3.

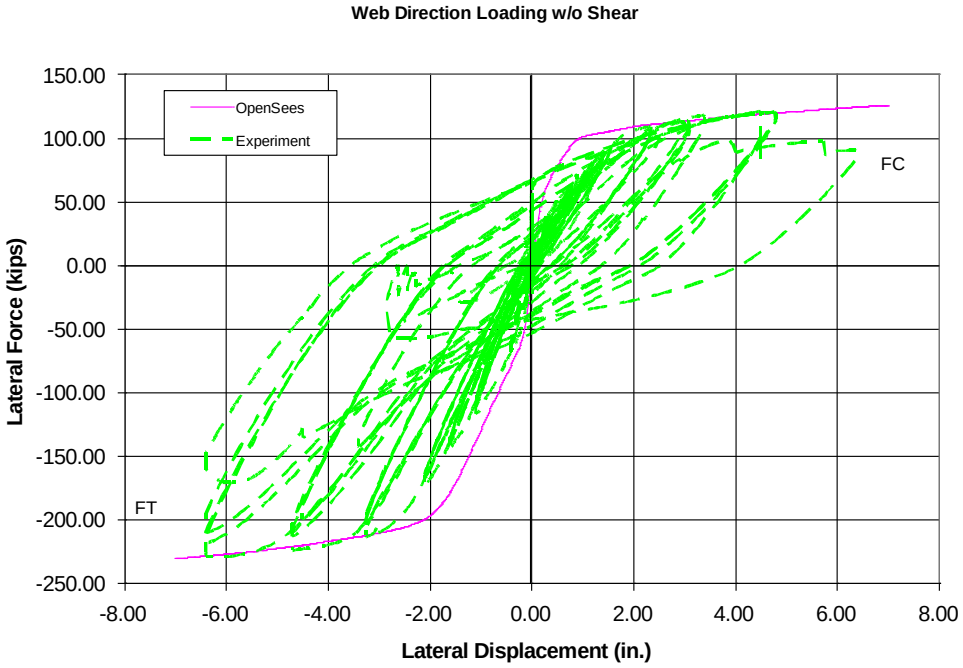

Figure 5.24 Comparison of Predicted Monotonic Envelope of NTW1 in the Web Direction with Experimental Data (shear deformation was not included)

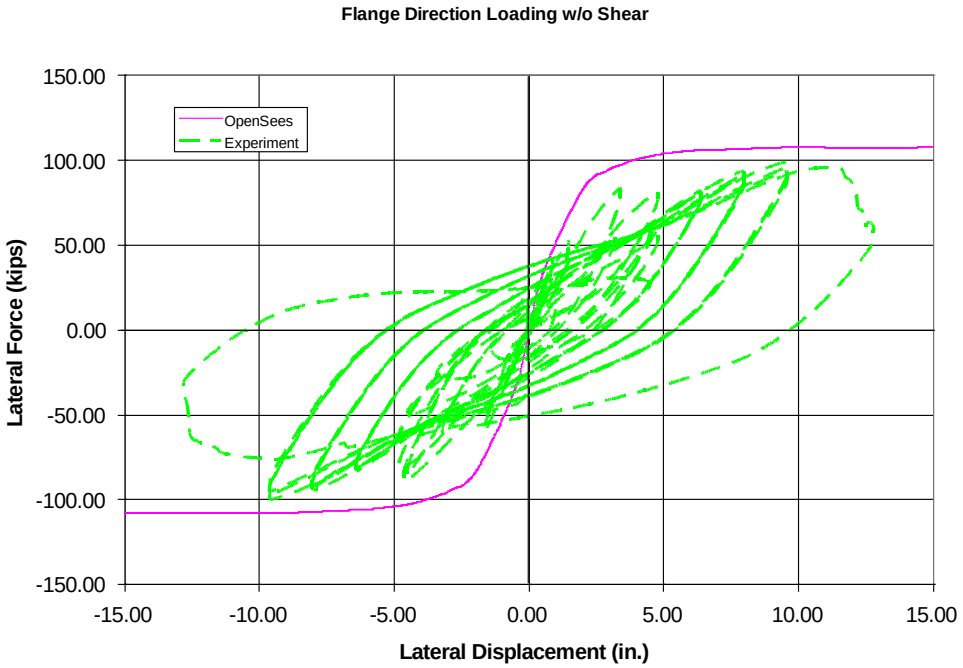

Figure 5.25 Comparison of Predicted Monotonic Envelope of NTW1 in the Flange Direction with Experimental Data (shear deformation was not included)

The reason for ignoring the effects of shear deformation in the original analysis was that the aspect ratio of the wall was greater than three, suggesting flexural dominant response of the wall. However, the experimental data clearly showed that shear deformations contributed to the overall wall response significantly. The fiber sections used in OpenSees did not account for the shear deformation of the specimen and had to be addressed separately. As with the models for rectangular walls, the method chosen to address this issue was to use a uniaxial material model to simulate the force-distortion relationship using *Pinching4* available in OpenSees. The envelope of the *Pinghing4* material model suitable for NTW1 was determined by selecting four points in the experimental force-distortion graph in both the positive and negative quadrants. The parameters for reloading/unloading were selected by comparing the cyclic behavior of the material model to the recorded shear distortion in NTW1. The *Pinching4* model as included to capture the shear deformation for the first floor of NTW1 is compared with the experimental data in Figure 5.26, which shows that the analytical model simulated the envelope and the reloading stiffness satisfactorily. However, the unloading stiffness and residual distortion were not generally well simulated. This discrepancy was due to the limitations of the chosen material model but the *Pinching4* model was the best material model available in OpenSees for this application.

Figure 5.27 shows the Origin-Centered Hysteretic model chosen for the simulation of the shear deformation in the second and third floors of NTW1. The *Origin-Centered Hysteretic* model was considered to be adequate to capture the shear deformation in the upper floors due to the limited inelastic shear deformations expected at these floor levels. Figure 5.28 compares the *Pinching4* material model used for the shear-distortion behavior in the direction parallel to the flange for the first floor of NTW1. The shear deformation above the third floor parallel to the web direction and above the first floor parallel to the flange direction was modeled using elastic material models, with stiffness of 448,074 k/rad and 40,508 k/rad for parallel to the web and flange directions, respectively. The decision to use elastic properties was based on observing no inelastic shear deformation in the second floor level in the flange direction, and observing no inelastic shear distortion of the fourth floor prior to failure in the web direction. The stiffness was chosen to match the average shear stiffness of the experimental response determined from the web and flange panel data.

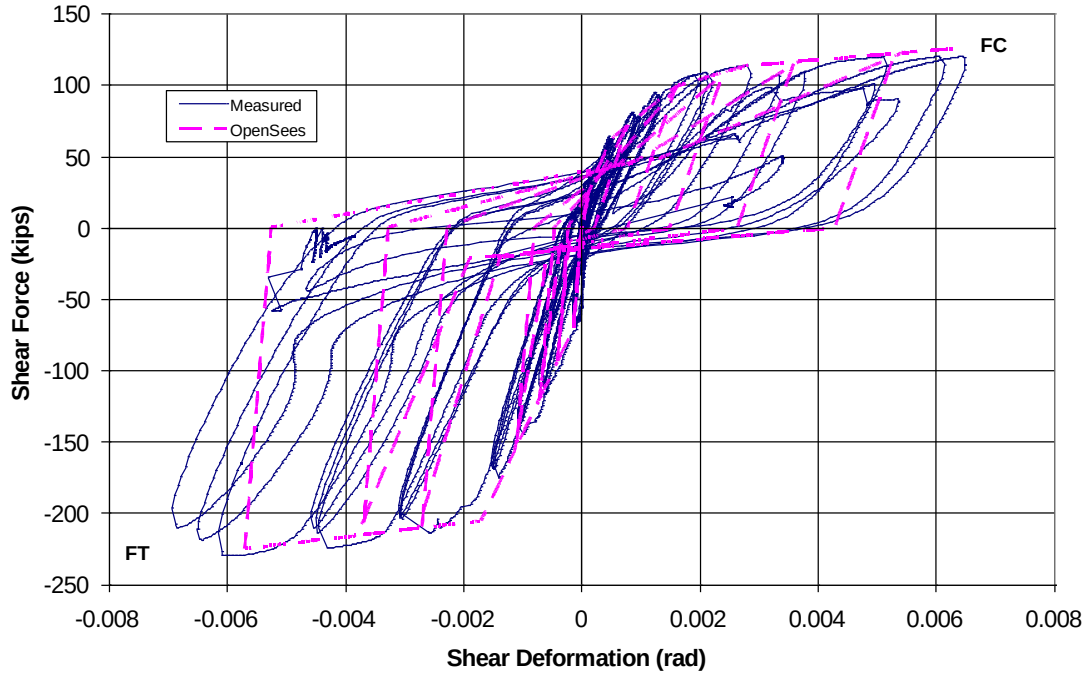

Figure 5.26 Comparison of Measured Shear Response for the First Floor of NTW1 in the Web Direction with the Response of Selected OpenSees Material Model

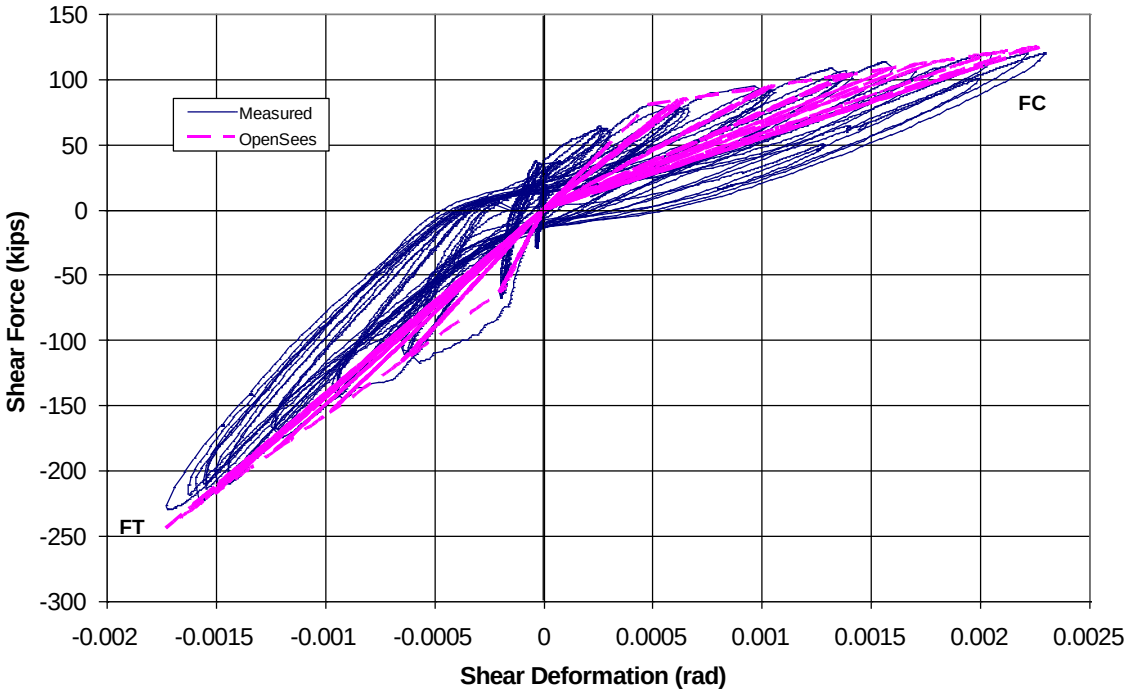

Figure 5.27 Comparison of Measured Shear Response for the Second Floor of NTW1 in Web Direction with the Response of Selected OpenSees Material Model

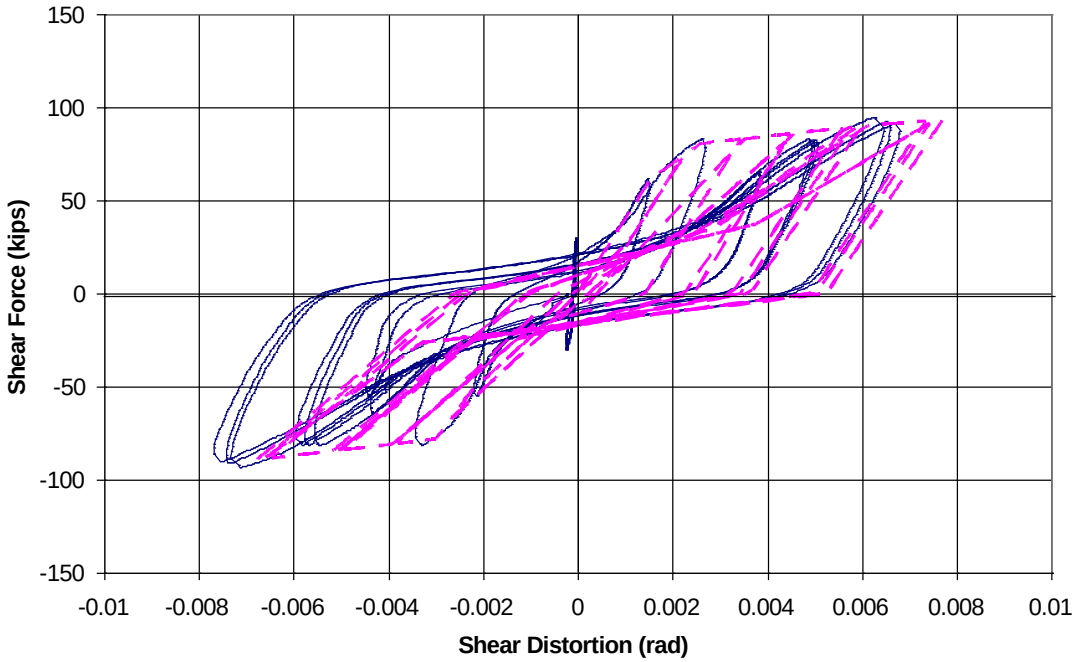

Figure 5.28 Comparison of Measured Shear Response for the First Floor of NTW1 in the Flange Direction with the Response of Selected OpenSees Material Model

Because different material models were used to simulate the shear behavior at each floor level, the OpenSees model had to be modified appropriately. The model used for the post-testing analysis consisted of one force-based beam-column element at each floor level. The shear response is a member level response; however, it is specified with the section definition in OpenSees. Even though the shear material is connected to the section, the shear does not modify the response of the fiber section. The shear material model was then aggregated onto the section used for the beam-column at each floor level. Thus the section uses the fiber discretization to determine the axial and flexural responses, and provides the shear force to the shear material to determine the shear distortion response. Aggregating the material model onto the section is conceptually similar to placing a shear spring in parallel with the beam-column element. This increased the number of elements and run time of the analysis.

Two issues related to the approach described above for including the shear deformation in the analysis are worthy of discussion. The shear deformation in each direction was calibrated against the test data from that direction only. Therefore, the shear deformation in the web

direction loading only included the shear behavior of the web, while the flange direction loading was created based only on the shear deformation of the flange. While this includes the major source of the shear deformation, the effect of the flange on the shear-distortion for the direction parallel to the web loading was not included. However, the data on the shear-distortion data from the flange during web direction loading did not show a clear pattern of response and was limited to 0.08 rad, and thus ignoring this component was not of a significant concern. A similar observation was made with regard to the effect of the shear deformation of the web on the flange direction response. Additionally, because the shear response is aggregated onto the section response in the two primary directions, the shear deformation in any arbitrary direction is simply the summation of the shear deformations obtained for the two directions separately. How accurately this reflects the real behavior of the T-wall needs to be examined. If this is not an accurate reflection of the behavior of the T-wall, this topic would deserve further research and appropriate modification to the fiber analysis in OpenSees.

5.7.1 Modeling of Shear Lag

Based on the results of an analysis of the second of two T-walls tested by Thomsen and Wallace [1993], a new fiber section was implemented in OpenSees by modifying the existing fiber section to include the effects of shear lag. The results from the Thomsen and Wallace T-wall indicated that significant shear lag should occur across the width of the flange, as illustrated in Figure 5.29. In order to understand the effect of shear lag, the new fiber section varied the strain passed down to the material models in the flange when the flange is placed in tension. The shape of the strain distribution was based on the average strain obtained from the LVDTs mounted at the base of the wall. The equation used for determining the strain across the flange width was:

$$\varepsilon = \varepsilon_0 + \Phi_y * z * \left(-0.1140527 * \left(\frac{B}{t} \right) * \left(\frac{2y}{B} \right)^2 + 1 \right) + \Phi_z * y \qquad \text{(Eqn. 5-1)}$$

where ε is the total uniaxial strain in the fiber, ε_0 is the strain due to axial load, Φ_y is the curvature about the local y-axis, Φ_z is the curvature about the local z-axis, B is the flange overhang length, t is the flange thickness, and z and y are respectively, the coordinates of the

fiber of interest relative to the centroid. Figure 5.30 illustrates the physical interpretation of the variables

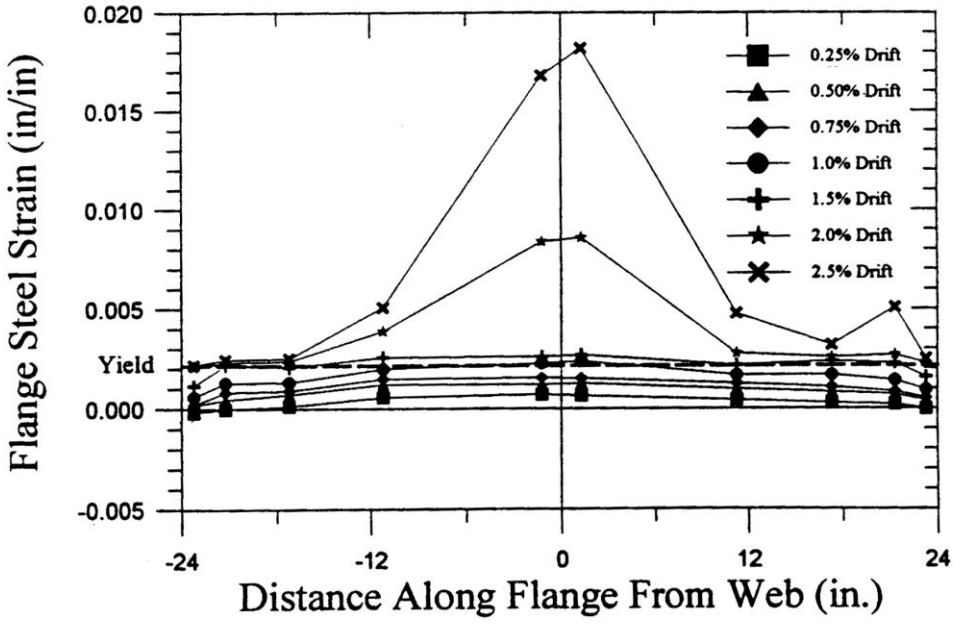

Figure 5.29 Strain Distribution across Flange near Base of T-wall from Thomsen & Wallace Specimen TW2 [Thomsen & Wallace, 1993]

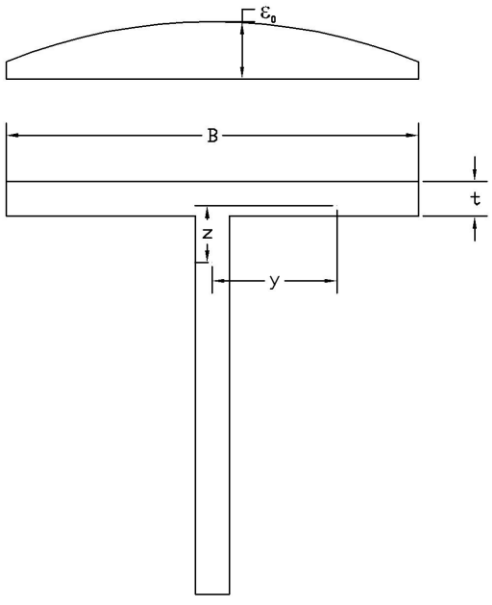

Figure 5.30 Variables used to Define Shear Lag Behavior

5.8 Comparison of Post-Test Analysis Results with Experimental data

5.8.1 Monotonic response comparison

Figures 5.31 and 5.32 show the monotonic response envelope after including the effects of shear and shear lag. The monotonic envelope is well captured in the two orthogonal directions. The discrepancy seen in the flange direction after yielding is caused by the damage that occurred during loading in the web direction prior to loading in the flange direction. The experimental response would be closer to the monotonic envelope if the load path had focused on the flange direction rather than the web direction. This is confirmed by the cyclic comparison presented in the next section as well as the study presented in Appendix B.

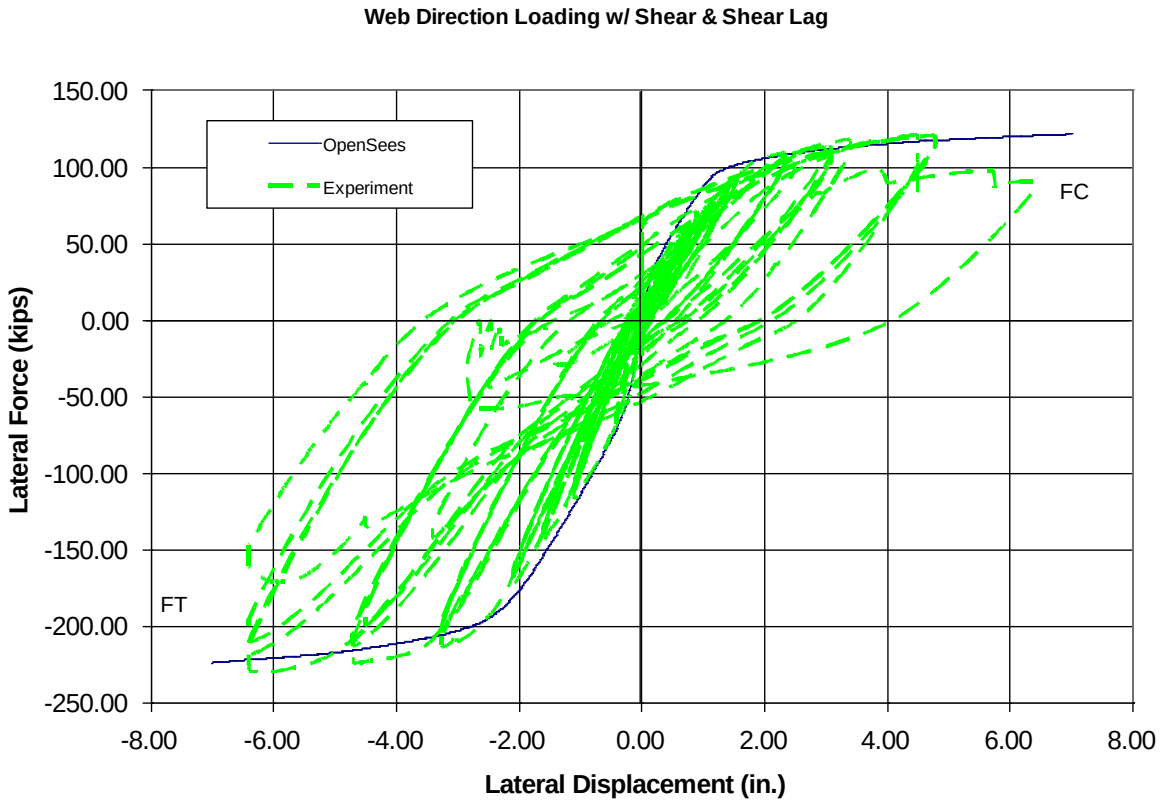

Figure 5.31 Comparison of Monotonic Envelope of NTW1 in the Web Direction Including the Effects of Shear and Shear Lag with Experimental Response

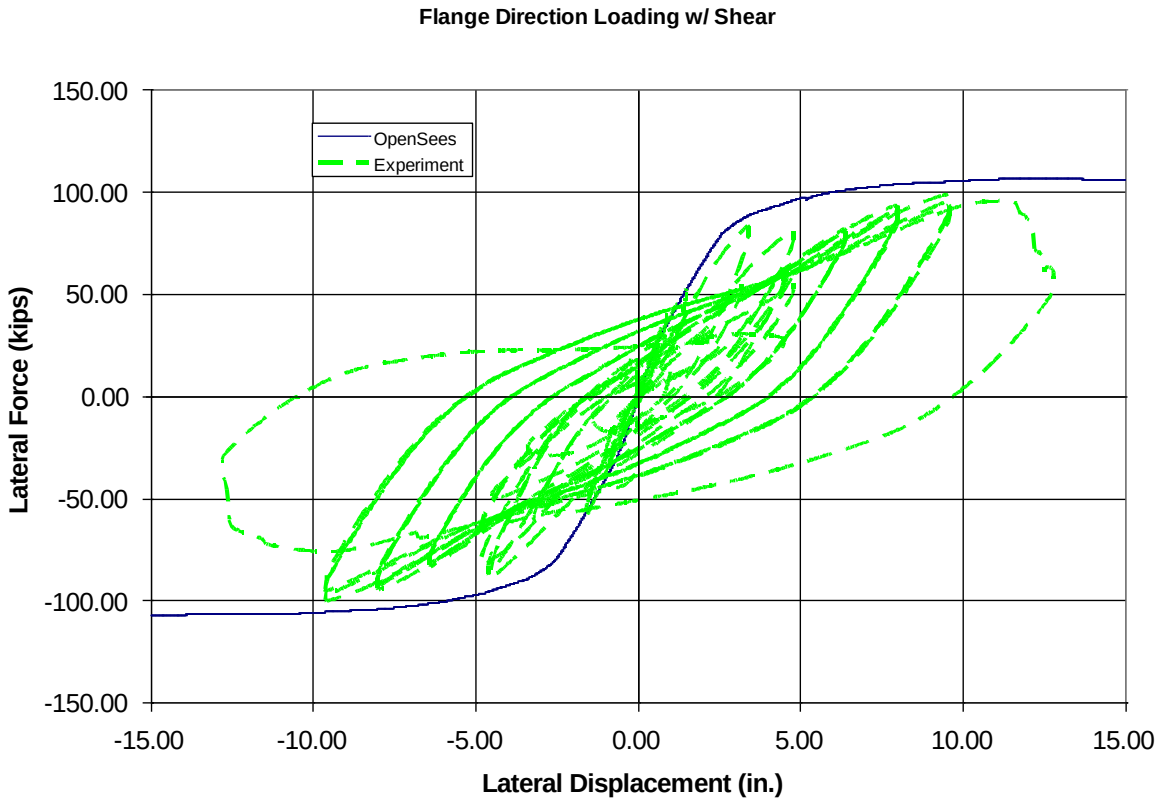

Figure 5.32 Comparison of Monotonic Envelope of NTW1 in the Flange Direction Including the Effects of Shear and Shear Lag with Experimental Response

5.8.2 Cyclic Response Comparison

The measured and calculated cyclic responses of NTW1 to the load path defined in Figures 5.19 and 5.20 are shown in Figures 5.33 and 5.34 for the flange and web directions, respectively. For the post-testing analysis, the concrete was modeled using the modified Chang and Mander concrete model and the test day concrete properties. As shown, the OpenSees simulation accurately captured the force-displacement response of NTW1 in the flange direction. The unloading, reloading, and residual displacements were well simulated by the analysis model. However, in the web direction although the simulated response is satisfactory, the OpenSees model did not capture the response as accurately as it did in the flange direction. This can be seen in Figures 5.35 and 5.36 that show the lateral force versus cumulative displacement for the web and flange direction responses, respectively. These figures give a different view of the

comparison between the OpenSees model and measured responses. In addition, Figures 5.37 and 5.38 show the same force versus cumulative displacement responses, but they present close-up views of the initial region in order to examine the responses in the elastic region. Overall, Figures 5.35 to 5.38 more clearly show many of the observations made in the force-displacement responses in Figures 5.33 and 5.34. Furthermore, they show how accurately the OpenSees model simulated the behavior of NTW1 in both elastic and inelastic regions despite subjecting NTW1 to a complex load path. There were some differences in the flange-in-tension direction response after developing flexural cracks at a drift of 0.15% and prior to yielding of the longitudinal reinforcement in the flange. In the flange direction, the measured and OpenSees responses were almost identical, supporting the conclusion that the plane section remain plane assumption for bending parallel to the flange is an acceptable assumption of the section behavior in that direction.

In neither the flange nor the web direction response is any pinching of the response near the origin evident either in the analytical or measured response. The walls were designed to code requirements and were detailed with adequate shear reinforcement to prevent shear failure. Thus it is not surprising that pinching of the global force-displacement response. Repeat cycles at a particular displacement level did not show continuing degradation, also as expected. Pinching of the response, rather than the large, open hysteretic loops seen in the response of NTW1 would be expected if the specimen were experiencing significant damage at each cycle, such as during failure. Pinching of the force-displacement response would be indicative of poor detailing and adequate shear reinforcement. However, the code requirements were adequate to prevent any pinching of the observed response.

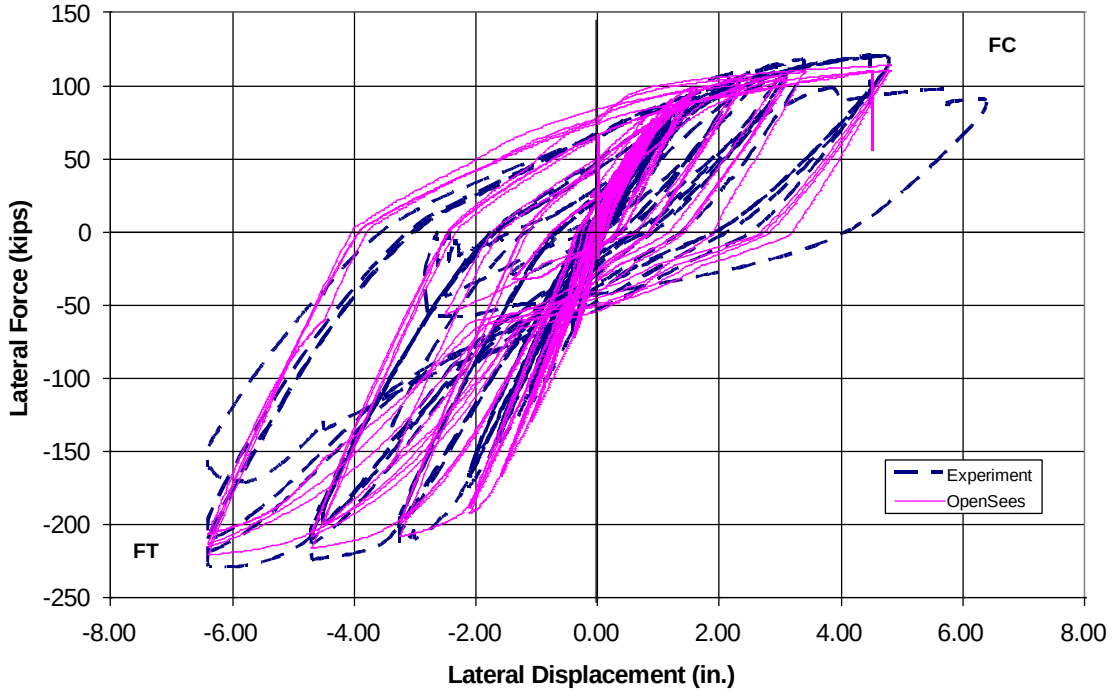

Figure 5.33 Measured and Calculated Force-Lateral Displacement Responses of NTW1 in the Web Direction

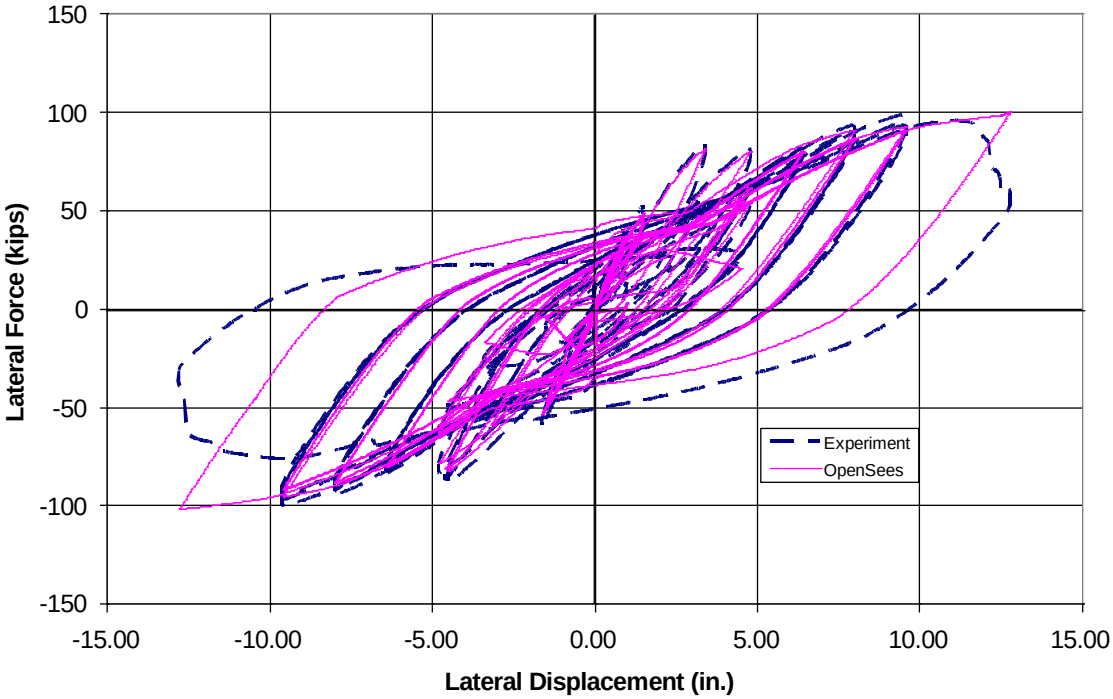

Figure 5.34 Measured and Calculated Force-Lateral Displacement Response of NTW1 in the Flange Direction

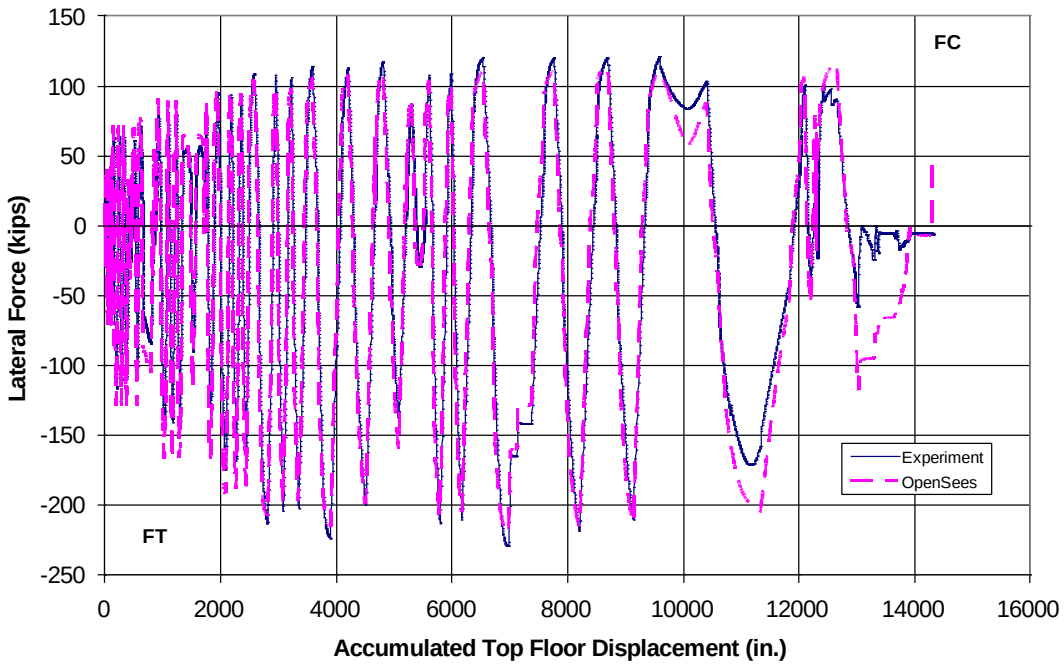

Figure 5.35 Comparison of Responses of NTW1 in the Web Direction as a Function of Cumulative Displacement

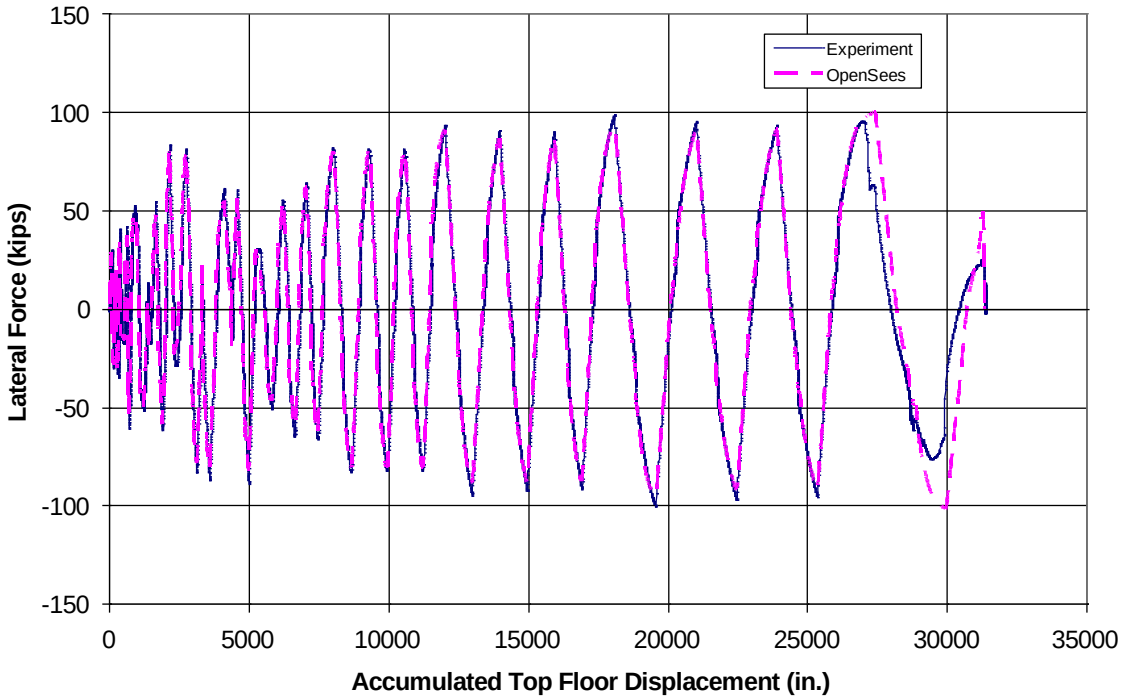

Figure 5.36 Comparison of Responses of NTW1 in the Flange Direction as a Function of Cumulative Displacement

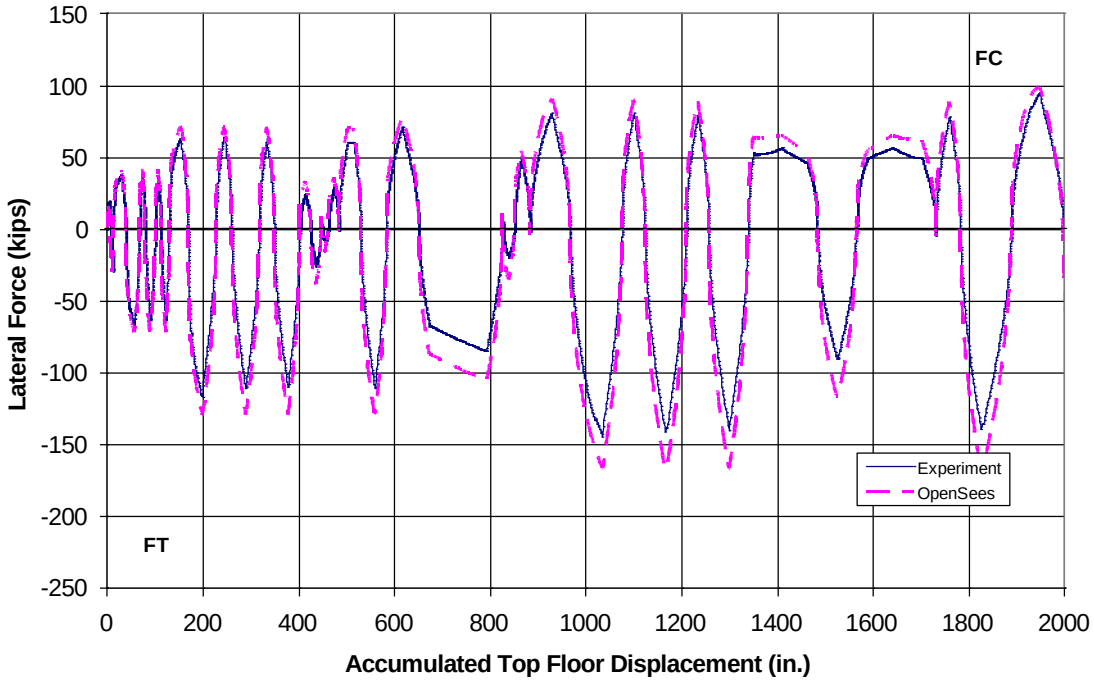

Figure 5.37 Comparison of Responses of NTW1 in the Web Direction as a Function of Cumulative Displacement in the Elastic Region

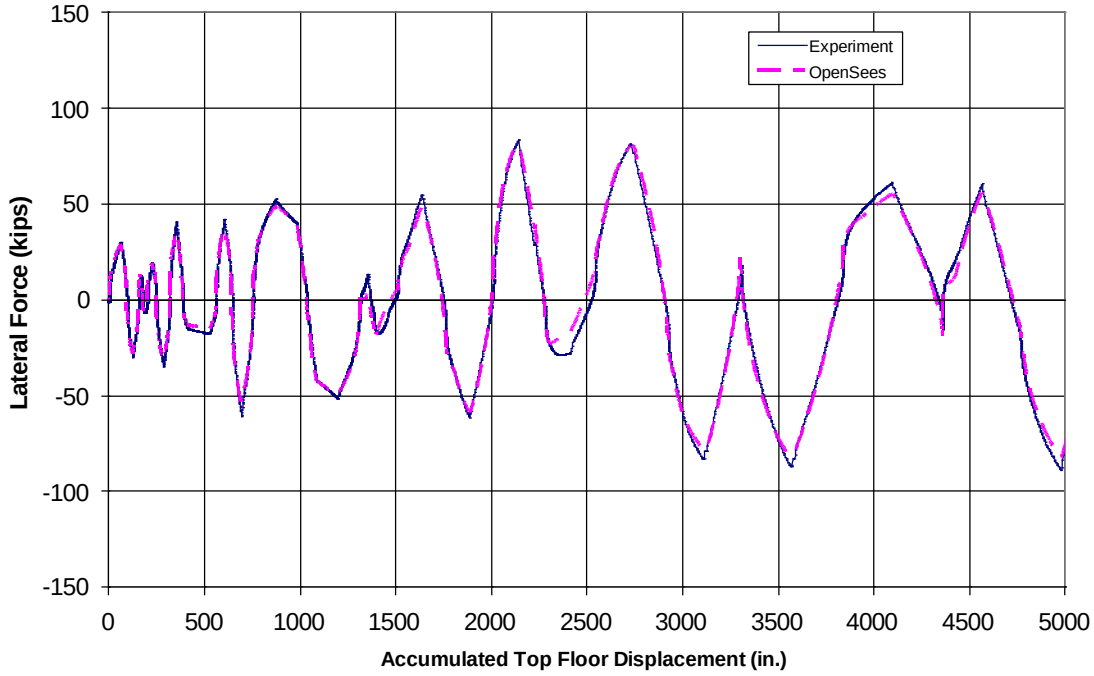

Figure 5.38 Comparison of Responses of NTW1 in the Flange Direction as a Function of Cumulative Displacement in the Elastic Region

5.8.3 First Floor Response

To ensure that the OpenSees model adequately captured the different deformation components accurately, the responses of NTW1 at the floor levels were also examined. It was expected that the first floor response would be more heavily influenced by the contribution of shear deformation. This provides an opportunity to more clearly examine the accuracy of the shear deformation component. The calculated and measured force-displacement responses of the first floor are shown in Figures 5.39 and 5.40 for the web and flange directions, respectively. The reported measured lateral displacement was the average of the displacements recorded by string potentiometers mounted to the flange and web tips. The OpenSees model did not capture the first floor response in both directions as good as it did for the top floor responses. Figure 5.39 and 5.40 show the first floor peak and residual displacements were overestimated by the analysis. However, as seen in Figure 5.39, the web direction response was captured within a reasonable degree of accuracy. Figure 5.41 and 5.42 show the first floor displacement as a function of the measurement number for the web and flange directions, respectively. In this perspective, it is easier to see that the analysis simulates the lateral displacement within 5 to 10% for the web direction, with a few exceptions where the difference being significantly larger. The measurement number is the number of times a measurement was taken In the flange direction. This approach for defining the x-axis was performed because the displacement from OpenSees at the first floor level was significantly larger than the measured displacement, the peak displacements are off by 40% in some places; however, at regions between the peaks the displacement is simulated within 15%. The cause of the discrepancy at the peaks was due to the shear distortion overestimating the shear deformation at higher levels in the positive direction, see Figure 5.28. This would have led to the over simulation of the lateral displacement. The faster unloading of the *Pinching4* material allowed the shear distortion to quickly return to the proper level causing the response between peaks to be better captured.

As noted, significant damage to NTW1 occurred in the plastic hinge region at drifts above 2%. The wall was heavily cracked with some spalling of the cover concrete near the toes, seen in Figure 5.43 and 5.44. Figure 5.43 shows the boundary element located at the flange tip, while Figure 5.44 shows the web tip. Large diagonal cracks formed between the boundary elements along the length of the flange and web. Additionally, truss action can develop in the

plastic hinge after the diagonal cracks form in the web. The truss action, which can potentially carry a significant portion of the lateral load [Park and Priestley, 1998], facilitates the interaction between the shear and flexural actions. Due to this interaction, the strains in the longitudinal reinforcement increases as it participate in both flexural and shear action. Similarly, the concrete strain will be different than that calculated from the plane sections remain plane assumption. This interaction was not explicitly modeled in the OpenSees analysis. It is possible that lack of explicit modeling of the shear-flexure contributed to the differences seen between the measured and calculated response at the first floor, particularly in the direction parallel to the flange.

In NTW1, the strain data from the longitudinal reinforcement showed that the strain obtained at 18 in. above the wall-foundation interface was higher than strains recorded at the interface. Figure 5.45 shows the strain profile for a bar located in the flange tip boundary element at 1% drift. The difference in strain could be due to the confinement effect of the foundation. This effect of the foundation was not included in the OpenSees model. The OpenSees model did not include the foundation because it was not thought to significantly influence the wall behavior, nor could this behavior be included easily in the OpenSees model due to the choice of using beam-column elements to model the wall.

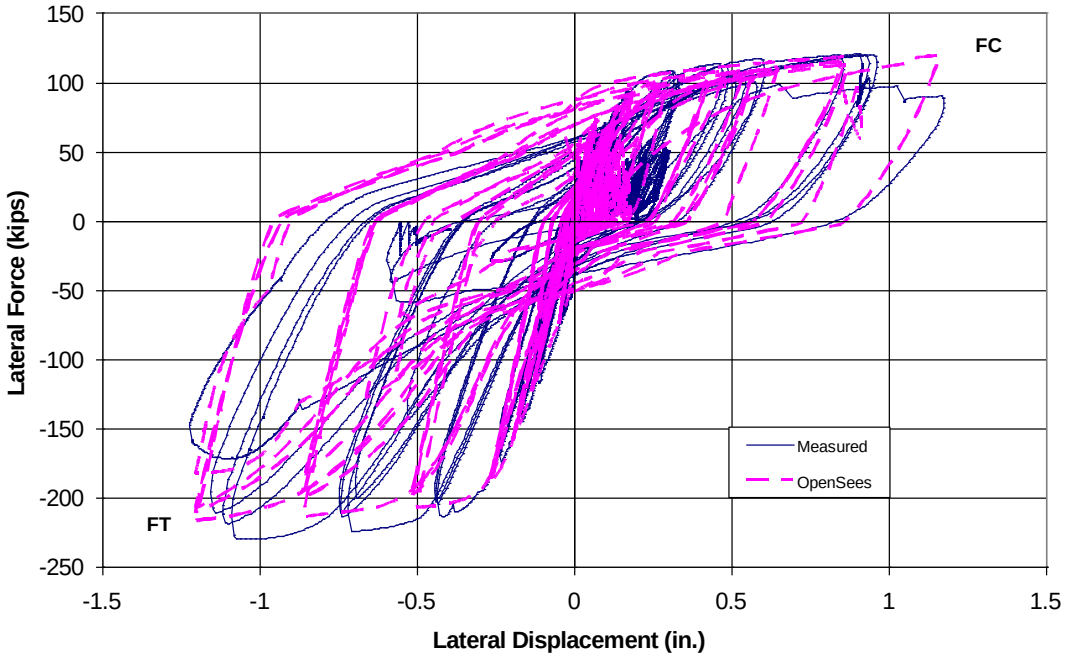

Figure 5.39 Measured and Calculated First Floor Force-Displacement Responses of NTW1 in the Web Direction

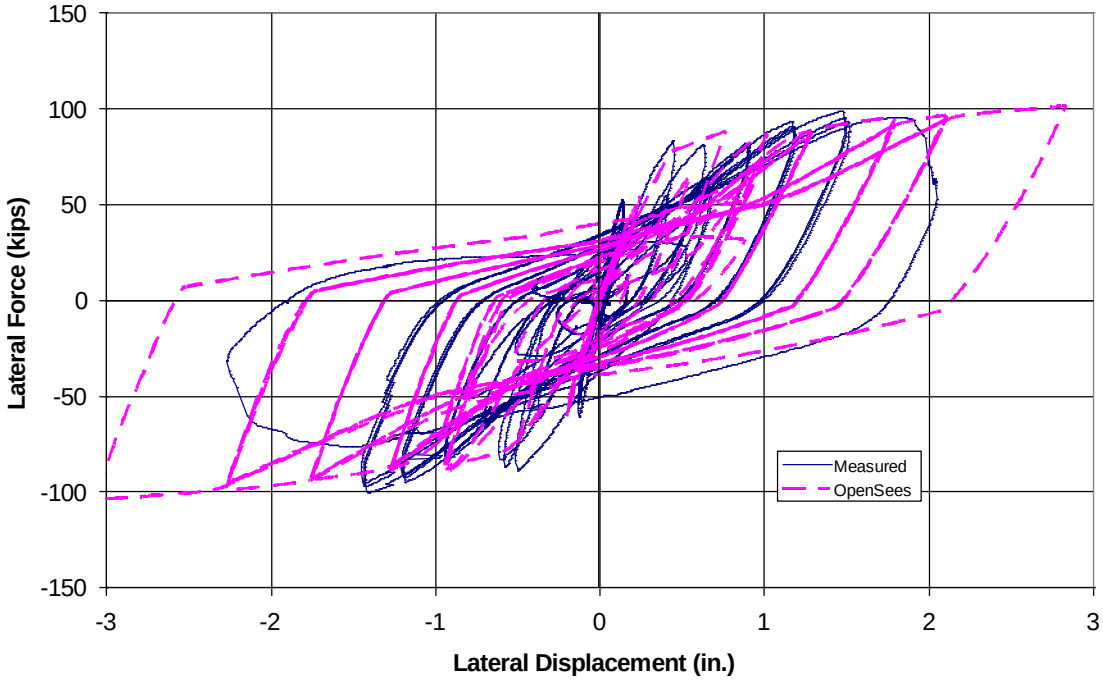

Figure 5.40 Measured and Calculated First Floor Force-Displacement Responses of NTW1 in the Flange Direction

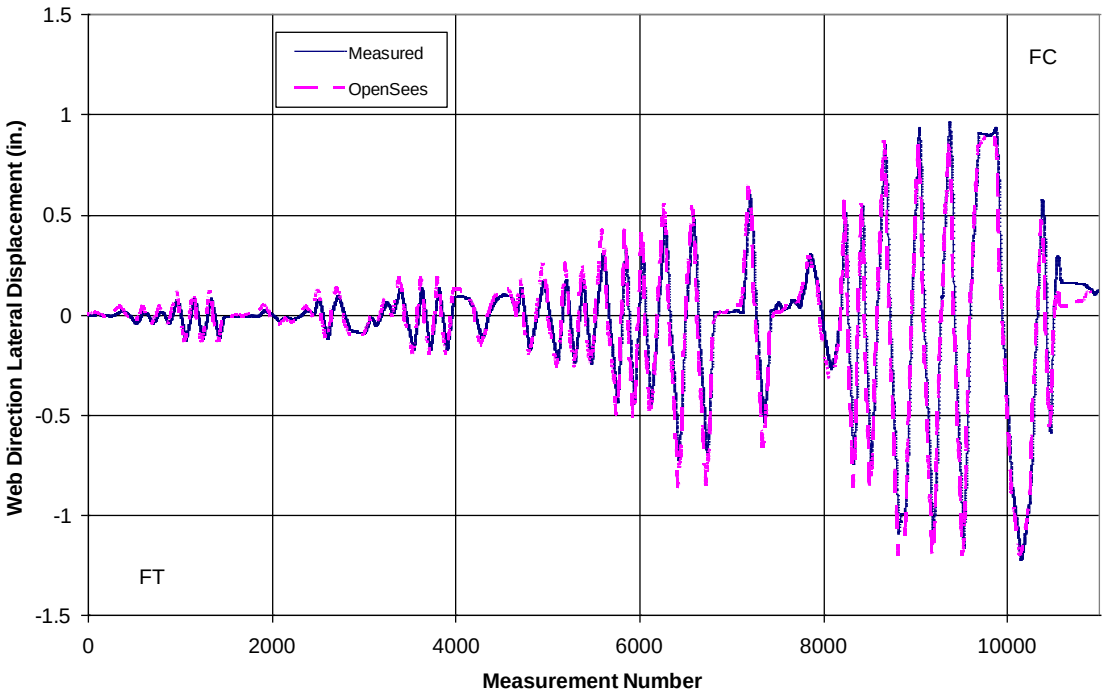

Figure 5.41 Comparison of First Floor Displacement of NTW1 in the Web Direction as a Function of Measurement Number

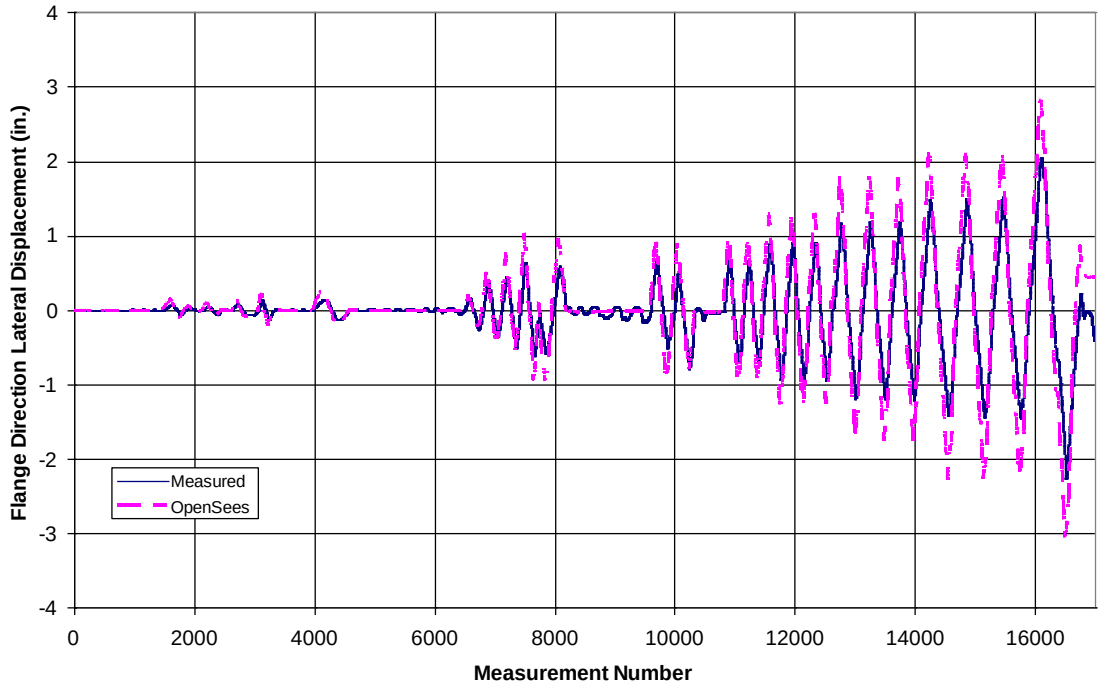

Figure 5.42 Comparison of First Floor Displacement of NTW1 in the Flange Direction as a Function of Measurement Number

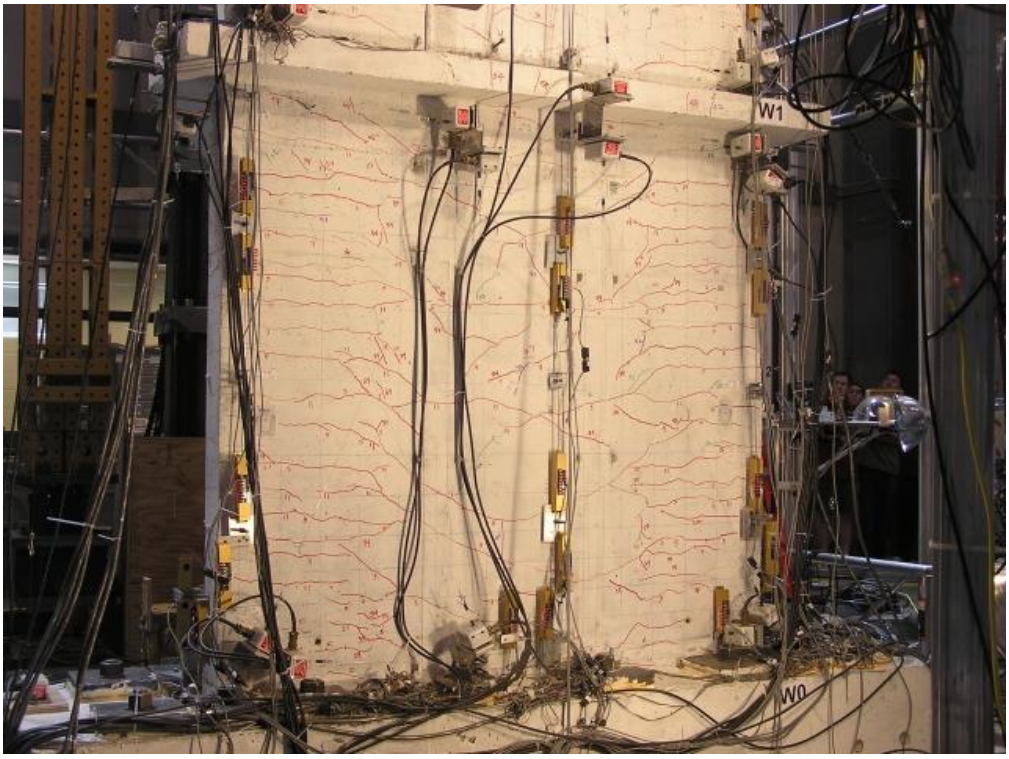

Figure 5.43 Condition of Flange at First Floor after subjected to 1% Drift Cycles

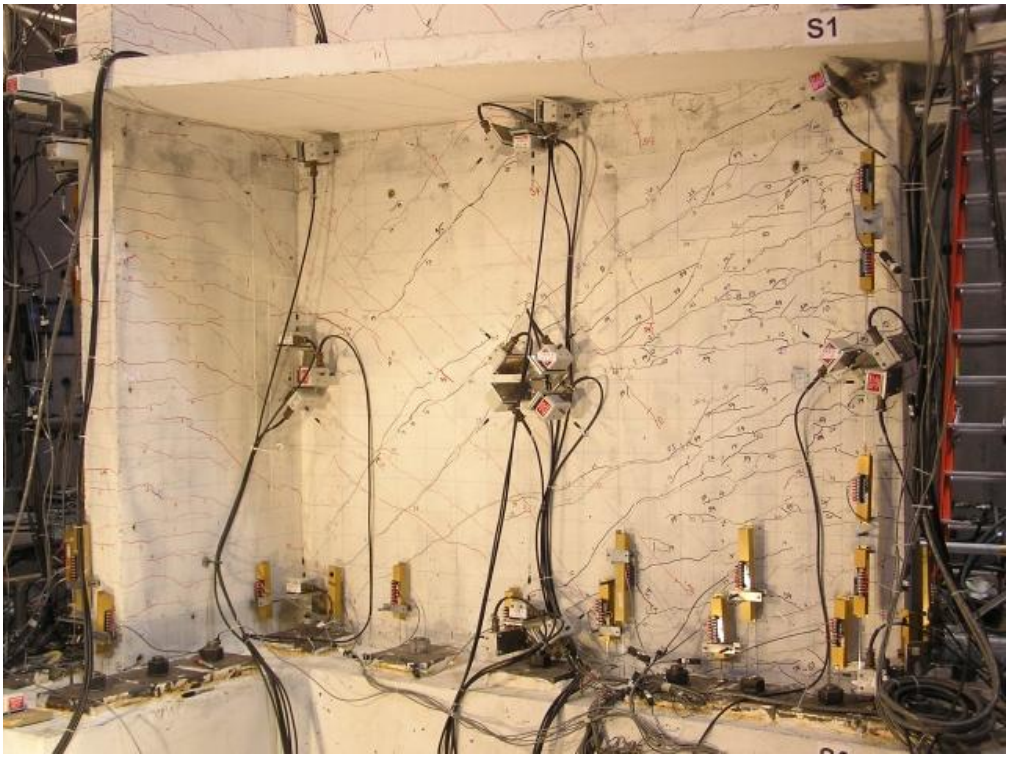

Figure 5.44 Condition of Web at First Floor After Subjected to 1% Drift Cycles

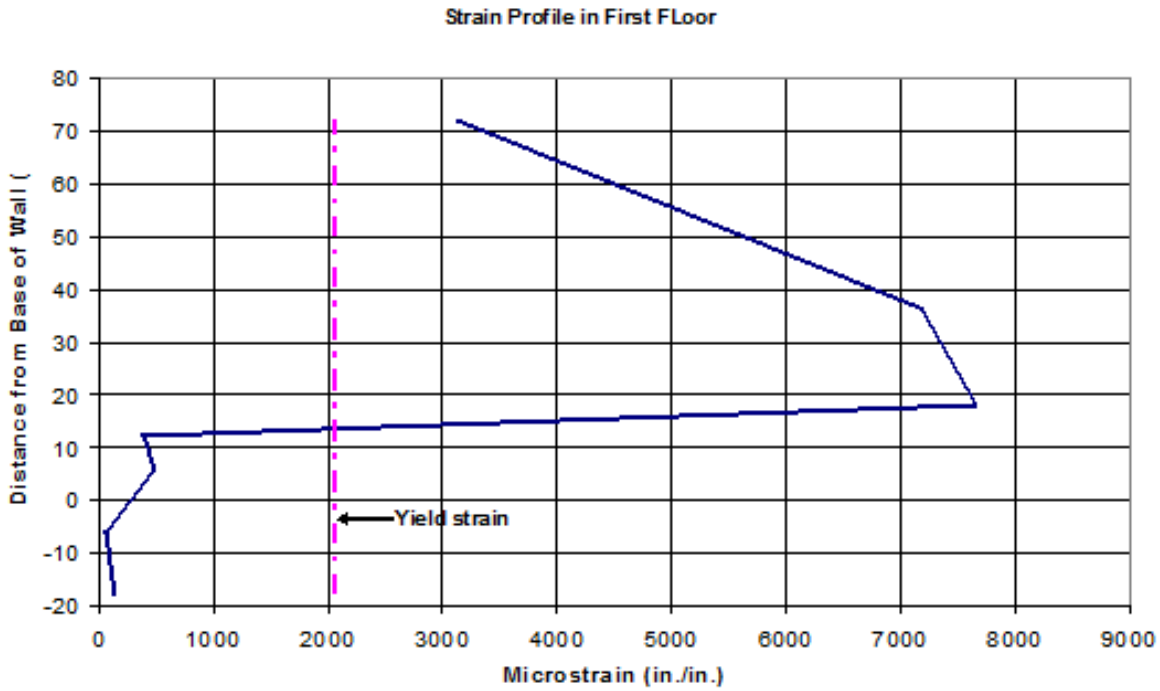

Figure 5.45 Measured Strain in a Longitudinal Reinforcement Bar in the Flange Boundary Element at 1% Drift.

Another source for the discrepancies between the measured and calculated responses of NTW1 could be due to the simple material model used to simulate the shear response. Figures 5.26 and 5.28 shows that the *Pinching4* model did not simulate the first floor level shear response perfectly. The lower floor level displacements are influenced more by the shear response than lateral displacement at the top of the wall. As noted previously, the inaccurate simulation of the unloading stiffness was due to the simple unloading rules of Pinching4 dominating the unloading response of the model. However, the Pinching4 model was found to be the best one available at the time of modeling NTW1 to simulate the shear response of the first floor level.

5.8.4 Second Floor Response

The calculated lateral displacement response of NTW1 at the second floor was also compared to the measured experimental data. The lateral movements of both flange tips and the web tip were measured using string potentiometers during the test. The responses from each of the three instruments were averaged to determine the experimental response. As seen in Figures

5.46 and 5.47, the second floor response was better simulated by the OpenSees model than the first floor response. The improved simulation was likely caused by the increased contribution of flexure to the total deformation and decreased influence of any foundation effects, along with other reasons discussed in Section 5.8.2.

Figures 5.48 and 5.49 compare the measured lateral displacement of NTW1 and that from the OpenSees analysis as a function of the measurement number for the web and flange direction, respectively. As noted previously, this perspective allows the accuracy of the analysis to be seen more clearly. In Figures 5.48 and 5.49, the OpenSees analysis typically overestimated the lateral displacement by approximately 10% in the web direction and 15% in the flange direction at the peak displacements. Displacements between the peaks are simulated within 5-10% of the measured displacements. There are isolated peaks where the OpenSees analysis over predicted the lateral displacement by as much as 15% in the web direction and 20% in the flange direction. While not as well simulated as the global response, the second floor response shows that the model is simulating the behavior of the wall better outside of the first floor. The adequate simulation seen for the second floor response confirms that improving the model performance in the critical region of the first floor level will improve the response of the analytical model at the second floor as well. Similar to the global force-displacement responses, the residual displacements were somewhat poorly captured by the model.

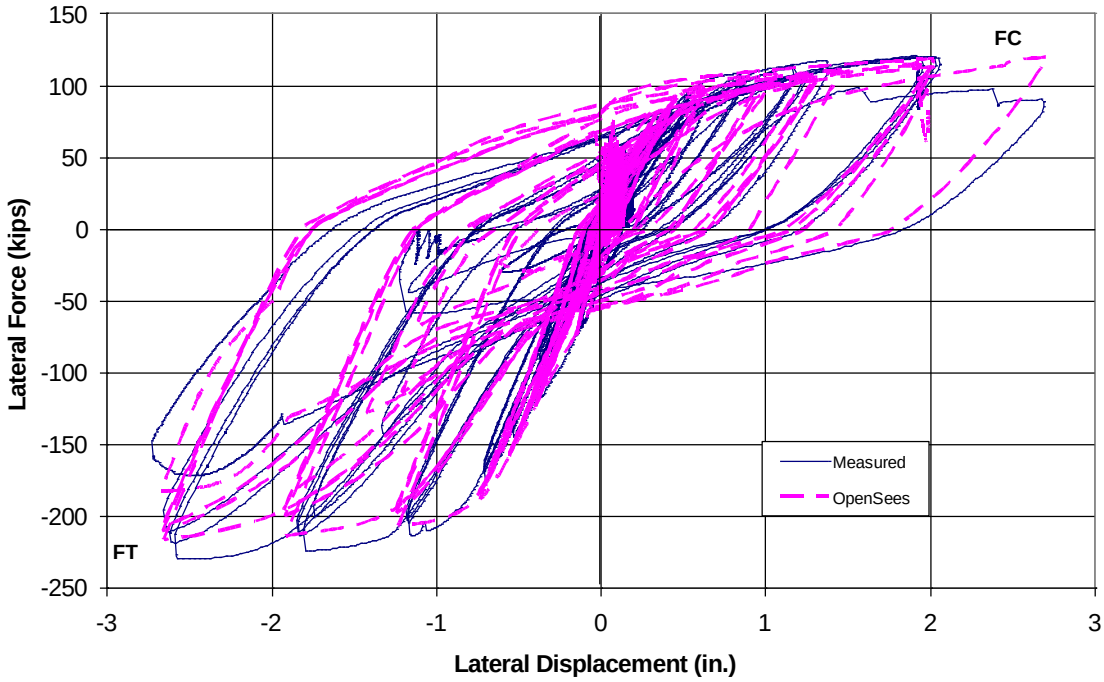

Figure 5.46 Measured and Calculated Second Floor Force-Lateral Displacement Responses of NTW1 in the Web Direction

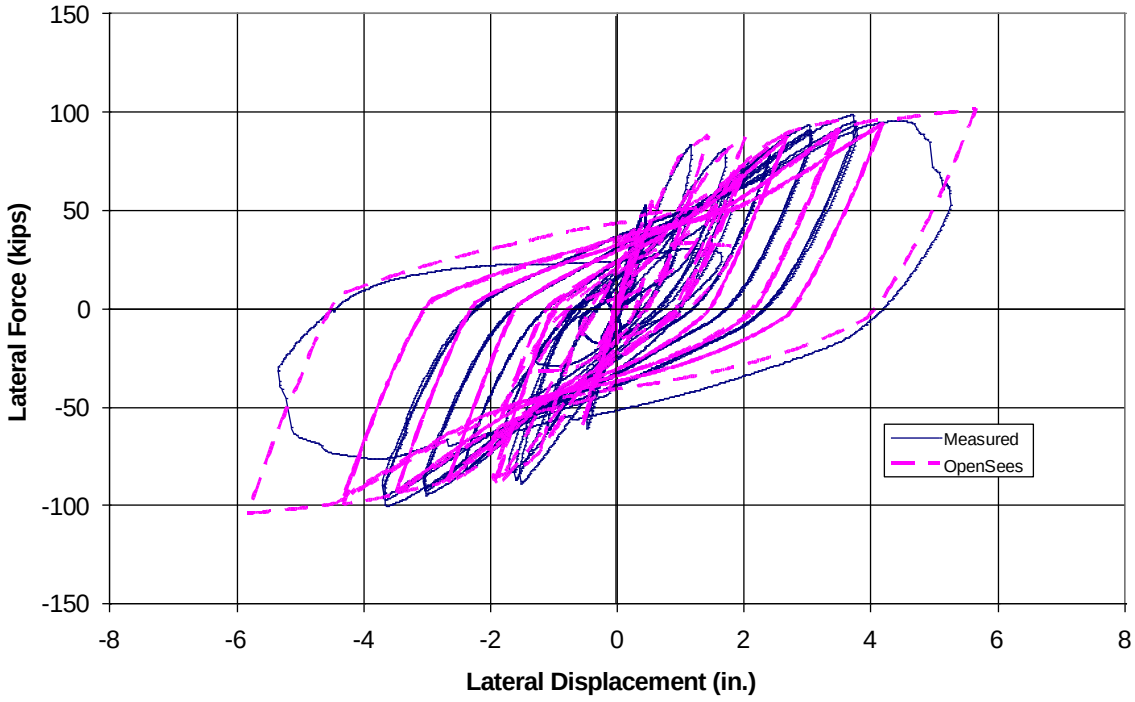

Figure 5.47 Measured and Calculated Second Floor Force-Lateral Displacement Responses of NTW1 in the Flange Direction

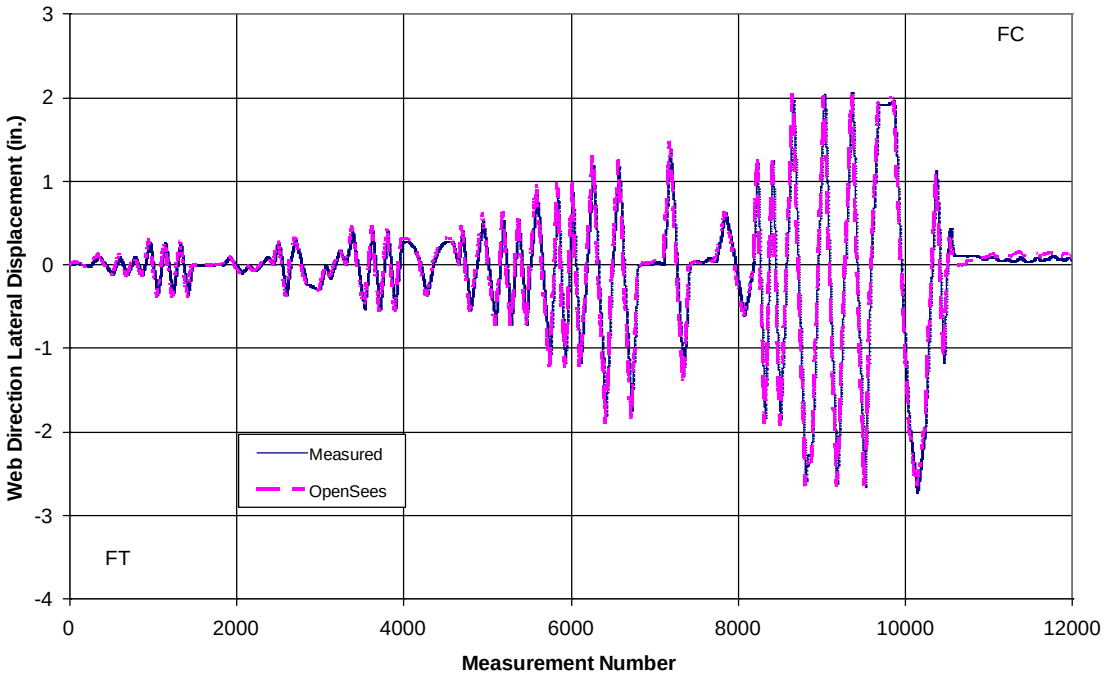

Figure 5.48 Comparison of Second Floor Displacement of NTW1 in the Web Direction as a Function of Measurement Number

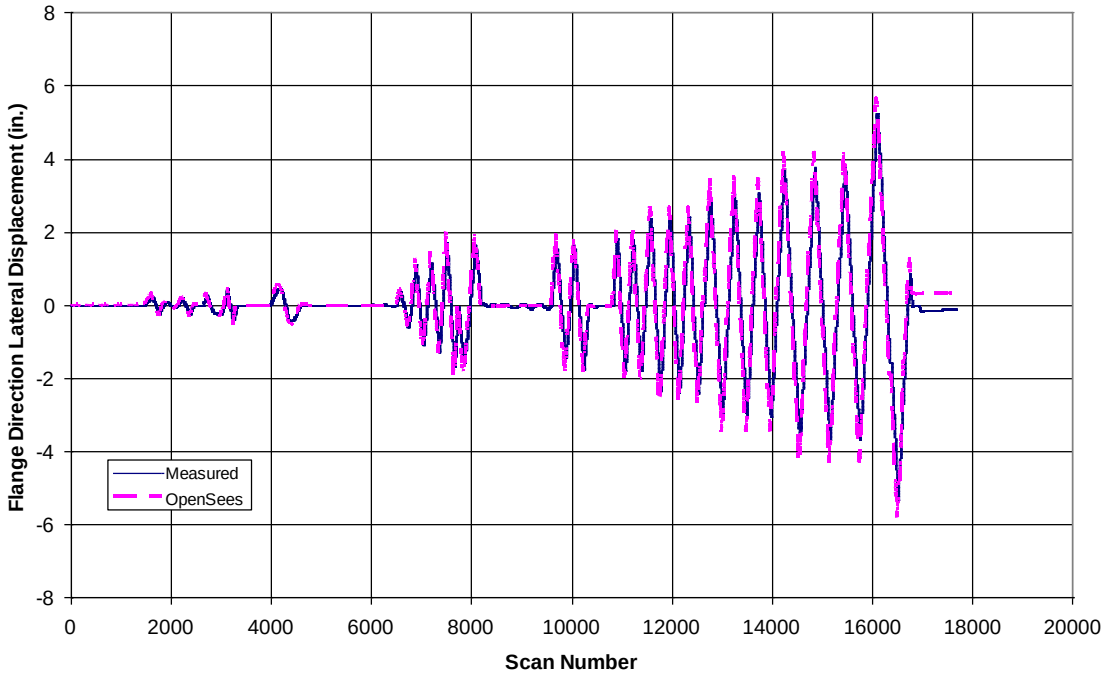

Figure 5.49 Comparison of Second Floor Displacement of NTW1 in the Flange Direction as a Function of Measurement Number

5.8.5 Components of Lateral Deformation

The lateral displacement measured in the test of NTW1 was decomposed into the various components, including the flexural component, shear component, and strain penetration component. A method used for doing the same for bridge joints by Sritharan and Priestley [Sritharan et al., 1996] was followed to decompose the lateral displacement into various components based on the measurements recorded by LVDTs and string potentiometers. Figures 5.50 and 5.51 compare the calculated and analytical contribution of the flexural, shear, and strain penetration displacement components as a fraction of the total first floor displacement for the web and flange directions, respectively. Each line represents the displacement of the component alone. Figure 5.50 shows that the OpenSees analysis is capturing the contribution of the shear and flexure with a reasonable degree of accuracy in the flange-in-tension direction. However, in the flange-in-compression direction the shear and flexure contribution are almost equal, and the flexural contribution is overestimated and the shear contribution underestimated. The large increase in shear distortion and thus higher shear contribution in the flange-in-compression direction compared to the flange-in-tension direction was also observed by Thomsen and Wallace in their test of specimen TW2 as discussed in Chapter 2. This behavior was attributed to inelastic shear deformation resulting from inelastic flexural response [Orakcal and Wallace, 2006]. The contribution of strain penetration was well captured by the analysis. Slightly lower contribution was recorded in the flange-in-compression direction compared to the analysis. The components were determined from the data for positive displacement in the parallel to the flange direction. Since the response was symmetrical the displacement components were not determined for the negative direction. In the flange direction the flexural component is adequately captured, but the shear contribution is underestimated. The measured strain penetration contribution is poorly captured; however, the decomposition shows strain penetration contribution was equal to shear deformation. This is not possible and is attributed to instrument malfunction.

The contribution of each component to the total top displacement is presented in Figure 5.52. The analysis accurately captures all the components of the lateral displacement at the top of the wall. The strain penetration contribution is shown for the top of the wall displacement, which indicates that the model is capturing the strain penetration up to a displacement of 1.36 in.

Beyond this displacement the contribution of strain penetration decreases, which is contrary to the fact that the strain penetration should increase for increasing displacements, particularly in the nonlinear range. The flexural contribution is very well captured by the analysis at all displacement levels. Overall the shear contribution at the top of the wall is adequately simulated. Due to the instrumentation, the top of the wall displacement cannot be decomposed in the flange direction. The shear distortion was not measured in the web direction above the second floor for the flange direction. Thus it is impossible to separate the lateral displacement that is due to flexural deformation and that due to shear distortion of the wall. Thus comparison of the displacement components cannot be presented. However, Figure 5.53 shows the theoretical displacement components from the OpenSees analysis.

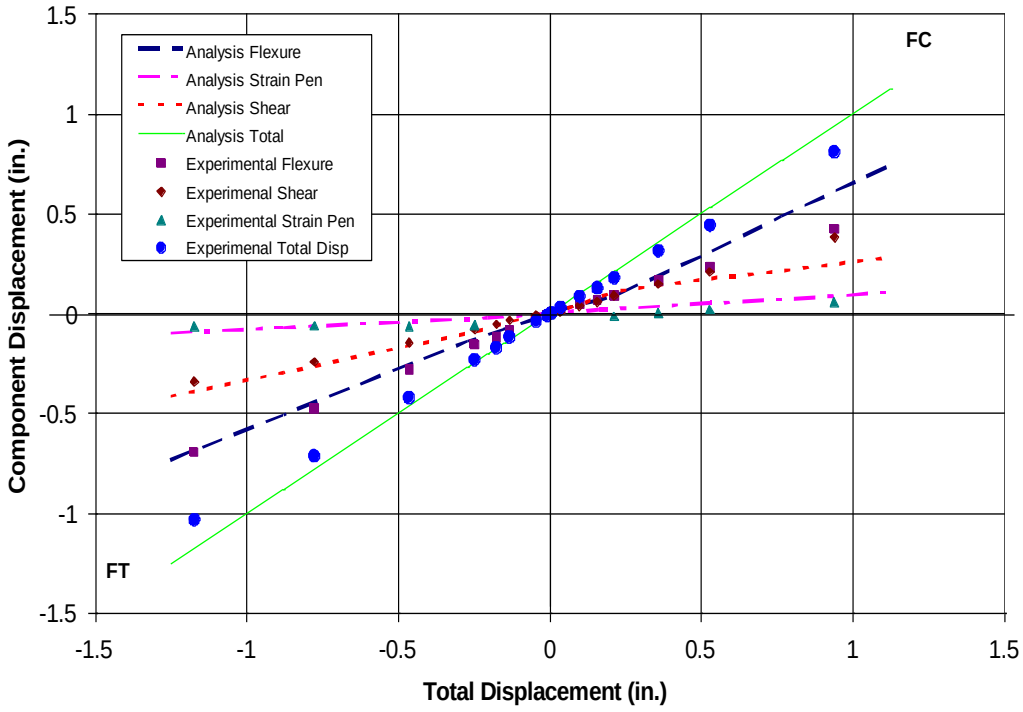

Figure 5.50 Comparison of the First Floor lateral Displacement Components in the Web Direction

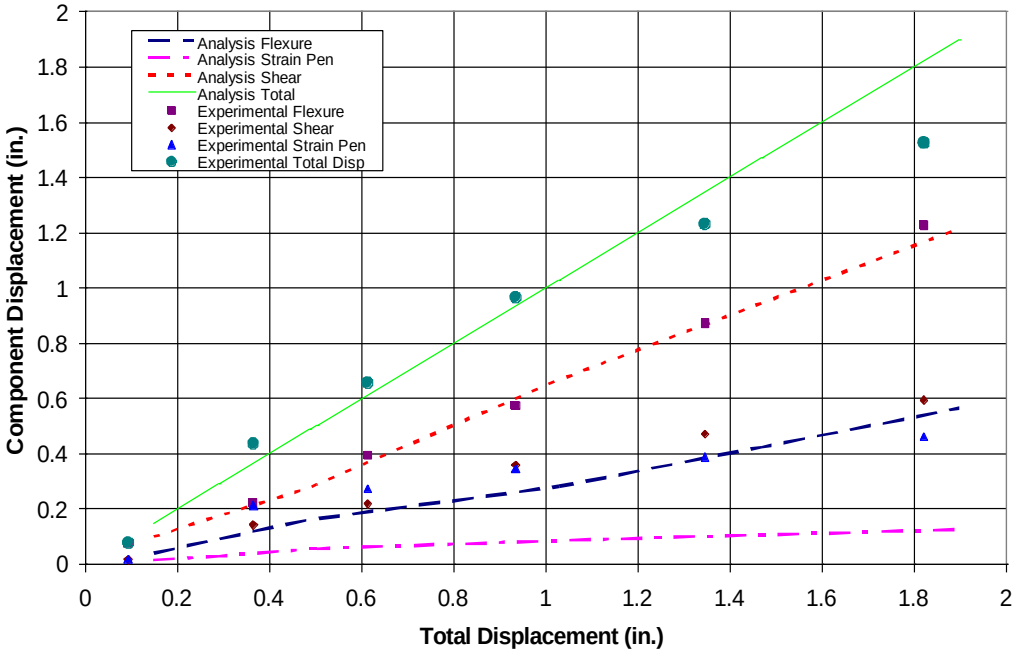

Figure 5.51 Comparison of the First Floor Lateral Displacement Components in the Flange Direction

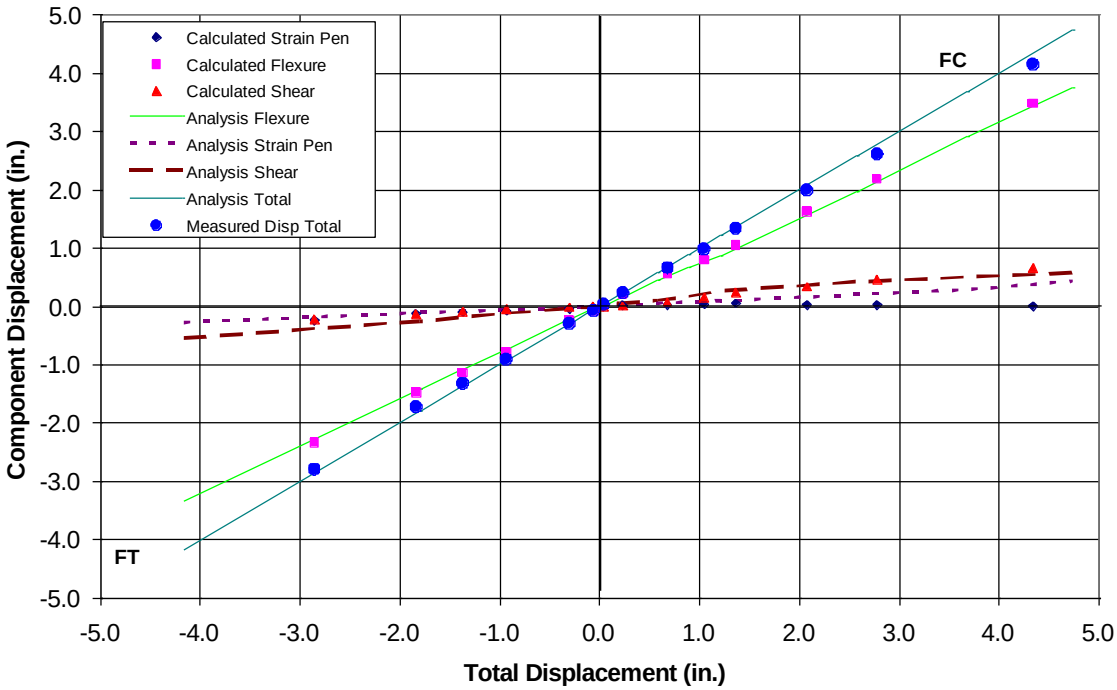

Figure 5.52 Comparison of the Wall Top Lateral Displacement Components in the Web Direction

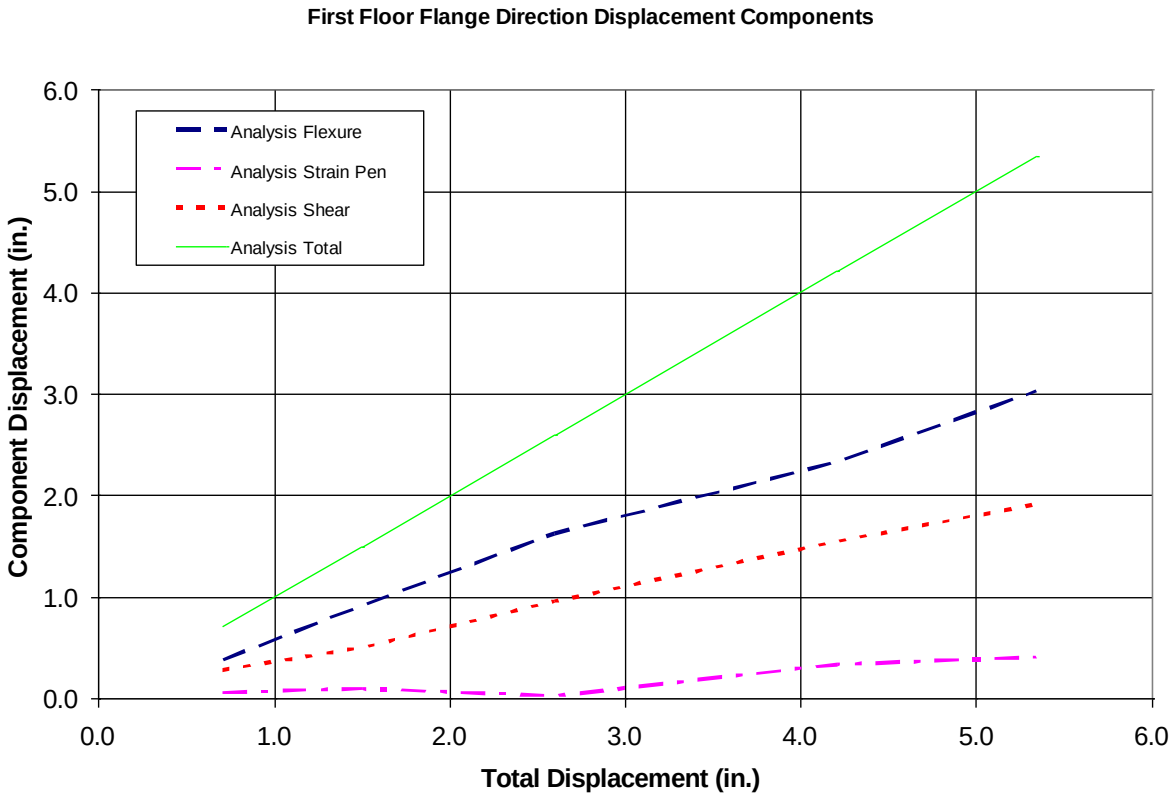

Figure 5.53 Comparison of the Wall Top Lateral Displacement Components in the Flange Direction

5.8.6 Multidirectional Load Path

As detailed in the load path in Section 5.4 (see Figures 5.12 and 5.16 and in Table 5.2), NTW1 was subjected to complex load paths, which had a pentagon shape and an "hourglass" shape. These paths were chosen to examine the ability of the analysis model to predict the behavior of NTW1 under complex bi-directional load. The pentagon shape was targeted at approximately 50% of the yield displacement at any given direction, which was achieved by making the load path to approximate the expected shape of the yield surface of NTW1. Due to the effects of shear lag and shear-flexure interaction, the strain in the critical reinforcement at the base of the wall in any given direction of loading was not expected to be at a constant value. However, the load path did allow the accuracy of the analysis model under complex loading in the elastic region to be evaluated. The hourglass shape was conducted at approximately 2% drift level. This path allowed the analysis in the nonlinear range to be evaluated.

Figure 5.54 to 5.57 show the comparison of experimental and analysis results from the pentagon shape loading in the elastic region, which shows that the analysis model of NTW1 satisfactorily captured the response in both the flange and web directions. Figure 5.54 shows the displacement at the top of the wall from the analytical model and the average experimental value obtained from potentiometer readings. It is seen that the OpenSees model experienced slightly larger displacements at the top of the wall in comparison to the average measured lateral displacement at the top of the wall. The overestimation of the wall top displacement in the model was due to the difference between the actual stiffness of the top block and that was modeled in OpenSees by applying the displacements at an artificial control point above the wall. Figure 5.55 shows the comparison between the measured force resistance at the top of the wall and that determined by the OpenSees analysis. Figures 5.56 and 5.57 show the force-displacement comparison in the web and flange directions, respectively, for the pentagon load path. Given the complexity of the load path, OpenSees model captured the response well under this multidirectional displacement path. The flange direction force-displacement was better simulated than the web direction response. One possible source for the somewhat large discrepancy in the web direction response is that shear lag that occurs in this direction of response is expected to be dominant in the elastic range and this could have influenced the analysis result. The other possible source of the discrepancy is the post-peak behavior of concrete in tension. Although the post-peak behavior of concrete would affect both directions, it would be more prominent in the flange-in-tension direction due to the larger area of concrete in tension in the flange. However, the response of the wall in the nonlinear range will be less sensitive to these effects.

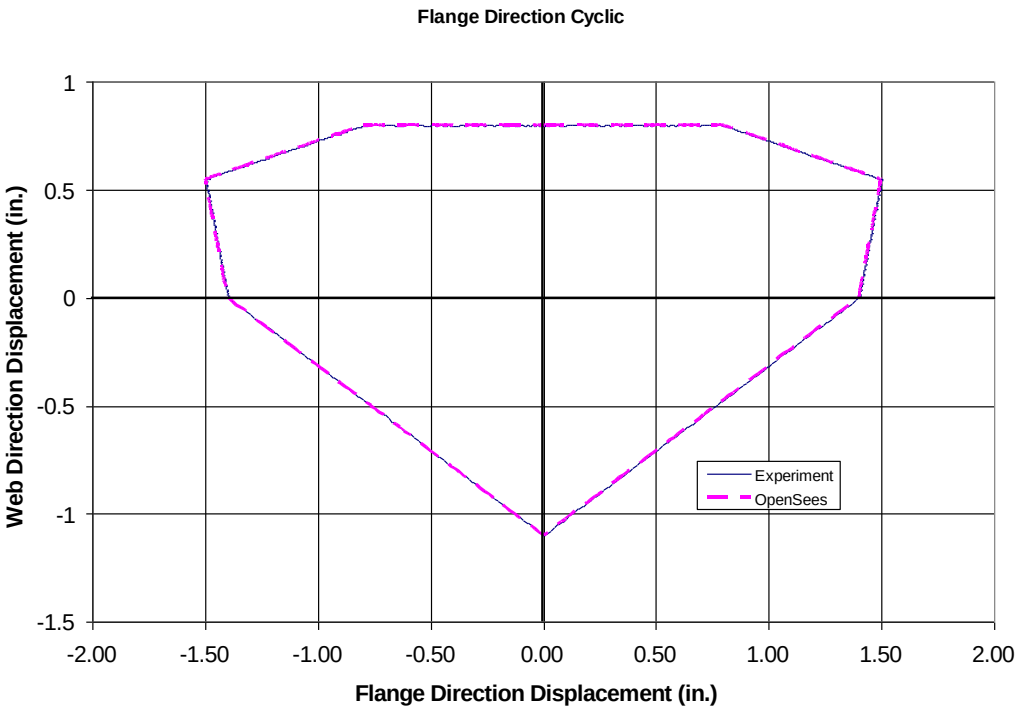

Figure 5.54 Comparison of Displacements at the Top of NTW1 for the Pentagon Shape Load Path at 50% of Yield

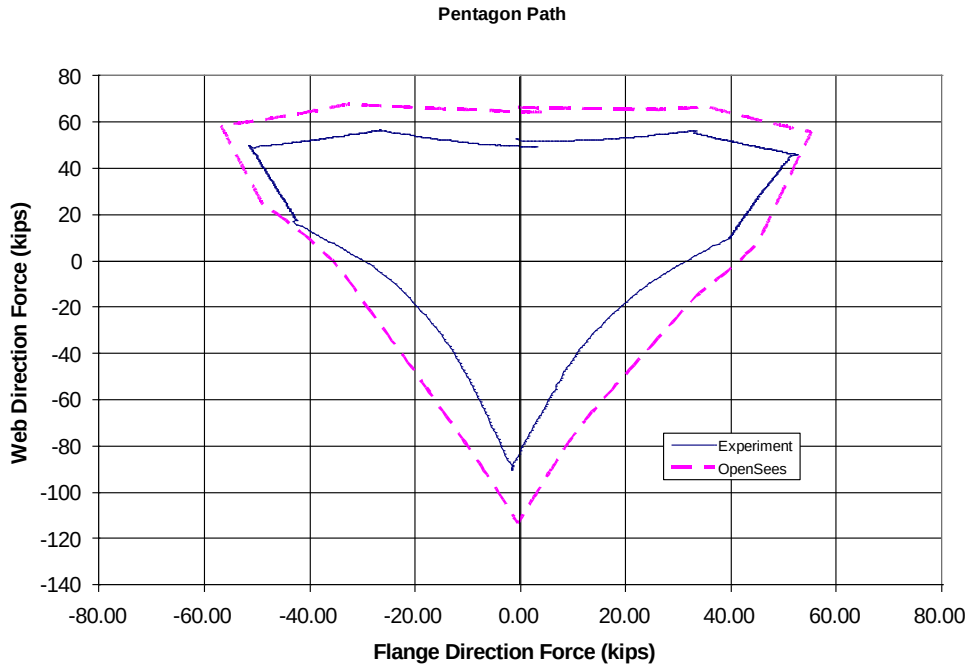

Figure 5.55 Comparison of Forces at the Top of NTW1 for the Pentagon Shape Load Path at 50% of Yield

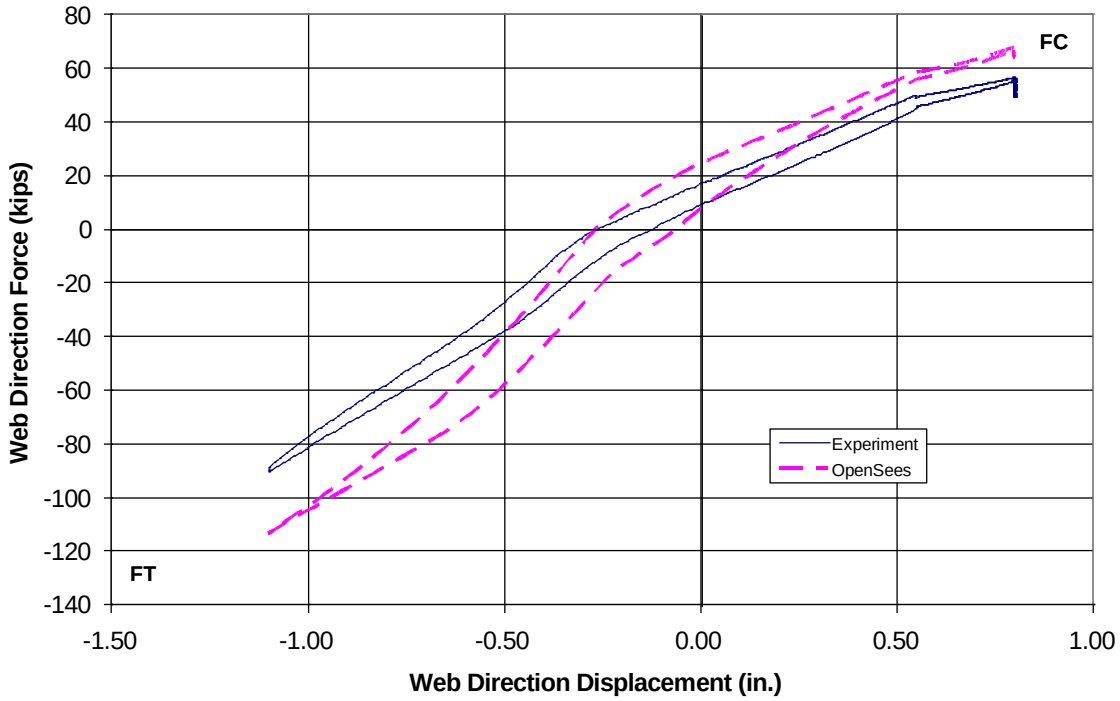

Figure 5.56 Comparison of Force-Displacement Response of NTW1 for the Pentagon Shape Load Path at 50% Yield in the Web Direction

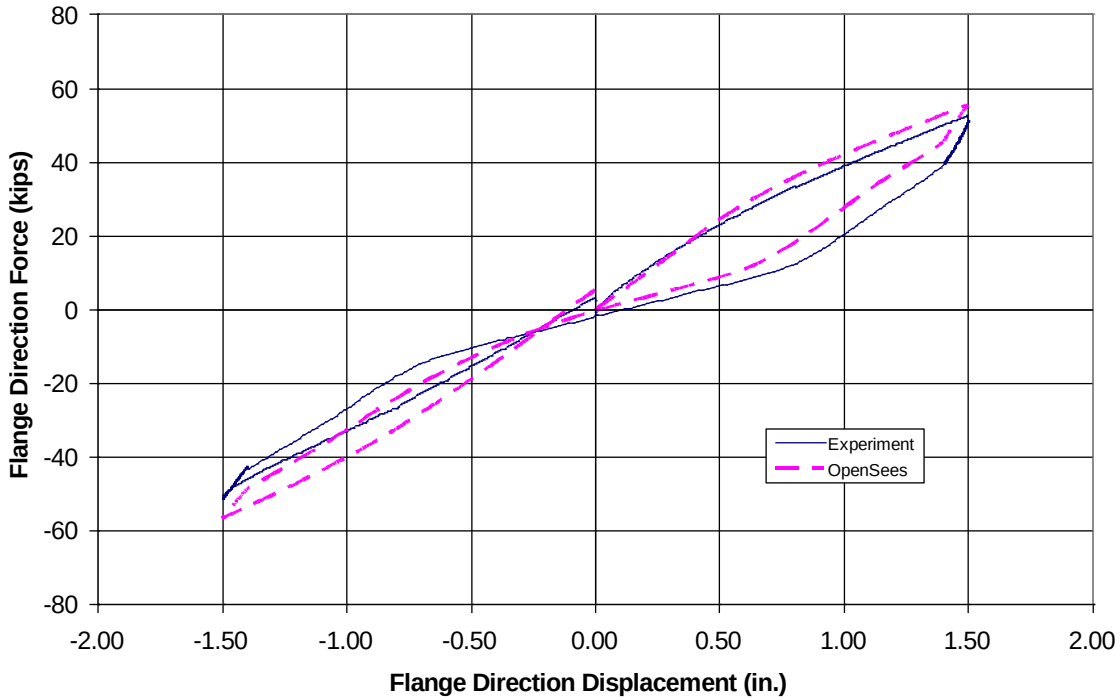

Figure 5.57 Comparison of Force-Displacement Response of NTW1 for the Pentagon Shape Load Path at 50% Yield in the Flange Direction

The results of hourglass shape load path conducted at 2.0% drift level are shown in Figure 5.58 to 5.61. At this displacement level, all longitudinal reinforcement in the critical regions of the web and flange was taken well into the inelastic range, and the wall was fully cracked under the influence of both flexure and shear actions (see Figure 5.62). Figure 5.58 shows the target displacement comparison at the top of the wall; the OpenSees analysis simulated the displacement targets at the top of the wall in comparison to the measured values. Figure 5.59 presents the comparison between the measured lateral force resistance and the results from the OpenSees analysis. The force-displacement response comparisons for the web and flange directions for the hourglass load path are shown in Figures 5.60 and 5.61 respectively. The force-displacement responses compared in these figures confirm that they were well captured by the OpenSees model. A slight over prediction seen for the flange-in-tension direction in Figure 5.60 was due to the fact that crushing of concrete began to occur in the web tip of NTW1. The lateral force-displacement response in the flange directions are compared in Figure 5.58. Again a good comparison is seen between the measured and analytical responses except for the first half cycle which led to some over prediction of the force resistance. This discrepancy may also be attributed to the fact that the flange had experienced some damage due to testing in the web direction, which may not have been adequately captured by the analytical model. Figure 5.62 shows significant cracking and damage prior to starting the hourglass load path. Figure 5.63 shows that the longitudinal reinforcement in the web tip had buckled during the hourglass load path, which occurred as the peak displacement of -6.38 in. was reached in the flange-in-tension direction. Upon deconstruction of the wall following testing, three bars in the web tip were found to have buckled over a number of the transverse stirrups (see Figure 5.63). This failure mode, however, was not included by the OpenSees model. The material models used in the OpenSees model of NTW1 did not have the ability to capture the buckling of the longitudinal reinforcement. During testing, crushing of concrete outside the confined region of the web boundary element was also observed in the web tip, which was accounted for in the analytical model through appropriate definition of concrete fibers.

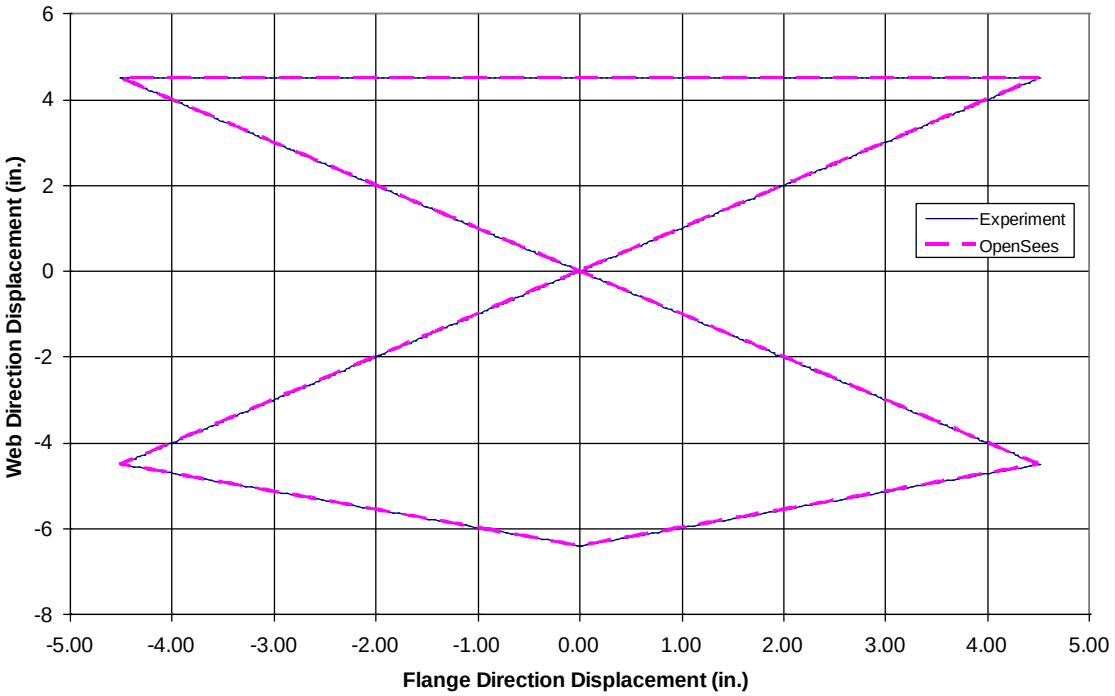

Figure 5.58 Comparison of Displacements at the Top of NTW1 for the Hourglass Shape Load Path at 2% Drift

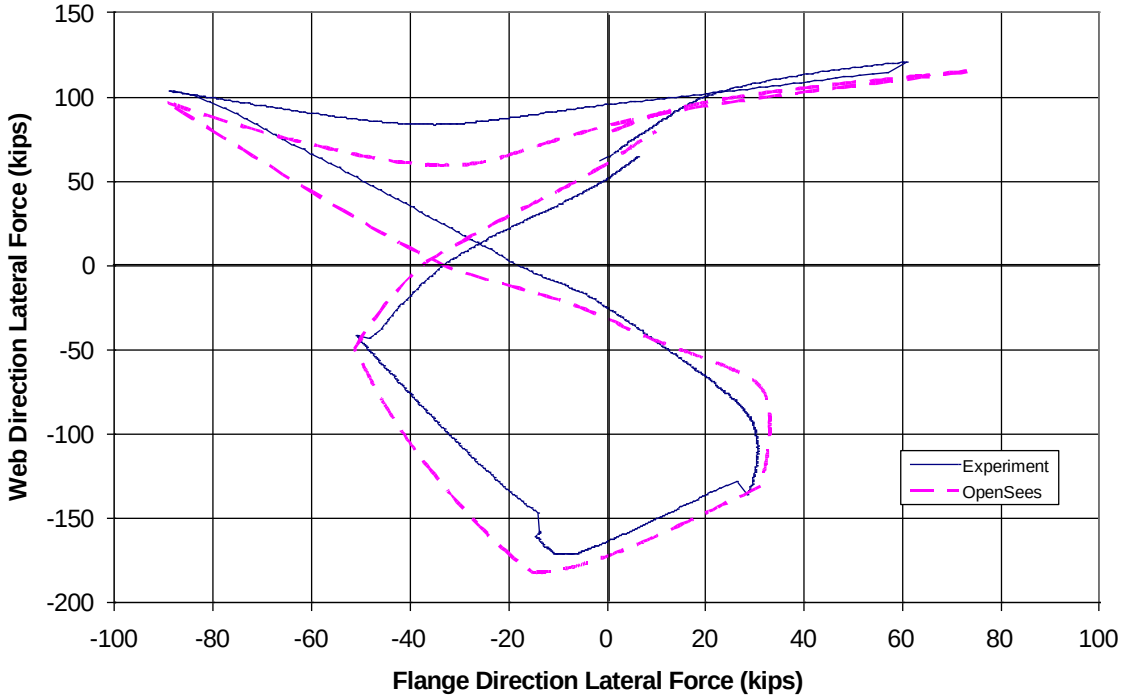

Figure 5.59 Comparison of Forces at the Top of NTW1 for the Hourglass Shape Load Path at 2% Drift

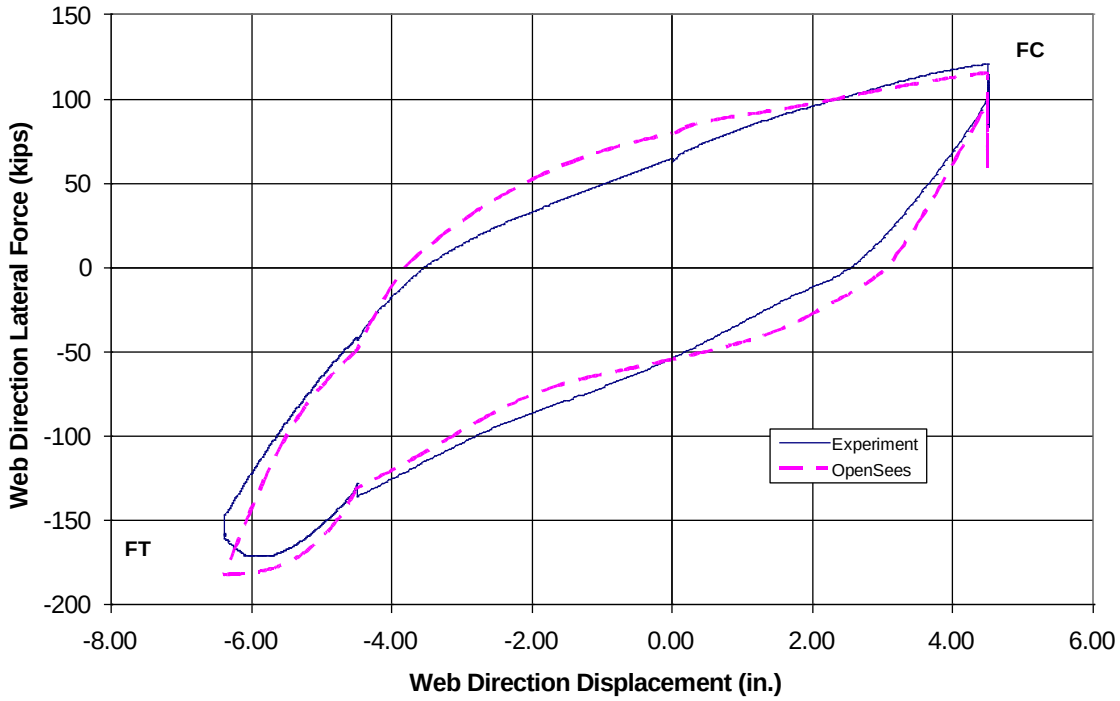

Figure 5.60 Comparison of Force-Displacement Response of NTW1 for the Hourglass Shape Load Path at 2 % Lateral Drift in the Web Direction

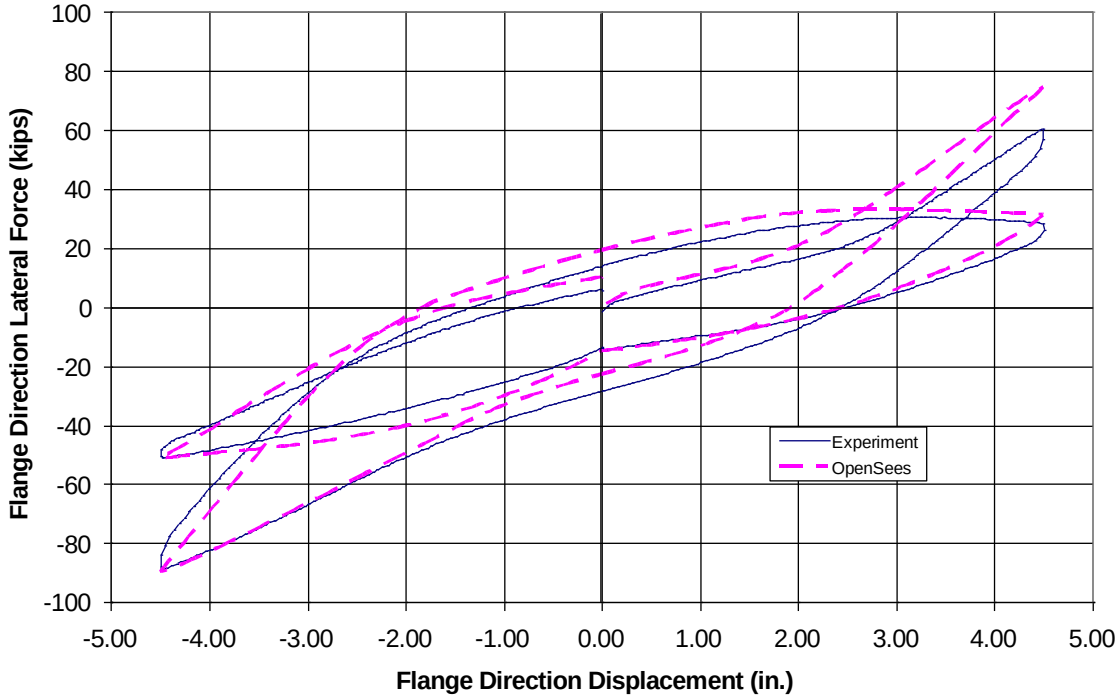

Figure 5.61 Comparison of Force-Displacement Response of NTW1 for the Hourglass Shape Load Path at 2% Lateral Drift in the Flange Direction

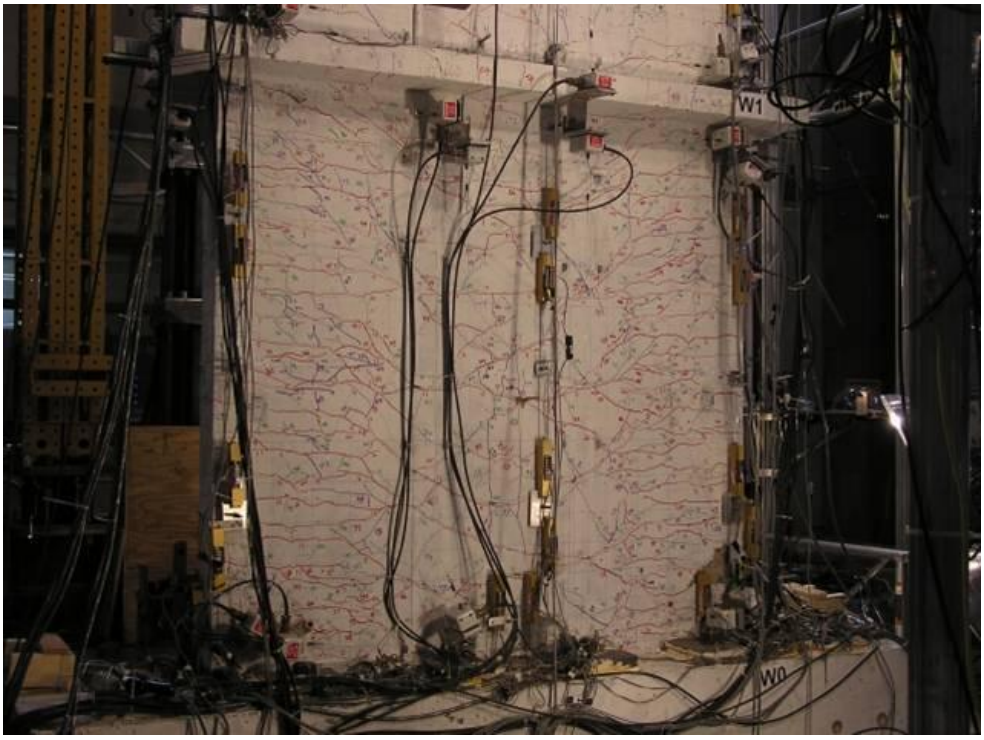

Figure 5.62 Back of the First Floor Flange of NTW1 Prior to Beginning of the Hourglass Shape Load Path

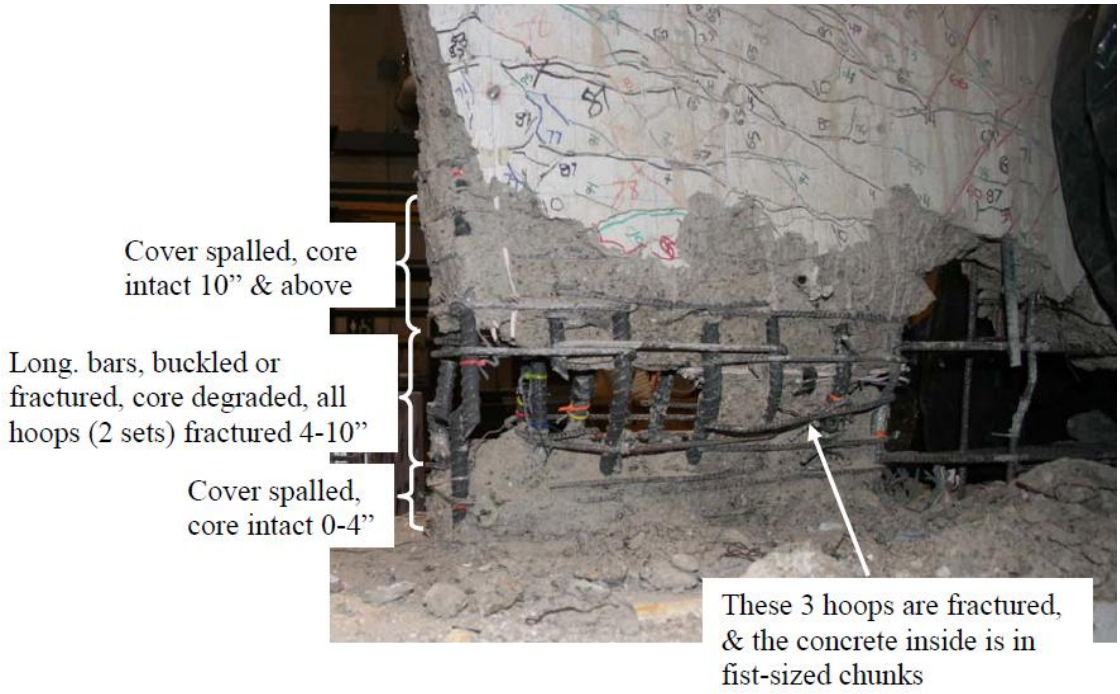

Figure 5.63 Buckling of the Longitudinal Reinforcement in the Web Tip Boundary Element of NTW1 at 2% drift

5.8.7 Strain Profile Comparison

Adequate simulation of the local response, including strains and neutral axis depths at the critical region, is important from a design perspective. Also, strain is a better predictor of damage to the structure at a particular location than a global parameter such as lateral displacement. Therefore, adequate simulation of local strains should be considered as an important feature when evaluating the adequacy of a particular modeling approach. The strains recorded nominally at six inches above the base were used for the comparison purposes since this location had the most complete set of gages, giving the most complete strain profiles.

Figures 5.64 and 5.65 show the strain profiles established at the first peak various displacements parallel to the length of the web for the flange-in-compression and flange-in-tension direction. The analysis satisfactorily captured the location of the neutral axis depth in both the flange-in-compression and flange-in-tension directions of loading. Figure 5.64 also shows the analysis captured the curvature up to the yield cycles. The strain and curvature of cycles below yield are particularly well captured by the analysis. The strain profile for the flange-in-tension direction was only plotted up to the yielding condition. Above yield, some gages in the flange malfunctioned, not providing adequate data to develop the strain profiles.

Under the flange direction of loading, a sufficient number of data was not obtained that was adequate to establish the strain profiles. Several strain gages in the flange failed prior to the majority of the flange direction testing began. Since this direction was not tested heavily until after the web tip experienced buckling of the longitudinal bars, the bars in the flange had been subjected to large strains in previous load cycles. As shown in Figure 5.66, a strain profile for the flange direction loading was established at 0.25% of the yield displacement, which shows a good agreement between the experimental and analytical OpenSees model.

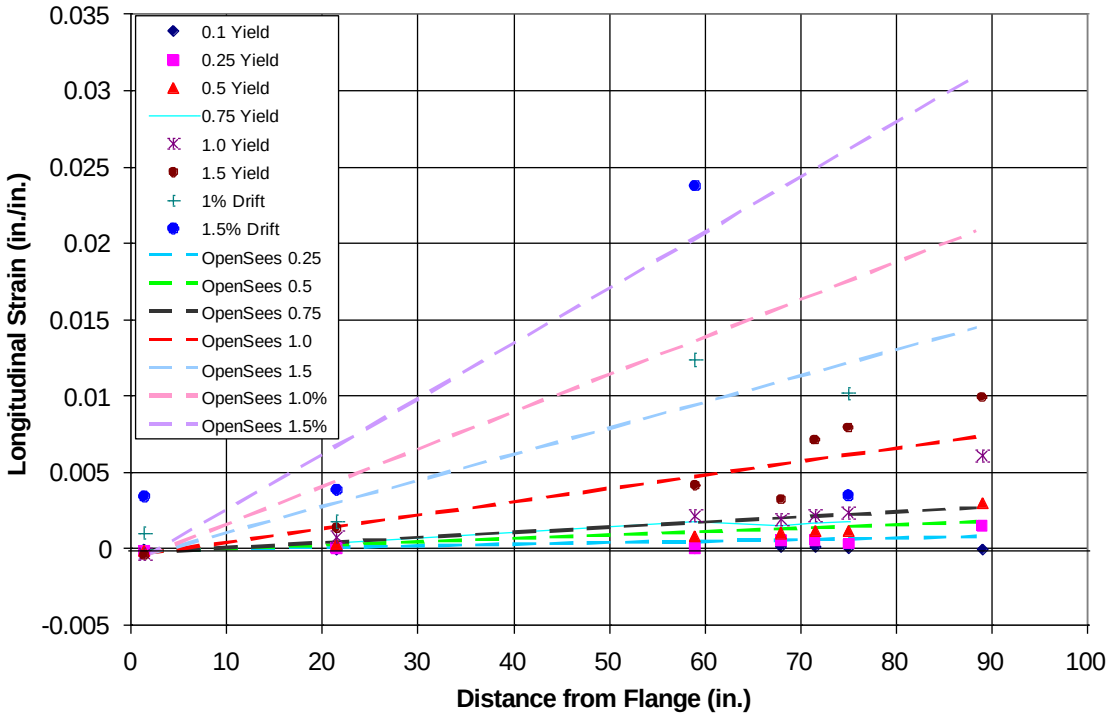

Figure 5.64 Comparison of Strain Profiles for the Flange-in-Compression Direction Response of NTW1

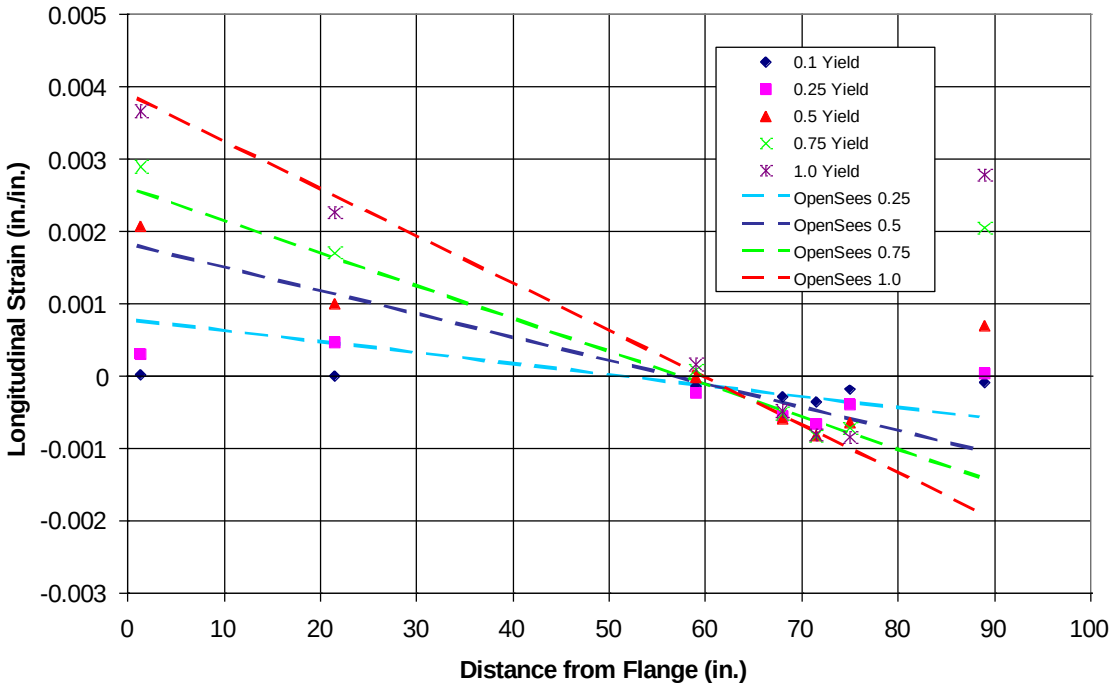

Figure 5.65 Comparison of Strain Profiles for the Flange-in-Tension Direction Response of NTW1

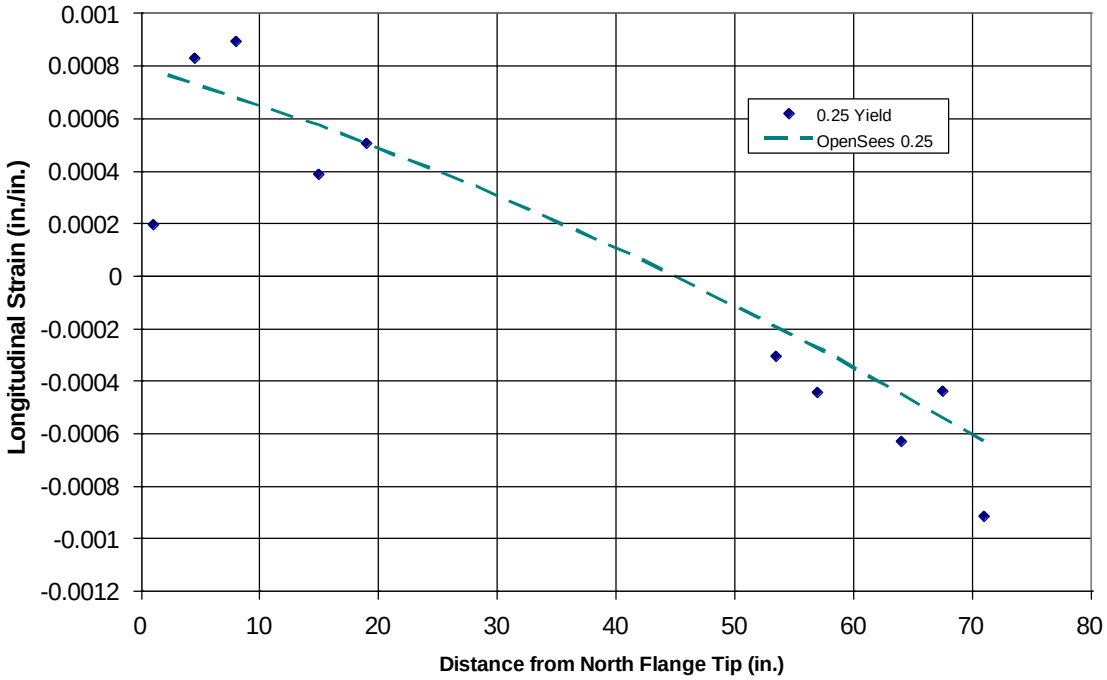

Figure 5.66 Comparison of Strain Profiles for the Flange Direction Response of NTW1

Chapter 6
Analysis of NTW2

6.0 Introduction

This chapter presents the analysis conducted prior to the testing of the second T-wall unit, NTW2. Post-testing analysis is not presented in this chapter, and was not conducted as part of this investigation. The analysis of NTW1 in Chapter 5 showed that a fiber-based model can adequately capture the experimental response of a T-wall subjected to multi-directional loading. The goal of the second T-wall analysis was to predict the response of NTW2 using the measured material properties and the experience gained from post-testing analysis of NTW1 and compare results with experimental data. Furthermore, post-testing analysis similar to that was conducted for NTW1 was not expected to provide significantly further information on the simulation of T-walls beyond what was learned in NTW1. The local response was not significantly examined because of discrepancies observed in the global response due to differences between NTW2 and other T-walls analyzed.

6.1 Description of NTW2

The second T-wall specimen, referred to as NTW2, was designed based on the observed response of NTW1 to the multidirectional loading. The reinforcement details were modified to improve the performance of the wall when subjected to multi-directional loading similar to that was used for testing NTW1. The reinforcement details used for NTW2 are shown in Figure 6.1. The same gross dimensions of NTW2 were identical to those of NTW1 since both walls, represented the same prototype wall at 50% scale. The total amount of longitudinal steel in the flange was similar to that in NTW1. A perfect match of the total reinforcement area was not possible as the number, size, and distribution of the longitudinal bars were altered; thus, NTW2 had approximately 0.88 sq in. or 9.4% less steel area in the flange than NTW1. A critical change in the detailing was that the amount of steel in the boundary elements of the NTW2 flange was reduced, and more steel was distributed along the length of the flange. Contrary to the current

design practice, the researchers felt that having more distributed steel would provide better crack control and allow for smaller, more distributed diagonal cracks to form, rather than allowing large concentrated cracks to develop as observed in NTW1 (see Figure 5.22). A complete discussion of crack distribution and the effects of reinforcement are discussed later in this chapter. The distributed steel in the web was not modified from that used in NTW1. However, the boundary element in the web tip was extended deeper into the web by increasing the confined concrete region because crushing of concrete just outside of the boundary element in NTW1 (see Section 5.4). Additionally, the arrangement of the confinement reinforcement in the web tip was modified from that used in NTW1. A number of the transverse reinforcement hoops with 135º hooks opened up during testing of NTW1, which led to loss of confinement to concrete [Brueggen, 2009]. The loss of transverse reinforcement would also lead to premature buckling of the longitudinal reinforcement as seen in the web tip of NTW1. The hoops were rearranged such that the 135º hooks were positioned away from the web tip as much as possible, as seen in Figure 6.1. In NTW1, continuous longitudinal reinforcement without any splices was used over the entire wall height. In NTW2, the longitudinal reinforcement was spliced at the first floor level. Tests of rectangular walls conducted as part of the PreNEESR project showed that splicing the longitudinal reinforcement at the foundation interface led to concentration of damage at the interface and leading to fracture of longitudinal reinforcement when compared to equivalent walls designed with continuous reinforcement without splices or mechanical couplers located at the foundation interface. For more information on the rectangular walls, readers are directed to the Johnson [2007] and Chapter 4 of this report. Relocating the splice to the first floor level was investigated to determine if this would be an acceptable location for a construction splice.

In addition to investigating the effects of the improved reinforcement details, NTW2 was used to further investigate the ability of the MAST facility to simulate the critical behavior of the prototype T-wall using shorter specimens. Instead of constructing four of the six stories of the prototype wall like in NTW1, only the bottom two stories of NTW2 were constructed and tested. The MAST control capabilities were then used to apply the same shear-to-moment ratio along the height of the test wall. While the axial load was not added for two additional missing floors, this issue was addressed partway through the test. The increase in axial load is shown in Section

6.3 as part of the load path applied to both NTW2 and the OpenSees simulation.

The connection details of the base block to the strong floor or the base block reinforcement details were not modified from NTW1. Since the actuators could only be placed at certain heights, the reduced height of NTW2 required the base block height to be increased. Additionally, the base block was constructed in two pieces to allow the wall to be constructed in the staging area at the MAST facility. Figure 6.2 shows the two-part construction of the base block used for NTW2.

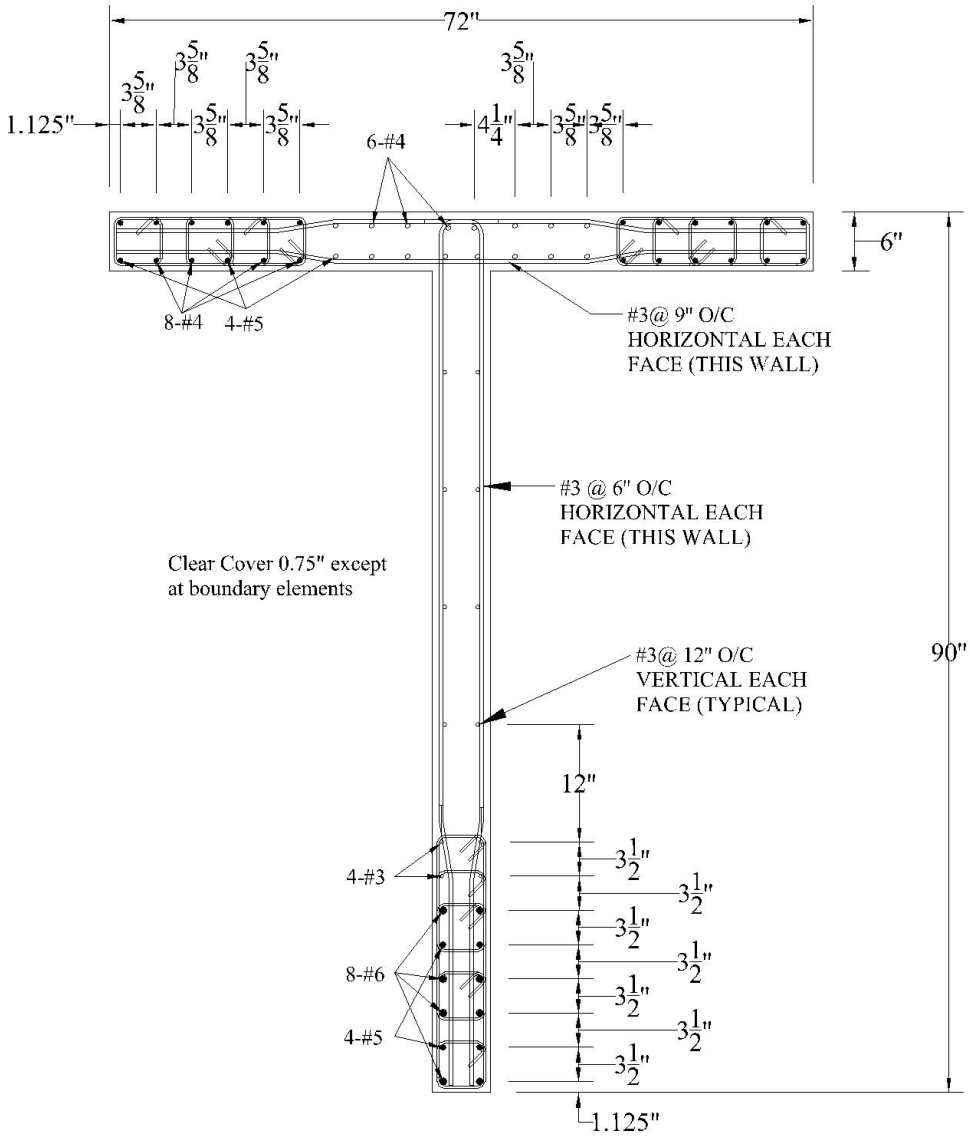

Figure 6.1 Cross-Sectional Dimensions and Reinforcement Details of Test Specimen NTW2

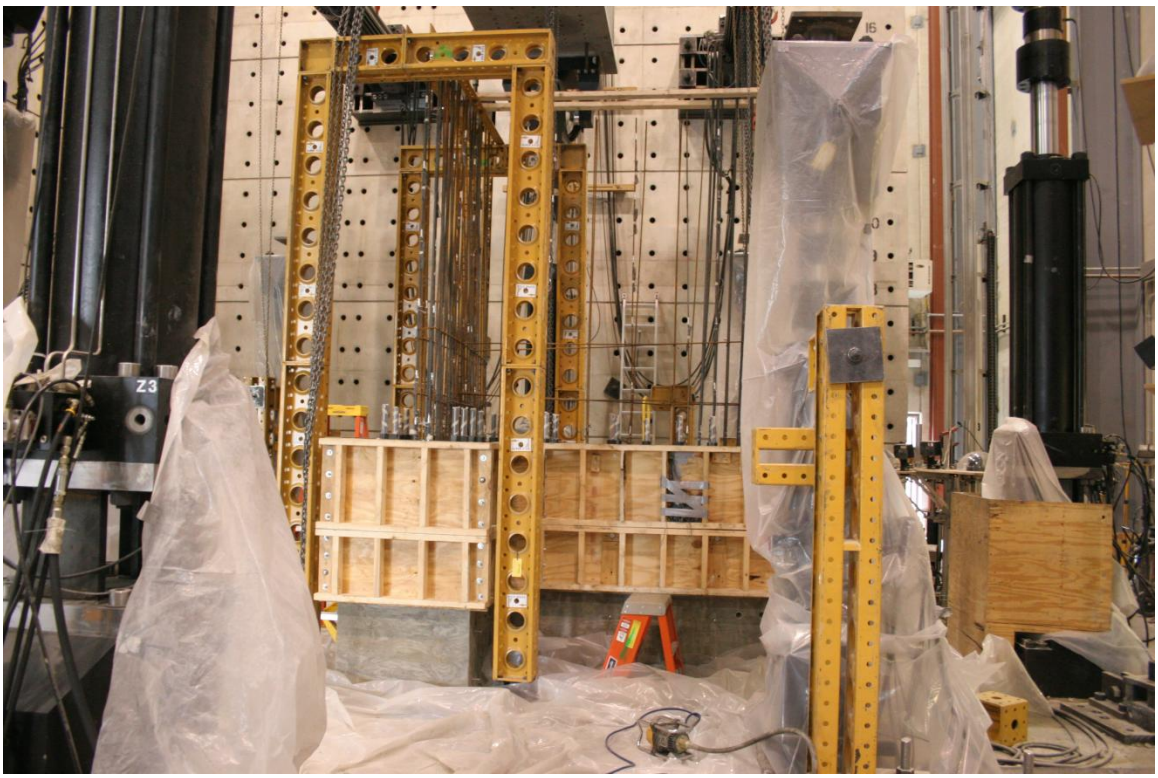

Figure 6.2 Two-part Base Block used for NTW2 to Expedite Construction

6.2 Description of Analysis Model

An OpenSees model for NTW2 was developed in a similar manner to the NTW1 analysis model used for the post-test analysis. The post-test model of NTW1 was established to accurately simulate the behavior of the T-wall by including the effects of shear lag, shear deformation, and strain penetration as shown in Figures 5.33 and 5.34. The test wall NTW2 provided an opportunity to evaluate the predictive capabilities of the modeling approach proposed for flanged walls based on experimental data and analysis results of NTW1 as well as TW2 tested by Thomsen and Wallace [1993].

As with NTW1, a single force-based nonlinear beam-column was used to model the first floor level. However, since the longitudinal reinforcement was spliced at the second floor level, three beam-column elements were used to model the second floor of NTW2. One beam-column element modeled the splice region and was assigned a section that had twice the area of steel as the section used for regions outside of the splice. The length of the splice region was determined to be 25.5 in. which extended upwards from 5 in. above the first floor level. The length of the

splice region was determined based on the equations for bond stress given by Priestley et al. [1996]. NTW2 had a story height of 72 in., leading to the wall model being 144 in. tall for the two stories that were constructed and tested. For an accurate shear-to-moment ratio to be applied to the critical region of the wall in the model, the displacements were applied at a control point located 312 in. above the base of the wall. The top of the wall and the control point were connected using a rigid element, see Figure 6.3.

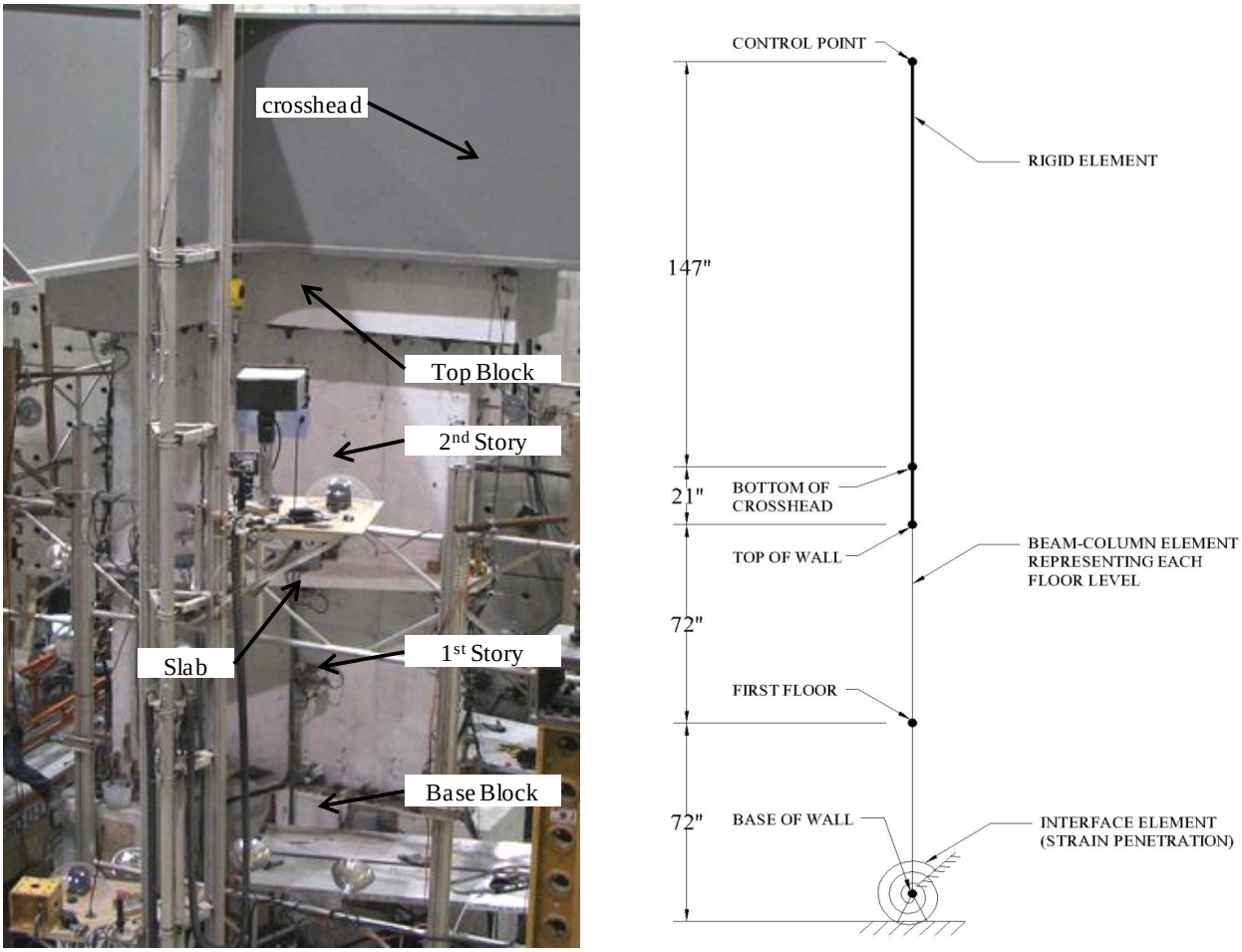

a) Full view of NTW2 specimen

b) Schematic of the analytical model of NTW2

Figure 6.3 Full view of NTW2 test setup and Schematic of the analytical model of NTW2.

The fiber section that included the effects of shear lag described in Section 5.7.1 was used for all the beam-column elements modeling NTW2. The cross section of NTW2 was discretized using fibers to simulate the confined and unconfined concrete and the longitudinal steel similar

to the procedure used for modeling of NTW1. A fiber size of 0.25 in. by 0.25 in. was used to discretize the wall cross section of NTW2. Further details on the discretization used for NTW1 and NTW2 may be found in Section 5.3. The confined and unconfined concrete behavior was modeled using the modified Chang and Mander model discussed in Chapter 3. The confined concrete properties were defined based on the measured unconfined concrete and steel strengths as well as the details of the confinement reinforcement. The peak tensile strength of concrete was based on split cylinder tests conducted on the day before testing of NTW2 started. The longitudinal reinforcement was again modeled using the modified Menegotto-Pinto steel model that is available in OpenSees. The parameters for the longitudinal reinforcement material model were taken from monotonic tension tests on the reinforcement conducted at UMN. The material properties for the unconfined concrete and steel fibers are summarized in Tables 6.1 and 6.2, respectively. The concrete behavior was the same in the sections modeling both the non-spliced wall reinforcement and the spliced reinforcement.

As with NTW1, the effects of shear deformation were included by aggregating a uniaxial material model simulating the shear deformation response onto the previously defined fiber sections. Because the horizontal shear reinforcement of NTW2 was similar to NTW1, the shear deformation model defined for NTW1 was used for the shear-deformation model of NTW2. The distribution of the longitudinal steel in the flange would reduce the shear deformation of the flange in NTW2. Due to the lack of information, no adjustment to the shear model was made. As discussed in Section 5.7, although the shear deformation is handled as an element level response, the shear-deformation behavior was defined and connected to a particular section, rather than an element. This required that the shear deformation behavior be aggregated onto the NTW2 fiber sections defined for the spliced and non-spliced regions.

The effects of strain penetration at the interface between the wall and the base block were handled in the same manner as in NTW1. A zero-length element was used with a section similar to the section of the wall without any splices for the longitudinal reinforcement. The steel material model was replaced with the strain penetration model developed and implemented in OpenSees by Zhao and Sritharan [2007].

Table 6.1: Concrete Properties used for the Analysis of NTW2				
f'_c (ksi)	ε_c (in./in.)	E_c (ksi)	f_t (ksi)	ε_t (in./in.)
5.80*	0.00218	4769.33	0.571*	0.0002395

*Average results obtained from three test cylinders; all other values assumed based on concrete model presented in Chapter 3

Table 6.2: Reinforcement Properties for the Analysis of NTW2			
Bar Size	Yield Stress (ksi)	Elastic Modulus (ksi)	Strain Hardening Ratio
#3	63.8*	29000	0.02
#4	72.1*	29000	0.02
#5	70.7*	29000	0.02
#6	70.7*	29000	0.02

*Average results from monotonic tension tests of three coupons; all other values were assumed based on typical reinforcement steel behavior

The difference between the cross head location 21 in. above the wall, where displacements were actually applied to the test specimen, and the control point where displacements were applied to the analytical model posed a challenge for defining the load path targets for NTW2. This is because the same load path that the NTW1 floors experienced was selected for NTW2 to simplify comparisons between the performances of the two walls, thereby removing any path-dependent effects on the wall responses. This required that the displacement targets for both the crosshead location and control point had to be developed for NTW2 such that they matched the recorded second floor displacements of NTW1.

Two methods were investigated to determine how the recorded peak displacements at the second floor of NTW1 could be scaled up to the crosshead and control point locations for the testing and analysis of NTW2. The first method was based on the assumption that both the top block and the rigid element connecting the top block to the control point would remain elastic during all stages of loading. The additional displacement was calculated as a function of the recorded lateral force applied to NTW1. The second method was to determine the displacement at the control point and crosshead locations as functions of the analytical displacements at the

second floor and fourth floor levels. The ratio of the displacement at the control point to the displacement at the second floor level and the ratio of the displacement at the crosshead to the displacement to the at fourth floor level were determined from the analysis. The two ratios could then be used to scale up the recorded peak second floor displacements to the control point and crosshead locations. The second method was found to give more consistent values for the determining the displacements at the crosshead and control point for all loading ranges of NTW1, and thus this method was selected to determine the displacement targets at the cross head and control point for NTW2. Consequently, the recorded peak displacements from NTW1 were multiplied by the appropriate ratio, shown in Table 6.3, to determine the displacement targets for the crosshead and the control point location of NTW2. The second floor displacements were monitored and compared with the recorded NTW1 displacements at the same location. The displacement of the second floor level of NTW2 was within 0.1 in. of the displacements recorded for NTW1.

Table 6.3: Displacement Ratio Used to Scale NTW1 Second Floor Displacements

Direction	Control Point Location	Crosshead Location
Flange-in-Tension	1.153	2.229
Flange-in-Compression	1.141	2.133
Flange	1.125	2.003

The base block of NTW2 was connected to the strong floor with ten three-in. diameter threaded Dywidag bars. The height of the base block provided adequate anchorage for the wall longitudinal reinforcement. Consequently, the base block was represented with a node in the analysis model and the degrees-of-freedom of this node was fixed in all directions. The base block was instrumented with LVDTs and string potentiometers in order to monitor the base block during testing, because there was some concern that the increased height of the base block and its two-piece construction would cause it to distort during testing. No movement or rotation of the base block or relative movement between the two pieces was recorded during testing; validating the assumed fixed boundary condition used for the base block.

An axial load of 186.5 kips was applied to NTW2 initially; however, as stated earlier in Section 6.1, the axial load was later increased to 201.4 kips to account for the weight of the

missing third and fourth floors. This required the analysis of NTW2 to be conducted in several different loading stages. The first stage modeled the 186.5 kips of axial load when it was applied to the wall, then lateral displacements were applied to the model in the next stage. In the third stage, the axial load was increased to 201.2 kips, and the remaining displacement history was applied to the model in the fourth and final stage.

6.3 Multidirectional Load Path

As previously noted in Section 6.1, the load path for NTW2 was selected primarily to match the displacements measured at the second floor level of NTW1. The improved reinforcement details were expected to allow NTW2 to be displaced further in both the flange and web directions than those experienced by NTW1. As in NTW1, positive displacement in the web direction places the flange in compression, while negative displacement places the flange in tension. Incorporating the factors from Table 6.3, Table 6.4 presents the displacements targets established for the crosshead. Graphical representations of the applied displacement path are shown in Figures 6.4 through 6.18.

Table 6.4: Applied Displacement Targets For NTW2 at the crosshead

Load Step	Load Description	Parallel Flange (in.)	Parallel Web (in.)
0	Apply Axial Load of 186.5 kips	0.0	0.0
1-3	25% First Yield Displacement in Web Direction	0.0	0.062
		0.0	-0.073
4-6	50% First Yield Displacement in Web Direction	0.0	0.127
		0.0	-0.166
7	25% First Yield Displacement in Flange Direction	0.16	0.0
		-0.155	0.0
8	25% First Yield Displacement in 45º Direction	0.044	0.046
		-0.04	-0.061
9	25% First Yield Displacement in (100% Flange + 30% Web) Direction	0.118	-0.03
		-0.159	0.06

Table 6.4 Cont'd			
Load Step	**Load Description**	**Parallel Flange (in.)**	**Parallel Web (in.)**
10	50% First Yield Displacement in Web Direction	0.0	0.127
		0.0	-0.168
11	75% First Yield Displacement in 45º Direction	0.269	0.296
		-0.245	-0.263
12	75% First Yield Displacement in (100% Flange + 30% Web) Direction	0.435	-0.124
		-0.592	0.225
13-15	75% First of Yield Displacement in Web Direction	0.0	0.40
		0.0	-0.51
	Increase Axial Load on Specimen to 201.2 k	0.0	0.0
16	75% First Yield Displacement in Web Direction	0.0	0.40
		0.0	-0.51
17	50% First Yield Pentagram Shaped Load Path	0.0	0.127
		0.116	0.127
		0.417	0.0
		0.0	-0.168
		-0.417	0.0
		-0.116	0.127
		0.0	0.127
18	75% First Yield Displacement in Web Direction	0.0	0.4
		0.0	-0.51
19-21	100% First Yield Displacement in Web Direction	0.0	0.616
		0.0	-0.733
22-24	150% First Yield Displacement in Web Direction	0.0	0.924
		0.0	-1.1
25-27	1% & 1.5% Drift in Web Direction	0.0	1.62
		0.0	-2.403
28	1% & 1.5% Drift in 100% Web + 30% Flange	0.43	1.330
		-0.68	-2.010

Table 6.4 Cont'd			
Load Step	**Load Description**	**Parallel Flange (in.)**	**Parallel Web (in.)**
29	1% Drift in Flange Direction	1.25	0.0
		-1.25	0.0
30	1.5% Drift in 45º Direction	1.3	1.56
		-1.45	-1.53
31	1.5% Drift in Flange Direction	1.91	0.0
		-1.91	0.0
32	1.5% Drift in 100% Flange + 30% Web Direction	-1.81	0.7
		1.85	-0.69
33-34	1% & 1.5% Drift in Web Direction	0.0	1.616
		0.0	-2.403
35-37	1.5% & 2% Drift in Web Direction	0.0	2.46
		0.0	-3.15
38	2.0% Drift Hourglass Displacement Path	1.81	2.21
		-1.81	2.21
		0.0	0.0
		1.90	-2.26
		0.0	-3.15
		-1.90	-2.26
39	2% & 2.5% Drift in Web Direction	0.0	2.78
		0.0	-3.89
41	1.5% Drift in Flange Direction	1.91	0.0
		-1.91	0.0
42-44	2% Drift in Flange Direction	2.69	0.0
		-2.69	0.0
45-47	2.5% Drift in Flange Direction	3.41	0.0
		-3.41	0.0
48-50	3% Drift in Flange Direction	4.15	0.0
		-4.15	0.0

51-52	4% Drift in Flange Direction	5.95	0.0
		-5.95	0.0

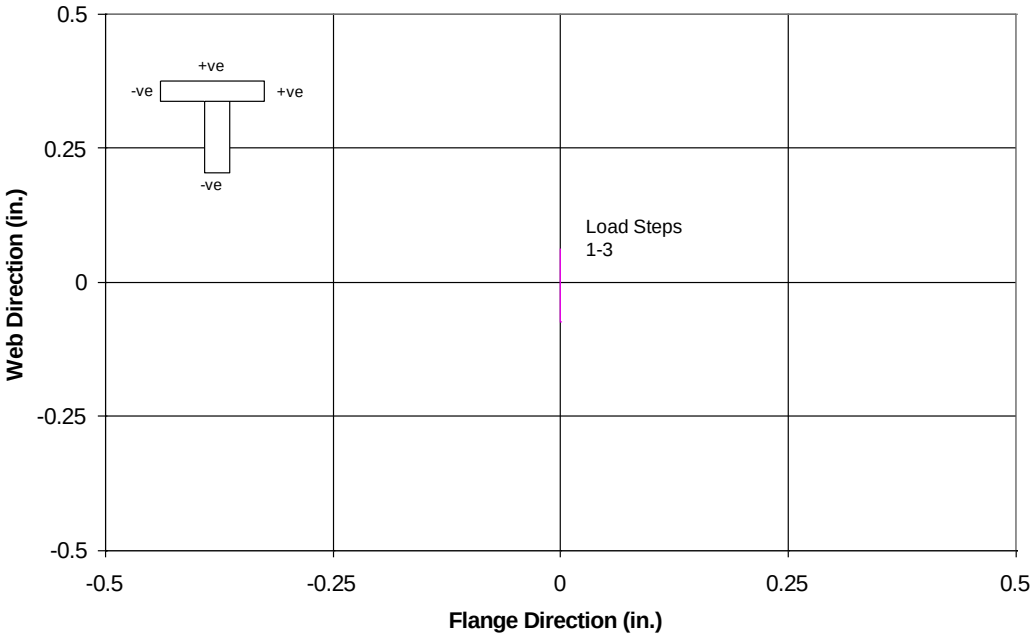

Figure 6.4 Load Steps 1 to 3 to Test NTW2 in the Web Direction at 25% of First Yield Displacement.

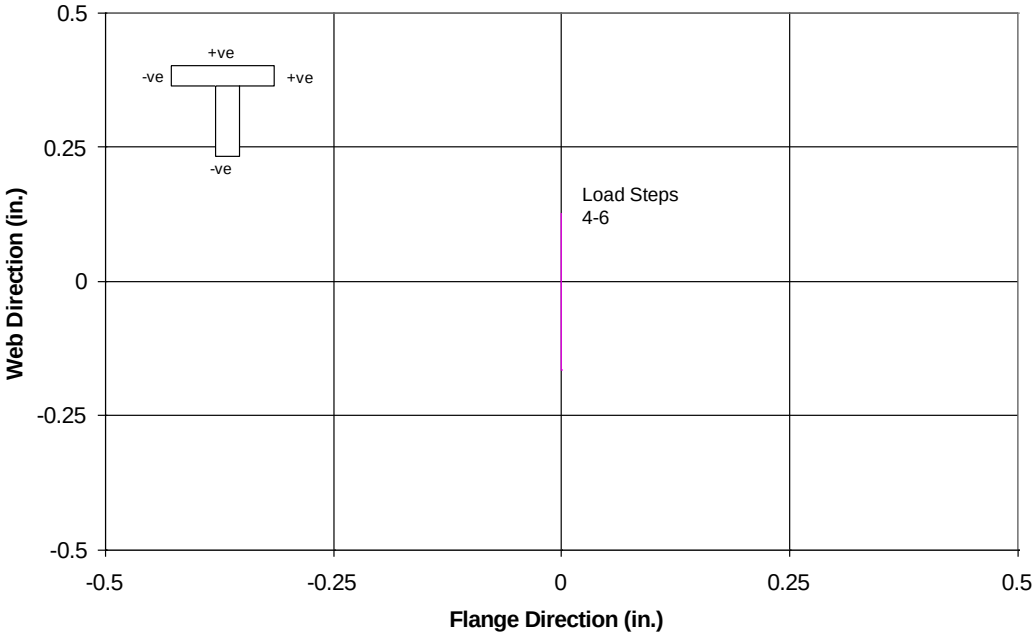

Figure 6.5 Load Steps 4-6 to Test NTW2 in the Web Direction at 50% of First Yield Displacement

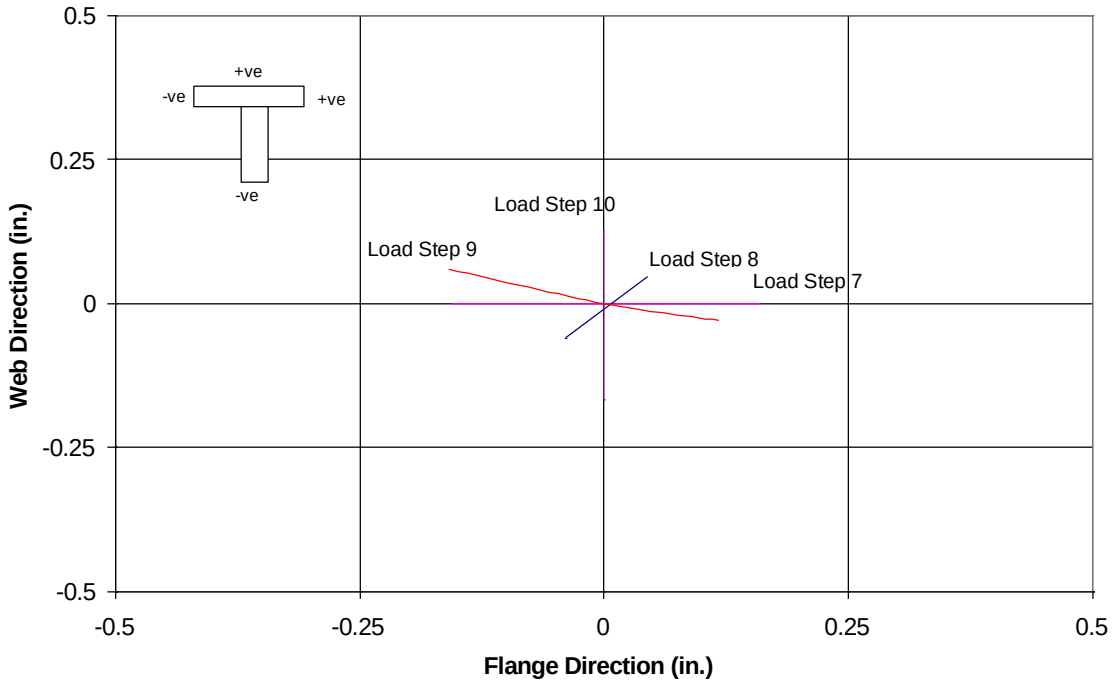

Figure 6.6 Load Steps 7 to 10 to Test NTW2 at 45º, Parallel to the Web, and 100+30 Directions at 25% of First Yield Displacement, and Repeat of 50% of First Yield in Web Direction

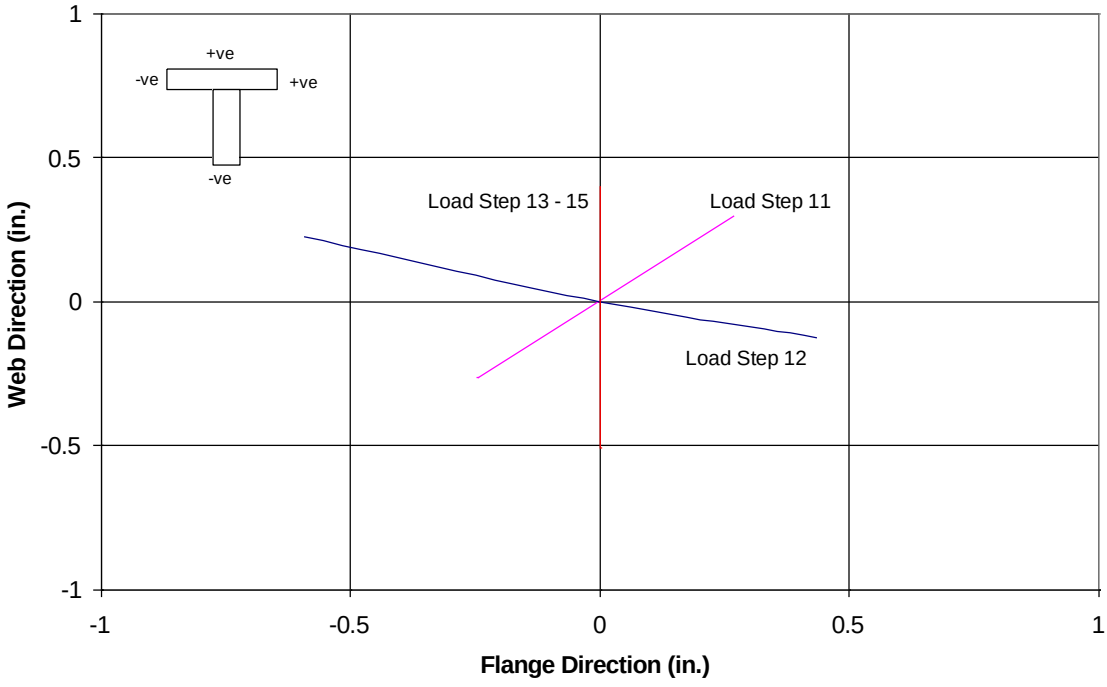

Figure 6.7 Load Steps 11 to 15 to Test NTW2 at 45º, 100+30, and Web Direction at 75% of First Yield Displacement

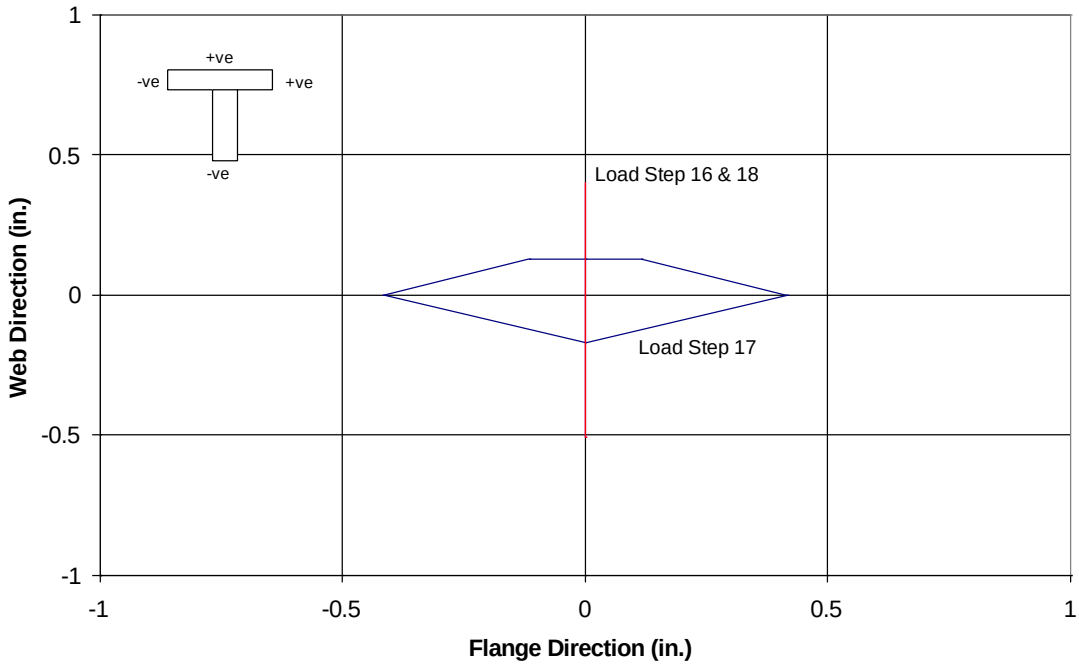

Figure 6.8 Load Step 16 to Test NTW2 Web Direction at 75% First Yield Displacement, Load Step 17 to Test 50% First Yield Pentagon Load Path, and Load Step 18 Repeat Web Direction at 75% First Yield Displacement

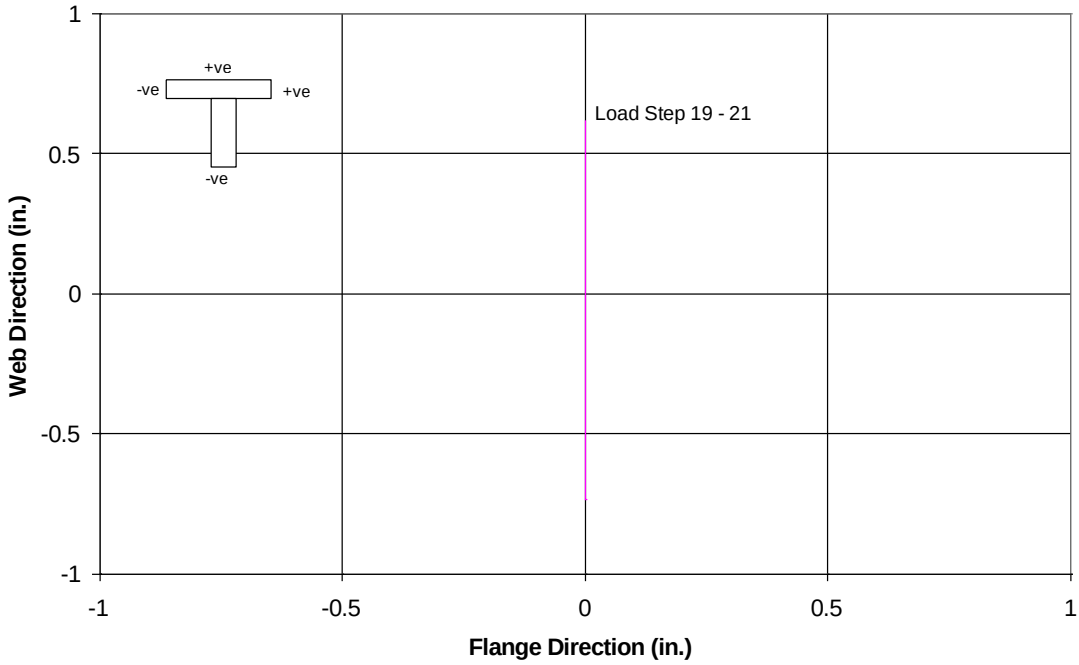

Figure 6.9 Load Steps 19 to 21 to Test NTW2 in the Web Direction at 100% First Yield Displacement

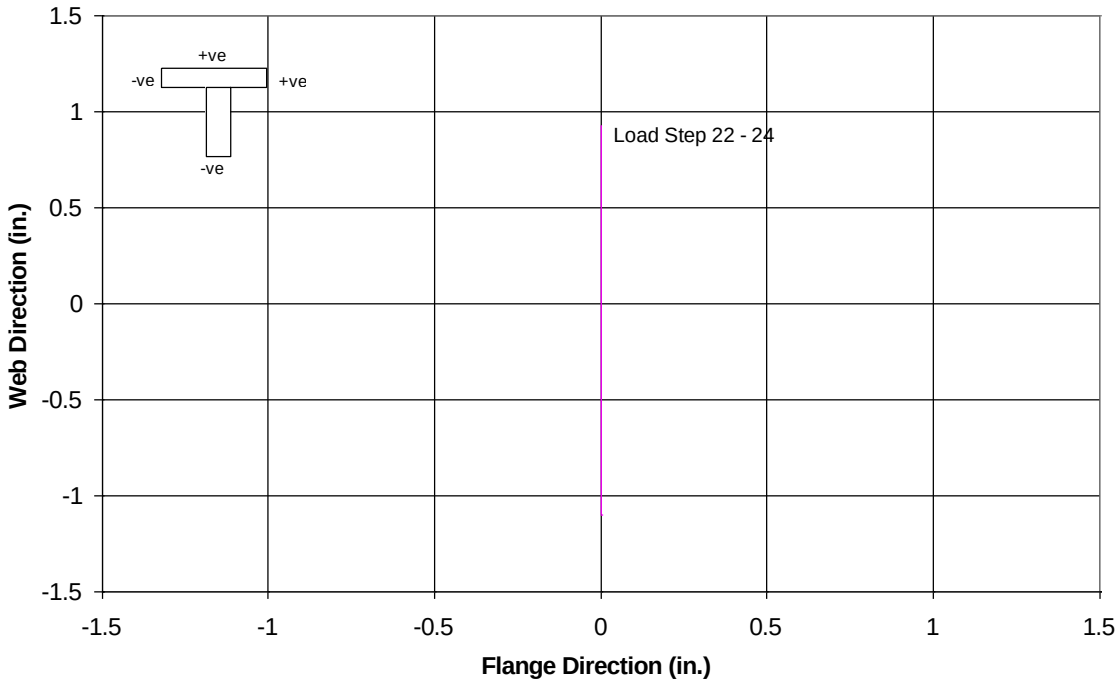

Figure 6.10 Load Steps 22 to 24, to Test NTW2 in the Web Direction of 150% First Yield Displacement

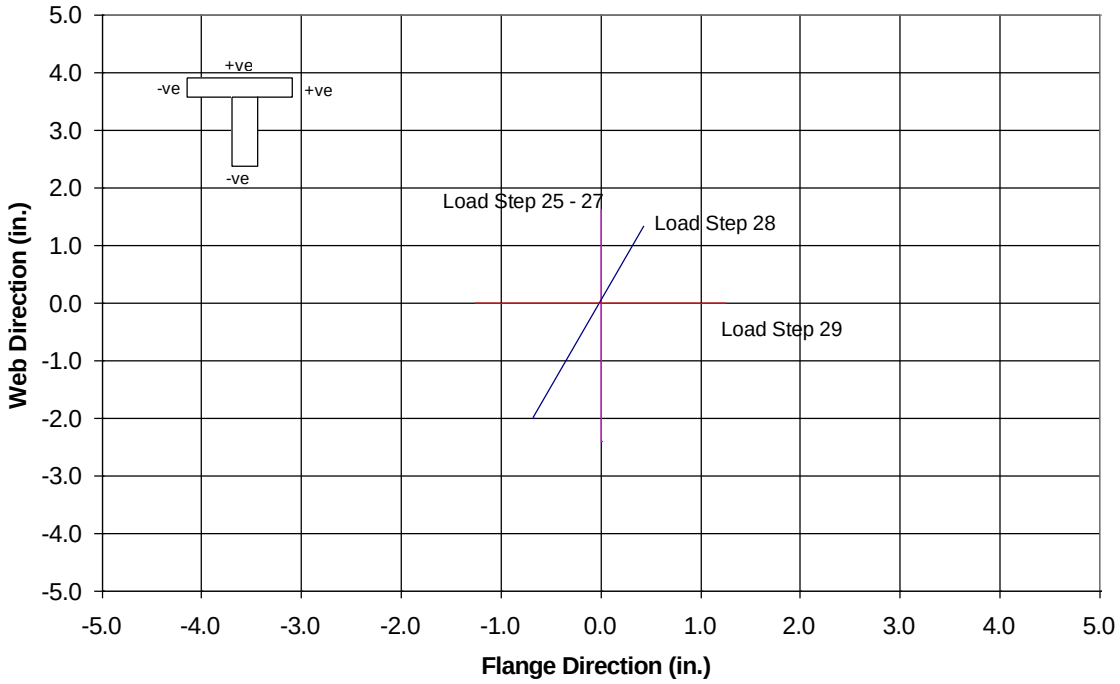

Figure 6.11 Load Steps 25 to 29 to Test NTW2 in Multidirectional Loadings at 1% and 1.5% Drift Levels

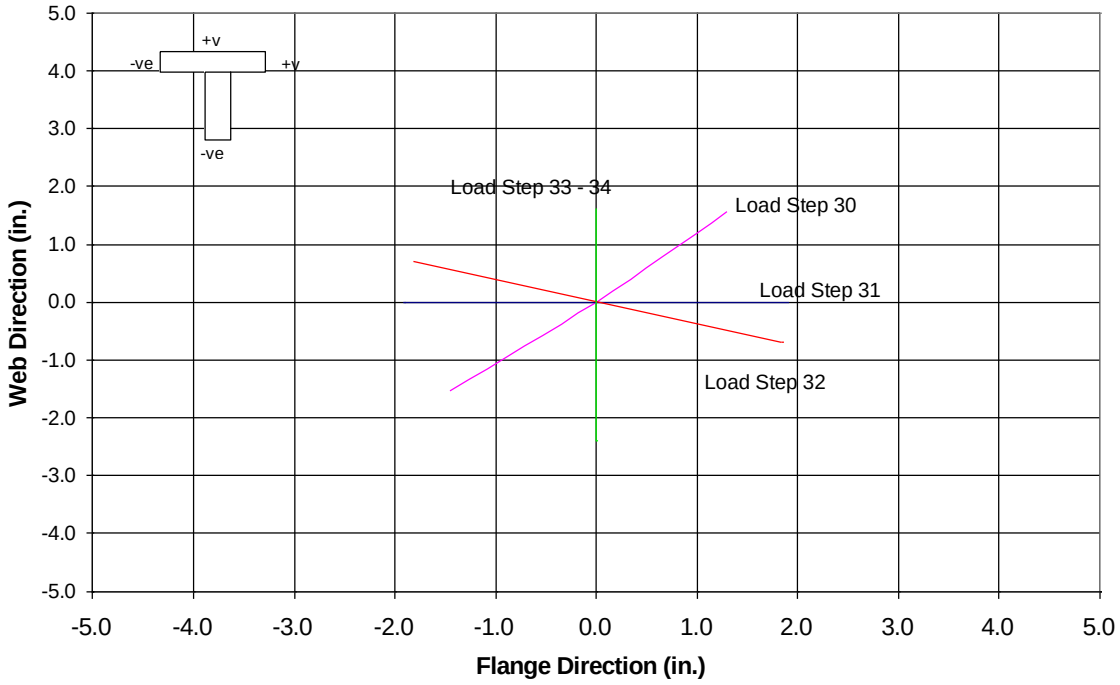

Figure 6.12 Load Steps 30-34 to Test NTW2 in Multidirectional Loadings at 1% and 1.5% Drift Levels

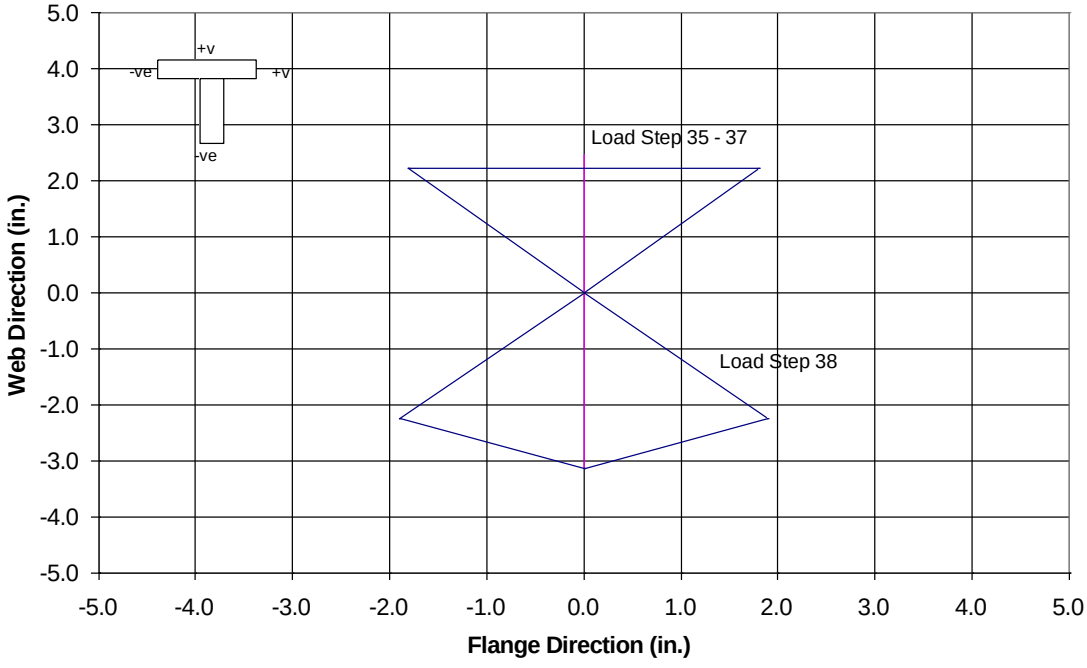

Figure 6.13 Load Steps 35-37, to Test NTW2 at 1.5% and 2.0% Drift in the Web Direction and Load Step 38 to Test 2% "Hourglass" Displacement Path

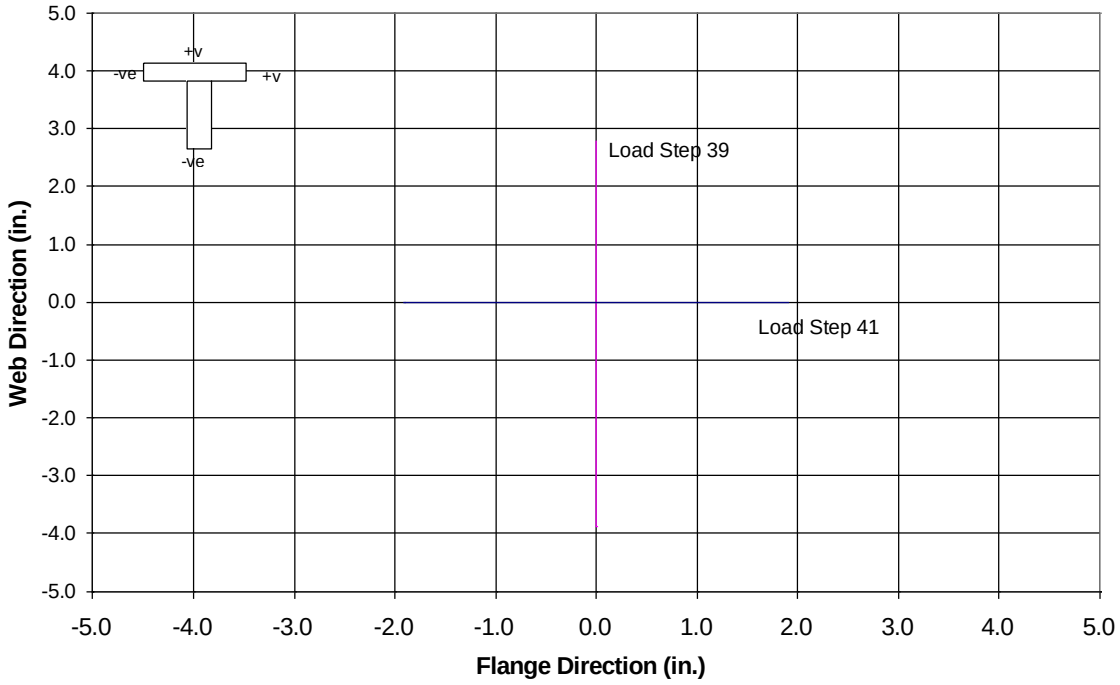

Figure 6.14 Load Steps 39 and 41, to Test NTW2 at 2.0% and 2.5% Drift in the Web Direction and 1.5% Drift in the Flange Direction

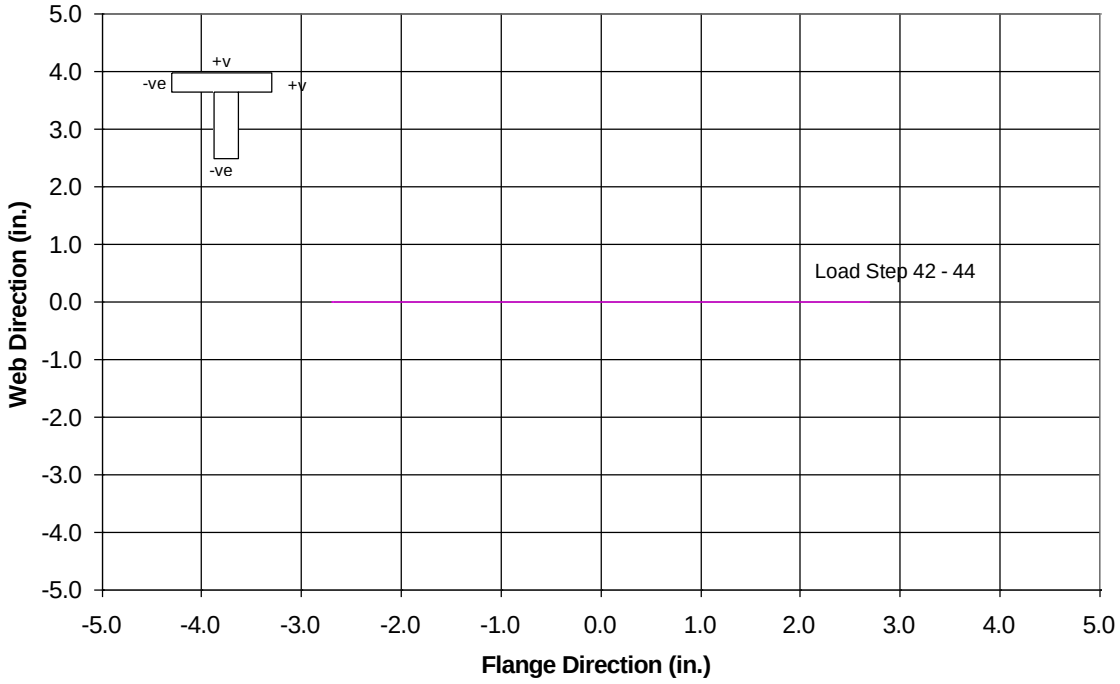

Figure 6.15 Load Steps 42-44 to Test NTW2 at 2.0% Drift in the Flange Direction

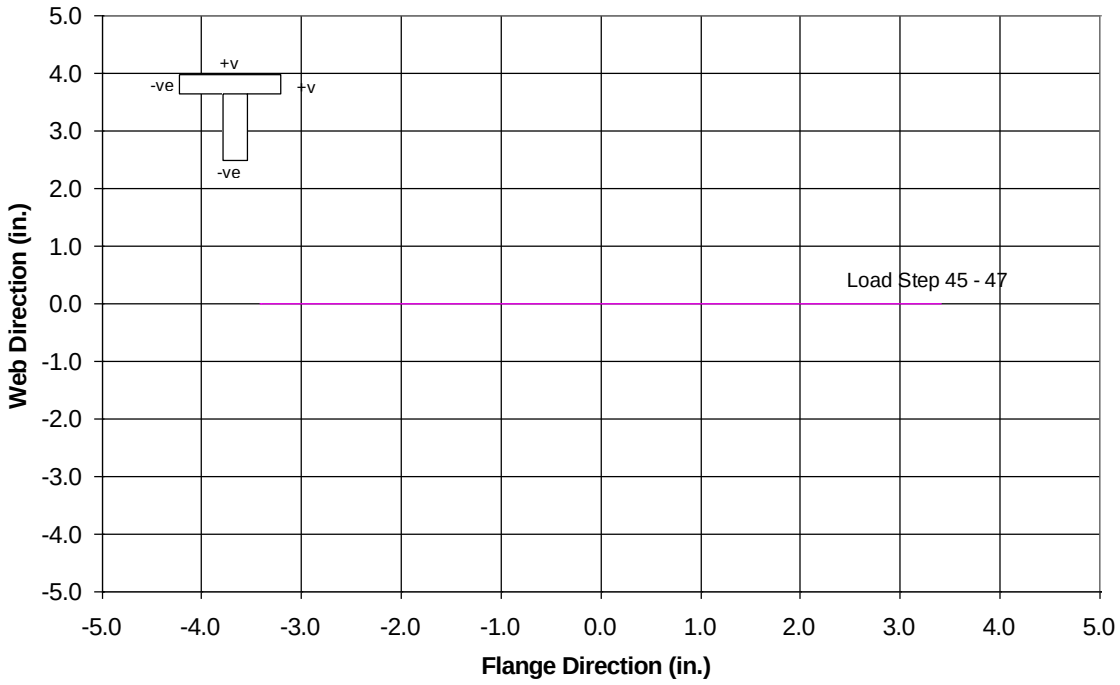

Figure 6.16 Load Steps 45-47 to Test NTW2 at 2.5% Drift in the Flange Direction

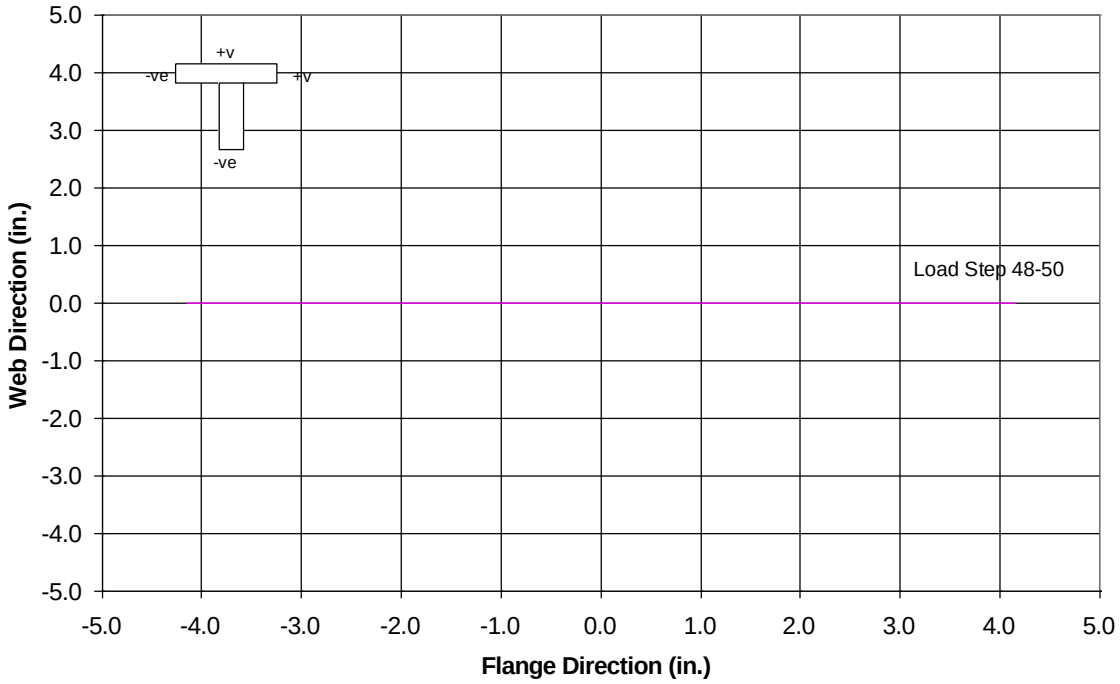

Figure 6.17 Load Steps 48-50 to Test NTW2 at 3.0% Drift in the Flange Direction

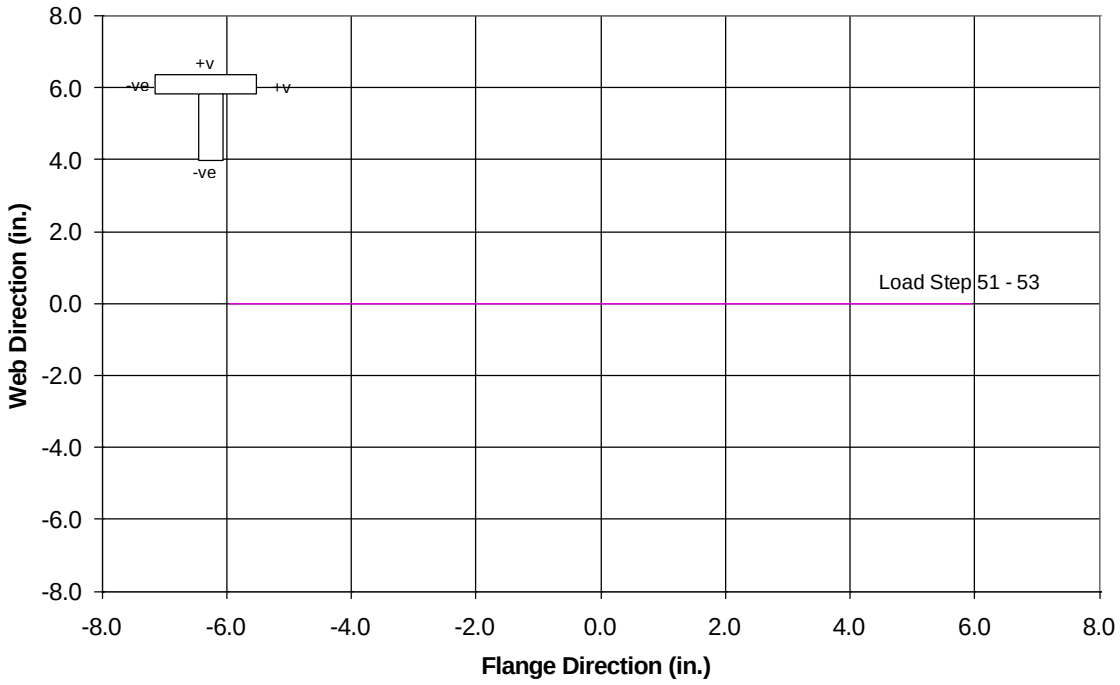

Figure 6.18 Load Steps 51-52 to Test NTW2 at 4.0% Drift in the Flange Direction

The displacements at the control point were applied to the NTW2 analytical model. Figures 6.19 and 6.20 compares the experimental and analytical displacements applied at the second floor of NTW2 as a function of the measurement number in the flange and web directions, respectively. Again, the measurement number refers to the number of times data was recorded during the test, which is also referred to as a "scan number". The second floor displacement of the analytical model was nearly identical to the recorded displacement of the test specimen. The OpenSees displacement was always within 0.07 in. in the flange direction and 0.05 in. in the web direction for the peak values obtained from the recorded potentiometer measurements. The lateral force could not be plotted as a function of the cumulative displacement because the minor differences in applied displacements quickly accumulate and make any useful comparison as a function of cumulative displacement impossible. Figure 6.21 compares the recorded second floor displacements in the flange and web directions between NTW1 and NTW2.

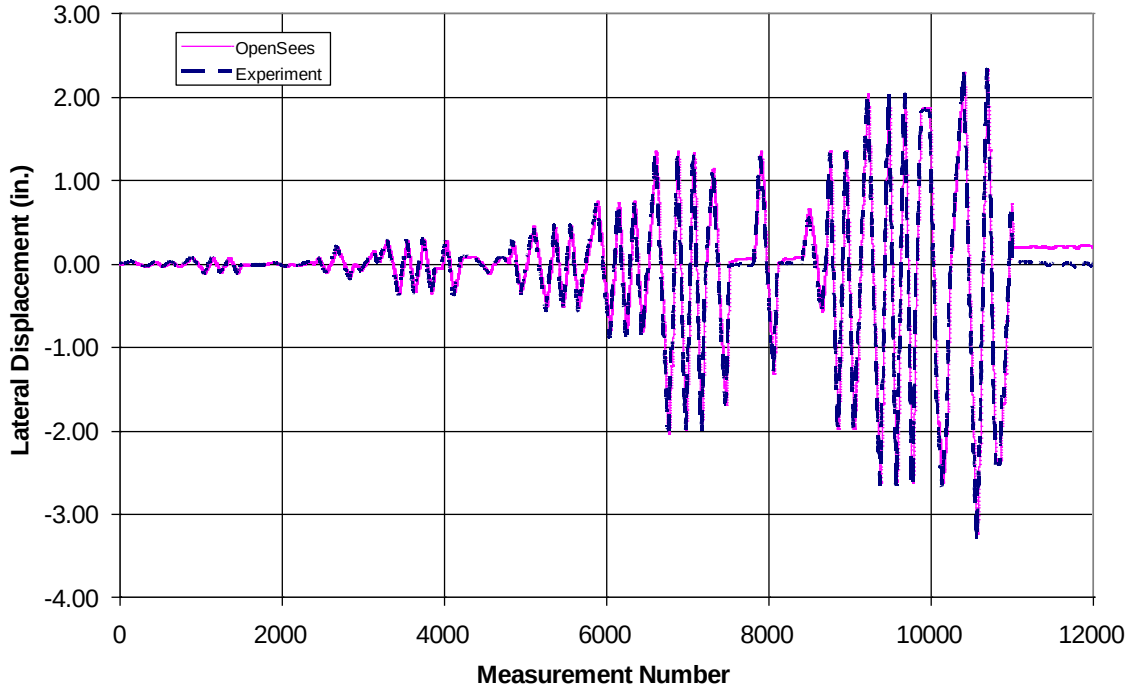

Figure 6.19 Comparison of Second Floor Displacement of NTW2 in the Web Direction as a Function of Measurement Number

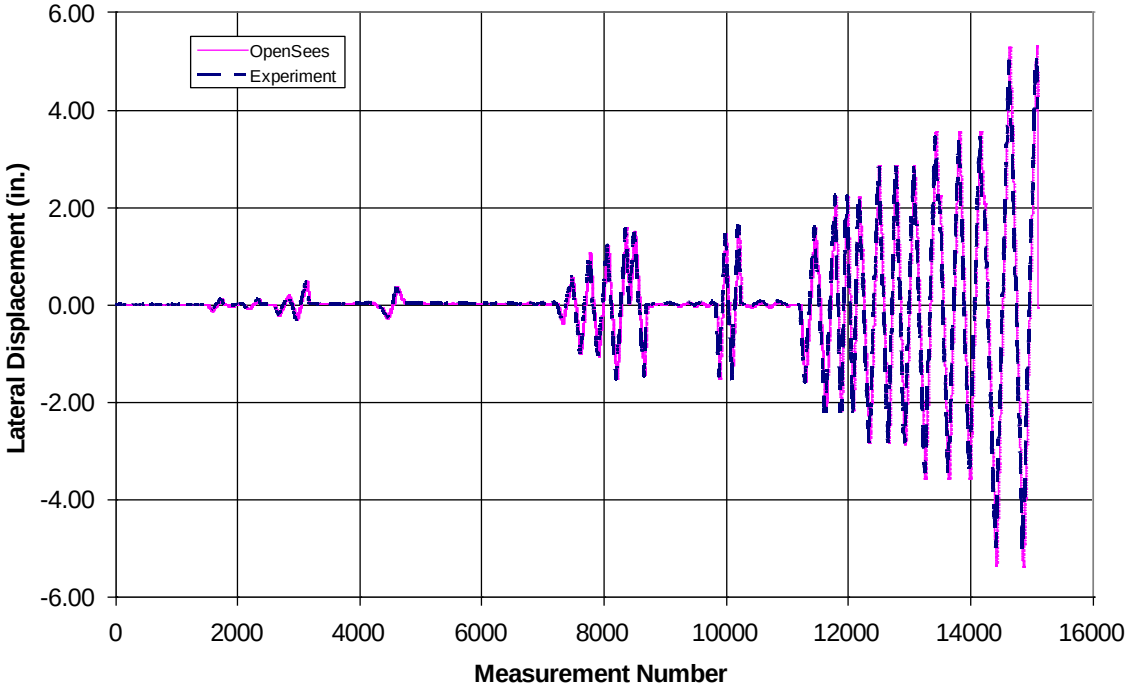

Figure 6.20 Comparison of Second Floor Displacement of NTW2 in the Flange Direction as a Function of Measurement Number

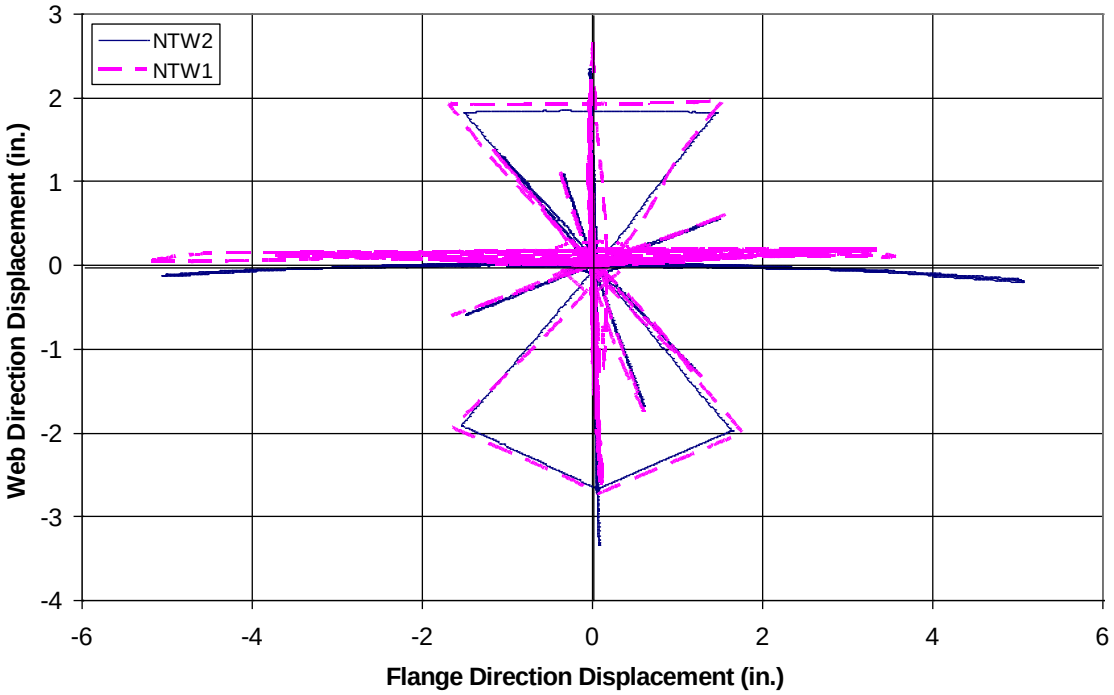

Figure 6.21 Comparison of Second Floor Displacements Recorded for NTW1 and NTW2 in the Flange and Web Directions

6.4 Summary of Response

NTW2 was subjected to the load path described in Section 6.3 beginning on November 29 and was completed on December 6, 2007. As with NTW1, the testing of NTW2 took 7 days to complete. NTW2 showed a significantly different pattern of cracking compared to that observed in NTW1. NTW2 exhibited small, well distributed flexural cracks in the flange. Additionally, very few diagonal shear cracks were observed in the flange during testing. Figure 6.22 shows the flange of NTW2 after yielding of the longitudinal reinforcement in the flange. The web of NTW2 exhibited the same crack pattern observed for NTW1. Figure 6.23 shows the large diagonal cracks outside the boundary elements and the fine well distributed cracks in the boundary elements. The increased distributed steel in the flange led to better crack control than in the web where the longitudinal reinforcement was concentrated in the web tip boundary element. As with NTW1, NTW2 exhibited a very stable response with the second and third cycles at a load level exhibiting the negligible degradation in the force resistance.

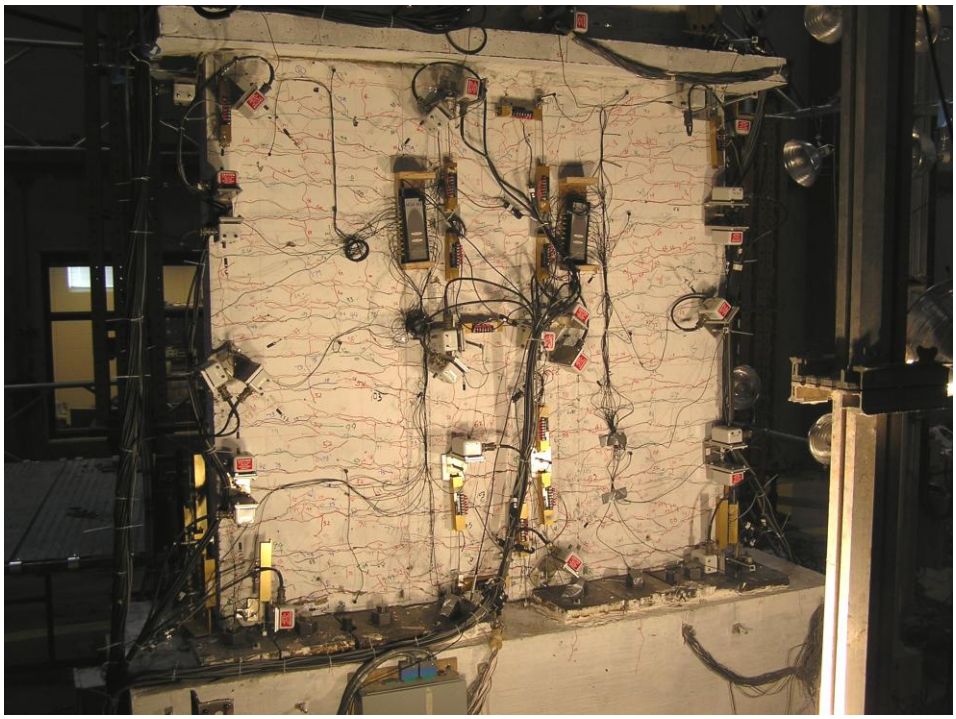

Figure 6.22 Flange of NTW2 after Yielding of the Longitudinal Reinforcement

Figure 6.23 Web of NTW2 after Yielding of the Longitudinal Reinforcement

Failure in the web direction was caused by buckling of the longitudinal reinforcement in the web direction. The revised detailing of the web tip boundary element compared to NTW1 was effective in delaying the buckling of the longitudinal reinforcement until 2.5% lateral drift. Following failure in the web direction, NTW2 was unloaded and returned to approximately zero residual displacement.

NTW2 was then cycled in the flange direction until the longitudinal reinforcement in the flange tip boundary elements buckled at approximately 4% drift. NTW1 experienced bucking of the longitudinal reinforcement in the flange boundary elements at 3% lateral drift, while NTW2 exhibited a stable response on all three cycles at 3% lateral drift.

Overall NTW2 exhibited a very good performance. It was displaced further in both the web and flange direction than NTW1. Additionally, the cracks in the flange were well controlled by the distributed steel in the flange. The splice at the first floor level performed well with no relative movement recorded between the spliced bars. A complete discussion of the experimental response of NTW2 can be found in Brueggen [2009].

6.5 Comparison of Analytical and Experimental Results

This section presents comparison of the experimental and analytical responses at the global and local levels. Since the improvements to the OpenSees capabilities were made the emphasis of the NTW2 analysis was placed in predictability of an OpenSees model using available capabilities. Consequently, no post-test analysis was performed, but appropriate recommendations to further improve the fiber-based analysis of non-rectangular walls are made.

6.5.1 Force-Displacement Responses

The lateral force-displacement responses in the web and flange directions are shown in Figures 6.24 and 6.25, respectively. The experimental response in each direction shows the average of the recorded string potentiometer displacements measured at the flange tips and the force resistance recorded by load cells connected to the actuators during the test. The analytical response was taken from the lateral displacement recorded at the node representing the second floor level of NTW2 while the force resistance was established from the member forces at the bottom end of the beam-column element modeling the wall at the first floor level. As seen in

Figure 6.24, the web direction response was generally well captured by the analytical model until strength degradation experienced in NTW2 due to buckling of the longitudinal reinforcement in the web tip boundary element at a lateral displacement of -3.89 inches. A good agreement between the experimental and simulated force-displacement are observed in terms of the force resistance in the flange-in-compression loading direction, the unloading/reloading stiffness, and the residual displacements after unloading from peak lateral displacements.

The force resistance in the flange-in-tension loading direction was underestimated by the analysis by approximately 5%. Figure 6.25 shows the flange direction response was not as well predicted as the web direction response. The peak lateral resistance and the reloading stiffness were significantly over predicted in the displacement range of 1.8 to 3.5 inches. Similar to NTW1, pinching of the global response was not observed in either the predicted nor measured response. Figures 6.26 and 6.27 compare the measured and simulated lateral force resistance versus the measurement number for the web and flange directions, respectively. In this perspective, the accuracy of the wall response simulation in the web direction is evident. The underestimation of the force in the web direction was likely due not capturing the shear lag in the flange accurately and its corresponding effect on the tensile strain distribution along the flange. The second possible source that could have contributed to this discrepancy was the inaccuracy in the shear deformation of NTW2, which could have affected both directions of loading although larger error should be expected in the flange-in-tension direction due to the increased shear force in that direction.

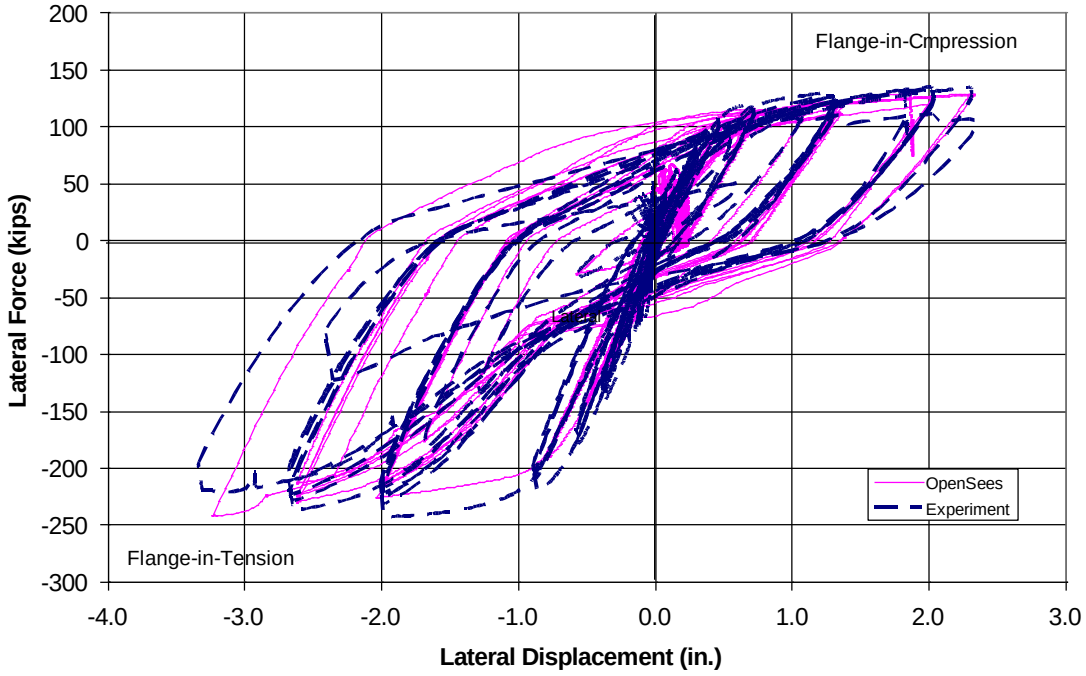

Figure 6.24 Measured and Predicted Force-Displacement Responses of NTW2 in the Web Direction

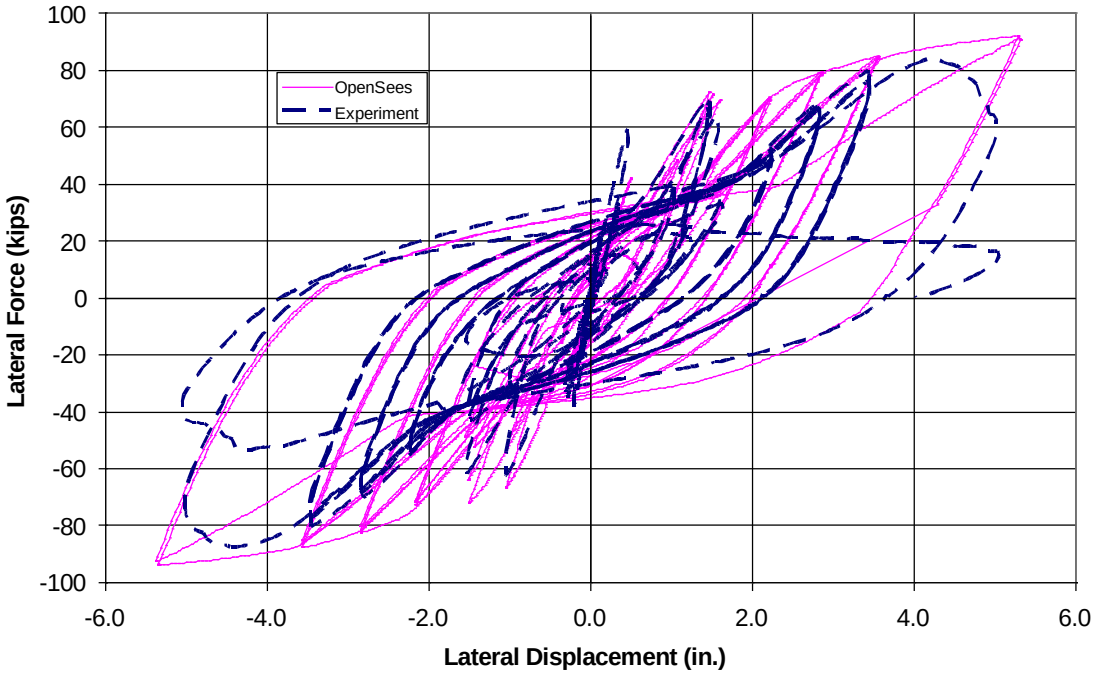

Figure 6.25 Measured and Predicted Force-Displacement Responses of NTW2 in the Flange Direction

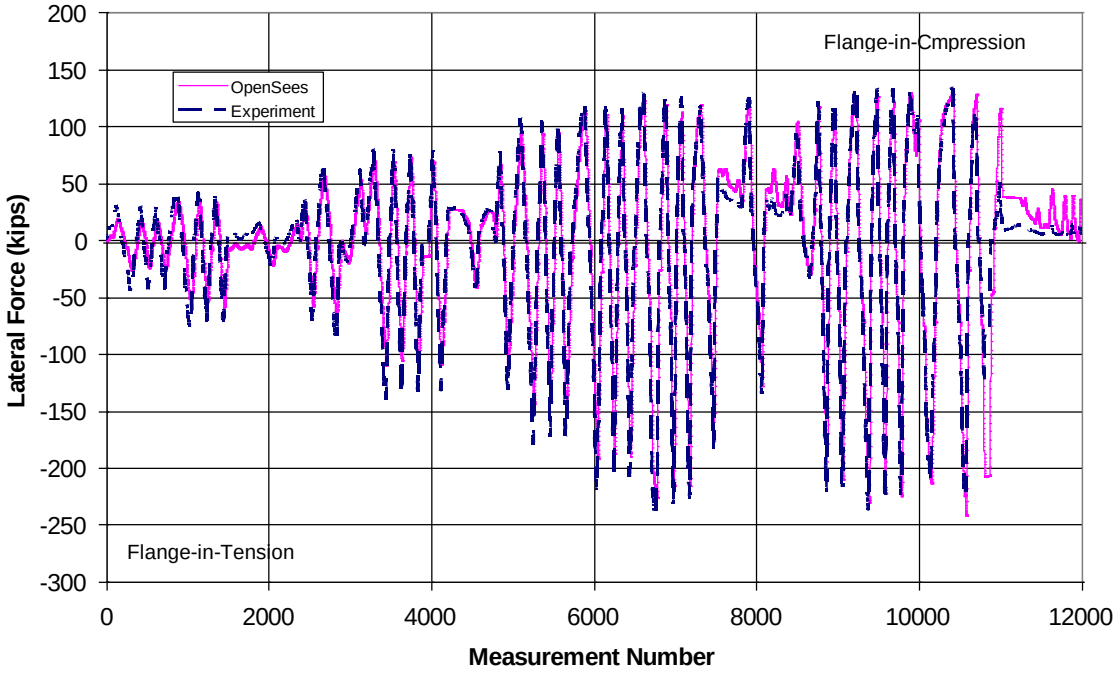

Figure 6.26 Measured and Predicted Force Resistance of NTW2 in the Web Direction as a Function of Measurement Number

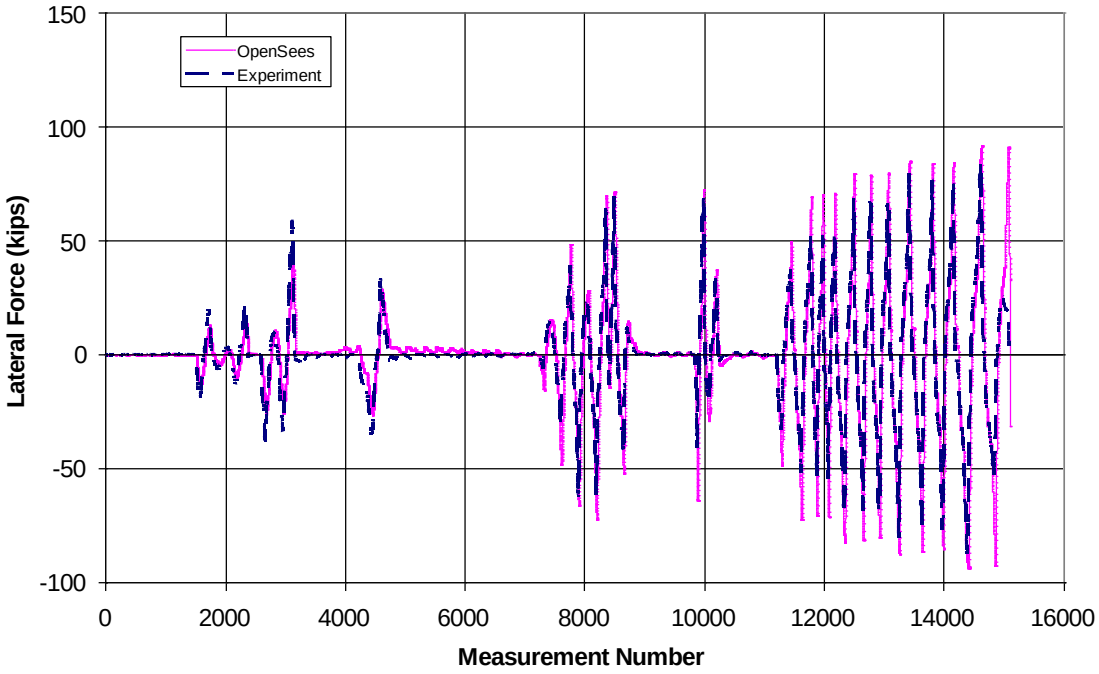

Figure 6.27 Measured and Predicted Force Resistance of NTW2 in the Flange Direction as a Function of Measurement Number

The strain distribution due to shear lag that was used in the section definition of NTW2 was based on the observed strain distribution in NTW1 and TW2 (TW2 was the second T-wall tested by Thomsen and Wallace [1993]). Both of those walls had low amounts of distributed steel between the boundary elements, while NTW2 had a large portion of the longitudinal steel in the flange that was distributed along the flange length. The distribution of the steel can influence the shear stiffness of the unstiffened portion of the flange, referred hereafter as the "free flange overhang". Increased shear stiffness of the free flange overhang will likely decrease the influence of shear lag, thereby increasing the lateral force resistance. Although this phenomenon was expected, this issue was not addressed due to the lack of information to handle this behavior in the NTW2 model. Figure 6.28 compares the experimental response of NTW2 with simulated response in the web direction that was obtained with the "plane sections remain plane" assumption ignoring the shear lag effects. As expected, the analytical response shows a higher stiffness than that found with the inclusion of shear lag. The higher stiffness observed in the experiment is, therefore, attributed to the decreased influence of shear lag due to the increased shear stiffness of the free flange. Figure 6.29 shows the strain distribution recorded along the length of the flange in NTW2 at 1.5 yield displacement and the predicted strain distribution from the equation used to include the effects of shear lag. The experimental strain was taken from the strain gages located nominally 6 inches about the base block. Although the data is erratic it is seen that the effects of shear lag are noticeably over estimated for NTW2 by the OpenSees analysis.

The shear deformation response of NTW2 was modeled based on that used for the post-test simulation of NTW1. The assumption was made that the shear deformation would not be significantly different in the web between the two walls, because the shear reinforcement in the web was not modified from NTW1. Figure 6.30 shows the comparison between the shear deformation response measured in the web of NTW2 and the shear deformation response of OpenSees model at the first floor level. The difference in the shear deformation behavior would also significantly contribute to alleviating the discrepancy seen in the web direction force-displacement response. The measured response is stiffer than was used in the analysis. The distributed flange reinforcement may have provided more doweling in the web direction, increasing the shear stiffness in that direction. The decreased shear stiffness would decrease the

stiffness of the wall model. Since the analysis was conducted in displacement control, this softening would lead to a decreased lateral resistance, and thus increasing the analysis shear stiffness would increase the lateral force resistance and reduce the discrepancy seen in Figure 6.24.

The flange direction response showed in Figures 6.25 and 6.27 indicate that the OpenSees analysis did not capture the force-displacement response in flange direction as good as the web direction response. The discrepancies are attributed to a number of different actions: 1) damage due to previous load cycles, 2) error in the residual strains and stresses from the multidirectional loading patterns resulting from inaccurate simulation of shear lag effects, and 3) the shear-distortion response that was taken from the response of NTW1.

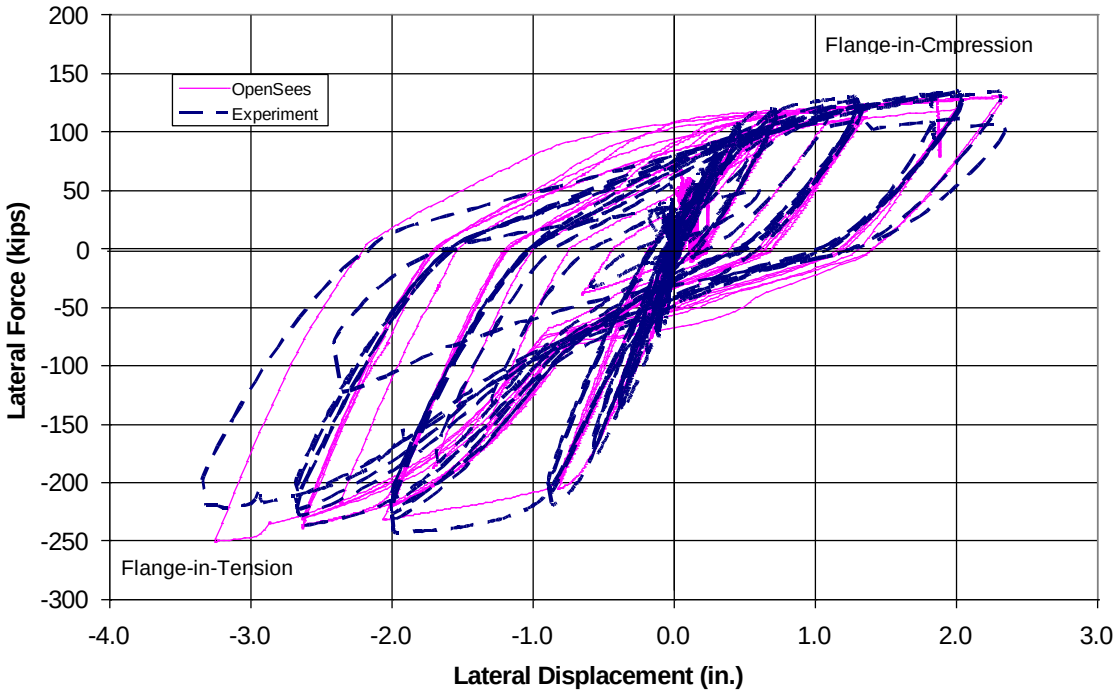

Figure 6.28 Measured and Predicted Force Resistance of NTW2 in the Web Direction as a Function of Measurement Number

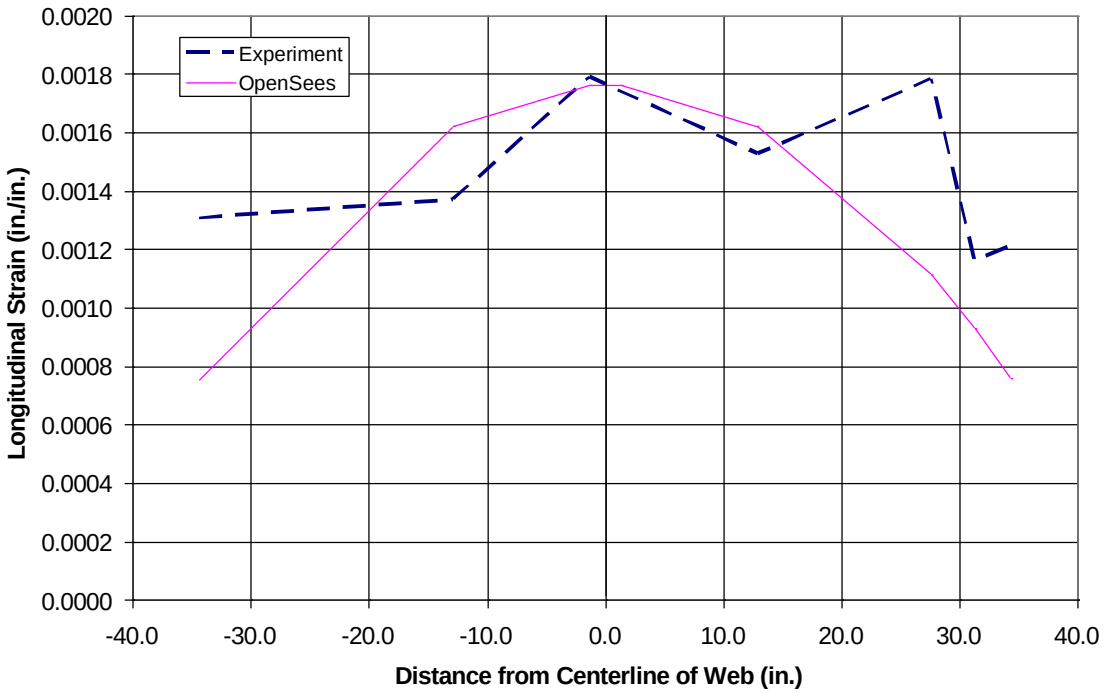

Figure 6.29 Comparison of Measured Strain Distribution in the Flange with that simulated by the OpenSees Model with Shear Lag at 0.75 First Yield Displacement in Web Direction

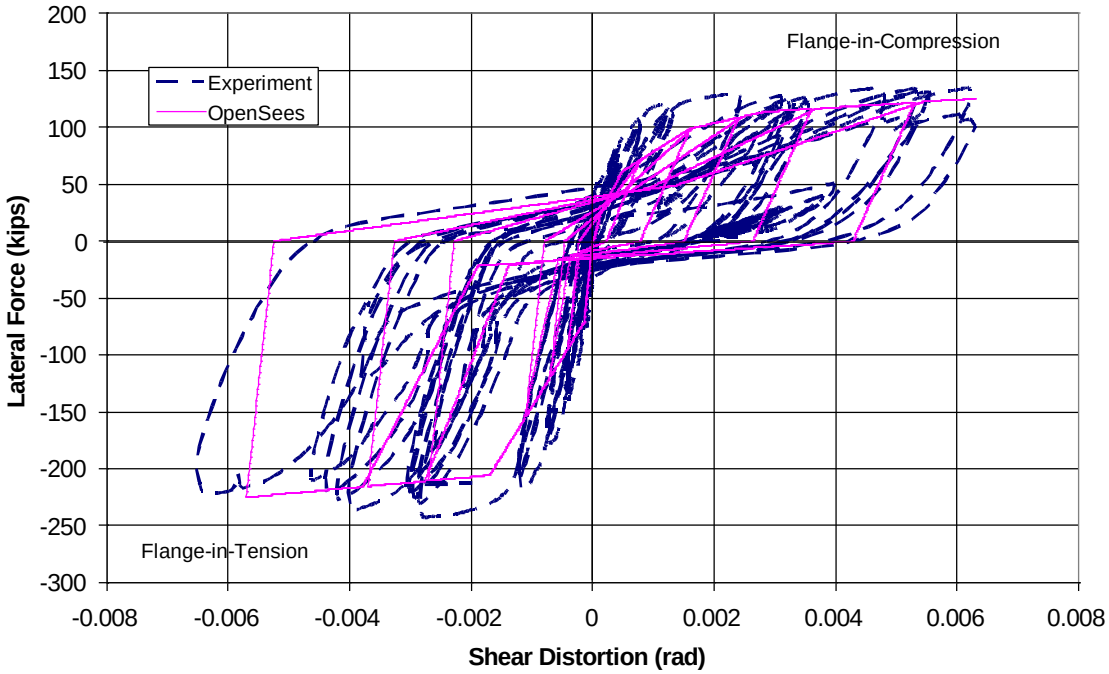

Figure 6.30 Comparison of Measured Shear Response for the First Floor of NTW2 in the Web Direction with the Response of NTW1 OpenSees Material Model

The selected displacement targets typically loaded NTW2 in the parallel to the web direction first at a particular displacement or drift level. This caused moderate to significant damage to the flange of the wall depending on the drift level. For example, the flange was heavily cracked due to the applied loading in the web direction at first yield of the longitudinal reinforcement, see Figure 6.31. If this damage was not fully captured in the simulation as was the cased based on the study reported in Appendix B, it could account for some of the overestimation of the wall resistance in the flange direction. If the shear lag effect was overestimated in the web direction loading, it would be expected that the damage would be underpredicted in the flange tips, as discussed earlier. This would lead to the over prediction of the lateral force resistance seen in the Figure 6.25 and 6.27.

The load path for NTW1 and NTW2 included displacements in the web, flange, and skewed directions with the first load cycles predominately in the web direction. When the flange was placed in tension that caused inelastic strains in the longitudinal reinforcement and then unloaded during web direction loading, the reinforcement fibers were subjected to residual strains. When the wall was then displaced in the flange direction, the strength and stiffness of the wall in this direction were influenced by the residual strains in the longitudinal reinforcement fibers in the flange. Furthermore, the shear lag effect that existed when the flange was in tension during web direction loading lowered the strain at the flange tips. Maintaining accurate estimations of tensile strains in the flange tips is critical for obtaining good force resistance estimation of the wall in the flange direction loading. Thus, overestimation of the effects of shear lag led to an overestimation of both the stiffness and force resistance in the flange direction response. Figure 6.32 shows the flange direction cyclic behavior of NTW2 for the analysis that was repeated after removing the effects of shear lag. When shear lag was removed, the reloading stiffness was somewhat reduced compared to when shear lag was present in the analysis as shown in Figure 6.25. The reduced stiffness is due to the increased strain and damage in the flange tips. Figure 6.33 shows the comparison of the strain in a longitudinal reinforcement fiber in the flange tip boundary element for the two analyses with and without shear lag effects. As can be seen, the strain in the flange tips was larger when shear lag was not included, leading to a larger residual strain after unloading and thus the reduced lateral stiffness observed in the force displacement response without the effects of shear lag. The overestimation of the stiffness was

thus partially influenced by the incorrect simulation of the strain distribution across the flange width during web direction loading.

As stated in the description of the NTW2 model in Section 6.2, the shear stiffness was taken directly from the model used for the analysis of NTW1. The comparison of the shear deformation response of the OpenSees NTW2 model with the measured first floor response is presented in Figure 6.34, which shows that the selected model did not accurately simulate the shear behavior of NTW2 in the flange direction. The decision to distribute the longitudinal steel in the flange would have significantly altered the shear deformation behavior of the flange of NTW2. While it was expected that shear behavior would be altered by the distributed longitudinal steel, information was not available to indicate how the shear model should be modified to account for the change from concentrated to distributed steel. It appears that the shear model significantly overestimated the stiffness of the wall in the positive direction and underestimated the stiffness in the negative direction due to the asymmetric behavior observed for the measured response. The cause for asymmetry response in both the measured data is not clear at this stage, but such an anomaly will influence the cyclic response of NTW2. The applied loading typically started by displacing the flange in the positive displacement (flange-in-compression direction), which might have had some influence on the observed asymmetric behavior. Pending further investigation of this issue, it is stated that the generally poor simulation of the shear strength and stiffness in the flange direction would contribute to the discrepancies observed in the responses in the flange direction.

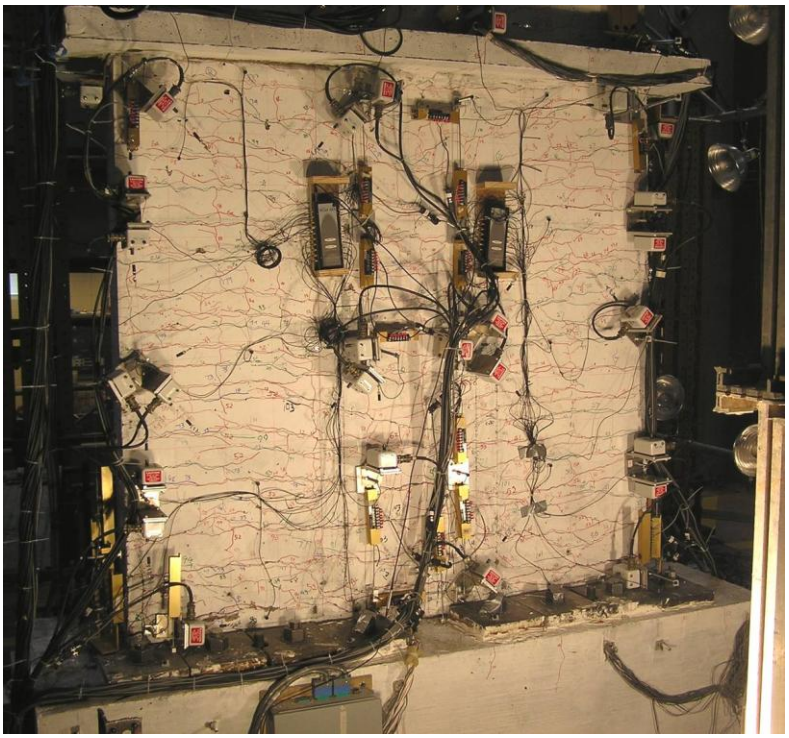

Figure 6.31 Back of Flange of NTW2 following Displacement Beyond First Yield in the Web Direction

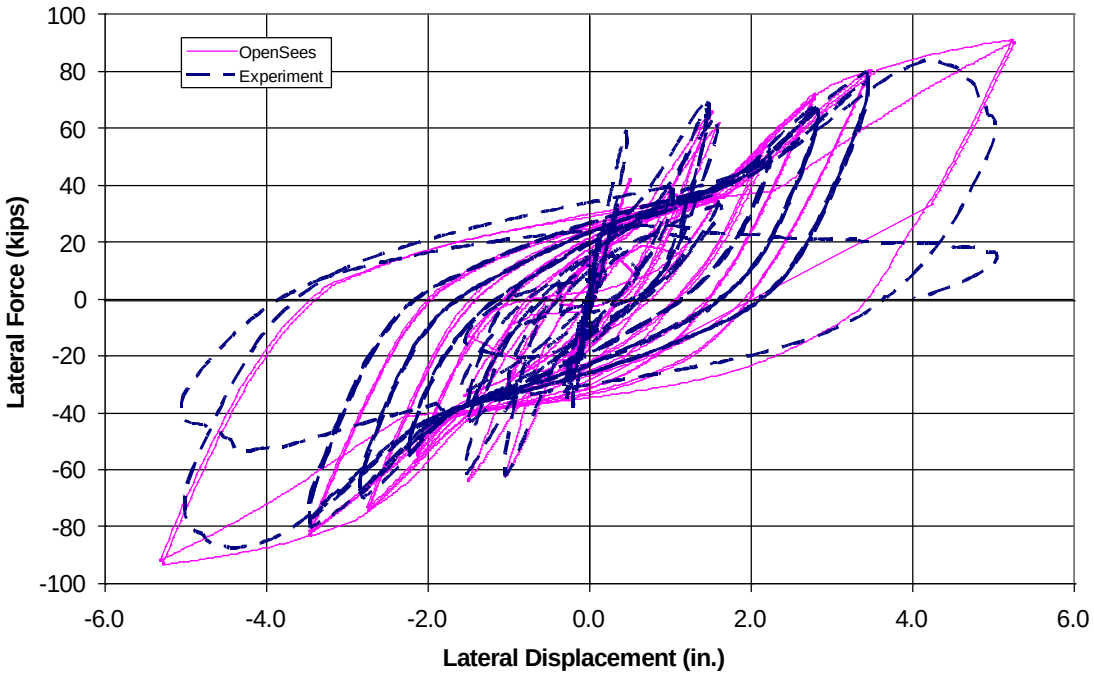

Figure 6.32 Measured and Predicted Force-Displacement Responses of NTW2 in the Flange Direction without Accounting for Shear Lag in the Web Direction Loading

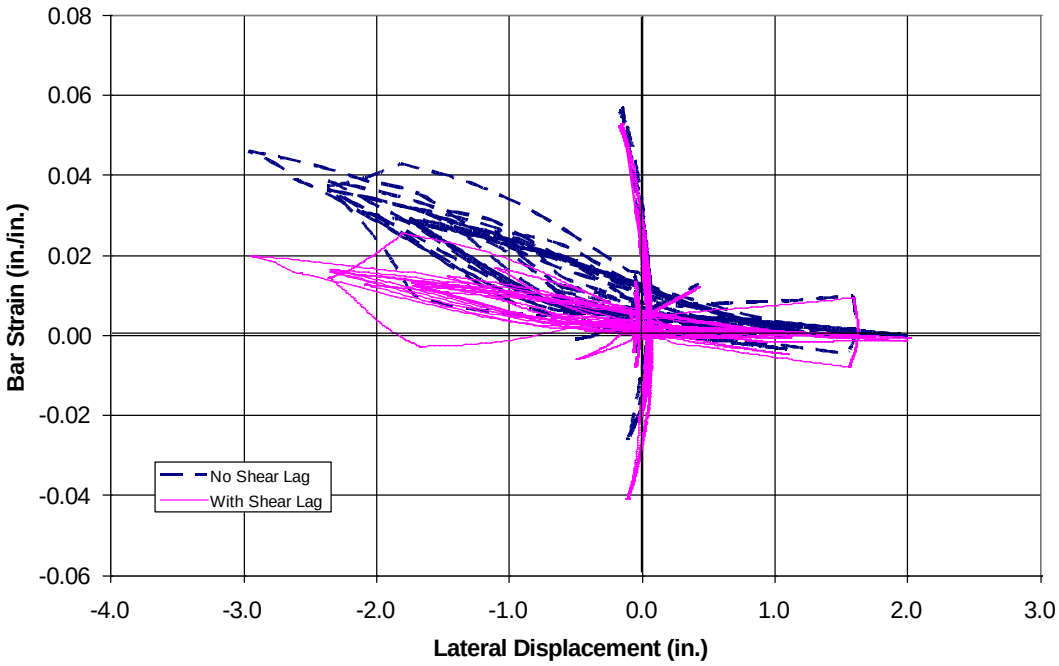

Figure 6.33 Strain in a Longitudinal Reinforcement Fiber in the Flange Boundary Element Located Furthest from Web Centerline and Web Tip With and Without the Effects of Shear Lag

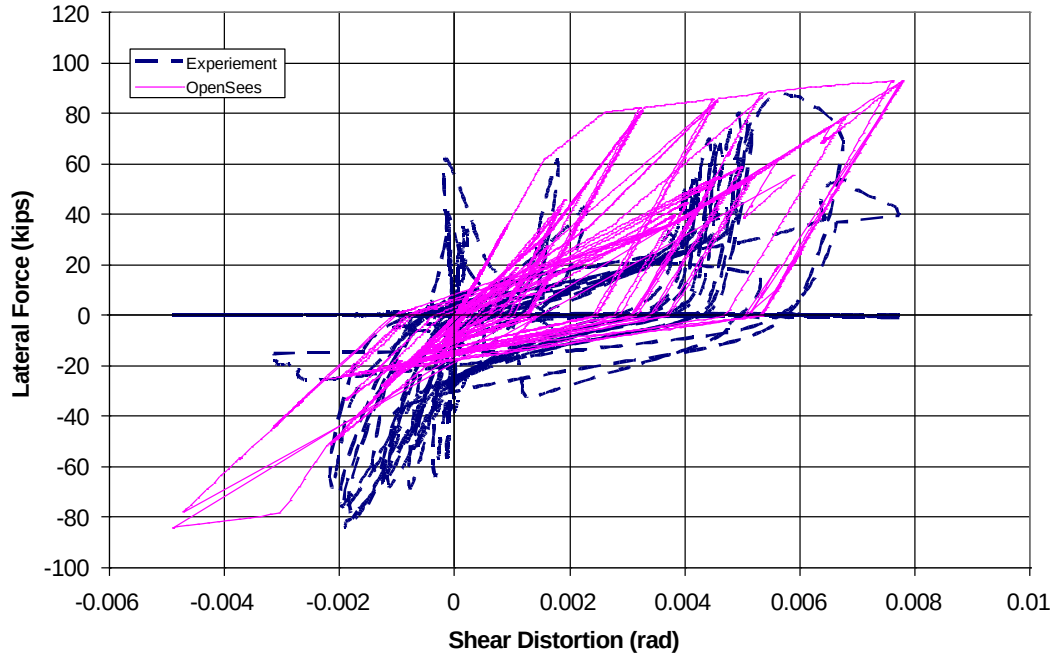

Figure 6.34 Comparison of Measured Shear Response at the First Floor of NTW2 in the Flange Direction with that Predicted by the OpenSees Model

6.5.2 Multidirectional Load Paths

Figure 6.35 compares the second floor displacements for the pentagon-shaped load path applied to NTW2 at 50% of the theoretical first yield. In this figure, the experimental response represents the average of the two string potentiometers attached to the flange tips. It is seen that the OpenSees model was subjected to nearly the same displacement path as the experimental unit NTW2. Figure 6.36 compares the measured and analytical force resistance surfaces corresponding to the load path in Figure 6.35, which shows a good agreement between the predicted and experimental results except at the peak displacements. Furthermore, Figures 6.37 and 6.38 show the force-displacement responses for the pentagon-shaped load path for the web and flange directions, respectively. In the web direction, the peak force was well predicted by the analysis even though the shear was not well simulated. However, the significant discrepancies in the shear response did not develop until after yielding of the longitudinal reinforcement. Though small, NTW2 experienced larger residual displacements than that exhibited by its analytical model. The amounts of residual displacement were somewhat unexpected because this cycle was at 50% of the yield displacement, and that the wall had not been previously displaced beyond the first yield limit state. The most likely source of the residual displacement was progressive cracking and associated damage of concrete during previous load cycles. However, the unloading and reloading stiffnesses of NTW2 were well estimated by the analysis in the web direction. In the flange direction, NTW2 showed slightly stiffer response and increased residual displacements than were recorded by the analysis model, leading to under prediction of the peak forces by as much as 25%. As with the web direction, a slightly larger residual displacement was recorded when unloading from positive peak displacement during testing than observed in the analytical response. The increased residual displacement led to a somewhat larger experimental cyclic loop, and increased energy dissipation than the analytical response.

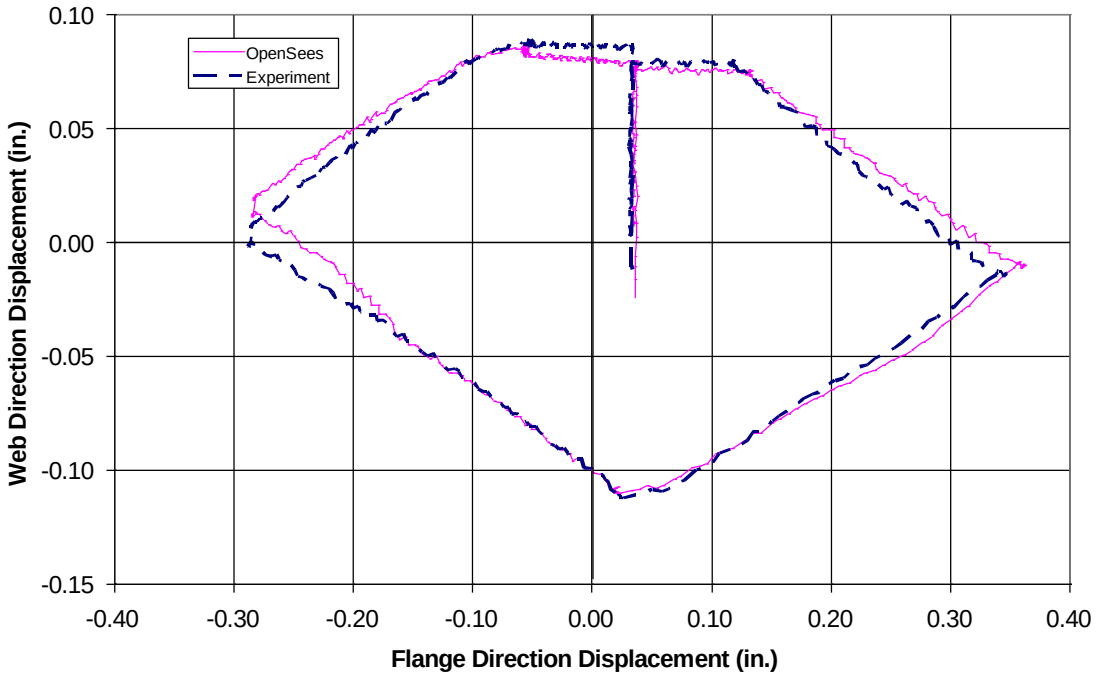

Figure 6.35 Comparison of Displacements at the Top of the Second Floor of NTW2 for the Pentagon Shape Load Path at 50% of the Theoretical First Yield

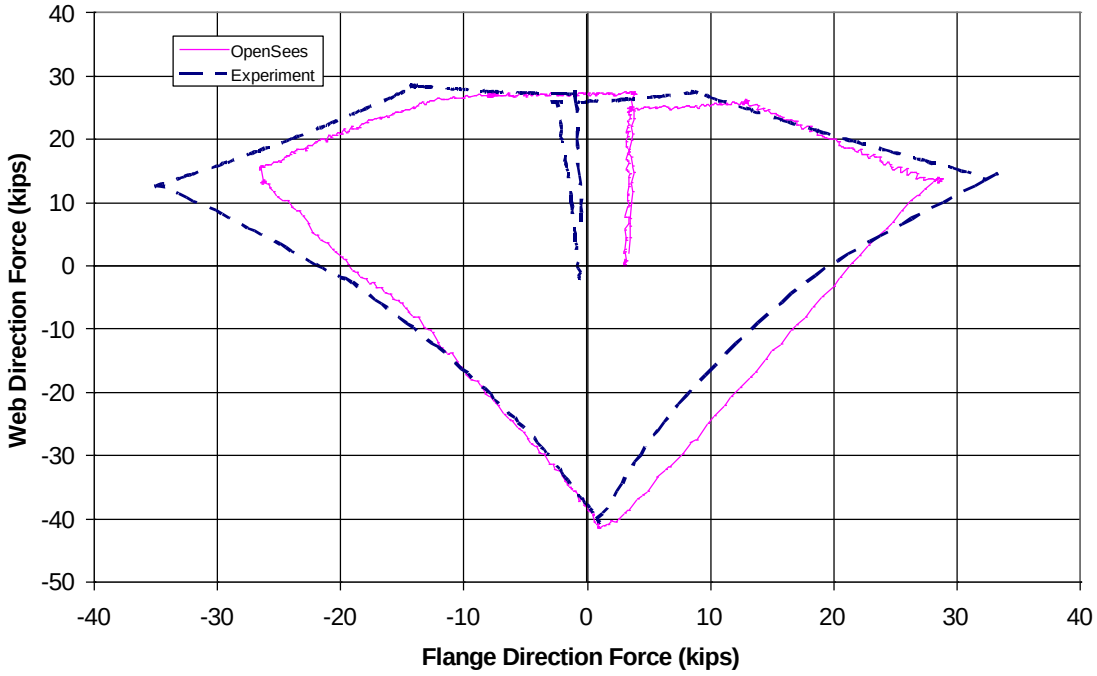

Figure 6.36 Comparison of Forces at the Top of the Second Floor of NTW2 for the Pentagon Shape Load Path at 50% of the Theoretical First Yield

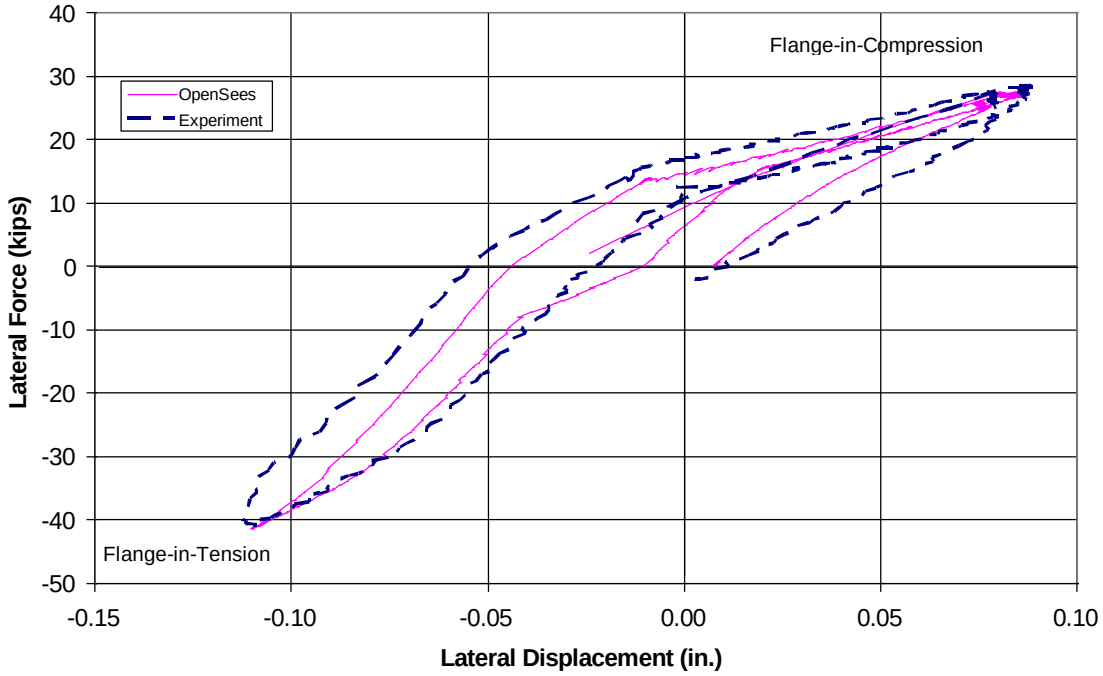

Figure 6.37 Comparison of Force-Displacements Response of NTW2 at the Second Floor for the Pentagon Load Path at 50% of the Theoretical First Yield in the Web Direction

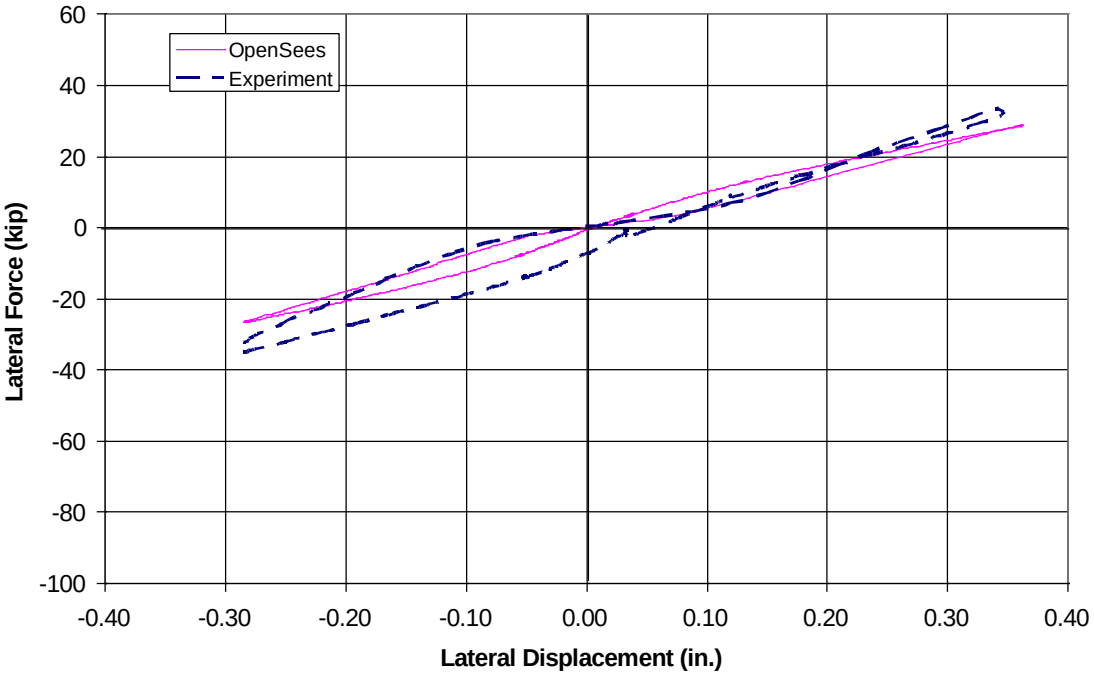

Figure 6.38 Comparison of Force-Displacements Response of NTW2 at the Second Floor for the Pentagon Load Path at 50% of the Theoretical First Yield in the Flange Direction

Figure 6.39 compares the experimental and analytical hourglass load path that subjected NTW2 to 2% lateral drift, which confirms that the test and analytical models were subjected to nearly the same bi-directional lateral displacements. Figure 6.40 shows the lateral force resistance surfaces of the experimental and analytical models for the hourglass shaped load path. It is seen that the peak forces are well simulated by the analysis; however, the force resistance while moving from one peak to the next was not well captured which can be examined more closely by examining the response in the two primary directions. Figures 6.41 and 6.42 show the force-displacement response of NTW2 in the web and flange directions, respectively, for the load path shown in Figure 6.39. The web direction response was almost exactly predicted by the model in both the flange-in-compression and the flange-in-tension directions. The reason this response was well simulated was because the discrepancies in the shear have decreased and the nonlinear strains make the effects of shear lag on the lateral force resistance small. The peak forces were accurately captured, so were the unloading and reloading stiffnesses. Between the peaks, the force in the flange-in-compression loading direction was underpredicted by approximately 20% at the largest difference being at about -0.5 in. of displacement. In the flange direction, the overall shape and stiffness of the response loops were satisfactorily predicted given the complexity of the load path. The flange direction response was more accurately predicted in the positive direction; however, in the negative displacement direction, the force was overestimated by as much as 40%. This overestimation was also seen in the simulation of NTW1 for the hourglass shaped load path, in Section 5.8.6. As explained for NTW1 response, the discrepancy was likely caused by not accurately simulating the accumulated damage in the flange direction that was present prior to beginning this specific load path.

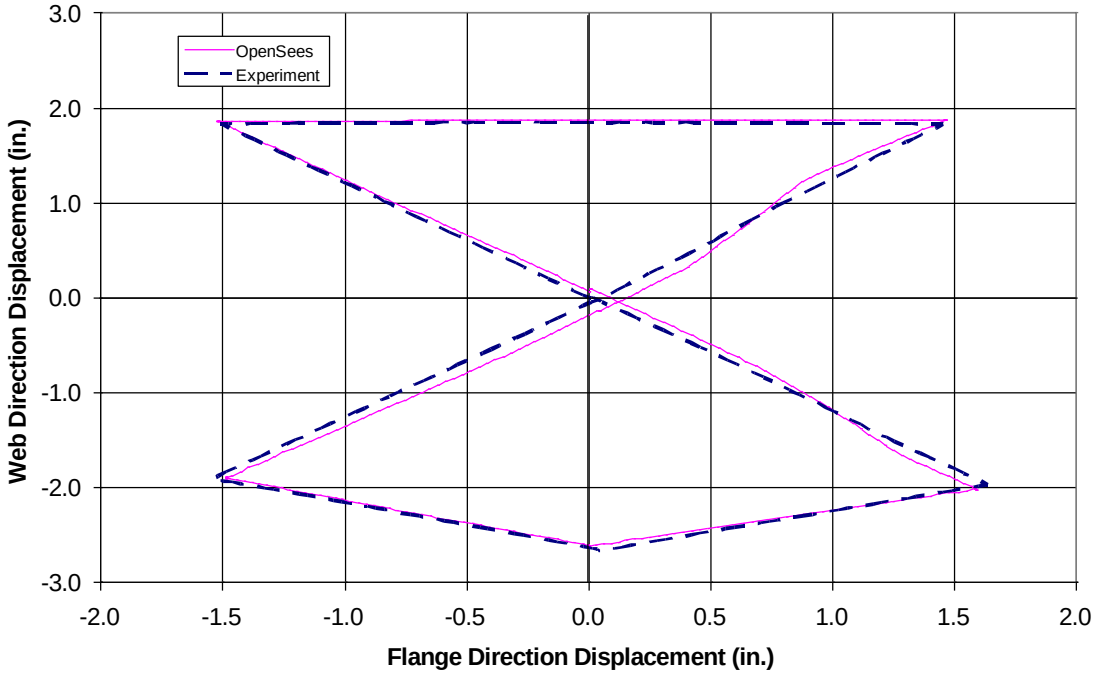

Figure 6.39 Comparison of Displacements at the Top of the Second Floor of NTW2 for the Hourglass Shape Load Path at 2% Lateral Drift

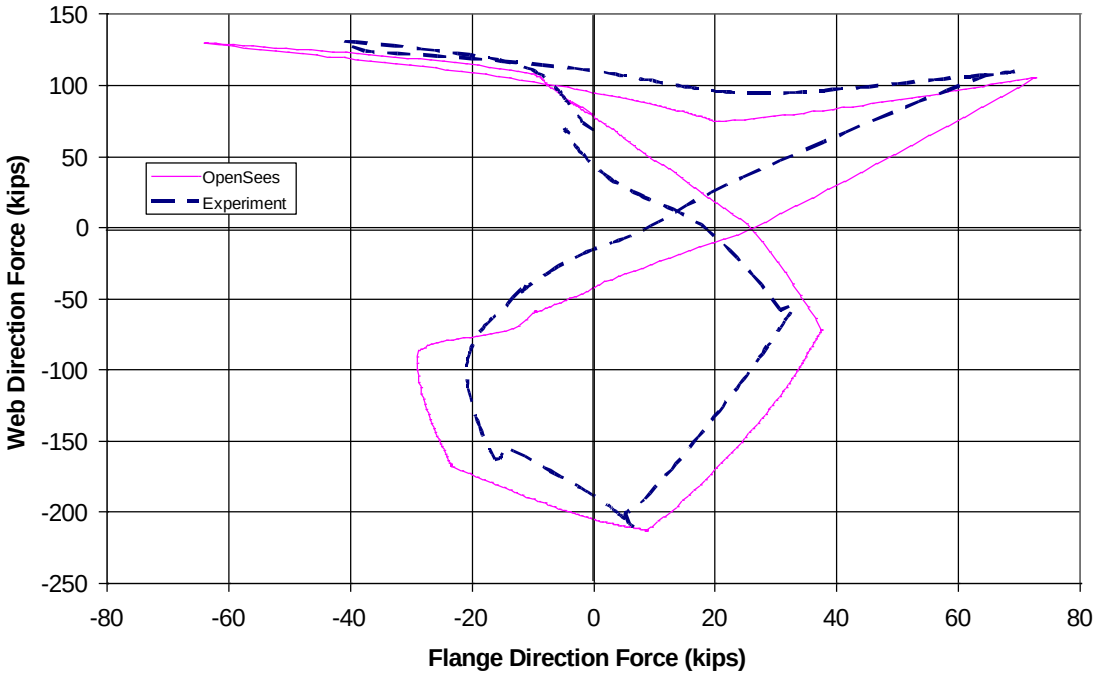

Figure 6.40 Comparison of Forces at the Top of the Second Floor of NTW2 for the Hourglass Shape Load Path at 2% Lateral Drift

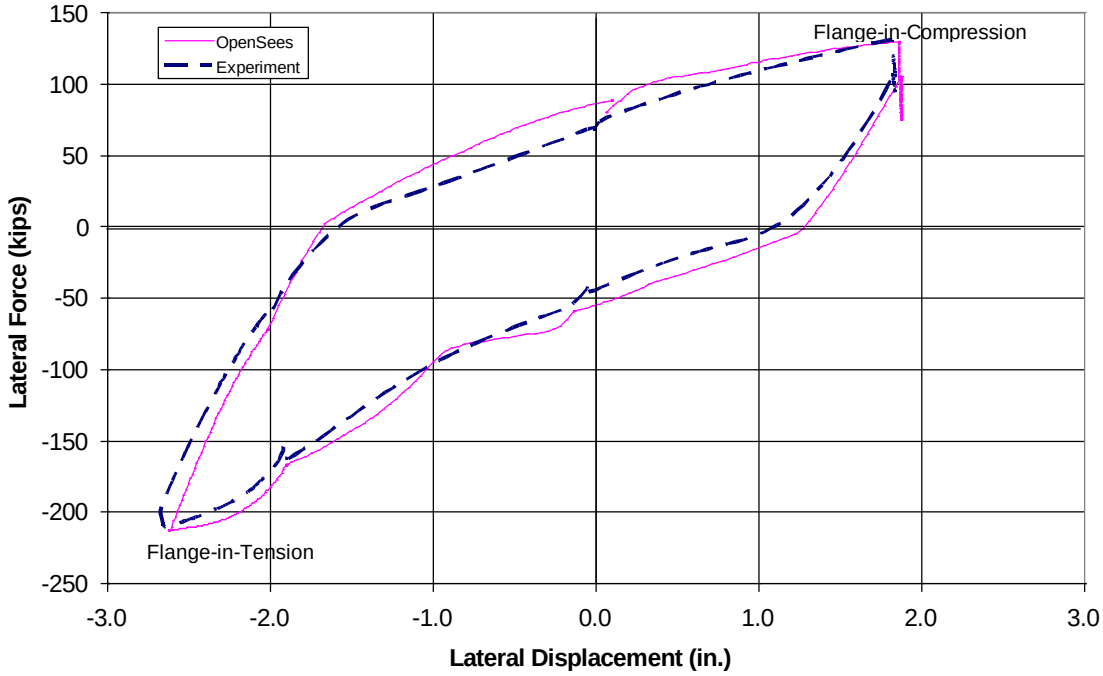

Figure 6.41 Comparison of Force-Displacement Response of NTW2 at the Second Floor Level for the Hourglass Shape Load Path at 2% Lateral Drift in the Web Direction

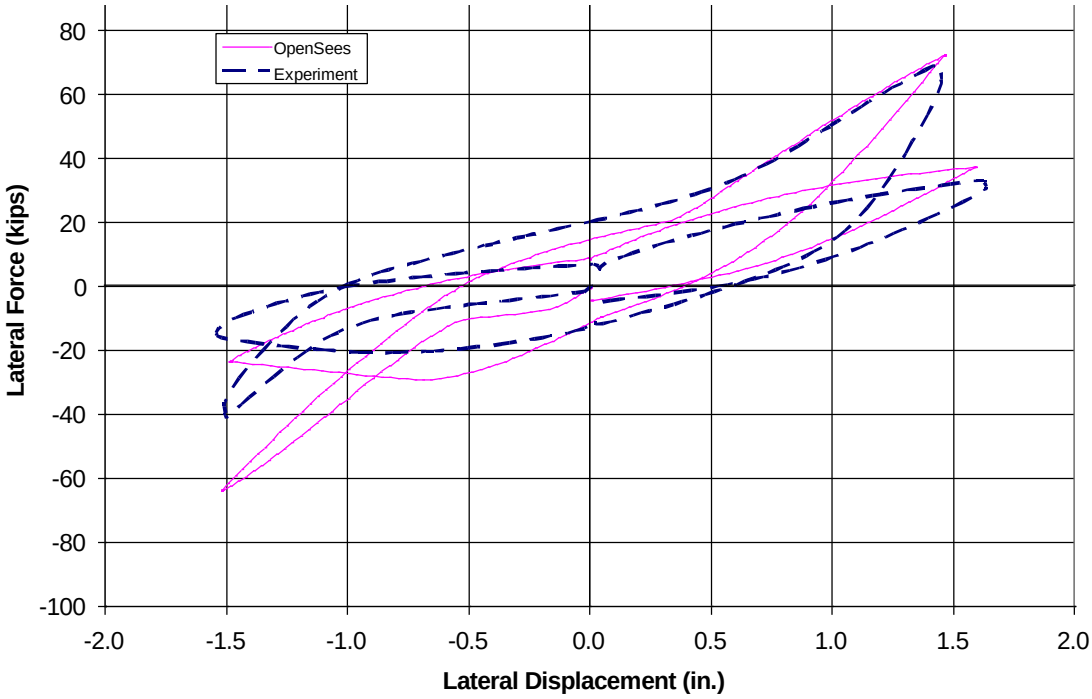

Figure 6.42 Comparison of Force-Displacement Response of NTW2 at the Second Floor Level for the Hourglass Shape Load Path at 2% Lateral Drift in the Flange Direction

6.5.3 First Floor Response

To examine the accuracy of the local responses, the force-displacement responses established at the first floor of NTW2 is shown in Figures 6.43 and 6.44 for the web and flange directions, respectively. The first floor response was not captured as accurately as the second floor response in both directions, which is partly due to the discrepancies between the measured lateral displacements and those imposed to the analytical model. Overall, the web direction response of NTW2 at the first floor level was not well captured by the analysis. Figure 6.24 shows that the elastic stiffness of NTW2 in this loading direction was significantly higher than the OpenSees model. In particular, the flange-in-tension direction had noticeable underestimation of the lateral stiffness of the T-wall by the analysis model. As should be expected, the first floor lateral displacement was heavily influenced by the contribution of the shear distortion of the first floor panel. Figure 6.30 shown earlier indicated that the OpenSees shear material model underpredicted the shear stiffness of the section in the web direction after cracking but before yielding of the longitudinal reinforcement, which is believed to have reduced the stiffness of the analytical model and led to over prediction of the lateral displacement in the elastic range. Additionally, overestimating shear lag effects in the analytical model and the corresponding difference in the strain distribution in the flange shown in Figure 6.29 would have decreased the stiffness if the analysis model in the flange-in-tension direction. Figure 6.44 shows that in the flange direction of response, the overestimation of the theoretical wall resistance after subjecting NTW2 to the multidirectional loading was similar to that observed for the second floor response (See Figure 6.25). The unloading and reloading stiffness was well captured at the first floor level, but the residual displacements were over predicted.

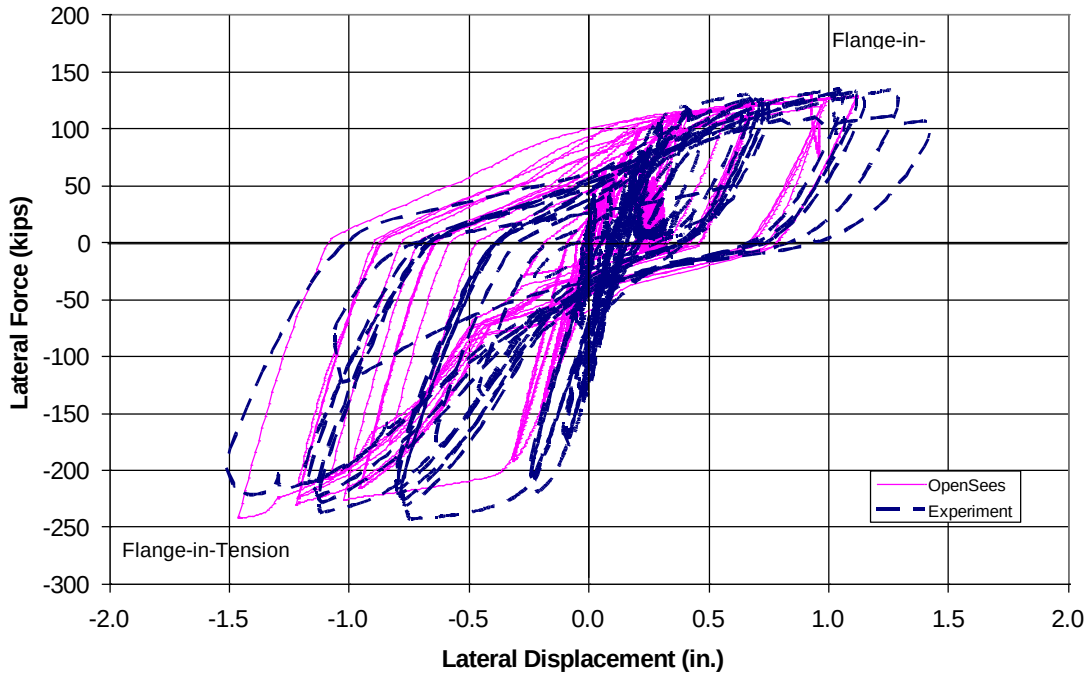

Figure 6.43 Measured and Calculated First Floor Force-Displacement Responses of NTW2 in the Web Direction

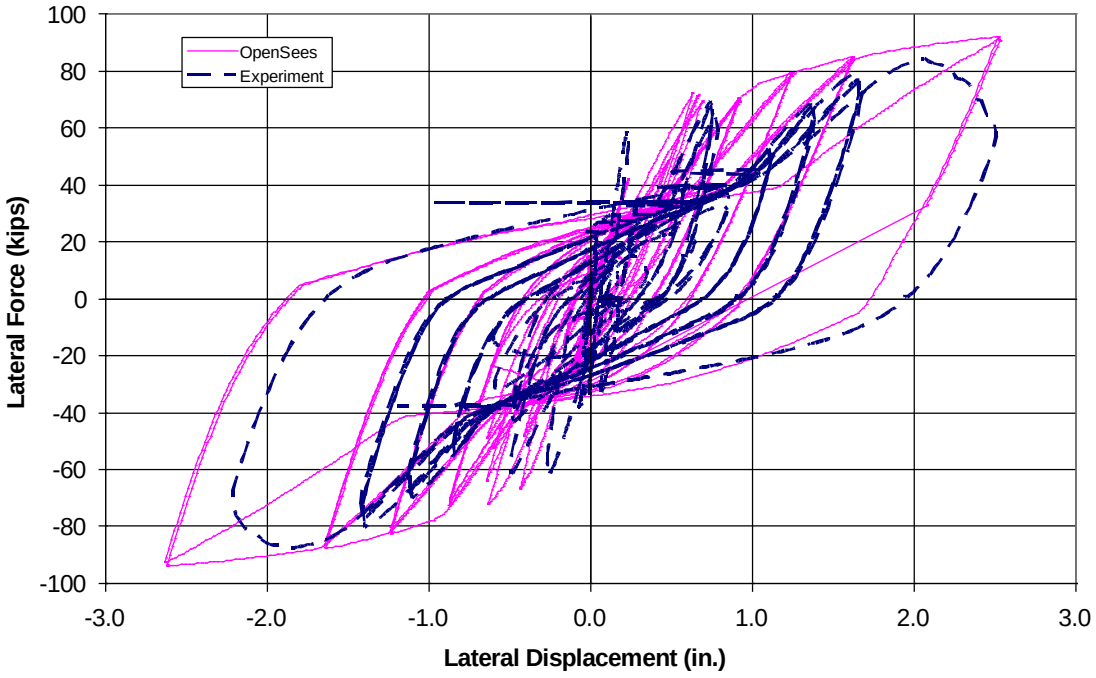

Figure 6.44 Measured and Calculated First Floor Force-Displacement Responses of NTW2 in the Flange Direction

Figure 6.45 and 6.46 compare the measured and analytical first floor lateral displacement of NTW2 as a function of the measurement number in the web and flange directions. It is evident that the OpenSees model was subjected to larger lateral displacements in both directions than was experienced by NTW2 during testing. It is also evident that NTW2 had residual displacements much earlier than was predicted by the OpenSees model. This again suggests that NTW2 experienced larger than predicted flexural actions due to reduced shear stiffness than anticipated based on the analytical response.

Furthermore, the predicted flexural behavior of NTW2 would have been also influenced by the simple modeling technique used for the spliced region at the second floor level. In comparison to the modeling technique used for the rectangular wall with a conventional splice (RWS) in Chapter 4, a simpler approach was used to model the splice in NTW2. This is because the prediction of NTW2 response was done prior to completing the analysis of RWS and the splice in RWS was located in the plastic hinge region. To realize the increased flexural contribution in NTW2, Figure 6.47 shows the comparison of the recorded strains in the first floor of NTW1 and NTW2 for a longitudinal rebar located in the web tip at a drift of 1.5%. As can be seen, NTW2 had higher strains in the reinforcement than were recorded for NTW1. This is due to restricting the length of the plastic hinge and placing more rotational demand on the plastic hinge of NTW2. As previously noted, this potential restriction was attempted to be captured by the analysis by increasing the area of the reinforcement fibers in the spliced region. However, the first floor results indicate that the restriction the splice placed on the plastic hinge formation was not fully captured by the OpenSees analysis.

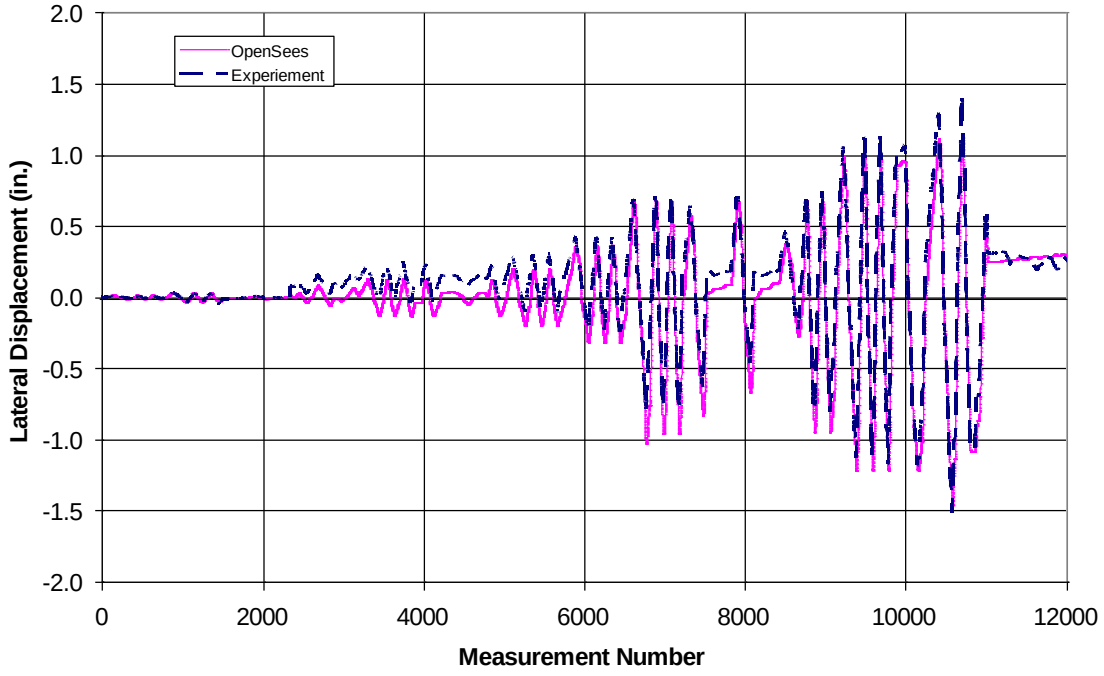

Figure 6.45 Comparison of First Floor Displacement of NTW2 in the Web Direction as a Function of Measurement Number

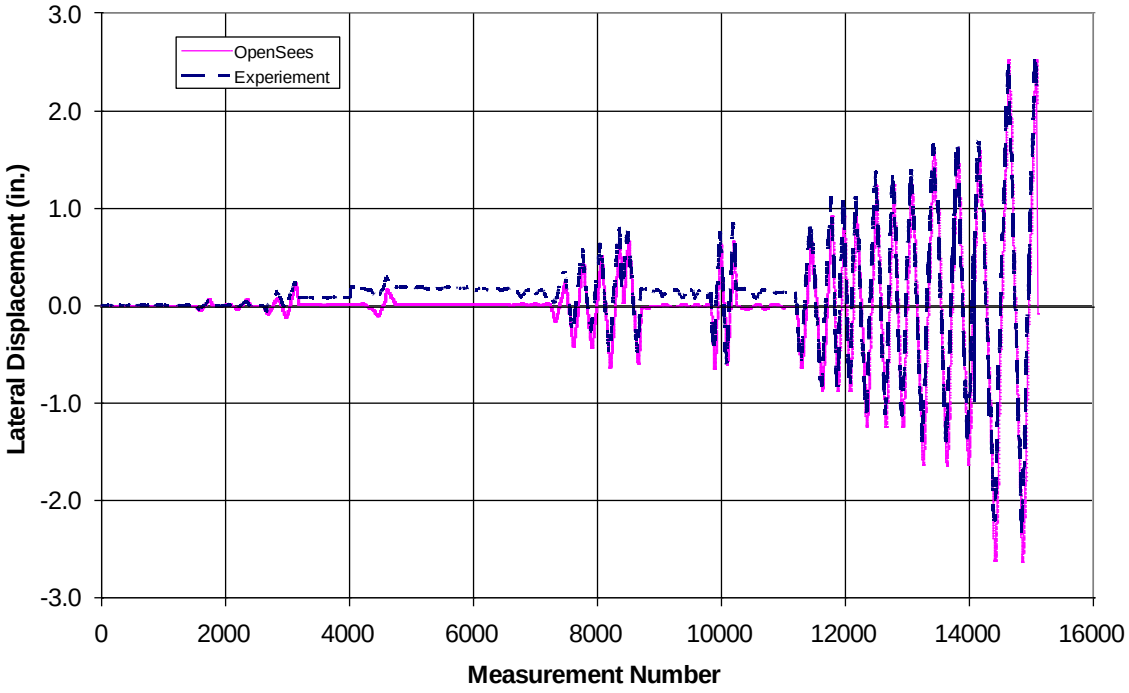

Figure 6.46 Comparison of First Floor Displacement of NTW2 in the Flange Direction as a Function of Measurement Number

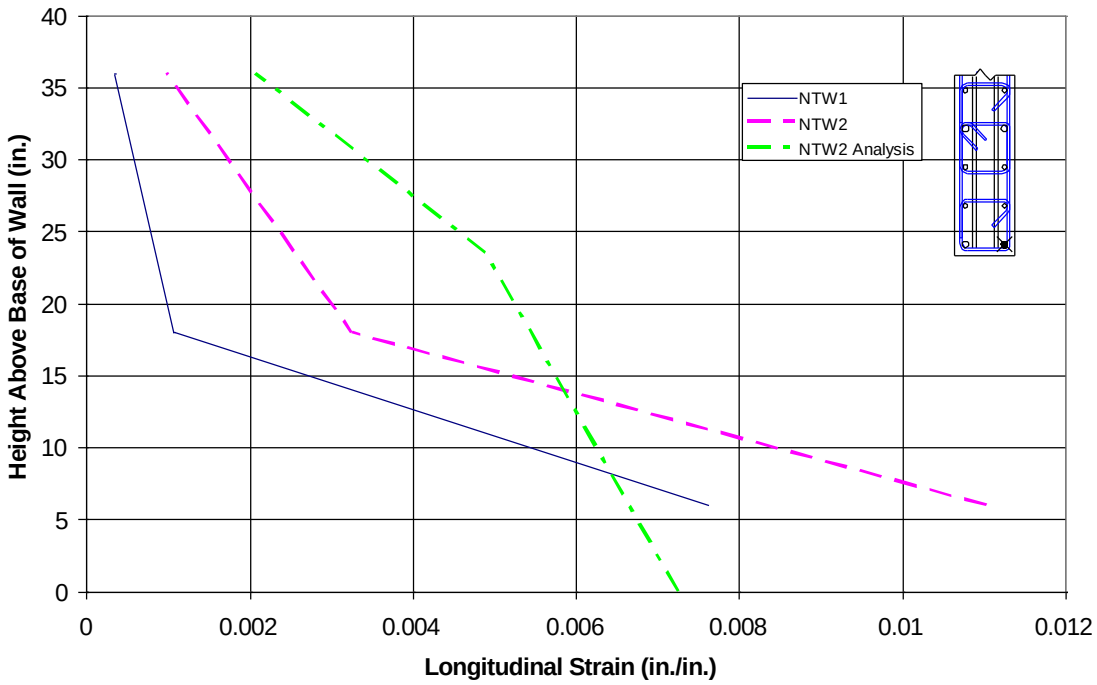

Figure 6.47 Comparison of Longitudinal Strains in the Web Tip of NTW1 and NTW2 at 1.5% Drift in the Web Direction

6.5.4 Local Response

As demonstrated for the first floor response, the accuracy of the local response was reduced due to inadequate simulation of the effects of shear lag and shear distortion in both web and flange directions.

Since the web direction response was the best predicted response by the OpenSees analysis, the local response in this direction was examined in detail. Figure 6.48 and 6.49 show the strain distribution along the web for the flange-in-compression and the flange-in-tension loading directions at different stages. Figure 6.48 shows that for the flange-in-compression direction, the OpenSees analysis accurately predicted the strain distribution, section curvature, and location of the neutral axis. This was expected because the flange-in-compression direction does not have the effects of shear lag, and the global and first floor force-displacement responses were the best simulated by the analysis model.

Figure 6.49 shows that the strain distribution was not accurately simulated for the flange-in-tension direction loading, even though the global force-displacement was reasonably predicted

by the analysis. The overestimation of the shear lag effects in the flange-in-tension direction would have made the analysis model more flexible, thus inducing lower tensile strain at a given target displacement.

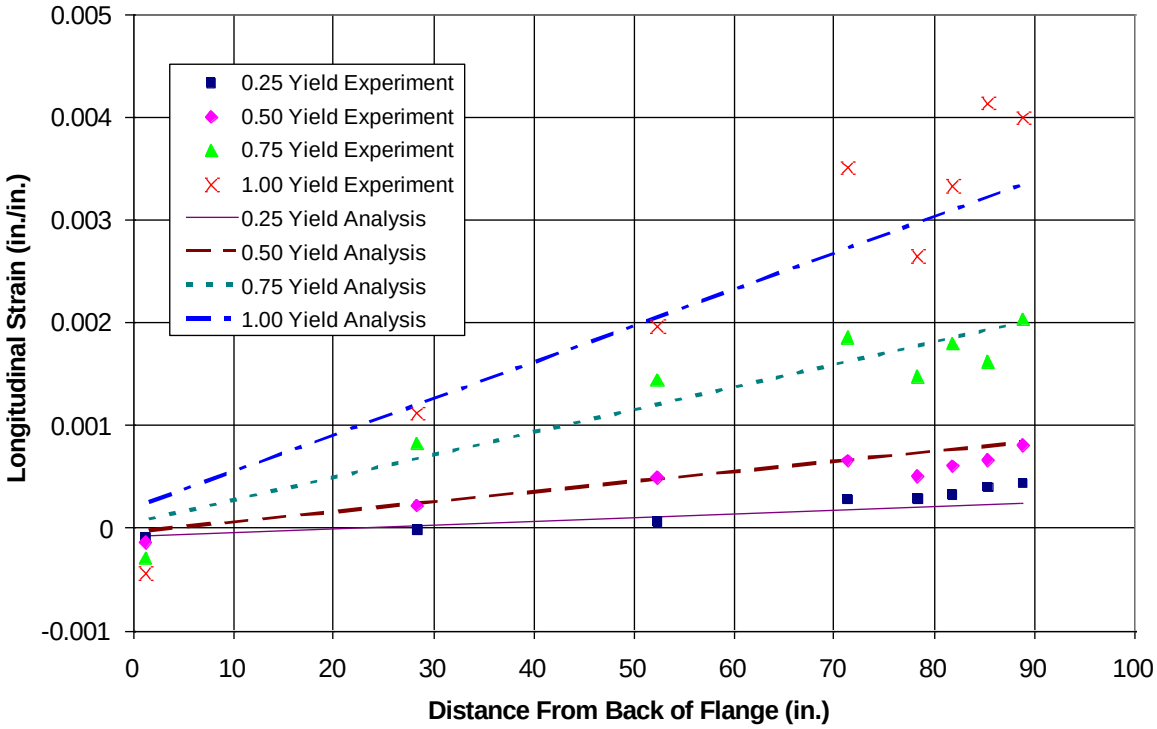

Figure 6.48 Comparisons of Strain Profiles for the Flange-in-Compression Direction Response for NTW2

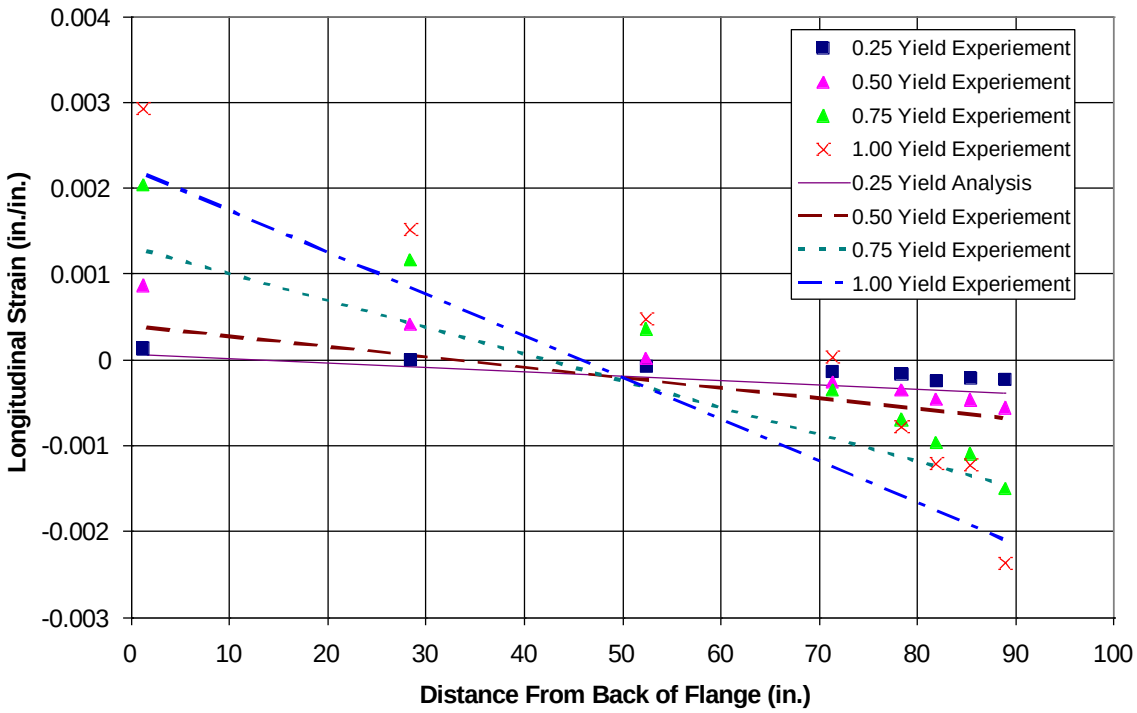

Figure 6.49 Comparisons of Strain Profiles for the Flange-in-Tension Direction Response for NTW2

6.5.5 Comments on Shear Lag Effects

The analytical and experimental responses of NTW2 in both the flange and web directions implied that the shear lag was not accurately captured in the NTW2 analysis model. As previously noted, the shear lag behavior depends on the shear stiffness of the free flange overhang which is influenced by:

- free flange length to thickness ratio,
- longitudinal reinforcement distribution along the flange,
- amount of longitudinal reinforcement in the flange, and
- spacing and diameter of transverse reinforcement spacing.

The original shear lag function used in the section definition of the NTW2 model included the strain distribution function using a B/t ratio (see Section 5.7.1). However, the other factors were not included in the section. The abstraction built into the design of the OpenSees

framework makes it difficult for the section code to determine the size, location, and distribution of the longitudinal reinforcement. A section only knows the location of a fiber and its associated material model. The section is unaware if a particular material model is a concrete or steel material model. Thus it cannot internally determine if the longitudinal steel is concentrated in the flange tips, or distributed along the flange length.

The strain distribution function developed to account for the shear lag effects was from the test data of NTW1 and TW2 (see details in Section 5.7.1), which is reproduced below:

$$\varepsilon = \varepsilon_0 + \Phi_y * z * \left(-0.1140527 * \left(\frac{B}{t} \right) * \left(\frac{2y}{B} \right)^2 + 1 \right) + \Phi_z * y \qquad \text{(Eqn. 6-1)}$$

In both NTW1 and TW2 walls, boundary elements were used and most of the longitudinal reinforcement was grouped at the flange tips. NTW2 had a different longitudinal reinforcement distribution in the flange with a large portion of the longitudinal reinforcement distributed along the flange. Analysis of the strain distribution in the flange of NTW2 indicates that the measured strains in the longitudinal reinforcement of the flange more closely followed Eqn. 6-2:

$$\varepsilon = \varepsilon_0 + \Phi_y * z * \left(-0.0764606 * \left(\frac{B}{t} \right) * \left(\frac{2y}{B} \right)^2 + 1 \right) + \Phi_z * y \qquad \text{(Eqn. 6-2)}$$

Based on the analysis of NTW1 and NTW2, it is obvious that the strain distribution function requires a variable that includes the influence of all aforementioned parameters. Including all the parameters that influence the shear stiffness of the free flange width in one variable would result in a strain distribution function that is of the following form:

$$\varepsilon = \varepsilon_0 + K * \varphi_y * z + \varphi_z * y \qquad \text{(Eqn. 6-3)}$$

Where ε is the strain in the fiber of interest, φ_y is the curvature about the local y-axis, φ_z is the curvature about the local z-axis, K is the shear lag variable including the previously mentioned factors, and y and z are the local coordinates of the fiber of interest. An investigation for determining the variable K is beyond the scope of this study. However, it is noted that not enough data currently exists for such an investigation and that a detailed analytical and experimental study is required to determine the influence of each parameter on the shear lag and strain distribution.

Until such an investigation is conducted, Eqns. 6.1 and 6.2 may be used as a guidance to include the shear lag effects based on the longitudinal reinforcement details in the flange of the

T-wall under consideration. If the majority of the longitudinal reinforcement is grouped in boundary elements located at the flange tips, then Eqn. 6.1 should be used for the analysis to capture the effects of shear lag; however, if the longitudinal reinforcement is distributed then Eqn. 6.2 is more suitable. The two cases represented by NTW1 and NTW2 provide an upper and lower bound for the effects of shear lag in the web direction of loading.

Chapter 7
Summary, Conclusions and Recommendations

7.1 Summary of Analysis and Testing

Three rectangular and two T-shaped concrete walls were designed and tested at 1/2-scale at the University of Minnesota's Multi-Axial Testing Facility as part of a PreNEESR project. The two T-wall specimens, referred to as NTW1 and NTW2, had identical cross-sectional dimensions but with different reinforcement details. NTW1 modeled four stories of a six-story prototype wall with the reinforcement details that are typical of the current industry practice. NTW2 modeled only 2 stories with improved reinforced details in the flange and web. The three rectangular walls, referred to as RWN, RWC and RWS, replicated the moment resistance of the prototype T-wall in the web direction and investigated the influence of the longitudinal reinforcement anchorage on the lateral load behavior of walls. RWN, RWC and RWS were, respectively, detailed with no splices, couplers and conventional code-based lap splices at the base of walls. The rectangular walls were subjected in-plane lateral loading while the T-walls were tested under multi-directional loading. The experimental findings of rectangular and T-walls are presented in Johnson (2007) and Brueggen (2009), respectively. This report has presented the fiber-based analysis of all walls investigated as part of this project.

Until the incipient failure occurred, all rectangular walls were subjected to the same load protocol that was determined based on pretest moment-curvature analyses of the wall sections. The load protocol used progressively increasing cyclic lateral displacements with full reversals and the full details of the applied displacement histories are presented in Section 4.2. Similarly, both T-walls were subjected to the same load protocol that included axial loads and lateral cyclic loads in the parallel to the web direction, parallel to the flange direction, and in inclined directions that subjected the walls to both the web and flange direction displacements. Additionally, the walls were subjected to complex multidirectional load paths in both the elastic and inelastic regions. These load paths were intended to investigate the performance of the walls

under multidirectional loading and the ability of the fiber-based models to capture the non-rectangular wall behavior under complex load paths. Complete details of the load paths applied to NTW1 and NTW2 are found in Sections 5.4 and 6.3, respectively.

The analysis of structural walls subjected to in-plane or multi-directional loading requires that a number of issues be addressed in the development of the analysis model. Those issues are: 1) nonlinear material behavior, including the effects of cracking and confinement of concrete as well as yielding and strain hardening of the mild steel reinforcement; 2) shear deformation of the walls; 3) interaction between the shear and flexural deformations; 4) the effects of shear lag in the flange in nonrectangular walls (e.g., T-walls); 5) strain penetration effects at the wall-to-foundation interface; and 6) influence of anchorage details used for the longitudinal reinforcement (e.g., couplers, lap splices etc.). The OpenSees models used for the analysis of the rectangular walls and T-shaped walls; NTW1 and NTW2 were designed to include the effects of these issues, except for the flexure-shear interaction and local slip of reinforcing bars within the lap splice, which was observed in RWS. Full descriptions of the analytical models used for the specimens were presented in Sections 4.3, 5.3 and 6.2.

The models used for the analysis in this report used fiber-based beam-column elements that were available in the OpenSees analysis software. A fiber-based approach was selected because the simplification of the material model based on uniaxial behavior enabled more accurate representation of the concrete and steel reinforcement behavior in modeling the wall response. Additionally, the strain distribution induced in the fiber elements of the walls could be modified to include the effects of shear lag. The fiber-based approach also enabled the effects of strain penetration at the wall-to-foundation interface to be included through the use of an interface element and a material model suitable for defining the local slip at the interface as a function of the stress in the longitudinal reinforcing bar, thus capturing the strain penetration effects in a rational manner. However, the fiber-based approach does have two drawbacks. First, the shear distortion is handled at the element level, and thus the analysis requires that the shear deformation of the wall in the flange and web directions be considered separately from the flexural behavior. Second, the separation of the shear and flexure behaviors makes it difficult for the shear-flexure interaction to be handled as directly as desired. However, a careful definition of the shear deformation can allow the nonlinear behavior of shear and flexure to occur

simultaneously as other researchers have observed this to be the case due to shear-flexure interaction.

Both pre- and post-test analyses were conducted for the three rectangular walls and NTW1, while only a pre-test analysis was conducted for NTW2. The pre-test analyses of the rectangular walls and NTW1 showed the importance of using a more realistic concrete cyclic model in analytical simulations of structural walls. The most sophisticated model available in OpenSees was the Kent-Park concrete model, which did not adequately represent the cyclic behavior of concrete. Thus a modified version of a cyclic concrete model proposed by Chang and Mander [1995] was implemented in OpenSees. Additionally, the pre-test analysis of the rectangular walls and NTW1 ignored the effects of shear deformation because it was assumed that the wall response would be flexure dominated due to their aspect ratios being greater than 2.5. However, the shear deformation contributed significantly to the lateral displacement of these walls, particularly at the first floor level. Finally, the effects of shear lag were ignored in the pre-test analysis of NTW1. While this approach did not significantly affect the global force-displacement response, the accuracy of the local responses such as the strains and location of the neutral axis in the critical region of the walls was compromised. The post-test analysis of NTW1 corrected these deficiencies by incorporating the modified Chang and Mander concrete model, shear behavior in the beam-column element, and strain variation in the flange due to shear lag. These modifications significantly improved the accuracy of the simulation of NTW1 as it was found both the global and local responses of NTW1 were closely compared with experimental results. A similar observation was also made for the post-test analyses of the rectangular walls which used the modified Chang and Mander concrete model and included the shear deformation in the beam-column element,

The post-test model of NTW1 included four beam-column elements to model the four stories of the test specimen and one interface element for the wall-to-foundation connection. Both the beam-column and interface elements used concrete and steel fibers to discretize the cross-section. The uniaxial material models for the fiber sections were defined using stress-strain relationships for the concrete and longitudinal reinforcement, and stress-slip relationships for the strain penetration material. The same procedure was followed for modeling the rectangular walls and four to ten beam-column elements were used in each model depending on the splice detail.

The second T-wall, NTW2, provided the opportunity to learn from the post-testing analysis of NTW1 and attempt to predict the response of NTW2 for the proposed multi-directional loading. The response of NTW2 was simulated using four beam-column elements to simulate the two story wall specimen and one interface element to capture the strain penetration effects at the wall-to-foundation connection. The longitudinal reinforcement was spliced at the second floor level in the test specimen, requiring three beam-column elements be used for the second floor in the OpenSees model. Fiber sections were used to represent the cross-section details of the wall while the shear-distortion response was aggregated onto the section using a pinching model. Using the observed shear behavior of NTW1 and a new fiber section that included the shear lag effects, the response of NTW2 was predicted prior to the test. When compared to the experimental results, the force-displacement response was found to be well predicted in the web direction; however, the response was less accurately predicted in the flange direction. The discrepancy in the flange direction response was due to inaccurate simulation of the strain distribution in the flange due to shear lag and the shear deformations. Both of these features in NTW2 were affected by the use of distributed longitudinal steel instead of concentrating them in the boundary elements of the flange as used in NTW1.

7.2 Conclusions

7.2.1 Global Response of Rectangular Walls

The force-based beam-column elements with fiber sections adequately captured the global cyclic force-displacement response for all the three rectangular walls. The calculated peak forces were within 5% of the experimental values while the loading, unloading and reloading stiffnesses were simulated with good accuracy. The initial stiffness of the walls was also well captured. For all three rectangular walls, the response in the direction that subjected the #6 and #5 bars in tension was better simulated than the response that subjected the #9 bars in tension. The discrepancy between the experimental and analytical results in the #9 bar in tension direction was caused primarily due to not adequately capturing the shear degradation during the repeated loading to the same lateral displacement. Since the best available approach was used in the analytical simulation, further improvement of the analysis of walls in OpenSees requires integration of a new shear model.

The global lateral displacement response of the rectangular walls was decomposed into deformation components due to flexure, shear and strain penetration to further validate the OpenSees models. The analytical models captured the flexural deformations at the top of the wall with good accuracy. The flexural component contributed 70 to 80% of the total top displacement for RWN and RWC. In RWS, the flexural contribution reduced from 70 % to 50% as the top lateral displacement increased, presumably due to increased slip of the reinforcement in the plastic hinge region.

The analytical model for RWN also captured the deformations due to shear and strain penetration at the top of the wall with sufficient accuracy. The deformations due to shear and strain penetration contributed 10 to 20% and 8 to 10%, respectively, to the top lateral displacement in RWN. In RWC, for drifts higher than 1%, the analytical models over predicted the lateral deformation due to strain penetration and under predicted the shear deformation by 30 to 50% and 10 to 27% respectively. Similarly, for RWS at lateral drift greater than 0.75%, the analytical model over predicted the lateral deformation due to strain penetration by 30 to 170%

In conclusion, the analytical models satisfactorily captured the total global response as well as the contributions due to flexure, shear and strain penetration. However, the accuracy of the analytical simulation could be further improved through introduction of an improved shear model.

7.2.2 Global Response of T-walls

The beam-column elements with fiber sections adequately simulated the response of the T-walls subjected to the multi-directional loading. The force-displacement response at the top of the wall was satisfactorily captured by the post-test analysis conducted for NTW1 and by the pre-test analysis of NTW2, both of which are discussed in detail below. In each of these models, an improved concrete hysteretic model and a strain penetration model, which implemented into OpenSees as part of this study, were incorporated. In addition, the models accounted for the shear lag effects and shear deformation as accurately as possible within the current capabilities of OpenSees.

The model of NTW1 yielded a very good simulation of the force-displacement response, giving forces within 5 to 10% of the measured lateral force resistance for a given displacement in

both the flange and web directions. The hourglass and pentagon load paths chosen to investigate the wall behavior to complex multi-directional loads were well simulated by the analysis model, in terms of the lateral force resistance and stiffness. The two dimensional force surfaces generated by the analysis model for the elastic and inelastic multidirectional displacement paths were compared to the experimental results, and they were found to be within 5-15% of the measured values.

The lateral displacement response of NTW1 was decomposed into the contributions due to flexural deformation, shear deformation, and strain penetration. The flexural component was particularly well captured by the analysis model; the analysis and experiment both determined the flexural component to contribute 84% of the lateral deformation for the flange-in-compression direction and 85% for the flange-in-tension direction. The strain penetration was captured satisfactorily. However, the analytical model for the slip versus bar stress could be improved, which would lead to an improved simulation of the strain penetration component. The experimental data showed that the strain penetration contribution to the total lateral displacement was 4% in the flange-in-compression direction and 10% in the flange-in-tension direction, while the analysis showed an 8% contribution in both directions. The shear deformation contribution was the least accurately modeled, which requires further improvements as found from the analysis of the rectangular concrete walls. The test data revealed that the contribution of shear deformation to the total lateral displacement was 12% in the flange-in-compression direction and 5% in the flange-in-tension direction. However, the shear contribution in the analysis was found to be about 8% in the flange-in-compression direction and 7% in the flange-in-tension direction at the peak displacements. Additionally, the material model used in this study to capture the shear-distortion behavior is difficult to use and its limited capabilities do not facilitate accurate capturing of the unloading and reloading portions of the shear response. A material model that is specifically designed to model the shear-distortion response of reinforced concrete flexural members would lead to an increased accuracy of the shear and total responses of concrete walls in OpenSees. The total displacement could not be decomposed into different components for the flange direction, because the shear of the flange was not measured above the second floor. Analytically, the contribution of shear to the total displacement was 36% indicating that shear played a larger role in the flange direction response than in the web direction response.

Using the material information available prior to or on day of testing, the analysis model of NTW2 was found to predict the force-displacement response within 15-25% of the measured experimental results. The OpenSees prediction did not capture the stiffness of the wall as accurately as it did for NTW1; however, this was due to NTW2 having a different shear stiffness than NTW1 resulting from minimizing the amount of longitudinal reinforcement in the boundary elements of the flange. Overall, the web direction force-displacement response was predicted within 10% of the experimental response, while the flange direction response was over predicted by as much as 25% at some peak displacements. Similar trends were reflected when the response of the wall to the multidirectional load paths were compared to the experimental results. In the web direction, the analysis predicted the forces within 5 to 10 %, while in the flange direction the analysis over predicted the lateral force resistance by as much as 25%.

Modeling the shear lag effects and shear response of NTW2 based on the observed NTW1 response and the observed difference in the shear stiffness between those of NTW2 and NTW1 affected the results in two ways. First, NTW2 showed a stiffer shear deformation response in the web and flange directions than that used in the OpenSees analysis, leading to under prediction of lateral force resistance in the web direction. Second, the increased shear stiffness of the flange due to the distributed longitudinal reinforcement decreased the effects of shear lag in NTW2, thereby increasing the stiffness of the wall in the flange-in-tension direction loading than that expected from the OpenSees results. The decreased effects of shear lag in NTW2 also led to the over prediction of the flange direction response, due to the under prediction of damage to the flange tips.

7.2.3 Local Responses

Accuracy of the analysis models cannot be sufficiently evaluated based only on the comparison of global responses. Appropriate local response parameters should also be examined. Accurate simulation of the local response is important for two reasons. First, the local response provides a better measure of damage in the structure and in performance-based design methods, which are being more frequently used; design limits are specified using local response parameters. Second, accurate prediction of the local response is a better measure of the capability of the modeling approach. Predicting the local response accurately requires the analytical model

to properly model the various components of lateral displacement. Compensation of errors associated with predicting different displacement components may lead to accurate prediction of the global force-displacement of a structure; however, the local response will not be accurate.

For the rectangular walls, the various components of lateral displacement at the first panel level were examined. The analytical models for all the three walls over predicted the flexural deformation at the first panel level by 10 to 40%, depending on the top displacement. At the higher top displacements, percentage of error was smaller. Similar to global response observations, the strain penetration component was over estimated by the analytical model in RWC and RWS.

The local responses of NTW1 were well captured by the post-test analysis. The calculated neutral axis depth and section curvature at the wall base were satisfactory in both the web and flange directions loading upto the theoretical first yield displacements. The location of the neutral axis was found to be within 0.5 inch of the location determined from the recorded strains for both the web and flange directions, this corresponded to an error of approximately 5%. The strains in the longitudinal reinforcement were simulated within 10 to 20% by the analysis.

In comparison to NTW1, the local responses of NTW2 were not as well predicted. The strain profile and the neutral axis depth were accurately predicted in the flange-in-compression loading direction. The location of the neutral axis was predicted within one-half inch. This direction was the best simulated by the analysis due to not being influenced by the effects of shear lag. In the flange-in-tension direction, the location of the neutral axis was incorrectly predicted, and was off by as much as 10 inches. Such a large error is misleading because it is due to the combination of the discrepancies in the shear deformation and shear lag effects. Improved simulation of these two effects would likely have increased the accuracy of the local response to be similar to that observed for the post-test analysis of NTW1. The inadequate simulation of the shear lag effects and shear deformation primarily led to relatively poor prediction of the local responses in that direction. The post-test analysis of NTW1 and accurate prediction of the flange-in-compression response of NTW2 indicate that, when the shear lag and shear deformation are accurately simulated, the prediction of global and local responses of non-rectangular walls will be greatly improved when the modeling technique used in this study is adopted.

7.3 Recommendations for Modeling Structural Walls

Based on the investigation in this report, the following recommendations are made for the simulation of structural walls and wall systems subjected to multidirectional or seismic loading:

- Beam-column elements with fiber sections can accurately simulate the response of structural walls to multidirectional loading and capture the contribution of various lateral deformation components of rectangular and non-rectangular walls. The beam-column elements offer significant advantages due to their ease of use, computational efficiency, familiarity to engineering community, and ease of model construction.
- The effects of shear deformation and strain penetration should be accurately modeled in rectangular and nonrectangular walls. In addition, the effects of shear lag should be included in the analysis of nonrectangular walls. Various material models and sections are becoming available in OpenSees that enable these capabilities.
- The material models selected for the analysis dictate the accuracy of hysteretic simulation of the wall behavior. The modified Chang and Mander concrete model introduced in this report is appropriate for use in the simulation of structural walls subjected to multidirectional loads. Similarly the model proposed by Zhao and Sritharan (2007) is appropriate for accounting for the effects of strain penetration.
- The response of the wall will be significantly influenced by the splice details used for the longitudinal reinforcement, especially when the splice is located within the plastic hinge region. Therefore, the splices of the wall reinforcement should be appropriately modeled to accurately capture the global and local wall responses. Conventional lap splices may be modeled as an equivalent bar with varying cross sectional area along the splice length.

7.4 Recommendations for Future Research

The investigation presented in this report has addressed several challenges associated with the analytical simulation of nonrectangular walls subjected to multidirectional loading and in-plane response of rectangular walls that were detailed with different anchorages for the longitudinal reinforcement. A number of issues have become apparent through the course of this investigation, which deserve further investigation as detailed below.

- Shear lag, which is dictated by the shear stiffness of the free flange, has a significant influence on the stiffness of the nonrectangular walls in both the flange-in-tension and flange direction responses. A combination of analytical and experimental investigation on how the shear stiffness of the flange influences the shape of the shear lag function and development of a function that is appropriate for implementation in a fiber section would be appropriate.
- Development of a material model that is appropriate for simulating the shear-distortion of reinforced concrete walls and columns is necessary for OpenSees. It is also important to address the effects of flexure-shear interaction in this model development.
- More data are needed to refine the shape of the bar stress vs. loaded end slip for the bond slip material model. While the indication from this study is that the method used for capturing the strain penetration effects is appropriate, accuracy of the analysis can be improved by improving the stress vs. slip relationship.
- Since the design codes continue to permit the use of conventional lap splices in the plastic hinge region of concrete walls, a material model that has the ability to capture the local slip within the lap spliced region of the wall would be valuable.

References

[1] National Information Service for Earthquake Engineering, University of California, Berkeley. Aug. 2005 <http://nisee.berkeley.edu/images/servlet/EqiisDetail?slide=S3364>

[2] National Information Service for Earthquake Engineering, University of California, Berkeley. Aug. 2005 <http://nisee.berkeley.edu/images/servlet/EqiisDetail?slide=S343>

[3] National Information Service for Earthquake Engineering, University of California, Berkeley. Aug. 2005 <http://nisee.berkeley.edu/images/servlet/EqiisDetail?slide=S3309>

Abrams, D.P., "Laboratory Definitions of Behavior for Structural Components and Building Systems," ACI Special Publication 127, Vol. 127, No. 4, pp. 91-152, April 1991.

ACI Committee 318, [2002] "Building Code Requirements for Structural Concrete," American Concrete Institute, Farmington Hills, Michigan, 2002.

Ali, A., and Wight, J.K., "Reinforced Concrete Structural Walls with Staggered Opening Configurations Under Reversed Cyclic Loading," Report No. UMCE 90-05, Department of Civil Engineering, University of Michigan, Ann Arbor, April 1990.

Belbari, A. and Hsu, T. [1991] "Constitutive Laws of Concrete in Tension and Reinforcing Bars Stiffened By Concrete," *ACI Structural Journal*, Vol. 94, No. 4, pp. 465-474.

Bolander, J., and Wright, J. [1991] "Finite Element Modeling of Shear Wall Dominate Buildings" *Journal of Structural Engineering*, Vol. 117, No. 6, pp. 1719-1739

Bruggen, B. L. [2009] "Performance of T-shaped reinforced concrete shear walls under multi directional loading", Doctoral dissertation (under preparation), University of Minnesota, MN.

Chang, G.A., and Mander, J.B. [1994] "Seismic Energy Based Fatigue Damage Analysis of Bridge Columns: Part 1 – Evaluation of Seismic Capacity," NCEER Technical Report No. NCEER-94-0006, State University of New York, Buffalo, NY.

Chang, s. [2004] "Shear Lag Effect in Simply Supported Prestressed Concrete Box Girders" *Journal of Bridge Engineering*, Vol. 9, No. 2, pp. 178-184.

Cho, J.Y., Pincheira, A. (2006) "Inelastic Analysis of Reinforced Concrete Columns with Short Lap Splices Subjected to Reversed Cyclic Loads", *ACI Structural Journal*, V. 103, No.2, pp 280-290.

Coull, A. and Bose, B. [1975] "Simplified analysis of frame-tube structures," *Journal of the Structural Division*, Vol. 117, No. 12, pp. 3623-3644.

Coull, A., and Abu El Magd, S., [1980] "Analysis of wide flanged shear wall structures," *Reinforced Concrete Structures Subjected to Wind and Earthquake Forces,* ACI Special Publication 65, Paper No. SP63-23, pp. 575-607.

Dazio, A. [2006] "Some Aspects of RC Walls Modeling using Fiber Elements," *Proceedings of the NEES/UCSD Workshop Analytical Model of Reinforced Concrete Walls,* San Diego, CA December, 2006.

Defries-Skene, A. and Scordelis, A. [1964] "Direct stiffness solution for folded plates," *Journal of the Structural Division,* Vol. 90 No. 4, pp. 15-48.

Deshmukh, K., Thiagarajan, G., and Heausler, T. [2006] "Numerical Modeling of Seven Story Reinforced Model Using SAP," *NEES/UCSD Workshop on Analytical Modeling of Reinforced Concrete Walls*, San Diego, CA December 2006.

Evans, H., and Taherian, A. [1977] "The prediction of shear lag effect in box girders," *Proceedings of the Institution of Civil Engineers,* Part 2, 69, Thomas Telford Services Ltd., London pg. 1065-1075.

Fintel, Mark, "Performance of Buildings With Shear Walla in Earthquakes of the Last Thirty Years," PCI Journal, Precast/Prestressed Concrete Institute, Vol. 40, No. 3, pp. 62-80, May-June 1995.

Fischinger, M., and Isakovic, T. [2006] "NEES Blind Prediction Testing on RC Wall Building Slice, Multiple-Vertical-Line-Element Model," *Proceedings of the NEES/UCSD Workshop Analytical Model of Reinforced Concrete Walls,* San Diego, CA December, 2006.

Foutch, D. and Chang, P. [1982] "A shear lag anomaly," *Journal of Structural Engineering*, Vol. 108, No. 7, pp. 1653-1658.

Goodsir, W.J. [1985] "The Design of Coupled Frame-Wall Structures for Seismic Actions," Research Report 85-8, Department of Civil Engineering, University of Canterbury, Christchurch, New Zealand, August 1985.

Grange, S., Mazars, J., and Koronis, P. [2006] "Seven-Story Building Slice Earthquake Blind Prediction Contest: A Simplified Model Using Multi fiber Timoshenko Beams" *Proceedings of the NEES/UCSD Workshop Analytical Model of Reinforced Concrete Walls,* San Diego, CA December, 2006.

Hachem, M. [2006] "Earthquake Analysis of Seven-Story Shear Wall Building using ADINA," *NEES/UCSD Workshop on Analytical Modeling of Reinforced Concrete Walls,* San Diego, CA December 2006.

Haji-Kazemi, H. and Company, M. [2002] "Exact Method of Analysis of Shear Lag in Framed Tube Structures" *The Structural Design of Tall Buildings,* Vol. 11, pp. 375-388.

Johnson, B. M. "Longitudinal Reinforcement anchorage Detailing effects on RC shear wall Behavior", Master of Science Thesis, University of Minnesota, 2007, 391 pp.

Kelly, T. [2006] "A Blind Prediction Test of Nonlinear Analysis Procedures for Reinforced Concrete Shear Walls," *Bulletin of the New Zealand Society for Earthquake Engineering,* Vol. 40, No. 4. pp. 142-158.

Kelly, T. [2006] "NCEES Blind Prediction Test: Practitioner Entry From Holmes Consulting Group, New Zealand," *NEES/UCSD Workshop on Analytical Modeling of Reinforced Concrete Walls,* San Diego, CA December 2006.

Kwan AKH. 1996. "Shear lag in shear/core walls", Journal of Structural Engineering, ASCE 122(9): 1097-1104

Lefas, I.D., Kotsovos, M.D. (1990), "Strength and Deformation Characteristics of Reinforced Concrete Walls under Load Reversals", ACI Structural Journal, vol. 87, no. 6, November-December 1990, pp. 716-726.

Mander, J.B., Priestley, M.J.N., and Park, R., [1988] "Theoretical Stress-Strain Model for Confined Concrete," *Journal of Structural Engineering*, American Society of Civil Engineering, Vol. 114, No. 8, August 1988.

Massone, Leonardo M., and Wallace, John W., "Load Deformation Response of Slender Reinforced Concrete Walls," ACI Structural Journal, American Concrete Institute, Vol. 101, No. 1, January-February 2004.

Martinelli, P., and Filippou, F. [2006] *"Numerical Simulation of the Shake Table Test of a Full Scale, Seven Story Shear Wall Specimen," Proceedings of the NEES/UCSD Workshop Analytical Model of Reinforced Concrete Walls, San Diego,* CA December, 2006.

Martinelli, L. [2008] "Modeling Shear-Flexure Interaction in Reinforced Concrete Elements Subjected to Cyclic Lateral Loading", *ACI Structural Journal,* V. 105, No. 6, pp 675-684.

Mazzoni, S., McKenna, F., Scott, M.H., Fenves, G.L. [2006] "Open System for Earthquake Engineering Simulation," Pacific Earthquake Engineering Research Center, University of California, Berkeley, California, Ver. 1.7.4.

Moaveni, B., He, X., Conte, J., and Restrepo, J. [2006] "System Identification of a Seven-Story Reinforced Concrete Shear Wall Building Slice Tested on the UCSD-NEES Shake Table," *NEES/UCSD Workshop on Analytical Modeling of Reinforced Concrete Walls,* San Diego, CA December 2006.

Moffatt, K., and Dowling, P., [1975] "Shear lag in steel box girder bridges," *The Structural Engineer,* Vol. 53, No. 10, pp. 439-448.

Narina, Jung (2007), "Preliminary design of Shear Wall specimens tested with MAST", Master of Science Thesis, University of Minnesota, 2007, 257 pp.

Neuenhofer, A., and Filippou, F.C. [1997] "Evaluation of Nonlinear Frame Finite-Element Models," *ASCE Journal of Structural Engineering*, Vol. 123, No. 7, pp. 958-966.

Oesterle, R.G., Aristizabal-Ochoa, J.D., Fiorato, A.E., Russel, H.E., and Corley, W.G., "Earthquake Resistant Structural Walls – Tests of Isolated Walls – Phase II," Report to the National Science Foundation, Construction Technology Laboratories, Portland Cement Association, Skokie, Illinois, October 1979.

Oesterle, R.G., Fiorato, A.E., Johal, L.S., Carpenter, J.E., Russel, H.E. and Corley, W.G., "Earthquake Resistant Structural Walls – Tests of Isolated Walls," Report to the National Science Foundation, Construction Technology Laboratories, Portland Cement Association, Skokie, Illinois, November 1976.

Open System for Earthquake Engineering Simulation (OpenSees) User Manual (1.7.5), 2007, http://opensees.berkeley.edu/.

Orakcal, K., and Wallace, J.W. [2006] "Flexural Modeling of Reinforced Concrete Walls – Experimental Verification," *ACI Structural Journal*, Vol. 103, No. 2, pp. 196-205.

Orakcal, K., Wallace, J.W., and Conte, J.P., [2004] "Nonlinear Modeling and Analysis of Slender Reinforced Concrete Walls*," ACI Structural Journal,* Vol. 101, No. 5, pp. 688-698.

Palermo, D., and Vecchio, F.J. [2004] "Compression Field Modeling of Reinforced Concrete Subjected to Reversed Loading: Verification," *ACI Structural Journal*, Vol. 101, No. 2, pp.155-164.

Pang, X. and Hsu, T. [1992] "Constitutive Laws of Reinforced Concrete in Shear," Research Report UHCEE92-1, Department of Civil Engineering, University of Houston, TX.

Park, R., and Paulay, T. [1975] "Reinforced Concrete Structures," New York: John Wiley and Sons.

Paulay, T. and Priestley, M.J.N., "Seismic Design of Reinforced Concrete and Masonry Buildings," John Wiley and Sons, New York, 1992.

Paulay, T., Priestly, M.J.N., and Synge, A.J., "Ductility in Earthquake Resisting Squat Shear Walls," Proceedings ACI Journal, American Concrete Institute, Vol. 79, No. 4, pp. 257-269, August 1982.

Petrangeli, M.; Pinto, P. E., and Ciampi, V., "Fiber Element for Cyclic Bending and Shear of RC Structures, I: Theory," Journal of Engineering Mechanics, V. 125, No. 9, 1999, pp. 994-1001.

Pilakoutas K, Elnashai, AS., “Cyclic behaviour of RC cantilever walls, Part I: Experimental results”, ACI Structural Journal 1995; 92(3), pp.271–281.

Riva, P., Meda, A., and Giuriani E., “Cyclic behaviour of a full scale RC structural wall”, Engineering Structures, V.25 (2003), pp. 835-845.

Shiu, K.N., Daniel, J.L., Aristizabal-Ochoa, J.D., Fiorato, A.E., and Corley, W.G., “Earthquake Resistant Structural Walls – Tests of Walls With and Without Openings,” Report to the National Science Foundation, Construction Technology Laboratories, Portland Cement Association, Skokie, Illinois, July 1981.

Sittipunt, C., and Wood, S.L. [1993] “Finite Element Analysis of Reinforced Concrete Shear Walls,” Report to the National Science Foundation, Department of Civil Engineering, University of Illinois at Urbana-Champaign, December 1993.

Song, Q., and Scordelis, A., [1990a] “Formulas for shear lag effect of T-, I-, and box beams,” Journal of Structural Engineering, Vol. 116, No. 5, pp. 1306-1318.

Song, Q., and Scordelis, A., [1990b] “Shear lag analysis of T-, I-, and box beams,” *Journal of Structural Engineering*, Vol. 116, No. 5, pp. 1290-1305.

Sritharan, S. "Analysis of Concrete Bridge Joints Subjected to Seismic Actions," Doctoral Dissertation, University of California, San Diego, California, 1998, 407 pp.

Sritharan, S., Priestley, N., and Seible, F. "Nonlinear Finite Element Analyses Of Concrete Bridge Joint Systems Subjected To Seismic Actions," Finite Elements in Analysis and Design. V. 36, 2000, pp. 215-233.

Tasnimi AA (2000). “Strength and deformation of mid-rise shear walls under load reversal”. Engineering Structures, Vol.22, pp.311–322.

Taucer, Fabio F., E. Spacone, and F. C. Filippou. [1991] “A Fiber Beam-Column Element for Seismic Response Analysis of Reinforced Concrete Structures. Report No. UCB/EERC-91/17,” Earthquake Engineering Research Center, College of Engineering, University of California, Berkeley.

Thomsen, J.H., and Wallace, J.W. [1995] “Displacement-Based Design of RC Structural Walls: An Experimental Investigation of Walls with Rectangular and T-Shaped Cross-Sections,” Report to the National Science Foundation, Department of Civil Engineering, Clarkson University, Potsdam, New York.

Zhang, Y.H. & Wang, Z.H. (2000), “Seismic behaviour of reinforced concrete shear walls subjected to high axial load”, ACI Structural Journal, vol. 97, no. 5, pp. 739-750.

Zhao, J., and Sritharan, S. [2007] "Modeling of Strain Penetration Effects in Fiber-Based Analysis of Reinforced Concrete Structures," *ACI Structural Journal*, Vol. 104, No. 2, pp. 133-141.

APPENDIX - A
Effects of Strain Penetration

Presented in this appendix in a paper format are the significance of strain penetration and the modeling technique that was developed in the PreNEESR project to account for the strain penetration effects in fiber-based analysis of concrete members. This analytical technique was implemented in OpenSees (as Bond_SP01 material model), which is being currently used by several users.

MODELING OF STRAIN PENETRATION EFFECTS IN FIBER-BASED ANALYSIS OF REINFORCED CONCRETE STRUCTURES

Jian Zhao and Sri Sritharan

(*This manuscript has been published in the ACI Concrete Journal in 2007*)

Biography: ACI member **Jian Zhao** is an assistant professor in the Department of Civil Engineering and Mechanics at the University of Wisconsin at Milwaukee, WI. He received his BS and MS from Tongji University, Shanghai, China and PhD from the University of Minnesota, Minneapolis, MN and served as a post-doctoral researcher at Iowa State University, Ames, IA. His research interests include behavior of reinforced concrete structures and earthquake engineering.

ACI member **Sri Sritharan** is an associate professor in the Department of Civil, Construction and Environmental Engineering at Iowa State University. He received his PhD from the University of California at San Diego, CA. He is the secretary of ACI Committee 341 (Earthquake-Resistant Concrete Bridges) and an associate member of ACI Committee 445 (Shear and Torsion). His research interests include seismic design of concrete structures and earthquake engineering.

ABSTRACT

In flexural concrete members, strain penetration occurs along longitudinal reinforcing bars that are fully anchored into connecting concrete members, causing bar slip along a partial anchorage length and thus end rotations to the flexural members at the connection intersections. Ignoring the strain penetration in linear and nonlinear analyses of concrete structures will underestimate the deflections and member elongation, and overestimate the stiffness, hysteretic energy dissipation capacities, strains and section curvature. Focusing on the member end rotation due to strain penetration along reinforcing bars anchored in footings and bridge joints, this paper introduces a hysteretic model for the reinforcing bar stress vs. slip response that can be integrated into fiber-based analysis of concrete structures using a zero-length section element. The ability of the proposed hysteretic model to capture the strain penetration effects is demonstrated by

simulating the measured global and local responses of two concrete columns and a bridge tee-joint system. Unless the strain penetration effects are satisfactorily modeled, it is shown that the analysis of concrete structures will appreciably underestimate the local response parameters that are used to quantify structural damage.
Keywords: reinforced concrete; seismic analysis; strain penetration; fiber analysis; bond slip; column; wall; bridge bent; OpenSees.

INTRODUCTION

There is a growing demand for developing reliable numerical simulation tools that can assist with improving safety of concrete buildings and bridges under extreme lateral loads, as well as advancing seismic design of these structures by addressing multiple performance limits. For reinforced concrete structures subjected to moderate to large earthquakes, capturing the structural response and damage states require accurate modeling of localized inelastic deformations occurring at the member end regions as identified by shaded areas 1 and 2 in Figure A.1. These member end deformations consist of two components: 1) the flexural deformation that causes inelastic strains in the longitudinal bars and concrete, and 2) the member end rotation, as indicated by arrows in Figure A.1, due to reinforcement slip. This slip, which is characteristically different from that which occurs to the entire bar embedment length due to poor anchorage condition,[1] results from strain penetration along a portion of the fully anchored bars into the adjoining concrete members (e.g., footings and joints) during the elastic and inelastic response of the structure. As demonstrated by Sritharan et al.[1], ignoring the strain penetration component may appear to produce satisfactory force-displacement response of the structural system by overestimating the flexural action for a given lateral load. However, this approach will appreciably overestimate the strains and section curvatures in the critical inelastic regions of the member, thereby over predicting the structural damage. These strain increases do not necessarily lead to a significant increase in the moment resistance at the section level because the increase in the resultant force magnitudes will be compensated by reduction in the moment arms. As a result, the force-displacement response of the member appears to be unaffected. Since the objective of the finite element analyses is to produce satisfactory global and local responses, an accurate representation of the strain penetration effects is critical when developing finite element models of concrete structures.

In beam-column joints of building frames, plastic hinges are designed to form at the beam ends (see shaded area 2 in Figure A.1). As a result, the beam longitudinal bars experience the bond slip due to strain penetration that occurs along the bars into the joint. In this case, the beam bar anchorage can be increased only by increasing the column width. Furthermore, the beam bars embedded in the interior joints of a frame structure responding to earthquake loads will be subjected simultaneously to tension at one end and compression at the other end. This condition, combined with the effects of load reversals, will progressively damage bond along the entire length of the beam bar within the joint, which is likely to cause slippage of the entire bar within the joint. Hence, the bond-slip of beam bars within the joint is expected to be relatively more sensitive to the concrete strength, column width, and joint force transfer mechanism than the vertical bars anchored in footings and bridge joints.

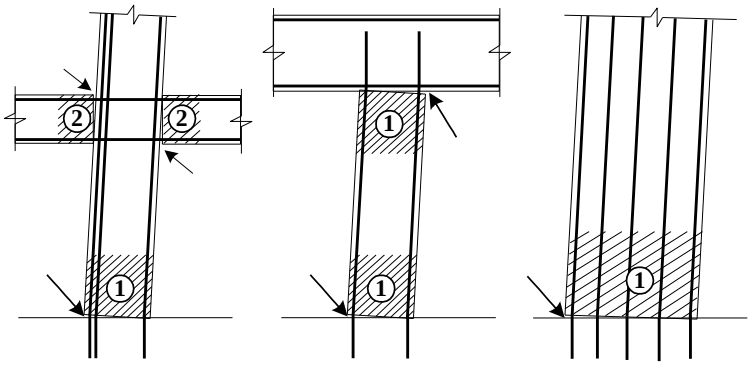

Figure A.1 Schematic representation of typical inelastic regions in well-designed concrete structures

Unlike the beam bars anchored into the interior building joints, the column and wall longitudinal bars extended into footings and bridge joints are typically designed with generous anchorage length (shaded area 1 in Figure A.1). Furthermore, the bars anchored into footings are often detailed with 90° hooks at the ends to improve constructability. In these cases, the embedded longitudinal bars that are loaded only at one end experience slip along a portion of the anchorage length and utilize end bearing to transfer forces when they are subjected to compression.[2] Hence, the monotonic and cyclic behavior of anchored bars (e.g., bar stress vs. slip responses) at the intersection between a flexural member and a footing/bridge joint is expected to be different from that occurring at the building joint interfaces. For these reasons, the hysteretic bar stress vs. slip response of these bars anchored in footings and bridge joints will be

relatively more stable and dependable. This hypothesis was evident in the cyclic load tests documented by Lin on a few bars that were fully anchored in concrete with straight and hooked ends.[3]

RESEARCH SIGNIFICANCE

A significant effort has been invested to model the bond slip of beam bars anchored into building joints while studies on the strain penetration effects of longitudinal bars into footings and bridge joints are very scarce. Recognizing that the member end rotation at the footing and bridge joint interfaces can be reliably simulated using zero-length section elements, this paper proposes constitutive models for the bar slip due to strain penetration. Using two cantilever columns and a bridge T-joint system, it is shown that fiber-based analyses incorporating the zero-length section elements with the proposed constitutive model can accurately capture both the global and local responses of concrete structures.

BACKGROUND

Strain penetration that represents gradual transferring of longitudinal bar forces to the surrounding concrete in the connecting member is described in Figure A.2. The loaded end of the anchored bar exhibits slip at the connection interface resulting from the accumulative strain difference between the bar and concrete within the connecting member. As a result, a crack forms and an end rotation occurs to the flexural member at the connection interface.

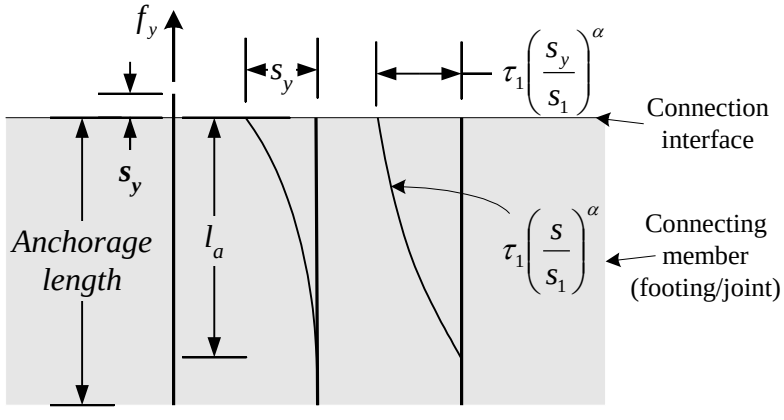

Figure A.2 Bond-slip due to strain penetration of an adequately anchored bar at yield

The strain penetration and the associated end rotation greatly influence the elastic and inelastic flexural deformations localized strains and curvature in the critical regions, and stiffness of the flexural members. For example, experimental studies have generally reported that the end rotation due to strain penetration contributes up to 35 percent to the lateral deformation of flexural members[4-6]. Ignoring the strain penetration also affects the energy dissipation capacity of the members to a lesser extent. Nonetheless, the strain penetration effects have been frequently neglected in analyses of concrete structures because, as noted above, it may not significantly affect the overall force-displacement response

Presented below is a brief discussion on the available modeling methods for the bond-slip rotation resulting from strain penetration, followed by details of the analytical method used in this study.

Previous Analytical Methods

Researchers have made significant efforts to model the bond slip of bars anchored into building joints. These efforts range from establishing the local bond stress vs. slip relation[7-11] to quantifying the bond slip effects at the member level through various analytical means.[12-17] General 3-D solid finite element models incorporating gap/interface elements have been used to capture the interaction between anchored longitudinal steel bars and surrounding concrete.[12-15] In these studies, local bond stress vs. slip models such as that developed by Eligehausen et al.[7] were used to describe the constitutive relation of the interface elements. While the suitability of modeling concrete as a homogeneous material at a dimension as small as the bar deformation needs further investigation, the required fine mesh of elements makes this analytical approach prohibitively expensive. Hence, such a general finite element analysis cannot be extended for the simulation of structural responses.

To lower the computational cost, special fiber-based beam-column elements have been formulated that consider the slippage of the reinforcing bars in the state determination at a section level.[17-19] The reinforcement slippage is quantified by analyzing the bar anchorage in the concrete between the adjacent integration points of the beam-column element. Although this special element formulation combines the simplicity of the fiber-based concept (that is discussed in the next section) and accuracy of the finite element analysis, modeling of strain penetration effects is still expensive due to the extensive discretization required to satisfactorily capture the behavior of reinforcing bars embedded in concrete. This makes the structure-level simulation

inefficient. Furthermore, this analysis approach has been shown to adequately predict the force-displacement response of flexural members; however, its ability to predict section-level responses (e.g., strains and curvature) has not been demonstrated.

With referenced to the above mentioned approaches, it should be noted that some controversy has arisen. The local bond-slip models utilized in these approaches (e.g., Eligehausen et al.) were developed using short reinforcing bars anchored in concrete, allowing the bars to slip when they were subjected to small strains. Shima et al. (1997a and 1987b) and Mayer and Eligehausen (1998) have suggested that bond condition of these bars may not be similar to that of fully anchored bars that experience high inelastic strains.

On a macroscopic level, nonlinear rotational springs have been used at the end of beam-column elements to include the member end rotation due to strain penetration effects.[20, 21] The monotonic properties of the rotational springs are typically established using empirical methods, and the modified Takeda model[20] has been used to describe the cyclic behavior of the rotational springs. Despite the simplicity, the strain penetration effects can't be accurately represented using the rotational springs due to their empirical nature.

The spring model concept has been further advanced by introducing super-elements to model the member end rotation in 2-D frame analyses, in which uniaxial springs are used to represent the slippage of the outermost longitudinal bars in the section.[22, 23] The constitutive model (i.e., bar force vs. slip relationship) for the uniaxial springs is established separately by analyzing the anchorage of the extreme bars. In this analysis, the bond stress distributions along the elastic and inelastic portions of the anchored bar are assumed as adopted by Ciampi et al.,[24] from which a multi-linear bar stress distribution along the anchorage length is established. Using a theoretical stress-strain model for the reinforcing steel, the corresponding strain distribution and thus the slip of the bar at the loaded end are determined. The member end rotation is found by dividing the slip determined for the extreme tension reinforcing bar by the distance to the location of the reinforcement from the neutral axis. This distance, which is determined through a section analysis, is usually assumed to be constant and independent of the bar slip. The monotonic curve established for the moment vs. end rotation relation is often simplified as a piecewise linear curve, and multi-linear unloading-reloading rules are specified so that the frame analyses can be performed under cyclic loading.

The deficiencies of the spring model concept may be attributed to the following: 1) the assumed bond stress distribution along the bar is not experimentally justified; 2) the bond slip estimated at the loaded end of the bar is strongly influenced by the theoretical stress-strain model used for the reinforcing steel; and 3) end rotations are underestimated at small displacements due to the use of a constant neutral axis depth. In addition, the spring models may not be reliably extended to capture the bond-slip rotation of a generalized flexural member (that has an arbitrary cross-section and is subjected to bi-directional loading).

Fiber-based Analysis

The general fiber analysis concept is briefly reviewed prior to introducing its application to model the strain penetration effects in reinforced concrete flexural members. In this concept, the flexural member is represented by unidirectional steel and concrete fibers, making the description of the corresponding material models relatively easy. Because the steel and concrete fiber responses are specified in the direction of the member length, the fiber analysis can be used to model the behavior of flexural members regardless of the cross-sectional shape or the direction of lateral loading.

The fiber analysis typically follows the direct stiffness method, in which solving the equilibrium equation of the overall system yields the nodal displacements.[19, 20] After the element displacements are extracted from the nodal displacements, the element forces are determined and the member stiffness is upgraded, based on which the global stiffness matrix is assembled for the next time step. The stiffness and forces of the fiber-based elements are obtained by numerically integrating the section stiffness and forces corresponding to a section deformation (i.e., axial strain $\bar{\varepsilon}$ and curvature φ).

The section deformation is calculated through interpolating the element end deformations (i.e., displacement and rotation) at the integration points. From the section deformation, the strain in each fiber (ε) is obtained using the plane sections remain plane assumption. For example, the fiber strain is calculated using $\varepsilon = \bar{\varepsilon} + \varphi y$, where y is the distance of the fiber from the centroid of the section. The fiber stress and stiffness are updated according to the material models, followed by upgrading of the section force resultant and the corresponding stiffness. The neutral axis position of the section at an integration point is determined through an iterative procedure, which balances the force resultants at the section level as well as at the member level as shown in Figure A.3a.

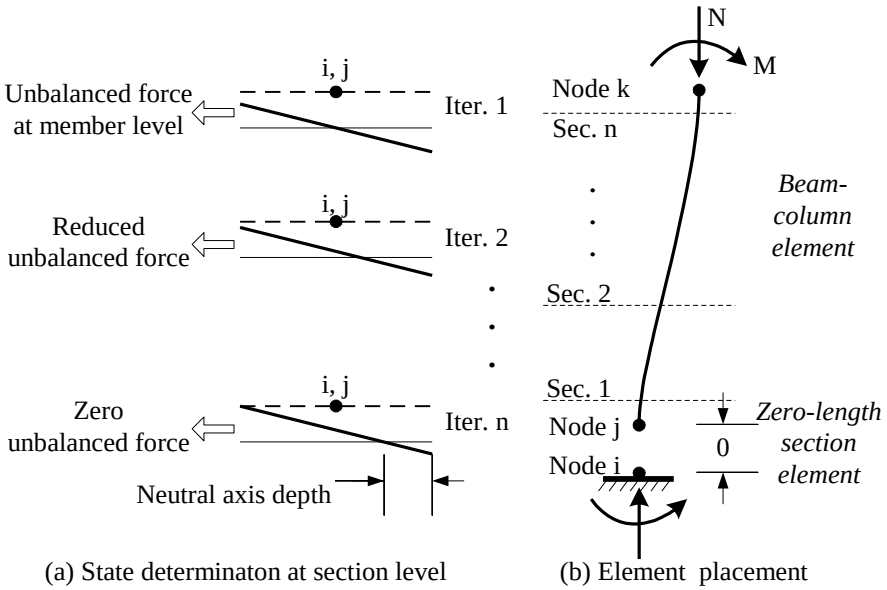

Figure A.3 Fiber-based modelling of strain penetration effects

Although shear-flexure interaction is not typically integrated in the element formulation and the built-in plane-section assumption may not be appropriate for shear-dominant member behavior, fiber analysis remains the most economic and accurate means to capture seismic behavior of concrete structures.[19, 20] In addition, if the member end rotation due to bond slip resulting from strain penetration effects can be accurately modeled, fiber analysis has the potential to accurately predict the localized structural responses such as bar strains and section curvature. Using the zero-length section element available in OpenSees (Open System for Earthquake Engineering Simulation),[26] it is shown in this paper that the end rotation due to bond slip can be accurately accounted for in fiber-based analysis of concrete structures.

OpenSees is a collection of application program interfaces and various elements, material models, solution procedures, and equation solvers bound together with a language interpreter. The framework is meant to represent a set of modules that are contributed by developers and can be used to build application programs (executables). OpenSees was preferred in the study reported in this paper because it is an open source package and is being increasingly used by the earthquake engineering research community.

Zero-Length Section Element

A zero-length section element in OpenSees contains one section (that corresponds to one integration point), which defines the stress resultant–deformation response of that element. To

place a zero-length section element, a duplicate node is required between a fiber-based beam-column element and an adjoining concrete element as shown in Figure A.3b. The translational degree-of-freedom of this new node (node *j* in Figure A.3b) should be constrained to the other node (node *i* in Figure A.3b) to prevent sliding of the beam-column element under lateral loading because the shear resistance is not included in the zero-length section element.

The zero-length section element available in OpenSees is assumed to have a unit length such that the element deformations (i.e., elongation and rotation) are equal to the section deformations (i.e., axial strain and curvature). Because of the unit-length assumption, a stress vs. displacement relationship is required for each fiber to upgrade the forces and stiffness of the section element. Zero-length section elements have been generally used for section analyses, which calculate the curvature of a section corresponding to an applied moment. Described below is a method that uses a zero-length section element to capture the member end rotation resulting from the strain penetration effects.

PROPOSED METHOD

As shown in Figure A.3b, the zero-length section element is placed at the intersection between the flexural member and an adjoining member representing a footing or joint. The material model for the steel fibers in the section element represents the bar slip instead of strain for a given bar stress. A material model should also be established for the concrete fibers of the zero-length section element. Because of the fiber representation of the section at the member interface, the proposed approach models the bond slip of the longitudinal bars individually during the state determination of the zero-length section element. Hence, this approach is amenable to the fiber analysis concept and allows the strain penetration effects to be captured during flexural analysis of concrete members regardless of the cross-sectional shape and direction of the lateral load.

The concept of using a zero-length section element to capture strain penetration effects is equally applicable to beam bars anchored into interior buildings joints. This application of the proposed concept requires further research and is beyond the scope of this paper. Focusing on capturing the bond slip due to strain penetration along fully anchored bars into concrete footings and bridge joints suitable material models for the zero-length section element are presented below.

Material Model for Steel Fibers

Given the anchorage condition of the reinforcing bars into footings and bridge joints, the material model for the steel fibers in the zero-length section element must accurately represent the bond slip of fully anchored bars loaded only at one end. To minimize the error in the material model for the steel fibers, the previously discussed approaches involving local bond-slip and steel stress-strain models were not preferred to establish the bar stress vs. loaded-end slip relationship. Instead, a theoretical model based on measured bar stress and loaded end slip from testing of steel reinforcing bars that were anchored in concrete with long embedment length is advocated in this paper.

Monotonic Curve

It is proposed that the monotonic bar stress (σ) vs. loaded-end slip (s) relationship can be described using a straight line for the elastic region and a curvilinear portion for the post-yield region as shown in Figure A.4. The slope of the straight line was taken as K, whereas the curvilinear portion was represented by,

$$\tilde{\sigma} = \frac{\dfrac{\tilde{s}}{\mu - \tilde{s}}}{\left[\left(\dfrac{1}{\mu \cdot b}\right)^{R_e} + \left(\dfrac{\tilde{s}}{\mu - \tilde{s}}\right)^{R_e}\right]^{1/R_e}}, \tag{A.1}$$

where $\tilde{\sigma} = \dfrac{\sigma - f_y}{f_u - f_y}$ is the normalized bar stress, $\tilde{s} = \dfrac{s - s_y}{s_y}$ is the normalized bar slip, $\mu = \dfrac{s_u - s_y}{s_y}$ is the ductility coefficient, b is the stiffness reduction factor, which represents the ratio of the initial slope of the curvilinear portion at the onset of yielding to the slope in the elastic region (K), f_y and f_u are, respectively, the yield and ultimate strengths of the steel reinforcing bar, and s_y and s_u correspond to the loaded-end slips when bar stresses are f_y and f_u, respectively.

According to Eq. (A.1), as the bar stress approaches the yield strength, ($\tilde{s}/\mu - \tilde{s}$) becomes zero, the slip approaches the yield slip (s_y), and the slope of the curve approaches the initial slope (bK). Furthermore, as the bar stress approaches the ultimate strength, ($\tilde{s}/\mu - \tilde{s}$) becomes infinity, the slip approaches the ultimate slip (s_u), and the slope of the curve approaches zero. To

maintain a zero slope near the ultimate strength of the bar, the value of factor R_e should be slightly greater than one and was taken as 1.01 for the analyses reported in this paper. The remaining parameters that are required to construct the bar stress vs. slip response envelope are s_y, s_u and b.

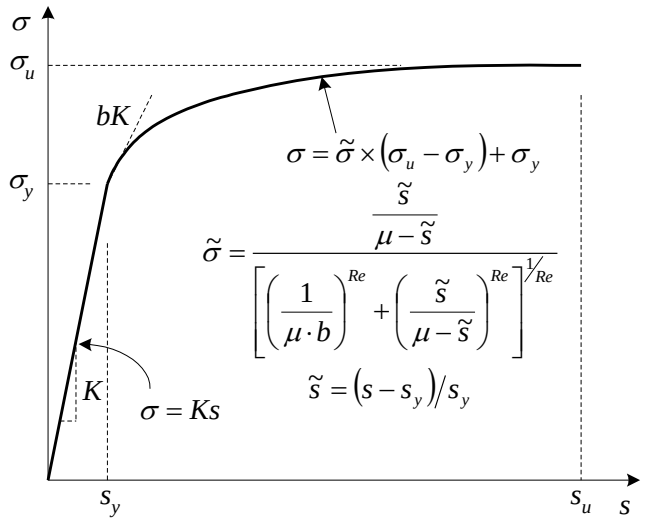

Figure A.4 Envelope curve for the bar stress vs. loaded-end slip relationship

The pull-out test data available in the literature for deformed steel reinforcing bars were used to establish a suitable value for s_y. Ensuring that the bar had sufficient anchorage during testing, only the pull-out tests that used a bar embedment length equal to or greater than the minimum anchorage length ($l_{a,\min}$) specified by Eq. (A.2) were selected for this purpose (see Table A.1). The minimum anchorage length was determined equating the bar stress to σ_y at the loaded end and assuming an average bond stress of $1.75\sqrt{f_c'}$ (where f_c' is the concrete compressive strength in MPa) over $l_{a,\min}$. This average bond stress, which is comparable to that used by Lowes and Altoontash,[23] was established assuming a linear slip distribution along $l_{a,\min}$ and the local bond stress reaching a maximum value of $2.5\sqrt{f_c'(\text{MPa})}$ at the loaded end.[7] Accordingly,

$$l_{a,min} = \frac{f_y \pi d_b{}^2/4}{1.75\sqrt{f_c'}\pi d_b} = \frac{1}{7}\frac{f_y}{\sqrt{f_c'}} d_b, \qquad \text{(A.2)}$$

where d_b is the bar diameter (mm).

Given the different values for variables d_b, f_y, and f_c' in the tests summarized in Table A.1 and the dependency of the yield slip on these variables, Eq. (A.3) was established from a linear regression analysis as represented in Figure A.5 to determine the suitable value for s_y.

$$s_y(mm) = 2.54\left(\frac{d_b(mm)}{8437}\frac{f_y(MPa)}{\sqrt{f_c'(MPa)}}(2\alpha+1)\right)^{1/\alpha} + 0.34, \quad \text{(A.3)}$$

where α is the parameter used in the local bond-slip relation as illustrated in Figure A.2 and was taken as 0.4 in this study in accordance with CEB-FIP Model Code 90 (MC90).[33]

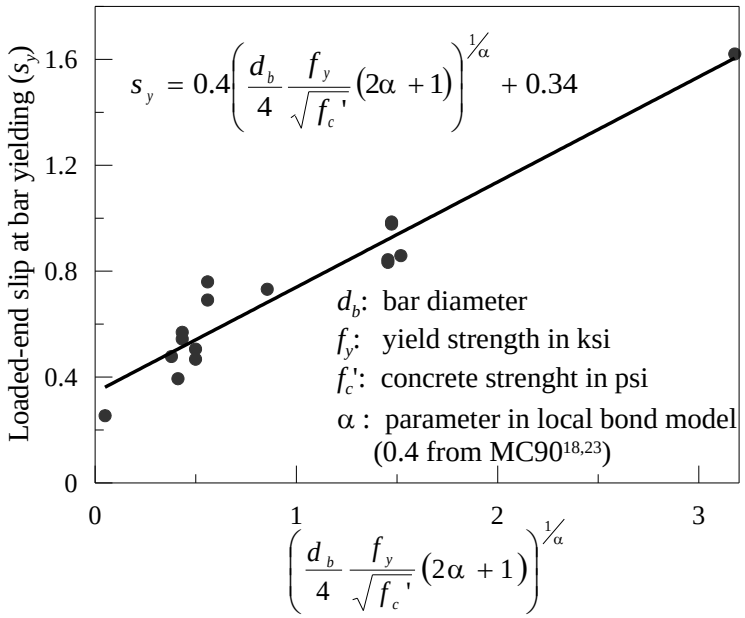

Figure A.5 Determination of bar slip at the yield strength

As observed for the yield slip, it is conceivable that the loaded-end slip at the bar ultimate strength (s_u) and the stiffness reduction factor (b) are also functions of steel and concrete properties as well as the bar diameter. However, sufficient experimental data were not available to establish these functions from regression analyses; most of the tests summarized in Table A.1 were terminated soon after reaching the yield slip. The limited test information available in the literature indicated that $s_u = 30 \sim 40 s_y$ and $b = 0.3 \sim 0.5$ would be appropriate. Furthermore, in the absence of sufficient experimental data, it is suggested that Eqs. (A.1) and (A.3) be used for sufficiently anchored bars with both straight and hooked ends under tension and compression loads. This suggestion should not introduce any significant error in the simulation of flexural members subjected to low axial loads (e.g., bridge columns and concrete walls in low- and mid-

rise buildings). As more data become available, appropriate empirical equations suitable for defining s_u and b can be developed.

Table A.1–Results of pull-out tests of deformed steel reinforcing bars

ID	f_c' (MPa)	d_b (mm)	l_a (mm)	f_y (Mpa)	s_y (mm)	$l_{a,\,\min}$ (mm)	Reference
1	37.6	10.2	673.1	403.3	0.3	95.5	Maekawa et al.[28]
2	19.6	19.1	762.0	350.3	0.5	215.4	Shima et al.[29]
3	19.6	19.1	762.0	610.2	0.9	375.3	
4	19.6	19.1	762.0	819.8	1.6	504.2	
5	28.6	12.7	266.7	708.8	0.5	240.4	Mathey et al.[30]
6	28.6	12.7	266.7	708.8	0.5	240.4	
7	26.1	12.7	355.6	708.8	0.8	251.6	
8	26.1	12.7	355.6	708.8	0.7	251.6	
9	32.1	12.7	431.8	708.8	0.6	227.1	
10	32.1	12.7	431.8	708.8	0.5	227.1	
11	27.7	25.4	711.2	537.8	1.0	370.7	
12	27.7	25.4	711.2	537.8	1.0	370.7	
13	28.0	25.4	863.6	537.8	0.8	368.8	
14	28.0	25.4	863.6	537.8	0.8	368.8	
15	28.8	19.1	609.6	438.5	0.4	222.6	Ueda et al.[31]
16	32.5	25.4	635.0	468.8	0.7	298.2	Viwathanatepa et al.[32]

The applicability of Eq. (A.1) to describe the bar stress vs. loaded-end slip response under monotonic loading is demonstrated in Figure A.6 by comparing experimental data from two bar pull-out tests with the corresponding theoretical curves. The parameters used for establishing the theoretical curves are included in the figure, for which the yield slips (s_y) were obtained using Eq. (A.3). The ultimate slip (s_u) reported in Figure A.6a was a measured value while s_u included in Figure A.6b was an estimated value based on the above recommendation. The b values were chosen in recognition of the observed initial slope of the hardening portion of the curves. A good agreement is seen between the theoretical curves and experimental data, indicating that Eq. (A.1) is capable of capturing the strain penetration effects in the analytical simulation of concrete flexural members.

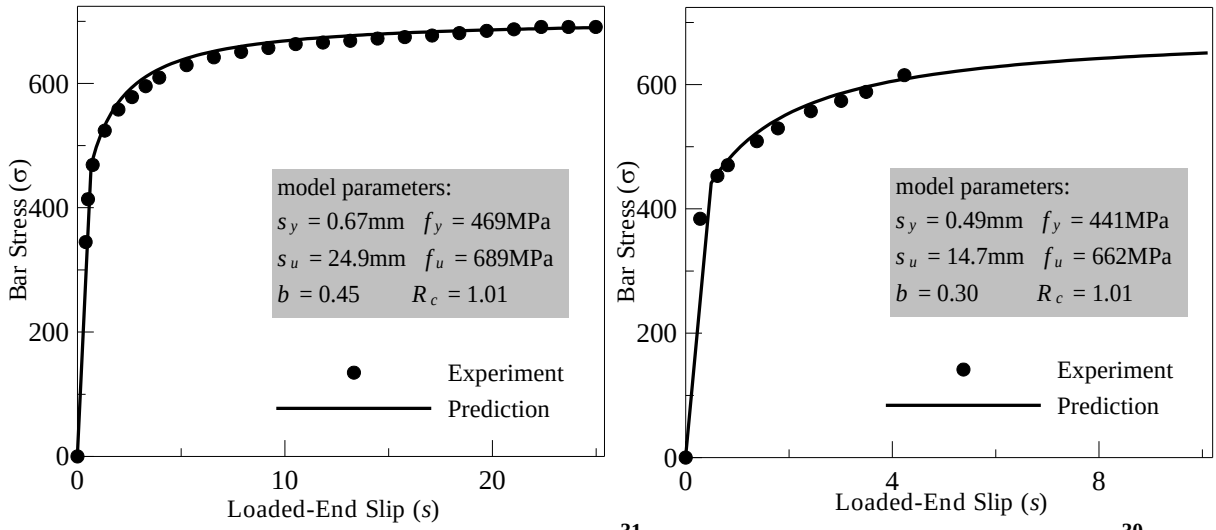

(a) Specimen #3 in Viwathanatepa et al.[31] **(b) Specimen S64 in Ueda et al.[30]**

Figure A.6–Experimental and analytical response of bar stress vs. loaded-end slip

Hysteretic Rules

To employ the proposed model for capturing the strain penetration effects in flexural members subjected to reversed cyclic loading, suitable hysteretic rules must be established for the bar stress vs. slip relationship. Using the experimental data reported by Lin[3] on cyclic response of a few well-anchored bars and observed cyclic response of columns reported in the next section, the following hysteretic rules were established (see Figure A.7 for a graphical description):

- Prior to unloading, the maximum and minimum bar stresses and the corresponding slips are compared with the history values, and the variables (*maxrs*, *maxrl*) and (*minrs*, *minrl*) as indicated in Figure A.7 are updated if necessary.
- Unloading and reloading in any direction follows the linear elastic portion of the monotonic curve if the bar slip prior to unloading has never exceeded $+s_y$ or $-s_y$.
- When the bar slip has exceeded $+s_y$ or $-s_y$, the unloading in any direction follows a straight line with the elastic slope K until the bar stress reaches zero. The intersection between the straight unloading line and the s-axis is located as (*rsvg*, 0).
- A reloading path as defined by Eq. (A.4) is followed from the intersection point (*rsvg*, 0).

$$\sigma = \sigma^{*} maxrl \text{ or } \sigma = \sigma^{*} minrl \qquad \text{(A.4a)}$$

$$\sigma^* = \frac{\dfrac{s^*}{s_{uy} - s^*}}{\left[\left(\dfrac{1}{s_{uy}}\right)^{R_c} + \left(\dfrac{s^*}{s_{uy} - s^*}\right)^{R_c}\right]^{1/R_c}}, \tag{A.4b}$$

$$s^* = \frac{s - rsvg}{s'_y} \tag{A.4c}$$

$$s_{uy} = \frac{maxrl - rsvg}{s'_y} \text{ or } \frac{minrl - rsvg}{s'_y} \tag{A.4d}$$

where σ^* is the bar stress ratio, s^* is the slip ratio, s_{uy} is the stress limit ratio, and s'_y is the elastic recovered slip determined by the return stress divided by the initial slope (K) as shown in Figure A.7.

In Eq. (A.4), coefficient $R_{c,}$ with typical values in the range of 0.5 to 1.0, defines the shape of the reloading curve. Depending on the anchorage detail and the corresponding mechanism, it is possible for a bar with sufficient anchorage length to exhibit pinching hysteretic behavior in the bar stress vs. slip response, especially when it is anchored into a joint. The coefficient R_c will permit the effects of this pinching characteristic to be accounted for in the analytical simulation of the flexural member. The lower end value of R_c will represent significant pinching behavior while a value of 1.0 will produce no pinching effect as shown in Figure A.8. A comprehensive test program is required to establish a procedure to determine the value of R_c. For demonstration purposes, suitable R_c values were chosen in the next section by comparing the cyclic analysis results with the measured force-displacement responses of the test units. In the absence of test data, the R_c values chosen for the examples may be used in the fiber-based analysis of similar structural problems.

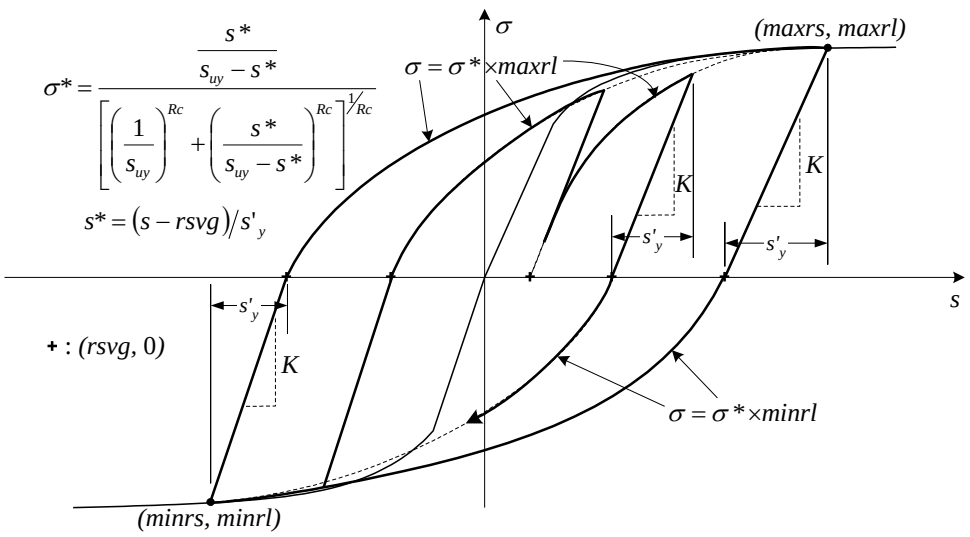

Figure A.7 Hysteretic model for the bar stress vs. loaded-end slip relationship

Material Model for Concrete Fibers

Similar to the model proposed for the steel fibers, a material model describing the monotonic response and hysteretic rules is also required for the concrete fibers. The combination of using the zero-length section element and enforcing the plane section assumption at the end of the flexural member imposes high deformations to the extreme concrete fibers in the zero-length element. These deformations were found to translate to concrete compressive strains in the order of 0.15 for the test columns described in the following section. According to the confinement model of Mander et al.[34], these strains are significantly greater than the strain capacity, ε_{cu}, that was estimated for the core concrete section of the columns used in following section. The maximum concrete strain that is expected to develop at the end of a flexural member will be somewhere in the range between ε_{cu} and 0.15. This is because the concrete at the end of the flexural member would benefit from additional confinement that would be provided by the adjoining member. Furthermore, the plane section assumption will be violated at the end section of the flexural member due to the penetration effects.

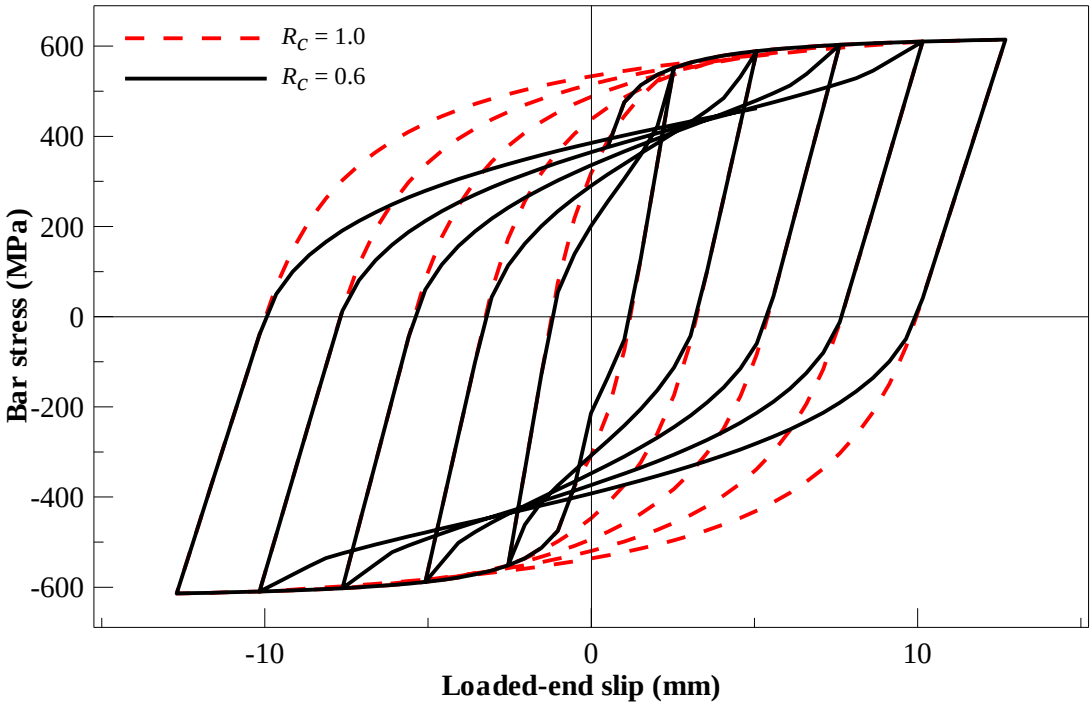

Figure A.8 The influence of parameter R_c on the cyclic bar stress vs. slip relation

In light of the discussion presented above, the concrete fibers in the zero-length was assumed to follow the Kent-Scott-Park stress-strain model and the corresponding hysteretic rules available in OpenSees through the material model known as *Concrete01*. To accommodate the large deformations expected to the extreme concrete fibers in the zero-length element, a perfectly plastic behavior was assumed for concrete in *Concrete01* once the strength reduces to 80% of the confined compressive strength. A parametric study involving the three test units described below indicated that the simulation results were not very sensitive to the compressive strain chosen to trigger the perfectly plastic behavior for concrete.

EXAMPLES OF APPLICATION

To demonstrate the applicability of the zero-length section element with the proposed material models and the corresponding improvements to the analysis results, cyclic responses of two concrete columns and a bridge tee-joint system were simulated using OpenSees (Ver. 1.5) and the results were compared with the experimental data. For all examples, the existing *Concrete01* and *Steel01* elements were used, respectively, to model the concrete and steel fibers within each element. *Steel01* does not include any ratcheting effects. For the analytical

simulations that included the strain penetration effects, the model parameters were determined as follows: the yield slips were calculated as per Eq. (A.3) using the reported material properties; the ultimate bar strengths were taken as $1.5f_y$; the ultimate slips were approximated to $35s_y$; the b factors were taken as 0.5; and the R_c factors were taken as 1.0 for the columns and 0.7 for the Tee-joint system. The reason for using two different R_c factors was that the longitudinal bars in the cantilever columns had ample anchorage length and 90° hooks at the end, whereas the column bars were terminated into the tee-joint with straight ends and an anchorage length of $22d_b$. A summary of the analysis results are presented below.

Short Rectangular Column

The first of the two cantilever columns studied was short rectangular column U6 that was designed and tested by Saatcioglu and Ozcebe.[22] The testing of this column was part of a study that evaluated the effects of confinement reinforcement specified in ACI 318-83 on the ductility capacity of short columns. As shown in the insert of FigureA.9, this column had a square cross section and a clear height of 1000 mm above the footing, and was modeled using five fiber-based beam-column elements. After subjecting the column to a constant axial load of 600 kN, the lateral-load cyclic testing was performed and the measured force-displacement response is included in Figure A.9. The test included sufficient instrumentation to isolate the displacement components due to member flexure, member shear, and strain penetration effects.

Also included in Figure A.9 are the simulated cyclic responses of the column with and without the zero-length section element to account for the strain penetration effects. (Note that the simulation with the strain penetration effects used the following model parameters: s_y = 0.56 mm, f_y = 437 MPa, b = 0.5, and R_c = 1.0.) Between the two analyses, the one which included the strain penetration effects closely simulated the measured response. Because the response of the test unit was influenced by shear deformation, which is not included in the beam-column elements available in OpenSees, the simulation with the strain penetration produced somewhat larger load resistance than the measured response for a given lateral displacement. The discrepancies between the measured and experimental results are even greater for the simulation that ignored the penetration effects. This particular analysis also markedly overestimated the elastic stiffness, yield strength, and the unloading stiffness of the test unit.

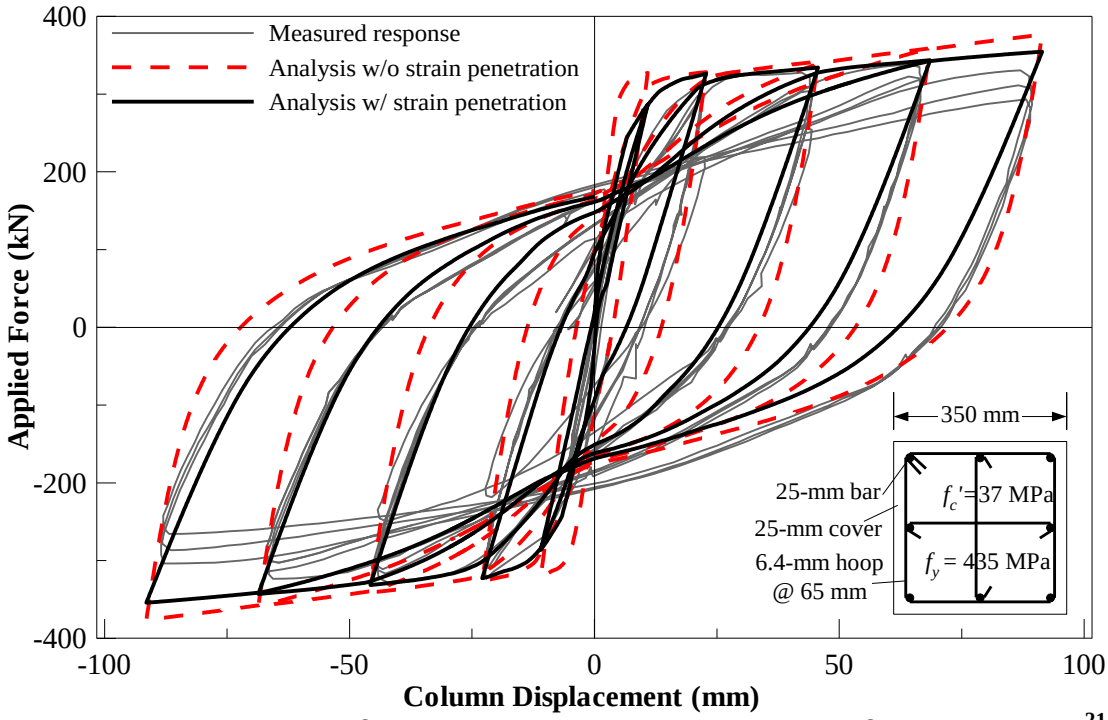

Figure A.9–Comparison of experimental and analytical results for specimen U6[21]

A further comparison between the analysis results and experimental results is presented in Figure A.10, which shows the lateral deflection along the column height at the yield lateral displacement (Δ_y) and $4\Delta_y$. In this figure, the measured displacements reflect the flexural displacements including the strain penetration effects, which were established by subtracting the measured shear displacements (approximately 20% at Δ_y and 10% at $4\Delta_y$) from the measured column total displacements. The analytical displacements corresponded to the measured lateral loads of 310 kN at Δ_y and 350 kN at $4\Delta_y$, and the contribution of the strain penetration effects to the column flexural deformation measured at the top was about 50% at Δ_y and 30% at $4\Delta_y$, respectively. For both cases, the analysis simulation that included the strain penetration effects very closely captured the measured flexural displacements along the height of the column. The simulated column displacements without the strain penetration effects were significantly low.

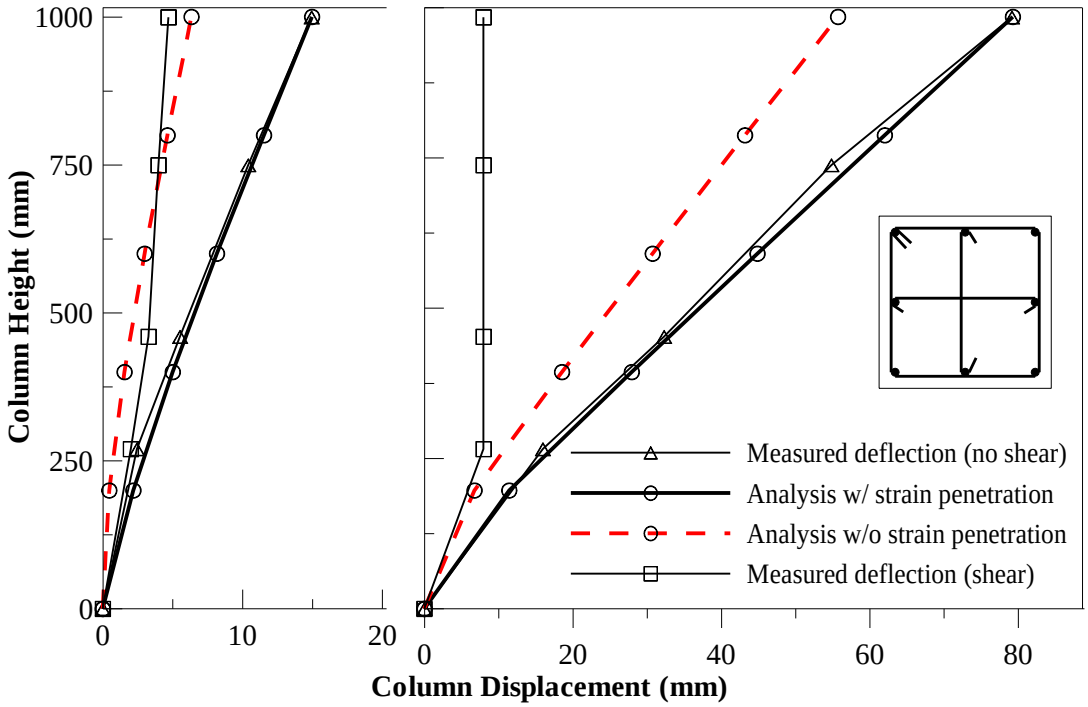

(a) at Δy **(b) at 4Δy**

Figure A.10–Comparison of deformation profile of specimen U6[21]

Tall Circular Column

The second column investigated in this study was that tested by Smith[35], which served as the reference column for an investigation on strategic relocation of plastic hinges in bridge columns. This column had a circular section as shown in the insert of Figure A.11 and a clear height of 3658 mm above the column footing. Under constant axial load of 1780 kN, the yield displacement of the column was reported to be 40 mm and the corresponding lateral load resistance was 259 kN. The failure of the column occurred due to fracture of the longitudinal reinforcing bars at the column base, after attaining lateral displacement of 323 mm with lateral resistance of 359 kN.

Figure A.11 compares the measured column top lateral displacement versus lateral force resistance with the analysis results, which were obtained with and without the zero-length element to capture the strain penetration effects and by modeling the column using five fiber-based beam-column elements. The analysis with the zero-length section element (with the following model parameters: s_y = 0.56 mm, f_y = 455 MPa, b = 0.5, and R_c = 1.0) more closely captured the measured response. In the pull-direction of loading, this analysis accurately predicted the lateral force resistance at the yield and maximum lateral displacements. In the

push-direction, the analysis appears to have somewhat overestimated the maximum force resistance due to the measured load resistance in this direction being slightly smaller than the pull direction. On the other hand, the analysis that ignored the strain penetration effects overestimated the ultimate lateral load resistance and greatly underestimated the column lateral deflection for a given lateral load. The influence of the strain penetration on the overall cyclic response of the column was not as pronounced as that seen in Figures. A.9 and A.10 because the strain penetration effects on the overall force-displacement response diminish with increasing column height.

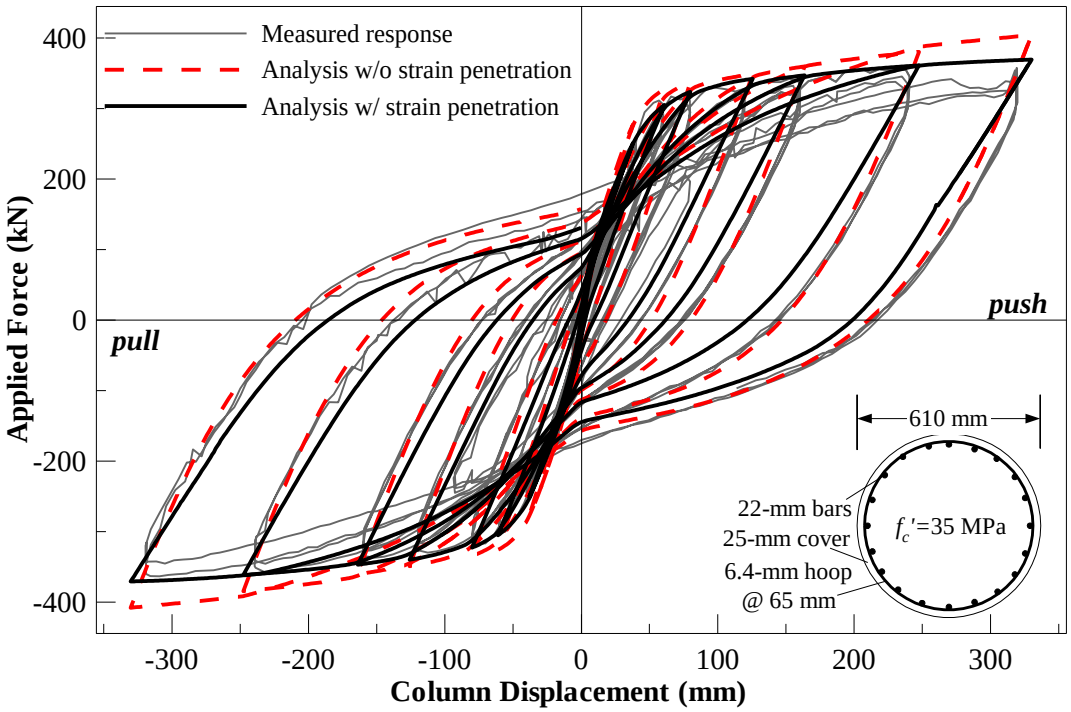

Figure A.11– Comparison of experimental and analytical results for the 'as built' column[34]

The column end rotation due to strain penetration reduces stress in the column longitudinal bars as is evident in Figure A.12. At the column yield displacement, the analysis that included the strain penetration effects correctly captured the strain distribution along a longitudinal extreme bar. The corresponding analysis without the strain penetration effects overestimated the bar strains in the plastic hinge region by about 30 percent. The strain gages in the hinge regions gradually failed when the column was subjected to inelastic displacements. Using the available data obtained at a column lateral displacement of 63 mm, Figure A.12b shows comparisons between the measured stain data and the calculated strain profiles. Again the analysis with the

zero-length section element produced strains that closely matched with the measured strains along the bar. The analysis that ignored the strain penetration effects greatly overestimated the bar strains by as much as 50%. The measured strains at the two locations are smaller than the predicted values by the analysis that included the strain penetration effects.

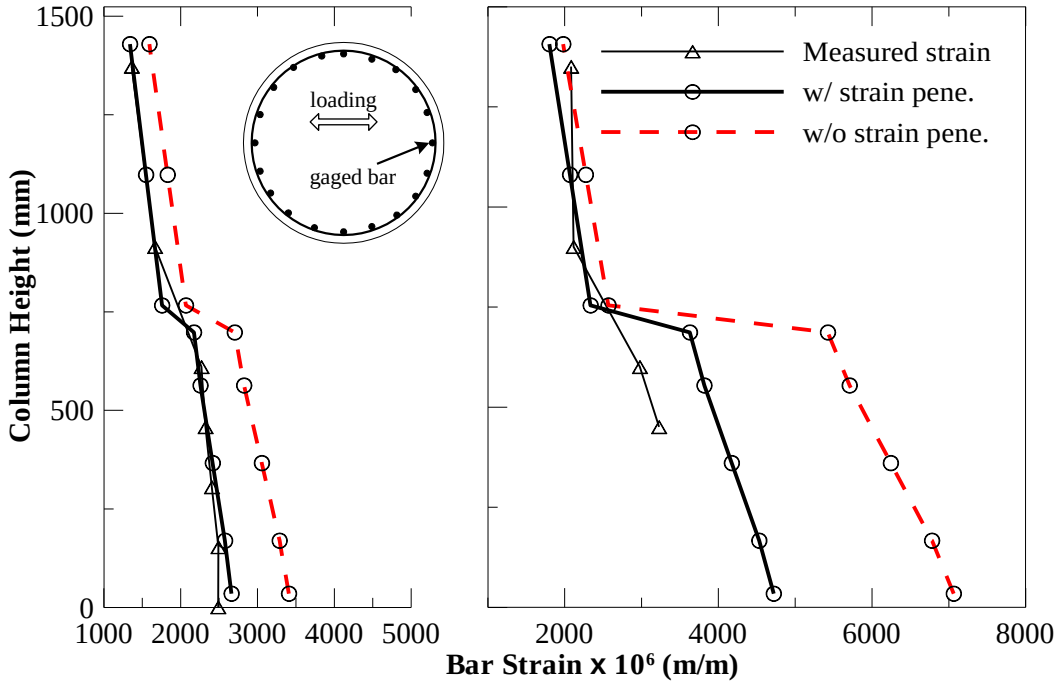

Figure A.12– Comparison of the strain of an extreme bar of the "as built" column[34]

Bridge Tee-Joint System

A bridge tee-joint system (specimen IC1) tested in an inverted position by Sritharan et al.[36] was studied to verify the feasibility of the proposed model for analyzing a structural system. This specimen with a conventional reinforced concrete cap beam, as schematically shown in Figure 13, was designed to evaluate new design details for the bridge cap beam-to-column joints. The concrete strengths on the day of testing were reported to be 31 MPa for the column and 40 MPa for the cap beam and joint. Under constant axial load of 400 kN, the column was subjected to cyclic lateral loading at a height of 1829 mm above the column-to-cap beam interface. The yield lateral displacement for the tee-joint system was reported to be 17 mm with the corresponding lateral resistance of 250 kN. The test joint experienced strength deterioration at

lateral displacement of 103 mm due to formation of large joint cracks and subsequent joint damage.

The simulation model included six fiber-based beam-column elements for the cap beam and four beam-column elements for the column. An additional fiber-based beam-column element with the elastic column section properties modeled the joint. The zero-length section element (with the model parameters of s_y = 0.51 mm, f_y = 448 MPa, b = 0.5, and R_c = 0.7) was located between this elastic element and the adjoining column element.

Figure A.13 compares the measured force-displacement hysteresis response of the test unit with the analytical results obtained with and without the strain penetration effects. The analysis, which included the strain penetration effects, produced force-displacement response that closely matched with the measured response in both loading directions. The joint shear failure experienced by the test unit towards the end of testing was not accounted for in the analytical model, and hence the analysis slightly overestimated the force resistance at the maximum displacement. On the other hand, the analysis that did not include the strain penetration effects overestimated both the lateral load resistance and the unloading-reloading stiffness.

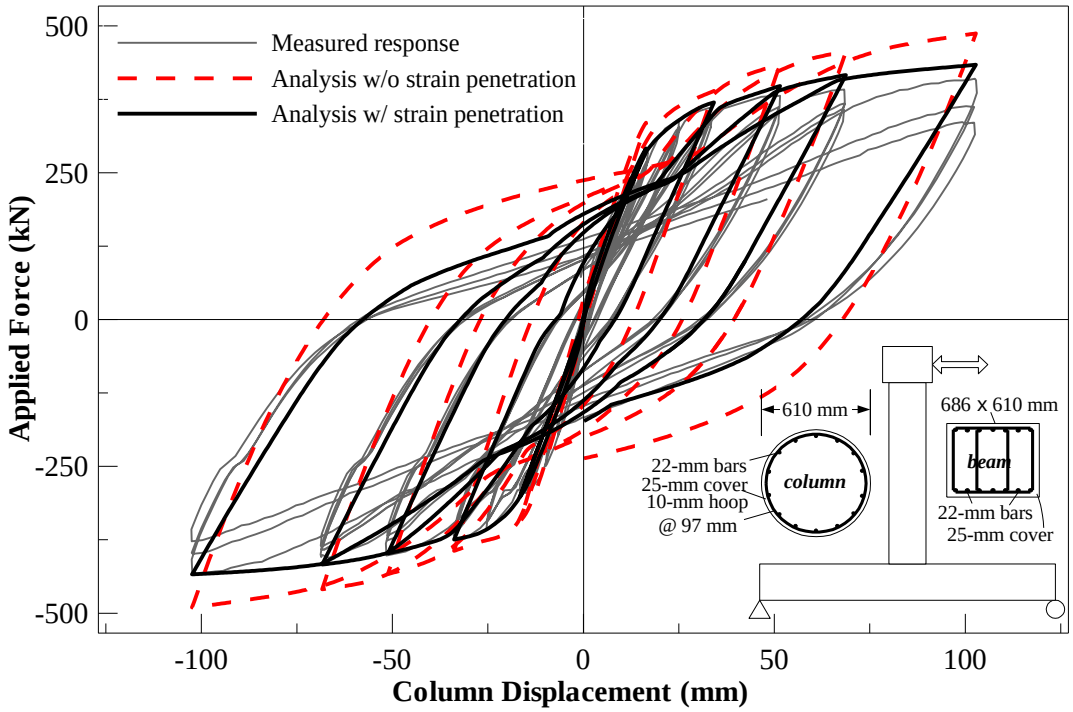

Figure A.13–Comparison of experimental and analytical results for specimen IC1[35]

The advantages of incorporating the strain penetration effects in the analysis is more pronounced in FigureA.14, in which the column moment vs. curvature histories at the beam-to-column intersection are compared. The analysis that ignored the strain penetration effects overestimated the column end curvature by approximately 90% towards the end of the test, indicating that the bar slip due to strain penetration greatly affects the local response measures that are indicative of damage to the plastic hinge region. A significant improvement to the moment-curvature response prediction was obtained when the analysis included the strain penetration effects. However, the predicted moment-curvature hysteretic loops are noticeably broad along the reloading path prior to intersecting the curvature axis. This discrepancy is expected to be diminished when the values of the model parameters, especially s_u, b, and R_c, are refined. As previously discussed, an experimental investigation designed to quantify the bar stress vs. slip response as a function of anchorage detail, bar diameter and material properties will improve selection of parameters for the steel fibers in the zero-length section element. Nonetheless, the tee-joint analysis results were adequate to emphasize the merit of the zero-length element concept and the proposed constitutive models to capture the strain penetration effects in fiber-based analysis of flexural concrete members.

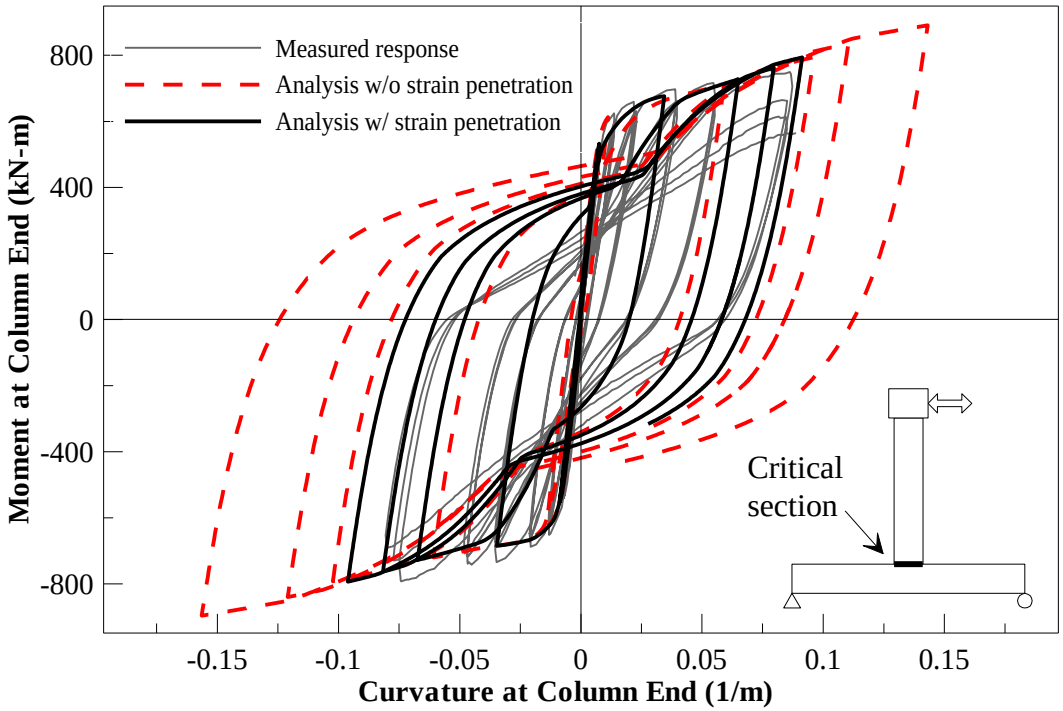

Figure A.14–Comparison of moment vs. column end curvature of specimen IC1[35]

CONCLUSIONS

Well-designed flexural concrete members experience rotations at the fixed end(s) due to bond slip that occurs as a result of strain penetrating along fully anchored longitudinal bars into the adjoining concrete members. Focusing on column and wall longitudinal bars anchored in footings and bridge joints, an efficient method is proposed in this paper to model the bond slip rotation using a zero-length section element that can be employed in nonlinear fiber-based analysis of concrete structures. A constitutive model that expresses the bar stress vs. loaded-end slip response was developed for the steel fibers of the zero-length section element using suitable experimental data reported in the literature. The adequacy of the proposed monotonic response for the steel fibers was illustrated by comparing the theoretical and measured bar stress vs. loaded-end slip responses of two pull-out tests conducted on well-anchored bars in concrete. Because of the lack of cyclic test data in the literature, the hysteretic rules for the bar stress vs. loaded-end slip response were established using the available test data and observed responses of concrete members under cyclic loading.

Advantages of the proposed method to improve fiber-based analysis of concrete structures was demonstrated by simulating cyclic response of two concrete cantilever columns and a bridge tee-joint system. Simulated responses were compared with the observed responses at both global and local levels. The analyses that utilized the proposed method to model the strain penetration effects satisfactorily captured the deflections, force vs. displacement hysteresis responses, strains in the longitudinal reinforcing bar and section curvature of the test units. When the strain penetration effects were ignored, the force resistance at a given lateral displacement was overestimated, along with portraying larger hysteresis loops. Most importantly, the local response parameters such as the steel strain and section curvature, which indicate the extent of structural damage, were grossly overestimated.

Based on these observations, it was concluded that 1) the strain penetration effects should not be ignored in the analysis of concrete members, and 2) the zero-length section element incorporating the proposed constitutive model for the steel fibers can be used in nonlinear fiber-based analysis to accurately capture the strain penetration effects and thus the global and local responses of concrete flexural members. The proposed method is versatile in that it can be used for modeling concrete flexural members without limiting cross-sectional shapes or direction of the lateral load. In addition, the proposed constitutive model for the bar stress vs. slip response

can be employed to capture the strain penetration effects in models of concrete structures developed using other types of elements.

ACKNOWLEDGMENTS

The study reported in this paper is based upon work supported by the National Science Foundation (NSF) under Grant No. CMS-0324559. The authors gratefully acknowledge the support of Dr. Steven McCabe, who serves as the program director for this grant. The authors also thank the collaborators of this project, especially Professor Cathy French, Suzanne Nakaki and Professor Ricardo López for their valuable feedback on the proposed method for capturing the strain penetration effects. Any opinions, findings, and conclusions or recommendations expressed in this material are those of the authors and do not necessarily reflect the views of NSF.

NOTATION

b = stiffness reduction factor

d_b = bar diameter

f_c' = concrete compressive strength

f_y = bar yield strength

f_u = bar ultimate strength

K = initial slope of bar stress vs. loaded-end slip relation

l_a = anchorage length

$l_{a,\min}$ = the minimum anchorage length

R_c = power index of the unloading/reloading curve

R_e = power index of the envelope curve

s = loaded-end slip

$\tilde{s}$ = normalized loaded-end slip

s^* = slip ratio

s_1 = slip corresponding to the peak local bond stress

s_u = loaded-end slip when bar stress equals to the bar ultimate strength

s_{uy} = stress limit ratio

s_y = loaded-end slip when bar stress equals to the bar yield strength

s'_y = elastic recorvered slip

α = power index of the local bond-slip relation

$\bar{\varepsilon}$ = axial strain of a section

ε = fiber strain

φ = curvature of a section

μ = ductility coefficient

τ = local bond stress

τ_1 = peak local bond stress

σ = bar stress

$\tilde{\sigma}$ = normalized bar stress

σ^* = bar stress ratio

REFERENCES

1. Sritharan, S., Priestley, N., and Seible, F. "Nonlinear Finite Element Analyses Of Concrete Bridge Joint Systems Subjected To Seismic Actions," *Finite Elements in Analysis and Design*. V. 36, 2000, pp. 215-233.
2. Sritharan, S., Vander Werff, J., Abendroth, R. E., Wassef, W., and Greimann, L., "Seismic Performance of a Concrete/Steel Integral Bridge Pier System," ASCE *Journal of Structural Engineering*, (In press).
3. Lin, I., "Anchorage characteristics for reinforcing bars subjected to reversed cyclic loading," Doctoral Dissertation, University of Washington, Seattle, WA, 1981, 326 pp.
4. Kowalsky, M., Priestley, N., and Seible, F., "Shear And Flexural Behavior Of Lightweight Concrete Bridge Columns In Seismic Regions," *ACI Structural Journal*, V. 96, No. 1, Jan.-Feb. 1999, pp. 136-148.
5. Calderone, A., Lehman, D., and Moehle, J., "Behavior of Reinforced Concrete Bridge Columns Having Varying Aspect Ratios and Varying Lengths of Confinement," Report No. PEER 2000-08, 2000, University of California, Berkeley, CA.
6. Saatcioglu, M., Alsiwat, J. and Ozcebe, G. "Hysteretic Behavior of Anchorage Slip in R/C Members," ASCE *Journal of Structural Engineering*, V. 118, No. 9, 1992, pp. 2439-2458.
7. Eligehausen R., Popov E., and Bertero V. "Local bond stress-slip relationships of deformed bars under generalized excitations," Report No. UCB/EERC 83-23, 1983, University of California, Berkeley.
8. Hawkins, N., Lin, I., and Ueda, T. "Anchorage of reinforcing bars for seismic forces." *ACI Structural Journal*, V. 84, No. 5, Sept.-Oct. 1987, pp. 407-418.
9. Popov, E. "Bond and anchorage of reinforcing bars under cyclic loading," *ACI Journal*, V. 81, No. 4, July-August 1984, pp. 340-349.
10. Shima, H., Chou, L., and Okamura, H., "Bond-slip-strain relationship of deformed bars embedded in massive concrete," *Concrete Library of JSCE*, N0. 10, Dec. 1987, pp 79-94.
11. Malvar, L., "Bond of reinforcement under controlled confinement." *ACI Material Journal*, V. 89, No. 6, Nov.-Dec. 1992, pp. 593-601.
12. Gilard, C. and Bastien, J., "Finite-element bond-slip model for concrete columns under cyclic loads." ASCE *Journal of Structural Engineering*. V. 128, No. 12, 2002, pp. 1502-1510.

13. Salem, H and Maekawa, K., "Pre- and post-yield Finite element method simulation of bond of ribbed reinforcing bars." ASCE *Journal of Structural Engineering*. V. 130, No. 4, 2004, pp. 671-680.
14. Lundgren, K. "Three-dimensional modeling of bond in reinforced concrete," Ph.D. thesis, 1999, Chalmers University of Technology, Göteborg, Sweden. 143 pp.
15. Lowes, L. "Finite Element Modeling of Reinforced Concrete Beam-Column Bridge Connections," Doctoral Dissertation, 1999, University of California, Berkeley.
16. Filippou, F., Popov, E., and Bertero, V. "Effect of bond deterioration on hysteretic behavior of concrete joints." Report No. UCB/EERC 83-19, 1983, University of California, Berkeley.
17. Monti, G. and Spacone, E. "Reinforced concrete fiber beam element with bond-slip." ASCE *Journal of Structural Engineering*. V. 126, No. 6, 2000, pp. 654-661.
18. Spacone, E., Filippou, F., and Taucer, F., "Fiber beam-column model for nonlinear analysis of R/C frames. Part I: Formulation," *Earthquake Engineering and Structural Dynamics*, Vol 25, 1996, pp. 711–725.
19. Spacone, E., Filippou, F., and Taucer, F. "Fiber beam-column model for nonlinear analysis of R/C frames. Part II: Applications," *Earthquake Engineering and Structural Dynamics*, Vol 25, 1996, pp. 727–742.
20. Otani, S. "Inelastic analysis of R/C frame structures," *Journal of the Structural Division*, Vol. 100, No. ST7, July, 1974, pp. 1433-1449.
21. Priestley, N., Seible, F., and Calvi, G., *Seismic Design and Retrofit of Bridges*, Wiley-Interscience. Hoboken, NJ 07030. 1996, 704 pp.
22. Saatcioglu, M. and Ozcebe, G. "Response of reinforced concrete columns to simulated seismic loading," *ACI Structural Journal*, V. 86, No. 6, Nov.-Dec. 1989, pp. 3-12.
23. Lowes, L. and Altoontash, A. "Modeling reinforced concrete beam-column joints subjected to cyclic loading," ASCE *Journal of Structural Engineering*, Vol. 129, No. 12, 2003, pp. 1686-1697.
24. Ciampi V., Eligehausen R., Bertero V., and Popov E., "Analytical model for concrete anchorages of reinforcing bars under generalized excitations," Report No. UCB/EERC 82-83, University of California, Berkeley, 1982.
25. Sritharan, S. "Analysis of Concrete Bridge Joints Subjected to Seismic Actions," Doctoral Dissertation, University of California, San Diego, California, 1998, 407 pp.

26. Open System for Earthquake Engineering Simulation (OpenSees) User Manual (V 1.5), 2004, http://opensees.berkeley.edu/.
27. Building Code Requirements for Structural Concrete (ACI 318-02), American Concrete Institute, Farmington Hills, MI. 2002.
28. Maekawa, K., Pimanmas, A., and Okamura, H., *Nonlinear mechanics of reinforced concrete*. 2003. Spon Press, 29 west 35th street, New York, NY 10001. pp. 392-398.
29. Shima, H., Chou, L., and Okamura, H., "Bond characteristic in post-yield range of deformed bars," *Concrete Library of JSCE*, No. 10, Dec. 1987, pp. 113-124.
30. Mathey, R. and Watstein, D., "Investigation of bond in beam and pull-out specimens with high-yield-strength deformed bars," *Journal of the American Concrete Institute*, Vol. 32, No. 9, Mar. 1961. pp. 1071-1090.
31. Ueda, T., Lin, I., and Hawkins, N. "Beam Bar Anchorage in Exterior Column-Beam Connections," *ACI Structural Journal*, V. 83, No. 3, May-June 1986, pp. 412-422.
32. Viwathanatepa, S., Popov, E., and Bertero, V., "Effects of generalized loadings on bond of reinforcing bars embedded in confined concrete blocks," Report No. EERC-79-22. University of California, Berkeley, CA., 1979.
33. FIB, Bulletin 10, "Bond of reinforcement in concrete", State of the art report prepared by Task Group Bond Models, former CEB, Task Group 5.2. fib, Case Postale 88, CH-1015 Lausanne , August 2000, 427 pp.
34. Mander, J., Priestley, M., and Park, R. "Observed stress-strain behavior of confined concrete," ASCE *Journal of Structural Engineering*, V01. 112, No. 8, August, 1988, pp.1827-1849.
35. Smith, P. E., "Strategic relocation of plastic hinges in bridge columns," MS Thesis, University of California, San Diego, California, 1996, 137 pp.
36. Sritharan, S., Priestley, N, and Seible, F., "Seismic response of column/cap beam tee connections with cap beam prestressing," Report No. SSRP-96/09, University of California, San Diego, California, 1996, 295 pp.

APPENDIX-B

Appendix B presents a model used in the blind prediction contest conducted by the University of California at San Diego (UCSD) on the response of a 7-story building slice. This model is similar to the models used for the analysis of NTW1 and NTW2 and showed that the modeling approach can be used for a dynamic analysis.

LESSONS LEARNED FROM SEISMIC ANALYSIS OF A 7-STORY CONCRETE TEST BUILDING

Jonathan D. Waugh

PhD Candidate, Iowa State University, Dept. of Civil, Construction, and Environmental Engineering, 407 Town Engineering Building, Ames, IA 50011, USA

Sri Sritharan

Associate Professor and Assistant Chair, Iowa State University, Dept. of Civil, Construction, and Environmental Engineering, 406 Town Engineering Building, Ames, IA 50011, USA

A uniaxial shake table test of a full-scale slice of a seven-story reinforced concrete wall building was performed at the University of California, San Diego. A 2D analytical model that primarily employed fiber-based beam-column elements was used for a blind prediction of the global response of the building to the imposed input accelerations. An improved analytical model, which adequately simulates the building's dynamic response and comparison of measured and analytical results, is presented. The lessons learned from participation in the blind prediction with particular attention to the effects of issues commonly ignored in analytical modeling of concrete buildings are included.

Keywords*:* concrete; wall; multistory building; shake table testing; seismic; dynamic; analysis; nonlinear

Introduction

In the fall of 2005, a portion of a full-scale seven-story concrete building, which hereafter is referred to as the test building, was constructed and tested under unidirectional earthquake motions using an outdoor shake table at the University of California, San Diego (UCSD). A capacity-based design approach was used to determine the structural details of the building elements, which led to smaller member dimensions and reduced amounts of reinforcing steel than those typically required by a traditional design code approach [Restrepo, 2006]. The smaller member sizes and reduced reinforcing steel created a more flexible structure that was

both economical and easier to construct, while satisfying criteria to produce ductile response for the building under the selected seismic input motions.

A blind prediction contest was held from April to May 2006, in which teams of practicing engineers, researchers, and students from all over the world participated and predicted the expected response of the test structure using the construction details and measured engineering material properties made available to them. The time histories of the four input motions, named EQ1, EQ2, EQ3, and EQ4, were also provided as part of the contest. The model used for the blind prediction by the writers, hereafter referred to as the original model, used OpenSees [Mazzoni *et al.*, 2004] with fiber sections. Other participants used various modeling approaches including: 3D solid elements, plain stress elements, multiple vertical line elements, and elastic beam elements [Restrepo, 2006]. The original model under predicted the overturning moments by 30-40%, story shear forces by 20-40%, and the residual displacements by 50-70%. The lateral displacement envelope was adequately predicted for EQ1 and EQ3, and under predicted for EQ2 and EQ4. In general, the floor accelerations were the best predicted quantities for events EQ1, EQ2, and EQ3, where the original model predicted values within 20% of the floor accelerations recorded for the test building. For EQ4, the floor accelerations were over predicted by 20-35%. The response of the building to EQ3, particularly the overturning moments, was difficult for participants to capture [Restrepo, 2006, Trevor, 2007]. A full description and discussion of the original model and corresponding results can be found in Waugh and Sritharan [2006].

A number of components were responsible for the discrepancies between the results from the original model and the recorded test data. The components that were ignored in the original model were the couple generated by the gravity columns, the stiffening effect of the link slab, and the flexibility of the shake table and foundation. Most of the participants made similar decisions about the importance of modeling these portions of the structure, as shown in the papers found in the proceedings of the NEES/UCSD Workshop on the Analytical Modeling of Reinforced Concrete Walls [Restrepo, 2006]. However, the excluded structural elements played an important role in the overall response, and thus influenced the accuracy of the predicted response parameters. Additionally, the structure had limited nonstructural elements, which in general significantly contribute to viscous damping, causing most of the analytical models to experience an excessive amount of viscous damping.

In this paper, an improved analytical model by addressing the shortcomings in the original model is presented. This model, hereafter referred to as the improved model, builds on the strengths of the original model and adds additional features that are typically ignored when modeling multi-story buildings. The most significant feature is the inclusion of the effects of gravity columns, which is given full treatment in this paper due to its significance to seismic design practice.

A brief description of the test building and testing methodology are presented first to show how the structure was constructed and tested at UCSD. Next, the description of the improved analytical model used to characterize the response of the test building using measured properties is presented, with emphasis on overcoming the limitations of the original model. The analytical results, including envelopes for design forces, floor level displacements, and inter-story drift ratio and time histories for the base moment, top floor displacement, and top floor acceleration, of the structure are then presented and compared with the experimental data. Finally, based on the comparison of results, lessons learned from participation in the blind prediction contest and recommendations to improve seismic modeling of buildings consisting of structural walls and gravity columns are presented.

Test Building and Test Methodology

Figures B.1a and B.1b show, respectively, the floor plan and elevation of the test building which consisted of a 4.88 m long cast-in-place (CIP) flange wall, a 3.66 m long CIP web wall, and a C-shaped precast, segmental pier with unbonded post-tensioning. The web wall primarily provided the lateral force resistance in the earthquake loading direction, while the flange wall and precast pier primarily provided transverse stability and torsional resistance for the test building. In addition, four pin-ended Dywidag prestressing bars, 44.5 mm diameter for the first story and 25.4 mm diameter for the second story and above, were used as columns within each story. The Dywidag bars were grouted inside 101.6 mm diameter, 8.6 mm thick steel pipes to prevent them from experiencing buckling. Due to the pin-ended connections, these columns were assumed in design to act as gravity columns and not to contribute to lateral force resistance. The floor at each level was 3.66 m wide, 8.13 m long, and 203.2 mm thick reinforced concrete slab, and was supported by the web wall and four steel columns.

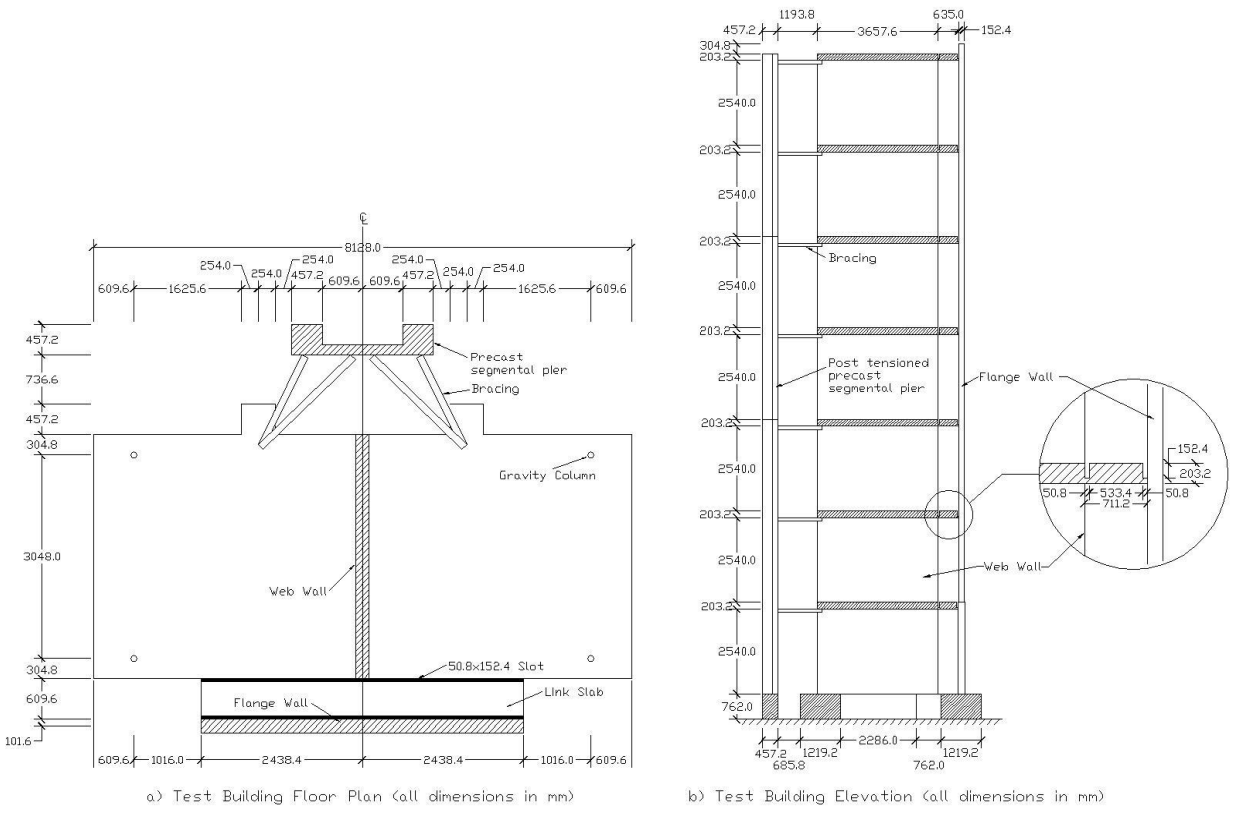

Figure B.1 Plan and Elevation of the Test Building [after NEES7Story, 2006].

Both the flange and web walls had fixed connections to their shake table, while the precast pier connection to the shake table was designed to act as a pin in the loading direction while providing large moment resistance in the orthogonal direction. This was achieved by orienting the post-tensioning tie-downs to the shake table in the direction orthogonal to the direction of the shaking such that it led to insignificant moment resistance in the direction of loading. Discussions with researchers at UCSD confirmed that the contribution of the pier to the system flexural resistance was small, and that a pin was the best idealization. However, the researchers never stated the exact contribution of the pier to the moment resistance. The flange wall and the precast pier were designed to have pin connections to the floor slab. Figure B.1b includes a magnification of the link slab connecting the main floor slab and web wall to the flange wall. The link slab incorporated two 152.4 mm deep by 50.8 mm wide slots in the slab

near the flange wall to accomplish the pin connection to the main floor slab. The pin connection between the pier and the floor slab was accomplished by using steel angles bolted to the floor slab and precast pier. The bolted connections and the limited moment capacity of the angles prevented the transfer of moment from the main floor slab to the pier.

The shake table testing of the building included several input motions, which were: one low amplitude white noise, three low intensity earthquakes, and one high intensity earthquake. The low intensity earthquake records chosen were the longitudinal (EQ1) and transverse (EQ2) components from the 1971 San Fernando earthquake recorded at site: *vnuy*, and the longitudinal component from the 1994 Northridge earthquake at site: *whox* (EQ3). The high intensity record was the 360º component taken from *Sylmar Olive View Med* (EQ4) that was recorded in the 1994 Northridge earthquake located near the epicenter of the earthquake [NEES7Story, 2006]. The strongest 30 seconds of ground motions EQ1, EQ2, EQ3, and EQ4 are shown in Figure B.2, the response spectra for the motions are shown in Figure B.3 assuming 5% viscous damping. The input ground motions for the blind prediction were given at both 50 and 240 Hz; the 50 Hz motions were selected for the dynamic analyses reported in this paper. The low intensity earthquakes were expected to cause limited damage to the test building while the high intensity earthquake was anticipated to cause significant damage to the building. In all cases, the plastic hinge and the associated damage was expected to concentrate in the first floor level of the test building.

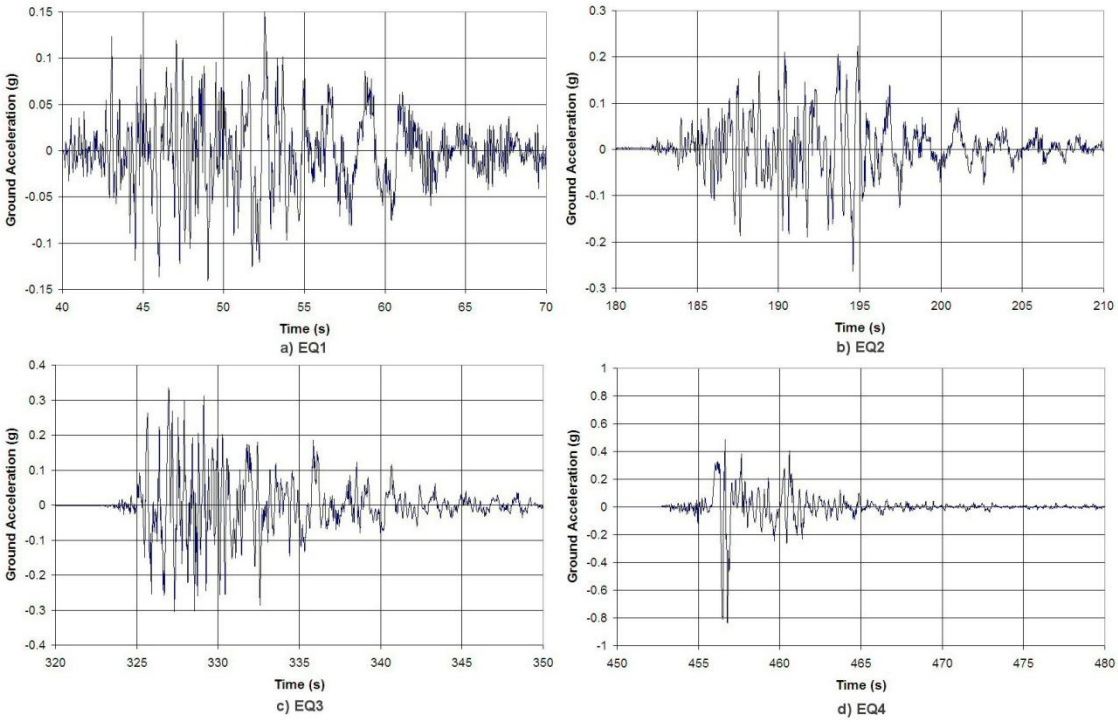

Figure B.2 Earthquake Input Motions used for the Shake Table Test

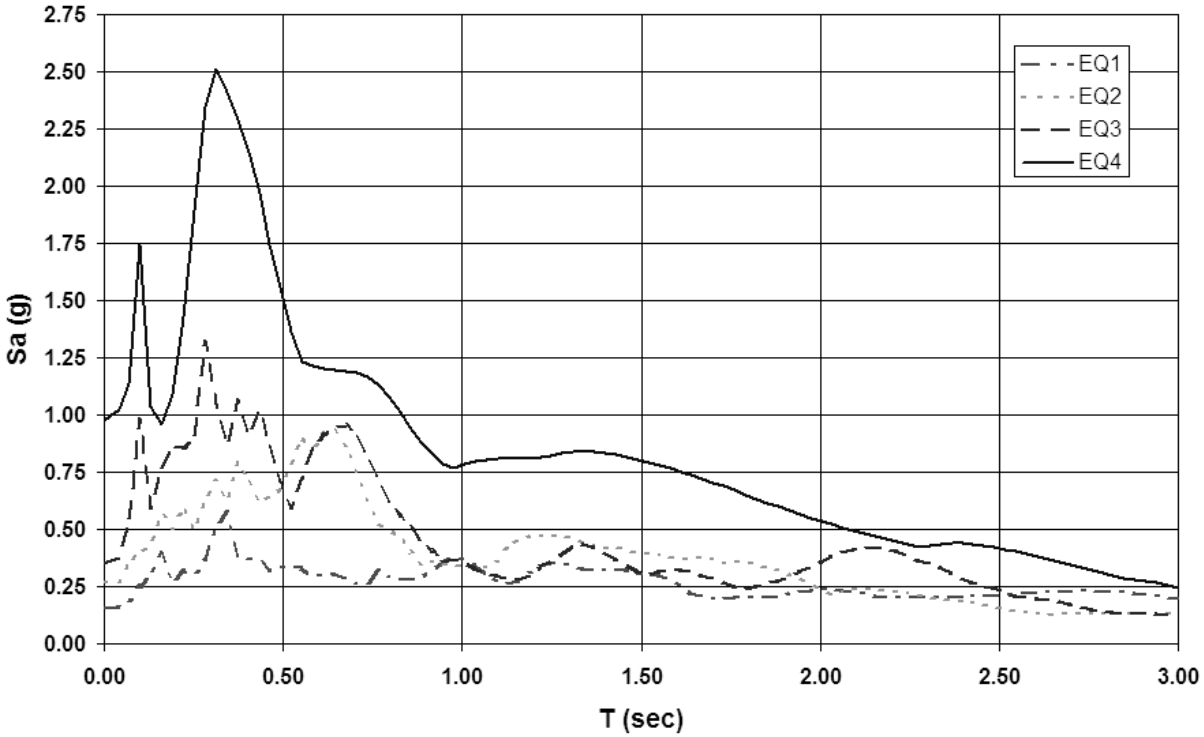

Figure B.3 Earthquake Input Motions Response Spectra with 5% Damping

Analytical Model and Key Features

The original model used for the blind prediction contest was a simple centerline model that included the web wall, flange wall, and post-tensioned segmental pier. As previously stated, this model was generally satisfactory in predicting the displacements and accelerations, but not overturning moments. The concept and relevant details of the improved model, together with discussion of critical issues that eliminated the deficiencies of the original model are presented below.

Overview

As noted, both the original and improved models of the test building were created to balance the need for accuracy with the desire for a relatively simple model that would run quickly and could be built based on the geometry and measured material properties. Because the accelerations were only applied in one direction, a two dimensional model parallel to the web wall was preferred. OpenSees [Mazzoni *et al*., 2004] was selected as the analysis software because of its use in an ongoing PreNEESR project that focuses on concrete wall buildings [Sritharan *et al.*, 2005]. As part of this project the capabilities of OpenSees for analyzing walls have been studied and new features have been added [e.g., Zhao and Sritharan, 2007].

The seismic mass of the structure was lumped at the floor levels to simplify the model and expedite the analysis. The mass corresponding to each floor was calculated by determining the mass of the floor slab and one half story height of the flange wall, web wall, pier, and gravity columns above and below the floor, and concentrated at the floor level nodes. The weight of the structure was also applied as point loads on the nodes at each floor level to account for the gravity effects. Table B.1 summarizes the point loads and masses applied to the model.

The number of elements and nodes in the improved analytical model maintains the simplicity and efficiency of the original model. A diagram delineating the improved OpenSees model is shown in Figure B.4, which had a total of 83 nodes and 81 elements including 56 beam-column elements, 22 truss elements, and three zero-length interface elements. In comparison, the models used by other participants had as many as 3143 elements and 3360 nodes [Restrepo, 2006].

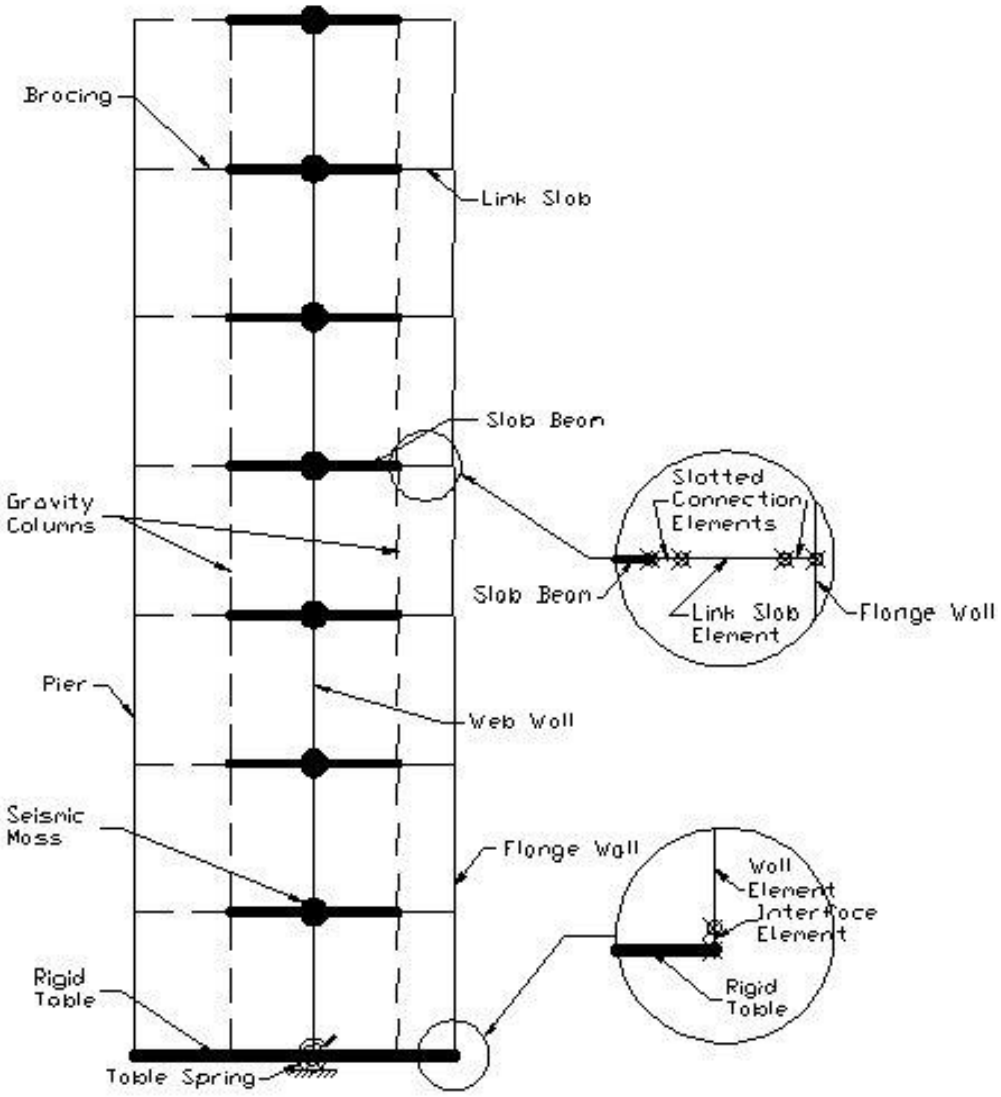

Figure B.4 Schematic of the Improved OpenSees Model Diagram of the Test Building

Table B.1: Nodal Gravity Forces and Masses

Location	Nodal Force (kN)	Mass (kN*s^2/m)
1st Floor Web Wall	46.26	4.72
1st Floor Flange Wall	61.70	6.29
1st Floor Pier	36.14	3.68
2nd –6th Floor Web Walls	105.87	10.79
2nd –6th Floor Flange Walls	60.50	6.16
2nd –6th Floor Piers	36.14	3.68
7th Floor Web Wall	71.17	7.25
7th Floor Flange Wall	19.57	1.99
7th Floor Pier	36.14	3.68

Lateral Force Resisting System

Based on the previous work done in modeling the response of structural walls to cyclic displacements by the writers, the flange and web walls of the test building were modeled using fiber-based beam-column elements. Due to difficulties in obtaining compatible forces and deformations for the force-based beam-column elements modeling the flange and web walls in the dynamic analysis, displacement-based beam-column elements were chosen. However, the first story web and flange walls were modeled using the force-based beam-column elements because they are considered to be a better choice for modeling the plastic hinge regions [Neuenhofer and Filippou, 1997]. The beam-column elements were assigned fiber sections that discretely modeled the reinforcement as well as confined and unconfined concrete regions. The first floor web wall section was discretized using 100 confined concrete fibers and 302 unconfined concrete fibers, while the first floor flange wall section was discretized with 20 confined concrete and 456 unconfined concrete fibers. The sections for the upper level flange wall used 60 unconfined concrete fibers to discretize the wall, while the upper level web wall section used 72 unconfined concrete fibers. A single beam-column element with five integration points along the element length was used to represent each wall within each story. The choice of five integration points for the beam-column elements was based on discussions with Prof. Filippou, the experience of the OpenSees community, and the author's work on simulating the response of concrete walls for a NSF/NEES funded project.

The fibers representing the longitudinal reinforcement in the various elements were located according to the as-built drawings shown in Figures B.5a and B.5b, which depict the dimensions and reinforcement details of the flange and web walls at the first floor and for floors two through seven, respectively. The confined concrete properties were calculated using the given transverse reinforcement details and the confined concrete model proposed by Mander *et al*. [1988], and were assigned to the fibers for the appropriate regions of the cross-sections for the first story of the building model. The upper stories had no confinement reinforcement and thus the concrete was modeled using unconfined concrete fibers. Material models "Steel02" and "Concrete03" in OpenSees were used to model the reinforcing steel and concrete behavior. The properties for the unconfined concrete and steel reinforcement material models were chosen to closely match the experimental stress-strain behavior established for these materials. Figures B.6a and B.6b show the measured and modeled monotonic stress-strain curves for the

unconfined concrete in the first story walls, and the #4 (d_b=12.7 mm, where d_b is the bar diameter) longitudinal bars used in the flange and web walls, respectively. It can be seen that the chosen concrete model adequately captures the unconfined concrete behavior. The behavior of the reinforcing steel was accurately modeled up to a strain of about 0.06 and significant discrepancies between measured and modeled behaviors expected at larger strains. To account for the low cycle fatigue behavior, the fracture strain for the longitudinal reinforcement was taken as 0.06 and thus the steel reinforcement strains were limited to 0.06 during the analysis. The tension capacity of concrete was modeled using a peak tensile strength of $0.59\sqrt{f'_c}$ with nonlinear post-peak softening following the University of Houston model presented by Hsu [1993], where f'_c is in MPa. Figure B.6c and 6d show the cyclic response characteristics of the steel and concrete material models, while the parameters used for the concrete and reinforcement material models in the analysis are given in Tables B.2 and B.3, respectively.

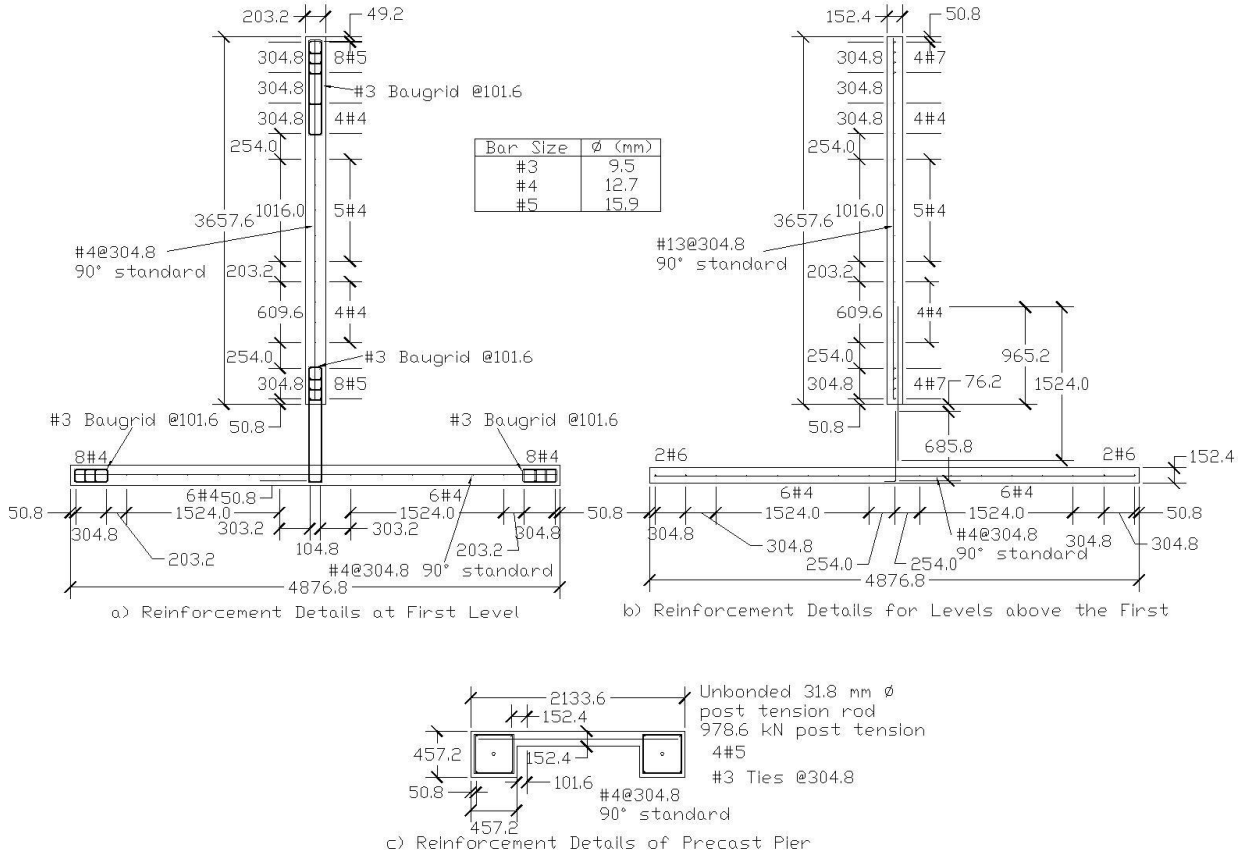

Figure B.5 Wall and Pier Reinforcement Details [after NEES7Story, 2006]

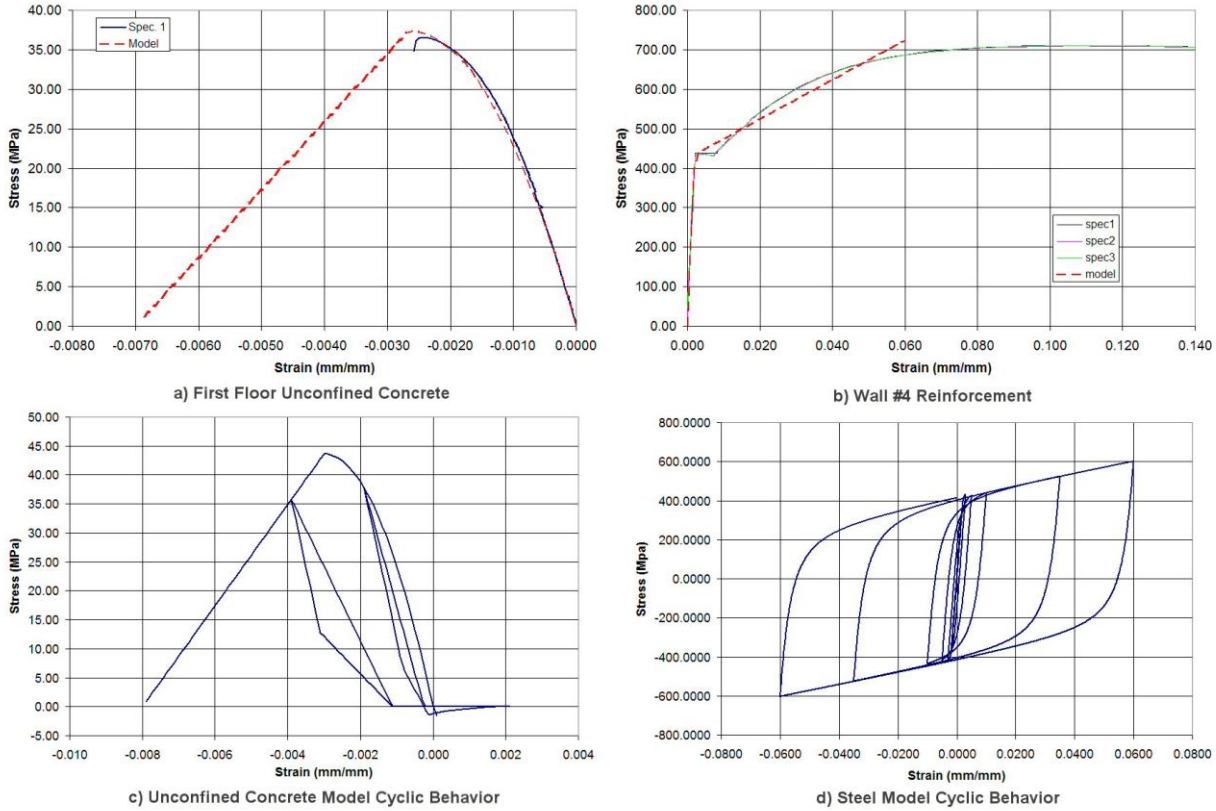

Figure B.6 Material Model Comparisons

The strain penetration effects resulting from anchoring the wall longitudinal reinforcing bars into the base block were included in the model using a zero-length section element with the same cross-section as the wall elements above it. However, the steel material model in this element was replaced with the strain penetration model developed by Zhao and Sritharan [2007] which describes the total bar slip due to strain penetration as a function of stress in the bar. This accounted for the additional flexibility resulting from the wall end rotation due to penetration of strain along the longitudinal reinforcement into the foundation block. The bottom node on the interface element was fixed for all degrees-of-freedom while the top node was only restrained against lateral translation. The bottom ends of the beam-column elements modeling the first story flange and web walls of the building were connected to the top nodes of the interface elements.

The unbonded post-tensioned pier was also modeled using displacement beam-column elements. A fiber section was used to represent the pier cross-section shown in Figure B.5c. The section was defined using 40 unconfined concrete fibers; the material properties used for the pier

Table B.2: Concrete Material Properties as defined in OpenSees

Location	Peak Compressive Stress (MPa)	Peak Compressive Strain (mm/mm)	Ultimate Compressive Stress (MPa)	Ultimate Compressive Strain (mm/mm)	Peak Tension Stress (MPa)	Peak Tension Strain (mm/mm)
First Level Walls Unconfined	37.4*	0.002664*	0.0	0.007	3.8	0.000135
Second – Sixth Level Walls	39.3*	0.002307*	0.0	0.007	3.9	0.000144
Precast Segmental Pier	38.8*	0.002375*	0.0	0.007	3.9	0.000119
Slab Beams & Link Slab	37.4*	0.002664*	0.0	0.007	3.8	0.000136

* Based on the average response of tested concrete cylinders

concrete and reinforcement are included in Tables B.2 and B.3, respectively. Similar to the flange and web walls, single beam-column element with five integration points along the element was used to represent the pier in each story. Anticipating primarily an elastic response, the unbonded post-tensioning rods in the pier were modeled using a single truss element that was given an elastic perfectly plastic material behavior and an initial strain to simulate the effect of prestress. The truss element shared the nodes at the top and bottom of the beam-column element modeling precast pier without any additional constraints along the height of the pier. Since the pier base moment resistance was negligibly small and had limited impact on the overall response, this simple approach was deemed appropriate. The boundary condition at the base of the pier was assumed to be pinned and thus free to rock at the connection between the pier and the shake table during the excitation of the structure. A dynamic analysis with the pier fixed at the base only increases the base moment by 3%. As stated earlier, the researchers at UCSD stated a pinned base was the proper idealization. The braces connecting the pier to the floor slab (see Figure B.1a) were modeled using truss elements and the Steel02 material model. The truss elements connected the nodes at floor levels on the post-tensioned pier to the nodes at the end of the floor slab elements.

Table B.3: Steel Material Properties as defined in OpenSees

Size & Location	Yield Stress (MPa)	Young's Modulus (MPa)	Strain Hardening Ratio
#4 - Flange and Web Walls	434.4*	199,948*	0.025
#5 - Flange and Web Walls	434.4*	199,948*	0.0225
#6 - Flange and Web Walls	475.7*	199,948*	0.025
#7 - Flange and Web Walls	461.9*	199,948*	0.025
#4 - Precast Pier	461.9*	199,948*	0.025
#5 – Precast Pier	489.5*	199,948*	0.025
Pier Bracing	248.2	199,948	0.01
Gravity Columns	879.1	199,948	0.01

*** Based on the average response of tested reinforcement bars**

Floor Slabs and Gravity Columns

As previously stated, the gravity columns were very important to the overall structural response, but were ignored in the original model. Consistent with the design assumptions, most participants in the blind prediction did not model the floor slab and columns because the specially detailed pinned connections at the column ends were intended to remove them from providing the lateral load resistance. However, the influence of the gravity columns and floor slab on the overall force-displacement response of the test building was evident during testing, and was confirmed by Panagioutou and Restrepo [2006] using a pushover analysis of the building. The primary reason for this influence was that the columns developed significant axial strains during testing due to their interactions with the floor slab. Consequently, the columns closer to the compression side of the web wall were subjected to compression forces and those near the tension side of the web wall were subjected to tensile forces. This enabled a large moment couple to be developed due to the distance of 3.05 m between the compression and tension columns and effectively contributing up to 24% to the lateral force resistance of the test building. The interaction between the floor slabs and gravity columns were dictated by the flexural stiffness of the floors, fixed connection between the slab and walls, and axial constraints imposed to the floor slabs by the gravity columns. Therefore, it was expected that the extent of the flexural cracking of the concrete floor slab occurring perpendicular to the direction from the compression region of the web wall to the tension columns and tension region of the web wall to the compression columns to have influenced the amount of force developed in the gravity columns. Figure B. 7 shows a part of the ANSYS [Swanson Analysis Systems, 1992] model

created to understand the interaction between the floor slab and gravity columns. The ANSYS model included the web wall, floor slab, and four gravity columns per floor for the seven floors in the building slice. The floor slab and web wall were modeled using the concrete element Solid65, but the flange wall was not modeled. This element is an eight node brick element that incorporated tension cracking and compression crushing of the concrete material, but the latter capability of the model was turned off because crushing of concrete can prematurely occur in an ANSYS analysis as reported by Barbosa and Ribeiro [1998]. The effect of the confined concrete was modeled by modifying the uniaxial behavior defined for the material in the boundary elements of the web wall using the confined concrete model of Mander *et al.* [1988]. The longitudinal and transverse reinforcement in the Solid65 element is smeared across the element area and defined with orientation relative to the global coordinate system and a uniaxial material model describing its stress-strain characteristics. The nodes along the top of the wall in the model were constrained to displace equally parallel to the length of the web wall. The behavior of this 3D model was studied by imposing monotonic displacement that followed the first mode response of the test building.

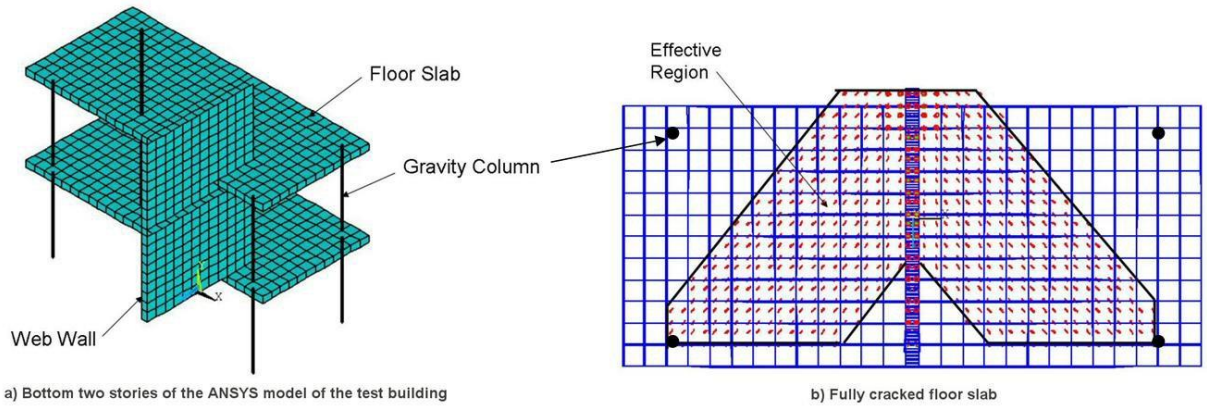

Figure B.7 ANSYS Model used to understand the 3D Effects of the Floor Slab

The 3D slab effect was introduced into the 2D OpenSees model using a beam-column element at each floor level. A bilinear moment-curvature envelope was selected to define the section behavior of this element. The initial slope of the moment-curvature relation is based on the uncracked slab properties with the flexural stiffness of 1130 and 3390 MN-m-rad for positive and negative moments, respectively. The two different stiffness values are due to the different reinforcement mats in the top and bottom of the slab. The moment at the transition between the

two linear portions was defined by the flexural cracking moment occurring over an effective width of the width of the slab. This moment was estimated to be 152.5 kN-m, based on an effective slab width of 11.5 times the slab thickness (or 2.33 m) that was determined from the ANSYS analysis results (se Figure B.6b). A post cracking stiffness ratio of 20% determined using the nominal strength and the corresponding curvature of the slab section over the effective width defined the second slope. This approach for modeling the 3D effects of slab-gravity column interaction in the 2D OpenSees model was validated by comparing the axial force induced in the columns vs. inter-story displacement with that obtained from the ANSYS model. Figure B.8a showing this relationship at the first story level confirms that the 3D effects of the slab-column interaction in the 2D model was satisfactory, while 7b shows the origin centered hysteretic model used for the moment-curvature behavior of the section of the beam-column element.

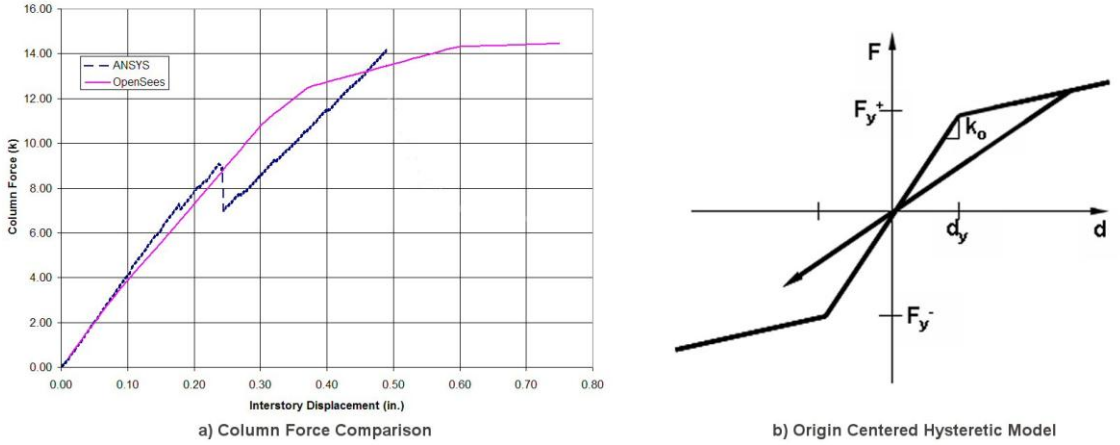

Figure B.8 Calibration of Axial Force Induced in Columns vs. Interstory Displacement and the Model chosen for the Cyclic Behavior

The columns were modeled using truss elements with the appropriate cross sectional area to simulate the axial constraints provided by the Dywidag bars. Since the OpenSees model was only 2D, the area of the two columns on each end of the web wall were modeled with a single truss element with twice the area of a single column. Small rigid links were used to model the thickness of the floor slab to accurately simulate the clear length of the gravity columns.

Link Slab Connection

Similar to the gravity columns, the effects of the link slabs were typically overlooked by the participants in the blind prediction contest. The link slab shown in Figures B.1a and B.1b refers to where notches were cut in the portion of floor slab connecting the flange and web walls. The intent of the detail was to minimize the moment resistance at the flange wall-to-slab interface while allowing the transfer of in-plane inertia forces. Despite minimizing the moment, a significant shear along the length of the notch was possible, which, in turn, increased the axial load in the web wall. Panagioutou and Restrepo [2006] observed this stiffening effect in their pushover model and showed that it almost doubled the axial load on the web wall when yielding of the horizontal notch reinforcement occurred as observed in the test.

In the original model, the effect of the notches was included by constraining the lateral displacements of the flange and web wall, while the rotational DOFs for the flange and web wall nodes were not constrained. Other participants in the contest used similar approaches by using either constraint equations or truss elements to model the effect of the link slab; however, neither approach captures the axial stiffening of the web wall and associated increase in the lateral force resistance. In the improved model, the link slab was modeled using three beam-column elements with fiber sections. Two beam-column elements were used to model each of the reduced sections of the slot, and the third beam-column element modeled the slab between the slots. The cross-sections for both the slab and slot sections were modeled using fibers representing the unconfined concrete and longitudinal reinforcement. This approach allowed yielding of the slab reinforcement along the notch, imposing the appropriate amount of additional axial load on the web wall. The additional axial load increases the resistance of the web wall by approximately 16%.

The beam-columns elements modeling the notch did not include the effects of shear deformation. If the notch regions sustained significant shear deformation is unknown. It was not mentioned by the UCSD researchers in their discussions of the behavior of the link slab.

Table and Foundation Flexibility

The connection between the test building and the shake table was modeled in the boundary conditions for the wall and pier elements. However, the shake table and foundation as a whole experienced some rotation and the building's response was influenced by the rotational

stiffness of the table. The table flexibility was neglected in the original model. As shown in Figure B.4, a zero-length elastic rotational spring was used to account for this additional flexibility in the improved model; rigid beams were used to link the rotational spring to the bases of the web and flange walls, gravity columns, and precast pier. Table B.4 lists the rotational stiffness of the table and foundation measured in each direction by the UCSD researchers for each of the ground motions. As indicated in the table, the average rotational stiffness obtained from the stiffness reported for the two directions during testing of EQ2, EQ3, and EQ4 was used in the improved analytical model. The rotational stiffness reported for EQ1 was relatively high compared to the values for the other events and thus was not included when finding the average value. This approximation was used since the effects of all earthquakes were examined in one analysis and the expected error in displacement due to underestimating the table stiffness for EQ1 was expected to be less than 5%. With this average value representing the rotational stiffness, one node of the rotational spring was fully fixed against deformation while the other node was allowed to rotate parallel to the web wall.

Table B. 4: Base Spring Rotational Stiffness

Rotational Spring stiffness due to combined flexibility of table and foundation (kips-ft/rad)*10^7	EQ1	EQ2	EQ3	EQ4	Model
Direction 1	1.326	0.883	0.711	0.711	0.7904
Direction 2	1.378	0.888	0.684	0.746	0.7904

Influence of Shear Deformation

Experimental research has shown that shear deformation can contribute significantly to the lateral displacement, especially at the lower floor levels, even in slender, flexure dominated walls [e.g., Thomsen & Wallace, 1995]. The effects of shear deformation need to be included to better simulate the lateral displacement, especially at the lower floor levels. The fiber sections used for the wall in the original model did not include any shear effects in the section formulation, requiring the shear response to be handled separately.

Some of the other participants did not have to separately handle the shear deformation because the modeling approach they used included the effects of shear within their chosen elements. However, OpenSees does not have an option for including shear in the element definition and the fiber sections used in the analysis sums the uniaxial response of the fibers to determine the axial and moment resistance of the section. Because the fibers have zero resistance to transverse loads, the shear deformation cannot be determined by the section. In the original model an estimate of the additional lateral displacement due to shear deformation was added during post-processing of the results. The method selected to incorporate shear deformation in the improved model was to aggregate a shear force-deformation response onto the fiber sections used to model the web walls. Because the small lateral force resisted by the flange wall and the short dimension parallel the shear force, the shear deformation of the flange wall was neglected. Aggregating the shear response does not cause the axial strains seen by the fibers due to curvature of the wall to change, neglecting the possible flexure-shear interaction.

The lateral force versus shear deformation hysteretic response of the web wall was modeled using a uniaxial material model. Figure B.9 shows the "pinching4" material model available in OpenSees that was used for this purpose at the first floor level. A minimum of three points with an optional fourth point are needed to define the response envelope of this model. Because the measured shear deformation of the web wall was not available, only three points were defined for the pinching model as follows: 1) point 1 was defined using the lateral force corresponding to the first flexural cracking of the web wall (111.2 kN) and the uncracked shear stiffness, 2) point 2 was defined using the lateral force that was expected to cause flexural yielding of the longitudinal reinforcement (311.4 kN) and effective shear stiffness, and 3) point 3 was defined using the ultimate lateral force resistance (467.1 kN) and post-yield shear stiffness. The uncracked shear stiffness was obtained according to Park and Paulay [1975] for an uncracked rectangular beam. The effective shear stiffness to the uncracked shear stiffness was taken as the same ratio as the flexural stiffness at yield to the gross flexural stiffness; this ratio was determined to be 20% of the uncracked stiffness. This choice to relate the cracked shear and flexural stiffness was based on observations of the behavior of RW2 and TW2 tested by Thomsen and Wallace [1993], RWN and NTW1 tested by Brueggen, *et al.* [2007], and the rectangular walls tested by Oesterle, *et al.* [1979]. Furthermore, research by Massone and Wallace [2004] has shown that when inelastic flexural action occurs, inelastic shear action also

begins because of coupling of the two responses. In order to simulate this coupling, the lateral force at yield was used to define the point when the tangent stiffness changes from the effective shear stiffness to the post-yield shear stiffness. The post-yield stiffness was defined based on the observed shear force versus deformation responses of NTW1 and RWN from the PreNEESR wall tests [Brueggen *et al.*, 2007] and RW2 and TW2 tested by Thomsen and Wallace [1995]. Based on those data sets, the post-yield shear stiffness should be approximately 1.0% of the effective shear stiffness. Shear stiffness for the second floor and above was modeled using an elastic material model with stiffness equal to 35% of the uncracked shear stiffness to reflect the cracking of the wall.

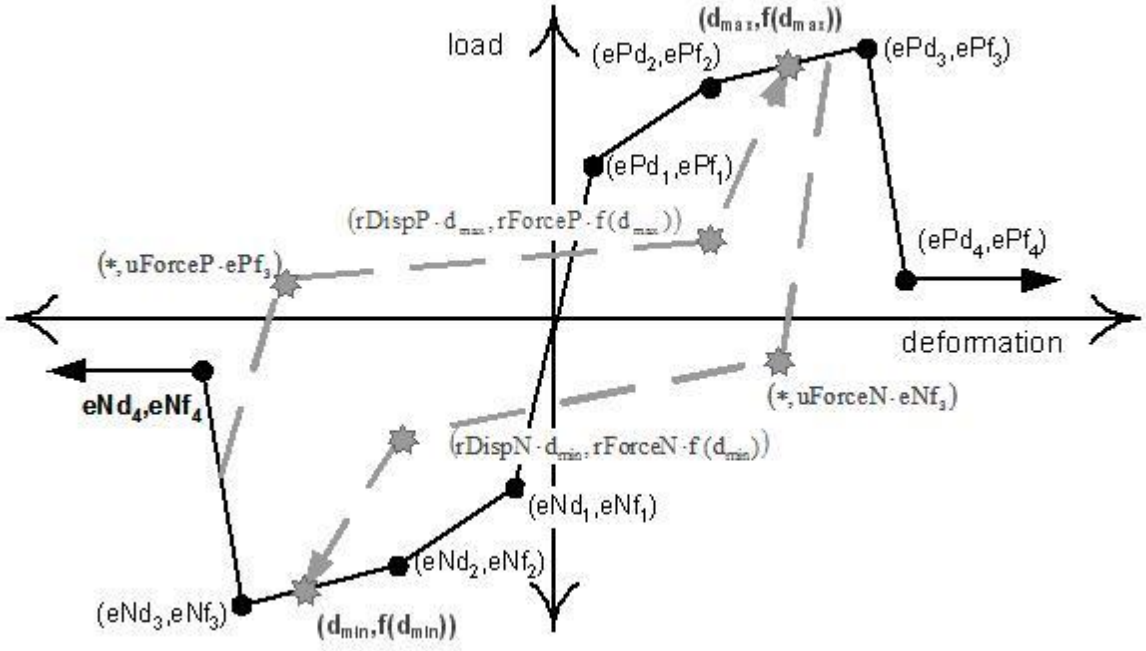

Figure B.9 Pinching4 Material Model used to account for the Shear Deformation Contribution [Mazzoni et al., 2004]

Viscous Damping

OpenSees includes Rayleigh damping as an option to capture the effects of the viscous damping during dynamic analysis. In a nonlinear system, the stiffness matrix used for calculating the damping matrix can have a significant impact on the results of the analysis. In the original model, Rayleigh damping was used in conjunction with the current stiffness matrix,

allowing damping to decay as damage accumulated. The coefficients needed to define the Rayleigh damping were obtained assuming five percent viscous damping for the first and third modes that were found from cracked section properties.

Priestley and Grant [2004] recommended that stiffness proportional damping be used for nonlinear analysis because Rayleigh damping heavily weights the mass matrix, leading to an almost constant damping matrix during a nonlinear response of the structure regardless of the degradation that occurred to the stiffness of the structure. Furthermore, test observations by Moaveni, *et al.* [2006] indicated approximately three percent damping on the first longitudinal mode when testing to white noise. However, Panagioutou and Restrepo [2006] used only 0.3 percent damping for the first longitudinal mode for accurate simulation of the test building's response to earthquake input motions. Such low damping may have been due to excluding the nonstructural elements in the test structure and flexural cracking over a lower height due to the reduced longitudinal reinforcement in the test building. Consequently, in the improved model the stiffness proportional viscous damping corresponded to 0.5% damping on the uncracked first mode period and 0.8% damping on the uncracked third mode period. This corresponded to 0.02% and 0.5% viscous damping, respectively, on the cracked first and third mode responses of the building. The damping was determined from the tangent stiffness matrix to capture the reduction in viscous damping after yield as recommended by Priestley and Grant.

Dynamic Analysis

The input accelerations shown in Figure B.2 were applied to the base of the building model in the direction parallel to the web wall. Using the Newmark's constant average acceleration method for the integrator, the analysis was conducted at a time increment of 0.02 seconds to limit the amount of output that must be post-processed. However, when the analysis failed to converge 10 substeps were carried out at 0.002 seconds to find a solution, and then the time step was increased back to 0.02 seconds.

In order to account for the effects of accumulated structural damage on the response of the test building, all input motions were concatenated. Six seconds of zero ground acceleration was added between the earthquake records to allow the structure to come to rest prior to being subjected to the next base input motion. The low accelerations at the end of the ground motions combined with the six seconds of padding were adequate for the structure to return to rest. The

total applied ground motion record to the test building was slightly more than 522 seconds long from start to finish. The entire analysis took approximately 45 minutes to run on a 2.0 GHz Pentium IV based computer with 1 GB of RAM running Windows XP.

Comparison of Results

The capabilities of the improved model can be seen best by comparing key time history responses with the measured data provided for the test building [NEES7Story 2006]. For this purpose, top floor displacement, base moment, and top floor acceleration are used. This is followed by comparison of envelope responses for variables that are of interest from a design viewpoint.

Time History Responses

Top Floor Displacement

The top floor displacement time history is shown in Figure B.10 with a, b, c, and d representing, respectively, the response during the most intense 30 seconds of EQ1, EQ2, EQ3, and EQ4. The figures show that the period of the test building was well captured by the analysis model for all earthquake intensities, except around 12-15 seconds into the EQ4 motion. Table 5 shows the period of the structure at various stages of loading. The analytical model simulates the period of the structure within one second, except for following EQ2. Additionally, all the significant peak displacements recorded during EQ1, EQ2, and EQ4 were generally well simulated, and were within 5% of the measured values. The peaks on EQ3 were under predicted by as much as 25%.

The cause of the discrepancy for the EQ3 event was extensively studied, because similar discrepancies were observed in the predictions by other participants (e.g., Kelly, 2007]. The fact that EQ2 and EQ3 were comparable in earthquake intensity was the primary cause for large discrepancies in the response of EQ3 and the unloading and reloading behaviors of the material models rather than their envelopes had a large influence on the analytical response of EQ3. Typically, the envelope response of materials is more accurately characterized than their reloading and unloading action. This hypothesis was confirmed by scaling the accelerations of EQ2 by 0.6 without altering the other events and rerunning the analysis. This modification significantly improved the EQ3 response of the test building, bringing the peak displacements

within 5% of the measured values. The concrete material model used for the analysis here had very simple unloading and reloading behavior as shown in Figure B.6c. The poor simulation of EQ3 would be improved by using a concrete material model that has a hysteretic behavior which better simulates the unloading and reloading behavior of the concrete. Furthermore, the pinching4 model may not be adequately simulating the shear deformation of the web wall; however, without the measured data for the shear deformation, the accuracy of the shear behavior cannot be evaluated. The simple unloading and reloading behavior of the "pinching4" model was also expected to have influenced the response of the test building to EQ3.

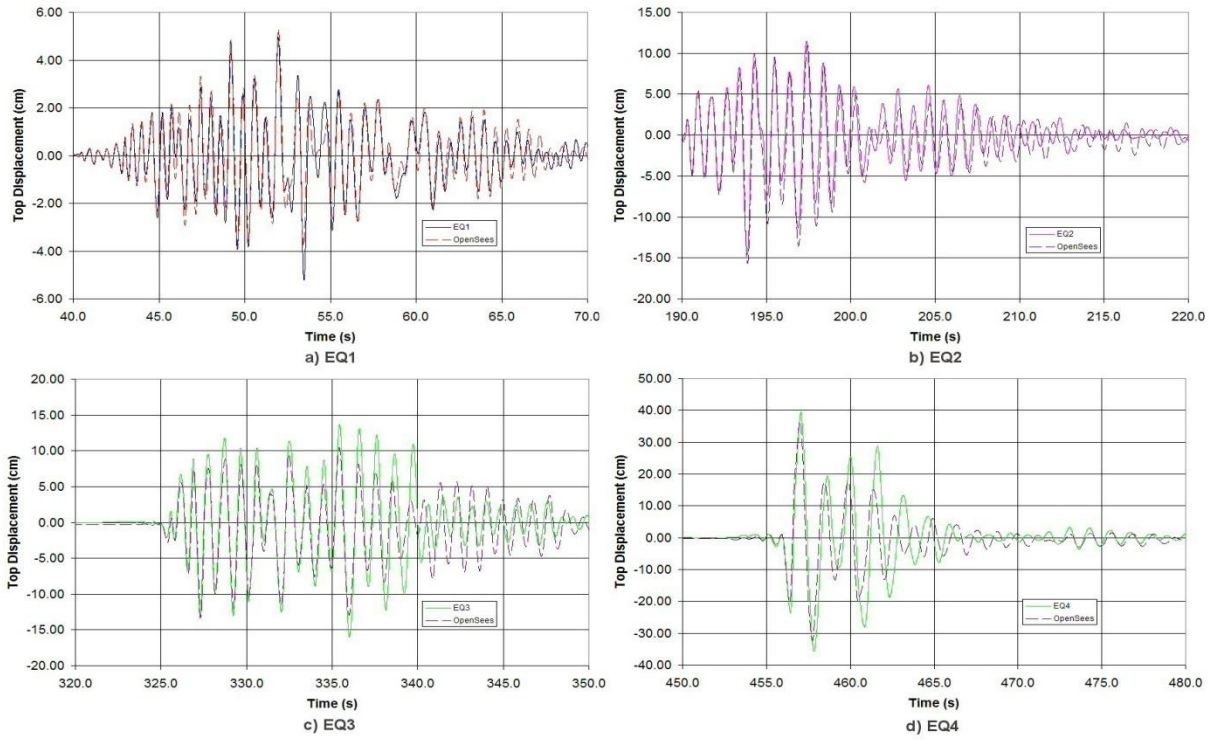

Figure B.10 Comparisons of Measured and Simulated Displacement Time Histories

A second possible explanation is the softening seen in Table B.5 for the period following EQ2. This softening could have some influence on the discrepancies in the response to EQ3. However, if it was due to the softening observed in the period, it would be expected that the OpenSees results would overestimate the peak displacement, which was not seen in the comparison of the response to motion EQ3. However, based on the improvement seen when the magnitude of EQ2 is decreased, the softening observed in the period follow EQ2 is not the primary cause of the discrepancies seen in the response of EQ3.

Table B.5: Comparison of Measured and Calculated Structure Fundamental Period		
	Measured Period (s)	Calculated Period (s)
Before Testing	0.526	0.519
Following EQ1	0.613	0.620
Following EQ2	0.826	0.873
Following EQ3	0.893	0.90
Following EQ4	0.980	0.974

Base Overturning Moment

The base moment was determined by summing the moments at the base of the web and flange walls, and the couple generated by the gravity columns that had about 10 to 24% contribution to the base overturning moment. Time history comparison for the base moment is shown in Figure B.11, in which many of the characteristics observed for the top floor displacement time history are also seen in the base moment plot comparison.

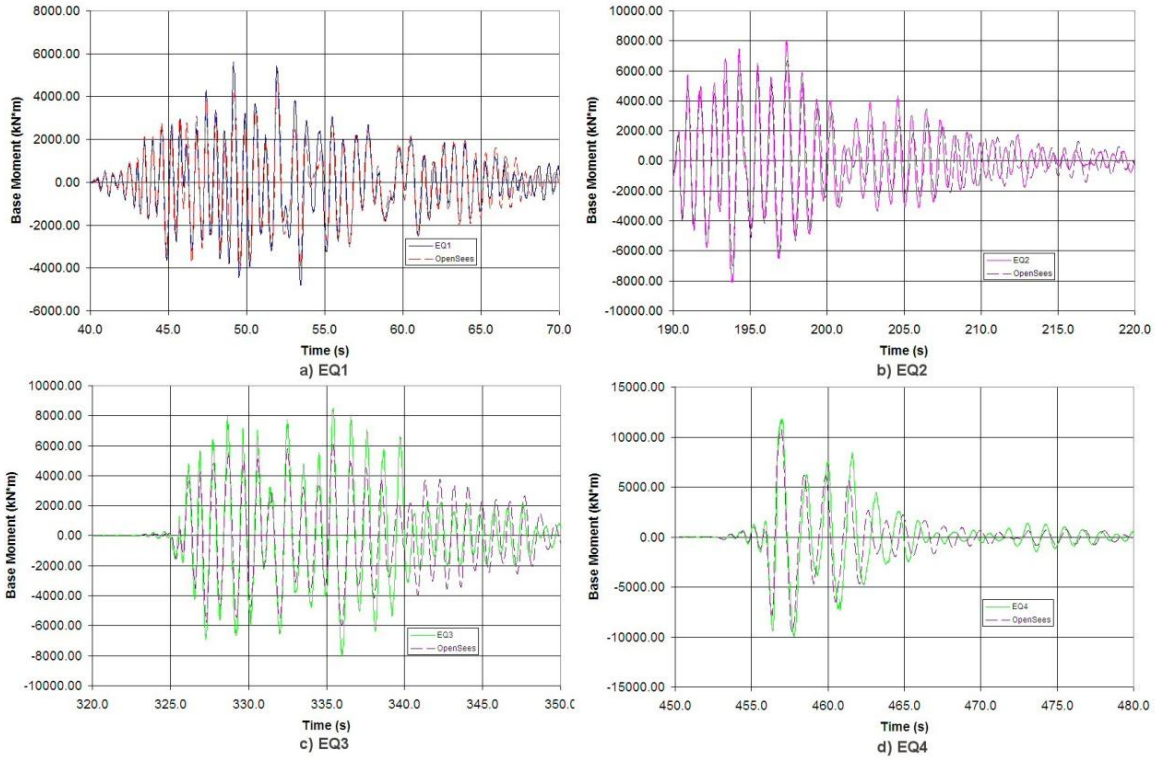

Figure B.11 Comparisons of Measured and Simulated Base Moment Time Histories

The period of the structure was well captured, showing that the analysis adequately captured the damage and subsequent softening of the structural stiffness. The peak values were

generally well captured and are within 10-15% of the measured values for EQ1, EQ2, and EQ4. As previously noted, the response of EQ3 is poorly simulated giving results within 25% of the measured values for the aforementioned reasons.

Top Floor Acceleration

The top floor acceleration time histories for all ground motions are shown in Figure B. 12. The acceleration time history shows the expected response considering the under prediction of the lateral displacement. The period of the structure was again well captured by the analysis; however, the peak values are typically over predicted by the analysis by approximately 10-20% when compared with the responses measured during the test.

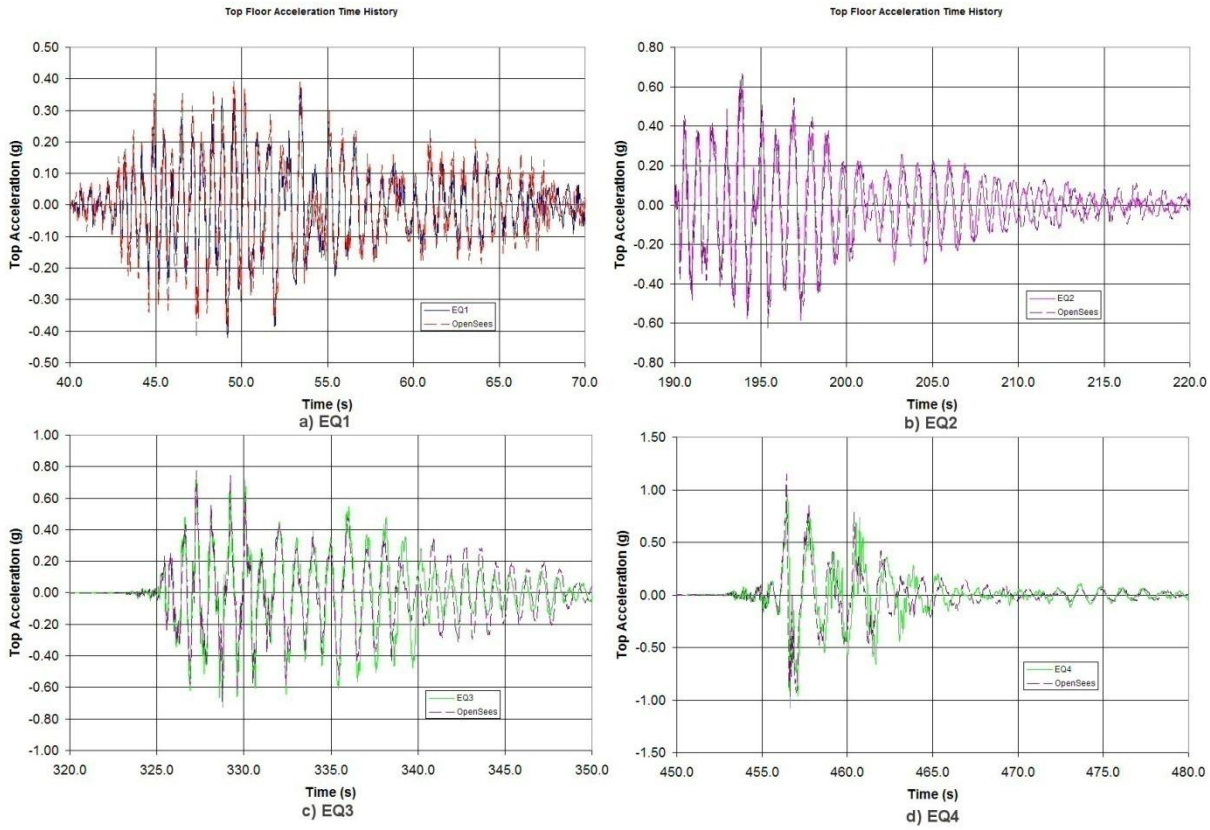

Figure B.12 Comparisons of Measured and Simulated Acceleration Time Histories

The simulation of the top floor acceleration was generally considered satisfactory given the large time step used for the input excitations used for the analysis and analysis time step. Simulation of the accelerations in a dynamic analysis can be sensitive to the time step used in the analysis and it typically requires a small time step to obtain accurate acceleration responses.

The large time step used in the analysis allows a good simulation of the floor level accelerations without requiring an extensive amount of computational time needed to use a small time step and post-process the corresponding analysis output.

Envelope Responses

The envelope responses of the test building model along with their experimental values are shown in Figure B.13 with a, b, c, and d representing the lateral displacement, inter-story drift, overturning moment, and story shear, respectively. The comparisons of the envelopes are discussed below in recognition of their influence on design.

Lateral Displacement

The floor level lateral displacements shown in Figure B.13a are generally well simulated, with the exception of EQ3. The displacements of EQ3 were under predicted by about 17%. For the rest of the ground motions, the predicted lateral floor displacements were within 10% of the recorded values during the shake table tests. The top floor displacements were generally better captured than the first floor displacements. This could be due to the influence of the shear deformation, since shear deformation has a larger impact on the lower floor level displacements.

The peak average inter-story drift obtained from the top floor displacement divided by the height of the building is used in the design of the structure. Despite designing the building as a flexible structure, the test building did not experience excessive lateral drifts. The maximum average drift ratios were 0.27% for EQ1, 0.81% for EQ2, and 1.88% for EQ4, and the corresponding measured values were 0.27%, 0.76%, and 2.06%, respectively. As expected, a poor comparison was expected for EQ3 response and the calculated and measured peak average drifts for this event were 0.69% and 0.83%, respectively.

Interstory Drift Ratio

An accurate simulation of the interstory drift is important to predict the damage to structural as well as nonstructural elements. The interstory drift ratios, shown in Figure B.13b, were well simulated by the analysis were within 10% of the experimental values for EQ1, EQ2, and EQ4. The EQ3 interstory drift was poorly simulated with results being within 20% of the measured values for the reasons previously discussed.

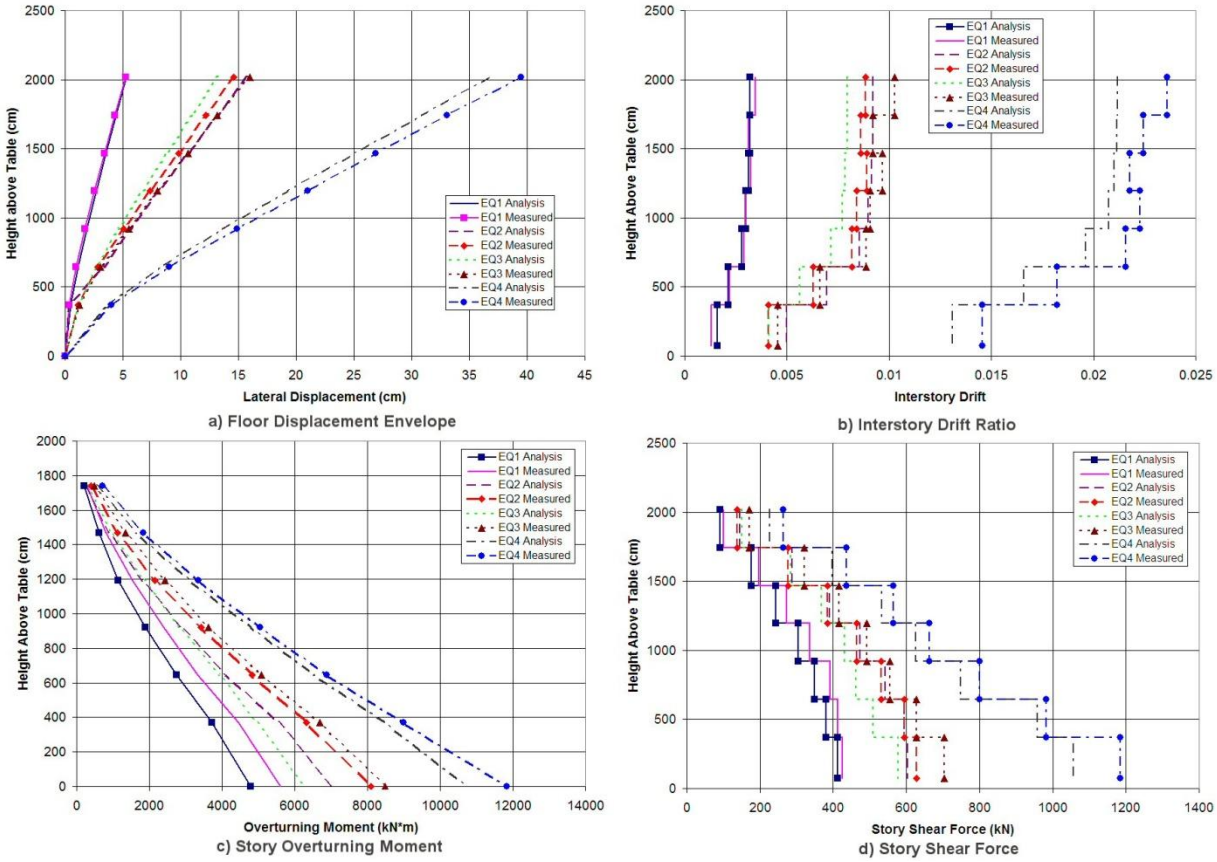

Figure B.13 Comparisons of Measured and Simulated Response Envelopes

Overturning Moment Envelope

The overturning moments, shown in Figure B.13c, were generally under predicted by the analysis compared to the envelopes established from the measured data. If the results for EQ3 are ignored, then the analytical results were within 5-15% of the recorded values. The results for EQ3 were within 25% of the measured values except for the top two floors, where they were under predicted by 30-40%. The moment generated by the gravity columns contributed approximately 20% of the overturning moment resistance for EQ2, EQ3, and EQ4, while approximately 10% for EQ1.

The difference between the measured and calculated overturning moments is believed to be due to the influence of the higher mode effects, which might not have been as well captured as the first mode response. However, it is noted that the time history shown in Figure B.11 for the base moment was generally well simulated as a function of time.

Story Shear Forces

The story shear forces, depicted in Figure B.13d, show a similar trend to that observed for the overturning moments. The analysis under predicted the measured responses by approximately 5-15% for EQ1, EQ2, and EQ4; however, EQ3 was under predicted by approximately 25%. As stated before, the analytical response of the test building during EQ3 was controlled by the unloading and reloading behavior of the material models and improvements to the cyclic behavior of the material models would improve the analytical response of the building to EQ3. Overall, the story shear forces were adequately captured, and an accurate prediction of the shear demand would help ensure that shear failure of the walls would not control the seismic behavior of the building.

Summary, Conclusions, and Lessons Learned

A 2D centerline model was created in OpenSees for a full-scale portion of a building that was designed and subjected to shake table tests at UCSD. This model emphasized simplicity and ease of creation based on the geometry and material properties. The original model used beam-column elements to model the flange and web walls, and the post-tensioned pier that was used primarily to provide stability to the test building. The improved model added elements ignored in the original model such as the link slab, gravity columns, and a rotational spring to simulate the flexibility of the shake table, all of which led to significant improvements to the analytical model. The link slab and notches were modeled with beam-column elements, providing the stiffening of the web wall observed in the test. The gravity columns contributed to the lateral resistance by developing axial tension and compression in the columns located at opposite ends of the web wall, thereby creating a moment couple. The axial loads in the columns were controlled by the 3D deformation of the floor slabs. A 3D ANSYS analysis was conducted to determine an effective slab width of 11.5 times the slab thickness, which was used to define the behavior of a beam-column element at each floor level to capture the corresponding effect in the 2D OpenSees model. The improved model remains simple and easy to construct, while giving accurate simulation of the structural response.

The conclusions drawn from the analysis of a large system such as the test building studied herein are:

- Simple, computationally efficient 2D models with fiber sections that satisfactorily account for any 3D effect are sufficient to predict the response of concrete wall buildings subjected to unidirectional earthquake motions. In this study, the effect that the floor slabs had on the axial load in the gravity columns was investigated using a 3D ANSYS model and such an effort will not be needed if an effective floor slab width needed to include in the 2D model is known.
- Inclusion of the gravity columns, link slab, and table flexibility were required to accurately capture the response of the structure to the earthquake input motions. Neglecting these components in the original model significantly affected the ability of the model to predict the dynamic response of the building.
- The gravity columns contributed significantly to the overturning moment in the structure. The couple generated by the axial load in the columns contributed 10-24% to the overturning moment. The contribution of the gravity columns generally increased as the intensity of the earthquake motions increased.
- The time history responses for the top floor displacement, base overturning moment, and top floor acceleration were well predicted by the improved 2D model for EQ1, EQ2, and EQ4 motions. The analysis gave results within 5% of the measured values for displacement while the base overturning moments and top floor acceleration peak values were within 10-15%.
- When subjected to input motions EQ1, EQ2, and EQ4, the improved 2D model gave results that were within 5-15% of the envelope for displacement, interstory drift, overturning moment, and story shear forces.
- Under input motion EQ3, the discrepancies between the analytical responses and the measured values were as large as 25%. This was due to EQ3 having a similar peak intensity to EQ2, which made response of the test building to EQ3 to be dependent heavily on the unloading and reloading behavior of the material models used in the analysis.
- Despite the building being designed as a flexible structure, the earthquake analysis of the test building did not produce excessive floor displacements or unacceptably large interstory drift ratios, which is encouraging and consistent with the test observations.

- The participation in the blind prediction and follow up analysis of the 7-story building provided a number of lessons about simulating the response of a complex system. These lessons are:
- Although gravity load resisting systems are frequently ignored in the seismic design and analysis of structures, they can significantly contribute to the lateral load resistance of a building. This situation may be expected if gravity columns are subjected to axial forces resulting from their interaction wit the floor slabs during lateral movement of the building, enabling moment couples to be generated. Since the distance between gravity columns is typically large, the resulting couple will be significant and should not be ignored.
- In dynamic analysis of concrete buildings, a 5% viscous damping is routinely assumed. At very low intensity of shaking, it was reported that the test building exhibited a damping ratio in the range of 2 – 6%. However, it appears that for a concrete building with almost no nonstructural elements and flexural cracking occurring within lower stories of the building, a significantly lower viscous damping ratio in the range of 0.3-1.0% should be expected.
- Stiffness proportional damping is preferred over Rayleigh damping for dynamic analysis of concrete buildings designed to respond nonlinearly. This is because it allows the viscous damping to decline as hysteretic damping increases. This follows the recommendation of Priestley and Grant [2004] regarding viscous damping in concrete structures.
- Accurate representation of the material response envelopes likely leads to satisfactory peak response of the structure subjected to earthquake loads that push the structure to respond in a virgin territory. However, accurate representation of the unloading and reloading paths of the models used for the material and shear behavior are critical when assessing the performance of a structure subjected to earthquake motions of intensities that do not dominate the structural response in a virgin territory. This should be expected when a structure is subjected to earthquakes of similar or lower intensities than those of the previously used input motions.

Acknowledgments:

The study presented in this paper was undertaken as part of a ongoing PreNEESR project, supported by the National Science Foundation through grant no. CMS-0324559. The authors gratefully acknowledge the support of S. McCabe and D. Foutch, who have served as program directors for this grant. The authors would also like to thank Silvia Mazzoni, Frank Mckenna, Gregry Fenves, and PEER for creating OpenSees and providing guidance and assistance to users of the program. Finally, the authors would like to thank NEES-UCSD for sharing the data from the 7-Story Building test and hosting the NEES/UCSD Seminar on Analytical Modeling of Reinforced Concrete Walls for Earthquake Resistance. Any opinions, findings, and conclusions or recommendations expressed in this material are those of the authors and do not necessarily reflect the views of NSF.

References:

- Barbosa, A. F., and Ribeiro, G. O. [1998] "Analysis of Reinforced Concrete Structures Using ANSYS Nonlinear Concrete Model," In: Idelsohn, S., Onat, E., and Dvorkin, E., (Eds.), *Computational Mechanics: New Trends and Applications*, pp. 1-7.
- Brueggen, B., Waugh, J., Aaleti, S., Johnson, B., French, C., Sritharan, S., Nakaki, S. [2007] "Tests of Structural Walls to Determine Deformation Contributions of Interest for Performance Based Design," *Proceedings of the 2007 Structures Congress*, American Society of Civil Engineers, Reston, VA.
- Hsu, T.C. [1993] Unified Theory of Reinforced Concrete. Boca Raton, FL, CRC Press.
- Kelly, T. [2007] "A Blind Prediction Test of Nonlinear Analysis Procedures for Reinforced Concrete Shear Walls," *New Zealand Society for Earthquake Engineering Bulletin*, Vol. 40, No. 3, pp. 142-159.
- Mander, J.B., Priestley, M.J.N., and Park, R. [1988] "Theoretical Stress-Strain Model for Confined Concrete," *Journal of Structural Engineering*, Vol. 114, No. 8, pp. 1804-1826.
- Massone, L.M., and Wallace, J.W. [2004] "Load Deformation Response of Slender Reinforced Concrete Walls," *ACI Structural Journal*, Vol. 101, No. 1, pp. 103-113.

- Mazzoni, S., McKenna, F., Scott, M.H., Fenves, G.L. [2004] "Open System for Earthquake Engineering Simulation," *Pacific Earthquake Engineering Research Center*, University of California, Berkeley California, Ver. 1.6.0.
- Moaveni, B., He, X., Conte, J.P., and Restrepo, J.I. [2006] "System Identification of a Seven-Story Reinforced Concrete Shear Wall Building Slice Tested on the UCSD-NEES Shake Table," *NEES-UCSD Workshop on the Analytical Model of Reinforced Concrete Walls*, San Diego, CA.
- NEES7Story [2006] NEES @ UCSD Seven Story Building-Slice Earthquake Blind Prediction Contest. http://nees.ucsd.edu/7story.html, accessed June 13, 2007.
- Neuenhofer, A., and Filippou, F.C. [1997] "Evaluation of Nonlinear Frame Finite-Element Models," *ASCE Journal of Structural Engineering*, Vol. 123, No. 7, pp. 958-966.
- Oesterle, R., Aristizabal-Ochoa, J., Fiorato, A., Russel, H., and Corley, W. [1979] "Earthquake Resistant Structural Walls – Tests of Isolated Walls – Phase II," *Report to the National Science Foundation*, Construction Technology Laboratories, Portland Cement Association, Skokie, IL.
- Panagiotou, M., and Restrepo, J. [2006] "Model Calibration for the UCSD 7-Story Building Slice", *NEES-UCSD Workshop on the Analytical Model of Reinforced Concrete Walls*, San Diego, CA.
- Park, R. and Paulay, T. [1975] *Reinforced Concrete Structures*, John Wiley & Sons, New York.
- Restrepo, J. [2006] "Proceedings of the NEES/UCSD Workshop Analytical Model of Reinforced Concrete Walls", *NEES-UCSD Workshop on the Analytical Model of Reinforced Concrete Walls*, San Diego, CA.
- Sritharan, S., Zhao. J., Waugh, J., and Govindarasu, M. [2005] "Nonrectangular Concrete Walls under Multi-directional Loads – Analytical simulation and remote participation in experimental research," *Proceeding of the First US-Portugal International Workshop on Grand Challenges in Earthquake Engineering*, Lamego, Portugal.
- Swanson Analysis System [1992] "Ansys User's Manual (for Ansys Revision 5.0) Part IV: Theory" *Swanson Analysis Systems*.

- Thomsen, J.H., and Wallace, J.W. [1995] "Displacement Based Design of RC Structural Walls: An Experimental Investigation of Walls with Rectangular and T-Shaped Cross-Sections," *Report to the National Science Foundation*, Department of Civil Engineering, Clarkson University, Potsdam, New York.
- Waugh, J. and Sritharan, S. [2006] "Description of Analysis Model Used for Predicting Behavior of 7-Story Test Building," *NEES-UCSD Workshop on the Analytical Model of Reinforced Concrete Walls*, San Diego, CA.
- Zhao, J. and Sritharan, S. [2007] "Modeling of Strain Penetration Effects in Fiber-Based Analysis of Reinforced Concrete Structures," *ACI Structural Journal*, 104(2), pp. 133-141.

APPENDIX - C
IREE Supplemental Award

As previously noted, the NSF IREE supplemental award enabled integration of international collaboration into the project through partnership with National Center for Research on Earthquake Engineering (NCREE) in Taiwan and introduction of a new precast wall system. The ISU research team of the IREE supplement award (PI: Sri Sritharan, Associate Professor; Student Researcher: Sriram Aaleti, a PhD Candidate) conducted an analytical investigation to improve the efficiency of precast wall systems in a previous study and introduced a new concept for a precast wall system (Aaleti and Sritharan 2007). The new wall system was expected to be a cost-effective as it can be designed to match the lateral load capacity of a comparable monolithic reinforced concrete wall. However, the viability of the concept was never proven through an experimental study.

Presented in this appendix are summary of results for the research made possible by the IREE supplemental award, which provides experimental validation for the lateral load behavior of the new precast wall system.

INTRODUCTION TO PREWEC AND KEY RESULTS OF A PROOF OF CONCEPT TEST

Sri Sritharan[1], Sriram Aaleti[2], Rick Henry[3], Keh-Chyuan Tsai[4], Kuang-Yen Liu[5]

[1]Associate Professor and Assistant Chair, Iowa State University, Ames, IA
[2]PhD Candidate, Iowa State University, Ames, IA
[3]PhD Student, University of Auckland, Auckland, New Zealand
[4]Director, National Center for Research on Earthquake Engineering (NCREE), Taiwan
[5]Associate Research Fellow, NCREE, Taiwan

(A paper submitted to the 2008 M. J. Nigel Priestley Symposium, King's beach, CA)

ABSTRACT

Introduced in this paper is a lateral load resisting system consisting of a Precast Wall with End Columns (or PreWEC) for seismic applications and results from a recent test that was performed to verify the concept of this new system. In this system, the wall and end columns are anchored individually to a foundation using unbonded post-tensioning. A newly designed, replaceable, low-cost mild steel connector is used to connect the wall and end columns horizontally, which also primarily acts as an energy dissipating element. The benefit of the new system is that it can be economically designed to have lateral load carrying capacity similar to that of a comparable reinforced concrete wall, while maintaining the advantages and properties of jointed wall systems. The proof test confirmed the viability of PreWEC for seismic applications and its superior performance over other currently available structural wall systems.

Introduction

With motivation to establish an economical precast lateral load resisting system for buildings, a new structural wall system consisting of a single PREcast Wall connected with two End Columns (or PreWEC), as shown in Figure C.1, has been recently introduced (Aaleti and Sritharan 2007). Steel columns, concrete filled steel tubes, or precast columns may be used as the end columns. The wall and columns are anchored to the foundation using unbonded post-tensioning and then joined horizontally using special energy dissipating connectors. The post-

tensioning tendons in the wall may be distributed evenly along the wall length or concentrated at the center of the wall. The use of unbonded post-tensioning tendons results in a constant strain in the tendons along the length and eliminates the development of large localized strains, thus allowing the wall system to undergo large lateral displacements without yielding the tendons. The debonding of the tendons also eliminates the development of large bond stresses in surrounding concrete and the associated tensile cracking.

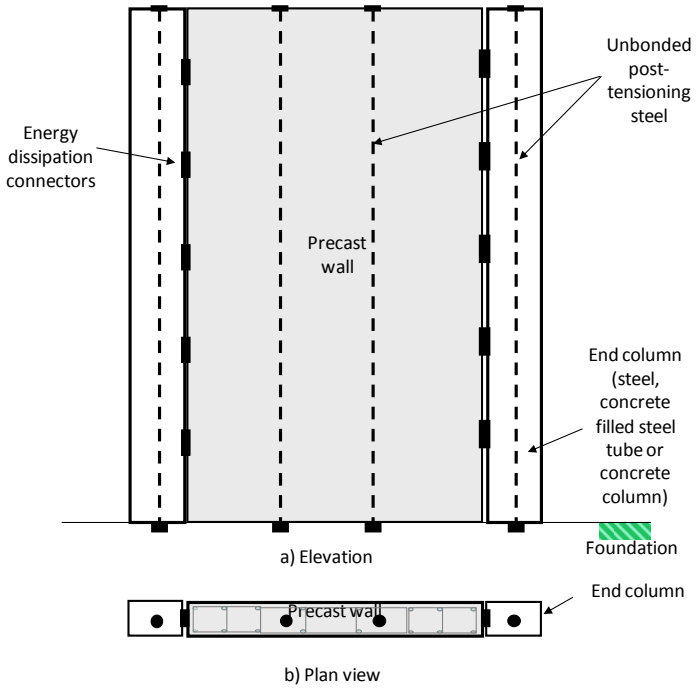

Figure C.1. The concept of PreWEC system.

The basic concept of this system is that it allows the wall and end columns to rock individually at the base when the PreWEC system is subjected to seismic lateral forces. The post-tensioned steel in the system is designed to remain elastic for the expected lateral forces up to the design-level earthquakes. As a result, the prestressing provides the necessary restoring force for the PreWEC system to recenter when the applied lateral force is removed, thus minimizing the residual displacements associated with earthquake loading. Another role of the prestressing is that it enables shear transfer to be achieved at the bases of wall and end columns through a friction mechanism. Special, replaceable connectors placed between the wall and end columns help dissipate the seismic energy by undergoing inelastic deformations when subjected to moderate to large earthquake loads. Therefore, the PreWEC system with the ability to dissipate

seismic energy, which minimizes structural damage and reduces residual displacements, is expected to be an economical alternative for seismic applications.

Connector Design

An extensive investigation combining analytical and experimental efforts was undertaken to establish a low-cost, easily replaceable connector suitable for the PreWEC system (Henry et al. 2008). After exploring different shapes and materials through finite element analyses, an oval-shaped, mild steel, connector (or o-connector) was determined to be the best choice to connect the wall and columns together horizontally (see Fig. C.2). while ensuring that the connector will deliver the adequate energy dissipation capacity for PreWEC. The o-connector dissipates energy by undergoing flexural yielding in the plane of loading and thus requires a restraint to prevent the connector from experiencing out-of-plane bending.

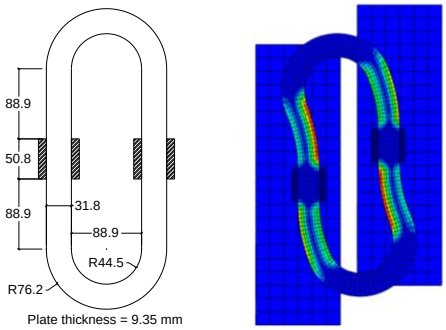

Figure C.2 Dimensions of an o-connector and its deformed shape demonstrated by a finite element model (1 mm = 0.0394 in.).

Figure C.2 shows a connector and the finite element model of it, which assumed that the connector would experience no out-of-plane bending. Shown in Figure C.3 are a set up used for testing a pair of o-connectors and the corresponding force-displacement response. As can been seen from this figure, the o-connector produces dependable response whose behavior was satisfactorily reproduced using a finite element model (FEM).

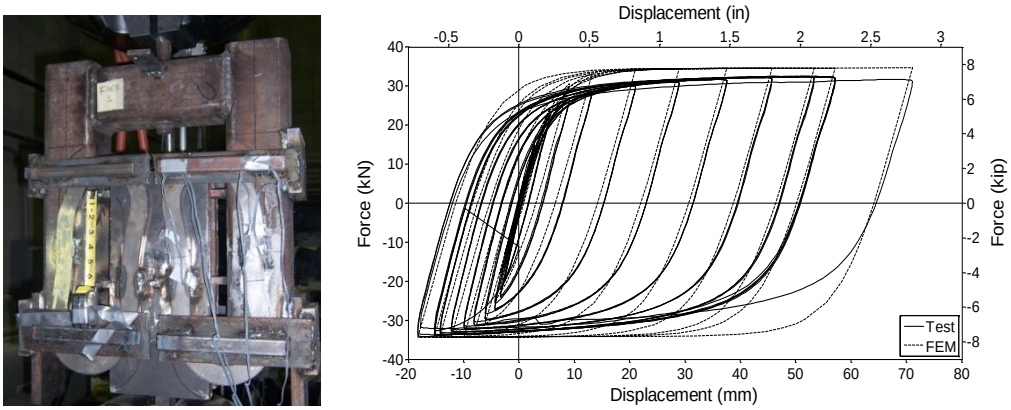

Figure C.3 Testing of a pair of o-connector and comparison of corresponding results with those obtained from a finite element analysis.

Detail of the Proof Test

With support from the International Research and Education and Engineering (IREE) program of the National Science Foundation and the National Science Council of Taiwan, a PreWEC system was designed, constructed and tested at the National Center for Research on Earthquake Engineering (NCREE) in Taiwan in March 2008. The 7.9 m (26-ft) tall test unit was designed to represent a prototype wall at ½-scale and used a ½-scale cast-in-place wall tested as part of a PreNEESR project as the reference wall (French et al. 2008). The PreNEESR project, funded by the National Science Foundation, is a joint effort between the University of Minnesota (PI: Cathy French), Iowa State University (PI: Sri Sritharan) and University of Puerto Rico at Mayagüez (PI: Ricardo López) that has focused on improving the behavior, analysis, and design of nonrectangular concrete walls subjected to multi-directional loads. The testing of wall in the PreNEESR project was conducted at the Multi-Axial Subassemblage Testing (MAST) facility of UMN that was established as part of the George E. Brown, Jr. Network for Earthquake Engineering (NEES) program.

The reference wall, referred to as RWN, was designed to comply with the current design practice and included continuous longitudinal mild steel reinforcing bars from the foundation to the top of the wall without any splices. Two different sets of longitudinal reinforcement were used in the boundary elements so that RWN can replicate the behavior of a T-wall (see Figure C.4). When designing the test unit of PreWEC (or PreWEC-1), its response was designed to

match or exceed the response of RWN in the direction that subjected the boundary element containing #5 and #6 bars in tension. Seismic performance of RWN was generally satisfactory, but it experienced significant damage to the wall as a result of forming a plastic hinge near the base as intended in the design.

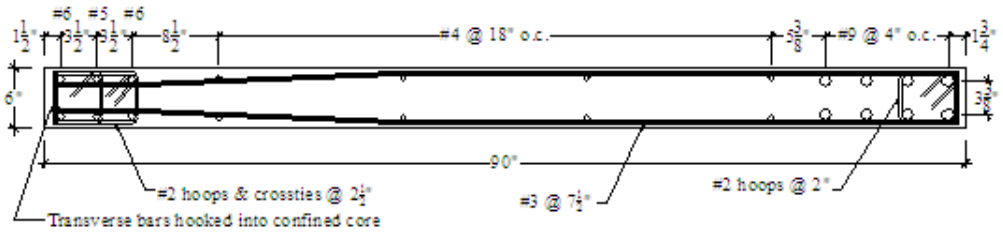

Figure C.4 Cross-sectional dimensions and reinforcement details of cast-in-place concrete wall RWN (1 in. = 25.4 mm).

Figure C.5 shows the cross sectional dimensions and reinforcement details of PreWEC-1. The precast wall in the test unit was lightly reinforced with mild steel reinforcement that was terminated within the wall panel. The post-tensioning tendon that secured the wall to the foundation was concentrated at the wall center. In addition to the confinement reinforcement shown in the boundary elements of the wall panel (see Figure C.5), a 0.61-m (2-ft) long, and 6.4 mm (0.25-in.) thick steel channel was attached to the bottom of the wall near the toe regions to minimize spalling of cover concrete at the base. Concrete filled steel tubes with cross-sectional dimensions of 203.2 mm x 152.4 mm (8 in. x 6 in.) were used as end columns. Prior to post-tensioning the columns and wall, 37 mm (1.5 inch) thick fiber reinforced grout was placed at the top of the foundation, which ensured uniform contact between the structural elements making up PreWEC-1 and foundation. Eight pairs of o-connectors having dimensions shown in Figure C.2a were used to link each column to the wall.

The PreWEC test unit was subjected to cyclic loading using the setup shown in Figure C.6 and by generally following the load protocol specified in ITG 5.1 (ACI Innovation Task Group 5, 2007a). The testing was continued up to lateral drifts of ±3.5%, with three full reversed cycles at each load step. As with RWN, no additional gravity load was applied to the test unit. If axial load had been included to simulate the gravity effects, the amount of post-tensioning would have been reduced by the same amount as the gravity load can effectively compensate for the role of prestressing.

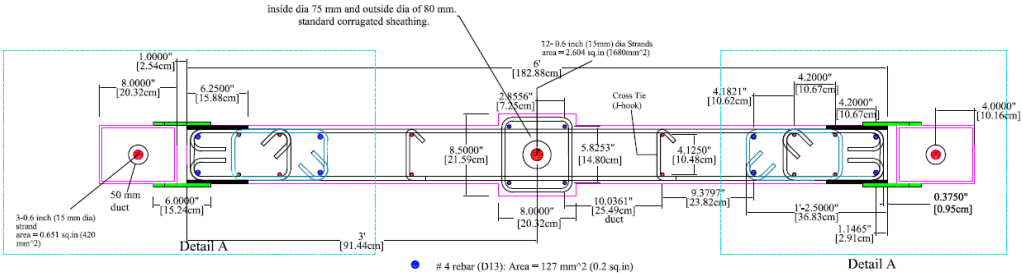

Figure C.5 Reinforcement Details of PreWEC-1.

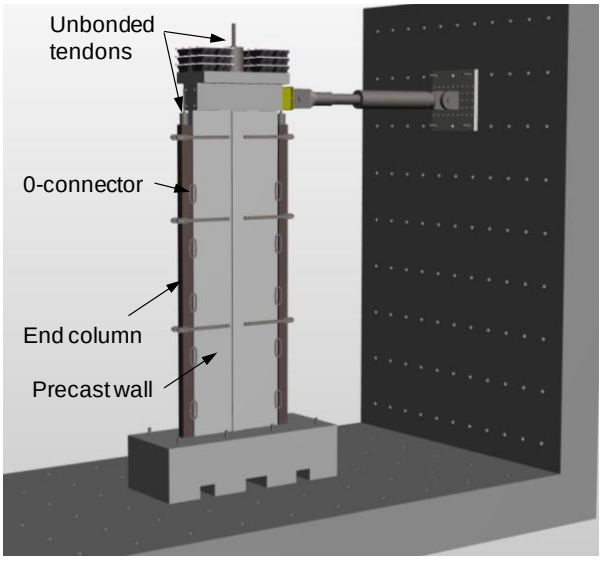

Figure C.6 Test setup used for PreWEC-1.

Test observations and key results

The PreWEC test unit performed superbly with negligible damage to the wall panel and no damage to the end columns. The damage to wall was limited to spalling of cover concrete in the bottom corners. The channel at the bottom of the wall experienced some bending and its impact on the response of the wall system especially during repeat of a similar test remains to be investigated. The o-connectors performed as expected and fulfilled their functional requirements. The connectors experienced progressive fracture at lateral drifts of ±3.5 percent; note that not all connectors fractured simultaneously during testing. Even after experiencing fracture in a connector, it was able to transmit forces as the fractured ends of the connector came

in full contact with each other. Consequently, the force-displacement response of the wall system was not affected by the fracture of the connectors, which gave another unique feature to the PreWEC system. Presented in Figure C.7 are the critical region of PreWEC-1 at 3% drift and a close-up of view of a connector at the same drift. Also included in this figure is the critical region of RWN at lateral drift of 2.5%. The minimal damage of PreWEC results from the use of unbonded post-tensioning is apparent in Figure C.7.

Figure C.8 shows the measured force-displacement response of PreWEC-1 and comparison of its response envelope with that of RWN. The cyclic force-displacement hysteretic response of PreWEC-1 was stable. There was no significant strength degradation between the successive cycles imposed at any drift. It is apparent from Figure 8b is that the response of PreWEC-1 superseded its cast-in-place counterpart RWN in terms of the elastic stiffness and lateral load resistance at any given lateral displacement. Note that the force-displacement response included in this figure for RWN assumes that the boundary elements at both ends of the wall contained #5 and #6 longitudinal bars, resulting in identical responses for the positive and negative displacement directions.

Two analytical methods, one based on a finite element model and the other based on a simplified analysis approach (Sritharan et al. 2007) were used to predict the system behavior under lateral loads. Both methods successfully captured the overall response of PreWEC-1 although the finite element model gave a closer comparison to the experimental results (see Figure C.8a). Both models satisfactorily captured their elastic stiffness of the test unit as well the response envelopes in the inelastic region.

The relative vertical movements that the o-connectors experienced in PreWEC-1 were recorded at multiple locations. As expected, almost all connectors experienced comparable deformations. Figure C.9 shows measured deformation of two connectors. As seen in the figure, the connectors experienced vertical displacements of up to 50 mm (2 in.).

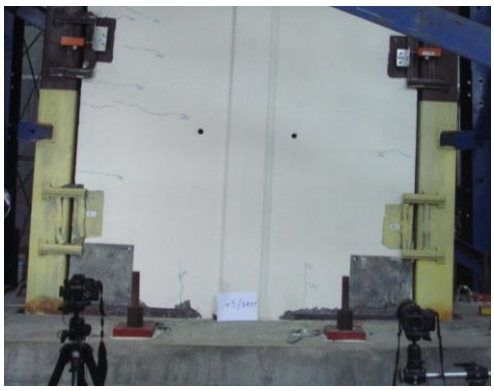

(a) PreWEC-1 at 3% drift

(b) PreWEC-1 at 3% drift

(c) Spalled region of wall in PreWEC-1

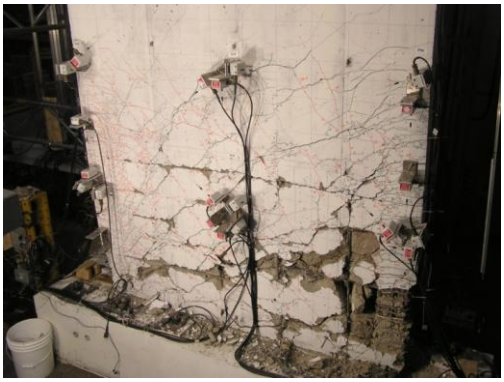

(d) RWN at 2.5% drift

Figure C.7 Observed response of test units.

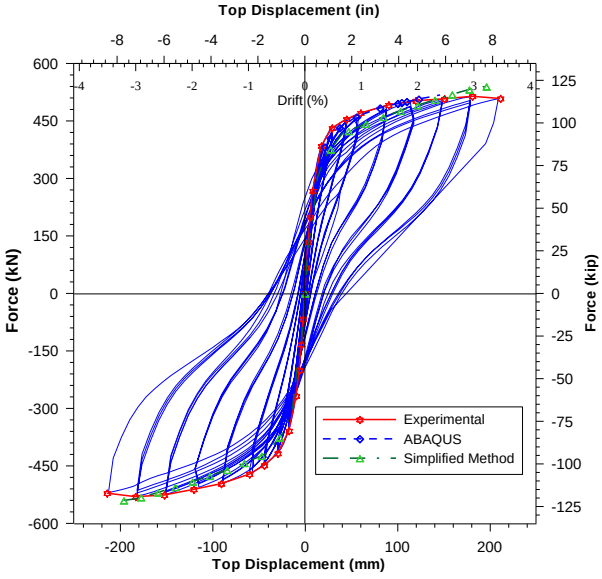

(a) Cyclic response of PreWEC-1

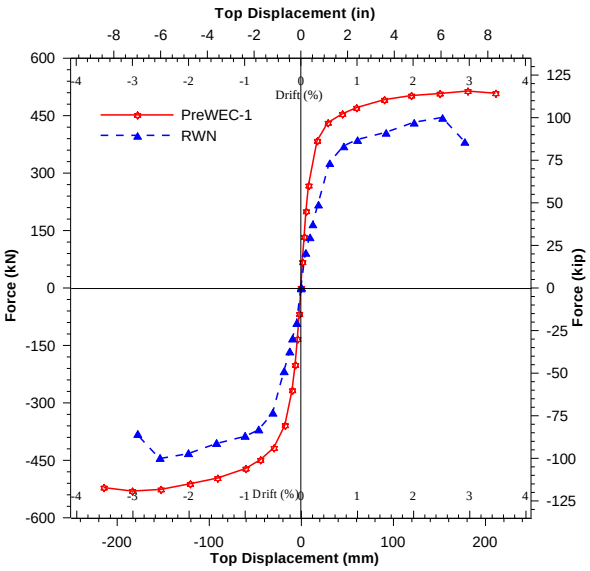

(b) Response envelopes of PreWEC-1 and RWN

Figure C.8 Responses of PreWEC-1 and the reference cast-in-place wall RWN.

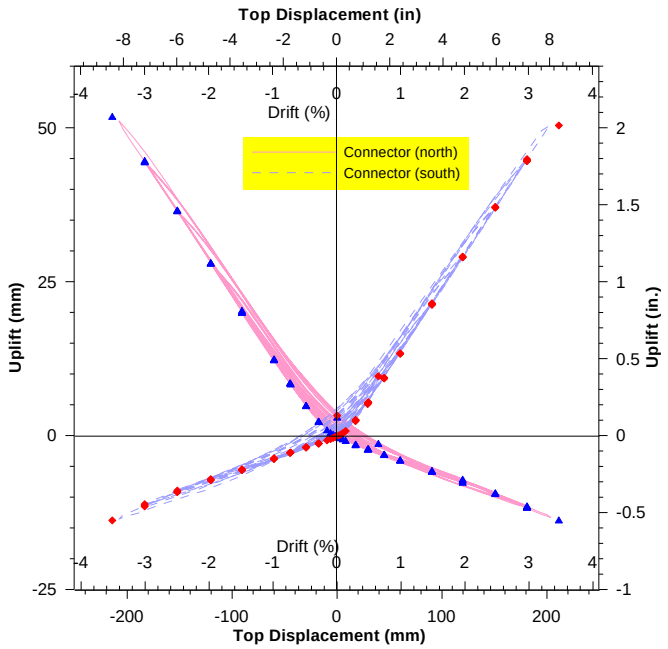

Figure C.9 Measured vertical deformation of the connectors.

Conclusions

Introduced in this paper is a new precast concrete wall system that combines a precast, unbonded, post-tensioned wall with two end columns using a set of special energy dissipation connectors. Similar to the wall, the end columns are also secured to the foundation using unbonded post-tensioning to make up the PreWEC system. Based on the test observations and experimental results of PreWEC-1 conducted through an international collaborative effort and the response of the reinforced concrete counterpart tested as part of a PreNEESR project, the following conclusions have been drawn:

- The lateral load behavior of the PreWEC system under simulated seismic testing was excellent and it performance superseded the comparable performance of the cast-in-plane reference concrete wall.
- The concrete wall in PreWEC experienced minor damage whereas the end columns experienced no damage. The wall damage was limited to repairable spalling of cover concrete to the end regions near the base. In comparison, the cast-in-place concrete wall experienced excessive damage in the plastic hinge region of the wall.
- The performance of the specially designed, low-cost energy dissipating connector was equally good. In addition to producing dependable cyclic behavior during the component

tests, the o-connector performed extremely well in the wall system and effectively contributed to energy dissipation. The connectors experienced progressive fracture at ±3.5% drift, but continued to perform well due to its ability to close the gap and continued to transfer forces.

- The analytical simulations, which were performed using a simplified method and a detailed finite element model, accurately captured the observed experimental force-displacement response of the PreWEC test unit.
- The collaboration effort by researchers from three countries, i.e., U.S., Taiwan and New Zealand, was very successful and it synergistically advanced the research and education of the PreWEC system.

Acknowledgements

The study reported in this paper is supported by the National Science Foundation through the International Research and Education in Engineering (IREE) program as a supplement to Grant No. CMS 0324559. Additional financial support for the experimental program reported in this paper was received from the National Science Council of Taiwan, while Rick Henry was supported by the Tertiary Education Commission in New Zealand. The authors also thank Doug Wood, the manager of the structural engineering laboratory at Iowa State University, and the technical staff of NCREE for their contribution to the testing of the connectors and PreWEC-1, respectively.

Any opinions, findings, and conclusions expressed in this paper are those of the authors, and do not necessarily represent those of the sponsor.

References

1. Aaleti, S., and Sritharan, S. (2007). "A Precast Wall with End Columns (PreWEC) for Seismic Applications", *Proc., 8th Pacific Conference on Earthquake Engineering*, Singapore, Paper 157.
2. ACI Innovation Task Group 5 2007a. Acceptance Criteria for Special Unbonded Post-Tensioned Structural Walls Based on Validation Testing. *ACI ITG 5.1-XX (Draft*), American Concrete Institute, Farmington Hills, MI.

3. French, C., Brueggen, B. and Johnson, B. (University of Minnesota); Sritharan, S., Waugh J. and Aaleti, S. (Iowa State University); López-Rodríguez, R. (University of Puerto Rico, Mayagüez); and Nakaki, S. (Nakaki-Bashaw Group, Inc.). (2008). "Collaborative Research: Testing and Analyses of Nonrectangular Walls under Multi-Directional Loads", *In Proceedings of the NSF CMMI Engineering Research and Innovation Conference*, January, Knoxville, Tennessee.
4. Henry, R., Aaleti, S., Sritharan, S. and Ingham, J. M. (2008). " Concept and Finite Element Modeling of New Steel Shear Connectors for Self-Centering Wall Systems", *Submitted to ASCE Journal Engineering Mechanics*.
5. Sritharan, S., Aaleti, S. and Thomas, D. (2007). "Seismic Analysis and Design of Precast Concrete Jointed Wall Systems", *ISU-ERI-Ames Report*, Department of Civil and Construction and Environmental Engineering, Iowa State University, Ames, Iowa.

APPENDIX - D
Use of IT Tool in Research Collaboration

This appendix summarizes how various IT tools were employed for real-time collaboration with researchers, especially those who were at the MAST facility, during testing of the large-scale concrete walls. In addition to utilizing them from the telepresence laboratory at ISU, these tools were also used during participation in experimental research from the University of Auckland and for a live experimental seminar presented from NCREE on the research conducted under the IREE program. In addition, several recommendations for improving the NEES IT tools are also presented, some which have already been implemented by NEESit.

Utilizing IT Capabilities for Remote Participation in Testing of Walls at NEES@Minnesota

Author:
Sri Sritharan, Associate Professor, Dept. of Civil, Construction and Environmental Engineering, Iowa State University, Ames, IA 50011, sri@isatste.edu

(This paper was presented at the 2007 ASCE Structures Congress, Long Beach, California)

Introduction

Researchers from the University of Minnesota (UMN), Iowa State University and the University of Puerto Rico at Mayagüez and a consulting engineer from the Nakaki Bashaw Group, Inc. in California have undertaken a collaborative PreNEESR project since 2004 (http://nees.umn.edu/projects/twall/). This project focuses on analytical and experimental efforts to investigate the behavior of nonrectangular structural walls subjected to multi-directional loading. The experimental component of the study utilizes the NEES Multi-Axial Subassemblage Testing (MAST) system at Minnesota (NEES@Minnesota). To date, large-scale testing of a T-shaped concrete wall and three rectangular walls has been completed. In each test, a variety of telepresence tools, including those developed and supported by the NEES Cyber infrastructure Center [1] were used to enable effective collaboration between the researchers at the test site at NEES@Minnesota (http://nees.umn.edu/) and those at the remote locations. The author of this paper was on sabbatical leave at the University of Auckland in New Zealand during testing of two rectangular walls. Consequently, the telepresence capabilities of NZNEES@Auckland (http://www.nznees.auckland.ac.nz/) together with the NEESit tools were used to continue the research project without compromising the real-time collaboration between researchers during the tests.

The wall tests conducted to date at NEES@Minnesota were the first NEES experiments to extensively use the telepresence tools and experience the benefits of real time capabilities to advance the simulation models. Consequently, these tests served as a test bed for various telepresence tools. While the benefits of real-time collaboration were realized satisfactorily in the experiments, improvements to the capabilities of telepresence tools were identified and recommended to NEESit. This paper provides a researcher's experience in remotely participating

in seismic tests, including the ability to interact with both people and equipment and manipulate test data in real time, and describes how different telepresence technologies were used in the project as well as some recommendations made towards improving capabilities of telepresence tools to enhance real-time research collaboration.

Testing of Walls

The overall scope of the project described in this paper is to investigate the behavior of nonrectangular concrete walls subjected to multi-directional loads. The project utilizes both rectangular and T-shaped concrete walls to examine the adequacy of reinforcement details prescribed in the design codes, validate and improve the existing analysis capabilities to predict the lateral load behavior of walls, understand the interaction between shear and flexural behavior of walls, and examine the influence of using splices and the couplers in the plastic hinge region of concrete walls. The experimental part of the study includes testing of three rectangular walls and two T-walls, of which four tests have been completed (see Figure D.1) and the last test to be performed on a T-wall is scheduled for summer 2007. Hundreds of sensors, 10 video cameras and eight still cameras were used in each completed wall test.

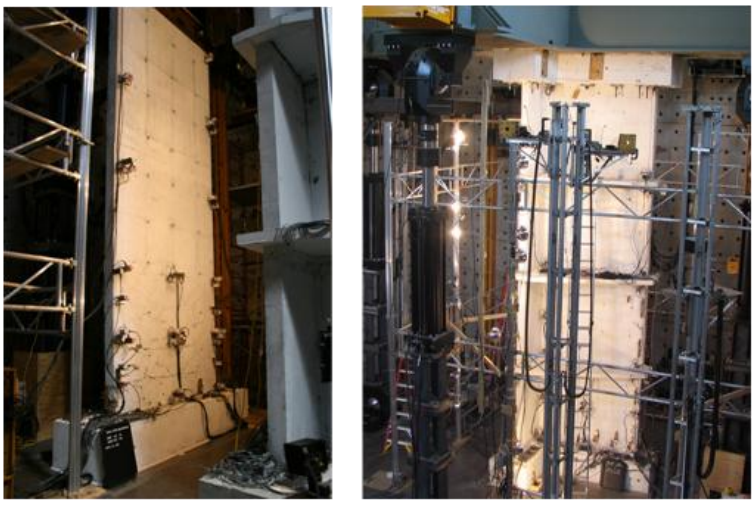

Figure D.1 Testing of Walls at NEES@Minnesota

Telepresence Tools and Capabilities

A variety of telepresence tools were utilized during testing of walls. A brief description of these tools and how they were used during testing to enhance effective participation of researchers, especially those who were at remote locations, are summarized below:

- WebEx – This is commercial software that enables internet teleconferencing by connecting regular phones and computers, providing capabilities necessary to support real-time meetings on the Web. Two sessions of WebEx were initiated and maintained during the entire test by the IT team of NEES@Minnesota. The first session shared the critical data collected by the data acquisition system (DAQ) in tabular and graphical forms (see Figure D.2). The second WebEx session shared a basic session of RDV (see details of RDV below) that displayed critical data streaming through a data turbine server at Minnesota. One of these WebEx sessions was also used to enable audio communication between researchers at different locations, which included researchers at the test floor who were equipped with wireless headsets that were linked to a phone connected to the WebEx session. These two WebEx sessions provided common ground for researchers to communicate effectively and make critical decisions.

Figure D.2 WEBEX Session that Displayed the data gathered by the data acquisition system

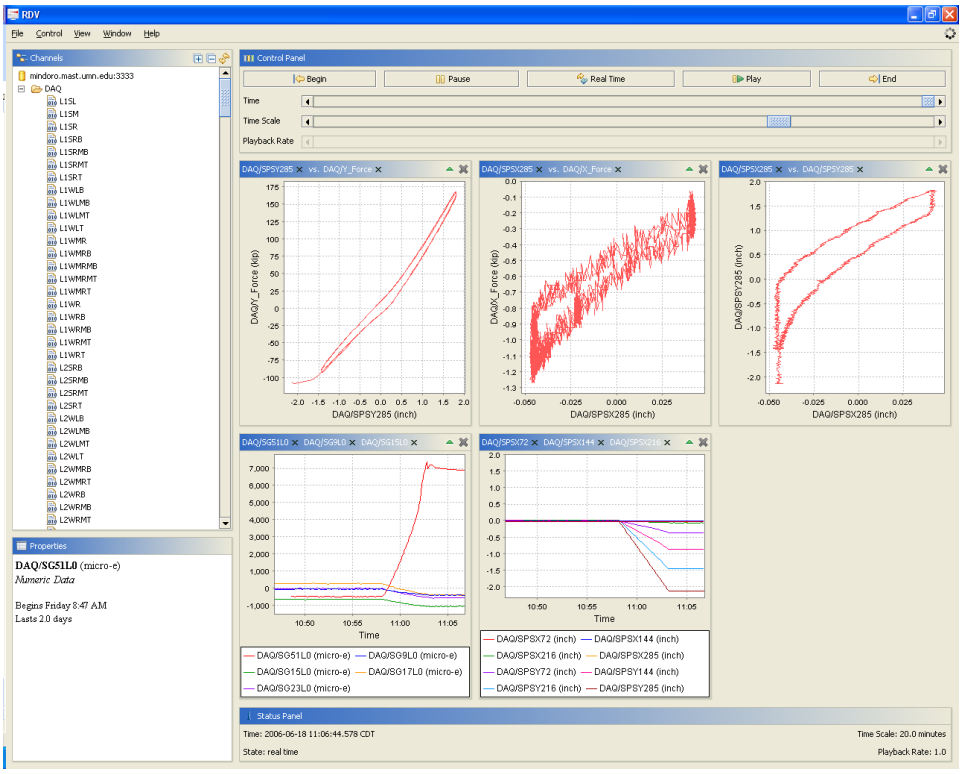

Figure D.3 RDV Session on a Remote Computer

- RDV (Real-Time Data Visualization Tool) – RDV enables viewing of video data and visualization of streaming instrumentation data in real-time. In addition to the RDV session shared through WebEx, several RDV sessions were administered at remote locations depending on the researchers' interest in the project. These sessions included data in tabular form, graphs of data channels as a function of time as well as X-Y plots, and limited video streams (see example in Figure D.3) and access the data in real-time from the data turbine server at NEES@Minnesota. To improve efficiency of RDV, mirroring the data turbine server at Minnesota to a local server at Iowa in real-time, and accessing the data from the local server was explored.
- FlexTPS (Flexible TelePresence System) – This is an open source software designed to enable remote viewing of live video and remote control operation of video and still cameras over the internet using a web browser on the user's computer. FlexTPS was primarily used during the tests to view live video from multiple cameras at a higher refresh rate than that used in RDV (see Figure D.4).
- Still Images – There was no special software available to archive high-resolution still images. Hence, the still images were taken, time stamped and made available to the researchers through a web server. By automating operation of most still cameras, the still images were made available almost instantaneously. Figure D.5 shows images appearing as thumbnails on the web, which were linked to large high-resolution images to visually inspect the extent of local damage occurred to the test walls.
- HCC (Hydraulic Control System Software) – HCC is a command entry and monitoring layer that provides a direct user interface to the MTS Controller of MAST at NEES@Minnesota [2]. HCC polls for and displays status information of MAST and enables precise control of it by allowing a remote user to specify the next target point through defining six degrees of freedom (DOF) for a control point. HCC was used during some segments of the tests to verify its capabilities and successfully operate MAST in Minnesota from a remote site in Iowa. Capabilities of HCC were also verified by operating MAST remotely from Auckland, New Zealand.
- MAST-RSVtool – In light of the limitations existed with the collaborative tools described above, the MAST Real-time System Visualization Tool (RSVtool) was developed locally at Iowa State University to enhance research collaboration in real-time [3]. The MAST-

RSVtool enables a remote researcher to 1) monitor the condition of the MAST hydraulic system (i.e., force and displacement of all MAST actuators) through progress bars and data viewer; 2) set soft limits (i.e., limits used by a remote user for research purposes and not for actuator control) for the MAST actuators; 3) monitor the load path effects on the test specimen, which was necessary to determine the critical paths for the next load cycles; and 4) compare the predicted force-displacement responses with measured responses, all in real-time.

- NZNEES@Auckland (http://www.nznees.auckland.ac.nz/) – NZNEES@Auckland provides a unique contribution to the capabilities that exist currently in earthquake engineering networks, and foster collaborative research in New Zealand and internationally. Included in NZNEES@Auckland is a Data Visualization Laboratory (DVL), connected to the New Zealand Kiwi Advanced Research and Education Network (KAREN). Using advance telepresence technologies, the DVL was designed to enable New Zealand researchers to effectively participate in experimental research. Using the above described IT tools, the author participated in two wall tests in real-time from NZNEES@Auckland (see Figure D.6).

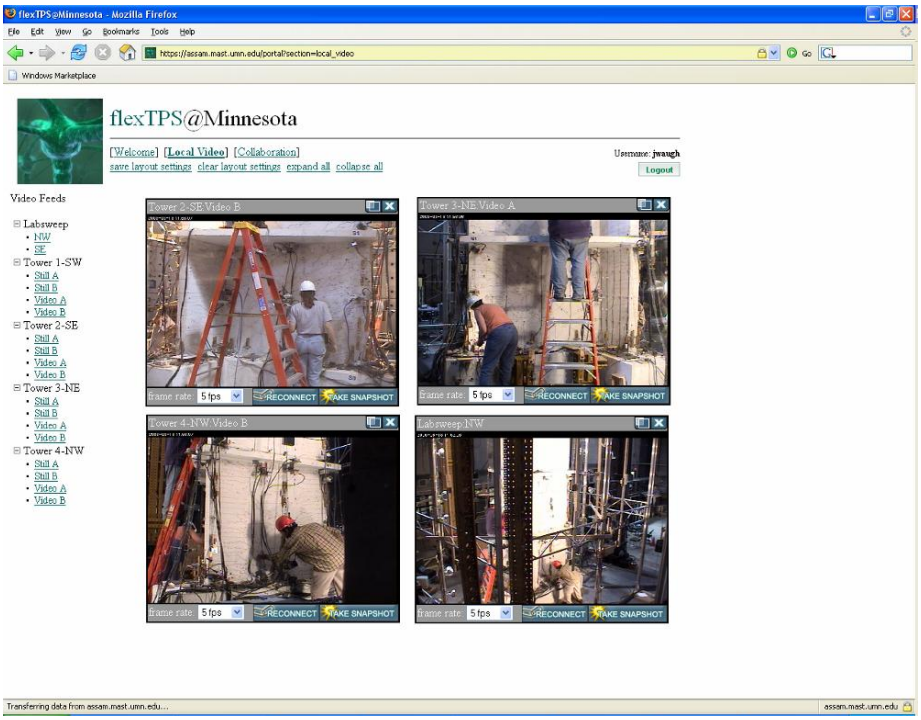

Figure D.4 FLEXTPS Session on a remote computer

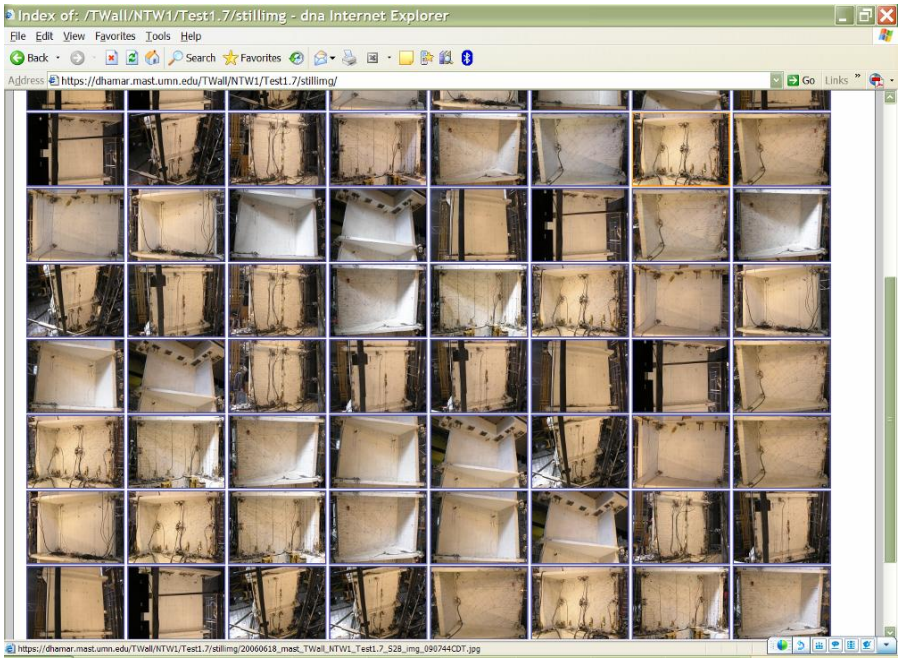

Figure D.5 Webpage showing thumbnails of high resolution still images

Figure D.6 Real-Time participation in a rectangular wall test at MAST lab from NZNEES@AUCKLAND

Various telepresence tools and their capabilities described above made researchers at remote locations to effectively participate during testing of walls at the NEES site in Minnesota.

The author participated in all four tests from either Iowa or Auckland, New Zealand. Although critical decisions during testing of walls were made collectively by researchers at the test and remote sites, the author had sole responsibility to make some of the decisions from a remote location for portions of the tests. Under no circumstances was the author felt that the information made available in real time was inadequate and that making a decision or contributing effectively for decision making during quasi-static wall tests was difficult. However, some limitations and possible improvements to the capabilities of the telepresence tools were identified and communicated to the NEESit team for their consideration. These requirements included: 1) incorporating discontinuous timelines into RDV; 2) enabling RDV to manipulate data and compare them with simulated results in real-time; 3) establishing robustness of the data turbine and RDV system as a whole; 4) providing specifications to guide remote researchers to realize the limitations of RDV based on the bandwidth and latency of the available network; 5) improving playback capabilities of RDV possibly by enabling history data to be uploaded individually in each window chosen within an RDV session; 6) adding audio capability to flexTPS; 7) integrating still images into the NEES telepresence portal; 8) promote mirroring of the data turbine server to a local server at a remote site in real time; 9) integration of a wireless video camera at the NEES equipment site that can be viewed through flexTPS; and 10) improving reliability of audio connections between wireless headsets and WebEx.

Concluding Remarks

Overall, the capabilities of the telepresence tools available to the researchers, especially those at remote locations in Iowa, Puerto Rico, California, and New Zealand, were sufficient. However, some difficulties and limitations were encountered with these tools. Recommendations to eliminate these limitations, along with potential new features for the telepresence technologies, were communicated to the NEESit team. Some of the recommendations made for improving RDV have been already implemented. The capabilities of the telepresence tools available today for NEES researchers are far superior than those available to the PreNEESR research team in 2004. As experienced with this PreNEESR project on non-rectangular walls, a key element for the rapid advancement of the NEES telepresence tools was the feedback that the NEESit team received from the NEES researchers. It is believed that further advancements to the telepresence tools can be made in this iterative process, ultimately providing

remote researchers with better access to NEES equipment sites that are designed to perform advanced experimental research.

Acknowledgement

The participation of the author in the PreNEES project was made possible by a grant (CMS-0324559) from the National Science Foundation. The author gratefully acknowledges the support of Dr. Douglas Foutch and Dr. Steven McCabe, who have served as program directors for this grant. The author also thanks the IT staff of NEESit, NEESinc, NEES@Minnesota and NZNEES@Auckland for their assistance that enabled the author to remotely contribute to research effectively during large-scale testing of walls at MAST. Any opinions, findings, and conclusions or recommendations expressed in this paper are those of the authors and do not necessarily reflect the views of the sponsor.

References

[1] NEESit, "Software for NEES Collaboratory", http://it.nees.org/software/index.php, 2007 (accessed).

[2] MAST Laboratory, "HCC User Guide Applying Loads and Displacements in the MAST Laboratory", *Report No. MAST-04-03, University of Minnesota*, 2004.

[3] Sritharan, S., Govindarasu, M., Zhao, J. and Fraiwan M., "A Real-time System Visualization Tool (RSVtool) for NEES-MAST to Facilitate Collaboration", *Feature Article, July Issue of Seismos* (http://it.nees.org/seismos/2005-07/index.php), NEES Cyberinfrastructure Center (NEESit) Newsletter, 2005.